

1 SEARCH FOR PRODUCTION OF A HIGGS BOSON AND A SINGLE TOP  
2 QUARK IN MULTILEPTON FINAL STATES IN pp COLLISIONS AT  $\sqrt{s} = 13$   
3 TeV

4 by

5 Jose Andres Monroy Montañez

# A DISSERTATION

7 Presented to the Faculty of

8 The Graduate College at the University of Nebraska

In Partial Fulfilment of Requirements

For the Degree of Doctor of Philosophy

11 Major: Physics and Astronomy

12 Under the Supervision of Professors Kenneth Bloom, Aaron Dominguez  
13 and Dr. Benjamin Stieger

14 Lincoln, Nebraska

15 July, 2018

16 SEARCH FOR PRODUCTION OF A HIGGS BOSON AND A SINGLE TOP QUARK IN  
17 MULTILEPTON FINAL STATES IN pp COLLISIONS AT  $\sqrt{s} = 13$  TeV

18 Jose Andres Monroy Montañez, Ph.D.

19 University of Nebraska, 2018

20 Adviser: Kenneth Bloom, Aaron Dominguez, Benjamin Stieger

21 The exciting work in high energy physics includes not only the analysis of the data taken by the  
22 experiment but also the development of detection systems. In this thesis, the results of a search for  
23 the production of a Higgs boson in association with a single top quark ( $tH$ ) are presented. This  
24 process is of particular interest due to its sensitivity to the relative sign of the top-Higgs coupling and  
25 the vector bosons-Higgs coupling. The focus is on leptonic signatures provided by the  $H \rightarrow WW$ ,  
26  $H \rightarrow \tau\tau$ , and  $H \rightarrow ZZ$  decay modes.

The analysis exploits final states with two same-sign leptons or three leptons and uses the 2016  
 data sample collected with the Compact Muon Solenoid (CMS) detector at the Large Hadron Collider  
 from proton-proton ( $pp$ ) collisions at a center of mass-energy of 13 TeV. Multivariate techniques are  
 used to discriminate the signal from the dominant backgrounds. The analysis yields a 95% confidence  
 level (C.L.) upper limit on the combined  $tH + t\bar{t}H$  production cross section times branching ratio  
 of 0.64 pb, with an expected limit of 0.32 pb, for a scenario with  $\kappa_t = -1.0$  and  $\kappa_V = 1.0$ . Values  
 of  $\kappa_t$  outside the range of -1.25 to +1.60 are excluded at 95% C.L., assuming  $\kappa_V = 1.0$ . Sensitivity  
 to CP mixing in the Higgs sector was investigated by considering scenarios for different values of  
 the mixing angle  $\alpha_{CP}$ . An upper limit on the combined  $tH + t\bar{t}H$  production cross section times  
 branching ratio of 0.6 pb is set for a scenario with  $\alpha_{CP} = 180^\circ$  which corresponds to the scenario  
 with  $\kappa_t = -1.0$  and  $\kappa_V = 1.0$ .

On the detection systems side, contributions to the construction of the CMS forward pixel detector (FPix) are presented; FPix is responsible for tracking with extreme accuracy the paths of particles emerging from the  $pp$  collisions at CMS. FPix is a modular detector composed of 672 modules built using a semiautomatic pick-and-place robotic system which integrates optical tools, pattern recognition algorithms, and glue dispensing subsystems to locate the constituent module parts on the work field and glue them together with a precision of  $10\ \mu\text{m}$ . Fully assembled modules were tested and characterized.

DEDICATION

## ACKNOWLEDGMENTS

47

---

## Table of Contents

---

48	<b>Table of Contents</b>	v
49	<b>List of Figures</b>	xi
50	<b>List of Tables</b>	xviii
51	<b>1 Introduction</b>	1
52	<b>2 Theoretical approach</b>	5
53	2.1 Introduction . . . . .	5
54	2.2 Standard model of particle physics . . . . .	6
55	2.2.1 Fermions . . . . .	8
56	2.2.2 Fundamental interactions . . . . .	15
57	2.2.3 Gauge invariance. . . . .	18
58	2.2.4 Gauge bosons . . . . .	21
59	2.3 Electroweak unification and the Higgs mechanism . . . . .	22
60	2.3.1 Spontaneous symmetry breaking (SSB) . . . . .	30
61	2.3.2 Higgs mechanism . . . . .	34
62	2.3.3 Masses of the gauge bosons . . . . .	36
63	2.3.4 Masses of the fermions . . . . .	37

64	2.3.5	The Higgs field . . . . .	38
65	2.3.6	Production of Higgs bosons at LHC . . . . .	39
66	2.3.7	Higgs boson decay channels . . . . .	44
67	2.4	Experimental status of the anomalous Higgs-fermion coupling . . . .	45
68	2.5	Associated production of a Higgs boson and a single top quark . . . .	47
69	2.6	CP-mixing in $tH$ processes . . . . .	52
70	<b>3</b>	<b>The CMS experiment at the LHC</b>	<b>57</b>
71	3.1	Introduction . . . . .	57
72	3.2	The LHC . . . . .	58
73	3.3	The CMS experiment . . . . .	68
74	3.3.1	CMS coordinate system . . . . .	71
75	3.3.2	Tracking system . . . . .	73
76	3.3.3	Silicon strip tracker . . . . .	76
77	3.3.4	Electromagnetic calorimeter . . . . .	77
78	3.3.5	Hadronic calorimeter . . . . .	79
79	3.3.6	Superconducting solenoid magnet . . . . .	80
80	3.3.7	Muon system . . . . .	82
81	3.3.8	CMS trigger system . . . . .	83
82	3.3.9	CMS computing . . . . .	84
83	<b>4</b>	<b>Event generation, simulation and reconstruction</b>	<b>89</b>
84	4.1	Introduction . . . . .	89
85	4.2	Event generation . . . . .	90
86	4.3	Monte Carlo Event Generators. . . . .	93
87	4.4	CMS detector simulation. . . . .	95
88	4.5	Event reconstruction. . . . .	97

89	4.5.1 Particle-Flow Algorithm. . . . .	97
90	4.5.2 Event reconstruction examples . . . . .	112
91	<b>5 Statistical methods</b>	<b>116</b>
92	5.1 Introduction . . . . .	116
93	5.2 Multivariate analysis . . . . .	116
94	5.2.1 Decision trees . . . . .	120
95	5.2.2 Boosted decision trees (BDT). . . . .	123
96	5.2.3 Overtraining . . . . .	125
97	5.2.4 Variable ranking . . . . .	126
98	5.2.5 BDT output example . . . . .	126
99	5.3 Statistical inference . . . . .	127
100	5.3.1 Nuisance parameters . . . . .	128
101	5.3.2 Maximum likelihood estimation method . . . . .	129
102	5.4 Upper limits . . . . .	130
103	5.5 Asymptotic limits . . . . .	135
104	<b>6 The inverted top-Higgs coupling</b>	<b>136</b>
105	6.1 Introduction . . . . .	136
106	6.2 $tHq$ signature . . . . .	139
107	6.3 Background processes . . . . .	141
108	6.4 Data and MC Samples . . . . .	143
109	6.4.1 Full 2016 data set . . . . .	143
110	6.4.2 Triggers . . . . .	144
111	6.4.3 MC samples . . . . .	148
112	6.5 Object Identification . . . . .	150
113	6.5.1 Lepton reconstruction and identification . . . . .	150

114	6.5.2 Lepton selection efficiency . . . . .	157
115	6.5.3 Jets and $b$ -jet tagging . . . . .	160
116	6.6 Event selection . . . . .	162
117	6.7 Background modeling and predictions . . . . .	163
118	6.7.1 $t\bar{t}V$ and diboson backgrounds . . . . .	164
119	6.7.2 Non-prompt and charge mis-ID backgrounds . . . . .	166
120	6.8 Pre-selection yields . . . . .	170
121	6.9 Signal discrimination . . . . .	173
122	6.9.1 MVA classifiers evaluation . . . . .	174
123	6.9.2 Discriminating variables . . . . .	174
124	6.9.3 BDTG classifiers response . . . . .	182
125	6.9.4 Additional discriminating variables . . . . .	183
126	6.9.5 Signal extraction procedure . . . . .	186
127	6.10 Forward jet mismodeling . . . . .	187
128	6.11 Signal model . . . . .	190
129	6.12 Systematic uncertainties . . . . .	194
130	6.13 Results . . . . .	197
131	6.13.1 $CL_S$ and cross section limits . . . . .	203
132	6.13.2 Best fit . . . . .	209
133	6.13.3 Effect of the nuisance parameters . . . . .	211
134	6.14 CP-mixing in $tH$ process . . . . .	214
135	<b>7 Phase 1 FPix upgrade module production</b>	<b>218</b>
136	7.1 Introduction . . . . .	218
137	7.2 CMS pixel detector upgrade . . . . .	219
138	7.3 Phase 1 FPix upgrade . . . . .	220

139	7.4 FPix module structure . . . . .	222
140	7.5 FPix module assembly . . . . .	223
141	7.5.1 Pick and place machine setup . . . . .	226
142	7.5.2 The gluing routine . . . . .	251
143	7.5.3 The encapsulation routine . . . . .	258
144	7.5.4 FPix module production yields . . . . .	268
145	<b>8 Conclusions</b>	<b>272</b>
146	8.1 Search for production of a Higgs boson and a single top quark . . . . .	272
147	8.2 Phase 1 FPix upgrade module production . . . . .	274
148	<b>A Datasets and triggers</b>	<b>276</b>
149	<b>B Additional plots</b>	<b>281</b>
150	B.1 Pre-selection kinematic variables . . . . .	281
151	B.2 BDTG input variables for $2lss$ channel . . . . .	285
152	B.3 Input variables distributions from BDTG classifiers . . . . .	286
153	B.4 Pulls and impacts . . . . .	290
154	<b>C Binning and selection optimization</b>	<b>293</b>
155	C.1 Binning and selection optimization . . . . .	293
156	C.2 Other binning strategies . . . . .	295
157	<b>D BDTG output variation with <math>\kappa_V</math> and <math>\kappa_t</math></b>	<b>298</b>
158	<b>E <math>tHq</math>-<math>t\bar{t}H</math> overlap</b>	<b>299</b>
159	<b>F Forward jet impact plots</b>	<b>301</b>
160	<b>G Cross section and branching ratio scalings</b>	<b>305</b>

161 Bibliography 312

162 References 313

---

## List of Figures

---

164	2.1	Standard Model of particle physics.	7
165	2.2	Transformations between quarks	14
166	2.3	Fundamental interactions in nature.	15
167	2.4	SM interactions diagrams	16
168	2.5	Neutral current processes	23
169	2.6	Spontaneous symmetry breaking mechanism	31
170	2.7	SSB Potential form	32
171	2.8	Potential for complex scalar field	33
172	2.9	SSB mechanism for complex scalar field	33
173	2.10	Proton-Proton collision	40
174	2.11	Proton PDFs	41
175	2.12	Higgs boson production mechanism Feynman diagrams	42
176	2.13	Higgs boson production cross section and decay branching ratios	43
177	2.14	$\kappa_t$ - $\kappa_V$ plot of the coupling modifiers. ATLAS and CMS combination.	46
178	2.15	Higgs boson production in association with a top quark	48
179	2.16	Cross section for $tHq$ process as a function of $\kappa_t$	51
180	2.17	Cross section for $tHW$ process as a function of $\kappa_{Htt}$	52

181	2.18 NLO cross section for $tX_0$ and $t\bar{t}X_0$ . . . . .	55
182	2.19 NLO cross section for $tWX_0$ , $t\bar{t}X_0$ . . . . .	56
183	3.1 CERN accelerator complex . . . . .	58
184	3.2 LHC protons source. First acceleration stage. . . . .	59
185	3.3 The LINAC2 accelerating system at CERN. . . . .	60
186	3.4 LHC layout and RF cavities module. . . . .	61
187	3.5 LHC dipole magnet. . . . .	63
188	3.6 Integrated luminosity delivered by LHC and recorded by CMS during 2016	65
189	3.7 LHC interaction points . . . . .	66
190	3.8 Multiple $pp$ collision bunch crossing at CMS. . . . .	68
191	3.9 Layout of the CMS detector . . . . .	69
192	3.10 CMS detector transverse slice . . . . .	70
193	3.11 CMS detector coordinate system . . . . .	72
194	3.12 CMS tracking system schematic view. . . . .	73
195	3.13 CMS pixel detector . . . . .	74
196	3.14 SST Schematic view. . . . .	76
197	3.15 CMS ECAL schematic view . . . . .	78
198	3.16 CMS HCAL schematic view . . . . .	80
199	3.17 CMS solenoid magnet . . . . .	81
200	3.18 CMS Muon system schematic view . . . . .	82
201	3.19 CMS Level-1 trigger architecture . . . . .	84
202	3.20 WLCG structure . . . . .	85
203	3.21 Data flow from CMS detector through hardware Tiers . . . . .	87
204	4.1 Event generation process. . . . .	90
205	4.2 Particle flow algorithm. . . . .	98

206	4.3	Stable cones identification . . . . .	106
207	4.4	Jet reconstruction. . . . .	107
208	4.5	Jet energy corrections. . . . .	109
209	4.6	Secondary vertex in a b-hadron decay. . . . .	111
210	4.7	HIG-13-004 Event 1 reconstruction. . . . .	113
211	4.8	$e\mu$ event reconstruction. . . . .	114
212	4.9	Recorded event reconstruction. . . . .	115
213	5.1	Scatter plots-MVA event classification. . . . .	118
214	5.2	Scalar test statistical. . . . .	119
215	5.3	Decision tree. . . . .	120
216	5.4	Decision tree output example. . . . .	123
217	5.5	BDT output example. . . . .	126
218	5.6	$t_r$ p.d.f. assuming each $H_0$ and $H_1$ . . . . .	132
219	5.7	Illustration of the $CL_s$ limit. . . . .	133
220	5.8	Example of Brazilian flag plot . . . . .	134
221	6.1	Analysis strategy workflow . . . . .	138
222	6.2	$tHq$ event signature . . . . .	140
223	6.3	$t\bar{t}$ and $t\bar{t}W$ events signature . . . . .	142
224	6.4	Trigger efficiency for the same-sign $\mu\mu$ category . . . . .	145
225	6.5	Trigger efficiency for the $e\mu$ category . . . . .	146
226	6.6	Trigger efficiency for the $3l$ category . . . . .	147
227	6.7	$tHq$ and $tHW$ cross section in the $\kappa_t$ - $\kappa_V$ phase space . . . . .	148
228	6.8	Tight vs loose lepton selection efficiencies in the $2lss$ channel. . . . .	159
229	6.9	Tight vs loose lepton selection efficiencies in the $3l$ channel. . . . .	160
230	6.10	Kinematic distributions in the diboson control region. . . . .	166

231	6.11	Fake rates . . . . .	169
232	6.12	Elecron mis-ID probabilities. . . . .	170
233	6.13	Discriminating variables for the event pre-selection. . . . .	172
234	6.14	MVA classifiers performance. . . . .	175
235	6.15	Diagrams for $tHq$ , $t\bar{t}$ , and $t\bar{t}W$ processes. . . . .	176
236	6.16	BDTG classifier Input variables distributions. . . . .	179
237	6.17	BDT input variables. Discrimination against $t\bar{t}$ and $t\bar{t}V$ in $3l$ channel. . .	180
238	6.18	Correlation matrices for the BDT input variables. . . . .	181
239	6.19	BDTG classifier response. Default parameters. . . . .	182
240	6.20	BDTG classifier output. . . . .	183
241	6.21	Additional discriminating variables distributions. . . . .	185
242	6.22	2D BDT classifier output planes . . . . .	186
243	6.23	Binning overlaid on the S/B ratio map on the plane of classifier outputs.	187
244	6.24	Kinematic distributions for forward jet mismodeling study. . . . .	189
245	6.25	Most forward jets $\eta$ distributions . . . . .	190
246	6.26	Scaling of the $tHq$ , $tHW$ , and $t\bar{t}H$ production cross section with $\kappa_t/\kappa_V$ . .	192
247	6.27	Fake rates closure test in the $3l$ selection. . . . .	197
248	6.28	Fake rates closure test. . . . .	199
249	6.29	Pre-fit BDT classifier outputs. . . . .	200
250	6.30	Pre-fit distributions in the final binning. . . . .	201
251	6.31	Post-fit distributions in the final binning. . . . .	202
252	6.32	Background-subtracted distributions in the final binning (ITC). . . . .	203
253	6.33	Background-subtracted distributions in the final binning (SM) . . . . .	204
254	6.34	Asymptotic limits on the combined $tH + t\bar{t}H$ $\sigma \times \text{BR}$ . . . . .	205
255	6.35	Asymptotic limits on the combined $tH + t\bar{t}H$ $\sigma \times \text{BR}$ , $\kappa_V = 0.5, 1.0, 1.5$ . .	206
256	6.36	Scan of $-2\Delta\log(\mathcal{L})$ for the combined fit of the $tH + t\bar{t}H$ signal strength.	207

257	6.37	Observed and a priori expected significance of the fit result. . . . .	210
258	6.38	Best fit values of the combined $tH + t\bar{t}H \sigma \times \text{BR}$ . . . . .	211
259	6.39	Post-fit pulls and impacts. . . . .	212
260	6.40	Post-fit pulls and impacts for a fit to the Asimov dataset. . . . .	213
261	6.41	BDT shape variations for five CP-mixing angles. . . . .	215
262	6.42	Asymptotic limits on the combined $tH + t\bar{t}H \sigma \times \text{BR}$ for CP-mixing angle.	217
263	7.1	Expected performance of the previous pixel detector in simulated $t\bar{t}$ events.	220
264	7.2	Layout of the upgraded and old pixel detectors. . . . .	221
265	7.3	FPix half disk design. . . . .	222
266	7.4	FPix module structure. . . . .	223
267	7.5	UNL module assembly work flow. . . . .	224
268	7.6	Full gluing and encapsulation setup . . . . .	227
269	7.7	Bare and full chucks . . . . .	227
270	7.8	BBM/HDI plate . . . . .	228
271	7.9	Glue reservoir plate . . . . .	229
272	7.10	Stamp and Weight tools in chucks . . . . .	229
273	7.11	Stamp and Weight tools . . . . .	230
274	7.12	Stamp patterns . . . . .	230
275	7.13	Test of amount of glue deposited. . . . .	231
276	7.14	Glue contact area test. . . . .	232
277	7.15	Grabber tool. . . . .	233
278	7.16	Pick and place tool. . . . .	234
279	7.17	Fiducial marks on tools. . . . .	235
280	7.18	Fiducial mark recognition. . . . .	236
281	7.19	Setup used to measure the GHCO . . . . .	238

282	7.20 Scratches scheme if the tool is not straight . . . . .	238
283	7.21 Dispensing system components. . . . .	243
284	7.22 Webcam setup. . . . .	244
285	7.23 Webcam setup calibration. . . . .	244
286	7.24 Needle tip offset measurement. . . . .	245
287	7.25 Wire bond region. . . . .	246
288	7.26 Sylgard deposition synchronization. . . . .	248
289	7.27 Time delay measurements. . . . .	249
290	7.28 Speed function for sylgard deposition. . . . .	250
291	7.29 Time delay functions. . . . .	250
292	7.30 Gluing routine workflow. . . . .	251
293	7.31 Gluing routine LabVIEW front panel . . . . .	252
294	7.32 Materials used during gluing stage . . . . .	253
295	7.33 Fiducial finder LabVIEW front panel . . . . .	254
296	7.34 Fiducial finder step LabVIEW front panel . . . . .	255
297	7.35 Gluing and pick-and-place LabVIEW front panels . . . . .	256
298	7.36 Gluing steps pictures. . . . .	257
299	7.37 Gluing session report. . . . .	258
300	7.38 ROC-HDI wirebonding. . . . .	259
301	7.39 Encapsulation workflow. . . . .	260
302	7.40 Encapsulation LabVIEW main front panel . . . . .	261
303	7.41 Encapsulation region. . . . .	262
304	7.42 Encapsulation reference positions. . . . .	264
305	7.43 Sylgard deposition LabVIEW front panel. . . . .	265
306	7.44 Encapsulation session report. . . . .	265
307	7.45 Encapsulation results. . . . .	266

308	7.46 Module in carrier. . . . .	267
309	7.47 Module assembly over time. . . . .	268
310	7.48 Module grade over time. . . . .	270
311	7.49 FPix installed in the CMS detector. . . . .	271
312	B.1 Input variables to the BDT, $3l$ channel. . . . .	282
313	B.2 Input variables to the BDT, $2lss - \mu^\pm\mu^\pm$ channel . . . . .	283
314	B.3 Input variables to the BDT, $2lss - e^\pm\mu^\pm$ channel . . . . .	284
315	B.4 Input variables to the BDT, $2lss$ channel . . . . .	285
316	B.5 BDT input variables. Discrimination against $t\bar{t}$ in $2lss$ channel. . . . .	286
317	B.6 BDT input variables. Discrimination against $t\bar{t}V$ in $2lss$ channel. . . . .	287
318	B.7 BDT input variables. Discrimination against $t\bar{t}$ in $3l$ channel. . . . .	288
319	B.8 BDT input variables. Discrimination against $t\bar{t}V$ in $3l$ channel. . . . .	289
320	B.9 Additional post-fit pulls and impacts. . . . .	291
321	B.10 Additional post-fit pulls and impacts for a fit to the Asimov dataset. . . . .	292
322	C.1 Binning combination scheme. . . . .	294
323	C.2 Binning by S/B regions for $2lss$ (left) and $3l$ (right). . . . .	296
324	C.3 Final bins (corresponding to S/B regions in the 2D plane) . . . . .	296
325	C.4 Binning into geometric regions using a $k$ -means algorithm. . . . .	297
326	C.5 Final bins using a $k$ -means algorithm. . . . .	297
327	D.1 BDTG output variation with $\kappa_V/\kappa_t$ . . . . .	298
328	F.1 Post-fit pulls and impacts with $p_T$ cut 25 GeV for the forward jet . . . . .	302
329	F.2 Post-fit pulls and impacts with $p_T$ cut 30 GeV for the forward jet . . . . .	303
330	F.3 Post-fit pulls and impacts with $p_T$ cut 25 GeV for the forward jet . . . . .	304

---

## List of Tables

---

332	2.1 Fermions of the SM. . . . .	8
333	2.2 Fermion masses. . . . .	9
334	2.3 Lepton properties. . . . .	11
335	2.4 Quark properties. . . . .	12
336	2.5 Fermion weak isospin and weak hypercharge multiplets. . . . .	13
337	2.6 Fundamental interactions features. . . . .	17
338	2.7 SM gauge bosons. . . . .	22
339	2.8 Higgs boson properties. . . . .	39
340	2.9 Predicted branching ratios for a SM Higgs boson with $m_H = 125 \text{ GeV}/c^2$ . . . . .	45
341	2.10 Predicted SM cross sections for $tH$ production at $\sqrt{s} = 13 \text{ TeV}$ . . . . .	50
342	2.11 Predicted enhancement of the $tHq$ and $tHW$ cross sections at LHC . . . . .	53
343	6.1 Trigger efficiency scale factors and associated uncertainties. . . . .	147
344	6.2 MC signal samples. . . . .	149
345	6.3 Effective areas, for electrons and muons. . . . .	154
346	6.4 Requirements on each of the three muon selections. . . . .	157
347	6.5 Criteria for each of the three electron selections. . . . .	158
348	6.6 Summary of event pre-selection. . . . .	163

349	6.7	Electron charge mis-ID probabilities.	170
350	6.8	Expected and observed yields for $35.9 \text{ fb}^{-1}$ after the pre-selection.	171
351	6.9	Signal yields split by decay channels of the Higgs boson.	173
352	6.10	Acceptance $\times$ efficiency for pre-selection cut.	173
353	6.11	BDTG input variables.	176
354	6.12	Configuration used in the final BDTG training.	182
355	6.13	Input variables ranking for BDTG classifiers	184
356	6.14	ROC-integral for all the testing cases.	185
357	6.15	Forward jet Data/MC scale factors.	191
358	6.16	$\kappa_t/\kappa_V$ ratios.	193
359	6.17	Pre-fit size of systematic uncertainties.	198
360	6.18	Expected and observed 95% C.L. cross section upper limits.	208
361	6.19	Expected and observed $\text{CL}_S$ limits on the signal strength.	209
362	6.20	Fit results for the ITC and SM scenarios	209
363	6.21	Best-fit signal strengths for a SM-like Higgs signal.	210
364	6.22	Cross sections for $tHq$ , $tHW$ and $t\bar{t}H$ as a function of $\cos(\alpha_{CP})$	214
365	6.23	Summary of expected and observed upper limits for CP-mixing angles.	216
366	7.1	Values of the needle tip height $h$ .	247
367	7.2	FPix module grading scheme.	269
368	A.1	Full 2016 dataset.	276
369	A.2	HLT paths.	277
370	A.3	$\kappa_V$ and $\kappa_t$ combinations.	278
371	A.4	List of background samples used in this analysis (CMSSW 80X).	279
372	A.5	Expected and observed upper limits.	280

373	C.1 Selection cuts optimization. . . . .	294
374	C.2 Limit variation as a function of bin size, $3l$ channel. . . . .	294
375	C.3 Limit variation as a function of bin size, $2lss$ channel. . . . .	295
376	E.1 Differences in event selection $tHq-t\bar{t}H$ multilepton analysis. . . . .	299
377	E.2 Individual and shared event yields $tHq-t\bar{t}H$ multilepton selections. . . . .	300
378	G.1 Scalings of Higgs decay branching ratios vs. $\kappa_t$ and $\kappa_V = 0.5$ . . . . .	306
379	G.2 Scalings of Higgs decay branching ratios vs. $\kappa_t$ and $\kappa_V = 1.0$ . . . . .	307
380	G.3 Scalings of Higgs decay branching ratios vs. $\kappa_t$ and $\kappa_V = 1.5$ . . . . .	308
381	G.4 Scalings of $\sigma \times \text{BR}$ for the signal components and $\kappa_V = 0.5$ . . . . .	309
382	G.5 Scalings of $\sigma \times \text{BR}$ for the signal components and $\kappa_V = 1.0$ . . . . .	310
383	G.6 Scalings of $\sigma \times \text{BR}$ for the signal components and $\kappa_V = 1.5$ . . . . .	311
384	G.7 Expected and observed upper limits for CP-mixing angles. . . . .	312

385

## CHAPTER 1

---

386

### Introduction

---

387 Over the last hundred years, exploration of nature at the atomic and subatomic  
388 scales has revealed the existence of the quantum world; several theories attempting to  
389 describe it have been created and many experiments to test them have been designed  
390 and executed.

391 This thesis explores three aspects of elementary particle physics. The theoretical  
392 aspect: the standard model (SM) of particle physics gathers the best understanding  
393 of nature that is consistent with the experimental data and although it is extremely  
394 successful, it is known that SM is not the final version of a theory of everything. The  
395 data analysis aspect: statistical methods have been developed in order to obtain the  
396 most from that experimental data. The instrumentation aspect: detection systems  
397 are under continuous research and development in order to extend their capabilities  
398 and sensitivity and improve their precision.

399 The context of SM is presented in Chapter 2, starting with a description of the  
400 basic components of the matter, quarks and leptons, and how they interact to produce  
401 the universe as it is. The language used in this description is the quantum field  
402 theory based on the principles of the gauge invariance, which states that the function  
403 describing the energy of a system is invariant under certain transformations; from

404 the physics point of view, that gauge invariance means that a physical system can  
405 be described by more than one mathematical model. Although the choice of the  
406 gauge could make, for instance, the mathematical treatment of the model more or  
407 less challenging, it does not have any effect on the observables of the physical system,  
408 i.e., a physical system is independent of the model used to describe it.

409 Interactions in the SM are represented in terms of the exchange of particles, known  
410 as gauge bosons. For instance, the electromagnetic interaction between two electrici-  
411 cally charged particles is modeled as the exchange of a photon, while the strong  
412 interaction between quarks is modeled as the exchange of gluons; hence, the photon  
413 and gluon are two of the gauge bosons. In addition, there is an interaction that ex-  
414 plains the mass of the elementary particles; this is the interaction with the so-called  
415 Higgs field.

416 In the SM, the Higgs boson is responsible for providing the mass to the elementary  
417 particles, and a fundamental part of characterization of the Higgs boson consists of  
418 finding the way it interacts with the rest of elementary particles, i.e., how the Higgs  
419 boson couples with other particles. In this thesis the coupling of the Higgs boson with  
420 the top quark is investigated; in particular, the search for the production of a Higgs  
421 boson in association with a single top quark ( $tH$ ) is considered; the focus is on the  
422  $H \rightarrow WW$ ,  $H \rightarrow \tau\tau$ , and  $H \rightarrow ZZ$  decay modes that provide leptonic signatures in  
423 the final state. This process is of special interest due to its sensitivity to the relative  
424 sign of the top-Higgs coupling and the vector bosons-Higgs coupling; in addition,  $tH$   
425 process is sensitive to charge-parity (CP) symmetry violation effects related with the  
426 Higgs boson. Thus, a description of the incorporation of the Higgs boson in the SM  
427 and the specifics of the  $tH$  process are also presented in Chapter 2.

428 The SM is a very successful theory, capable of explaining and making predictions  
429 about a vast number of natural phenomena, therefore, it is under constant testing

430 looking for evidences that verifies its predictions or that reveals the existence of  
 431 physics beyond it and highlight the road to this new physics. Currently, experiments  
 432 held at CERN<sup>1</sup> provide data from proton-proton collisions used to explore the SM.  
 433 The source of the data used in this thesis is the Compact Muon Solenoid experiment  
 434 (CMS) for which a description is presented in Chapter 3.

435 Thanks to increasing development in computing, tools like Monte Carlo (MC)  
 436 generators, simulation and reconstruction algorithms and software allow for evaluat-  
 437 ing the theory predictions and comparing them with real data. MC generators are  
 438 used to create a set of simulated data samples that reflect the theoretical principles  
 439 and details of the process under investigation, thus, predictions are obtained from the  
 440 numerical solution of the mathematical models; however, a direct comparison with  
 441 the data obtained from the experiments is not possible because of a variety of factors,  
 442 for instance, the presence of the detection systems. The effect of the detection sys-  
 443 tems can be simulated and attached to the MC data samples such that the resulting  
 444 samples account for these effects.

445 Experimental data are also processed; given that the whole detector is composed  
 446 of several subdetectors, the information coming from these subdetection systems is  
 447 combined to reconstruct the features of the particles produced after the proton-proton  
 448 collision. The process of matching the information from different subdetection sys-  
 449 tems is known as event reconstruction. The result of the event reconstruction is a set  
 450 of objects that are identified with the particles expected in the final state and that  
 451 are predicted by the theory; in the  $tH$  process case, those final state particles are  
 452 leptons and jets. Chapter 4 presents the details about the computational tools used  
 453 in this thesis.

454 The statistical tools used to treat the data samples are described in Chapter

---

<sup>1</sup> CERN stand for Conseil Européen pour la Recherche Nucléaire

455 5; these tools include the Boosted Decision Trees (BDT) method employed to dis-  
456 criminate signal and background events based on their features, and the statistical  
457 inference methods used to account for the uncertainties introduced in the analysis  
458 and to extract the upper limits on the  $tH + t\bar{t}H$  production cross section.

459 In Chapter 6, the search for the production of a Higgs boson in association with  
460 a single top quark ( $tH$ ) is presented. First, the features of the signal and background  
461 processes are described; then, the MC and data samples considered, and the strategies  
462 oriented to identify the physics objects are defined. The event selection proceeds in  
463 two steps; first, an event pre-selection based on the signal features is performed; later,  
464 the signal is extracted based on BDT discriminators. As a result, an upper limit on  
465 the  $tH + t\bar{t}H$  production cross section is set. Finally, the sensitivity to CP-mixing in  
466  $tH$  process is investigated and upper limits on the  $tH + t\bar{t}H$  production cross section  
467 are set.

468 In Chapter 7, the upgrade of the CMS forward pixel detection system (FPix)  
469 is presented. The HEP group at University of Nebraska - Lincoln (UNL) played  
470 a leading role in the so-called Phase 1 FPix upgrade, serving as a FPix modules  
471 assembly site; the assembly process was designed as a production line composed  
472 of several stages among which the gluing and encapsulation stages are described in  
473 detail. These stages were implemented using a semi-automated pick-and-place robotic  
474 system integrating vision, vacuum, and dispensing subsystems. The employment of  
475 the semi-automated setup, capable of providing a precision in location of about 10  
476  $\mu\text{m}$ , provides uniformity and speed up the module production. The commissioning of  
477 the assembly site started from scratch in late 2012 and by mid 2015 the production  
478 yields reached the same level as other experienced assembly sites.

479 Chapter 8 presents the conclusions from both analysis and hardware development  
480 sides.

481

## CHAPTER 2

482

### Theoretical approach

483

## 2.1 Introduction

484 The physical description of the universe is a challenge that physicists have faced by  
485 making theories that refine existing principles and proposing new ones in an attempt  
486 to embrace emerging facts and phenomena.

487 At the end of 1940s Julian Schwinger [1] and Richard P. Feynman [2], based on  
488 the work of Sin-Itiro Tomonaga [3], developed an electromagnetic theory consistent  
489 with special relativity and quantum mechanics that describes how matter and light  
490 interact; the so-called *quantum electrodynamics* (QED) was born.

491 QED has become the blueprint for developing theories that describe the universe.  
492 It was the first example of a quantum field theory (QFT), which is the theoretical  
493 framework for building quantum mechanical models that describes particles and their  
494 interactions. QFT is composed of a set of mathematical tools that combines classical  
495 fields, special relativity and quantum mechanics, while keeping the quantum point  
496 particles and locality ideas.

497 This chapter gives an overview of the standard model of particle physics, starting  
498 with a description of the particles and their interactions, followed by a description of  
499 the electroweak interaction, the Higgs boson and the associated production of Higgs

500 boson and a single top quark ( $tH$ ). The description contained in this chapter is based  
 501 on References [4–6].

## 502 2.2 Standard model of particle physics

503 The *standard model of particle physics (SM)* describes particle physics at the funda-  
 504 mental level in terms of a collection of interacting particles and fields. The full picture  
 505 of the SM is composed of three fields<sup>1</sup> whose excitations are interpreted as particles  
 506 called mediators or force-carriers, a set of fields whose excitations are interpreted as  
 507 elementary particles interacting through the exchange of those mediators, and a field  
 508 that gives the mass to elementary particles. Figure 2.1 shows a scheme of the SM  
 509 particles’ organization. In addition, for each of the particles in the scheme there exists  
 510 an antiparticle with the same mass and opposite quantum numbers. The existence of  
 511 antiparticles is a prediction of the relativistic quantum mechanics from the solution  
 512 of the Dirac equation for which a negative energy solution is also possible. In some  
 513 cases a particle is its own anti-particle, like photon or Higgs boson.

514 The mathematical formulation of the SM is based on group theory and the use of  
 515 Noether’s theorem [8] which states that for a physical system modeled by a Lagrangian  
 516 that is invariant under a group of transformations a conservation law is expected. For  
 517 instance, a system described by a time-independent Lagrangian is invariant (symmet-  
 518 ric) under time changes (transformations) with the total energy conservation law as  
 519 the expected conservation law. In QED, the charge operator ( $Q$ ) is the generator of  
 520 the  $U(1)$  symmetry which according to the Noether’s theorem means that there is a

---

<sup>1</sup> The formal and complete treatment of the SM is out of the scope of this document, however a plenty of textbooks describing it at several levels are available in the literature. The treatment in References [5, 6] is quite comprehensive and detailed. Note that gravitational field is not included in the standard model formulation

## Standard Model of Elementary Particles

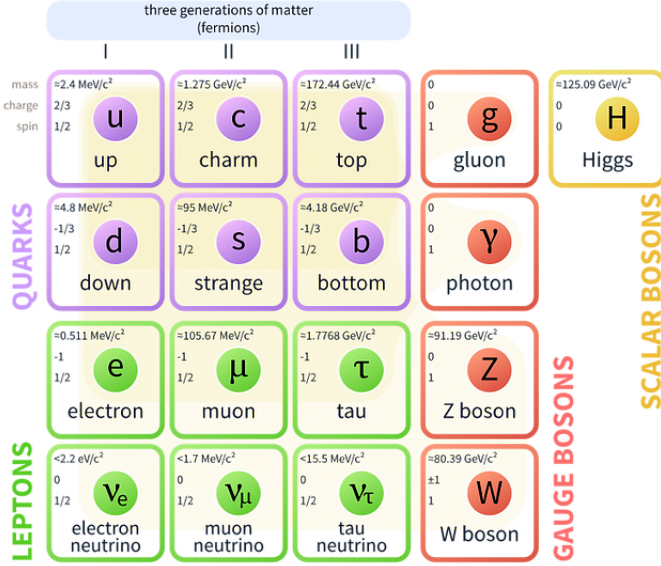


**Figure 2.1:** Schematic representation of the Standard Model of particle physics. The SM is a theoretical model intended to describe three of the four fundamental forces of the universe in terms of a set of particles and their interactions. [7].

521 conserved quantity; this conserved quantity is the electric charge and thus the law  
 522 conservation of electric charge is established.

523 In the SM, the symmetry group  $SU(3)_C \otimes SU(2)_L \otimes U(1)_Y$  describes three of the  
 524 four fundamental interactions in nature (see Section 2.2.2): strong interaction (SI),  
 525 weak interaction (WI) and electromagnetic interactions (EI) in terms of symmetries  
 526 associated to physical quantities:

- 527     • Strong:  $SU(3)_C$  associated to color charge  
 528     • Weak:  $SU(2)_L$  associated to weak isospin and chirality  
 529     • Electromagnetic:  $U(1)_Y$  associated to weak hypercharge and electric charge

530 It will be shown that the electromagnetic and weak interactions are combined in  
 531 the so-called electroweak interaction where chirality, hypercharge, weak isospin and

532 electric charge are the central concepts.

### 533 2.2.1 Fermions

534 The basic constituents of the ordinary matter at the lowest level, which form the set  
 535 of elementary particles in the SM formulation, are quarks and leptons. All of them  
 536 have spin 1/2, therefore they are classified as fermions since they obey Fermi-Dirac  
 537 statistics. There are six *flavors* of quarks and three of leptons organized in three  
 538 generations, or families, as shown in Table 2.1.

		Generation		
		1st	2nd	3rd
Leptons	Charged	Electron (e)	Moun( $\mu$ )	Tau ( $\tau$ )
	Neutral	Electron neutrino ( $\nu_e$ )	Muon neutrino ( $\nu_\mu$ )	Tau neutrino ( $\nu_\tau$ )
Quarks	Up-type	Up (u)	Charm (c)	Top (t)
	Down-type	Down (d)	Strange (s)	Bottom (b)

**Table 2.1:** Fermions of the SM. There are six flavors of quarks and three of leptons, organized in three generations, or families, composed of two pairs of closely related particles. The close relationship is motivated by the fact that each pair of particles is a member of an  $SU(2)_L$  doublet that has an associated invariance under isospin transformations. WI between leptons is limited to the members of the same generation; WI between quarks is not limited but greatly favored, to same generation members.

539 There is a mass hierarchy between generations (see Table 2.2), where the higher  
 540 generation particles decays to the lower one, which can explain why the ordinary  
 541 matter is made of particles from the first generation. In the SM, neutrinos are modeled  
 542 as massless particles so they are not subject to this mass hierarchy; however, today it  
 543 is known that neutrinos are massive so the hierarchy could be restated. The reason  
 544 behind this mass hierarchy is one of the most important open questions in particle  
 545 physics, and it becomes more puzzling when noticing that the mass difference between  
 546 first and second generation fermions is small compared to the mass difference with  
 547 respect to the third generation.

Lepton	Mass (MeV/c <sup>2</sup> )	Quark	Mass (MeV/c <sup>2</sup> )
e	0.51	u	2.2
$\mu$	105.65	c	$1.28 \times 10^3$
$\tau$	1776.86	t	$173.1 \times 10^3$
$\nu_e$	Unknown	d	4.7
$\nu_\mu$	Unknown	s	96
$\tau_\mu$	Unknown	b	$4.18 \times 10^3$

**Table 2.2:** Fermion masses [9]. Generations differ by mass in a way that has been interpreted as a mass hierarchy. Approximate values with no uncertainties are used, for comparison purpose.

548        Usually, the second and third generation fermions are produced in high energy  
 549        processes, like the ones recreated in particle accelerators.

550        **Leptons**

551        A lepton is an elementary particle that is not subject to the SI. As seen in Table 2.1,  
 552        there are two types of leptons, the charged ones (electron, muon and tau) and the  
 553        neutral ones (the three neutrinos). The electric charge (Q) is the property that gives  
 554        leptons the ability to participate in the EI. From the classical point of view, Q plays  
 555        a central role determining, among others, the strength of the electric field through  
 556        which the electromagnetic force is exerted. It is clear that neutrinos are not affected  
 557        by EI because they don't carry electric charge.

558        Another feature of the leptons that is fundamental in the mathematical description  
 559        of the SM is the chirality, which is closely related to spin and helicity. Helicity  
 560        defines the handedness of a particle by relating its spin and momentum such that  
 561        if they are parallel then the particle is right-handed; if spin and momentum are  
 562        antiparallel the particle is said to be left-handed. The study of parity conservation  
 563        (or violation) in  $\beta$ -decay has shown that only left-handed electrons/neutrinos or right-  
 564        handed positrons/anti-neutrinos are created [10]; the inclusion of that feature in the  
 565        theory was achieved by using projection operators for helicity, however, helicity is

566 frame dependent for massive particles which makes it not Lorentz invariant and then  
 567 another related attribute has to be used: *chirality*.

568 Chirality is a purely quantum attribute which makes it not so easy to describe in  
 569 graphical terms but it defines how the wave function of a particle transforms under  
 570 certain rotations. As with helicity, there are two chiral states, left-handed chiral (L)  
 571 and right-handed chiral (R). In the highly relativistic limit where  $E \approx p \gg m$  helicity  
 572 and chirality converge, becoming exactly the same for massless particles.

573 In the following, when referring to left-handed (right-handed) it will mean left-  
 574 handed chiral (right-handed chiral). The fundamental fact about chirality is that  
 575 while EI and SI are not sensitive to chirality, in WI left-handed and right-handed  
 576 fermions are treated asymmetrically, such that only left-handed fermions and right-  
 577 handed anti-fermions are allowed to couple to WI mediators, which is a violation of  
 578 parity. The way to translate this statement in a formal mathematical formulation is  
 579 based on the isospin symmetry group  $SU(2)_L$ .

580 Each generation of leptons is seen as a weak isospin doublet.<sup>2</sup> The left-handed  
 581 charged lepton and its associated left-handed neutrino are arranged in doublets of  
 582 weak isospin  $T=1/2$  while their right-handed partners are singlets:

$$\begin{pmatrix} \nu_l \\ l \end{pmatrix}_L, l_R := \begin{pmatrix} \nu_e \\ e \end{pmatrix}_L, \begin{pmatrix} \nu_\mu \\ \mu \end{pmatrix}_L, \begin{pmatrix} \nu_\tau \\ \tau \end{pmatrix}_L, e_R, \mu_R, \tau_R, \nu_{eR}, \nu_{\mu R}, \nu_{\tau R} \quad (2.1)$$

583 The isospin third component refers to the eigenvalues of the weak isospin operator  
 584 which for doublets is  $T_3 = \pm 1/2$ , while for singlets it is  $T_3 = 0$ . The physical meaning  
 585 of this doublet-singlet arrangement falls in that the WI couples the two particles in  
 586 the doublet by exchanging the interaction mediator while the singlet member is not  
 587 involved in WI. The main properties of the leptons are summarized in Table 2.3.

---

<sup>2</sup> The weak isospin is an analogy of the isospin symmetry in strong interaction where neutron and proton are affected equally by strong force but differ in their charge.

Lepton	Q(e)	$T_3$	$L_e$	$L_\mu$	$L_\tau$	Lifetime (s)
Electron (e)	-1	-1/2	1	0	0	Stable
Electron neutrino( $\nu_e$ )	0	1/2	1	0	0	Unknown
Muon ( $\mu$ )	-1	-1/2	0	1	0	$2.19 \times 10^{-6}$
Muon neutrino ( $\nu_\mu$ )	0	1/2	0	1	0	Unknown
Tau ( $\tau$ )	-1	-1/2	0	0	1	$290.3 \times 10^{-15}$
Tau neutrino ( $\nu_\tau$ )	0	1/2	0	0	1	Unknown

**Table 2.3:** Lepton properties [9]. Q: electric charge,  $T_3$ : weak isospin. Only left-handed leptons and right-handed anti-leptons participate in the WI. Anti-particles with inverted  $T_3$ , Q and lepton number complete the leptons set but are not listed. Right-handed leptons and left-handed anti-leptons, neither listed, form weak isospin singlets with  $T_3 = 0$  and do not take part in the weak interaction.

588        Although all three flavor neutrinos have been observed, their masses remain un-  
 589        known and only some estimations have been made [11]. The main reason is that  
 590        the flavor eigenstates are not the same as the mass eigenstates which implies that  
 591        when a neutrino is created its mass state is a linear combination of the three mass  
 592        eigenstates and experiments can only probe the squared difference of the masses. The  
 593        Pontecorvo-Maki-Nakagawa-Sakata (PMNS) mixing matrix encodes the relationship  
 594        between flavor and mass eigenstates.

## 595        Quarks

596        Quarks are the basic constituents of protons and neutrons. The way quarks join to  
 597        form bound states, called *hadrons*, is through the SI. Quarks are affected by all the  
 598        fundamental interactions which means that they carry all the four types of charges:  
 599        color, electric charge, weak isospin and mass.

600        Table 2.4 summarizes the features of quarks, among which the most remarkable  
 601        is their fractional electric charge. Note that fractional charge is not a problem, given  
 602        that quarks are not found isolated, but serves to explain how composed particles are  
 603        formed out of two or more valence quarks<sup>3</sup>.

---

<sup>3</sup> Hadrons can contain an indefinite number of virtual quarks and gluons, known as the quark and gluon sea, but only the valence quarks determine hadrons' quantum numbers.

Flavor	$Q(e)$	$I_3$	$T_3$	B	C	S	T	$B'$	Y	Color
Up (u)	2/3	1/2	1/2	1/3	0	0	0	0	1/3	r,b,g
Charm (c)	2/3	0	1/2	1/3	1	0	0	0	4/3	r,b,g
Top(t)	2/3	0	1/2	1/3	0	0	1	0	4/3	r,b,g
Down(d)	-1/3	-1/2	-1/2	1/3	0	0	0	0	1/3	r,b,g
Strange(s)	-1/3	0	-1/2	1/3	0	-1	0	0	-2/3	r,b,g
Bottom(b)	-1/3	0	-1/2	1/3	0	0	0	-1	-2/3	r,b,g

**Table 2.4:** Quark properties [9]. Q: electric charge,  $I_3$ : isospin,  $T_3$ : weak isospin, B: baryon number, C: charmness, S: strangeness, T: topness,  $B'$ : bottomness, Y: hypercharge. Anti-quarks posses the same mass and spin as quarks but all charges (color, flavor numbers) have opposite sign.

- 604        Color charge is responsible for the SI between quarks and is the symmetry ( $SU(3)_C$ )  
 605        that defines the formalism to describe SI. There are three colors: red (r), blue (b)  
 606        and green (g) and their corresponding three anti-colors; thus each quark carries one  
 607        color unit while anti-quarks carries one anti-color unit. As explained in Section 2.2.2,  
 608        quarks are not allowed to be isolated due to the color confinement effect, hence, their  
 609        features have been studied indirectly by observing their bound states created when
- 610        • one quark with a color charge is attracted by an anti-quark with the correspond-  
 611        ing anti-color charge forming a colorless particle called a *meson*.
- 612        • three quarks (anti-quarks) with different color (anti-color) charges are attracted  
 613        among them forming a colorless particle called a *baryon* (*anti-baryon*).
- 614        In practice, when a quark is left alone isolated a process called *hadronization* occurs  
 615        where the quark emits gluons (see Section 2.2.4) which eventually will generate new  
 616        quark-antiquark pairs and so on; those quarks will recombine to form hadrons that  
 617        will decay into leptons. This proliferation of particles looks like a *jet* coming from  
 618        the isolated quark. More details about the hadronization process and jet structure  
 619        will be given in chapter4.
- 620        In the first version of the quark model (1964), M. Gell-Mann [12] and G. Zweig  
 621        [13, 14] developed a consistent way to classify hadrons according to their properties.

622 Only three quarks (u, d, s) were involved in a scheme in which all baryons have baryon  
 623 number B=1 and therefore quarks have B=1/3; non-baryons have B=0. Baryon  
 624 number is conserved in SI and EI which means that single quarks cannot be created  
 625 but in pairs  $q - \bar{q}$ .

626 The scheme organizes baryons in a two-dimensional space ( $I_3$  - Y); Y (hypercharge)  
 627 and  $I_3$  (isospin) are quantum numbers related by the Gell-Mann-Nishijima formula  
 628 [15, 16]:

$$Q = I_3 + \frac{Y}{2} \quad (2.2)$$

629 where  $Y = B + S + C + T + B'$  are the quantum numbers listed in Table 2.4.

	Quarks			$T_3$	$Y_W$	Leptons			$T_3$	$Y_W$
Doublets	$(\frac{u}{d'})_L$	$(\frac{c}{s'})_L$	$(\frac{t}{b'})_L$	$(\frac{1/2}{-1/2})$	1/3	$(\nu_e)_L$	$(\nu_\mu)_L$	$(\nu_\tau)_L$	$(\frac{1/2}{-1/2})$	-1
Singlets	$u_R$	$c_R$	$t_R$	0	4/3	$\nu_{eR}$	$\nu_{\mu R}$	$\nu_{\tau R}$	0	-2
	$d'_R$	$s'_R$	$b'_R$	0	-2/3	$e_R$	$\mu_R$	$\tau_R$		

**Table 2.5:** Fermion weak isospin and weak hypercharge multiplets. Weak hypercharge is calculated through the Gell-Mann-Nishijima formula 2.2 but using the weak isospin and charge for quarks.

630 There are six quark flavors organized in three generations (see Table 2.1) follow-  
 631 ing a mass hierarchy which, again, implies that higher generations decay to first  
 632 generation quarks.

633 Isospin doublets of quarks are also defined (see Table 2.5), and same as for neu-  
 634 trinos, the WI eigenstates are not the same as the mass eigenstates which means  
 635 that members of different quark generations are connected by the WI mediator; thus,  
 636 up-type quarks are coupled not to down-type quarks (the mass eigenstates) directly  
 637 but to a superposition of down-type quarks ( $q'_d$ ; the weak eigenstates) via WI accor-  
 638 ding to:

$$q'_d = V_{CKM} q_d \quad (2.3)$$

$$\begin{pmatrix} d' \\ s' \\ b' \end{pmatrix} = \begin{pmatrix} V_{ud} & V_{us} & V_{ub} \\ V_{cd} & V_{cs} & V_{cb} \\ V_{td} & V_{ts} & V_{tb} \end{pmatrix} \begin{pmatrix} d \\ s \\ b \end{pmatrix} \quad (2.4)$$

639 where  $V_{CKM}$  is known as Cabibbo-Kobayashi-Maskawa (CKM) mixing matrix [17,18]  
640 given by

$$\begin{pmatrix} |V_{ud}| & |V_{us}| & |V_{ub}| \\ |V_{cd}| & |V_{cs}| & |V_{cb}| \\ |V_{td}| & |V_{ts}| & |V_{tb}| \end{pmatrix} = \begin{pmatrix} 0.97427 \pm 0.00015 & 0.22534 \pm 0.00065 & 0.00351^{+0.00015}_{-0.00014} \\ 0.22520 \pm 0.00065 & 0.97344 \pm 0.00016 & 0.0412^{+0.0011}_{-0.0005} \\ 0.00867^{+0.00029}_{-0.00031} & 0.0404^{+0.0011}_{-0.0005} & 0.999146^{+0.000021}_{-0.000046} \end{pmatrix}. \quad (2.5)$$

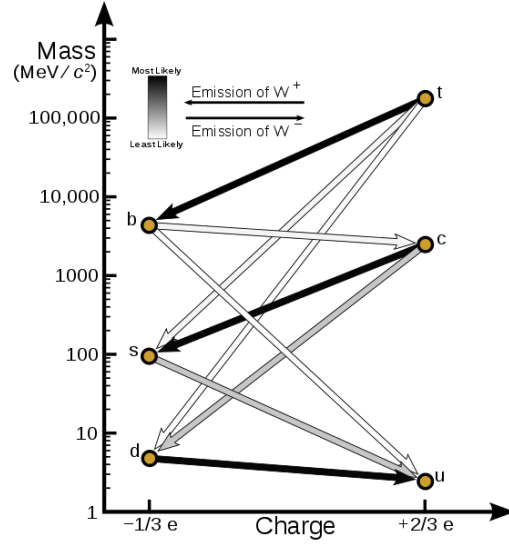


**Figure 2.2:** Transformations between quarks through the exchange of a WI. Higher generations quarks decay to first generation quarks by emitting a W boson. The arrow color indicates the likelihood of the transition according to the grey scale in the top left side which represent the CKM matrix parameters [19].

641 The weak decays of quarks are represented in the diagram of Figure 2.2; again,  
642 the CKM matrix plays a central role since it contains the probabilities for the differ-  
643 ent quark decay channels, in particular, note that quark decays are greatly favored

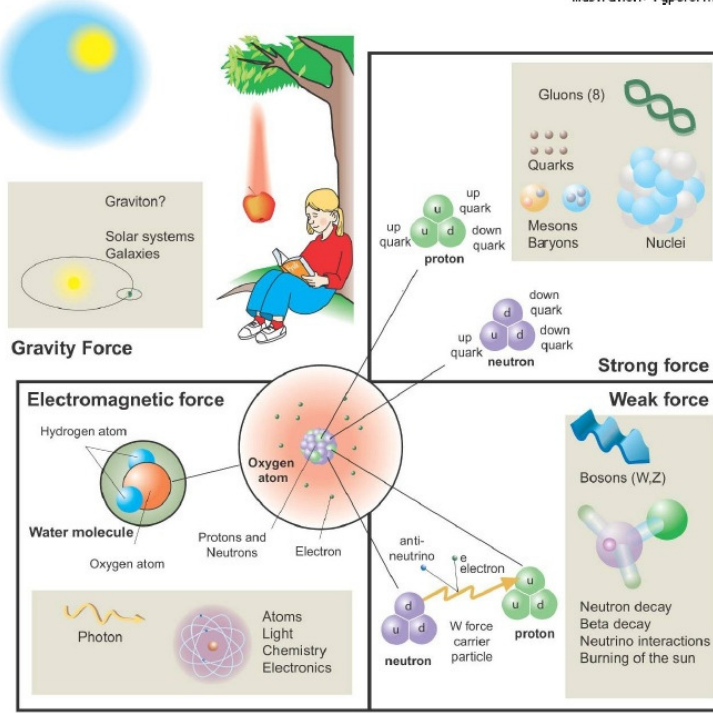
644 between generation members.

645 CKM matrix is a  $3 \times 3$  unitary matrix parametrized by three mixing angles and  
 646 the *CP-mixing phase*; the latter is the parameter responsible for the Charge-Parity  
 647 symmetry violation (CP-violation) in the SM. The fact that the top quark decays  
 648 almost all the time to a bottom quark is exploited in this thesis when making the  
 649 selection of the signal events by requiring the presence of a jet tagged as a jet coming  
 650 from a  $b$  quark in the final state.

## 651 2.2.2 Fundamental interactions

### Fundamental interactions.

Illustration: Typoform



Summer School KPI 15 August 2009

**Figure 2.3:** Fundamental interactions in nature. Despite the many manifestations of forces in nature, we can track all of them back to one of the fundamental interactions. The most common forces are gravity and electromagnetic given that all of us are subject and experience them in everyday life.

652 Even though there are many manifestations of force in nature, like the ones rep-  
 653 resented in Figure 2.3, we can classify all of them in four fundamental interactions:

- 654     ● *Electromagnetic interaction (EI)* affects particles that are *electrically charged*,  
 655       like electrons and protons. Figure 2.4a. shows a graphical representation, known  
 656       as *Feynman diagram*, of electron-electron scattering.
- 657     ● *Strong interaction (SI)* described by Quantum Chromodynamics (QCD). Hadrons  
 658       like the proton and the neutron have internal structure given that they are com-  
 659       posed of two or more valence quarks<sup>4</sup>. Quarks have fractional electric charge  
 660       which means that they are subject to electromagnetic interaction and in the case  
 661       of the proton they should break apart due to electrostatic repulsion; however,  
 662       quarks are held together inside the hadrons against their electrostatic repulsion  
 663       by the *Strong Force* through the exchange of *gluons*. The analog to the electric  
 664       charge is the *color charge*. Electrons and photons are elementary particles as  
 665       quarks but they don't carry color charge, therefore they are not subject to SI. A  
 666       Feynman diagram for gluon exchange between quarks is shown in Figure 2.4b.

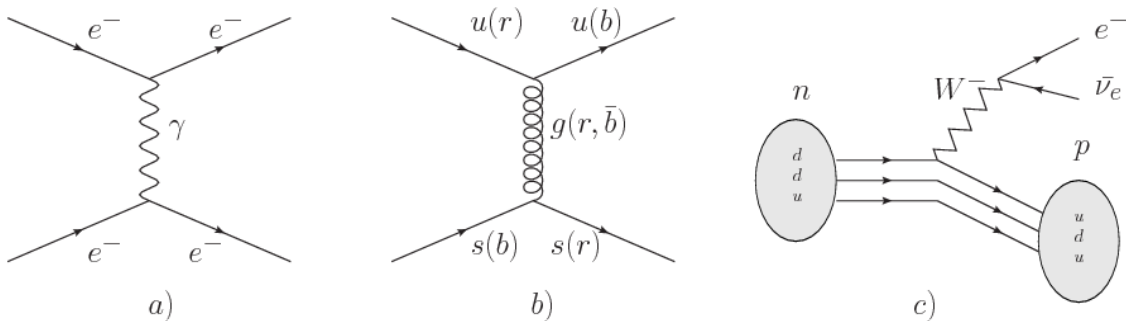


**Figure 2.4:** Feynman diagrams representing the interactions in SM; a) EI: e-e scattering; b) SI: gluon exchange between quarks ; c) WI:  $\beta$ -decay

- 667     ● *Weak interaction (WI)* described by the weak theory (WT), is responsible, for  
 668       instance, for the radioactive decay in atoms and the deuterium production

<sup>4</sup> Particles made of four and five quarks are exotic states not so common.

669 within the sun. Quarks and leptons are the particles affected by the weak  
 670 interaction; they possess a property called *flavor charge* (see 2.2.1) which can  
 671 be changed by emitting or absorbing one weak force mediator. There are three  
 672 mediators of the *weak force* known as  $Z$  boson in the case of electrically neutral  
 673 flavor changes and  $W^\pm$  bosons in the case of electrically charged flavor changes.  
 674 The *weak isospin* is the WI analog to electric charge in EI, and color charge in  
 675 SI, and defines how quarks and leptons are affected by the weak force. Figure  
 676 2.4c. shows the Feynman diagram of  $\beta$ -decay where a neutron (n) is transformed  
 677 in a proton (p) by emitting a  $W^-$  particle.

- 678 • *Gravitational interaction (GI)* described by General Theory of Relativity (GR).  
 679 It is responsible for the structure of galaxies and black holes as well as the  
 680 expansion of the universe. As a classical theory, in the sense that it can be  
 681 formulated without even appeal to the concept of quantization, it implies that  
 682 the space-time is a continuum and predictions can be made without limitation  
 683 to the precision of the measurement tools. The latter represents a direct con-  
 684 tradiction of the quantum mechanics principles. Gravity is deterministic while  
 685 quantum mechanics is probabilistic; despite that, efforts to develop a quantum  
 686 theory of gravity have predicted the *graviton* as mediator of the gravitational  
 687 force<sup>5</sup>.

Interaction	Acts on	Relative strength	Range (m)	Mediators
Electromagnetic (QED)	Electrically charged particles	$10^{-2}$	Infinite	Photon
Strong (QCD)	Quarks and gluons	1	$10^{-15}$	Gluon
Weak (WI)	Leptons and quarks	$10^{-6}$	$10^{-18}$	$W^\pm$ , Z
Gravitational (GI)	Massive particles	$10^{-39}$	Infinite	Graviton

**Table 2.6:** Fundamental interactions features [20].

<sup>5</sup> Actually a wide variety of theories have been developed in an attempt to describe gravity; some famous examples are string theory and supergravity.

688       Table 2.6 summarizes the main features of the fundamental interactions. The  
 689       strength of the interactions is represented by the coupling constants which depend  
 690       on the energy scale at which the interaction is evaluated, therefore, it is the relative  
 691       strength of the fundamental forces that reveals the meaning of strong and weak; in  
 692       a context where the relative strength of the SI is 1, the EI is about hundred times  
 693       weaker and WI is about million times weaker than the SI. A good description on how  
 694       the relative strength and range of the fundamental interactions are calculated can  
 695       be found in References [20, 21]. In the everyday life, only EI and GI are explicitly  
 696       experienced due to the range of these interactions; i.e., at the human scale distances  
 697       only EI and GI have appreciable effects, in contrast to SI which at distances greater  
 698       than  $10^{-15}$ m become negligible. Is it important to clarify that the weakness of the  
 699       WI is attributed to the fact that its mediators are highly massive which affects the  
 700       propagators of the interaction, as a result, the effect of the coupling constant is  
 701       reduced.

### 702       **2.2.3      Gauge invariance.**

703       QED was built successfully on the basis of the classical electrodynamics theory (CED)  
 704       of Maxwell and Lorentz, following theoretical and experimental requirements imposed  
 705       by

- 706           • Lorentz invariance: independence on the reference frame.
- 707           • Locality: interacting fields are evaluated at the same space-time point to avoid  
                 action at a distance.
- 709           • Renormalizability: physical predictions are finite and well defined.

- 710        • Particle spectrum, symmetries and conservation laws already known must emerge  
 711              from the theory.
- 712        • Local gauge invariance.

713        The gauge invariance requirement reflects the fact that the fundamental fields  
 714        cannot be directly measured but associated fields which are the observables. Electric  
 715        (**E**) and magnetic (**B**) fields in CED are associated with the electric scalar potential  
 716         $V$  and the vector potential **A**. In particular, **E** can be obtained by measuring the  
 717        change in the space of the scalar potential ( $\Delta V$ ); however, two scalar potentials  
 718        differing by a constant  $f$  correspond to the same electric field. The same happens  
 719        in the case of the vector potential **A**; thus, different configurations of the associated  
 720        fields result in the same set of values of the observables. The freedom in choosing one  
 721        particular configuration is known as *gauge freedom*; the transformation law connecting  
 722        two configurations is known as *gauge transformation* and the fact that the observables  
 723        are not affected by a gauge transformation is called *gauge invariance*.

724        When the gauge transformation:

$$\begin{aligned} \mathbf{A} &\rightarrow \mathbf{A} - \nabla f \\ V &\rightarrow V - \frac{\partial f}{\partial t} \end{aligned} \tag{2.6}$$

725        is applied to Maxwell equations, they are still satisfied and the fields remain invariant.  
 726        Thus, CED is invariant under gauge transformations and is called a *gauge theory*.  
 727        The set of all gauge transformations form the *symmetry group* of the theory, which  
 728        according to the group theory, has a set of *group generators*. The number of group  
 729        generators determine the number of *gauge fields* of the theory.

730 As mentioned in the first lines of Section 2.2, QED has one symmetry group ( $U(1)$ )  
 731 with one group generator (the  $Q$  operator) and one gauge field (the electromagnetic  
 732 field  $A^\mu$ ). In CED there is not a clear definition, beyond the historical convention,  
 733 of which fields are the fundamental and which are the associated, but in QED the  
 734 fundamental field is  $A^\mu$ . When a gauge theory is quantized, the gauge fields are  
 735 quantized and their quanta are called *gauge bosons*. The word boson characterizes  
 736 particles with integer spin which obey Bose-Einstein statistics.

737 As will be detailed in Section 2.3, interactions between particles in a system can  
 738 be obtained by considering first the Lagrangian density of free particles in the sys-  
 739 tem, which of course is incomplete because the interaction terms have been left out,  
 740 and demanding global phase transformation invariance. Global phase transforma-  
 741 tion means that a gauge transformation is performed identically to every point  
 742 in the space<sup>6</sup> and the Lagrangian remains invariant. Then, the global transforma-  
 743 tion is promoted to a local phase transformation (this time the gauge transformation  
 744 depends on the position in space) and again invariance is required.

745 Due to the space dependence of the local transformation, the Lagrangian density is  
 746 not invariant anymore. In order to reinstate the gauge invariance, the gauge covariant  
 747 derivative is introduced in the Lagrangian and with it the gauge field responsible for  
 748 the interaction between particles in the system. The new Lagrangian density is gauge  
 749 invariant, includes the interaction terms needed to account for the interactions and  
 750 provides a way to explain the interaction between particles through the exchange of  
 751 the gauge boson.

752 This recipe was used to build QED and the theories that aim to explain the  
 753 fundamental interactions.

---

<sup>6</sup> Here space corresponds to the 4-dimensional space i.e. space-time.

754 **2.2.4 Gauge bosons**

755 The importance of the gauge bosons comes from the fact that they are the force  
 756 mediators or force carriers. The features of the gauge bosons reflect those of the fields  
 757 they represent and they are extracted from the Lagrangian density used to describe  
 758 the interactions. In Section 2.3, it will be shown how the gauge bosons of the EI and  
 759 WI emerge from the electroweak Lagrangian. The SI gauge bosons features are also  
 760 extracted from the SI Lagrangian but it is not detailed in this document. The main  
 761 features of the SM gauge bosons will be briefly presented below and summarized in  
 762 Table 2.7.

763 • **Photon.** EI occurs when the photon couples to (is exchanged between) parti-  
 764 cles carrying electric charge; however, The photon itself does not carry electric  
 765 charge, therefore, there is no coupling between photons. Given that the photon  
 766 is massless the EI is of infinite range, i.e., electrically charged particles interact  
 767 even if they are located far away one from each other; this also implies that  
 768 photons always move with the speed of light.

769 • **Gluon.** SI is mediated by gluons which just as photons are massless. They  
 770 carry one unit of color charge and one unit of anticolor charge, hence, gluons  
 771 can couple to other gluons. As a result, the range of the SI is not infinite  
 772 but very short due to the attraction between gluons, giving rise to the *color*  
 773 *confinement* which explains why color charged particles cannot be isolated but  
 774 live within composite particles, like quarks inside protons.

775 • **W, Z.**  $W^\pm$  and Z, are massive which explains their short-range. Given that  
 776 the WI is the only interaction that can change the flavor of the interacting  
 777 particles, the W boson is the responsible for the nuclear transmutation where

778        a neutron is converted into a proton or vice versa with the involvement of an  
 779        electron and a neutrino (see Figure 2.4c). The Z boson is the responsible for the  
 780        neutral weak processes like neutrino elastic scattering where no electric charge  
 781        but momentum transference is involved. WI gauge bosons carry isospin charge  
 782        which makes interaction between them possible.

Interaction	Mediator	Electric charge (e)	Color charge	Weak Isospin	mass (GeV/c <sup>2</sup> )
Electromagnetic	Photon ( $\gamma$ )	0	No	0	0
Strong	Gluon (g)	0	Yes -octet	No	0
Weak	$W^\pm$	$\pm 1$	No	$\pm 1$	$80.385 \pm 0.015$
	Z	0	No	0	$91.188 \pm 0.002$

**Table 2.7:** SM gauge bosons main features [9].

783        **2.3 Electroweak unification and the Higgs**  
 784        **mechanism**

785        Physicists dream of building a theory that contains all the interactions in one single  
 786        interaction, i.e., showing that at some scale in energy all the four fundamental inter-  
 787        actions are unified and only one interaction emerges in a *Theory of everything*. The  
 788        first sign of the feasibility of such unification came from success in the construction  
 789        of the CED. Einstein spent years trying to reach that full unification, which by 1920  
 790        only involved electromagnetism and gravity, with no success; however, a new par-  
 791        tial unification was achieved in the 1960's, when S.Glashow [22], A.Salam [23] and  
 792        S.Weinberg [24] independently proposed that electromagnetic and weak interactions  
 793        are two manifestations of a more general interaction called *electroweak interaction*  
 794        (*EWI*). EWI was developed by following the useful prescription provided by QED  
 795        and the gauge invariance principles.

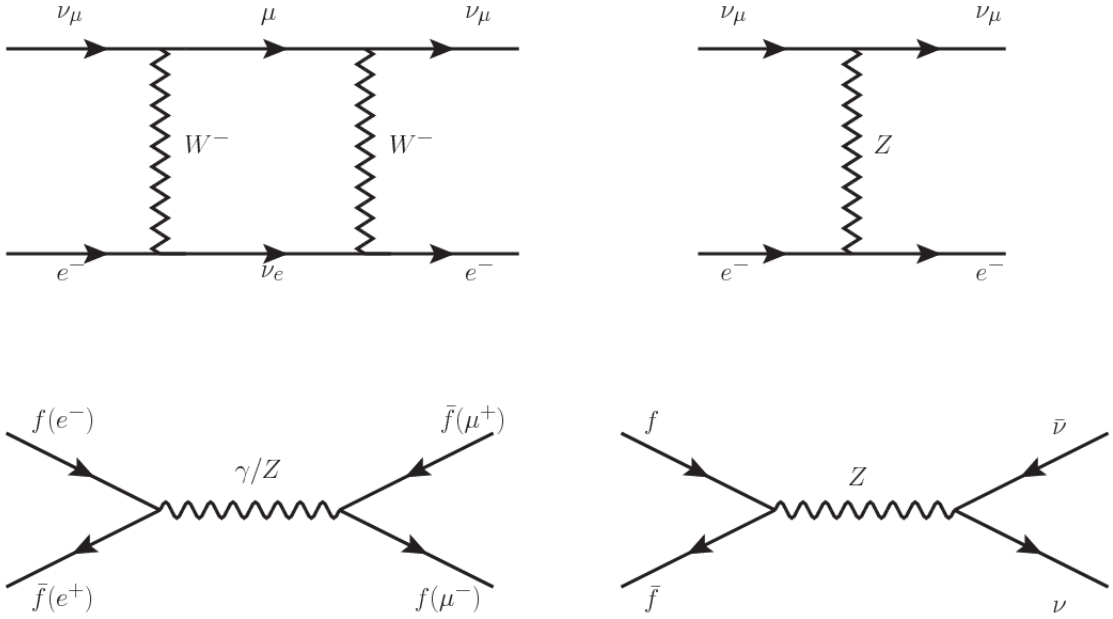


**Figure 2.5:** Top:  $\nu_\mu - e^-$  scattering going through charged currents (left) and neutral currents (right). Bottom: neutral current processes for charged fermions (left) and involving neutrinos (right). While neutral current processes involving only charged fermions can proceed through EI or WI, those involving neutrinos can only proceed via WI.

796        The *classic* weak theory developed by Fermi, did not have the concept of the W  
 797        boson but instead it was treated as a point interaction with the dimensionful constant  
 798         $G_F$  associated with it. It works really well at low energies very far off the W mass  
 799        shell. When going up in energy, the theory of weak interactions involving the W  
 800        boson is capable of explaining the  $\beta$ -decay and in general the processes mediated by  
 801         $W^\pm$  bosons. However, there were some processes like the  $\nu_\mu - e^-$  scattering which  
 802        would require the exchange of two W bosons (see Figure 2.5 top diagrams) giving  
 803        rise to divergent loop integrals and then non-finite predictions. The EWI theory, by  
 804        including neutral currents involving fermions via the exchange of a neutral bosons Z,  
 805        overcomes those divergences and the predictions become realistic.

806        Neutral weak interaction vertices conserve flavor in the same way as the electro-  
 807        magnetic vertices do, but additionally, the Z boson can couple to neutrinos which

808 implies that processes involving charged fermions can proceed through EI or WI but  
 809 processes involving neutrinos can proceed only through WI.

810 The prescription to build a gauge theory of the WI consists of proposing a free  
 811 field Lagrangian density that includes the particles involved; next, by requesting  
 812 invariance under global phase transformations first and generalizing to local phase  
 813 transformations invariance later, the conserved currents are identified and interactions  
 814 are generated by introducing gauge fields. Given that the goal is to include the EI  
 815 and WI in a single theory, the group symmetry considered should be a combination of  
 816  $SU(2)_L$  and  $U(1)_{em}$ , however the latter cannot be used directly because the EI treats  
 817 left and right-handed particles indistinctly in contrast to the former. Fortunately, the  
 818 weak hypercharge, which is a combination of the weak isospin and the electric charge  
 819 (Eqn. 2.2) is suitable to be used since it is conserved by the EI and WI. Thus, the  
 820 symmetry group to be considered is

$$G \equiv SU(2)_L \otimes U(1)_Y \quad (2.7)$$

821 The following treatment applies to any of the fermion generations, but for sim-  
 822 plicity the first generation of leptons will be considered [5, 6, 25, 26].

823 Given the first generation of leptons

$$\psi_1 = \begin{pmatrix} \nu_e \\ e^- \end{pmatrix}_L, \quad \psi_2 = \nu_{eR}, \quad \psi_3 = e_R^- \quad (2.8)$$

824 the charged fermionic currents are given by

$$J_\mu \equiv J_\mu^+ = \bar{\nu}_{eL} \gamma_\mu e_L, \quad J_\mu^\dagger \equiv J_\mu^- = \bar{e}_L \gamma_\mu \nu_{eL} \quad (2.9)$$

825 and the free Lagrangian is given by

$$\mathcal{L}_0 = \sum_{j=1}^3 i\bar{\psi}_j(x)\gamma^\mu\partial_\mu\psi_j(x). \quad (2.10)$$

826 Mass terms are included directly in the QED free Lagrangians since they preserve  
 827 the invariance under the symmetry transformations involved which treat left and right  
 828 handed particles similarly, however mass terms of the form

$$m_W^2 W_\mu^\dagger(x) W^\mu(x) + \frac{1}{2} m_Z^2 Z_\mu(x) Z^\mu(x) - m_e \bar{\psi}_e(x) \psi_e(x) \quad (2.11)$$

829 which represent the mass of  $W^\pm$ , Z and electrons, are not invariant under G transfor-  
 830 mations, therefore the gauge fields described by the EWI are in principle massless.

831 Experiments have shown that the EWI gauge fields are not massless [27–30];  
 832 however, they have to acquire mass through a mechanism compatible with the gauge  
 833 invariance; that mechanism is known as the *Higgs mechanism* and will be considered  
 834 later in this Section. The global transformations in the combined symmetry group G  
 835 can be written as

$$\begin{aligned} \psi_1(x) &\xrightarrow{G} \psi'_1(x) \equiv U_Y U_L \psi_1(x), \\ \psi_2(x) &\xrightarrow{G} \psi'_2(x) \equiv U_Y \psi_2(x), \\ \psi_3(x) &\xrightarrow{G} \psi'_3(x) \equiv U_Y \psi_3(x) \end{aligned} \quad (2.12)$$

836 where  $U_L$  represent the  $SU(2)_L$  transformation acting only on the weak isospin dou-  
 837 blet and  $U_Y$  represent the  $U(1)_Y$  transformation acting on all the weak isospin mul-  
 838 tiplets. Explicitly

$$U_L \equiv \exp\left(i\frac{\sigma_i}{2}\alpha^i\right), \quad U_Y \equiv \exp(iy_i\beta) \quad (i = 1, 2, 3) \quad (2.13)$$

839 with  $\sigma_i$  the Pauli matrices and  $y_i$  the weak hypercharges. In order to promote the  
 840 transformations from global to local while keeping the invariance, it is required that  
 841  $\alpha^i = \alpha^i(x)$ ,  $\beta = \beta(x)$  and the replacement of the ordinary derivatives by the covariant  
 842 derivatives

$$\begin{aligned} D_\mu \psi_1(x) &\equiv \left[ \partial_\mu + ig\sigma_i W_\mu^i(x)/2 + ig'y_1 B_\mu(x) \right] \psi_1(x) \\ D_\mu \psi_2(x) &\equiv [\partial_\mu + ig'y_2 B_\mu(x)] \psi_2(x) \\ D_\mu \psi_3(x) &\equiv [\partial_\mu + ig'y_3 B_\mu(x)] \psi_3(x) \end{aligned} \quad (2.14)$$

843 introducing in this way four gauge fields,  $W_\mu^i(x)$  and  $B_\mu(x)$ , in the process. The  
 844 covariant derivatives (Eqn. 2.14) are required to transform in the same way as fermion  
 845 fields  $\psi_i(x)$  themselves, therefore, the gauge fields transform as:

$$\begin{aligned} B_\mu(x) &\xrightarrow{G} B'_\mu(x) \equiv B_\mu(x) - \frac{1}{g'} \partial_\mu \beta(x) \\ W_\mu^i(x) &\xrightarrow{G} W_\mu^{ii}(x) \equiv W_\mu^i(x) - \frac{i}{g} \partial_\mu \alpha_i(x) - \varepsilon_{ijk} \alpha_i(x) W_\mu^j(x). \end{aligned} \quad (2.15)$$

846 The G invariant version of the Lagrangian density 2.10 can be written as

$$\mathcal{L}_0 = \sum_{j=1}^3 i \bar{\psi}_j(x) \gamma^\mu D_\mu \psi_j(x) \quad (2.16)$$

847 where free massless fermion and gauge fields and fermion-gauge boson interactions  
 848 are included. The EWI Lagrangian density must additionally include kinetic terms  
 849 for the gauge fields ( $\mathcal{L}_G$ ) which are built from the field strengths, according to

$$B_{\mu\nu}(x) \equiv \partial_\mu B_\nu - \partial_\nu B_\mu \quad (2.17)$$

$$W_{\mu\nu}^i(x) \equiv \partial_\mu W_\nu^i(x) - \partial_\nu W_\mu^i(x) - g\varepsilon^{ijk}W_\mu^j W_\nu^k \quad (2.18)$$

850 the last term in Eqn. 2.18 is added in order to hold the gauge invariance; therefore,

$$\mathcal{L}_G = -\frac{1}{4}B_{\mu\nu}(x)B^{\mu\nu}(x) - \frac{1}{4}W_{\mu\nu}^i(x)W_i^{\mu\nu}(x) \quad (2.19)$$

851 which contains not only the free gauge fields contributions, but also the gauge fields  
 852 self-interactions and interactions among them.

853 The three weak isospin conserved currents resulting from the  $SU(2)_L$  symmetry  
 854 are given by

$$J_\mu^i(x) = \frac{1}{2}\bar{\psi}_1(x)\gamma_\mu\sigma^i\psi_1(x) \quad (2.20)$$

855 while the weak hypercharge conserved current resulting from the  $U(1)_Y$  symmetry is  
 856 given by

$$J_\mu^Y = \sum_{j=1}^3 \bar{\psi}_j(x)\gamma_\mu y_j\psi_j(x) \quad (2.21)$$

857 In order to evaluate the electroweak interactions modeled by an isovector field  
 858  $W_\mu^i$  that couples to isospin currents  $J_\mu^i$  with strength  $g$  and additionally the singlet  
 859 field  $B_\mu$  which couples to the weak hypercharge current  $J_\mu^Y$  with strength  $g'/2$ . The  
 860 interaction Lagrangian density to be considered is

$$\mathcal{L}_I = -gJ^{i\mu}(x)W_\mu^i(x) - \frac{g'}{2}J^{Y\mu}(x)B_\mu(x) \quad (2.22)$$

861 Note that the weak isospin currents are not the same as the charged fermionic cur-  
 862 rents that were used to describe the WI (Eqn. 2.9), since the weak isospin eigenstates  
 863 are not the same as the mass eigenstates, but they are closely related

$$J_\mu = \frac{1}{2}(J_\mu^1 + iJ_\mu^2), \quad J_\mu^\dagger = \frac{1}{2}(J_\mu^1 - iJ_\mu^2). \quad (2.23)$$

864 The same happens with the gauge fields  $W_\mu^i$  which are related to the mass eigen-  
 865 states  $W^\pm$  by

$$W_\mu^+ = \frac{1}{\sqrt{2}}(W_\mu^1 - iW_\mu^2), \quad W_\mu^- = \frac{1}{\sqrt{2}}(W_\mu^1 + iW_\mu^2). \quad (2.24)$$

866 The fact that there are three weak isospin conserved currents is an indication that  
 867 in addition to the charged fermionic currents, which couple charged to neutral leptons,  
 868 there should be a neutral fermionic current that does not involve electric charge  
 869 exchange; therefore, it couples neutral fermions or fermions of the same electric charge.  
 870 The third weak isospin current contains a term that is similar to the electromagnetic  
 871 current ( $j_\mu^{em}$ ), indicating that there is a relation between them and resembling the  
 872 Gell-Mann-Nishijima formula 2.2 adapted to electroweak interactions

$$Q = T_3 + \frac{Y_W}{2}. \quad (2.25)$$

873 Just as  $Q$  generates the  $U(1)_{em}$  symmetry, the weak hypercharge generates the  
 874  $U(1)_Y$  symmetry as said before. It is possible to write the relationship in terms of  
 875 the currents as

$$j_\mu^{em} = J_\mu^3 + \frac{1}{2}J_\mu^Y. \quad (2.26)$$

876 The neutral gauge fields  $W_\mu^3$  and  $B_\mu$  cannot be directly identified with the  $Z$

and the photon fields since the photon interacts similarly with left and right-handed fermions; however, they are related through a linear combination given by

$$A_\mu = B_\mu \cos \theta_W + W_\mu^3 \sin \theta_W \quad (2.27)$$

$$Z_\mu = -B_\mu \sin \theta_W + W_\mu^3 \cos \theta_W$$

where  $\theta_W$  is known as the *Weinberg angle*. The interaction Lagrangian is now given by

$$\begin{aligned} \mathcal{L}_I = & -\frac{g}{\sqrt{2}}(J^\mu W_\mu^+ + J^{\mu\dagger} W_\mu^-) - \left(g \sin \theta_W J_\mu^3 + g' \cos \theta_W \frac{J_\mu^Y}{2}\right) A^\mu \\ & - \left(g \cos \theta_W J_\mu^3 - g' \sin \theta_W \frac{J_\mu^Y}{2}\right) Z^\mu \end{aligned} \quad (2.28)$$

the first term is the weak charged current interaction, while the second term is the electromagnetic interaction under the condition

$$g \sin \theta_W = g' \cos \theta_W = e, \quad \frac{g'}{g} = \tan \theta_W \quad (2.29)$$

contained in the Eqn.2.26; the third term is the neutral weak current.

882

883 Note that the neutral fields transformation given by the Eqn. 2.27 can be written  
884 in terms of the coupling constants  $g$  and  $g'$  as:

$$A_\mu = \frac{g' W_\mu^3 + g B_\mu}{\sqrt{g^2 + g'^2}}, \quad Z_\mu = \frac{g W_\mu^3 - g' B_\mu}{\sqrt{g^2 + g'^2}}. \quad (2.30)$$

885 So far, the Lagrangian density describing the non-massive EWI is:

$$\mathcal{L}_{nmEWI} = \mathcal{L}_0 + \mathcal{L}_G \quad (2.31)$$

886 where fermion and gauge fields have been considered massless because their regular  
 887 mass terms are manifestly non invariant under  $G$  transformations; therefore, masses  
 888 have to be generated in a gauge invariant way. The mechanism by which this goal is  
 889 achieved is known as the *Higgs mechanism* and is closely connected to the concept of  
 890 *spontaneous symmetry breaking*.

### 891 2.3.1 Spontaneous symmetry breaking (SSB)

892 Figure 2.6 left shows a steel nail (top) which is subject to an external force; the form  
 893 of the potential energy is also shown (bottom).

894 Before reaching the critical force value, the system has rotational symmetry with  
 895 respect to the nail axis; however, after the critical force value is reached the nail buck-  
 896 les (top right). The form of the potential energy (bottom right) changes appearing a  
 897 set of infinity minima but preserving its rotational symmetry. Right before the nail  
 898 buckles there is no indication of the direction the nail will bend because any of the  
 899 directions are equivalent, but once the nail bends, choosing a direction, an arbitrary  
 900 minimal energy state (ground state) is selected and it does not share the system's  
 901 rotational symmetry. This mechanism for reaching an asymmetric ground state is  
 902 known as *spontaneous symmetry breaking*.

903 The lesson from this analysis is that the way to introduce the SSB mechanism  
 904 into a system is by adding the appropriate potential to it.

905 Figure 2.7 shows a plot of the potential  $V(\phi)$  in the case of a scalar field  $\phi$

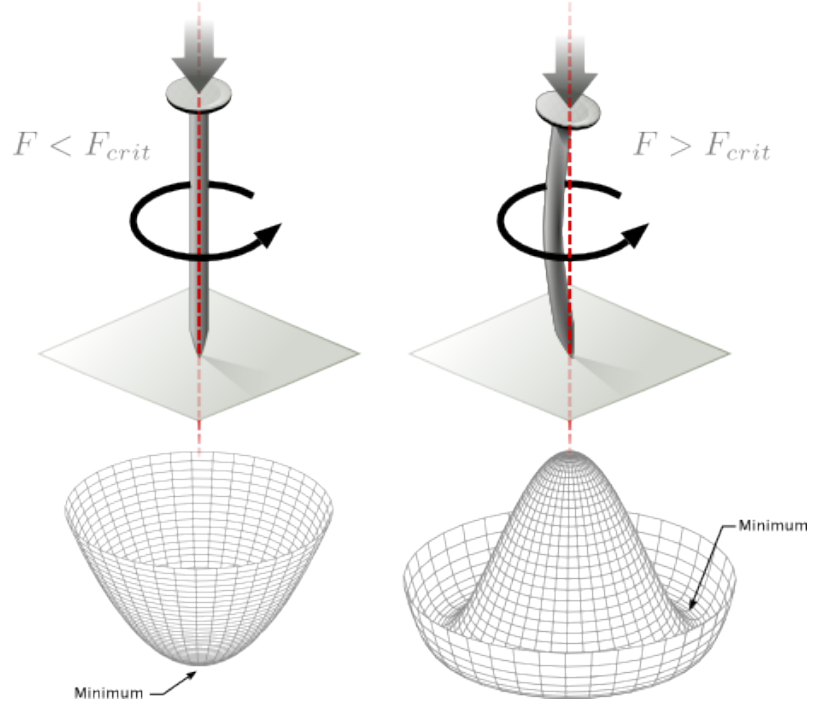


**Figure 2.6:** Spontaneous symmetry breaking mechanism. The steel nail, subject to an external force (top left), has rotational symmetry with respect to its axis. When the external force overcomes a critical value the nail buckles (top right) choosing a minimal energy state (ground state) and thus *breaking spontaneously the rotational symmetry*. The potential energy (bottom) changes but holds the rotational symmetry; however, an infinite number of asymmetric ground states are generated and circularly distributed in the bottom of the potential [31].

$$V(\phi) = \mu^2 \phi^\dagger \phi + \lambda (\phi^\dagger \phi)^2 \quad (2.32)$$

906     If  $\mu^2 > 0$  the potential has only one minimum at  $\phi = 0$  and describes a scalar field  
 907    with mass  $\mu$ . If  $\mu^2 < 0$  the potential has a local maximum at  $\phi = 0$  and two minima  
 908    at  $\phi = \pm\sqrt{-\mu^2/\lambda}$  which enables the SSB mechanism to work.

909     In the case of a complex scalar field  $\phi(x)$

$$\phi(x) = \frac{1}{\sqrt{2}}(\phi_1 + i\phi_2) \quad (2.33)$$

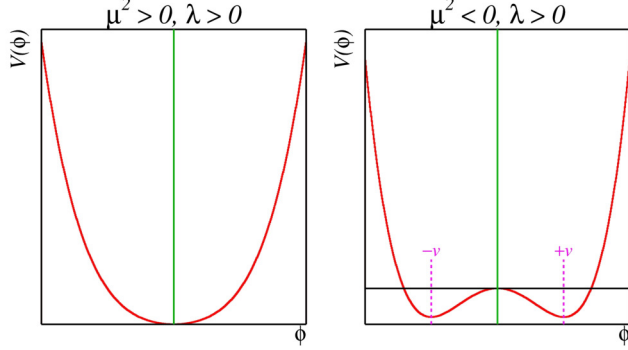


**Figure 2.7:** Shape of the potential  $V(\phi)$  for  $\lambda > 0$  and:  $\mu^2 > 0$  (left) and  $\mu^2 < 0$  (right). The case  $\mu^2 < 0$  corresponds to the potential suitable for introducing the SSB mechanism by choosing one of the two ground states which are connected via reflection symmetry. [31].

910 the Lagrangian (invariant under global  $U(1)$  transformations) is given by

$$\mathcal{L} = (\partial_\mu \phi)^\dagger (\partial^\mu \phi) - V(\phi), \quad V(\phi) = \mu^2 \phi^\dagger \phi + \lambda (\phi^\dagger \phi)^2 \quad (2.34)$$

911 where an appropriate potential has been added in order to introduce the SSB.

912 As seen in Figure 2.8, the potential has now an infinite number of minima circularly  
913 distributed along the  $\xi$ -direction which makes possible the occurrence of the SSB by  
914 choosing an arbitrary ground state; for instance,  $\xi = 0$ , i.e.  $\phi_1 = v, \phi_2 = 0$

$$\phi_0 = \frac{v}{\sqrt{2}} \exp(i\xi) \xrightarrow{\text{SSB}} \phi_0 = \frac{v}{\sqrt{2}} \quad (2.35)$$

915 As usual, excitations over the ground state are studied by making an expansion  
916 about it; thus, the excitations can be parametrized as:

$$\phi(x) = \frac{1}{\sqrt{2}}(v + \eta(x) + i\xi(x)) \quad (2.36)$$

917 which when substituted into Eqn. 2.34 produces a Lagrangian in terms of the new  
918 fields  $\eta$  and  $\xi$

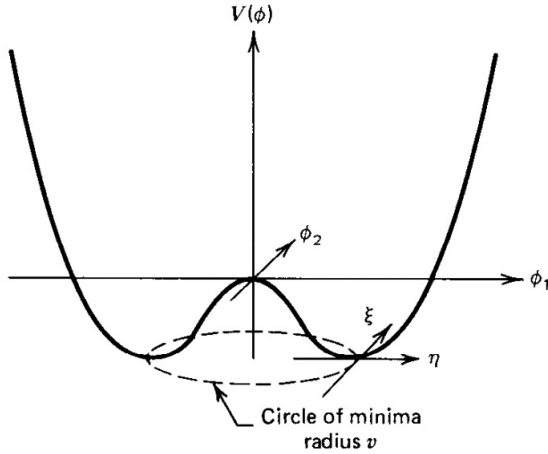


**Figure 2.8:** Potential for complex scalar field. There is a circle of minima of radius  $v$  along the  $\xi$ -direction [6].

$$\mathcal{L}' = \frac{1}{2}(\partial_\mu \xi)^2 + \frac{1}{2}(\partial_\mu \eta)^2 + \mu^2 \eta^2 - V(\phi_0) - \lambda v \eta (\eta^2 + \xi^2) - \frac{\lambda}{4}(\eta^2 + \xi^2)^2 \quad (2.37)$$

where the last two terms represent the interactions and self-interaction between the two fields  $\eta$  and  $\xi$ . The particular feature of the SSB mechanism is revealed when looking to the first three terms of  $\mathcal{L}'$ . Before the SSB, only the massless  $\phi$  field is present in the system; after the SSB there are two fields of which the  $\eta$ -field has acquired mass  $m_\eta = \sqrt{-2\mu^2}$  while the  $\xi$ -field is still massless (see Figure 2.9).

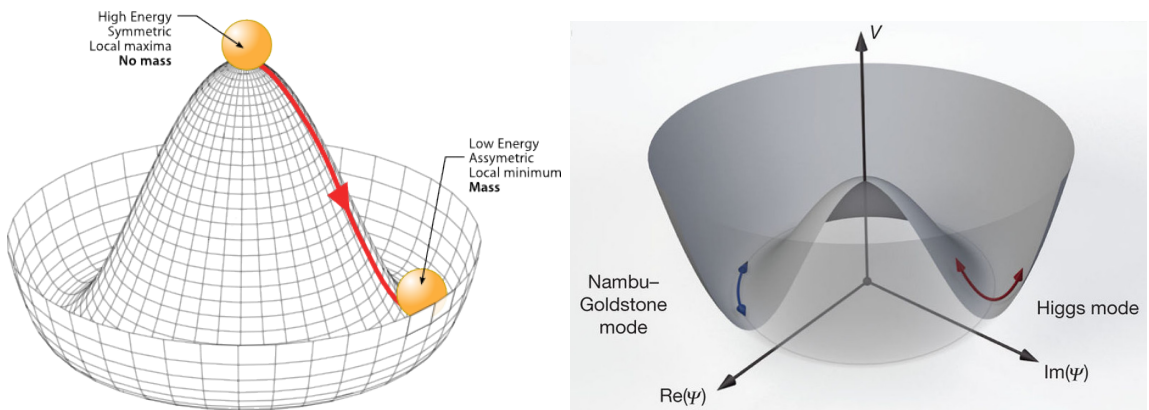


**Figure 2.9:** SSB mechanism for a complex scalar field [31, 32].

924     Thus, the SSB mechanism serves as a method to generate mass but as a side  
 925     effect a massless field is introduced in the system. This fact is known as the Gold-  
 926     stone theorem and states that a massless scalar field appears in the system for each  
 927     continuous symmetry spontaneously broken. Another version of the Goldstone theo-  
 928     rem states that “*if a Lagrangian is invariant under a continuous symmetry group  $G$ ,*  
 929     *but the vacuum is only invariant under a subgroup  $H \subset G$ , then there must exist as*  
 930     *many massless spin-0 particles (Nambu-Goldstone bosons) as broken generators.*” [26]  
 931     The Nambu-Goldstone boson can be understood considering that the potential in the  
 932      $\xi$  – direction is flat so excitations in that direction are not energy consuming and  
 933     thus represent a massless state.

### 934     **2.3.2 Higgs mechanism**

935     When the SSB mechanism is introduced in the formulation of the EWI in an attempt  
 936     to generate the mass of the so far massless gauge bosons and fermions, an interesting  
 937     effect is revealed. In order to keep the  $G$  symmetry group invariance and generate  
 938     the mass of the EW gauge bosons, a  $G$  invariant Lagrangian density ( $\mathcal{L}_S$ ) has to be  
 939     added to the non massive EWI Lagrangian (Eqn. 2.31)

$$\mathcal{L}_S = (D_\mu \phi)^\dagger (D^\mu \phi) - \mu^2 \phi^\dagger \phi - \lambda (\phi^\dagger \phi)^2, \quad \lambda > 0, \mu^2 < 0 \quad (2.38)$$

$$D_\mu \phi = \left( i\partial_\mu - g \frac{\sigma_i}{2} W_\mu^i - g' \frac{Y}{2} B_\mu \right) \phi \quad (2.39)$$

940      $\phi$  has to be an isospin doublet of complex scalar fields so it preserves the  $G$  invariance;  
 941     thus  $\phi$  can be defined as:

$$\phi = \begin{pmatrix} \phi^+ \\ \phi^0 \end{pmatrix} \equiv \frac{1}{\sqrt{2}} \begin{pmatrix} \phi_1 + i\phi_2 \\ \phi_3 + i\phi_4 \end{pmatrix}. \quad (2.40)$$

942 The minima of the potential are defined by

$$\phi^\dagger \phi = \frac{1}{2} (\phi_1^2 + \phi_2^2 + \phi_3^2 + \phi_4^2) = -\frac{\mu^2}{2\lambda}. \quad (2.41)$$

943 The choice of the ground state is critical. By choosing a ground state, invariant  
 944 under  $U(1)_{em}$  gauge symmetry, the photon will remain massless and the  $W^\pm$  and  $Z$   
 945 bosons masses will be generated which is exactly what is needed. In that sense, the  
 946 best choice corresponds to a weak isospin doublet with  $T_3 = -1/2$ ,  $Y_W = 1$  and  $Q = 0$   
 947 which defines a ground state with  $\phi_1 = \phi_2 = \phi_4$  and  $\phi_3 = v$ :

$$\phi_0 \equiv \frac{1}{\sqrt{2}} \begin{pmatrix} 0 \\ v \end{pmatrix}, \quad v^2 \equiv -\frac{\mu^2}{\lambda}. \quad (2.42)$$

948 where the vacuum expectation value  $v$  is fixed by the Fermi coupling  $G_F$  according  
 949 to  $v = (\sqrt{2}G_F)^{1/2} \approx 246$  GeV.

950 The G symmetry has been broken and three Nambu-Goldstone bosons will appear.  
 951 The next step is to expand  $\phi$  about the chosen ground state as:

$$\phi(x) = \frac{1}{\sqrt{2}} \exp \left( \frac{i}{v} \sigma_i \theta^i(x) \right) \begin{pmatrix} 0 \\ v + H(x) \end{pmatrix} \approx \frac{1}{\sqrt{2}} \begin{pmatrix} \theta_1(x) + i\theta_2(x) \\ v + H(x) - i\theta_3(x) \end{pmatrix} \quad (2.43)$$

952 to describe fluctuations from the ground state  $\phi_0$ . The fields  $\theta_i(x)$  represent the  
 953 Nambu-Goldstone bosons while  $H(x)$  is known as *Higgs field*. The fundamental fea-  
 954 ture of the parametrization used is that the dependence on the  $\theta_i(x)$  fields is factored  
 955 out in a global phase that can be eliminated by taking the physical *unitary gauge*

956  $\theta_i(x) = 0$ . Therefore the expansion about the ground state is given by:

$$\phi(x) \frac{1}{\sqrt{2}} \begin{pmatrix} 0 \\ v + H(x) \end{pmatrix} \quad (2.44)$$

957 which when substituted into  $\mathcal{L}_S$  (Eqn. 2.38) results in a Lagrangian containing the  
 958 now massive three gauge bosons  $W^\pm, Z$ , one massless gauge boson (photon) and  
 959 the new Higgs field ( $H$ ). The three degrees of freedom corresponding to the Nambu-  
 960 Goldstone bosons are now integrated into the massive gauge bosons as their lon-  
 961 gitudinal polarizations which were not available when they were massless particles.  
 962 The effect by which vector boson fields acquire mass after an spontaneous symmetry  
 963 breaking, but without an explicit gauge invariance breaking is known as the *Higgs*  
 964 *mechanism*.

965 The mechanism was proposed by three independent groups: F.Englert and R.Brout  
 966 in August 1964 [33], P.Higgs in October 1964 [34] and G.Guralnik, C.Hagen and  
 967 T.Kibble in November 1964 [35]; however, its importance was not realized until  
 968 S.Glashow [22], A.Salam [23] and S.Weinberg [24], independently, proposed that elec-  
 969 tromagnetic and weak interactions are two manifestations of a more general interac-  
 970 tion called *electroweak interaction* in 1967.

### 971 2.3.3 Masses of the gauge bosons

972 The masses of the gauge bosons are extracted by evaluating the kinetic part of La-  
 973 grangian  $\mathcal{L}_S$  in the ground state (known also as the vacuum expectation value), i.e.,

$$\left| \left( \partial_\mu - ig \frac{\sigma_i}{2} W_\mu^i - i \frac{g'}{2} B_\mu \right) \phi_0 \right|^2 = \left( \frac{1}{2} vg \right)^2 W_\mu^+ W^{-\mu} + \frac{1}{8} v^2 (W_\mu^3, B_\mu) \begin{pmatrix} g^2 & -gg' \\ -gg' & g'^2 \end{pmatrix} \begin{pmatrix} W^{3\mu} \\ B^\mu \end{pmatrix} \quad (2.45)$$

974 comparing with the typical mass term for a charged boson  $M_W^2 W^+ W^-$

$$M_W = \frac{1}{2} v g. \quad (2.46)$$

The second term in the right side of the Eqn.2.45 comprises the masses of the neutral bosons, but it needs to be written in terms of the gauge fields  $Z_\mu$  and  $A_\mu$  in order to be compared to the typical mass terms for neutral bosons, therefore using Eqn. 2.30

$$\begin{aligned} \frac{1}{8} v^2 [g^2 (W_\mu^3)^2 - 2gg' W_\mu^3 B^\mu + g'^2 B_\mu^2] &= \frac{1}{8} v^2 [g W_\mu^3 - g' B_\mu]^2 + 0[g' W_\mu^3 + g B_\mu]^2 \quad (2.47) \\ &= \frac{1}{8} v^2 [\sqrt{g^2 + g'^2} Z_\mu]^2 + 0[\sqrt{g^2 + g'^2} A_\mu]^2 \end{aligned}$$

975 and then

$$M_Z = \frac{1}{2} v \sqrt{g^2 + g'^2}, \quad M_A = 0 \quad (2.48)$$

### 976 2.3.4 Masses of the fermions

977 The lepton mass terms can be generated by introducing a gauge invariant Lagrangian

978 term describing the Yukawa coupling between the lepton field and the Higgs field

$$\mathcal{L}_{Yl} = -G_l \left[ (\bar{\nu}_l, \bar{l})_L \begin{pmatrix} \phi^+ \\ \phi^0 \end{pmatrix} l_R + \bar{l}_R (\phi^-, \bar{\phi}^0) \begin{pmatrix} \nu_l \\ l \end{pmatrix} \right], \quad l = e, \mu, \tau. \quad (2.49)$$

979 After the SSB and replacing the usual field expansion about the ground state

980 (Eqn.2.42) into  $\mathcal{L}_{Yl}$ , the mass term arises

$$\mathcal{L}_{Yl} = -m_l (\bar{l}_L l_R + \bar{l}_R l_L) - \frac{m_l}{v} (\bar{l}_L l_R + \bar{l}_R l_L) H = -m_l \bar{l} l \left( 1 + \frac{H}{v} \right) \quad (2.50)$$

981

$$m_l = \frac{G_l}{\sqrt{2}} v \quad (2.51)$$

982 where the additional term represents the lepton-Higgs interaction. The quark masses  
 983 are generated in a similar way as lepton masses but for the upper member of the  
 984 quark doublet a different Higgs doublet is needed:

$$\phi_c = -i\sigma_2\phi^* = \begin{pmatrix} -\bar{\phi}^0 \\ \phi^- \end{pmatrix}. \quad (2.52)$$

985 Additionally, given that the quark isospin doublets are not constructed in terms  
 986 of the mass eigenstates but in terms of the flavor eigenstates, as shown in Table 2.5,  
 987 the coupling parameters will be related to the CKM matrix elements; thus, the quark  
 988 Lagrangian is given by:

$$\mathcal{L}_{Yq} = -G_d^{i,j}(\bar{u}_i, \bar{d}'_i)_L \begin{pmatrix} \phi^+ \\ \phi^0 \end{pmatrix} d_{jR} - G_u^{i,j}(\bar{u}_i, \bar{d}''_i)_L \begin{pmatrix} -\bar{\phi}^0 \\ \phi^- \end{pmatrix} u_{jR} + h.c. \quad (2.53)$$

989 with  $i,j=1,2,3$ . After SSB and expansion about the ground state, the diagonal form  
 990 of  $\mathcal{L}_{Yq}$  is:

$$\mathcal{L}_{Yq} = -m_d^i \bar{d}_i d_i \left(1 + \frac{H}{v}\right) - m_u^i \bar{u}_i u_i \left(1 + \frac{H}{v}\right) \quad (2.54)$$

991 Fermion masses depend on arbitrary couplings  $G_l$  and  $G_{u,d}$  and are not predicted  
 992 by the theory.

### 993 2.3.5 The Higgs field

994 After the characterization of the fermions and gauge bosons as well as their interac-  
 995 tions, it is necessary to characterize the Higgs field itself. The Lagrangian  $\mathcal{L}_S$  in Eqn.

996 2.38 written in terms of the gauge bosons is given by

$$\mathcal{L}_S = \frac{1}{4}\lambda v^4 + \mathcal{L}_H + \mathcal{L}_{HV} \quad (2.55)$$

997  $\mathcal{L}_H = \frac{1}{2}\partial_\mu H\partial^\mu H - \frac{1}{2}m_H^2 H^2 - \frac{1}{2v}m_H^2 H^3 - \frac{1}{8v^2}m_H^2 H^4 \quad (2.56)$

998  $\mathcal{L}_{HV} = m_H^2 W_\mu^+ W^{\mu-} \left(1 + \frac{2}{v}H + \frac{2}{v^2}H^2\right) + \frac{1}{2}m_Z^2 Z_\mu Z^\mu \left(1 + \frac{2}{v}H + \frac{2}{v^2}H^2\right) \quad (2.57)$

999 The mass of the Higgs boson is deduced as usual from the mass term in the Lagrangian  
1000 resulting in:

$$m_H = \sqrt{-2\mu^2} = \sqrt{2\lambda}v \quad (2.58)$$

1001 however, it is not predicted by the theory either. The experimental measurement of  
1002 the Higgs boson mass have been performed by the *Compact Muon Solenoid (CMS)*  
1003 experiment and the *A Toroidal LHC Appartus (ATLAS)* experiments at the *Large  
1004 Hadron Collider(LHC)*, [36–38], and is presented in Table 2.8.

Property	Value
Electric charge	0
Color charge	0
Spin	0
Weak isospin	-1/2
Weak hypercharge	1
Parity	1
Mass (GeV/c <sup>2</sup> )	125.09±0.21 (stat.)±0.11 (syst.)

**Table 2.8:** Higgs boson properties. Higgs mass is not predicted by the theory and the value here corresponds to the experimental measurement.

### 1005 2.3.6 Production of Higgs bosons at LHC

1006 At the LHC, Higgs bosons are produced as a result of the collision of two counter-  
1007 rotating protons beams. A detailed description of the LHC machine will be presented  
1008 in chapter 3.

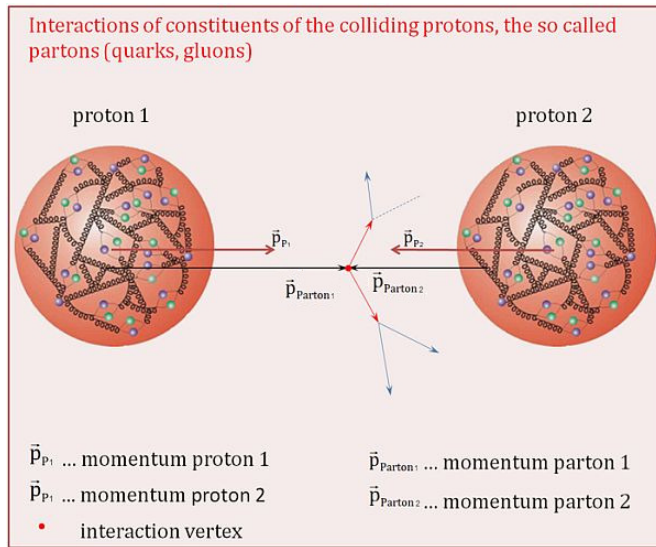


**Figure 2.10:** Proton-proton collision. Protons are composed of 3 valence quarks, a sea of quarks and gluons; therefore in a proton-proton collision, quarks and gluons are those who collide. [39].

1009 Protons are composed of quarks and these quarks are bound by gluons; however,  
1010 what is commonly called the quark content of the proton makes reference to the  
1011 valence quarks. In fact, a proton is not just a rigid entity with three balls in it all  
1012 tied up with springs, but the gluons exchanged by the valence quarks tend to split  
1013 spontaneously into quark-antiquark pairs or more gluons, creating *sea of quarks and*  
1014 *gluons* as represented in Figure 2.10.

In a proton-proton ( $pp$ ) collision, the proton's constituents, quarks and gluons, are those that collide. The  $pp$  cross section depends on the momentum of the colliding particles, reason for which it is needed to know how the momentum is distributed inside the proton. Quarks and gluons are known as partons, hence, the functions that describe how the proton momentum is distributed among partons inside it are called *parton distribution functions (PDFs)*; PDFs are determined from experimental data obtained in experiments where the internal structure of hadrons is tested, and depend on the momentum transfer  $Q$  and the fraction of momentum  $x$  carried by an

1023 specific parton. Figure 2.11 shows the proton PDFs ( $xf(x, Q^2)$ ) for two values of  $Q$ .

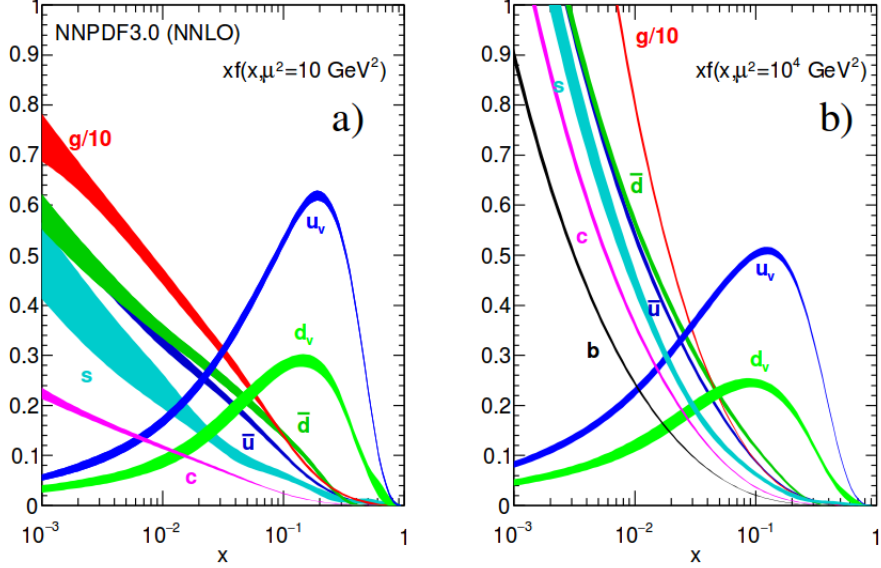


**Figure 2.11:** Proton PDFs for two values of  $Q^2$ : left.  $\mu^2 = Q^2 = 10 \text{ GeV}^2$ , right.  $\mu^2 = Q^2 = 10^4 \text{ GeV}^2$ .  $u_v$  and  $d_v$  correspond to the  $u$  and  $d$  valence quarks,  $s, c, b, \bar{u}, \bar{d}$  correspond to sea quarks, and  $g$  corresponds to gluons. Note that gluons carry a high fraction of the proton's momentum. [9]

1024 In physics, a common approach to study complex systems consists of starting  
 1025 with a simpler version of them, for which a well known description is available, and  
 1026 adding an additional *perturbation* which represents a small deviation from the known  
 1027 behavior. If the perturbation is small enough, the physical quantities associated with  
 1028 the perturbed system are expressed as a series of corrections to those of the simpler  
 1029 system. The perturbation series corresponds to an expansion in power series of a small  
 1030 parameter, therefore, the more terms are considered in the series (the higher order  
 1031 in the perturbation series), the more precise is the the description of the complex  
 1032 system. If the perturbation does not get progressively smaller, the strategy cannot  
 1033 be applied and new methods have to be employed.

1034 High energy systems, like the Higgs production at LHC explored in this thesis,  
 1035 usually can be treated perturbatively with the expansion made in terms of the cou-

pling constants. The overview presented here will be oriented specifically to the Higgs boson production mechanisms in  $pp$  collisions at LHC.

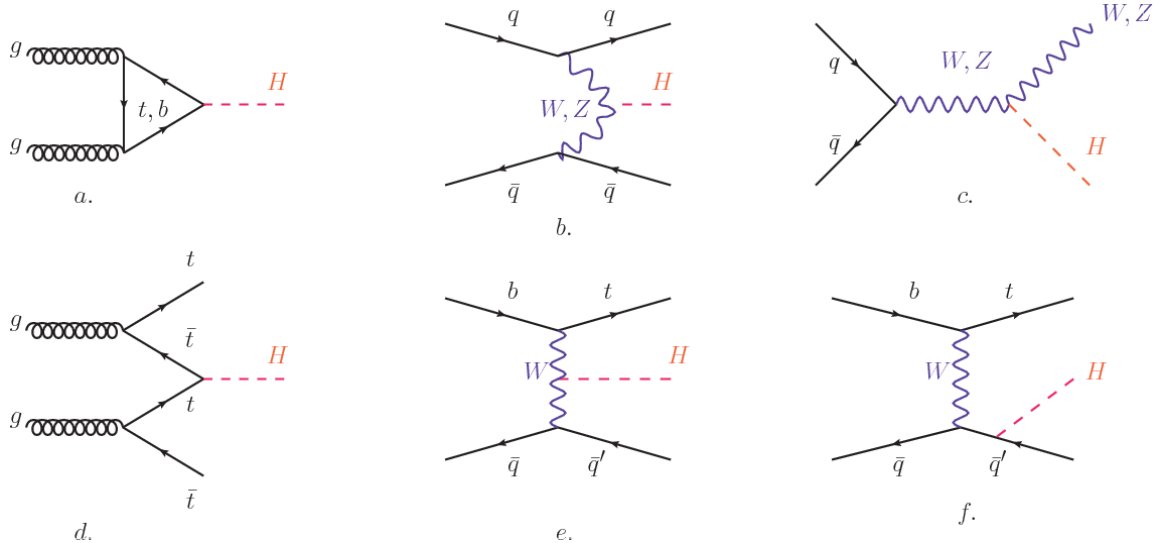


**Figure 2.12:** Main Higgs boson production mechanism Feynman diagrams. a. gluon-gluon fusion, b. vector boson fusion (VBF), c. Higgs-strahlung, d. Associated production with a top or bottom quark pair, e-f. associated production with a single top quark.

Figure 2.12 shows the Feynman diagrams for the leading order (first order LO) Higgs production processes at LHC; note that in these diagrams the incoming particles are not the protons themselves but the partons from the protons that actually participate in the interaction, hence, theorists typically calculate the cross section for the parton interaction, and then convolute that cross section with the information from the PDFs to get a production cross section that is actually measured in experiments. The cross section for Higgs production as a function of the center of mass-energy ( $\sqrt{s}$ ) for  $pp$  collisions is showed in Figure 2.13 left. The tags NLO (next to leading order), NNLO (next to next to leading order) and N3LO (next to next to next to leading order) make reference to the order at which the perturbation series have been considered while the tags QCD and EW correspond to the strong and electroweak coupling constants respectively.

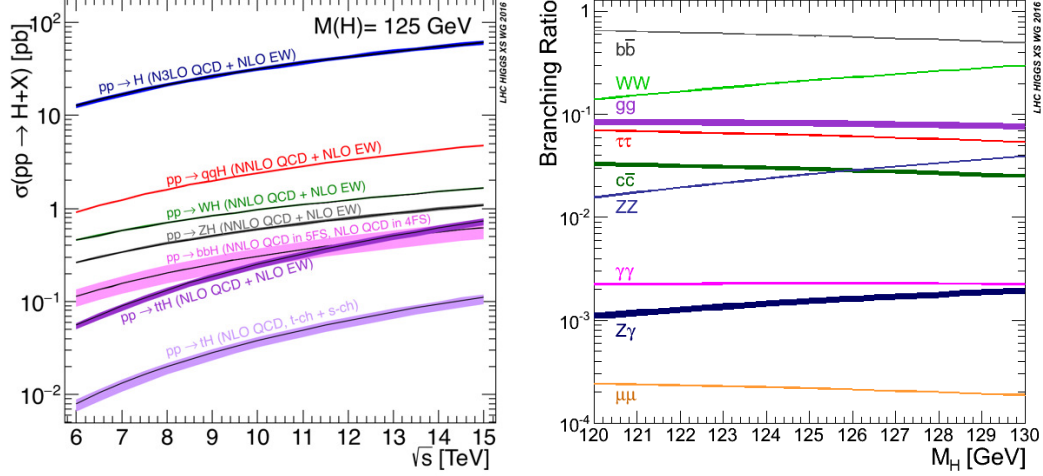


**Figure 2.13:** Higgs boson production cross sections (left) and decay branching ratios (right) for the main mechanisms. The VBF is indicated as  $qqH$  [40].

1050        The main production mechanism is the gluon fusion (Figure 2.12a and  $pp \rightarrow H$   
 1051        in Figure 2.13) given that gluons carry the highest fraction of momentum of the  
 1052        protons in  $pp$  colliders (as shown in Figure 2.11). Since the Higgs boson does not  
 1053        couple to gluons, the mechanism proceeds through the exchange of a virtual top-quark  
 1054        loop. Note that in this process the Higgs boson is produced alone, turning out to  
 1055        be problematic for some Higgs decays, because such absence of anything produced in  
 1056        association with the Higgs represent a trouble for triggering, however, this mechanism  
 1057        is experimentally clean when combined with the two-photon or the four-lepton decay  
 1058        channels (see Section 2.3.7).

1059        Vector boson fusion (Figure 2.12b and  $pp \rightarrow qqH$  in Figure 2.13) has the second  
 1060        largest production cross section. The scattering of two fermions is mediated by a weak  
 1061        gauge boson which later emits a Higgs boson. In the final state, the two fermions tend  
 1062        to be located in the central region of the detector; this kind of features are generally  
 1063        used as a signature when analyzing the datasets provided by the experiments<sup>7</sup>.

1064        In the Higgs-strahlung mechanism (Figure 2.12c and  $pp \rightarrow WH, pp \rightarrow ZH$  in

<sup>7</sup> More details about how to identify events of interest in this analysis will be given in chapter 6.

1065 Figure 2.13) two fermions annihilate to form a weak gauge boson. If the initial  
 1066 fermions have enough energy, the emergent boson might emit a Higgs boson.

1067 The associated production with a top or bottom quark pair and the associated  
 1068 production with a single top quark (Figure 2.12d-f and  $pp \rightarrow bbH, pp \rightarrow t\bar{t}H, pp \rightarrow tH$   
 1069 in Figure 2.13) have a smaller cross section than the main three mechanisms above,  
 1070 but they provide a good opportunity to test the Higgs-top coupling. The analysis  
 1071 reported in this thesis is developed using these production mechanisms. A detailed  
 1072 description of the  $tH$  mechanism will be given in Section 2.5.

### 1073 2.3.7 Higgs boson decay channels

1074 When a particle can decay through several modes, also known as channels, the prob-  
 1075 ability of decaying through a given channel is quantified by the *branching ratio (BR)*  
 1076 of the decay channel; thus, the BR is defined as the ratio of number of decays go-  
 1077 ing through that given channel to the total number of decays. In regard to the  
 1078 Higgs boson decay, the BR can be predicted with accuracy once the Higgs mass is  
 1079 known [41, 42]. In Figure 2.13 right, a plot of the BR as a function of the Higgs mass  
 1080 is presented; the largest predicted BR corresponds to the  $b\bar{b}$  pair decay channel (see  
 1081 Table 2.9) given that it is the heaviest particle pair whose on-shell<sup>8</sup> production is  
 1082 kinematically allowed in the decay.

1083 Decays to other lepton and quark pairs, like electron, strange, up, and down  
 1084 quark pairs not listed in the table, are also possible but their likelihood is too small  
 1085 to measure since they are very lightweight, hence, their interaction with the Higgs  
 1086 boson is very weak. On other hand, the decay to top quark pairs is heavily suppressed

---

<sup>8</sup> In general, on-shell or real particles are those which satisfy the energy-momentum relation ( $E^2 - |\vec{p}|^2 c^2 = m^2 c^4$ ); off-shell or virtual particles does not satisfy it which is possible under the uncertainty principle of quantum mechanics. Usually, virtual particles correspond to internal propagators in Feynman diagrams.

Decay channel	Branching ratio	Rel. uncertainty
$H \rightarrow b\bar{b}$	$5.84 \times 10^{-1}$	+3.2% – 3.3%
$H \rightarrow W^+W^-$	$2.14 \times 10^{-1}$	+4.3% – 4.2%
$H \rightarrow \tau^+\tau^-$	$6.27 \times 10^{-2}$	+5.7% – 5.7%
$H \rightarrow ZZ$	$2.62 \times 10^{-2}$	+4.3% – 4.1%
$H \rightarrow \gamma\gamma$	$2.27 \times 10^{-3}$	+5.0% – 4.9%
$H \rightarrow Z\gamma$	$1.53 \times 10^{-3}$	+9.0% – 8.9%
$H \rightarrow \mu^+\mu^-$	$2.18 \times 10^{-4}$	+6.0% – 5.9%

**Table 2.9:** Predicted branching ratios and the relative uncertainty for some decay channels of a SM Higgs boson with  $m_H = 125$  GeV/c<sup>2</sup> [9]

1087 due to the top quark mass ( $\approx 173$  GeV/c<sup>2</sup>).

1088 Decays to gluons proceed indirectly through a virtual top quark loop while the  
 1089 decays to photons proceed through a virtual W boson loop, therefore, their branching  
 1090 ratio is smaller compared to direct interaction decays. Same is true for the decay to  
 1091 a photon and a Z boson.

1092 In the case of decays to pairs of W and Z bosons, the decay proceed with one of  
 1093 the bosons being on-shell and the other being off-shell. The likelihood of the process  
 1094 diminish depending on how far off-shell are the virtual particles involved, hence, the  
 1095 branching ratio for W boson pairs is bigger than for Z boson pairs since Z boson mass  
 1096 is bigger than W boson mass.

1097 Note that the decay to a pair of virtual top quarks is possible, but the probability  
 1098 is way too small.

## 1099 2.4 Experimental status of the anomalous 1100 Higgs-fermion coupling

1101 ATLAS and CMS have performed analyses of the anomalous Higgs-fermion coupling  
 1102 by making likelihood scans for the two coupling modifiers,  $\kappa_f$  and  $\kappa_V$ , under the

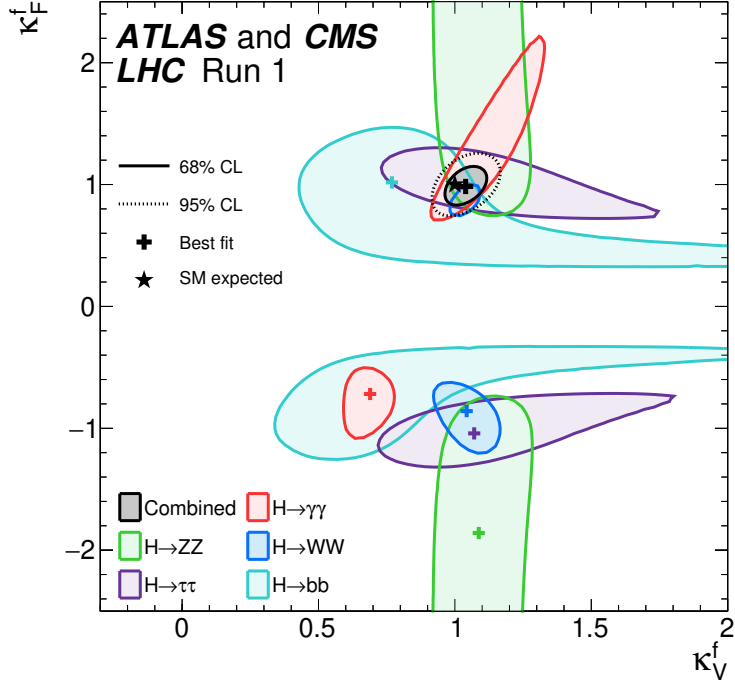


**Figure 2.14:** Combination of the ATLAS and CMS fits for coupling modifiers  $\kappa_t - \kappa_V$ ; also shown the individual decay channels combination and their global combination. No assumptions have been made on the sign of the coupling modifiers [44].

assumption that  $\kappa_Z = \kappa_W \equiv \kappa_V$  and  $\kappa_t = \kappa_\tau = \kappa_b \equiv \kappa_f$ . Figure 2.14 shows the

result of the combination of ATLAS and CMS fits; also the individual decay channels

combination and the global combination results are shown. Note that from this plot

there is limited information on the sign of the coupling since the only information

available about the sign of the coupling comes from decays rather than production.

While all the channels are compatible for positive values of the modifiers, for

negative values of  $\kappa_f$  there is no compatibility. The best fit for individual channels

is compatible with negative values of  $\kappa_f$  except for the  $H \rightarrow bb$  channel. The best

fit for the combination yields  $\kappa_f \geq 0$ , in contrast to the yields from the individual

channels; the reason of this yield resides in the  $H \rightarrow \gamma\gamma$  coupling.  $H \rightarrow \gamma\gamma$  decay

proceeds through a loop of either top quarks or W bosons, hence, this channel is

1114 sensitive to  $\kappa_t$  thanks to the interference of these two amplitude contributions; under  
 1115 the assumption that no beyond SM particles take part in the loops, a flipped sign  
 1116 of  $\kappa_t$  will increase the  $H \rightarrow \gamma\gamma$  branching fraction by a factor of  $\sim 2.4$  which is not  
 1117 supported by measurements; thus, this large asymmetry between the positive and  
 1118 negative coupling ratios in the  $H \rightarrow \gamma\gamma$  channel drives the yield of the global fit and  
 1119 would mean that the anomalous H-t coupling is excluded as stated in Reference [44],  
 1120 but there is a caveat, this exclusion holds only if no new particles contribute to the  
 1121 loop in the main diagram for that decay.

1122 Although the  $H \rightarrow bb$  channel is expected to be the most sensitive channel and  
 1123 its best fit value of  $\kappa_t$  is positive, and then the global fit yield is still supported,  
 1124 the contributions from all the other decay channels, small compared to the  $H \rightarrow bb$ ,  
 1125 indicate that the anomalous H-t coupling cannot be excluded completely, motivating  
 1126 to look at  $tH$  processes which can help with both, the limited information on the sign  
 1127 of the H-t coupling and the access to information from the Higgs boson production  
 1128 rather than from its decays. It will be shown in Section 2.5 that the same interference  
 1129 effect enhance the  $tH$  production rate and could reveal evidence of direct production  
 1130 of heavy new particles as predicted in composite and little Higgs models [45], or new  
 1131 physics related to Higgs boson mediated flavor changing neutral currents [46] as well  
 1132 as probes the CP-violating phase of the H-t coupling [47, 48].

## 1133 **2.5 Associated production of a Higgs boson and a 1134 single top quark**

1135 The production of Higgs boson in association with a top quark has been extensively  
 1136 studied [47, 49–52]. While measurements of the main Higgs production mechanisms

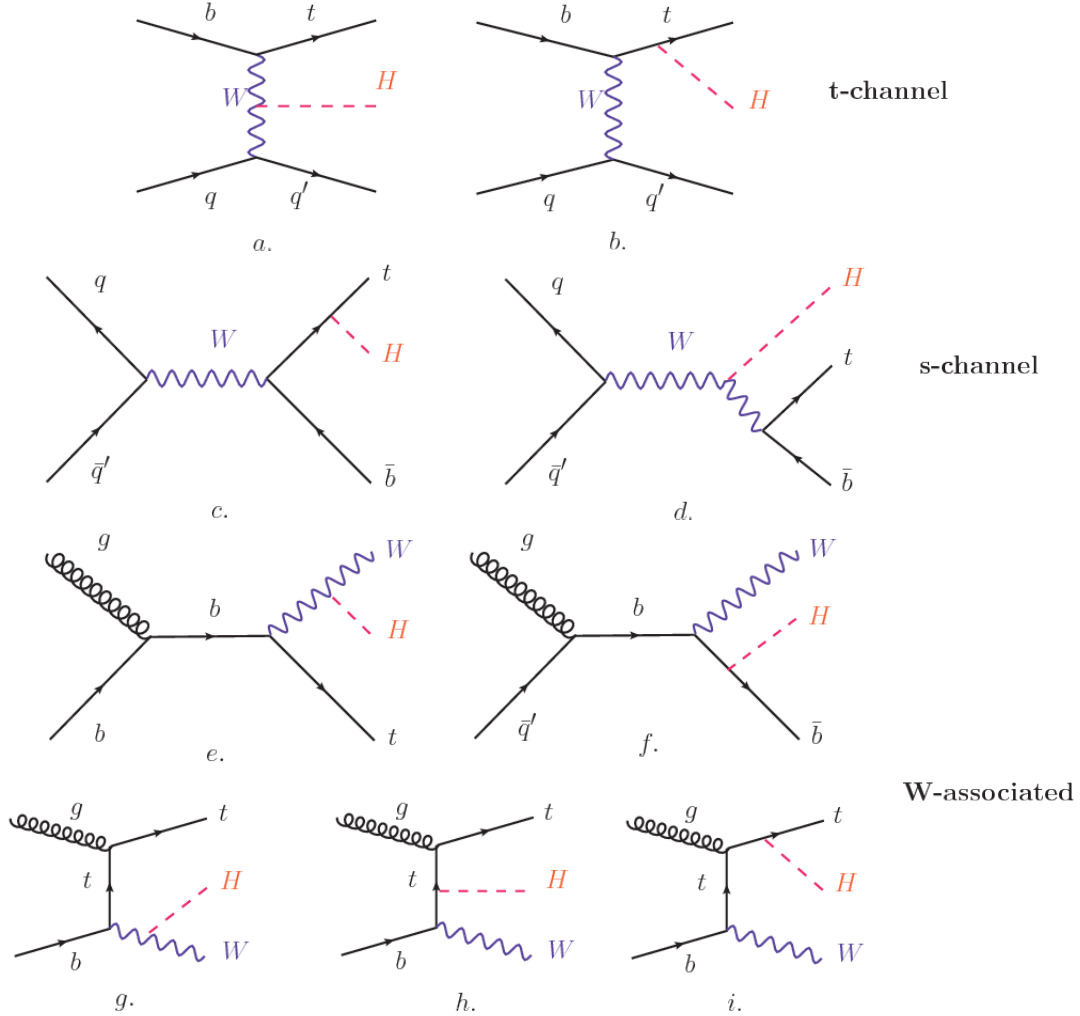


**Figure 2.15:** Associated Higgs boson production with a top quark mechanism Feynman diagrams. a.,b. t-channel ( $tHq$ ), c.,d. s-channel ( $tHb$ ), e-i. W-associated.

1137 rates are sensitive to the strength of the Higgs coupling to W boson or top quark,  
 1138 they are not sensitive to the relative sign between the two couplings. In this thesis,  
 1139 the Higgs boson production mechanism explored is the associated production with a  
 1140 single top quark ( $tH$ ) which offers sensitivity to the relative sign of the Higgs couplings  
 1141 to W boson and to top quark. The description given here is based on Reference [51].  
 1142 A process where two incoming particles interact and produce a final state with two  
 1143 particles can proceed in three called channels (see, for instance, Figure 2.15 omitting

the red line). The t-channel represents processes where an intermediate particle is emitted by one of the incoming particles and absorbed by the other. The s-channel represents processes where the two incoming particles merge into an intermediate particle which eventually will split into the particles in the final state. The third channel, u-channel, is similar to the t-channel but the two outgoing particles interchange their roles. These three channels are connected to the so-called Mandelstam variables

$$s = (p_1 + p_2)^2 = (p'_1 + p'_2)^2 \rightarrow \text{square of the center mass-energy.} \quad (2.59)$$

$$t = (p_1 - p'_1)^2 = (p'_2 - p_2)^2 \rightarrow \text{square of the four-momentum transfer.} \quad (2.60)$$

$$u = (p_1 - p'_2)^2 = (p'_1 - p_2)^2 \rightarrow \text{square of the crossed four-momentum transfer.} \quad (2.61)$$

$$s + t + u = m_1^2 + m_2^2 + m'_1^2 + m'_2^2 \quad (2.62)$$

which relate the momentum, energy and the angles of the incoming and outgoing particles in an scattering process of two particles to two particles. The importance of the Mandelstam variables reside in that they form a minimum set of variables needed to describe the kinematics of this scattering process; they are Lorentz invariant which makes them very useful when doing calculations.

The  $tH$  production, where Higgs boson can be radiated either from the top quark or from the W boson, is represented by the leading order Feynman diagrams in Figure 2.15. The cross section for the  $tH$  process is calculated, as usual, summing over the contributions from the different Feynman diagrams; therefore it depends on the interference between the contributions. In the SM, the interference for t-channel ( $tHq$  process) and W-associated ( $tHW$  process) production is destructive [49] resulting in the small cross sections presented in Table 2.10.

The s-channel contribution can be neglected. It will be shown that a deviation

tH production channel	Cross section (fb)
t-channel ( $pp \rightarrow tHq$ )	$70.79^{+2.99}_{-4.80}$
W-associated ( $pp \rightarrow tHW$ )	$15.61^{+0.83}_{-1.04}$
s-channel( $pp \rightarrow tHb$ )	$2.87^{+0.09}_{-0.08}$

**Table 2.10:** Predicted SM cross sections for  $tH$  production at  $\sqrt{s} = 13$  TeV [53, 54].

from the SM destructive interference would result in an enhancement of the  $tH$  cross section compared to that in SM, which could be used to get information about the sign of the Higgs-top coupling [51, 52]. In order to describe  $tH$  production processes, Feynman diagram 2.15b will be considered; there, the W boson is radiated by a quark in the proton and eventually it will interact with the b quark. In the high energy regime, the effective W approximation [55] is used to describe the process as the emission of an approximately on-shell W and its hard scattering with the b quark; i.e.  $Wb \rightarrow th$ . The scattering amplitude for the process is given by

$$\mathcal{A} = \frac{g}{\sqrt{2}} (\kappa_t - \kappa_V) \frac{m_t \sqrt{s}}{m_W v} A \left( \frac{t}{s}, \varphi; \xi_t, \xi_b \right) + \frac{g}{\sqrt{2}} \left( \kappa_V \frac{2m_W s}{v} \frac{1}{t} + (2\kappa_t - \kappa_V) \frac{m_t^2}{m_W v} \right) B \left( \frac{t}{s}, \varphi; \xi_t, \xi_b \right), \quad (2.63)$$

where  $\kappa_V \equiv g_{HVV}/g_{HVV}^{SM}$  and  $\kappa_t \equiv g_{Ht}/g_{Ht}^{SM} = y_t/y_t^{SM}$  are scaling factors that quantify possible deviations of the couplings from the SM values, Higgs-Vector boson (H-W) and Higgs-top (H-t) respectively, from the SM couplings;  $s = (p_W + p_b)^2$ ,  $t = (p_W - p_H)^2$ ,  $\varphi$  is the Higgs azimuthal angle around the  $z$  axis taken parallel to the direction of motion of the incoming W; A and B are functions describing the weak interaction in terms of the chiral states  $(\xi_t, \xi_b)$  of the quarks  $b$  and  $t$ . Terms that vanish in the high energy limit have been neglected as well as the Higgs and  $b$  quark masses<sup>9</sup>.

---

<sup>9</sup> A detailed explanation of the structure and approximations used to derive  $\mathcal{A}$  can be found in

1179        The scattering amplitude grows with energy like  $\sqrt{s}$  for  $\kappa_V \neq \kappa_t$ , in contrast to  
 1180    the SM ( $\kappa_t = \kappa_V = 1$ ), where the first term in 2.63 cancels out and the amplitude  
 1181    is constant for large s; therefore, a deviation from the SM predictions represents an  
 1182    enhancement in the  $tHq$  cross section. In particular, for a SM H-W coupling and  
 1183    a H-t coupling of inverted sign with respect to the SM ( $\kappa_V = -\kappa_t = 1$ ) the  $tHq$   
 1184    cross section is enhanced by a factor greater 10 as seen in the Figure 2.16 taken from  
 1185    Reference [51]; Reference [56] has reported similar enhancement results.

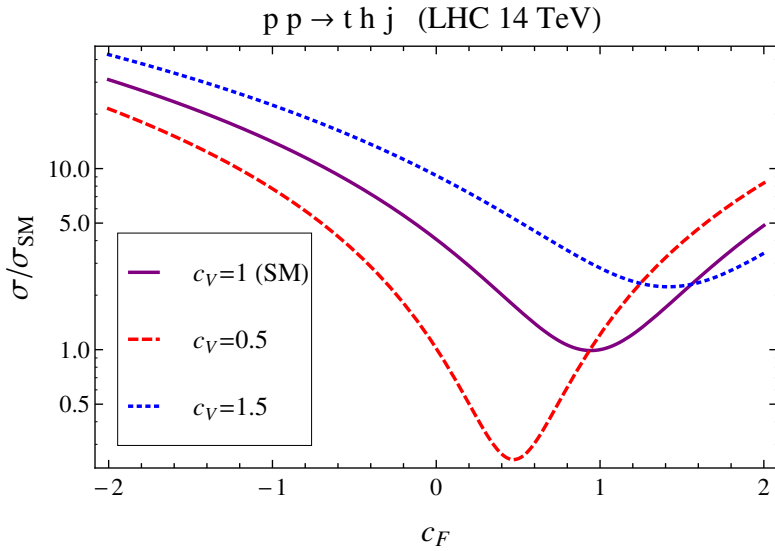


**Figure 2.16:** Cross section for  $tHq$  process as a function of  $\kappa_t$ , normalized to the SM, for three values of  $\kappa_V$ . In the plot  $c_f$  refers to the Higgs-fermion coupling which is dominated by the H-t coupling and represented here by  $\kappa_t$ . Solid, dashed and dotted lines correspond to  $c_V \rightarrow \kappa_V = 1, 0.5, 1.5$  respectively. Note that for the SM ( $\kappa_V = \kappa_t = 1$ ), the destructive effect of the interference is maximal.

1186        A similar analysis is valid for the W-associated channel but, in that case, the in-  
 1187    terference is more complicated since there are more than two contributions and an ad-  
 1188    ditional interference with the production of Higgs boson and a top pair process( $t\bar{t}H$ ).  
 1189    The calculations are made using the so-called Diagram Removal (DR) technique where  
 1190    interfering diagrams are removed (or added) from the calculations in order to evaluate

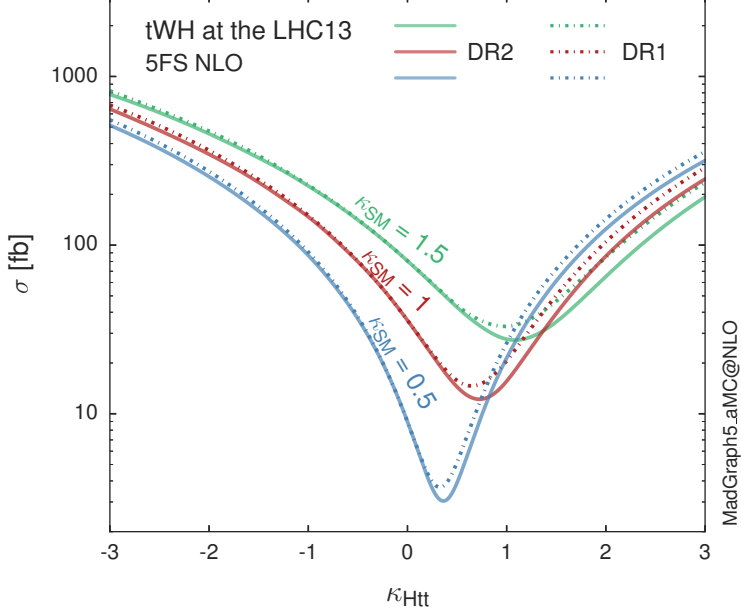


**Figure 2.17:** Cross section for  $tHW$  process as a function of  $\kappa_{Htt}$ , for three values of  $\kappa_{SM}$  at  $\sqrt{s} = 13$  TeV.  $\kappa_{Htt}^2 = \sigma_{Htt}/\sigma_{Htt}^{SM}$  is a simple re-scaling of the SM Higgs interactions.

the impact of the removed contributions. DR1 was defined to neglect  $t\bar{t}H$  interference while DR2 was defined to take  $t\bar{t}H$  interference into account [48]. As shown in Figure 2.17, the  $tHW$  cross section is enhanced from about 15 fb (SM:  $\kappa_{Htt} = 1$ ) to about 150 fb ( $\kappa_{Htt} = -1$ ). Differences between curves for DR1 and DR2 help to gauge the impact of the interference with  $t\bar{t}H$ . Results of the calculations of the  $tHq$  and  $tHW$  cross sections at  $\sqrt{s} = 13$  TeV can be found in Reference [57] and a summary of the results is presented in Table 2.11.

## 2.6 CP-mixing in $tH$ processes

In addition to the sensitivity to sign of the H-t coupling, the  $tHq$  and  $tHW$  processes have been proposed as a tool to investigate the possibility of a H-t coupling that does not conserve CP [47, 48, 58].

In this thesis, the sensitivity of  $tH$  processes to CP-mixing is also studied on the

	$\sqrt{s}$ TeV	$\kappa_t = 1$	$\kappa_t = -1$
$\sigma^{LO}(tHq)(\text{fb})$ [51]	8	$\approx 17.4$	$\approx 252.7$
	14	$\approx 80.4$	$\approx 1042$
$\sigma^{NLO}(tHq)(\text{fb})$ [51]	8	$18.28^{+0.42}_{-0.38}$	$233.8^{+4.6}_{-0.0}$
	14	$88.2^{+1.7}_{-0.0}$	$982.8^{+28}_{-0.0}$
$\sigma^{LO}(tHq)(\text{fb})$ [56]	14	$\approx 71.8$	$\approx 893$
$\sigma^{LO}(tHW)(\text{fb})$ [56]	14	$\approx 16.0$	$\approx 139$
$\sigma^{NLO}(tHq)(\text{fb})$ [57]	8	$18.69^{+8.62\%}_{-17.13\%}$	-
	13	$74.25^{+7.48\%}_{-15.35\%}$	$848^{+7.37\%}_{-13.70\%}$
	14	$90.10^{+7.34\%}_{-15.13\%}$	$1011^{+7.24\%}_{-13.39\%}$
$\sigma^{LO}(tHW)(\text{fb})$ [48]	13	$15.77^{+15.91\%}_{-15.76\%}$	-
$\sigma^{NLO}DR1(tHW)(\text{fb})$ [48]	13	$21.72^{+6.52\%}_{-5.24\%}$	$\approx 150$
$\sigma^{NLO}DR2(tHW)(\text{fb})$ [48]	13	$16.28^{+7.34\%}_{-15.13\%}$	$\approx 150$

**Table 2.11:** Predicted enhancement of the  $tHq$  and  $tHW$  cross sections at LHC for  $\kappa_V = 1$  and  $\kappa_t = \pm 1$  at LO and NLO; the cross section enhancement of more than a factor of 10 is due to the flipping in the sign of the H-t coupling with respect to the SM one.

1203 basis of References [47, 48] using the effective field theory framework where a generic  
 1204 particle ( $X_0$ ) of spin-0 and a general CP violating interaction with the top quark  
 1205 (Htt coupling), can couple to scalar and pseudo-scalar fermionic densities. The H-W  
 1206 interaction is assumed to be SM-like. The Lagrangian modeling the H-t interaction  
 1207 is given by

$$\mathcal{L}_0^t = -\bar{\psi}_t (c_\alpha \kappa_{Htt} g_{Htt} + i s_\alpha \kappa_{Att} g_{Att} \gamma_5) \psi_t X_0, \quad (2.64)$$

1208 where  $\alpha$  is the CP-mixing phase,  $c_\alpha \equiv \cos \alpha$  and  $s_\alpha \equiv \sin \alpha$ ,  $\kappa_{Htt}$  and  $\kappa_{Att}$  are real  
 1209 dimensionless re-scaling parameters<sup>10</sup> used to parametrize the magnitude of the CP-  
 1210 violating and CP-conserving parts of the amplitude. The model defines  $g_{Htt} = g_{Att} =$   
 1211  $m_t/v = y_t/\sqrt{2}$  with  $v \sim 246$  GeV the Higgs vacuum expectation value. In this  
 1212 parametrization, three special cases can be recovered

1213 • CP-even coupling  $\rightarrow \alpha = 0^\circ$

<sup>10</sup> analog to  $\kappa_t$  and  $\kappa_V$

1214 • CP-odd coupling  $\rightarrow \alpha = 90^\circ$

1215 • SM coupling  $\rightarrow \alpha = 0^\circ$  and  $\kappa_{Htt} = 1$

1216 The loop induced  $X_0$  coupling to gluons can also be described in terms of the  
1217 parametrization above, according to

$$\mathcal{L}_0^g = -\frac{1}{4} \left( c_\alpha \kappa_{Hgg} g_{Hgg} G_{\mu\nu}^a G^{a,\mu\nu} + s_\alpha \kappa_{Agg} g_{Agg} G_{\mu\nu}^a \tilde{G}^{a,\mu\nu} \right) X_0. \quad (2.65)$$

1218 where  $g_{Hgg} = -\alpha_s/3\pi v$  and  $g_{Agg} = \alpha_s/2\pi v$  and  $G_{\mu\nu}$  is the gluon field strength tensors.

1219 Under the assumption that the top quark dominates the gluon-fusion process at LHC  
1220 energies,  $\kappa_{Hgg} \rightarrow \kappa_{Htt}$  and  $\kappa_{Agg} \rightarrow \kappa_{Att}$ , so that the ratio between the gluon-gluon  
1221 fusion cross section for  $X_0$  and for the SM Higgs prediction can be written as

$$\frac{\sigma_{NLO}^{gg \rightarrow X_0}}{\sigma_{NLO,SM}^{gg \rightarrow H}} = c_\alpha^2 \kappa_{Htt}^2 + s_\alpha^2 \left( \kappa_{Att} \frac{g_{Agg}}{g_{Hgg}} \right)^2. \quad (2.66)$$

1222 If the re-scaling parameters are set to

$$\kappa_{Htt} = 1, \quad \kappa_{Att} = \left| \frac{g_{Hgg}}{g_{Agg}} \right| = \frac{2}{3}. \quad (2.67)$$

1223 the gluon-fusion SM cross section is reproduced for every value of the CP-mixing  
1224 angle  $\alpha$ ; therefore, by imposing that condition to the Lagrangian density 2.64, the  
1225 CP-mixing angle is not constrained by current data. Figure 2.18 shows the NLO cross  
1226 sections for t-channel  $tX_0$ (blue) and  $t\bar{t}X_0$  (red) associated production processes as a  
1227 function of the CP-mixing angle  $\alpha$ .  $X_0$  is a generic spin-0 particle with top quark  
1228 CP-violating coupling. Re-scaling factors  $\kappa_{Htt}$  and  $\kappa_{Att}$  have been set to reproduce  
1229 the SM gluon-fusion cross sections.

1230 It is interesting to notice that the  $tX_0$  cross section is enhanced, by a factor of  
1231 about 10, when a continuous rotation in the scalar-pseudoscalar plane is applied; this

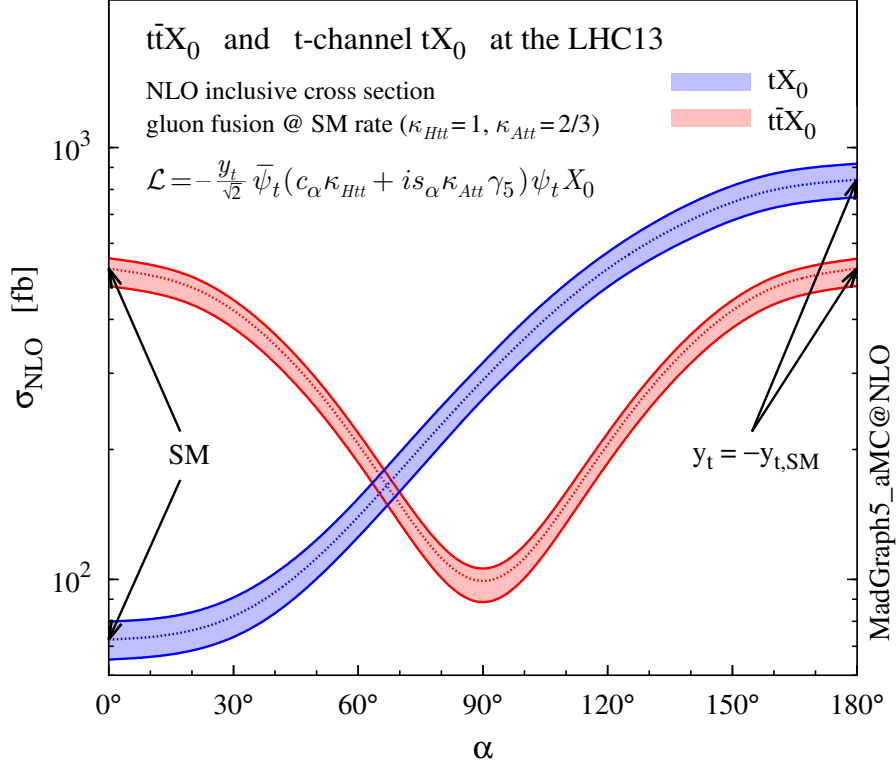


**Figure 2.18:** NLO cross sections for t-channel  $tX_0$ (blue) and  $t\bar{t}X_0$  (red) associated production processes as a function of the CP-mixing angle  $\alpha$ .  $X_0$  is a generic spin-0 particle with top quark CP-violating coupling [47].

enhancement is similar to the enhancement produced when the H-t coupling is flipped in sign with respect to the SM ( $y_t = -y_{t,SM}$  in the plot), as showed in Section 2.5. In contrast, the degeneracy in the  $t\bar{t}X_0$  cross section is still present given that it depends quadratically on the H-t coupling, but more interesting is to notice that  $t\bar{t}X_0$  cross section is exceeded by  $tX_0$  cross section after  $\alpha \sim 60^\circ$ .

A similar parametrization can be used to investigate the  $tHW$  process sensitivity to CP-violating H-t coupling. As said in 2.5, the interference in the W-associated channel is more complicated because there are more than two contributions and also there is interference with the  $t\bar{t}H$  production process.

Figure 2.19 shows the NLO cross sections for t-channel  $tX_0$ (blue),  $t\bar{t}X_0$  (red)

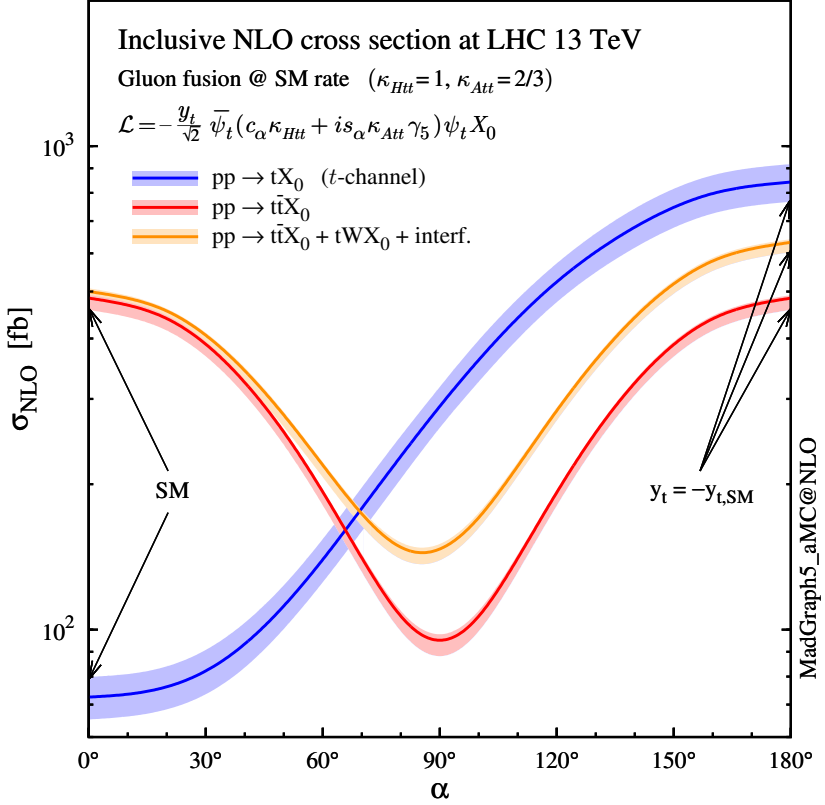


**Figure 2.19:** NLO cross sections for t-channel  $tX_0$  (blue),  $t\bar{t}X_0$  (red) associated production processes and combined  $tWX_0 + t\bar{t}X_0 + \text{interference}$  (orange) production as a function of the CP-mixing angle  $\alpha$  [47].

1242 associated production and for the combined  $tWX_0 + t\bar{t}X_0 + \text{interference}$  (orange) as  
 1243 a function of the CP-mixing angle. It is clear that the effect of the interference in the  
 1244 combined case is the lifting of the degeneracy present in the  $t\bar{t}X_0$  production. The  
 1245 constructive interference enhances the cross section from about 500 fb at SM ( $\alpha = 0$ )  
 1246 to about 600 fb ( $\alpha = 180^\circ \rightarrow y_t = -y_{t,SM}$ ).

1247 An analysis combining  $tHq$  and  $tHW$  processes will be made in this thesis taking  
 1248 advantage of the sensitivity improvement.

1249

## CHAPTER 3

1250

### The CMS experiment at the LHC

#### 1251 3.1 Introduction

1252 Located on the Swiss-French border, the European Council for Nuclear Research  
1253 (CERN) is the largest scientific organization leading particle physics research. About  
1254 13000 people in a broad range of roles including users, students, scientists, engineers,  
1255 among others, contribute to the data taking and analysis, with the goal of unveiling  
1256 the secrets of nature and revealing the fundamental structure of the universe. CERN  
1257 is also the home of the Large Hadron Collider (LHC), the largest particle accelerator  
1258 around the world, where protons (or heavy ions) traveling close to the speed of light,  
1259 are made to collide. These collisions open a window to investigate how particles (and  
1260 their constituents if they are composite) interact with each other, providing clues  
1261 about the laws of nature. This chapter presents an overview of the LHC structure  
1262 and operation. A detailed description of the CMS detector is offered, given that the  
1263 data used in this thesis have been taken with this detector.

## 1264 3.2 The LHC

1265 With 27 km of circumference, the LHC is currently the most powerful circular accelerator  
 1266 in the world. It is installed in the same tunnel where the Large Electron-Positron  
 1267 (LEP) collider was located, taking advantage of the existing infrastructure. The LHC  
 1268 is part of the CERN's accelerator complex composed of several successive accelerat-  
 1269 ing stages before the particles are injected into the LHC ring where they reach their  
 1270 maximum energy (see Figure 3.1).

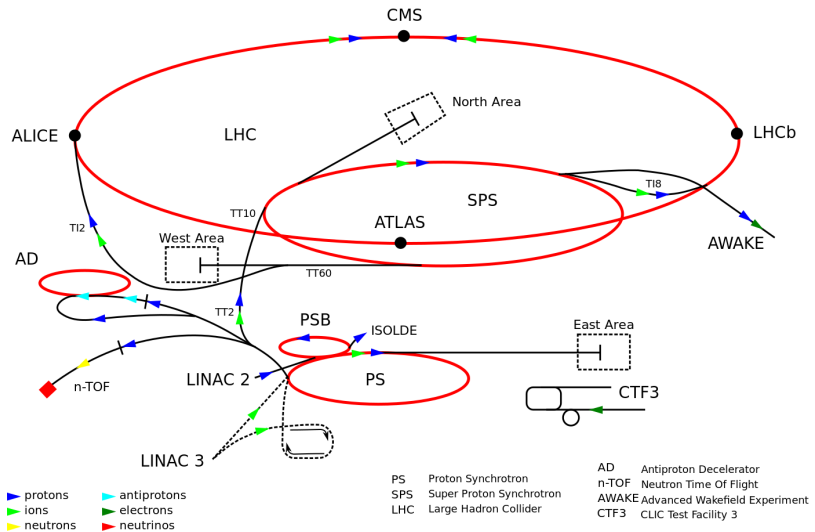


**Figure 3.1:** CERN accelerator complex. Blue arrows show the path followed by protons along the acceleration process [61].

1271 The LHC runs in three collision modes depending on the particles being acceler-  
 1272 ated

- 1273 • Proton-Proton collisions ( $pp$ ) for multiple physics experiments.
- 1274 • Lead-Lead collisions ( $Pb-Pb$ ) for heavy ion experiments.
- 1275 • Proton-Lead collisions ( $p-Pb$ ) for quark-gluon plasma experiments.

1276 In this thesis only  $pp$  collisions will be considered.

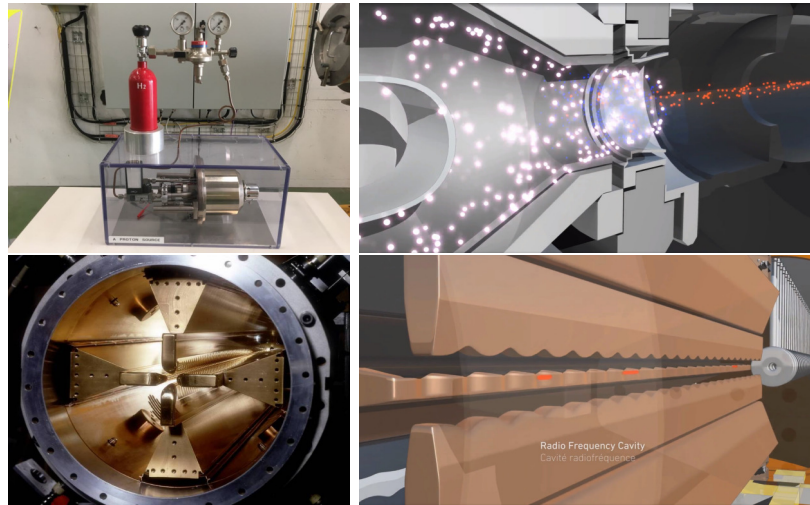


**Figure 3.2:** LHC protons source and the first acceleration stage. Top: the bottle contains hydrogen gas which is injected into the metal cylinder (white dots) to be broken down into electrons (blue dots) and protons (red dots); Bottom: the obtained protons are directed towards the radio frequency quadrupole which perform the first acceleration, focus the beam and create the bunches of protons. Left images are real pictures while right images are drawings [65, 66].

1277        Collection of protons starts with hydrogen atoms taken from a bottle, containing  
 1278        hydrogen gas, and injecting them in a metal cylinder; hydrogen atoms are broken  
 1279        down into electrons and protons by an intense electric field (see Figure 3.2 top).  
 1280        The resulting protons leave the metal cylinder towards a radio frequency quadrupole  
 1281        (RFQ) that focus the beam, accelerates the protons and creates the packets of protons  
 1282        called bunches. In the RFQ, an electric field is generated by a RF wave at a frequency  
 1283        that matches the resonance frequency of the cavity where the electrodes are contained.  
 1284        The beam of protons traveling on the RFQ axis experiences an alternating electric  
 1285        field gradient that generates the focusing forces.

1286        In order to accelerate the protons, a longitudinal time-varying electric field com-  
 1287        ponent is added to the system; it is done by giving the electrodes a sine-like profile as  
 1288        shown in Figure 3.2 bottom. By matching the speed and phase of the protons with  
 1289        the longitudinal electric field the bunching is performed; protons synchronized with

1290 the RFQ (synchronous protons) do not feel an accelerating force, but those protons in  
 1291 the beam that have more (or less) energy than the synchronous proton (asynchronous  
 1292 protons) will feel a decelerating (accelerating) force; therefore, asynchronous protons  
 1293 will oscillate around the synchronous ones forming bunches of protons [63]. From the  
 1294 RFQ protons emerge with energy 750 keV in bunches of about  $1.15 \times 10^{11}$  protons [64].

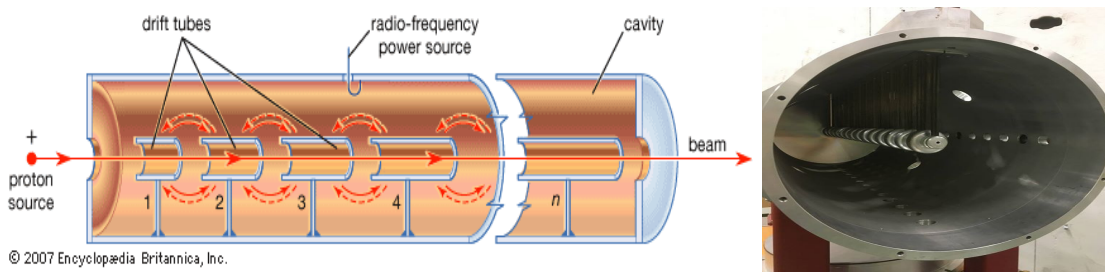


**Figure 3.3:** Left: drawing of the LINAC2 accelerating system at CERN. Electric fields generated by radio frequency (RF) create acceleration and deceleration zones inside the cavity; deceleration zones are blocked by drift tubes where quadrupole magnets focus the proton beam. Right: picture of a real RF cavity [67].

1295 Proton bunches coming from the RFQ go to the linear accelerator 2 (LINAC2)  
 1296 where they are accelerated to reach 50 MeV energy. In the LINAC2 stage, acceleration  
 1297 is performed using electric fields generated by radio frequency which create zones  
 1298 of acceleration and deceleration as shown in Figure 3.3. In the deceleration zones,  
 1299 the electric field is blocked using drift tubes where protons are free to drift while  
 1300 quadrupole magnets focus the beam.

1301 The beam coming from LINAC2 is injected into the proton synchrotron booster  
 1302 (PSB) to reach 1.4 GeV in energy. The next acceleration is provided at the proton  
 1303 synchrotron (PS) up to 26 GeV, followed by the injection into the super proton  
 1304 synchrotron (SPS) where protons are accelerated to 450 GeV. Finally, protons are  
 1305 injected into the LHC where they are accelerated to the target energy of 6.5 TeV.

1306 PSB, PS, SPS and LHC accelerate protons using the same RF acceleration tech-  
 1307 nique described before.

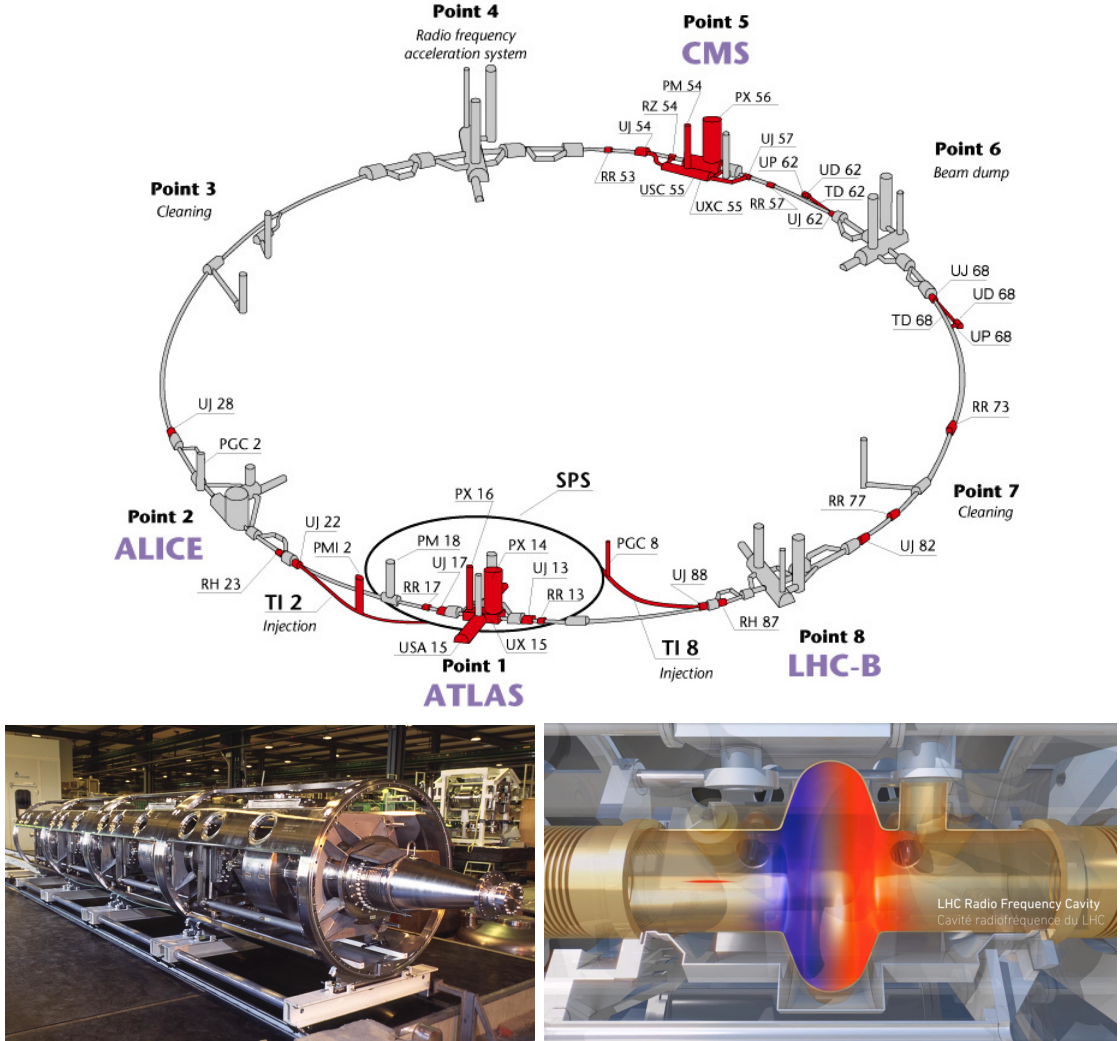


**Figure 3.4:** Top: LHC layout. The red zones indicate the infrastructure additions to the LEP installations, built to accommodate the ATLAS and CMS experiments which exceed the size of the former experiments located there [62]. Bottom: LHC RF cavities. A module (left picture) accommodates 4 cavities, each like the one in the right drawing, that accelerate protons and preserve the bunch structure of the beam. The color gradient pattern represents the strength of the electric field inside the cavity; red zone corresponds to the maximum of the oscillation electric field while the blue zone corresponds to the minimum. [66, 68]

1308        The LHC has a system of 16 RF cavities located in the so-called point 4, as  
 1309 shown in Figure 3.4 top, tuned at a frequency of 400 MHz. The bottom side of  
 1310 Figure 3.4 shows a picture of a RF module composed of 4 RF cavities working in a  
 1311 superconducting state at 4.5 K; also, a representation of the accelerating electric field

that accelerates the protons in the bunch is shown. The maximum of the oscillating electric field (red region) picks the proton bunches at the entrance of the cavity and keeps accelerating them through the whole cavity. The protons are carefully timed so that in addition to the acceleration effect the bunch structure of the beam is preserved.

While protons are accelerated in one section of the LHC ring, where the RF cavities are located, in the rest of their path they have to be kept in the curved trajectory defined by the LHC ring. Technically, LHC is not a perfect circle; RF, injection, beam dumping, beam cleaning and sections before and after the experimental points where protons collide are all straight sections. In total, there are 8 arcs 2.45 km long each and 8 straight sections 545 m long each. In order to curve the proton's trajectory in the arc sections, superconducting dipole magnets are used.

Inside the LHC ring, there are two proton beams traveling in opposite directions in two separated beam pipes; the beam pipes are kept at ultra-high vacuum ( $\sim 10^{-9}$ Pa) to ensure that there are no particles that interact with the proton beams. The superconducting dipole magnets used in LHC are made of a NbTi alloy, capable of transporting currents of about 12000 A when cooled at a temperature below 2K using liquid helium (see Figure 3.5).

Protons in the arc sections of LHC feel a centripetal force exerted by the dipole magnets; the magnitude of magnetic field needed to keep the protons in the LHC curved trayectomy can be found assuming that protons travel at  $v \approx c$ , using the standard values for proton mass and charge and the LHC radius, as

$$F_m = \frac{mv^2}{r} = qBv \rightarrow B = 8.33T \quad (3.1)$$

which is about 100000 times the Earth's magnetic field. A representation of the

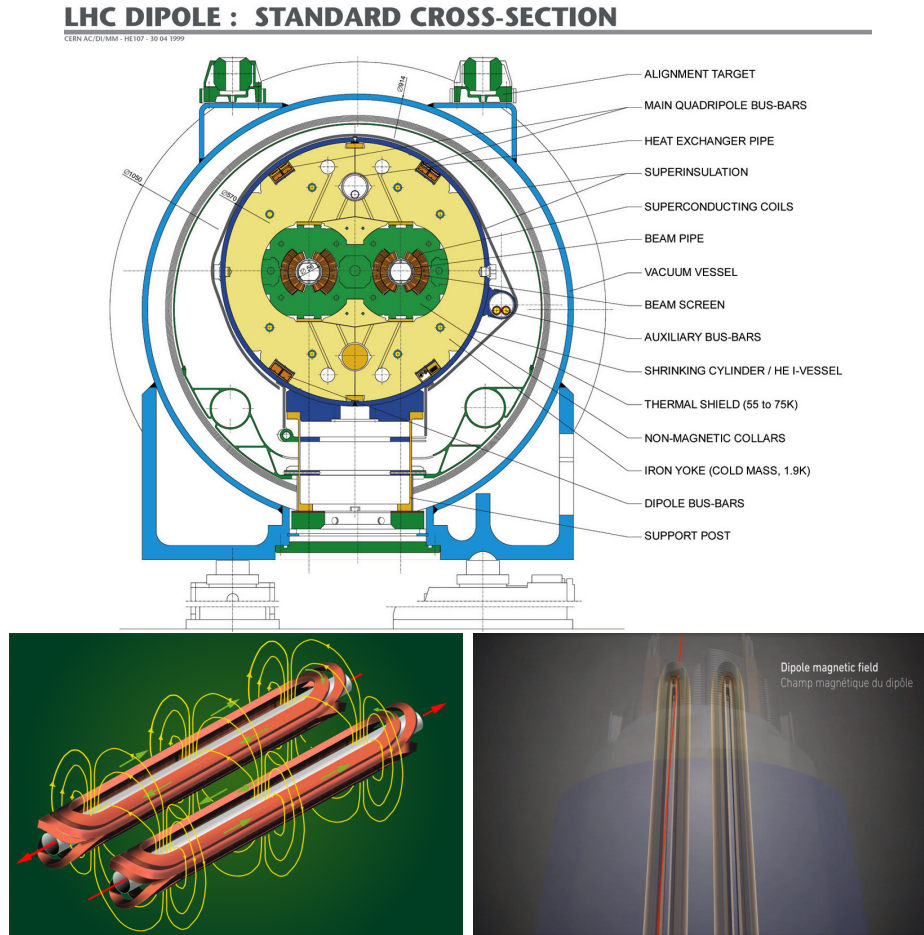


**Figure 3.5:** Top: LHC dipole magnet transverse view; cooling, shielding and mechanical support are indicated. Bottom left: Magnetic field generated by the dipole magnets; note that the direction of the field inside one beam pipe is opposite with respect to the other beam pipe which guarantee that both proton beams are curved in the same direction towards the center of the ring. The effect of the dipole magnetic field on the proton beam is represented on the bottom right side [66, 69, 70].

1335 magnetic field generated by the dipole magnets is shown on the bottom left side of  
 1336 Figure 3.5. The bending effect of the magnetic field on the proton beam is shown on  
 1337 the bottom right side of Figure 3.5. Note that the dipole magnets are not curved; the  
 1338 arc section of the LHC ring is composed of straight dipole magnets of about 15 m.  
 1339 In total there are 1232 dipole magnets along the LHC ring.

1340 In addition to the bending of the beam trajectory, the beam has to be focused. The

1341 focusing is performed by quadrupole magnets installed in a different straight section;  
 1342 in total 858 quadrupole magnets are installed along the LHC ring. Other effects like  
 1343 electromagnetic interaction among bunches, interaction with electron clouds from the  
 1344 beam pipe, the gravitational force on the protons, differences in energy among protons  
 1345 in the same bunch, among others, are corrected using sextupole and other magnetic  
 1346 multipoles.

1347 The two proton beams inside the LHC ring are made of bunches with a cylindrical  
 1348 shape of about 7.5 cm long and about 1 mm in diameter; when bunches are close to the  
 1349 interaction point (IP), the beam is focused up to a diameter of about 16  $\mu\text{m}$  in order  
 1350 to maximize the probability of collisions between protons. The number of collisions  
 1351 per second is proportional to the cross section of the bunches with the *luminosity* ( $L$ )  
 1352 as the proportionality factor, thus, the luminosity can be calculated using

$$L = fn \frac{N_1 N_2}{4\pi\sigma_x\sigma_y} \quad (3.2)$$

1353 where  $f$  is the revolution frequency,  $n$  is the number of bunches per beam,  $N_1$  and  $N_2$   
 1354 are the numbers of protons per bunch,  $\sigma_x$  and  $\sigma_y$  are the gaussian transverse sizes of  
 1355 the bunches. With the expected parameters, the LHC expected luminosity is about

$$f = \frac{v}{2\pi r_{LHC}} \approx \frac{3 \times 10^8 \text{ m/s}}{27 \text{ km}} \approx 11.1 \text{ kHz},$$

$$n = 2808$$

$$N_1 = N_2 \sim 1.5 \times 10^{11}$$

$$\sigma_x = \sigma_y = 16 \mu\text{m}$$

1356

$$L = 1.28 \times 10^{34} \text{ cm}^{-2} \text{ s}^{-1} = 1.28 \times 10^{-5} \text{ fb}^{-1} \text{ s}^{-1} \quad (3.3)$$

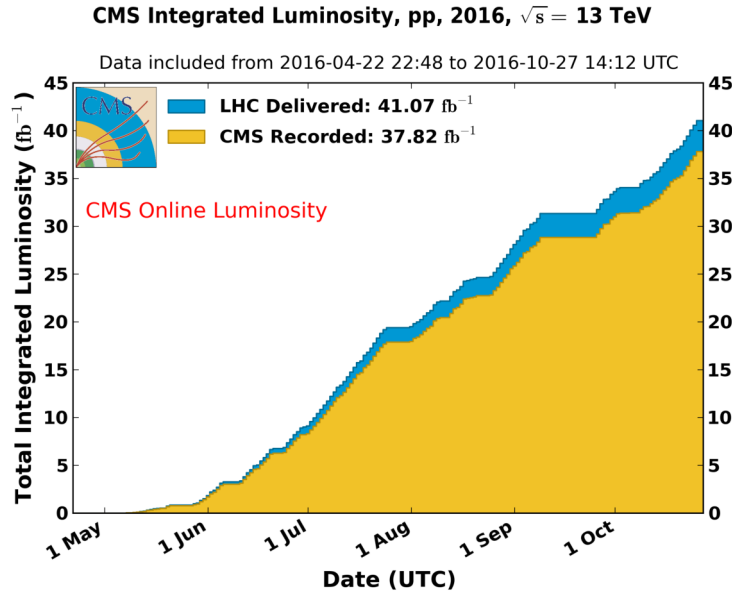


**Figure 3.6:** Integrated luminosity delivered by LHC and recorded by CMS during 2016. The difference between the delivered and the recorded luminosity is due to fails and issues occurred during the data taking in the CMS experiment [162].

1357        Luminosity is a fundamental aspect of LHC given that the bigger luminosity the  
 1358        bigger number of collisions, which means that for processes with a very small cross  
 1359        section the number of expected occurrences is increased and so the chances of being  
 1360        detected. The integrated luminosity, collected by the CMS experiment during 2016  
 1361        is shown in Figure 3.6; the data analyzed in this thesis corresponds to an integrated  
 1362        luminosity of  $35.9 \text{ fb}^{-1}$  at a center of mass-energy  $\sqrt{s} = 13 \text{ TeV}$ .

1363        One way to increase  $L$  is increasing the number of bunches in the beam. Cur-  
 1364        rently, the separation between two consecutive bunches in the beam is 7.5 m which  
 1365        corresponds to a time separation of 25 ns. In the full LHC ring the allowed number of  
 1366        bunches is  $n = 27 \text{ km}/7.5 \text{ m} = 3600$ ; however, there are some gaps in the bunch pat-  
 1367        tern intended for preparing the dumping and injection of the beam, thus, the proton  
 1368        beams are composed of 2808 bunches.

1369        Once the proton beams reach the desired energy, they are brought to cross each

1370 other producing  $pp$  collisions. The bunch crossing happens in precise places where  
 1371 the four LHC experiments are located, as seen in the top of Figure 3.7. In 2008  $pp$   
 1372 collisions of  $\sqrt{s} = 7$  TeV were performed; the energy was increased to 8 TeV in 2012  
 1373 and to 13 TeV in 2015.

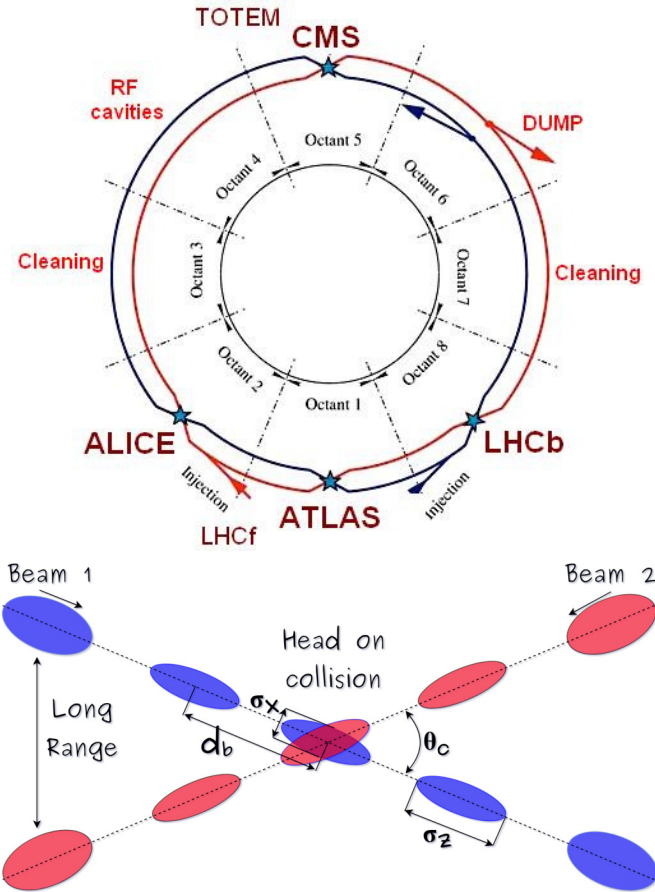


**Figure 3.7:** Top: LHC interaction points. Bunch crossing occurs where the LHC experiments are located [72]. Sections indicated as cleaning are dedicated to collimate the beam in order to protect the LHC ring from collisions with protons in very spreaded bunches. Bottom: bunch crossing scheme. Since the bunch crossing is not perfectly head-on, the luminosity is reduced in a factor of 17%; adapted from Reference [86].

1374 The CMS and ATLAS experiments are multi-purpose experiments, hence, they  
 1375 are enabled to explore physics in any of the LHC collision modes. LHCb experiment  
 1376 is optimized to explore bottom quark physics, while ALICE is optimized for heavy

1377 ion collisions searches; TOTEM and LHCf are dedicated to forward physics studies;  
 1378 MoEDAL (not indicated in the Figure) is intended for monopole or massive pseudo  
 1379 stable particles searches.

1380 At the IP there are two interesting details that need to be addressed. The first  
 1381 one is that the bunch crossing does not occur head-on but at a small crossing angle  $\theta_c$   
 1382 (280  $\mu$ rad in CMS and ATLAS) as shown in the bottom side of Figure 3.7, affecting  
 1383 the overlapping between bunches; the consequence is a reduction of about 17% in  
 1384 the luminosity (represented by a factor not included in eqn. 3.2). The second one  
 1385 is the occurrence of multiple  $pp$  collisions in the same bunch crossing; this effect is  
 1386 called *pileup* (PU). A fairly simple estimation of the PU follows from estimating the  
 1387 probability of collision between two protons, one from each of the bunches in the  
 1388 course of collision; it depends roughly on the ratio of proton size and the cross section  
 1389 of the bunch in the IP, i.e.,

$$P(pp - \text{collision}) \sim \frac{d_{\text{proton}}^2}{\sigma_x \sigma_y} = \frac{(1\text{fm})^2}{(16\mu\text{m})^2} \sim 4 \times 10^{-21} \quad (3.4)$$

1390 however, there are  $N = 1.15 \times 10^{11}$  protons in a bunch, thus the estimated number  
 1391 of collisions in a bunch crossing is

$$PU = N^2 * P(pp - \text{collision}) \sim 50pp \text{ collision per bunch crossing}, \quad (3.5)$$

1392 about 20 of which are inelastic. A multiple  $pp$  collision event in a bunch crossing at  
 1393 CMS is shown in Figure 3.8.

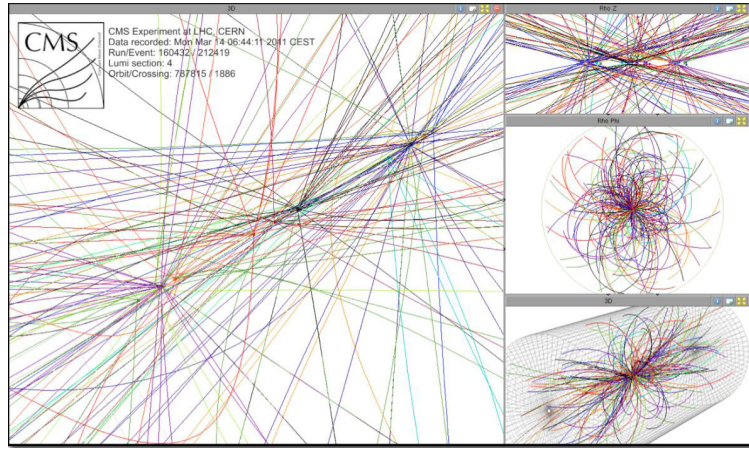


**Figure 3.8:** Multiple  $pp$  collision bunch crossing at CMS. [73].

### 1394 3.3 The CMS experiment

CMS is a general-purpose detector designed to conduct research in a wide range of physics from the standard model to new physics like extra dimensions and dark matter. Located at Point 5 in the LHC layout as shown in Figure 3.4, CMS is composed of several detection systems distributed in a cylindrical structure; in total, CMS weights about 12500 tons in a very compact 21.6 m long and 14.6 m diameter cylinder. It was built in 15 separate sections at the ground level and lowered to the cavern individually to be assembled. A complete and detailed description of the CMS detector and its components is given in Reference [74] on which this section is based. Figure 3.9 shows the layout of the CMS detector. The detection system is composed of (from the innermost to the outermost)

- 1405 • Pixel detector.
- 1406 • Silicon strip tracker.
- 1407 • Preshower detector.
- 1408 • Electromagnetic calorimeter.

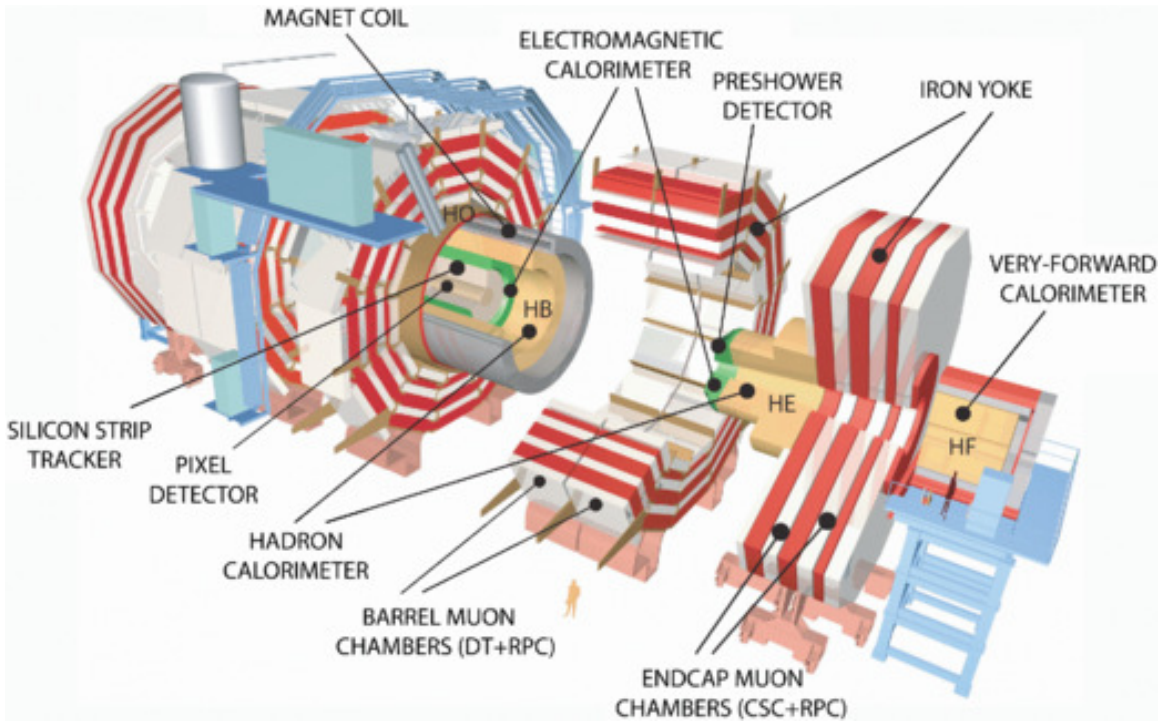


**Figure 3.9:** Layout of the CMS detector. The several subdetectors are indicated. The central region of the detector is referred as the barrel section while the endcaps are referred as the forward sections. [75].

1409        • Hadronic calorimeter.

1410        • Muon chambers (barrel and endcap)

1411        The central region of the detector is commonly referred as the barrel section while  
 1412        the endcaps are referred as the forward sections of the detector; thus, each subdetector  
 1413        is composed of a barrel section and a forward section.

1414        When a  $pp$  collision happens inside the CMS detector, many different particles are  
 1415        produced, but only some of them live long enough to be detected; they are electrons,  
 1416        photons, pions, kaons, protons, neutrons and muons; neutrinos are not detected by  
 1417        the CMS detector. Thus, the CMS detector was designed to detect those particles and  
 1418        measure their properties. Figure 3.10 shows a transverse slice of the CMS detector.  
 1419        The silicon tracker (pixel detector + strip tracker) is capable to register the track of

1420 the charged particles traversing it, while calorimeters (electromagnetic and hadronic)  
 1421 measure the energy of the particles that are absorbed by their materials. Considering  
 1422 the detectable particles, mentioned above, emerging from the IP, a basic description  
 1423 of the detection process is as follows.

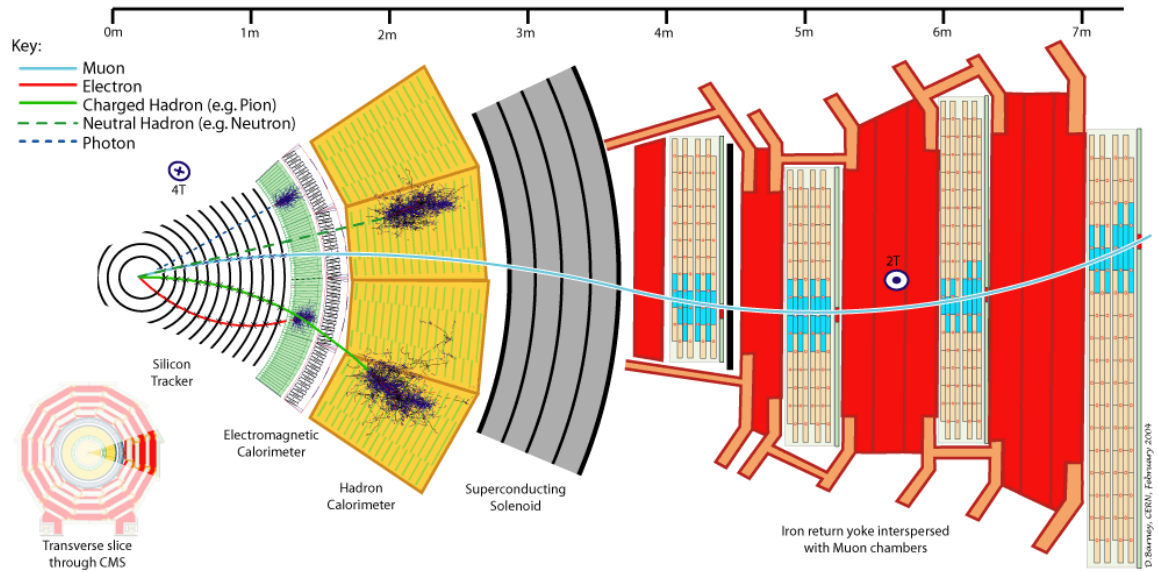


**Figure 3.10:** CMS detector transverse slice [76].

1424 A muon emerging from the IP, will create a track on the silicon tracker and on  
 1425 the muon chambers. The design of the CMS detector is driven by the requirements  
 1426 on the identification, momentum resolution and unambiguous charge determination  
 1427 of the muons; therefore, a large bending power is provided by the solenoid magnet  
 1428 made of superconducting cable capable of generating a 3.8 T magnetic field. The  
 1429 muon track is bent twice since the magnetic field inside the solenoid is directed along  
 1430 the  $z$ -direction but outside its direction is reversed. Muons interact very weakly with  
 1431 the calorimeters, therefore, it is not absorbed but escape away from the detector.

1432 An electron emerging from the IP will create a track along the tracker which will  
 1433 be bent due to the presence of the magnetic field, later, it will be absorbed in the  
 1434 electromagnetic calorimeter where its energy is measured.

1435 A photon will not leave a track because it is neutral, but it will be absorbed in  
 1436 the electromagnetic calorimeter.

1437 A neutral hadron, like the neutron, will not leave a track either but it will lose a  
 1438 small amount of its energy during its passage through the electromagnetic calorimeter  
 1439 and then it will be absorbed in the hadron calorimeter depositing the rest of its energy.

1440 A charged hadron, like the proton or  $\pi^\pm$ , will leave a curved track on the silicon  
 1441 tracker, some of its energy in the electromagnetic calorimeter and finally will be  
 1442 absorbed in the hadronic calorimeter.

1443 A more detailed description of each detection system will be presented in the  
 1444 following sections.

### 1445 3.3.1 CMS coordinate system

1446 The coordinate system used by CMS is centered on the geometrical center of the  
 1447 detector which is the nominal IP as shown in Figure 3.11<sup>1</sup>. The  $z$ -axis is parallel  
 1448 to the beam direction, while the  $Y$ -axis pointing vertically upward, and the  $X$ -axis  
 1449 pointing radially inward toward the center of the LHC.

1450 In addition to the common cartesian and cylindrical coordinate systems, two co-  
 1451 ordinates are of particular utility in particle physics: rapidity ( $y$ ) and pseudorapidity  
 1452 ( $\eta$ ), defined in connection to the polar angle  $\theta$ , energy and longitudinal momentum  
 1453 component (momentum along the  $z$ -axis) according to

$$y = \frac{1}{2} \ln \frac{E + p_z}{E - p_z} \quad \eta = -\ln \left( \tan \frac{\theta}{2} \right) \quad (3.6)$$

1454 Rapidity is related to the angle between the  $XY$ -plane and the direction in which  
 1455 the products of a collision are emitted; it has the nice property that the difference

---

<sup>1</sup> Not all the  $pp$  interaction occur at the nominal IP because of the bunch lenght, therefore, each  $pp$  collision has its own IP location

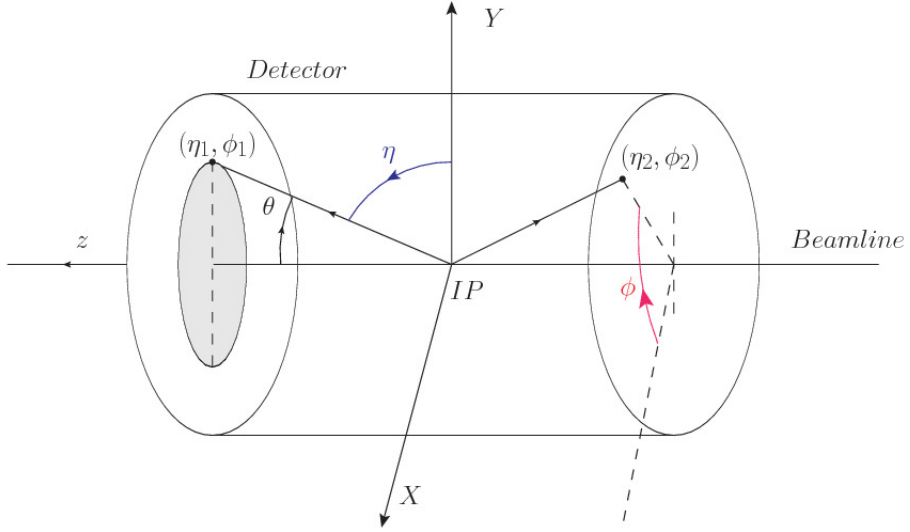


**Figure 3.11:** CMS detector coordinate system.

1456 between the rapidities of two particles is invariant with respect to Lorentz boosts  
 1457 along the  $z$ -axis, hence, data analysis becomes more simple when based on rapid-  
 1458 ity; however, it is not simple to measure the rapidity of highly relativistic particles,  
 1459 as those produced after  $pp$  collisions. Under the highly relativistic motion approxi-  
 1460 mation,  $y$  can be rewritten in terms of the polar angle, concluding that rapidity is  
 1461 approximately equal to the pseudorapidity defined above, i.e.,  $y \approx \eta$ . Note that  $\eta$   
 1462 is easier to measure than  $y$  given the direct relationship between the former and the  
 1463 polar angle.

1464 The angular distance between two objects in the detector ( $\Delta R$ ) is commonly used  
 1465 to judge the isolation of those object; it is defined in terms of their coordinates  $(\eta_1, \phi_1)$ ,  
 1466  $(\eta_2, \phi_2)$  as

$$\Delta R = \sqrt{(\Delta\eta)^2 - (\Delta\phi)^2} \quad (3.7)$$

### 1467 3.3.2 Tracking system

1468 The CMS tracking system is designed to provide a precise measurement of the trajectories (*track*) followed by the charged particles created after the  $pp$  collisions; also, the  
 1469 precise reconstruction of the primary and secondary origins of the tracks (*vertices*) is  
 1470 expected in an environment where, each 25 ns, the bunch crossing produces about 20  
 1471 inelastic collisions and about 1000 particles.  
 1472

1473 Physics requirements guiding the tracking system performance include the precise characterization of events involving gauge bosons, W and Z, and their leptonic  
 1474 decays for which an efficient isolated lepton and photon reconstruction is of capital  
 1475 importance, given that isolation is required to suppress background events to a level  
 1476 that allows observations of interesting processes like Higgs boson decays or beyond  
 1477 SM events.

1479 The ability to identify and reconstruct  $b$ -jets and B-hadrons within these jets is also  
 1480 a fundamental requirement, achieved through the ability to reconstruct accurately  
 1481 displaced vertices, given that  $b$ -jets are part of the signature of top quark physics, like  
 1482 the one treated in this thesis.

1483 An schematic view of the CMS tracking system is shown in Figure 3.12

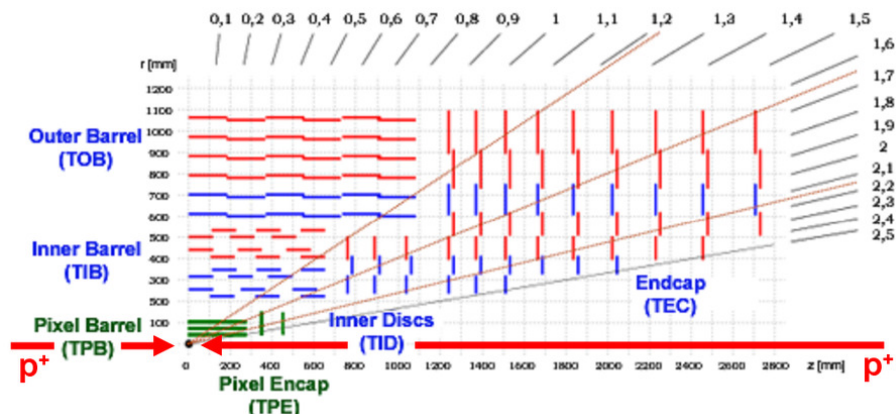


**Figure 3.12:** CMS tracking system schematic view [78].

1484 In order to satisfy these performance requirements, the tracking system uses two  
 1485 different detector subsystems arranged in concentric cylindrical volumes, the pixel  
 1486 detector and the silicon strip tracker; the pixel detector is located in the high particle  
 1487 density region ( $r < 20$  cm) while the silicon strip tracker is located in the medium and  
 1488 lower particle density regions  $20 \text{ cm} < r < 116$  cm.

1489 **Pixel detector**

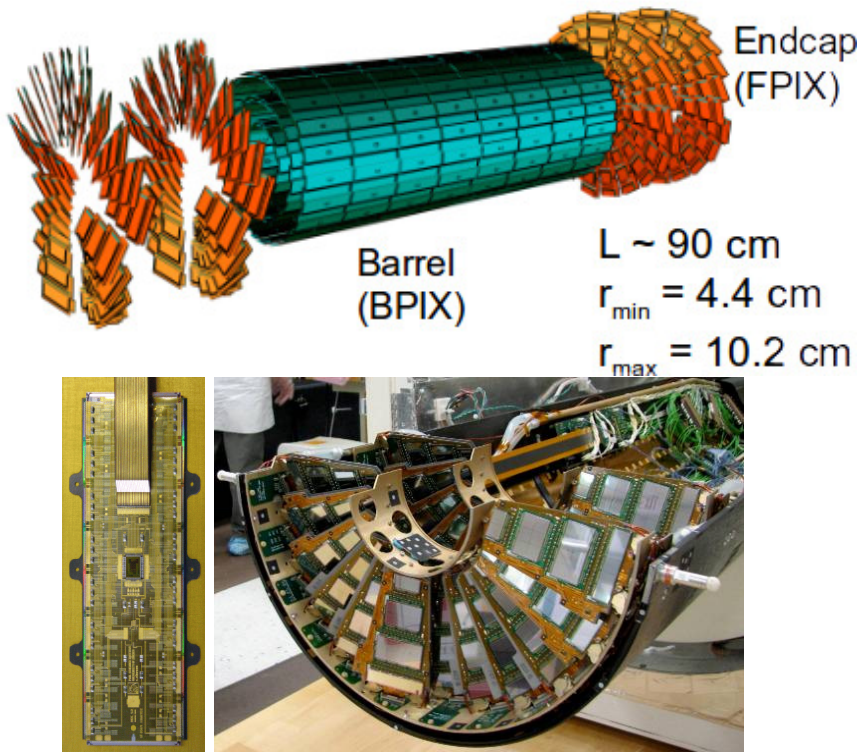


**Figure 3.13:** CMS pixel detector. Top: schematic view; Bottom: pictures of a barrel(BPIX) module(left) and forward modules(right) [74].

1490 The pixel detector was replaced during the 2016-2017 extended year-end technical  
 1491 stop, due to the increasingly challenging operating conditions like the higher particle  
 1492 flux and more radiation harsh environment, among others. The new one is responding  
 1493 as expected, reinforcing its crucial role in the successful way to fulfill the new LHC

1494 physics objectives after the discovery of the Higgs boson. Since the data sets used  
 1495 in this thesis were produced using the previous version of the pixel detector, it will  
 1496 be the subject of the description in this section. The last chapter of this thesis is  
 1497 dedicated to describe my contribution to the *Forward Pixel Phase 1 upgrade*.

1498 The pixel detector was composed of 1440 silicon pixel detector modules organized  
 1499 in three-barrel layers in the central region (BPix) and two disks in the forward region  
 1500 (FPix) as shown in the top side of Figure 3.13; it was designed to record efficiently  
 1501 and with high precision, up to  $20 \mu\text{m}$  in the  $XY$ -plane and  $20 \mu\text{m}$  in the  $z$ -direction,  
 1502 the first three space-points (*hits*) nearest to the IP region in the range  $|\eta| \leq 2.5$ . The  
 1503 first barrel layer was located at a radius of 44 mm from the beamline, while the third  
 1504 layer was located at a radius of 102 mm, closer to the strip tracker inner barrel layer  
 1505 (see Section 3.3.3) in order to reduce the rate of fake tracks. The high granularity of  
 1506 the detector is represented in its about 66 Mpixels, each of size  $100 \times 150 \mu\text{m}^2$ . The  
 1507 transverse momentum resolution of tracks can be measured with a resolution of 1-2%  
 1508 for muons of  $p_T = 100 \text{ GeV}$ .

1509 A charged particle passing through the pixel sensors produce ionization in them,  
 1510 giving energy for electrons to be removed from the silicon atoms, hence, creating  
 1511 electron-hole pairs. The collection of charges in the pixels generates an electrical  
 1512 signal that is read out by an electronic readout chip (ROC); each pixel has its own  
 1513 electronics which amplifies the signal. Combining the signal from the pixels activated  
 1514 by a traversing particle in the several layers of the detector allows one to reconstruct  
 1515 the particle's trajectory in 3D.

1516 Commonly, the charge produced by traversing of a particle is collected by and  
 1517 shared among several pixels; by interpolating between pixels, the spatial resolution  
 1518 is improved. In the barrel section the charge sharing in the  $r\phi$ -plane is due to the  
 1519 Lorentz effect. In the forward pixels the charge sharing is enhanced by arranging the

1520 blades in the turbine-like layout as shown in Figure 3.13 bottom left.

1521 **3.3.3 Silicon strip tracker**

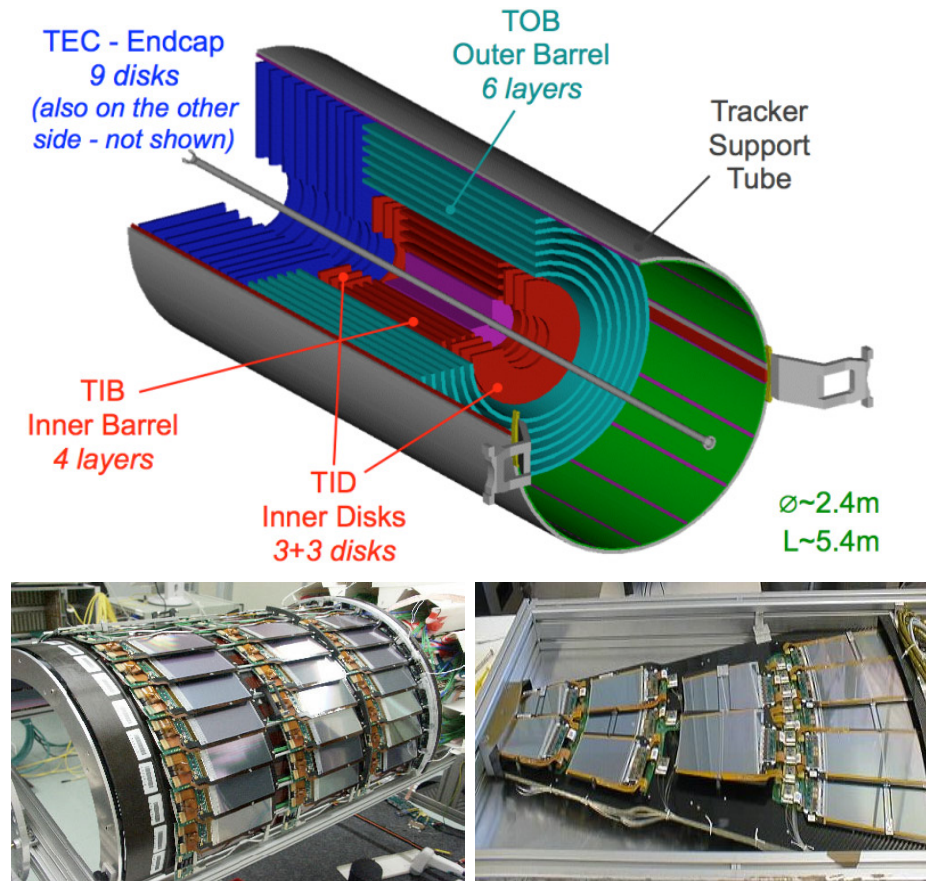


**Figure 3.14:** Top: CMS Silicon Strip Tracker (SST) schematic view. The SST is composed of the tracker inner barrel (TIB), the tracker inner disks (TID), the tracker outer barrel (TOB) and the tracker endcaps (TEC). Each part is made of silicon strip modules; the modules in blue represent two modules mounted back-to-back and rotated in the plane of the module by a stereo angle of 120 mrad in order to provide a 3-D reconstruction of the hit positions. Bottom: pictures of the TIB (left) and TEC (right) modules [80–82].

1522 The silicon strip tracker (SST) is the second stage in the CMS tracking system.

1523 The top side of Figure 3.14 shows a schematic of the SST. The inner tracker region is

1524 composed of the tracker inner barrel (TIB) and the tracker inner disks (TID) covering

1525 the region  $r < 55$  cm and  $|z| < 118$  cm. The TIB is composed of 4 layers while the

1526 TID is composed of 3 disks at each end. The silicon sensors in the inner tracker are 320  
 1527  $\mu\text{m}$  thick, providing a resolution of about 13-38  $\mu\text{m}$  in the  $r\phi$  position measurement.

1528 The modules indicated in blue in the schematic view of Figure 3.14 are two mod-  
 1529 ules mounted back-to-back and rotated in the plane of the module by a *stereo* angle  
 1530 of 100 mrad; the hits from these two modules, known as *stereo hits*, are combined to  
 1531 provide a measurement of the second coordinate ( $z$  in the barrel and  $r$  on the disks)  
 1532 allowing the reconstruction of hit positions in 3-D.

1533 The outer tracker region is composed of the tracker outer barrel (TOB) and the  
 1534 tracker endcaps (TEC). The six layers of the TOB offer coverage in the region  $r > 55$   
 1535 cm and  $|z| < 118$  cm, while the 9 disks of the TEC cover the region  $124 < |z| < 282$   
 1536 cm. The resolution offered by the outer tracker is about 13-38  $\mu\text{m}$  in the  $r\phi$  position  
 1537 measurement. The inner four TEC disks use silicon sensors 320  $\mu\text{m}$  thick; those in  
 1538 the TOB and the outer three TEC disks use silicon sensors of 500  $\mu\text{m}$  thickness. The  
 1539 silicon strips run parallel to the  $z$ -axis and the distance between strips varies from 80  
 1540  $\mu\text{m}$  in the inner TIB layers to 183  $\mu\text{m}$  in the inner TOB layers; in the endcaps the  
 1541 wedge-shaped sensors with radial strips, whose pitch range between 81  $\mu\text{m}$  at small  
 1542 radii and 205  $\mu\text{m}$  at large radii.

1543 The whole SST has 15148 silicon modules, 9.3 million silicon strips and cover a  
 1544 total active area of about 198  $\text{m}^2$ .

### 1545 3.3.4 Electromagnetic calorimeter

1546 The CMS electromagnetic calorimeter (ECAL) is designed to measure the energy of  
 1547 electrons and photons. It is composed of 75848 lead tungstate crystals which have a  
 1548 short radiation length (0.89 cm) and fast response, since 80% of the light is emitted  
 1549 within 25 ns; however, they are combined with Avalanche photodiodes (APDs) as

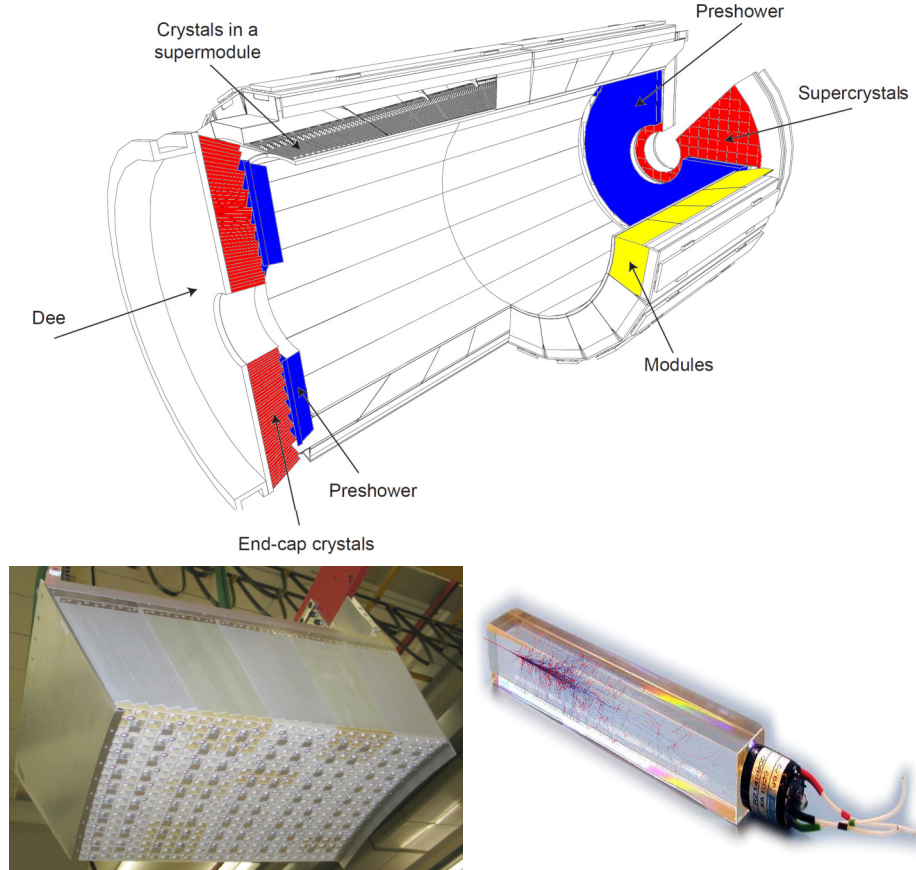


**Figure 3.15:** Top: CMS ECAL schematic view. Bottom: Module equipped with the crystals (left); ECAL crystal(right) with an artistic representation of an electromagnetic shower [74].

1550 photodetectors given that crystals themselves have a low light yield ( $30\gamma/\text{MeV}$ ). A  
 1551 schematic view of the ECAL is shown in Figure 3.15.

1552 Energy is measured when electrons and photons are absorbed by the crystals  
 1553 which generates an electromagnetic *shower*, as seen in bottom right picture of the  
 1554 Figure 3.15; the shower is seen as a *cluster* of energy which depending on the amount  
 1555 of energy deposited can involve several crystals. The ECAL barrel (EB) covers the  
 1556 region  $|\eta| < 1.479$ , using crystals of depth of 23 cm and  $2.2 \times 2.2 \text{ cm}^2$  transverse  
 1557 section; the ECAL endcap (EE) covers the region  $1.479 < |\eta| < 3.0$  using crystals of  
 1558 depth 22 cm and transverse section of  $2.86 \times 2.86 \text{ cm}^2$ ; the photodetectors used are

1559 vacuum phototriodes (VPTs). Each EE is divided in two structures called *Dees*.

1560 The preshower detector (ES) is installed in front of the EE and covers the region  
 1561  $1.653 < |\eta| < 2.6$ . The ES provides a precise measurement of the position of electro-  
 1562 magnetic showers, which allows to distinguish electrons and photon signals from  $\pi^0$   
 1563 decay signals. The ES is composed of a layer of lead radiators followed by a layer of  
 1564 silicon strip sensors. The lead radiators initiate electromagnetic showers when reached  
 1565 by photons and electrons, then, the strip sensors measure the deposited energy and  
 1566 the transverse shower profiles. The full ES thickness is 20 cm.

### 1567 3.3.5 Hadronic calorimeter

1568 Hadrons are not absorbed by the ECAL<sup>2</sup> but by the hadron calorimeter (HCAL),  
 1569 which is made of a combination of alternating brass absorber layers and silicon photo-  
 1570 multiplier(SiPM) layers; therefore, particles passing through the scintillator material  
 1571 produce showers, as in the ECAL, as a result of the inelastic scattering of the hadrons  
 1572 with the detector material. Since the particles are not absorbed in the scintillator,  
 1573 their energy is sampled; therefore the total energy is not measured but estimated from  
 1574 the energy clusters, which reduces the resolution of the detector. Brass was chosen  
 1575 as the absorber material due to its short interaction length ( $\lambda_I = 16.42$  cm) and its  
 1576 non-magnetivity. Figure 3.16 shows a schematic view of the CMS HCAL.

1577 The HCAL is divided into four sections; the Hadron Barrel (HB), the Hadron  
 1578 Outer (HO), the Hadron Endcap (HE) and the Hadron Forward (HF) sections. The  
 1579 HB covers the region  $0 < |\eta| < 1.4$ , while the HE covers the region  $1.3 < |\eta| < 3.0$ .  
 1580 The HF, made of quartz fiber scintillator and steel as absorption material, covers  
 1581 the forward region  $3.0 < |\eta| < 5.2$ . Both the HB and HF are located inside the  
 1582 solenoid. The HO is placed outside the magnet as an additional layer of scintillators

---

<sup>2</sup> Most hadrons are not absorbed, but few low-energy ones might be.

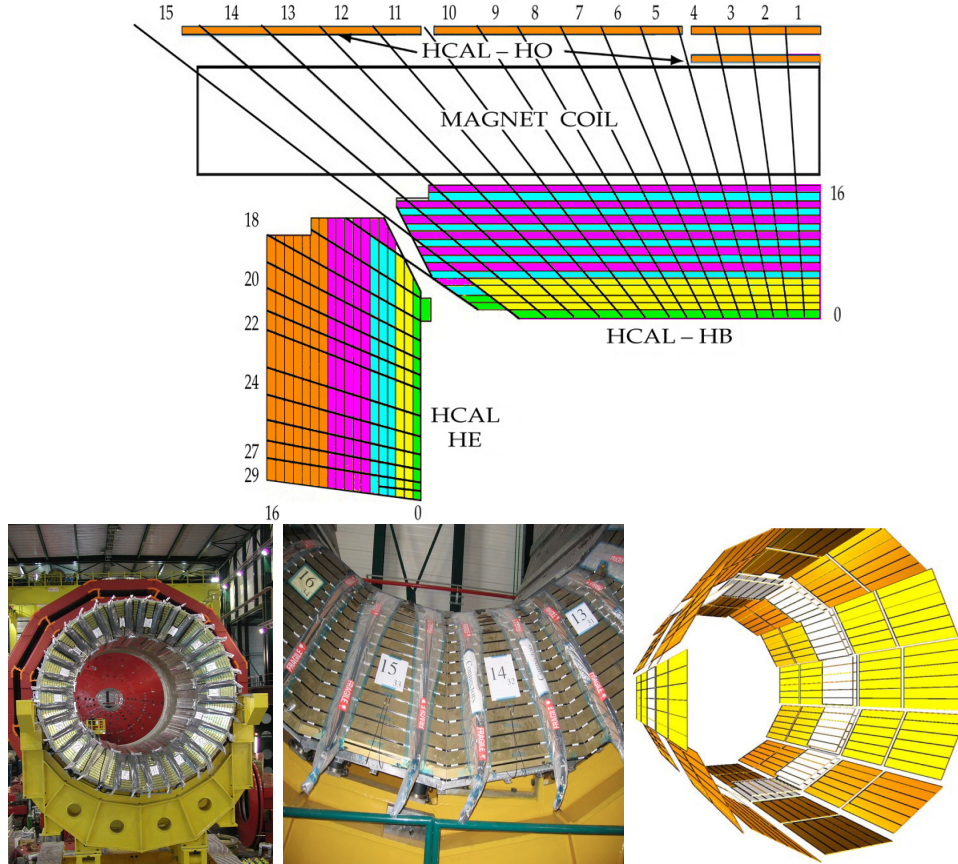


**Figure 3.16:** Top: CMS HCAL schematic view, the colors indicate the layers that are grouped into the same readout channels. Bottom: picture of a section of the HB; the absorber material is the golden region and scintillators are placed in between the absorber material (left and center). Schematic view of the HO (right). [83,84]

1583 with the purpose of measure the energy tails of particles passing through the HB and  
 1584 the magnet (see Figure 3.16 top and bottom right).

### 1585 **3.3.6 Superconducting solenoid magnet**

1586 The superconducting magnet installed in the CMS detector is designed to provide  
 1587 an intense and highly uniform magnetic field in the central part of the detector.  
 1588 In fact, the tracking system takes advantage of the bending power of the magnetic  
 1589 field to measure with precision the momentum of the particles that traverse it; the

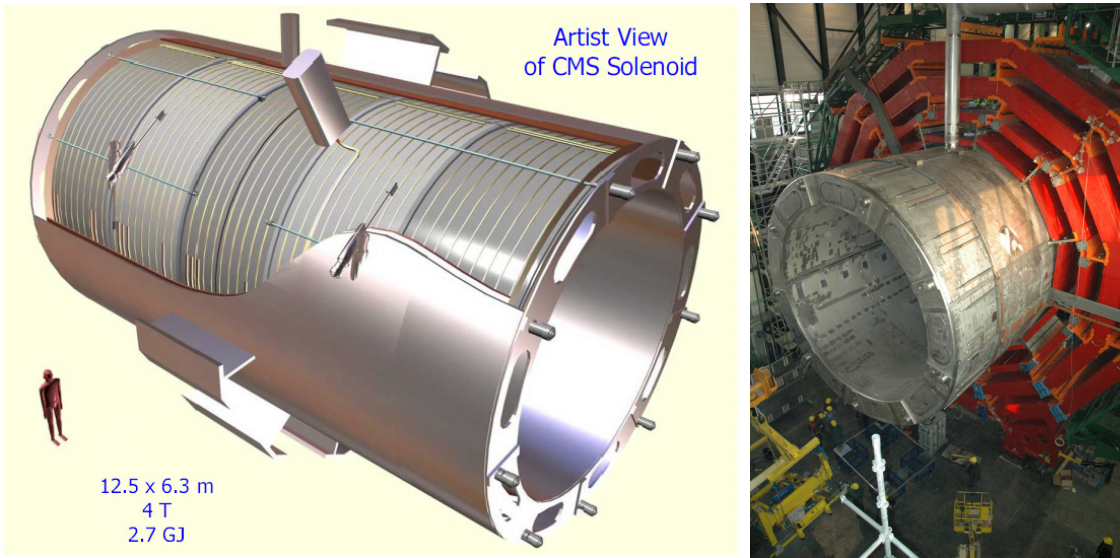


**Figure 3.17:** Artistic representation of the CMS solenoid magnet(left). The magnet is supported on an iron yoke (right) which also serves as the house of the muon detector and as mechanical support for the whole CMS detector [77].

1590 unambiguous determination of the sign for high momentum muons was a driving  
 1591 principle during the design of the magnet. The magnet has a diameter of 6.3 m, a  
 1592 length of 12.5 m and a cold mass of 220 ton; the generated magnetic field reaches a  
 1593 strength of 3.8T. Since it is made of Ni-Tb superconducting cable it has to operate at  
 1594 a temperature of 4.7 K by using a helium cryogenic system; the current circulating in  
 1595 the cables reaches 18800 A under normal running conditions. The left side of Figure  
 1596 3.17 shows an artistic view of the CMS magnet, while the right side shows a transverse  
 1597 view of the cold mass where the winding structure is visible.

1598 The yoke (see Figure 3.17), composed of 5 barrel wheels and 6 endcap disks made  
 1599 of iron, serves not only as the media for magnetic flux return but also provides housing  
 1600 for the muon detector system and structural stability to the full detector.

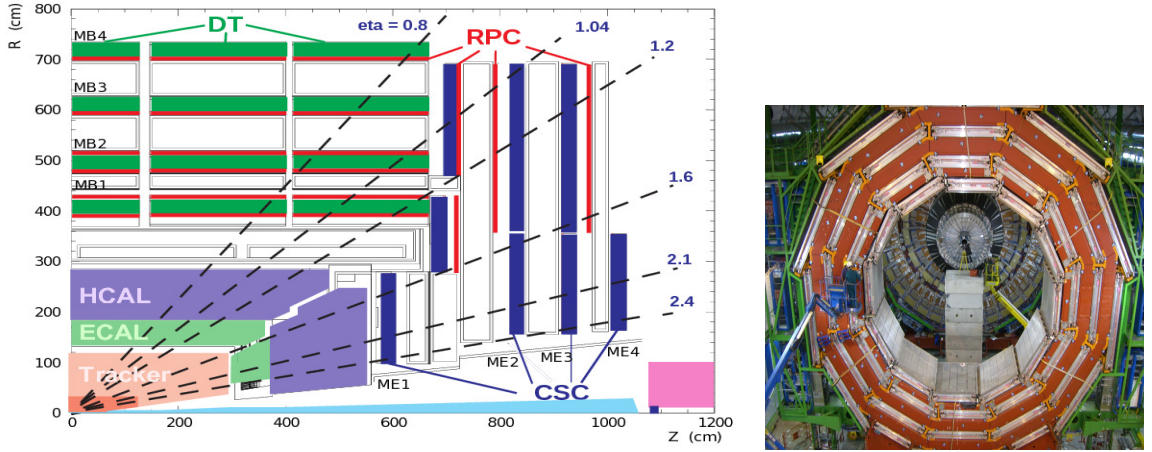


**Figure 3.18:** Left: CMS muon system schematic view; Right: one of the yoke rings with the muon DTs and RPCs installed; in the back it is possible to see the muon endcap [85].

### 1601 3.3.7 Muon system

1602 Muons are the only charged particles able to pass through all the CMS detector due  
 1603 to their low ionization energy loss; thus, muons can be separated easily from the  
 1604 high amount of particles produced in a  $pp$  collision. Also, muons are expected to be  
 1605 produced in the decay of several new particles; therefore, good detection of muons  
 1606 was one of the leading principles when designing the CMS detector.

1607 The CMS muon detection system (muon spectrometer) is embedded in the return  
 1608 yoke as seen in Figure 3.18. It is composed of three different detector types, the drift  
 1609 tube chambers (DT), cathode strip chambers (CSC), and resistive plate chambers  
 1610 (RPC); DT are located in the central region  $\eta < 1.2$  arranged in four layers of drift  
 1611 chambers filled with an Ar/CO<sub>2</sub> gas mixture.

1612 The muon endcaps are made of CSCs covering the region  $\eta < 2.4$  and filled with  
 1613 a mixture of Ar/CO<sub>2</sub>/CF<sub>4</sub>. The reason behind using a different detector type lies on  
 1614 the different conditions in the forward region like the higher muon rate and higher  
 1615 residual magnetic field compared to the central region.

1616 The third type of detector used in the muon system is a set of four disks of RPCs

1617 working in avalanche mode. The RPCs provide good spatial and time resolutions. The  
1618 track of high- $p_T$  muon candidates is built combining information from the tracking  
1619 system and the signal from up to six RPCs and four DT chambers.

1620 The muon tracks are reconstructed from the hits in the several layers of the muon  
1621 system.

### 1622 **3.3.8 CMS trigger system**

1623 CMS expects  $pp$  collisions every 25 ns, i.e., an interaction rate of 40 MHz for which  
1624 it is not possible to store the recorded data in full. In order to handle this high event  
1625 rate data, an online event selection, known as triggering, is performed; triggering  
1626 reduces the event rate to 100 Hz for storage and further offline analysis.

1627 The trigger system starts with a reduction of the event rate to 100 kHz in the  
1628 so-called *the level 1 trigger* (L1). L1 is based on dedicated programmable hardware  
1629 like Field Programmable Gate Arrays (FPGAs) and Application Specific Integrated  
1630 Circuits (ASICs), partly located in the detector itself; another portion is located in  
1631 the CMS underground cavern. Hit pattern information from the muon chambers  
1632 and the energy deposits in the calorimeter are used to decide if an event is accepted  
1633 or rejected, according to selection requirements previously defined, which reflect the  
1634 interesting physics processes. Figure 3.19 shows the L1 trigger architecture.

1635 The second stage in the trigger system is called *the high-level trigger* (HLT); events  
1636 accepted by L1 are passed to HLT in order to make an initial reconstruction of them.  
1637 HLT is software based and runs on a dedicated server farm, using selection algorithms  
1638 and high-level object definitions; the event rate at HLT is reduced to 100 Hz. The  
1639 first HLT stage takes information from the muon detectors and the calorimeters to  
1640 make the initial object reconstruction; in the next HLT stage, information from the

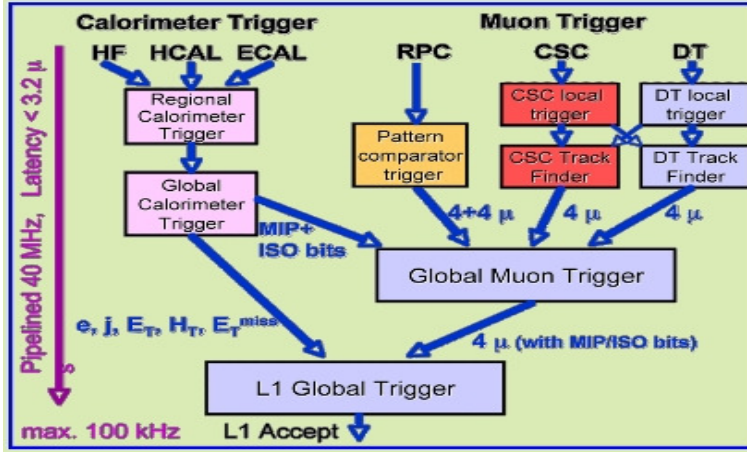


Figure 3.19: CMS Level-1 trigger architecture [86].

pixel and strip detectors is used to do first fast tracking and then full tracking online.

This initial object reconstruction is used in further steps of the trigger system.

Events and preliminary reconstructed physics objects from HLT are sent to be fully reconstructed at the CERN computing center known also as Tier-0 facility. Again, the pixel detector information provides high-quality seeds for the track reconstruction algorithm offline, primary vertex reconstruction, electron and photon identification, muon reconstruction,  $\tau$  identification, and b-tagging. After full reconstruction, data sets are made available for offline analyses.

Sometimes, a trigger *prescale* is introduced in order to reduce even further the event rate; thus, for a prescaling of ten only one of each ten events passing the trigger requirements is saved.

### 3.3.9 CMS computing

Data coming from the experiment have to be stored and made available for further analysis; in order to cope with all the tasks implied in the offline data processing, like transfer, simulation, reconstruction and reprocessing, among others, a large computing power is required. The CMS computing system is based on the distributed

1657 architecture concept, where users of the system and physical computer centers are  
 1658 distributed worldwide and interconnected by high-speed networks.

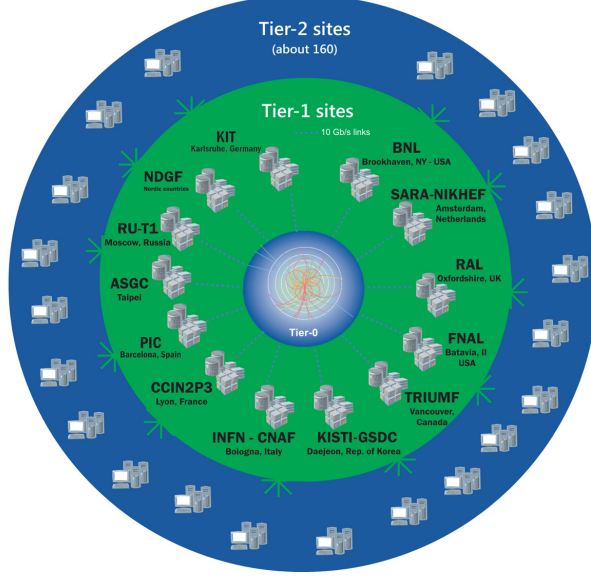


**Figure 3.20:** WLCG structure. The primary computer centers (Tier-0) are located at CERN (data center) and at the Wigner datacenter in Budapest. Tier-1 is composed of 13 centers and Tier-2 is composed of about 160 centers. [87].

1659 The worldwide LHC computing grid (WLCG) is the mechanism used to provide  
 1660 that distributed environment. WLCG is a tiered structure connecting computing  
 1661 centers around the world, which provides the necessary storage and computing facil-  
 1662 ities. The primary computing centers of the WLCG are located at the CERN and  
 1663 the Wigner datacenter in Budapest and are known as Tier-0 as shown in Figure 3.20.  
 1664 The main responsibilities for each tier level are [87]

- 1665 • **Tier-0:** initial reconstruction of recorded events and storage of the resulting  
 1666 datasets, the distribution of raw data to the Tier-1 centers.
- 1667 • **Tier-1:** provide storage capacity, support for the Grid, safe-keeping of a pro-  
 1668 portional share of raw and reconstructed data, large-scale reprocessing and safe-  
 1669 keeping of corresponding output, generation of simulated events, distribution

1670 of data to Tier 2s, safe-keeping of a share of simulated data produced at these  
1671 Tier 2s.

- 1672 • **Tier-2:** store sufficient data and provide adequate computing power for spe-  
1673 cific analysis tasks and proportional share of simulated event production and  
1674 reconstruction.

1675 Aside from the general computing strategy to manage the huge amount of data  
1676 produced by experiments, CMS uses a software framework to perform a variety of  
1677 processing, selection and analysis tasks. The central concept of the CMS data model  
1678 referred to as *event data model* (EDM) is the *Event*; therefore, an event is the unit  
1679 that contains the information from a single bunch crossing, any data derived from  
1680 that information like the reconstructed objects, and the details of the derivation.

1681 Events are passed as the input to the *physics modules* that obtain information  
1682 from them and create new information; for instance, *event data producers* add new  
1683 data into the events, *analyzers* produce an information summary from an event set,  
1684 *filters* perform selection and triggering.

1685 CMS uses several event formats with different levels of detail and precision

- 1686 • **Raw format:** events in this format contain the full recorded information from  
1687 the detector as well as trigger decision and other metadata. An extended version  
1688 of raw data is used to store information from the CMS Monte Carlo simulation  
1689 tools (see Chapter 4). Raw data are stored permanently, occupying about  
1690 2MB/event

- 1691 • **RECO format:** events in this format correspond to raw data that have been  
1692 submitted to reconstruction algorithms like primary and secondary vertex re-  
1693 construction, particle ID, and track finding. RECO events contain physics ob-

1694       jects and all the information used to reconstruct them; average size is about 0.5  
 1695       MB/event.

- 1696     • **AOD format:** Analysis Object Data (AOD) is the data format used in the  
   1697       physics analyses given that it contains the parameters describing the high-level  
   1698       physics objects in addition to enough information to allow a kinematic refitting if  
   1699       needed. AOD events are filtered versions of the RECO events to which skimming  
   1700       or other filtering have been applied, hence AOD events are subsets of RECO  
   1701       events. Requires about 100 kB/event.
- 1702     • **Non-event data** are data needed to interpret and reconstruct events. Some  
   1703       of the non-event data used by CMS contains information about the detector  
   1704       contraction and condition data like calibrations, alignment, and detector status.

1705       Figure 3.21 shows the data flow scheme between CMS detector and tiers.

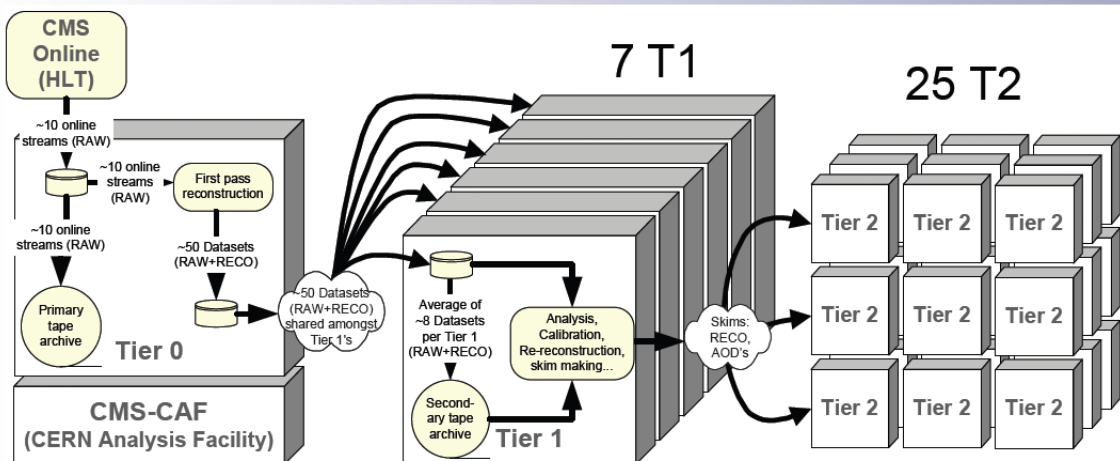


**Figure 3.21:** Data flow from CMS detector through tiers.

1706       The whole collection of software built as a framework is referred to as *CMSSW*. This  
 1707       framework provides the services needed by the simulation, calibration and alignment,  
 1708       and reconstruction modules that process event data, so that physicists can perform

1709 analysis. The CMSSW event processing model is composed of one executable, called  
1710 cmsRun, and several plug-in modules which contains all the tools (calibration, recon-  
1711 struction algorithms) needed to process an event. The same executable is used for  
1712 both detector data and Monte Carlo simulations [88].

1713

## CHAPTER 4

1714

### Event generation, simulation and reconstruction

1715

#### 4.1 Introduction

1716 The process of analyzing data recorded by the CMS experiment involves several stages  
1717 where the data are processed in order to interpret the information provided by all  
1718 the detection systems; in those stages, the particles produced after the  $pp$  collision  
1719 are identified by reconstructing their trajectories and measuring their features. In  
1720 addition, the SM provides a set of predictions that have to be compared with the  
1721 experimental results; however, in most of the cases, theoretical predictions are not  
1722 directly comparable to experimental results due to the diverse source of uncertainties  
1723 introduced by the experimental setup and theoretical approximations, among others.

1724 The strategy to face these conditions consists in using statistical methods imple-  
1725 mented in computational algorithms to produce numerical results that can be con-  
1726 trasted with the experimental results. These computational algorithms are commonly  
1727 known as Monte Carlo (MC) methods and, in the case of particle physics, they are  
1728 designed to apply the SM rules and produce predictions about the physical observ-  
1729 ables measured in the experiments. Since particle physics is governed by quantum  
1730 mechanics principles, predictions are not allowed from single events; therefore, a high  
1731 number of events are *generated* and predictions are produced in the form of statistical

1732 distributions for the observables. Effects of the detector presence are included in the  
 1733 predictions by introducing simulations of the detector itself.

1734 This chapter presents a description of the event generation strategy and the tools  
 1735 used to perform the detector simulation and physics objects reconstruction. A com-  
 1736 prehensive review of event generators for LHC physics can be found in Reference [89]  
 1737 on which this chapter is based.

## 1738 4.2 Event generation

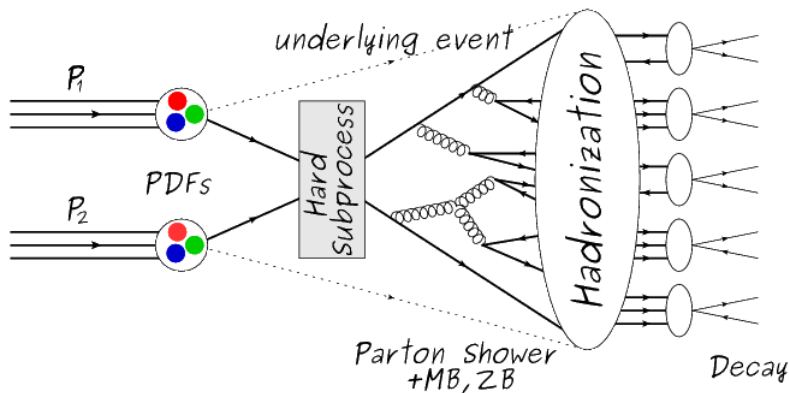


**Figure 4.1:** Event generation process. The actual interaction is generated in the hard subprocess. The parton shower describes the evolution of the partons from the hard subprocess. Modified from Reference [90].

1739 The event generation is intended to create events that mimic the behavior of  
 1740 actual events produced in collisions; they obey a sequence of steps from the particles  
 1741 collision hard process to the decay process into the final state. Figure 4.1 shows a  
 1742 schematic view of the event generation process; the fact that the full process can be  
 1743 treated as several independent steps is motivated by the QCD factorization theorem.

1744 Generation starts by taking into account the PDFs of the incoming particles.  
 1745 Event generators offer the option to chose from several PDF sets depending on the

particular process under simulation<sup>1</sup>; in the following,  $pp$  collisions will be considered. The *hard subprocess* describes the actual interaction between partons from the incoming protons; it is represented by the matrix element connecting the initial and final states of the interaction. Normally, the matrix element can be written as a sum over Feynman diagrams and consider interferences between terms in the summation. During the generation of the hard subprocess, the production cross section is calculated.

The order to which the cross section is calculated depends on the order of the Feynman diagrams involved in the calculation; therefore, radiative corrections are included by considering a higher order Feynman diagrams where QCD radiation dominates. Currently, cross sections calculated to LO do not offer a satisfactory description of the processes, i.e., the results are only reliable for the shape of distributions; therefore, NLO calculations have to be performed with the implication that the computing time needed is highly increased.

The final parton content of the hard subprocess is subjected to the *parton shower* which generates the gluon radiation. Parton shower evolves the partons, i.e., gluons split into quark-antiquark pairs and quarks with enough energy radiate gluons giving rise to further parton multiplication, following the DGLAP (Dokshitzer-Gribov-Lipatov-Altarelli-Parisi) equations. Showering continues until the energy scale is low enough to reach the non-perturbative limit.

In the simulation of LHC processes that involve  $b$  quarks, like the single top quark or Higgs associated production, it is needed to consider that the  $b$  quark is heavier than the proton; hence, the QCD interaction description is made in two different schemes [95]

---

<sup>1</sup> Tool in Reference [91] allows to plot different PDF sets under customizable conditions.

1770       • four-flavor (4F) scheme.  $b$  quarks appear only in the final state because they  
 1771       are heavier than the proton and therefore they can be produced only from the  
 1772       splitting of a gluon into pairs or singly in association with a  $t$  quark in high  
 1773       energy-scale interactions; furthermore, during the simulation, the  $b$ -PDFs are set  
 1774       to zero. Calculations in this scheme are more complicated due to the presence  
 1775       of the second  $b$  quark but the full kinematics is considered already at LO and  
 1776       therefore the accuracy of the description is better.

1777       • five-flavor (5F) scheme.  $b$  quarks are considered massless, therefore they can  
 1778       appear in both initial and final states since they can now be part of the proton;  
 1779       thus, during the simulation  $b$ -PDFs are not set to zero. In this scheme, calcu-  
 1780       lations are simpler than in the 4F scheme and possible logarithmic divergences  
 1781       are absorbed by the PDFs through the DGLAP evolution.

1782       In this thesis, the  $tHq$  events are generated using the 4F scheme in order to reduce  
 1783       uncertainties, while the  $tHW$  events are generated using the 5F scheme to eliminate  
 1784       LO interference with  $t\bar{t}H$  process [48].

1785       Partons involved in the  $pp$  collision are the focus of the simulation, however, the  
 1786       rest of the partons inside the incoming protons are also affected because the remnants  
 1787       are colored objects; also, multiple parton interactions can occur. The hadronization  
 1788       of the remnants and multiple parton interactions are known as *underlying event* and  
 1789       it has to be included in the simulation. In addition, multiple  $pp$  collisions in the same  
 1790       bunch crossing (pile-up mentioned in 3.2) occurs, actually in two forms

1791       • *in-time PU* which refers to multiple  $pp$  collision in the bunch crossing but that  
 1792       are not considered as primary vertices.

1793       • *Out-of-time PU* which refers to overlapping  $pp$  collisions from consecutive bunch  
 1794       crossings; this can occur due to the time-delays in the detection systems where  
 1795       information from one bunch crossing is assigned to the next or previous one.

1796       While the underlying event effects are included in generation using generator-  
 1797       specific tools, PU effects are added to the generation by overlying Minimum-bias (MB)  
 1798       and Zero-bias (ZB) events to the generated events. MB events are inelastic events  
 1799       selected by using a loose trigger with as little bias as possible, therefore accepting a  
 1800       large fraction of the overall inelastic event; ZB events correspond to random events  
 1801       recorded by the detector when collisions are likely. MB models in-time PU and ZB  
 1802       models out-of-time PU.

1803       The next step in the generation process is called *hadronization*. Since particles  
 1804       with a net color charge are not allowed to exits isolated, they have to recombine  
 1805       to form bound states. This is precisely the process by which the partons resulting  
 1806       from the parton shower arrange themselves as color singlets to form hadrons. At  
 1807       this step, the energy-scale is low and the strong coupling constant is large, therefore  
 1808       hadronization process is non-perturbative and the evolution of the partons is described  
 1809       using phenomenological models. Most of the baryons and mesons produced in the  
 1810       hadronization are unstable and hence they will decay in the detector.

1811       The last step in the generation process corresponds to the decay of the unstable  
 1812       particles generated during hadronization; it is also simulated in the hadronization  
 1813       step, based on the known branching ratios.

### 1814       **4.3 Monte Carlo Event Generators.**

1815       The event generation described in the previous section has been implemented in  
 1816       several software packages for which a brief description is given.

- 1817     • **PYTHIA 8.** It is a program designed to perform the generation of high energy  
 1818        physics events which describes the collisions between particles such as electrons  
 1819        and protons. Several theories and models are implemented in it, in order to  
 1820        describe physical aspects like hard and soft interaction, parton distributions,  
 1821        initial and final-state parton showers, multiple parton interactions, beam rem-  
 1822        nants, hadronization<sup>2</sup> and particle decay. Thanks to extensive testing, several  
 1823        optimized parametrizations, known as *tunings*, have been defined in order to  
 1824        improve the description of actual collisions to a high degree of precision; for  
 1825        analysis at  $\sqrt{s} = 13$  TeV, the underline event CUETP8M1 tune is employed [97].  
 1826        The calculation of the matrix element is performed at LO which is not enough  
 1827        for the current required level of precision; therefore, pythia is often used for  
 1828        parton shower, hadronization and decays, while other event generators are used  
 1829        to generate the matrix element at NLO.
- 1830     • **MadGraph5\_aMC@NLO.** MadGraph is a matrix element generator which  
 1831        calculates the amplitudes for all contributing Feynman diagrams of a given  
 1832        process but does not provide a parton shower while MC@NLO incorporates  
 1833        NLO QCD matrix elements consistently into a parton shower framework; thus,  
 1834        MadGraph5\_aMC@NLO, as a merger of the two event generators MadGraph5  
 1835        and aMC@NLO, is an event generator capable to calculate tree-level and NLO  
 1836        cross sections and perform the matching of those with the parton shower. It is  
 1837        one of the most frequently used matrix element generators; however, it has the  
 1838        particular feature of the presence of negative event weights which reduce the  
 1839        number of events used to reproduce the properties of the objects generated [98].
- 1840     • **POWHEG.** It is an NLO matrix element generator where the hardest emis-

---

<sup>2</sup> based in the Lund string model [96]

1841 sion of color charged particles is generated in such a way that the negative event  
 1842 weights issue of MadGraph5\_aMC@NLO is overcome; however, the method re-  
 1843 quires an interface with  $p_T$ -ordered parton shower or a parton shower generator  
 1844 where this highest emission can be vetoed in order to avoid double counting of  
 1845 this highest-energetic emission. PYTHIA is a commonly matched to POWHEG  
 1846 event generator [100].

1847 Events resulting from the whole generation process are known as MC events.

## 1848 **CMS detector simulation.**

1849 After generation, MC events contain the physics of the collisions but they are not  
 1850 ready to be compared to the events recorded by the experiment since these recorded  
 1851 events correspond to the response of the detection systems to the interaction with  
 1852 the particles traversing them. The simulation of the CMS detector has to be applied  
 1853 on top of the event generation; it is simulated with a MC toolkit for the simulation  
 1854 of particles passing through matter called Geant4 which is also able to simulate the  
 1855 electronic signals that would be measured by all detectors inside CMS.

1856 The simulation takes the generated particles contained in the MC events as input,  
 1857 makes them pass through the simulated geometry, and models physics processes that  
 1858 particles experience during their passage through matter. The full set of results from  
 1859 particle-matter interactions corresponds to the simulated hit which contains informa-  
 1860 tion about the energy loss, momentum and position. Particles of the input event are  
 1861 called *primary*, while the particles originating from GEANT4-modeled interactions of  
 1862 a primary particle with matter are called a *secondary*. Simulated hits are the input  
 1863 of subsequent modules that emulate the response of the detector readout system and

1864 triggers. The output from the emulated detection systems and triggers is known as  
 1865 digitization [101, 102].

1866 The modeling of the CMS detector corresponds to the accurate modeling of the  
 1867 interaction among particles, the detector material, and the magnetic field. This  
 1868 simulation procedure includes the following standard steps

1869 • Modeling of the Interaction Region.

1870 • Modeling of the particle passage through the hierarchy of volumes that compose  
 1871 CMS detector and of the accompanying physics processes.

1872 • Modeling of the effect of multiple interactions per beam crossing and/or the  
 1873 effect of events overlay ( Pile-Up simulation).

1874 • Modeling of the detector's electronics response, signal shape, noise, calibration  
 1875 constants (digitization).

1876 In addition to the full simulation, i.e., a detailed detector simulation, a faster  
 1877 simulation (FastSim) have been developed, that may be used where much larger  
 1878 statistics are required. In FastSim, detector material effects are parametrized and  
 1879 included in the hits; those hits are used as input of the same higher-level algorithms<sup>3</sup>  
 1880 used to analyze the recorded events. In this way, comparisons between fast and full  
 1881 simulations can be performed [104].

1882 After the full detector simulation, the output events can be directly compared  
 1883 to events actually recorded in the CMS detector. The collection of MC events that  
 1884 reproduces the expected physics for a given process is known as MC sample.

---

<sup>3</sup> track fitting, calorimeter clustering, b tagging, electron identification, jet reconstruction and calibration, trigger algorithms which will be considered in the next sections

1885 **4.5 Event reconstruction.**

1886 The CMS experiment use the *particle-flow event reconstruction algorithm (PF)* to do  
 1887 the reconstruction of particles produced in  $pp$  collisions. Next sections will present  
 1888 a basic description of the *Elements* used by PF (tracker tracks, energy clusters, and  
 1889 muon tracks), based in the References [105,106] where more detailed descriptions can  
 1890 be found.

1891 **4.5.1 Particle-Flow Algorithm.**

1892 Each of the several sub detection systems of the CMS detector is dedicated to identify  
 1893 an specific type of particles, i.e., photons and electrons are absorbed by the ECAL  
 1894 and their reconstruction is based on ECAL information; hadrons are reconstructed  
 1895 from clusters in the HCAL while muons are reconstructed from hits in the muon  
 1896 chambers. PF is designed to correlate signals from all the detector layers (tracks and  
 1897 energy clusters) in order to reconstruct and identify each final state particle and its  
 1898 properties as sketched in Figure 4.2.

1899 For instance, a charged hadron is identified by a geometrical connection, known  
 1900 as *link*, between one or more calorimeter clusters and a track in the tracker, provided  
 1901 there are no hits in the muon system; combining several measurements allows a better  
 1902 determination of the energy and charge sign of the charged hadron.

1903 **Charged-particle track reconstruction.**

1904 The strategy used by PF in order to reconstruct tracks is called *Iterative Tracking*  
 1905 which occurs in four steps

- 1906 • Seed generation where initial track candidates are found by looking for a combi-  
 1907 nation of hits in the pixel detector, strip tracker, and muon chambers. In total

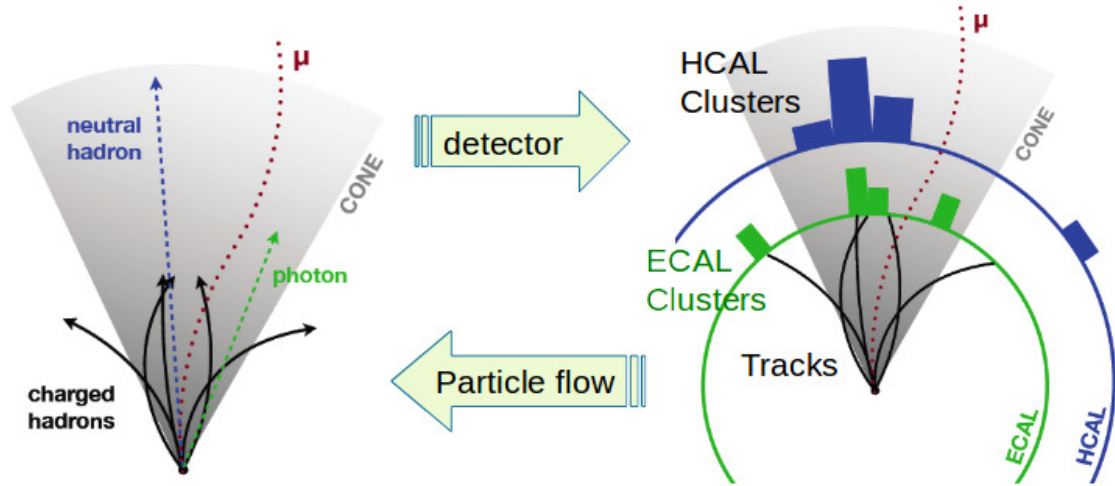


**Figure 4.2:** Particle flow algorithm. Information from the several CMS detection systems is provided as input to the algorithm which then combine it to identify and reconstruct all the particles in the final state and their properties. Reconstruction of simulated events is also performed by providing information from MC samples, detector and trigger simulation [107].

- 1908 ten iterations are performed, each one with a different seeding requirement.
- 1909 Seeds are used to estimate the trajectory parameters and uncertainties at the
- 1910 time of the full track reconstruction. Seeds are also considered track candidates.
- 1911 • Track finding using a tracking software known as Combinatorial Track Finder
- 1912 (CTF) [108]. The seed trajectories are extrapolated along the expected flight
- 1913 path of a charged particle, in agreement to the trajectory parameters obtained
- 1914 in the first step, in an attempt to find additional hits that can be assigned to
- 1915 the track candidates.
- 1916 • Track-fitting where the found tracks are passed as input to a module which
- 1917 provides the best estimate of the parameters of each trajectory.
- 1918 • Track selection where track candidates are submitted to a selection which dis-
- 1919 cards those that fail a set of defined quality criteria.
- 1920 Iterations differ in the seeding configuration and the final track selection as elab-

1921 orated in References [105, 106]. In the first iteration, high  $p_T$  tracks and tracks pro-  
 1922 duced near to the interaction region are identified and those hits are masked thereby  
 1923 reducing the combinatorial complexity. Next, iterations search for more complicated  
 1924 tracks, like low  $p_T$  tracks and tracks from b hadron decays, which tend to be displaced  
 1925 from the interaction region.

1926 **Vertex reconstruction.**

1927 During the track reconstruction, an extrapolation toward to the calorimeters is per-  
 1928 formed in order to match energy deposits; that extrapolation is performed also toward  
 1929 the beamline in order to find the origin of the track known as *vertex*. The vertex re-  
 1930 construction is performed by selecting from the available reconstructed tracks, those  
 1931 that are consistent with being originated in the interaction region where  $pp$  collisions  
 1932 are produced. The selection involves a requirement on the number of tracker (pixel  
 1933 and strip) hits and the goodness of the track fit.

1934 Selected tracks are clustered using a *deterministic annealing algorithm* (DA)<sup>4</sup>. A  
 1935 set of candidate vertices and their associated tracks, resulting from the DA, are then  
 1936 fitted with an *adaptive vertex fitter* (AVF) to produce the best estimate of the vertices  
 1937 locations.

1938 The  $p_T$  of the tracks associated to a reconstructed vertex is added, squared and  
 1939 used to organize the vertices; the vertex with the highest squared sum is designated  
 1940 as the *primary vertex* (PV) while the rest are designated as PU vertices.

1941 **Calorimeter clustering.**

1942 After traversing the CMS tracker system, electrons, photons and hadrons deposit their  
 1943 energy in the ECAL and HCAL cells. The PF clustering algorithm aims to provide

---

<sup>4</sup> DA algorithm and AVF are described in detail in References [110, 111]

1944 a high detection efficiency even for low-energy particles and an efficient distinction  
 1945 between close energy deposits. The clustering runs independently in the ECAL barrel  
 1946 and endcaps, HCAL barrel and endcaps, and the two preshower layers, following two  
 1947 steps

- 1948     • cells with an energy larger than a given seed threshold and larger than the energy  
              of the neighboring cells are identified as cluster seeds. The neighbor cells are  
              those that either share a side with the cluster seed candidate, or the eight closest  
              cells including cells that only share a corner with the seed candidate.
- 1952     • cells with at least a corner in common with a cell already in the cluster seed  
              and with an energy above a cell threshold are grouped into topological clusters.

1954       Clusters formed in this way are known as *particle-flow clusters*. With this cluster-  
 1955 ing strategy, it is possible to detect and measure the energy and direction of photons  
 1956 and neutral hadrons as well as differentiate these neutral particles from the charged  
 1957 hadron energy deposits. In cases involving charged hadrons for which the track pa-  
 1958 rameters are not determined accurately, for instance, low-quality and high- $p_T$  tracks,  
 1959 clustering helps in the energy measurements.

### 1960 **Electron track reconstruction.**

1961 Although the charged-particle track reconstruction described above works for elec-  
 1962 trons, they lose a significant fraction of their energy via bremsstrahlung photon radia-  
 1963 tion before reaching the ECAL; thus, the reconstruction performance depends on the  
 1964 ability to measure also the radiated energy. The reconstruction strategy, in this case,  
 1965 requires information from the tracking system and from the ECAL. Bremsstrahlung  
 1966 photons are emitted at similar  $\eta$  values to that of the electron but at different values  
 1967 of  $\phi$ ; therefore, the radiated energy can be recovered by grouping ECAL clusters in a

1968     $\eta$  window over a range of  $\phi$  around the electron direction. The group is called ECAL  
 1969    supercluster (SC) .

1970       Electron candidates from the track-seeding and ECAL super clustering are merged  
 1971    into a single collection which is submitted to a full electron tracking fit with a  
 1972    Gaussian-sum filter (GSF) [109]. The electron track and its associated ECAL su-  
 1973    percluster form a *particle-flow electron*.

1974    **Muon track reconstruction.**

1975    Given that the CMS detector is equipped with a muon spectrometer capable to iden-  
 1976    tify and measure the momentum of the muons traversing it, the muon reconstruction  
 1977    is not specific to PF; therefore, three different muon types are defined

1978       • *Standalone muon.* A clustering on the DTs or CSCs hits is performed to form  
 1979       track segments; those segments are used as seeds for the reconstruction in the  
 1980       muon spectrometer. All DTs, CSCs, and RPCs hits along the muon trajectory  
 1981       are combined and fitted to form the full track. The fitting output is called a  
 1982       *standalone-muon track*.

1983       • *Tracker muon.* Each track in the inner tracker with  $p_T$  larger than 0.5 GeV and  
 1984       a total momentum  $p$  larger than 2.5 GeV is extrapolated to the muon system.  
 1985       A *tracker muon track* corresponds to a extrapolated track that matches at least  
 1986       one muon segment.

1987       • *Global muon.* When tracks in the inner tracker (inner tracks) and standalone-muon  
 1988       tracks are matched and turn out being compatibles, their hits are combined and  
 1989       fitted to form a *global-muon track*.

1990        Global muons sharing the same inner track with tracker muons are merged into  
 1991      a single candidate. PF muon identification uses the muon energy deposits in ECAL,  
 1992      HCAL, and HO associated with the muon track to improve the muon identification.

1993 **Particle identification and reconstruction.**

1994      PF elements are connected by a linker algorithm that tests the connection between any  
 1995      pair of elements; if they are found to be linked, a geometrical distance that quantifies  
 1996      the quality of the link is assigned. Two elements may be linked indirectly through  
 1997      common elements. Linked elements form *PF blocks* and each PF block may contain  
 1998      elements originating in one or more particles. Links can be established between  
 1999      tracks, between calorimeter clusters, and between tracks and calorimeter clusters.  
 2000      The identification and reconstruction start with a PF block and proceed as follows

2001      • Muons. An *isolated global muon* is identified by evaluating the presence of  
 2002      inner track and energy deposits close to the global muon track in the  $(\eta, \phi)$   
 2003      plane, i.e., in a particular point of the global muon track, inner tracks and  
 2004      energy deposits are sought within a radius of  $\Delta R = 0.3$  (see eqn. 3.7) from  
 2005      the muon track; if they exit and the  $p_T$  of the found track added to the  $E_T$  of  
 2006      the found energy deposit does not exceed 10% of the muon  $p_T$  then the global  
 2007      muon is an isolated global muon. This isolation condition is stringent enough  
 2008      to reject hadrons misidentified as muons.

2009      *Non-isolated global muons* are identified using additional selection requirements  
 2010     on the number of track segments in the muon system and energy deposits along  
 2011     the muon track. Muons inside jets are identified with more stringent criteria  
 2012     in isolation and momentum as described in Reference [112]. The PF elements  
 2013     associated with an identified muon are masked from the PF block.

- 2014     • Electrons are identified and reconstructed as described above plus some additional requirements on fourteen variables like the amount of energy radiated, the distance between the extrapolated track position at the ECAL and the position of the associated ECAL supercluster, among others, which are combined in an specialized multivariate analysis strategy that improves the electron identification.
- 2015
- 2016
- 2017
- 2018
- 2019
- 2020     There are three methods for charge estimation; one is the sign of the curvature of the GSF track; a second method is based on matching a CTF track to a GSF track when at least one hit is shared in the innermost region. In the third method, the vector joining the beam spot and the SC position and the vector joining the beam spot and the first hit of the electron GSF track, are compared; the charge is estimated from the sign of the difference in  $\phi$  between these two vector. The electron charge is defined by the sign shared by at least two of the three estimates [157].
- 2021
- 2022
- 2023
- 2024
- 2025
- 2026
- 2027
- 2028     Tracks and clusters used to identify and reconstruct electrons are masked in the PF block.
- 2029
- 2030     • Isolated photons are identified from ECAL superclusters with  $E_T$  larger than 10 GeV, for which the energy deposited at a distance of 0.15, from the supercluster position on the  $(\eta, \phi)$  plane, does not exceed 10% of the supercluster energy; note that this is an isolation requirement. In addition, there must not be links to tracks. Clusters involved in the identification and reconstruction are masked in the PF block.
- 2031
- 2032
- 2033
- 2034
- 2035
- 2036     • Bremsstrahlung photons and prompt photons tend to convert to electron-positron pairs inside the tracker, therefore, a dedicated finder algorithm is used to link tracks that seem to originate from a photon conversion; in case those two tracks
- 2037
- 2038

2039        are compatible with the direction of a bremsstrahlung photon, they are also  
 2040        linked to the original electron track. Photon conversion tracks are also masked  
 2041        in the PF block.

- 2042        • The remaining elements in the PF block are used to identify hadrons. In the  
                 2043        region  $|\eta| \leq 2.5$ , neutral hadrons are identified with HCAL clusters not linked  
                 2044        to any track while photons from neutral pion decays are identified with ECAL  
                 2045        clusters without links to tracks. In the region  $|\eta| > 2.5$  ECAL clusters linked to  
                 2046        HCAL clusters are identified with a charged or neutral hadron shower; ECAL  
                 2047        clusters with no links are identified with photons. HCAL clusters not used yet,  
                 2048        are linked to one or more unlinked tracks and to an unlinked ECAL in order to  
                 2049        reconstruct charged-hadrons or a combination of photons and neutral hadrons  
                 2050        according to certain conditions on the calibrated calorimetric energy.
- 2051        • Charged-particle tracks may be liked together when they converge to a *sec-  
                 2052        ondary vertex (SV)* displaced from the IP where the PV and PU vertices are  
                 2053        reconstructed; at least three tracks are needed in that case, of which at most  
                 2054        one has to be an incoming track with hits in tracker region between a PV and  
                 2055        the SV.

2056        The linker algorithm, as well as the whole PF algorithm, has been validated and  
 2057        commissioned; results from that validation are presented in the Reference [105].

### 2058        **Jet reconstruction.**

2059        Quarks and gluons may be produced in the  $pp$  collisions, therefore, their hadronization  
 2060        will be seen in the detector as a shower of hadrons and their decay products in the  
 2061        form of a *jet*. Two classes of clustering algorithms have been developed based in  
 2062        their jet definition [113]:

2063     • Iterative cone algorithms (IC). Jets are defined in terms of circles of fixed radius  
 2064        $R$  in the  $\eta$ - $\phi$  plane, known as *stable cones*, for which the sum of the momenta  
 2065       of all the particles within the cone points in the same direction as the center  
 2066       of the circle. The seed of the iteration is the hardest non-isolated particle in  
 2067       the event, then, the resulting momentum direction is assigned as the new cone  
 2068       direction and a new iteration starts; iteration process stops when the cone is  
 2069       found to be stable.

2070     • Sequential recombination algorithms. The distance between non-isolated par-  
 2071       ticles is calculated; if that distance is below a threshold, these particles are  
 2072       recombined into a new object. The sequence is repeated until the separation  
 2073       between the recombined object and any other particle is above certain thres-  
 2074       hold; the recombined object is called a jet and the algorithm starts again with  
 2075       the remaining particles.

2076       Two conditions are of particular importance for the clustering algorithms, *infrared*  
 2077       *and collinear (IRC) safety*. In order to explain the concept of infrared (IR) safety,  
 2078       consider an event with three hard particles as shown in the top left side of Figure 4.3,  
 2079       two stable cones are found and then two jets are identified; if a soft gluon is added, as  
 2080       shown in the top right side of Figure 4.3, three stable cones are found and the three  
 2081       hard particles are now clustered into a single jet. If the addition of soft particles  
 2082       change the outcome of the clustering, then it is said that the algorithm is IR unsafe.  
 2083       Soft radiation is highly likely in perturbative QCD, which dominates the physics of  
 2084       the jets, and then IR unsafe effect leads to divergences [113].

2085       The concept of collinear safety can also be explained considering a three hard  
 2086       particles event, as shown in the bottom left side of Figure 4.3, where one stable cone  
 2087       containing all three particles is found and one jet is identified; if the hardest particle

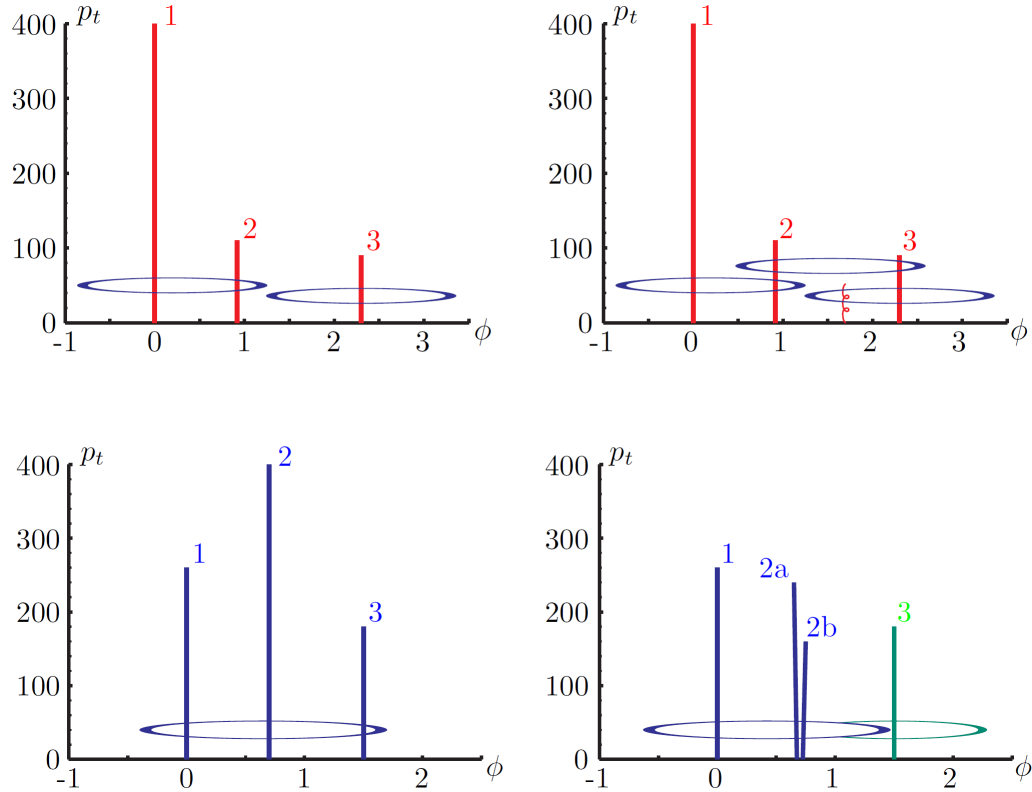


**Figure 4.3:** Stable cones identification using IC algorithms [113].

is split into two collinear particles (2a and 2b) in the bottom right side of Figure 4.3, then the clustering results in a different jet identification and the algorithm is said to be collinear unsafe. The collinear unsafe effect leads to divergences in jet cross section calculations [114].

It has been determined that IC algorithms are IRC unsafe, and therefore, they have to be replaced by algorithms that not only provide the finite perturbative results from theoretical computations, but also that are not highly dependent on underlying event and pileup effects which leads to significant corrections [113].

The sequential recombination algorithms arise as the IRC safe alternative used by the CMS experiment; in particular the anti- $k_t$  algorithm [114] which is a generalization of the previously existing  $k_t$  [115] and Cambridge/Aachen [116] jet clustering algorithms.

2100        The anti- $k_t$  algorithm is used to perform the jet reconstruction by clustering those  
 2101 PF particles within a cone (see Figure 4.4); previously, isolated electrons, isolated  
 2102 muons, and charged particles associated with other interaction vertices are excluded  
 2103 from the clustering.

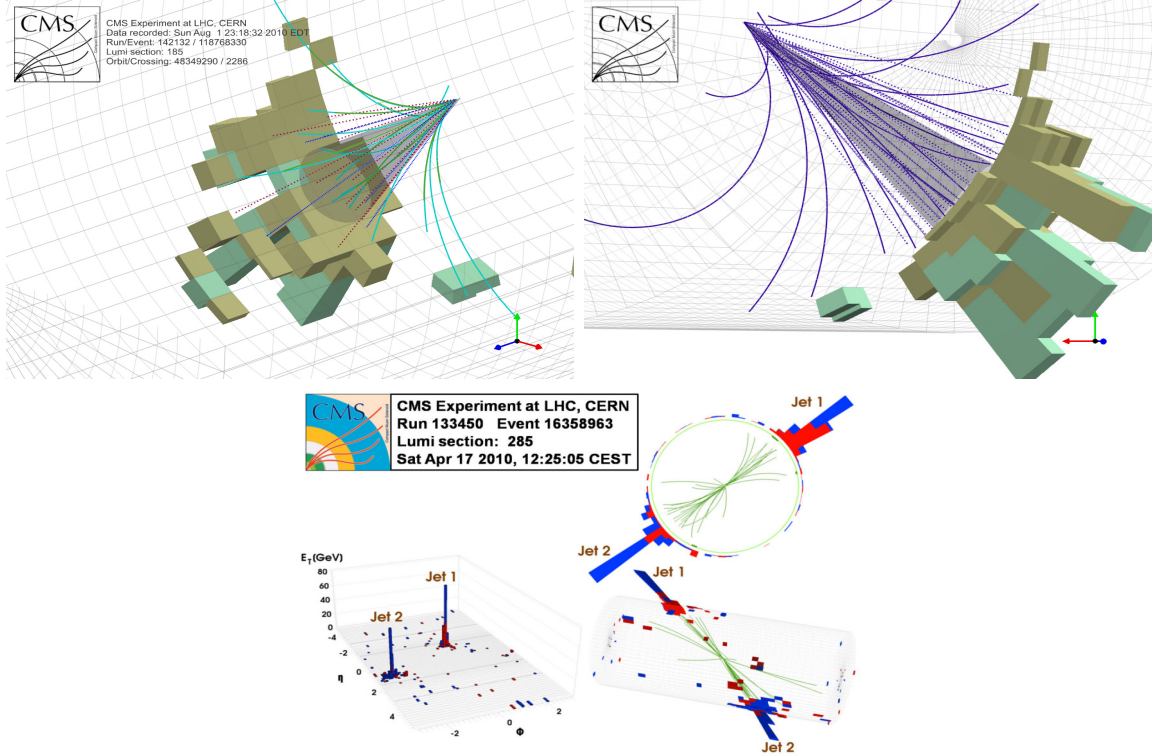


**Figure 4.4:** Jet reconstruction performed by the anti- $k_t$  algorithm. Top: Two different views of a CMS recorded event are presented. Continuous lines correspond to tracks left by charged particles in the tracker while dotted lines are the imaginary paths followed by neutral particles. The green cubes represent the ECAL cells while the blue ones represent the HCAL cells; in both cases, the height of the cube represent the amount of energy deposited in the cells [117]. Bottom: Reconstruction of a recorded event with two jets [118].

2104        The anti- $k_t$  algorithm proceeds in a sequential recombination of PF particles; the  
 2105 distance between particles  $i$  and  $j$  ( $d_{ij}$ ) and the distance between particles and the  
 2106 beam are defined as

$$\begin{aligned}
d_{ij} &= \min \left( \frac{1}{k_{ti}^2}, \frac{1}{k_{tj}^2} \right) \frac{\Delta_{ij}^2}{R^2} \\
d_{iB} &= \frac{1}{k_{ti}^2}
\end{aligned} \tag{4.1}$$

2107 where  $\Delta_{ij}^2 = (y_i - y_j)^2 + (\phi_i - \phi_j)^2$ ,  $k_{ti}$ ,  $y_i$  and  $\phi_i$  are the transverse momentum,  
 2108 rapidity and azimuth of particle  $i$  respectively and  $R$  is the called jet radius. For  
 2109 all the remaining PF particles, after removing the isolated ones,  $d_{ij}$  and  $d_{iB}$  are  
 2110 calculated<sup>5</sup> and the smallest is identified; if it is a  $d_{ij}$ , particles  $i$  and  $j$  are replaced  
 2111 with a new object whose momentum is the vectorial sum of the combined particles.  
 2112 If the smallest distance is a  $d_{iB}$  the clustering process ends, the object  $i$  (which at  
 2113 this stage should be a combination of several PF particles) is declared as a *Particle-*  
 2114 *flow-jet* (PF jet) and all the associated PF particles are removed from the detector.  
 2115 The clustering process is repeated until no PF particles remain.  $R$  is a free parameter  
 2116 that can be adjusted according to the specific analysis conditions; usually, two values  
 2117 are used,  $R=0.4$  and  $R=0.5$ , giving the name to the so-called AK4-jet and AK5-jet  
 2118 respectively.

2119 An advantage of the anti- $k_t$  algorithm over other clustering algorithms is the reg-  
 2120 ularity of the boundaries of the resulting jets. For all known IRC safe algorithms,  
 2121 soft radiation can introduce irregularities in the boundaries of the final jets; however,  
 2122 anti- $k_t$  algorithm is soft-resilient, meaning that jets shape is not affected by soft radia-  
 2123 tion, which is a valuable property considering that knowing the typical shape of jets  
 2124 makes experimental calibration of jets more simple. In addition, that soft-resilience  
 2125 is expected to simplify certain theoretical calculations and reduce the momentum-  
 2126 resolution loss caused by underlying-event (UE) and pileup contamination [114].

---

<sup>5</sup> Notice that this is a combinatorial calculation.

2127        The effect of the UE and pileup contamination over a jet identification, can be  
 2128        seen as if soft events are added to the jet; for instance, if a soft event representing UE  
 2129        or pileup is added to an event for which a set of jets J have been identified, and the  
 2130        clustering is rerun on that new extended event, the outcome will be different in two  
 2131        aspects: jets will contain some additional soft energy and the distribution of particles  
 2132        in jets may have change; that effect is called *back-reaction*. The back-reaction effect in  
 2133        the anti- $k_t$  algorithm is suppressed not by the amount of momentum added to the jet  
 2134        but by the jet transverse momentum  $p_{T,J}$ , which means that this strong suppression  
 2135        leads to a smaller correction due to EU and pileup effect [114].

2136 **Jet energy Corrections**

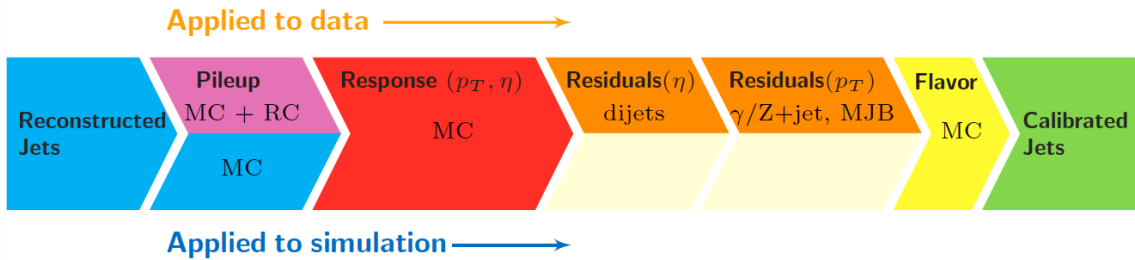


**Figure 4.5:** Jet energy correction diagram. Correction levels are applied sequentially in the indicated fixed order [120].

2137        Even though jets can be reconstructed efficiently, there are some effects that are  
 2138        not included in the reconstruction and that lead to discrepancies between the re-  
 2139        constructed results and the predicted results; in order to overcome these discrep-  
 2140        ancies, a factorized model has been designed in the form of jet energy corrections  
 2141        (JEC) [119,120] applied sequentially as shown in the diagram of Figure 4.5.

2142        At each level, the jet four-momentum is multiplied by a scaling factor based on  
 2143        jet properties, i.e.,  $\eta$ , flavor, etc.

- 2144        • Level 1 correction removes the energy coming from pile-up. The scale factor is

2145       determined using a MC sample of QCD dijet (2 jets) events with and without  
 2146       pileup overlay; it is parametrized in terms of the offset energy density  $\rho$ , jet  
 2147       area A, jet  $\eta$  and jet  $p_T$ . Different corrections are applied to data and MC due  
 2148       to the detector simulation.

- 2149     • MC-truth correction accounts for differences between the reconstructed jet en-  
           2150       ergy and the MC particle-level energy. The correction is determined on a QCD  
           2151       dijet MC sample and is parametrized in terms of the jet  $p_T$  and  $\eta$ .
- 2152     • Residuals correct remaining small differences within jet response in data and  
           2153       MC. The Residuals  $\eta$ -dependent correction compares jets of similar  $p_T$  in the  
           2154       barrel reference region. The Residuals  $p_T$ -dependent correct the jet absolute  
           2155       scale (JES vs  $p_T$ ).
- 2156     • Jet-flavor corrections are derived in the same way as MC-truth corrections but  
           2157       using QCD pure flavor samples.

2158 ***b*-tagging of jets.**

2159 A particular feature of the hadrons containing bottom quarks (b-hadrons) is that  
 2160 their lifetime is long enough to travel some distance before decaying, but it is not as  
 2161 long as those of light quark hadrons; therefore, when looking at the hadrons produced  
 2162 in  $pp$  collisions, b-hadrons decay typically inside the tracker rather than reaching the  
 2163 calorimeters as some light-hadrons do. As a result, a b-hadron decay gives rise to a  
 2164 displaced vertex (secondary vertex) with respect to the primary vertex as shown in  
 2165 Figure 4.6; the SV displacement is in the order of a few millimeters. A jet resulting  
 2166 from the decay of a b-hadron is called *b* jet; other jets are called light jets.

2167       Several methods to identify *b*-jets (*b*-tagging) have been developed; the method  
 2168 used in this thesis is known as *Combined Secondary Vertex* algorithm in its second

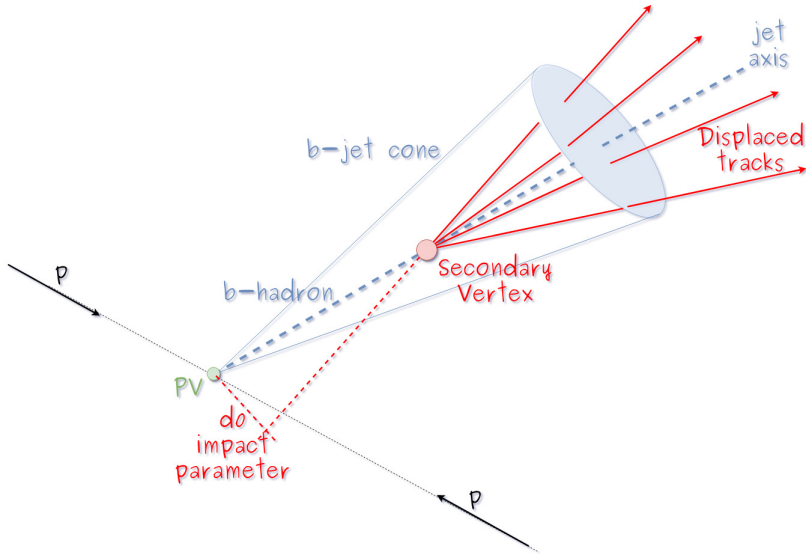


**Figure 4.6:** Secondary vertex in a b-hadron decay.

version (CSVv2) [121]. By using information of the impact parameter, the reconstructed secondary vertices, and the jet kinematics as input in a multivariate analysis that combines the discrimination power of each variable in one global discriminator variable, three working points (references): loose, medium and tight, are defined which quantify the probabilities of mistag jets from light quarks as jets from  $b$  quarks; 10, 1 and 0.1 % respectively. Although the mistagging probability decreases with the working point strength, the efficiency to correctly tag  $b$ -jets also decreases as 83, 69 and 49 % for the respective working point; therefore, a balance needs to be achieved according to the specific requirements of the analysis.

### Missing transverse energy.

The fact that proton bunches carry momentum along the  $z$ -axis implies that for each event it is expected that the momentum in the transverse plane is balanced. Imbalances are quantified by the missing transverse energy (MET) and are attributed to several sources including particles escaping undetected through the beam pipe,

2183 neutrinos produced in weak interactions processes which do not interact with the  
 2184 detector and thus escaping without leaving a sign, or even undiscovered particles  
 2185 predicted by models beyond the SM.

2186 The PF algorithm assigns the negative sum of the momenta of all reconstructed  
 2187 PF particles to the *particle-flow MET* according to

$$\vec{E}_T = - \sum_i \vec{p}_{T,i} \quad (4.2)$$

2188 JEC are propagated to the calculation of the  $\vec{E}_T$  as described in the Reference [122].

#### 2189 4.5.2 Event reconstruction examples

2190 Figures 4.7-4.9 show the results of the reconstruction performed on 3 recorded events.  
 2191 Descriptions are taken directly from the source.

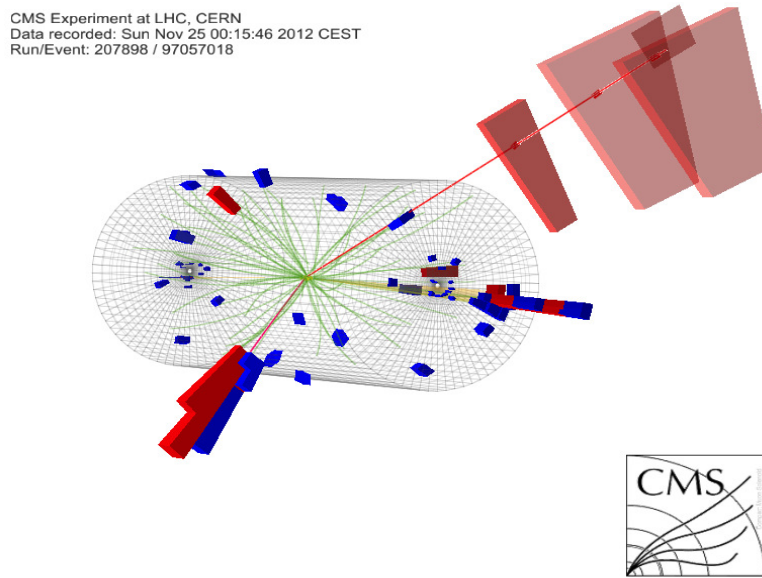


**Figure 4.7:** HIG-13-004 Event 1 reconstruction results; “HIG-13-004 Event 1: Event recorded with the CMS detector in 2012 at a proton-proton center-of-mass energy of 8 TeV. The event shows characteristics expected from the decay of the SM Higgs boson to a pair of  $\tau$  leptons. Such an event is characterized by the production of two forward-going jets, seen here in opposite endcaps. One of the  $\tau$  decays to a muon (red lines on the right) and neutrinos, while the other  $\tau$  decays into a charged hadron and a neutrino.” [123].

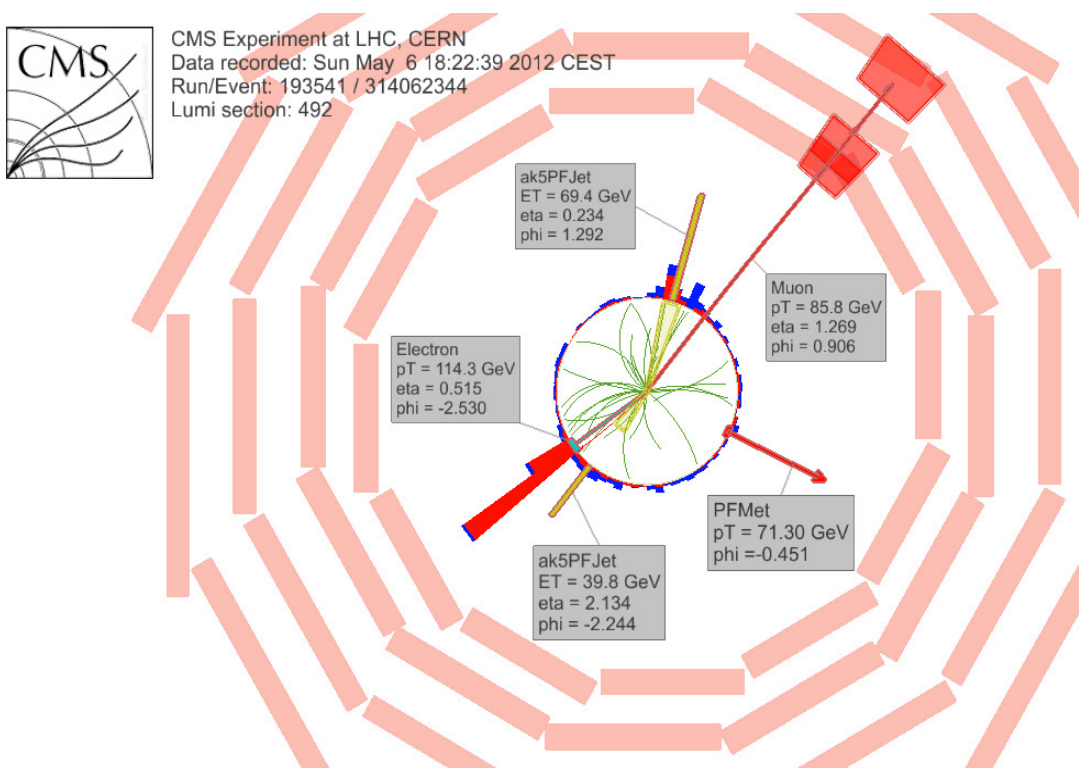


**Figure 4.8:**  $e\mu$  event reconstruction results; “An  $e\mu$  event candidate selected in 8 TeV data, as seen from the direction of the proton beams. The kinematics of the main objects used in the event selection are highlighted: two isolated leptons and two particle-flow jets. The reconstructed missing transverse energy is also displayed for reference” [124].

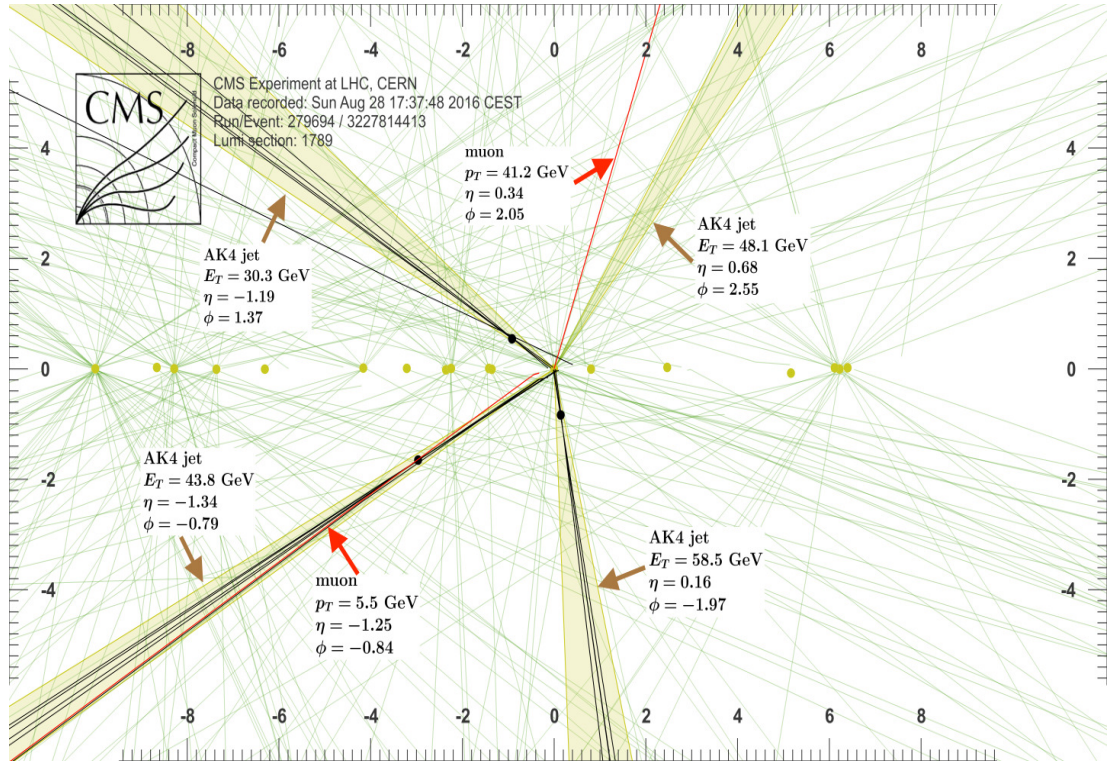


**Figure 4.9:** Recorded event reconstruction results; “Recorded event ( $\rho$ - $z$  projection) with three jets with  $p_T > 30$  GeV with one displaced muon track in 2016 data collected at 13 TeV. Each of the three jets has a displaced reconstructed vertex. The jet with  $p_T(j) = 43.8$  GeV,  $\eta(j) = -1.34$ ,  $\phi(j) = -0.79$  contains muon with  $p_T(\mu) = 5.5$  GeV,  $\eta(\mu) = -1.25$ ,  $\phi(\mu) = -0.84$ . Event contains reconstructed isolated muon with  $p_T(\mu) = 41.2$  GeV,  $\eta(\mu) = 0.34$ ,  $\phi(\mu) = 2.05$  and MET with  $p_T = 72.5$  GeV,  $\phi = -0.32$ . Jet candidates for a  $b$ -jet from top quark leptonic and hadronic decays are tagged by CSVv2T algorithm. One of the other two jets is tagged by CharmT algorithm. Tracks with  $p_T > 0.5$  GeV are shown. The number of reconstructed primary vertices is 18. Reconstructed  $m_T(W)$  is 101.8 GeV. Beam spot position correction is applied. Reconstructed primary vertices are shown in yellow color, while reconstructed displaced vertices and associated tracks are presented in black color. Dimensions are given in cm” [125].

2192

## CHAPTER 5

2193

### Statistical methods

#### 2194 5.1 Introduction

2195 In the course of analyzing the data sets provided by the CMS experiment and used in  
2196 this thesis, several statistical tools have been employed; in this chapter, a description  
2197 of these tools will be presented, starting with the general statement of the multivariate  
2198 analysis methods, followed by the particularities of the Boosted Decision Trees (BDT)  
2199 method and its application to the classification problem. Statistical inference methods  
2200 used will also be presented. This chapter is based mainly on References [126–128].

#### 2201 5.2 Multivariate analysis

2202 Multivariate data analysis (MVA) makes use of the statistical techniques developed to  
2203 analyze more than one variable at once, taking into account all the correlations among  
2204 variables. MVA is employed in a variety of fields like consumer and market research,  
2205 quality control and process optimization. Using MVA it is possible to identify the  
2206 dominant patterns in a data sample, like groups, outliers and trends, and determine  
2207 to which group a set of values belong; in the particle physics context, MVA methods  
2208 are used to perform the selection of certain type of events from a large data set.

2209 Processes with small cross section, such as the  $tHq$  process ( $\sigma_{SM}^{tHq}(13 \text{ TeV}) = 70.96$   
 2210 fb), are hard to detect in the presence of the processes with larger cross sections,  
 2211  $\sigma_{SM}^{t\bar{t}}(13 \text{ TeV}) = 823.44$  fb for instance; therefore, only a small fraction of the data  
 2212 contains events of interest (signal), the major part is signal-like events, which mimic  
 2213 signal characteristics but belong to different processes, so they are a background to  
 2214 the process of interest. This implies that it is not possible to say with certainty  
 2215 that a given event is a signal or a background and statistical methods should be  
 2216 involved. In that sense, the challenge can be formulated as one where a set of events  
 2217 have to be classified according to certain special features; these features correspond  
 2218 to the measurements of several parameters like energy or momentum, organized in a  
 2219 set of *input variables*. The measurements for each event can be written in a vector  
 2220  $\mathbf{x} = (x_1, \dots, x_n)$  for which

- 2221 •  $f(\mathbf{x}|s)$  is the probability density (*likelihood function*) that  $\mathbf{x}$  is the set of mea-  
 2222 sured values given that the event is a signal event (signal hypothesis).
- 2223 •  $f(\mathbf{x}|b)$  is the probability density (*likelihood function*) that  $\mathbf{x}$  is the set of mea-  
 2224 sured values given that the event is a background event (background hypothe-  
 2225 sis).

2226 Figure 5.1 shows three ways to perform a classification of events for which mea-  
 2227 surements of two properties, i.e., two input variables  $x_1$  and  $x_2$ , have been performed;  
 2228 blue circles represent signal events while red triangles represent background events.  
 2229 The classification on the left is *cut-based* requiring  $x_1 < c_1$  and  $x_2 < c_2$ ; usually  
 2230 the cut values ( $c_1$  and  $c_2$ ) are chosen according to some knowledge about the event  
 2231 process. In the middle plot, the classification is performed using a linear function of  
 2232 the input variables, hence the boundary is a straight line, while in the right plot the

2233 the relationship between input variables is not linear thus the boundary is not linear  
 2234 either.

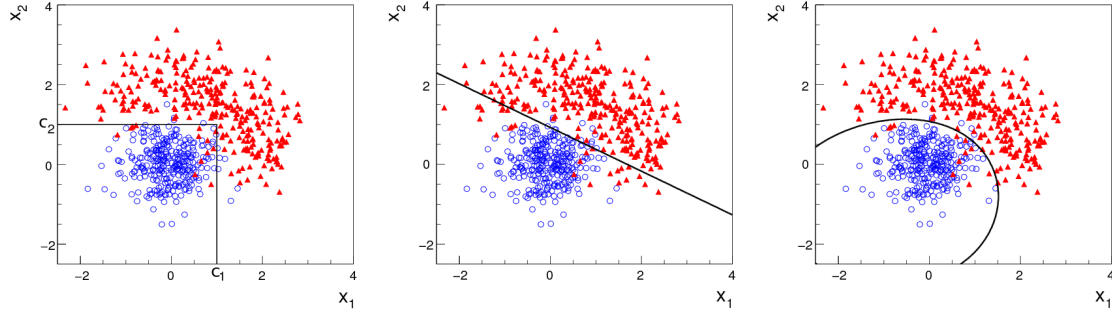


**Figure 5.1:** Scatter plots-MVA event classification. Distribution of two input variables  $x_1$  and  $x_2$  measured for a set of events; blue circles represent signal events and red triangles represent background events. The classification is based on cuts (left), linear boundary (center), and nonlinear boundary (right) [126]

2235 In general, the boundary can be parametrized in terms of the input variables such  
 2236 that the cut is set on the parametrization instead of on the variables, i.e.,  $y(\mathbf{x}) = y_{cut}$   
 2237 with  $y_{cut}$  being a constant; thus, the acceptance or rejection of an event is based on  
 2238 which side of the boundary the event is located. If  $y(\mathbf{x})$ , usually called *test statistic*,  
 2239 has functional form, it can be used to determine the probability distribution functions  
 2240  $p(y|s)$  and  $p(y|b)$  and then perform a test statistic with a single cut on the scalar  
 2241 variable  $y$ .

2242 Figure 5.2 shows an example of what would be the probability distribution func-  
 2243 tions under the signal and background hypotheses for a scalar test statistic with a cut  
 2244 on the classifier  $y$ . Note that the tails of the distributions indicate that some signal  
 2245 events fall in the rejection region and some background events fall on the acceptance  
 2246 region; therefore, it is convenient to define the *efficiency* with which events of a given  
 2247 type are accepted. The signal and background efficiencies are given by

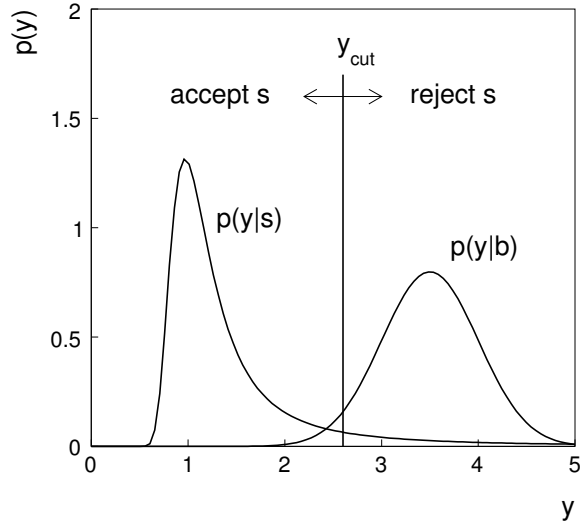


**Figure 5.2:** Distributions of the scalar test statistic  $y(\mathbf{x})$  under the signal and background hypotheses. [126]

$$\varepsilon_s = P(\text{accept event}|s) = \int_A f(\mathbf{x}|s) d\mathbf{x} = \int_{-\infty}^{y_{cut}} p(y|s) dy , \quad (5.1)$$

$$\varepsilon_b = P(\text{accept event}|b) = \int_A f(\mathbf{x}|b) d\mathbf{x} = \int_{-\infty}^{y_{cut}} p(y|b) dy , \quad (5.2)$$

where  $A$  is the acceptance region. If the background hypothesis is the *null hypothesis* ( $H_0$ ), the signal hypothesis would be *alternative hypothesis* ( $H_1$ ); in this context, the background efficiency corresponds to the significance level of the test ( $\alpha$ ) and describes the misidentification probability, while the signal efficiency corresponds to the power of the test ( $1-\beta$ )<sup>1</sup> and describes the probability of rejecting the background hypothesis if the signal hypothesis is true. What is sought in an analysis is to maximize the power of the test relative to the significance level, i.e., set a selection with the largest possible selection efficiency and the smallest possible misidentification probability.

---

<sup>1</sup>  $\beta$  is the fraction of signal events that fall out of the acceptance region.

### 2256 5.2.1 Decision trees

2257 For this thesis, the implementation of the MVA strategy, described above, is per-  
 2258 formed through decision trees by using the TMVA software package [127] included  
 2259 in the ROOT analysis framework [129]. In a simple picture, a decision tree classifies  
 2260 events according to their input variables values by setting a cut on each input variable  
 2261 and checking which events are on which side of the cut, just as proposed in the MVA  
 2262 strategy, but in addition, as a machine learning algorithm, decision trees offer the  
 2263 possibility to be trained and then perform the classification efficiently.

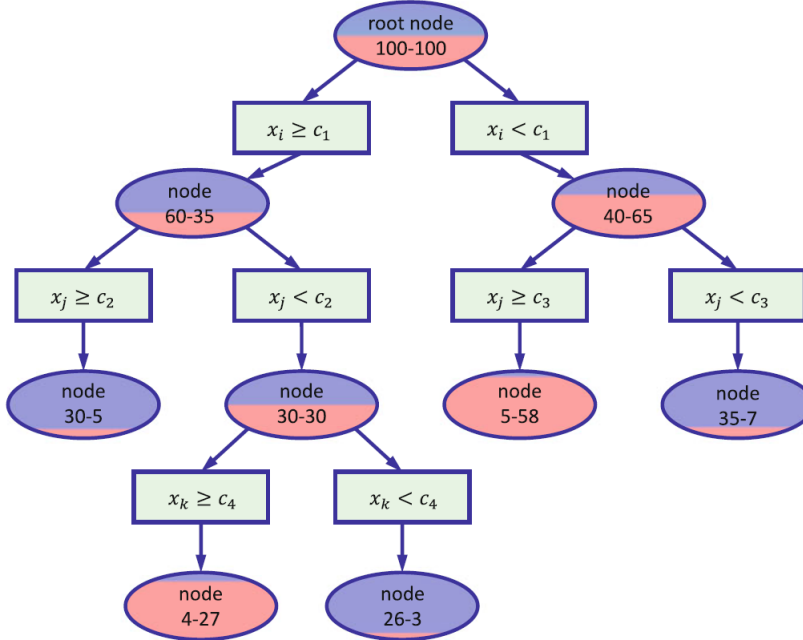


**Figure 5.3:** Example of a decision tree. Each node is fed with a MC sample mixing signal and background events (left-right numbers); nodes colors represent the relative number of signal/background events [128].

2264 The training or growing of a decision tree is the process where the rules for clas-  
 2265 sifying events are defined; this process is represented in Figure 5.3 and consists of  
 2266 several steps:

- 2267 • take MC samples of signal and background events and split them into two parts

2268 each; the first parts will be used in the decision tree training, while the second  
 2269 parts will be used for testing the final classifier obtained from the training.  
 2270 Each event has associated a set of input variables  $\mathbf{x} = (x_1, \dots, x_n)$  which serve  
 2271 to distinguish between signal and background events. The training sample is  
 2272 taken in at the *root node*.

- 2273     • Pick one variable, say  $x_i$ .
- 2274     • Pick one value of  $x_i$ , each event has its own value of  $x_i$ , and split the training  
     sample into two subsamples  $B_1$  and  $B_2$ ;  $B_1$  contains events for which  $x_i < c_1$   
     while  $B_2$  contains the rest of the training events;
- 2277     • scan all possible values of  $x_i$  and find the splitting value that provides the *best*  
     classification<sup>2</sup>, i.e.,  $B_1$  is mostly made of signal events while  $B_2$  is mostly made  
     of background events.
- 2280     • It is possible that variables other than the picked one produce a better classi-  
     fication, hence, all the variables have to be evaluated. Pick the next variable,  
     say  $x_j$ , and repeat the scan over its possible values.
- 2283     • At the end, all the variables and their values will have been scanned, the *best*  
     variable and splitting value will have been identified, say  $x_1, c_1$ , and there will  
     be two nodes fed with the subsamples  $B_1$  and  $B_2$ .

2286 Nodes are further split by repeating the decision process until a given number of  
 2287 final nodes is obtained, nodes are largely dominated by either signal or background  
 2288 events, or nodes have too few events to continue. Final nodes are called *leaves* and  
 2289 they are classified as signal or background leaves according to the class of the majority  
 2290 of events in them. Each *branch* in the tree corresponds to a sequence of cuts.

---

<sup>2</sup> Quality of the classification will be treated in the next paragraph.

2291       The quality of the classification at each node is evaluated through a separation  
 2292       criteria; there are several of them but the *Gini Index* ( $G$ ) is the one used in the  
 2293       decision trees trained for the analysis in this thesis.  $G$  is written in terms of the  
 2294       purity ( $P$ ), i.e., the fraction of signal events in the samples after the separation is  
 2295       made; it is given by

$$G = P(1 - P) \quad (5.3)$$

2296       note that  $P=0.5$  at the root node while  $G=0$  for pure leaves. For a node  $A$  split into  
 2297       two nodes  $B_1$  and  $B_2$  the  $G$  gain is

$$\Delta G = G(A) - G(B_1) - G(B_2). \quad (5.4)$$

2298       The *best* classification corresponds to that for which the gain of  $G$  is maximized;  
 2299       hence, the scanning over all the variables in an event and their values is of great  
 2300       importance.

2301       In order to provide a numerical output for the classification, events in a sig-  
 2302       nal(background) leaf are assigned an score of 1(-1) each, defining in this way the  
 2303       decision tree *classifier/weak learner* as

$$f(\mathbf{x}) = \begin{cases} 1 & \mathbf{x} \text{ in signal region,} \\ -1 & \mathbf{x} \text{ in background region.} \end{cases}$$

2304       Figure 5.4 shows an example of the classification of a sample of events, containing  
 2305       two variables, performed by a decision tree.

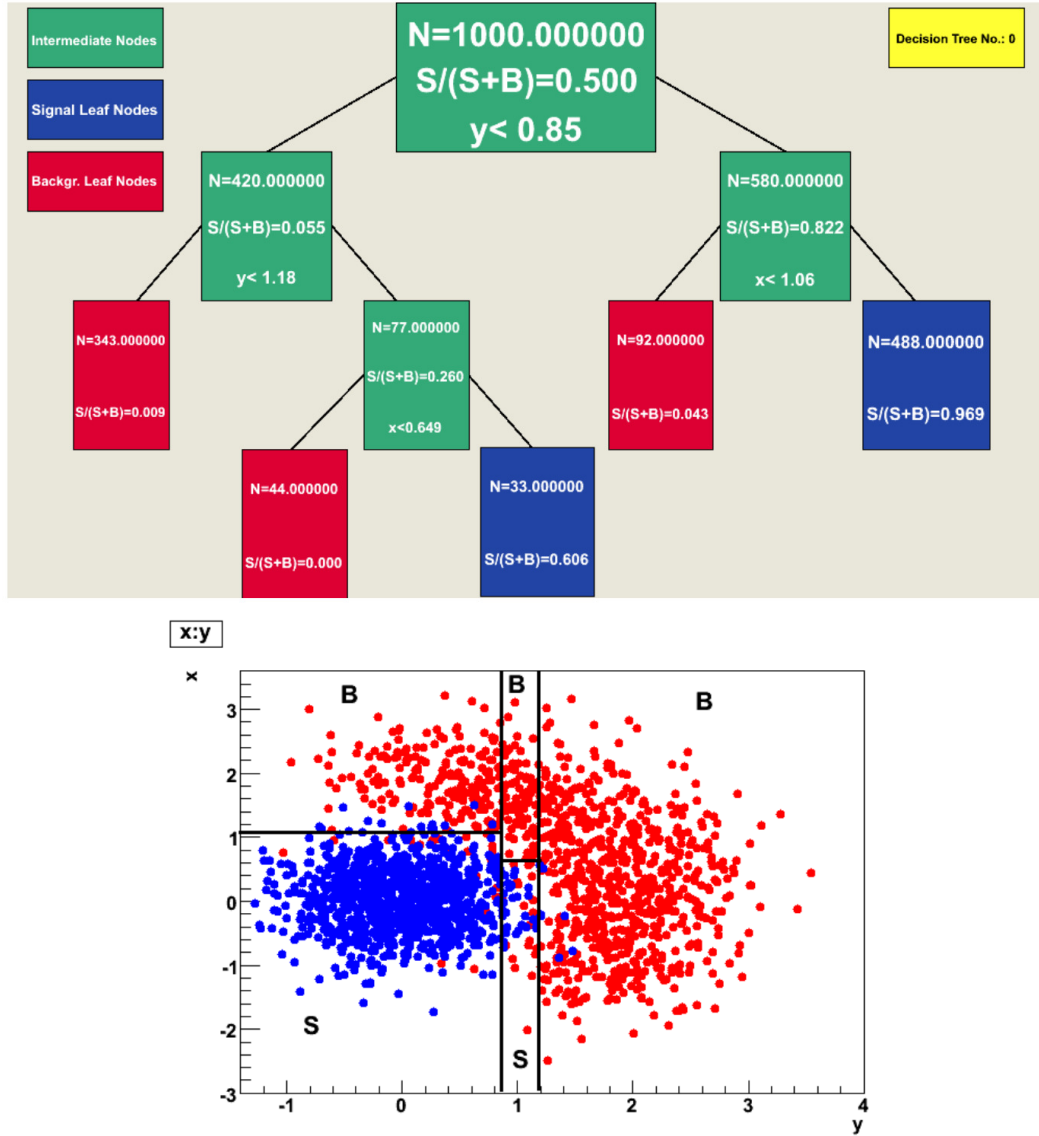


**Figure 5.4:** Example of a decision tree output. Each leaf, blue for signal events and red for background events, is represented by a region in the variables phase space [130].

### 2306 5.2.2 Boosted decision trees (BDT).

2307 Event misclassification occurs when a training event ends up in the wrong leaf, i.e., a  
 2308 signal event ends up in a background leaf or a background event ends up in a signal  
 2309 leaf. A way to correct it is to assign a weight to the misclassified events and train  
 2310 a second tree using the reweighted events; the event reweighting is performed by a

2311 boosting algorithm in such a way that when used in the training of a new decision  
 2312 tree the *boosted events* get correctly classified. The process is repeated iteratively  
 2313 adding a new tree to the forest and creating a set of classifiers, which are combined  
 2314 to create the next classifier; the final classifier offers more stability<sup>3</sup> and has a smaller  
 2315 misclassification rate than any individual ones. The resulting tree collection is known  
 2316 as a *boosted decision tree (BDT)*.

2317 Thus, purity of the sample is generalized to

$$P = \frac{\sum_s w_s}{\sum_s w_s + \sum_b w_b} \quad (5.5)$$

2318 where  $w_s$  and  $w_b$  are the weights of the signal and background events respectively;  
 2319 the Gini index is also generalized

$$G = \left( \sum_i^n w_i \right) P(1 - P) \quad (5.6)$$

2320 with  $n$  the number of events in the node. The final score of an event, after pass-  
 2321 ing through the forest, is calculated as the renormalized sum of all the individual  
 2322 (possibly weighted) scores; thus, high(low) score implies that the event is most likely  
 2323 signal(background).

2324 The boosting procedure, implemented in the *Gradient boosting* algorithm used in  
 2325 this thesis, produces a classifier  $F(\mathbf{x})$  which is the weighted sum of the individual  
 2326 classifiers obtained after each iteration, i.e.,

$$F(\mathbf{x}) = \sum_{m=1}^M \beta_m f(\mathbf{x}; a_m) \quad (5.7)$$

2327 where  $M$  is the number of trees in the forest. The *loss function*  $L(F, y)$  represents the

---

<sup>3</sup> Decision trees suffer from sensitivity to statistical fluctuations in the training sample which may lead to very different results with a small change in the training samples.

2328 deviation between the classifier  $F(\mathbf{x})$  response and the true value  $y$  obtained from the  
 2329 training sample (1 for signal events and -1 for background event), according to

$$L(F, y) = \ln(1 + e^{-2F(\mathbf{x})y}) \quad (5.8)$$

2330 thus, the reweighting is employed to ensure the minimization of the loss function; a  
 2331 more detailed description of the minimization procedure can be found in Reference  
 2332 [131]. The final classifier output is later used as a final discrimination variable, labeled  
 2333 as *BDT output/response*.

### 2334 5.2.3 Overtraining

2335 Decision trees offer the possibility to have as many nodes as desired in order to  
 2336 reduce the misclassification to zero (in theory); however, when a classifier is too much  
 2337 adjusted to a particular training sample, the classifier's response to a slightly different  
 2338 sample may leads to a completely different classification results; this effect is known  
 2339 as *overtraining*.

2340 An alternative to reduce the overtraining in BDTs consists in pruning the tree  
 2341 by removing statistically insignificant nodes after the tree growing is completed but  
 2342 this option is not available for BDTs with gradient boosting in the TMVA-toolkit,  
 2343 therefore, the overtraining has to be reduced by tuning the algorithm, number of  
 2344 nodes, minimum number of events in the leaves, etc. The overtraining can be evaluated  
 2345 by comparing the responses of the classifier when running over the training and  
 2346 test samples.

### 2347 5.2.4 Variable ranking

2348 BDTs have a couple of particular advantages related to the input variables; they are  
 2349 relatively insensitive to the number of input variables used in the vector  $\mathbf{x}$ . The  
 2350 ranking of the BDT input variables is determined by counting the number of times a  
 2351 variable is used to split decision tree nodes; in addition, the separation gain-squared  
 2352 achieved in the splitting and the number of events in the node are accounted by  
 2353 applying a weighting to that number. Thus, those variables with small or no power  
 2354 to separate signal and background events are rarely chosen to split the nodes, i.e., are  
 2355 effectively ignored.

2356 In addition, variables correlations play an important role for some MVA methods  
 2357 like the Fisher discriminant algorithm in which the first step consist of performing a  
 2358 linear transformation to a phase space where the correlations between variables are  
 2359 removed; in the case of BDT algorithm, correlations do not affect the performance.

### 2360 5.2.5 BDT output example

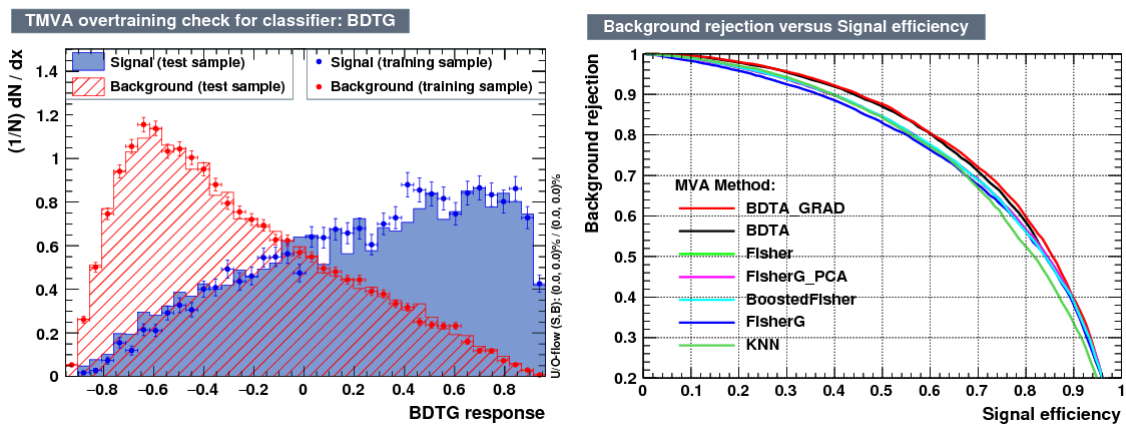


**Figure 5.5:** Left: Output distributions for the gradient boosted decision tree (BDTG) classifier using a sample of signal ( $pp \rightarrow tHq$ ) and background ( $pp \rightarrow tt$ ) events. Right: Background rejection vs signal efficiency (ROC curves) for various MVA classifiers running over the same sample used to produce the plot on the left.

2361       The left side of figure 5.5 shows the BDT output distributions for signal ( $pp \rightarrow$   
 2362      $tHq$ ) and background ( $pp \rightarrow t\bar{t}$ ) events; this plot is the equivalent to the one shown  
 2363     in Figure 5.2. A forest with 800 trees, maximum depth per tree = 3, and gradient  
 2364     boosting have been used as training parameters. The BDTG classifier offers a good  
 2365     separation power. There is a small overtraining in the signal distribution, while the  
 2366     background distribution is very well predicted which might indicate that the sample  
 2367     is composed of more background than signal events.

2368       The right side of figure 5.5 shows the background rejection vs signal efficiency  
 2369     curves for several combinations of MVA classifiers-boosting algorithms running over  
 2370     the same MC sample; these curves are known as ROC curves and give an indication of  
 2371     the performance of the classifier. In this particular example, the best performance is  
 2372     achieved with the BDTG classifier (BDTA\_GRAD), which motivated its use in this  
 2373     thesis and thus no other method is described; for other analyses, the performance  
 2374     might be better for a different method, and then a careful choice and optimization of  
 2375     the method is necessary.

### 2376     **5.3 Statistical inference**

2377       Once events are classified, the likelihood functions  $f(\mathbf{x}|s)$ ,  $f(\mathbf{x}|b)$  for signal and back-  
 2378     ground events are parametrized but the parameters that characterize them are still  
 2379     unknown, therefore, the next step consists of finding those parameters. In general,  
 2380     likelihood functions depend not only on the measurements but also on parameters  
 2381     ( $\theta_m$ ) that define their shapes; the process of estimating these *unknown parameters*  
 2382     and their uncertainties from the experimental data is called *inference*.

2383       The statistical inference tools used in this analysis are implemented in the RooFit  
 2384     toolkit [132] and COMBINE package [133] included in the CMSSW software framework.

2385 **5.3.1 Nuisance parameters**

2386 The unknown parameter vector  $\theta$  is made of two types of parameters: those pa-  
 2387 rameters that provide information about the physical observables of interest for the  
 2388 experiment or *parameters of interest*, and the *nuisance parameters* that are not of  
 2389 a direct interest for the experiment but that need to be included in the analysis in  
 2390 order to achieve a satisfactory description of the data; they represent effects of the  
 2391 detector response like the finite resolutions of the detection systems, miscalibrations,  
 2392 and in general any source of uncertainty introduced in the analysis.

2393 Nuisance parameters can be estimated from experimental data; for instance, data  
 2394 samples from a test beam are usually employed for calibration purposes. In cases  
 2395 where experimental samples are not availables, the estimation of nuisance parameters  
 2396 makes use of dedicated simulation programs to provide the required samples.

2397 The estimation of the unknown parameters involves certain deviations from their  
 2398 true values, hence, the measurement of the nuisance parameter is written in terms  
 2399 of an estimated value, also called central value,  $\hat{\theta}$  and its uncertainty  $\delta\theta$  using the  
 2400 notation

$$\theta = \hat{\theta} \pm \delta\theta \quad (5.9)$$

2401 where the interval  $[\hat{\theta} - \delta\theta, \hat{\theta} + \delta\theta]$  is called *confidence interval*; it is usually interpreted,  
 2402 in the limit of infinite number of experiments, as the interval where the true value  
 2403 of the unknown parameter  $\theta$  is contained with a probability of 0.6827 (if no other  
 2404 convention is stated); this interval represents the area under a Gaussian distribution  
 2405 in the interval  $\pm 1\sigma$ .

2406 Conventionally, uncertainties are split into two classes: *systematic*, associated with  
 2407 the systematic effects, and *statistical*, related only to fluctuations in data and having

2408 statistical nature.

### 2409 5.3.2 Maximum likelihood estimation method

2410 The estimation of the unknown parameters that are in best agreement with the ob-  
 2411 served data is performed through a function of the data sample that returns the  
 2412 estimate of those parameters; that function is called an *estimator*. Estimators are  
 2413 usually constructed using mathematical expressions encoded in computer programs.

2414 In this thesis, the estimator used is the likelihood function  $f(\mathbf{x}|\boldsymbol{\theta})$ <sup>4</sup> which depends  
 2415 on a set of measured variables  $\mathbf{x}$  and a set of unknown parameters  $\boldsymbol{\theta}$ . The likelihood  
 2416 function for N events in a sample is the combination of all the individual likelihood  
 2417 functions, i.e.,

$$L(\boldsymbol{\theta}) = \prod_{i=1}^N f(\mathbf{x}^i|\boldsymbol{\theta}) = \prod_{i=1}^N f(x_1^i, \dots, x_n^i; \theta_1, \dots, \theta_m) \quad (5.10)$$

2418 and the estimation method used is the *Maximum Likelihood Estimation* method  
 2419 (MLE); it is based on the combined likelihood function defined by eqn. 5.10 and  
 2420 the procedure seeks for the parameter set that corresponds to the maximum value of  
 2421 the combined likelihood function, i.e., the *maximum likelihood estimator* of the un-  
 2422 known parameter vector  $\boldsymbol{\theta}$  is the function that produces the vector of *best estimators*  
 2423  $\hat{\boldsymbol{\theta}}$  for which the likelihood function  $L(\boldsymbol{\theta})$  evaluated at the measured  $\mathbf{x}$  is maximum.

2424 Usually, the logarithm of the likelihood function is used in numerical algorithm  
 2425 implementations in order to avoid underflow the numerical precision of the computers  
 2426 due to the product of small likelihoods. In addition, it is common to minimize the  
 2427 negative logarithm of the likelihood function, therefore, the negative log-likelihood

---

<sup>4</sup> analogue to the likelihood functions described in previous sections

2428 function is

$$F(\boldsymbol{\theta}) = -\ln L(\boldsymbol{\theta}) = -\sum_{i=1}^N f(\mathbf{x}^i | \boldsymbol{\theta}). \quad (5.11)$$

2429 The minimization process is performed by the software MINUIT [134] imple-  
 2430 mented in the ROOT analysis framework. In case of data samples with large number  
 2431 of measurements, the computational resources necessary to calculate the likelihood  
 2432 function are too big; therefore, the parameter estimation is performed using binned  
 2433 distributions of the variables of interest for which the *binned likelihood function* is  
 2434 given by

$$L(\mathbf{x}|r, \boldsymbol{\theta}) = \prod_{i=1} \frac{(r \cdot s_i(\boldsymbol{\theta}) + b_i(\boldsymbol{\theta}))^{n_i}}{n_i!} e^{-r \cdot s_i(\boldsymbol{\theta}) - b_i(\boldsymbol{\theta})} \prod_{j=1} \frac{1}{\sqrt{2\pi}\sigma_{\theta_j}^2} e^{-(\theta_j - \theta_{0,j})^2/2\sigma_{\theta_j}^2}, \quad (5.12)$$

2435 with  $s_i$  and  $b_i$  the expected number of signal and background yields for the bin  $i$ ,  $n_i$  is  
 2436 the observed number of events in the bin  $i$  and  $r = \sigma/\sigma_{SM}$  is the signal strength. Note  
 2437 that the number of entries per bin follows a Poisson distribution. The effect of the  
 2438 nuisance parameters have been included in the likelihood function through Gaussian  
 2439 distributions that models the nuisance. The three parameters,  $r$ ,  $s_i$  and  $b_i$  are jointly  
 2440 fitted to estimate the value of  $r$ .

## 2441 5.4 Upper limits

2442 In this analysis, two hypotheses are considered; the background only hypothesis  
 2443 ( $H_0(b)$ ) and the signal plus background hypothesis ( $H_1(s + b)$ ), i.e., the sample of  
 2444 events is composed of background only events ( $r=0$ ) or it is a mixture of signal plus  
 2445 background events ( $r=1$ ). The exclusion of one hypothesis against the other means  
 2446 that the observed data sample better agrees with  $H_0$  or rather with  $H_1$ . In order  
 2447 to discriminate these hypotheses, a test statistic is constructed on the basis of the

2448 likelihood function evaluated for each of the hypothesis.

2449 The *Neyman-Pearson* lemma [135] states that the test statistic that provides the  
 2450 maximum power for  $H_1$  for a given significance level (background misidentification  
 2451 probability  $\alpha$ ), is given by the ratio of the likelihood functions  $L(\mathbf{x}|H_1)$  and  $L(\mathbf{x}|H_0)$ ;  
 2452 however, in order to use that definition it is necessary to know the true likelihood  
 2453 functions, which in practice is not always possible. Approximate functions obtained  
 2454 by numerical methods, like the BDT method described above, have to be used, so  
 2455 that the *profile likelihood* test statistic is defined by

$$\lambda(\mathbf{r}) = \frac{L(\mathbf{x}|r, \hat{\boldsymbol{\theta}}(r))}{L(\mathbf{x}|\hat{r}, \hat{\boldsymbol{\theta}})}, \quad (5.13)$$

2456 where,  $\hat{r}$  and  $\hat{\boldsymbol{\theta}}$  maximize the likelihood function, and  $\hat{\boldsymbol{\theta}}$  maximizes the likelihood  
 2457 function for a given value of the signal strength modifier  $r$ . In practice, the test  
 2458 statistic  $t_r$

$$t_r = -2\ln\lambda(r) \quad (5.14)$$

2459 is used to evaluate the presence of signal in the sample, since the minimum of  $t_r$  at  
 2460  $r = \hat{r}$  suggests the presence of signal with signal strength  $\hat{r}$ . The uncertainty interval  
 2461 for  $r$  is determined by the values of  $r$  for which  $t_r = +1$ .

2462 The expected probability density function (p.d.f)  $f(t_r|r, \boldsymbol{\theta})$  of the test statistic  $t_r$   
 2463 can be obtained numerically by generating MC samples where one hypothesis,  $H_0(b)$   
 2464 or  $H_1(s+b)$ , is assumed; thus, MC samples contain the possible values of  $t_r$  obtained  
 2465 from *pseudo-experiments* as shown in Figure 5.6. The probability that  $t_r$  takes a value  
 2466 equal or greater than the observed value ( $t_{r,obs}$ ) when a signal with a signal modifier  
 2467  $r$  is present in the data sample, is called the *p-value* of the observation; it can be  
 2468 calculated using

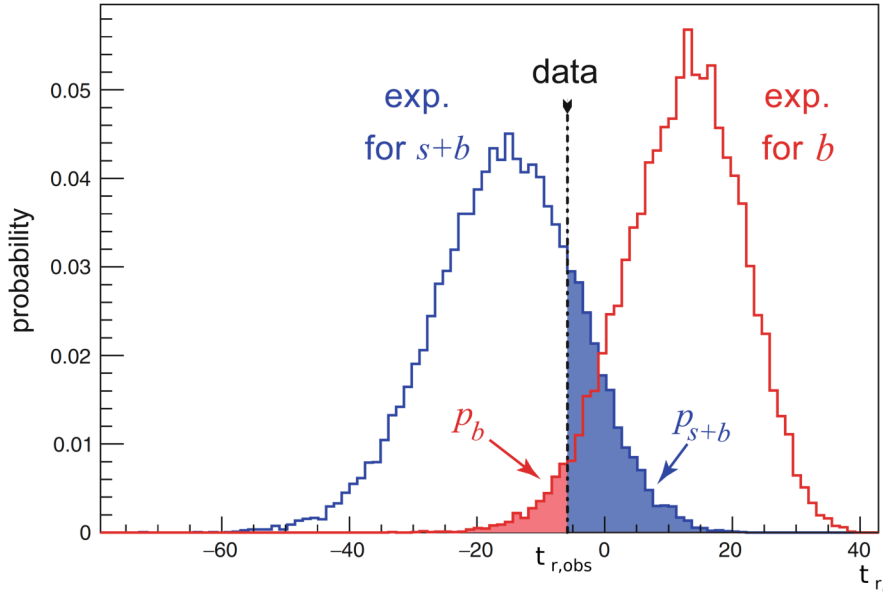


**Figure 5.6:**  $t_r$  p.d.f. from MC pseudo experiments assuming  $H_0$  (red) and  $H_1$  (blue). The black dashed line shows the value of the test statistic as measured from data. Adapted from Reference [128].

$$p_r = \int_{t_{r,obs}}^{\infty} f(t'_r | r, \boldsymbol{\theta}) dt'_r, \quad (5.15)$$

thus,  $p_r < 0.05$  means that, for that particular value of  $r$ ,  $H_1$  could be excluded at 95% Confidence Level (CL), i.e., if more measurements are taken, 95% of them will be in agreement with the  $H_0$  hypothesis; therefore, the CL is a measure of the reliability of a result. Other way to express the CL meaning is by saying that 95% confidence level means that if the measurements are repeated, the chance to get the same result is 95%.

The corresponding background-only p-value is given by

$$1 - p_b = \int_{t_{r,obs}}^{\infty} f(t'_r | 0, \boldsymbol{\theta}) dt'_r, \quad (5.16)$$

If the  $t_r$  p.d.f.s for both hypotheses are well separated, as shown in the top side

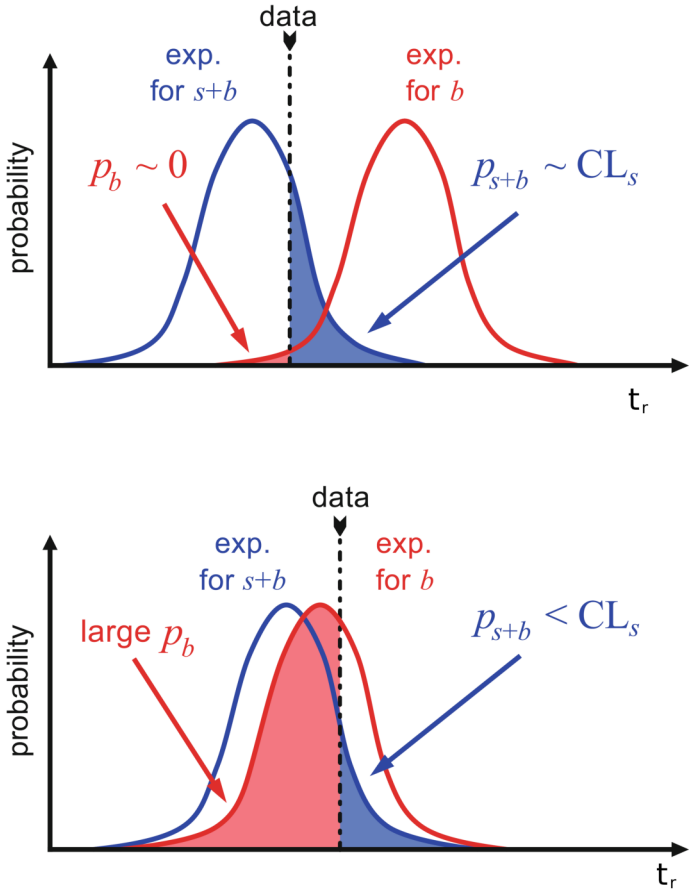


**Figure 5.7:**  $CL_s$  limit illustration. When the test statistic p.d.f. for the two hypotheses  $H_0$  and  $H_1$  are well separated (top) and when they are largely overlapped (bottom). Adapted from Reference [128].

of Figure 5.7, the experiment is sensitive to the presence of signal in the sample. If the signal presence is small, both p.d.f.s will be largely overlapped (bottom of Figure 5.7) and either the signal hypothesis could be rejected with not enough justification because the experiment is not sensitive to the signal or a fluctuation of the background could be misinterpreted as presence of signal with the corresponding rejection of the background-only hypothesis. These issues are corrected by using the modified p-value [136]

$$p'_r = \frac{p_r}{1 - p_b} \equiv CL_s. \quad (5.17)$$

If  $H_1$  is true, then  $p_b$  is small,  $CL_s \simeq p_r$  and  $H_0$  is rejected; if there is large overlap and a statistical fluctuation causes that  $p_b$  is large, then both numerator and denominator in Eqn. 5.17 become small but  $CL_s$  would allow the rejection of  $H_1$  even if there is poor sensitivity to signal.

The upper limit of the parameter of interest  $r^{up}$  is determined by excluding the range of values of  $r$  for which  $CL_s(r, \theta)$  is lower than the confidence level desired, normally 90% or 95%, e.g, scanning over  $r$  and finding the value for which  $p'^{up}_r = 0.05$ . The expected upper limit can be calculated using pseudo-experiments based on the background-only hypothesis and obtaining a distribution for  $r_{ps}^{up}$ ; the median of that distribution corresponds to the expected upper limit, while the  $\pm 1\sigma$  and  $\pm 2\sigma$  deviations correspond to the values of the distribution that defines the 68% and 95% of the area under the distribution centered in the median. It is usual to present all the information about the expected and observed limits in the so-called *Brazilian-flag plot* as the one shown in Figure 5.8. The solid line represent the observed  $CL_s$

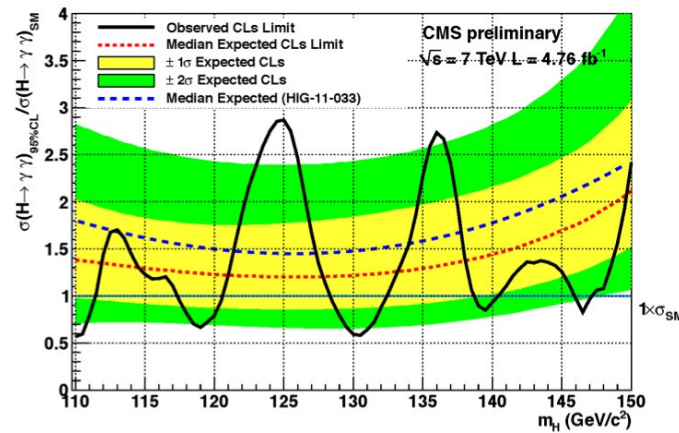


**Figure 5.8:** Brazilian flag plot of CMS experiment limits for Higgs boson decaying to photons [137].

## 2498 5.5 Asymptotic limits

2499 As said before, the complexity of the likelihood functions, the construction of test  
2500 statistics, and the calculation of the limits and their uncertainties is not always man-  
2501 ageable and requires extensive computational resources; in order to overcome those  
2502 issues, asymptotic approximations for likelihood-based test statistics, like the ones  
2503 described in previous sections, have been developed [138, 139] using Wilks's theorem.  
2504 Asymptotic approximations replace the construction of the test statistic p.d.f.s using  
2505 MC pseudo-experiments with the approximate calculation of the test statistic p.d.f.s  
2506 by employing the so-called *Asimov dataset*.

2507 The Asimov dataset is defined as the dataset that produces the true values of the  
2508 nuisance parameters when it is used to evaluate the estimators for all the parameters;  
2509 it is obtained by setting the values of the variables in the dataset to their expected  
2510 values [139].

2511 Limits calculated by using the asymptotic approximation and the Asimov dataset  
2512 are known as *asymptotic limits*.

2513

## CHAPTER 6

---

2514

# The inverted top-Higgs coupling

---

## 2515 6.1 Introduction

2516 Once the mass of the Higgs boson has been determined experimentally, the couplings  
 2517 to fermions and vector bosons are completely specified by the standard model. With  
 2518 the Higgs now observed and its mass measured [141], the coupling strengths can now  
 2519 be measured and compared to the predictions of the model.

2520 In order to test the Higgs-top coupling, several measurements have been per-  
 2521 formed, as stated in the chapter 2, but they are sensitive to the strength of the cou-  
 2522 pling only. The production of a Higgs boson in association with a single top quark  
 2523 ( $tH$ ) not only offers access to the sign of the coupling, but also to the CP-mixing  
 2524 phase of the Higgs couplings.

2525 This chapter presents the search for the associated production of a Higgs boson  
 2526 and a single top quark ( $tHq$ ) events, focusing on leptonic signatures provided by the  
 2527 Higgs decay modes to  $WW$ ,  $ZZ$ , and  $\tau\tau$ ; the 13 TeV dataset produced in 2016, with  
 2528 an integrated luminosity of  $35.9 \text{ fb}^{-1}$ , is used. The analysis exploits signatures with  
 2529 two leptons of the same sign ( $2lss$ ) channel and three leptons ( $3l$ ) channel in the final  
 2530 state.

2531 As shown in Section 2.5, the SM cross section of  $tHq$  process is affected by a

destructive interference between two contributions (see Figure 2.15), where the Higgs couples to either the W boson or the top quark; however, if the sign of the Higgs-top coupling is flipped with respect to the SM prediction, a large enhancement of the cross section occurs, making this analysis sensitive to such a deviation. A second process, where the Higgs boson and top quark are accompanied by a W boson ( $tHW$ ) has similar behavior, albeit with a weaker interference pattern and lower contribution to the cross section, therefore, a combination of both processes would increase the sensitivity to the sign of the coupling; in this analysis both contributions are combined and referred to as the  $tH$  channel. In order to provide the analysis with sensitivity to the strength of the coupling, the  $t\bar{t}H$  process is included as part of the signal; thus, the purpose of this analysis is to investigate the exclusion of the presence of the  $tH + t\bar{t}H$  processes in the SM under the assumption of the anomalous Higgs-top coupling modifier ( $\kappa_t = -1$ ) also known as the *Inverted Top Coupling* (ITC) scenario.

Constraints on the sign of the Higgs-top coupling ( $y_t$ ) have been derived from the decay rate of Higgs boson to photon pairs [50] and from the cross section for associated production of Higgs and Z bosons via gluon fusion [142], with recent results disfavoring negative signs of the coupling [44, 59, 143], although the negative sign coupling has not been completely excluded.

The analysis presented here expands previous analyses performed at 8 TeV [144, 145] and searches for associated production of  $t\bar{t}$  pair and a Higgs boson in the multilepton final state channel [146], by adjusting the object selections to the updated LHC running conditions at 13 TeV, improving the lepton identification, using more powerful multivariate analysis techniques for the signal extraction and a new yield interpretation; it also complements searches in  $H \rightarrow b\bar{b}$  [147].

The first sections present the characteristic  $tHq$  signature as well as the expected backgrounds. The MC samples, data sets, and the physics object definitions are then

described; after, the background predictions, the signal extraction, the statistical treatment of the selected events and the discussion of the systematic uncertainties are described. The final section presents the results for the exclusion limits as a function of the ratio of  $\kappa_t$  and the modifier of the Higgs-vector boson coupling  $\kappa_V$ .

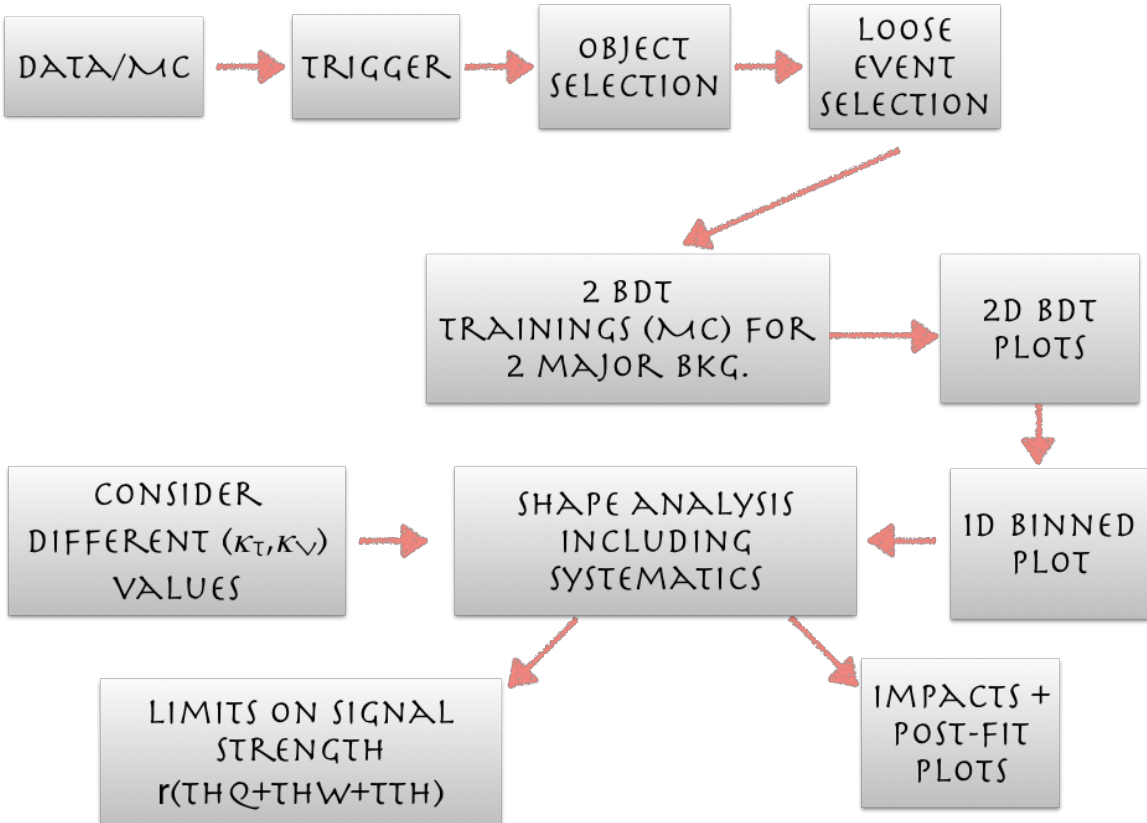


**Figure 6.1:** A schematic overview of the analysis workflow. Based on sets of optimized physics object definitions and selection criteria, signal and background events in a data sample are discriminated. The discrimination is performed by a BDT, previously trained using MC samples of the dominant backgrounds, using discriminant variables based on the  $b$ -jet multiplicity, the activity in the forward region of the detector, and the kinematic properties of leptons. The  $CL_s$  limits on the combined  $t\bar{t}H + tH$  production cross section, as a function of the relative coupling strengths are calculated.

The analysis is designed to efficiently identify and select prompt leptons from on-shell W and Z boson decays and to reject non-prompt leptons from  $b$  quark decays and spurious lepton signatures from hadronic jets. Events are then selected in the

2565  $2lss$  and  $3l$  channels, and are required to contain hadronic jets, some of which must  
 2566 be consistent with  $b$  quark hadronization. Finally, the signal yield is extracted by  
 2567 simultaneously fitting the output of two dedicated multivariate discriminants, trained  
 2568 to separate the  $tHq$  signal from the two dominant backgrounds which, as will be shown  
 2569 in Section 6.3, are  $t\bar{t}$ ,  $t\bar{t}W$  and  $t\bar{t}Z$  processes. The fit result is then used to set an  
 2570 upper limit on the combined  $t\bar{t}H + tH$  production cross section as a function of the  
 2571 relative coupling strengths of Higgs-top quark and Higgs-Vector boson. Figure 6.1  
 2572 shows an schematic overview of the analysis strategy workflow.

2573 The analysis has been made public by CMS as a Physics Analysis Summary [148]  
 2574 combining the result for the three lepton and two lepton same-sign channels; the  
 2575 content present in this chapter is based on that document and on References [146,151]  
 2576 unless another reference is stated. Currently, an effort to turn the analysis into a paper  
 2577 combining the multilepton and  $H \rightarrow b\bar{b}$  results is ongoing.

## 2578 6.2 $tHq$ signature

2579 In order to select events of  $tHq$  process, its features are translated into a set of  
 2580 selection rules; Figure 6.2 shows the Feynman diagram and a schematic view of the  
 2581  $tHq$  process from the  $pp$  collision (at partonic level) to the final state configuration.  
 2582 A single top quark is produced accompanied by a light quark, denoted as  $q$ ; this light  
 2583 quark is produced predominantly in the forward region of the detector. The Higgs  
 2584 boson can be either emitted by the exchanged  $W$  boson or directly by the singly  
 2585 produced top quark.

2586 Due to their high masses/short lifetimes, the top quark and Higgs boson decay  
 2587 within the detector after their production. The Higgs boson is required to decay  
 2588 into a  $W$  boson pair. The top quark almost always decays into a bottom quark and

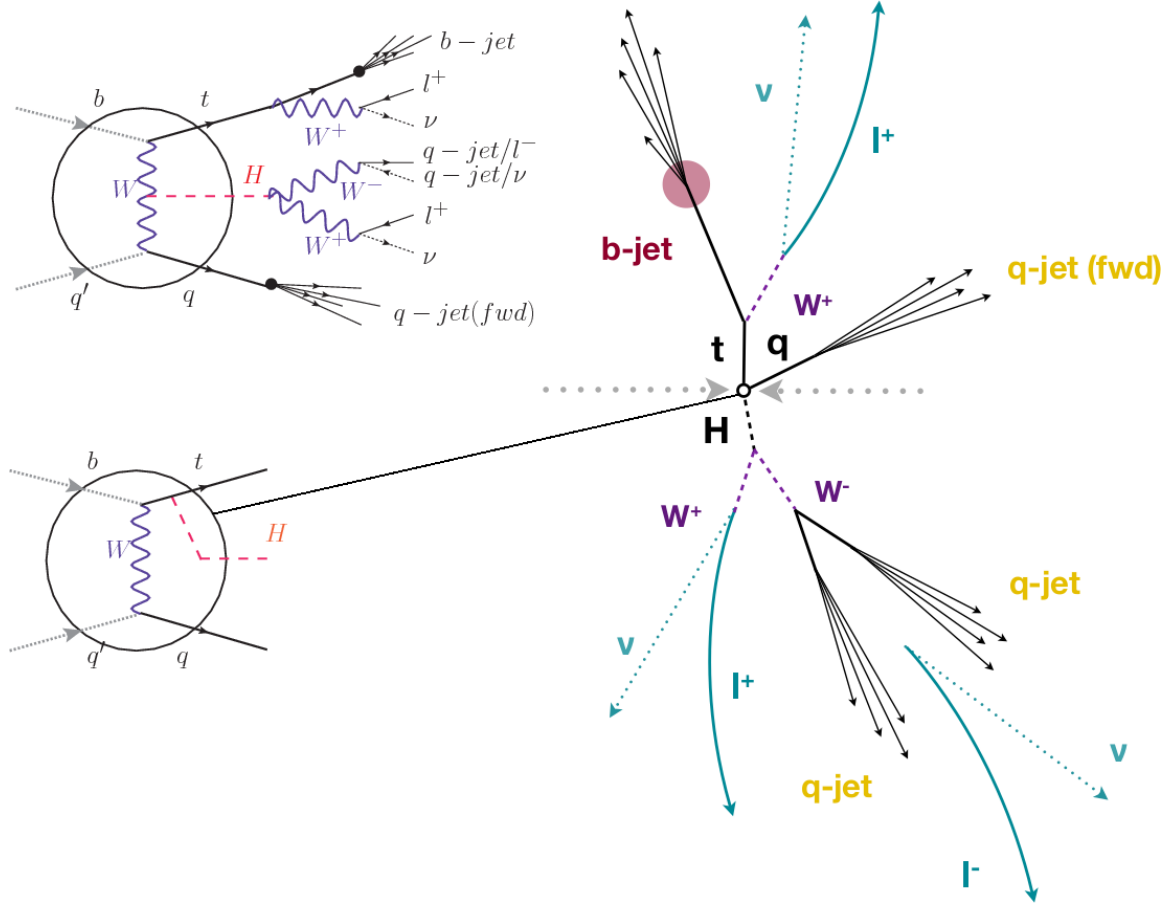


**Figure 6.2:**  $tHq$  event signature. Left: Feynman diagram including the whole evolution up to the final state for the case of the Higgs boson emitted by the  $W$  boson (top); Feynman diagram for the case where the Higgs boson is emitted by the top quark. Right: Schematic view as it would be seen in the detector; the circle in the Feynman diagrams on the left corresponds to the circle in the center of the schematic view as indicated by the line connecting them. In the  $2lss$  channel, one of the  $W$  bosons from the Higgs boson decays to two light-quark jets while in the  $3l$  channel both  $W$  bosons decay to leptons.

2589 a  $W$  boson, as encoded in the CMK matrix. The  $W$  bosons are required to decay  
 2590 leptonically either all the three in the  $3l$  channel or the pair with equal electrical  
 2591 charge in the  $2lss$  channel case;  $\tau$  leptons are not reconstructed separately and only  
 2592 their leptonic decays into either electrons or muons are considered in this analysis.

2593 In summary, the signal process is characterized by the final state with

- 2594     • one light-flavored forward jet,
- 2595     • one central b-jet,
- 2596     •  $2lss$  channel  $\rightarrow$  two leptons of the same sign, two neutrinos and two, often soft,
- 2597        jets,
- 2598     •  $3l$  channel  $\rightarrow$  three leptons, three neutrinos and no central light-flavored jets.

2599     The presence of neutrinos is inferred from the presence of MET.

2600     Note that,  $H \rightarrow ZZ$  and  $H \rightarrow \tau\tau$  decays can produce the same final state as for

2601      $H \rightarrow WW$  decay; therefore, they are also include in the analysis but they are not

2602     separately reconstructed.

### 2603     **6.3 Background processes**

2604     The background processes are those that can mimic the signal signature or at least

2605     can be reconstructed as signal as a result of certain circumstances. The backgrounds

2606     can be classified as

- 2607        • irreducible backgrounds: where genuine prompt leptons are produced in on-
- 2608            shell W and Z boson decays; they can be reliably estimated directly from MC
- 2609            simulated events, using higher-order cross sections (NLO or NNLO or higher as
- 2610            available) or data control regions for the overall normalization.
- 2611        • reducible backgrounds: where at least one of the leptons is *non-prompt*, i.e.,
- 2612            produced within a hadronic jet; genuine leptons from heavy flavor decays and
- 2613            misreconstructed jets, also known as *mis-ID leptons* are considered non-prompt
- 2614            leptons or or *fake leptons* as well as electrons from photon conversions. These
- 2615            non-prompt leptons leave tracks and hits in the detection systems as would a

2616 prompt lepton, but evaluation of the correlation of those hits with nearby jets is  
 2617 a way of removing them. The misassignment of electron charge in processes like  
 2618  $t\bar{t}$  or Drell-Yan, represents an additional source of background, but it is relevant  
 2619 only for the  $2lss$  channel. Reducible backgrounds are not well predicted by  
 2620 simulation, hence, they are estimated using data-driven methods.

2621 The main sources of background events for  $tHq$  process are the  $t\bar{t}$  process and  
 2622  $t\bar{t}V(V = W, Z, \gamma)$  processes. Figure 6.3 shows the signature for  $t\bar{t}$  and  $t\bar{t}W$  processes.

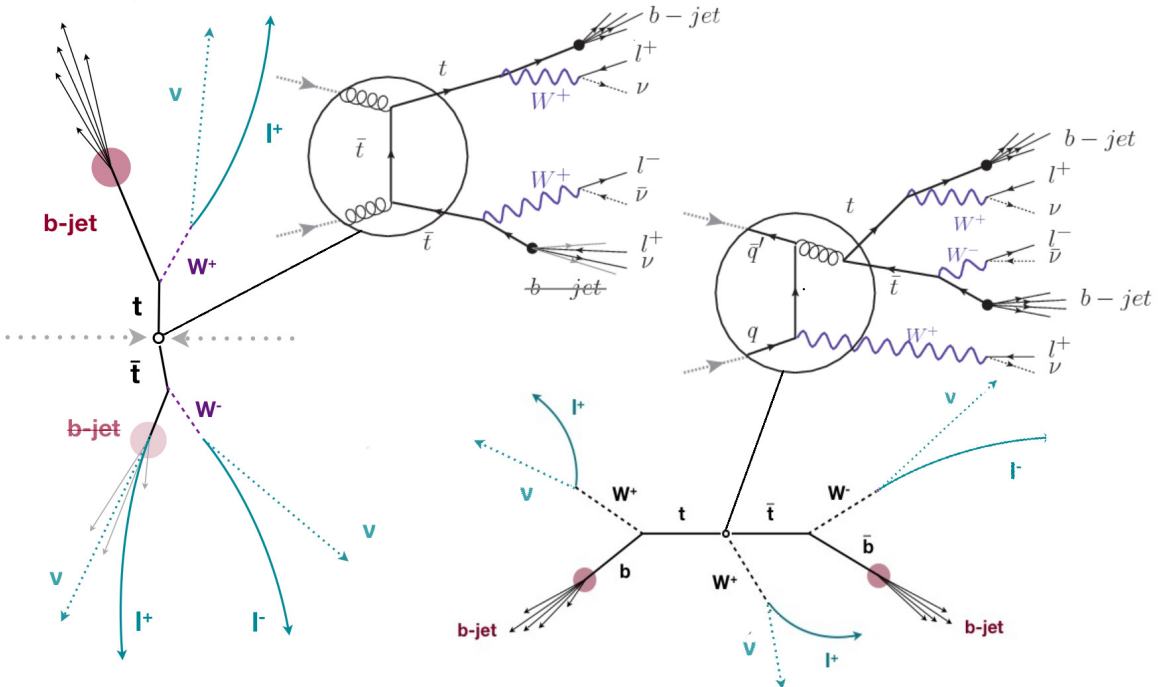


**Figure 6.3:**  $t\bar{t}$  (left) and  $t\bar{t}W$  (right) events signature as they would be seen in the detector; the Feynman diagrams including the whole evolution up to the final state are also shown. The  $t\bar{t}$  process signature is very similar to that of the signal process with one  $b$ -jet misidentified as a lepton (fake lepton indicated with the  $b$ -jet tag struck through) and no forward activity. The  $t\bar{t}W$  process presents a higher  $b$ -jet multiplicity compared to the signal process, a prompt lepton and no forward activity.

2623 The largest contribution to irreducible backgrounds comes from  $t\bar{t}W$  and  $t\bar{t}Z$   
 2624 processes for which the number of ( $b$ -)jets (( $b$ -)jet multiplicity) is higher than that  
 2625 of the signal events, while for other contributing background events,  $WZ$ ,  $ZZ$ , and

2626 rare SM processes like  $W^\pm W^\pm qq$ ,  $t\bar{t}t\bar{t}$ ,  $tZq$ ,  $tZW$ ,  $WWW$ ,  $WWZ$ ,  $WZZ$ ,  $ZZZ$ ,  
 2627 the ( $b-$ )jet multiplicity is lower compared to that of the signal events. None of the  
 2628 irreducible backgrounds present activity in the forward region of the detector.

2629 On the side of the reducible backgrounds, the largest contribution comes from the  
 2630  $t\bar{t}$  events which have a very similar signature to the signal events but does no present  
 2631 activity in the forward region of the detector either; A particular feature of the  $t\bar{t}$   
 2632 events is their charge-symmetry, which is different from the characteristics of signal  
 2633 events.

## 2634 6.4 Data and MC Samples

### 2635 6.4.1 Full 2016 data set

2636 The data set used in this analysis was collected by the CMS experiment during 2016,  
 2637 while running at  $\sqrt{s} = 13$  TeV, and corresponds to a total integrated luminosity  
 2638 of  $35.9 \text{ fb}^{-1}$ . Only periods when the CMS magnet was on were considered when  
 2639 selecting the data samples; that corresponds to the 23Sep2016 (Run B to G) and  
 2640 PromptReco (Run H) versions of the datasets.

2641 Multilepton final states with either two same-sign leptons or three leptons tar-  
 2642 get the case where the Higgs boson decays to a pair of W bosons,  $\tau$  leptons, or  
 2643 Z bosons, and where the top quark decays leptonically, hence, the SingleElectron,  
 2644 SingleMuon, DoubleEG, MuonEG, DoubleMuon dataset (see Table A.1) compose the full  
 2645 dataset. The selected sample has contributions from  $H \rightarrow WW (\sim 75\%)$ ,  $ZZ (\sim 25\%)$ ,  
 2646  $\tau\tau (\sim 5\%)$ .

2647 The quality of the data sets is evaluated by considering any observation reported  
 2648 from the CMS control room where the status of each detection system is monitored;

2649 thus, if ,for instance, an unusual behavior in the solenoid is reported, the data sets  
 2650 produced with the data taken at that are accordingly flagged. In fact, information  
 2651 about alignment, calibration, luminosity, detectors status, among others is used to  
 2652 qualify the data sets. Part of the qualification is make online (during the data tak-  
 2653 ing) while further qualifications are preformed offline when the data are stored and  
 2654 processed at the Tier-0 and Tier-1 data processing centers.

2655 Usually, during the offline qualification, experts from the sub detection systems  
 2656 teams check the data quality based on the performance of their subsystems by looking  
 2657 at histograms specifically tailored to catch relevant problems; then, a single boolean  
 2658 flag is assigned to describe the final quality result. Data are defined as *good for*  
 2659 *physics analysis* if all subdetectors, trigger and physics object (tracking, electron,  
 2660 muon, gamma, jet and MET) show the expected performance. A complete description  
 2661 of data certification strategy is documented in Reference [149].

2662 Qualification results include the information about the luminosity delivered by  
 2663 LHC, the luminosity recorded by CMS and the luminosity certified as Good for physics  
 2664 analysis. In particular, the *luminosity section* which is a sub-section of a run during  
 2665 which the instantaneous luminosity is unchanging; is used as the unit of accounting  
 2666 for integrated luminosity, hence, production data files contain one or many whole  
 2667 luminosity sections. The certified luminosity sections are listed in a JSON formatted  
 2668 file<sup>1</sup> known as the *golden JSON file* defined by the CMS experiment [150].

## 2669 6.4.2 Triggers

2670 The events considered are those online-reconstructed events triggered by one, two, or  
 2671 three leptons. Single-lepton triggers are included in order to boost the acceptance  
 2672 of events where the  $p_T$  of the sub-leading lepton falls below the threshold of the

---

<sup>1</sup> JSON stands for JavaScript Object Notation

2673 double-lepton triggers. The trigger efficiency is increased by including double-lepton  
 2674 triggers in the  $3l$  category, and single-lepton triggers in all categories; it is possible  
 2675 given the logical “or” of the trigger decisions of all the individual triggers in a given  
 2676 category. Table A.2 shows the lowest-threshold non-prescaled triggers present in the  
 2677 HLT menus for both Monte Carlo and data in 2016.

2678 **Trigger efficiency scale factors**

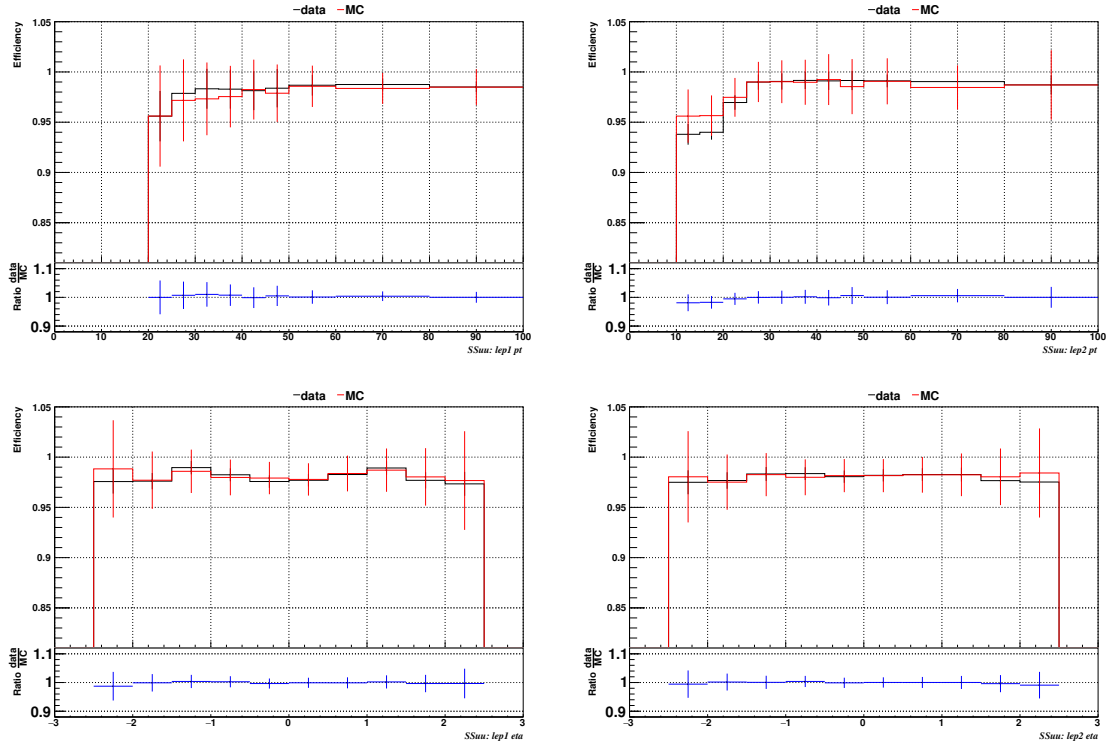


**Figure 6.4:** Comparison between data and MC trigger efficiencies in the same-sign  $\mu\mu$  category, as a function of the  $p_T$  (top) and  $\eta$  (bottom) of the leading lepton (left) and the sub-leading lepton (right). The lower panes show the data/MC ratio. [151].

2679 Trigger efficiency describes the probability of events to pass the trigger require-  
 2680 ments. It is measured in simulated events using generator information given that  
 2681 there is no trigger bias with the MC sample. Measuring the trigger efficiency in data  
 2682 requires a more elaborate procedure; first, select a set of events collected by a trigger

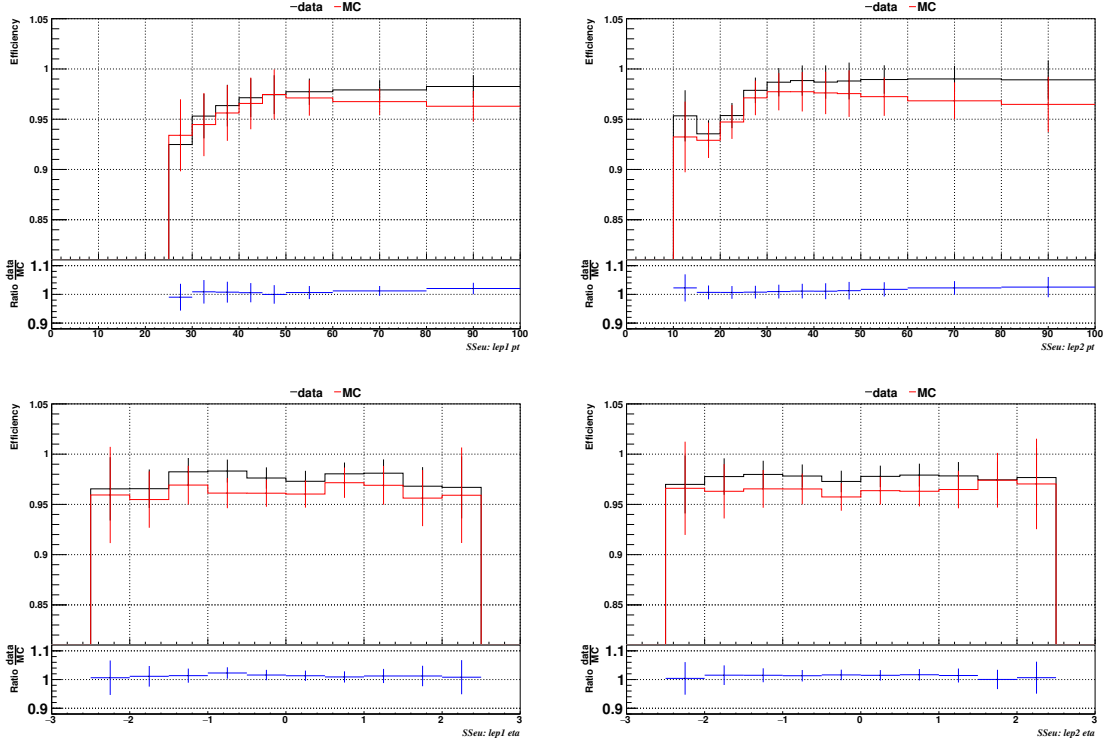


**Figure 6.5:** Comparison between data and MC trigger efficiencies in the same-sign  $e\mu$  category as a function of the  $p_T$  (top) and  $\eta$  (bottom) of the leading lepton (left) and the sub-leading lepton (right). The lower panes show the data/MC ratio. [151].

that is uncorrelated with the lepton triggers such that the selected events form an unbiased sample. In this analysis, that uncorrelated trigger is a MET trigger. Second step is looking for candidate events with exactly two leptons (exactly three leptons for the  $3l$  channel). Finally, measure the efficiency for the candidate events to pass the logical “or” of triggers being considered in a given event category as defined in Table A.2.

Comparisons between the data and MC efficiencies for each category, shown in Figures 6.4, 6.5, and 6.6, reveal that they are in good agreement; the difference is corrected by applying scale factors derived from the ratio between both efficiencies.

Applied flat scale factors in each category are shown in Table 6.1; they have been inherited from Reference [151].

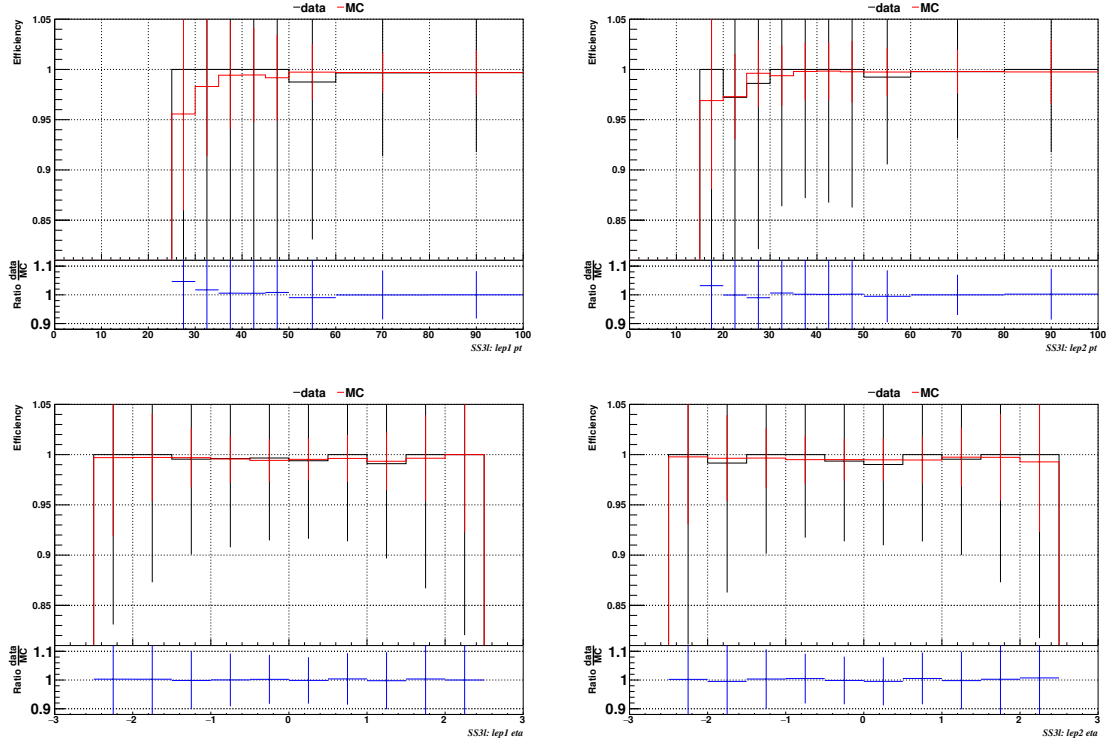


**Figure 6.6:** Comparison between data and MC trigger efficiencies in the  $3l$  category, as a function of the  $p_T$  (top) and  $\eta$  (bottom) of the leading lepton (left) and the sub-leading lepton (right). The lower panes show the data/MC ratio. [151].

Category	Scale Factor
ee	$1.01 \pm 0.02$
e $\mu$	$1.01 \pm 0.01$
$\mu\mu$	$1.00 \pm 0.01$
3l	$1.00 \pm 0.03$

**Table 6.1:** Trigger efficiency scale factors and associated uncertainties, shown here rounded to the nearest percent.

2694 **6.4.3 MC samples**

2695 Current event generators allow the adjustment of the kinematics of the generated  
 2696 events, based on an event-wise reweighting; in this way, several generation parameter  
 2697 phase spaces can be explored according to the experimental interests. The signal  
 2698 samples used in this analysis were generated in such a way that not only the  $\kappa_t = -1$   
 2699 case, but an extended range of  $\kappa_t$  and  $\kappa_V$  values may be investigated.

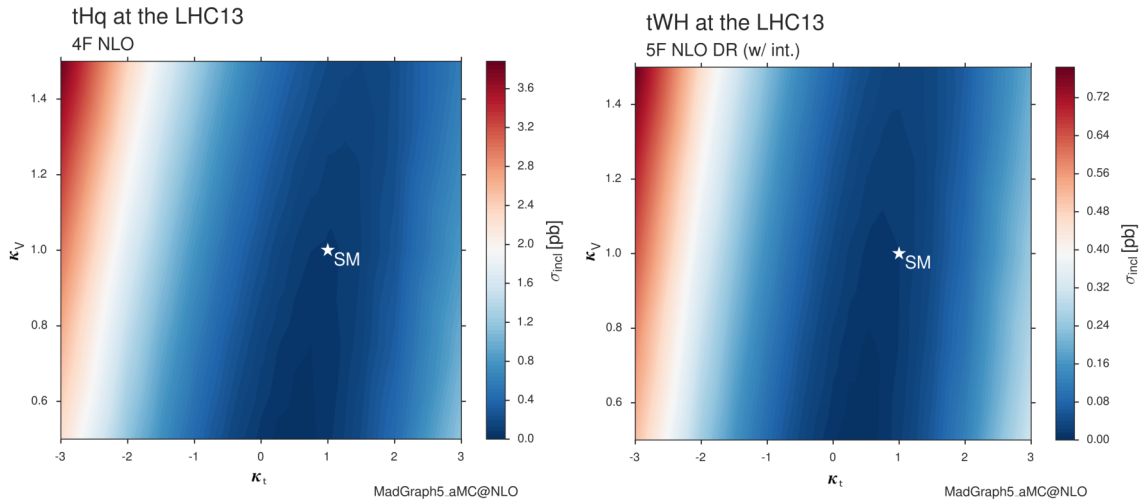


**Figure 6.7:**  $tHq$  and  $tHW$  cross section in the  $\kappa_t$ - $\kappa_V$  phase space [152].

2700 The  $tHq$  and  $tHW$  cross sections in the  $\kappa_t$ - $\kappa_V$  phase space are shown in Figure  
 2701 6.7. As said in Section 4.2, the  $tHq$  sample was generated using the 4F scheme  
 2702 which provides a better description of the additional  $b$  quark from the initial gluon  
 2703 splitting, while the  $tHW$  sample was generated using the 5F scheme in order to  
 2704 remove its interference with  $t\bar{t}H$  at LO.

2705 **MC signal samples**

2706 The two signal samples,  $tHq$  and  $tHW$ , correspond to the RunIISummer16MiniAODv2  
 2707 campaign produced with CMSSW\_80X; they were produced with MG5\_aMC@NLO  
 2708 (version 5.2.2.3), in LO mode at  $\sqrt{s} = 13$  TeV, and are normalized to NLO cross sec-

tions (see Table 6.2). The Higgs boson is assumed to be SM-like except for the values of its couplings to the top quark and W boson. Each sample was generated with a set of event weights corresponding to 51 different values of  $(\kappa_t, \kappa_V)$  couplings, accessible in terms of LHE event weights as shown in Table A.3; however, the main interest is the  $(\kappa_t = -1, \kappa_V = 1)$  case.

Sample	$\sigma$ [pb]	BF
/THQ_Hincl_13TeV-madgraph-pythia8_TuneCUETP8M1/	0.7927	0.324
/THW_Hincl_13TeV-madgraph-pythia8_TuneCUETP8M1/	0.1472	1.0
/tHJetToNonbb_M125_13TeV_amcatnloFXFX_madspin_pythia8_mWCutfix/	0.2151	1.0

**Table 6.2:** MC signal samples used in this analysis; cross section and branching fraction are also listed [152].

The  $t\bar{t}H$  sample was produced using AMC@NLO interfaced to PYTHIA 8 for the parton shower, and is scaled to NLO cross sections.

### MC background samples

Several MC generators were used to generate the samples of the background processes. The dominant background sources ( $t\bar{t}$ ,  $t\bar{t}W$ ,  $t\bar{t}Z$ ) were produced using AMC@NLO interfaced to PYTHIA8, and are scaled to NLO cross sections. Other minor background processes are simulated using POWHEG interfaced to PYTHIA, or bare PYTHIA as stated in the sample names in Table A.4. Pileup interactions are included in the simulation in order to reflect the observed multiplicity in data; the simulated events are weighted according to the actual pileup in data, estimated from the measured bunch-to-bunch instantaneous luminosity and the total inelastic cross section, 69.2 mb. All events are finally passed through a full simulation of the CMS detector using GEANT4, and reconstructed using the same algorithms as used for the data.

## 2728 6.5 Object Identification

2729 In this section, the specific definitions of the physical objects in terms of the recon-  
 2730 struction parameters are presented; thus, the details provided summarize and com-  
 2731 plement the descriptions presented in previous chapters. The object reconstruction  
 2732 and selection strategy used in this thesis are inherited from the analyses in Refer-  
 2733 ences [146, 151].

### 2734 6.5.1 Lepton reconstruction and identification

2735 Two types of leptons are defined in this analysis: *signal leptons* are those coming from  
 2736  $W, Z$  and  $\tau$  decays which usually are isolated from other particles; *background leptons*  
 2737 are defined as leptons produced in  $b$ -jet hadron decays, light-jets misidentification,  
 2738 and photon conversions; they are the same non-prompt leptons defined before.

2739 The process of reconstruction and identification of electron and muon candidates  
 2740 was described in chapter4, hence, the identification variables used in order to retain  
 2741 the highest possible efficiency for signal leptons while maximizing the rejection of  
 2742 background leptons are listed and described in the following sections <sup>2</sup>.

2743 The identification variables include not only observables related directly to the re-  
 2744 constructed leptons themselves, but also to the clustered energy deposits and charged  
 2745 particles in a cone around the lepton direction (jet-related variables); an initial loose  
 2746 preselection of leptons candidates is performed and then an MVA discriminator, re-  
 2747 ferred to as *lepton MVA* discriminator, is used to distinguish signal leptons from  
 2748 background leptons.

---

<sup>2</sup> The studies performed to optimize the identification are far from the scope of this thesis, therefore, only general descriptions are provided.

2749 **Muons**

2750 The Physics Objects Groups (POG) at CMS are in charge of studying and defining  
 2751 the set of selection criteria applied in the course of reconstruction and identification  
 2752 of particles. These selection criteria are implemented in the CMS framework in the  
 2753 form of several object identification working points according to the stringency of the  
 2754 requirements.

2755 The muon candidates are reconstructed by combining information from the tracker  
 2756 system and the muon detection system of CMS detector and the POG defined three  
 2757 working points for muon identification *MuonID* [155];

2758 • *POG Loose Muon ID* is a particle identified as a muon by the PF event re-  
 2759 construction and also reconstructed either as a global-muon or as an arbitrated  
 2760 tracker-muon. These identification criteria are designed to be highly efficient  
 2761 for prompt muons and for muons from heavy and light quark decays; they can  
 2762 be complemented by applying impact parameter cuts in analyses with prompt  
 2763 muon signals.

2764 • *POG Medium Muon ID* is a Loose muon with additional track-quality and  
 2765 muon-quality (spatial matching between the individual measurements in the  
 2766 tracker and the muon system) requirements. These identification criteria are  
 2767 designed to be highly efficient in the identification of the muons coming from  
 2768 decay in flight of heavy quarks so that they can be separated from muons coming  
 2769 from B meson decays as well as prompt muons. An additional category *MVA*  
 2770 *Prompt ID* is defined in these identification criteria directed to discriminated  
 2771 muons from B mesons and prompt muons (from W,Z and  $\tau$  decays). The  
 2772 Medium ID (+ MVA Prompt ID) provides the same fake rate as the Tight  
 2773 Muon ID but a higher efficiency on prompt and B-decays muons [156].

2774       • *POG Tight Muon ID* is a global muon with additional muon-quality require-  
 2775       ments Tight Muon ID selects a subset of the PF muons.

2776       Only muons within the muon system acceptance  $|\eta| < 2.4$  and minimum  $p_T$  of 5  
 2777       GeV are considered.

2778       **Electrons**

2779       Electrons are reconstructed using information from the tracker and from the electro-  
 2780       magnetic calorimeter and identified by an MVA algorithm (*MVA eID* discriminant)  
 2781       using the shape of the calorimetric shower variables like the shape in  $\eta$  and  $\phi$ , the  
 2782       cluster circularity, widths along  $\eta$  and  $\phi$ ; track-cluster matching variables relating  
 2783       the electron momentum at the point of closest approach to the beam spot ( $p_{in}$ ), the  
 2784       electron momentum extrapolated to the surface of the ECAL from the track at the  
 2785       exit of the tracker ( $p_{out}$ ), the  $\eta$  and  $\phi$  position of the supercluster (SC), the track  $\eta$   
 2786       and  $\phi$  position extrapolated from the innermost track hit; and track quality variables  
 2787       like  $\chi^2$  of the GSF tracks and the number of hits used by the GSF filter [157, 158].

2788       A loose selection based on  $\eta$ -dependent cuts on this discriminant is used to prese-  
 2789       lect electron candidates; the full shape of the discriminant is used in the lepton MVA  
 2790       selection to separate signal leptons from background leptons (as described in Section  
 2791       6.5.1).

2792       In order to reject electrons from photon conversions, electron candidates with  
 2793       missing hits in the pixel tracker layers or matched to a conversion secondary vertex  
 2794       are discarded. Electrons are selected for the analysis if they have  $p_T > 7$  GeV and  
 2795       are located within the tracker system acceptance region ( $|\eta| < 2.5$ ).

2796 **Lepton vertexing and pile-up rejection**

2797 The impact parameter in the transverse plane  $d_0$ , impact parameter along the  $z$ -axis  
 2798  $d_z$ , and the impact parameter significance in the detector space  $SIP_{3D}$  are considered  
 2799 to perform the identification and rejection of pile-up, misreconstructed tracks, and  
 2800 background leptons from b-hadron decays; pile-up and misreconstructed track miti-  
 2801 gation is achieved by imposing loose cuts on the impact parameter variables. The  
 2802 full shape of those variables is used in a lepton MVA classifier to achieve the best  
 2803 separation between the signal and the background leptons.

2804 **Lepton isolation**

2805 PF is able to recognize leptons from two different sources: on one side, leptons from  
 2806 the decays of heavy particles, such as W and Z bosons, which are normally isolated in  
 2807 space from the hadronic activity in the event; on the other side, leptons from decays  
 2808 of hadrons and jets misidentified as leptons, which are not isolated as the former. For  
 2809 highly boosted systems, like the lepton and the  $b$ -jet generated in the semileptonic  
 2810 decay of a boosted top, the decay products tend to be more closer and sometimes they  
 2811 even overlap; thus, the PF standard definition of isolation in terms of the separation  
 2812  $\Delta R$  between lepton candidates ( $l$ ) and other PF objects ( $i$ ) in the  $\eta$ - $\phi$  plane,

$$\Delta R = \sqrt{(\eta^l - \eta^i)^2 + (\phi^l - \phi^i)^2} < 0.3 \quad (6.1)$$

2813 which considers all the neutral, charged hadrons and photons in a cone around the  
 2814 leptons, is refocused to the local isolation of the leptons through the mini-isolation  
 2815  $I_{mini}$  [159] defined as the sum of particle flow candidates  $p_T$  within a cone around the

2816 lepton, corrected for the effects of pileup and divided by the lepton  $p_T$

$$I_{mini} = \frac{\sum_R p_T(h^\pm) - \max\left(0, \sum_R p_T(h^0) + p_T(\gamma) - \rho \mathcal{A} \left(\frac{R}{0.3}\right)^2\right)}{p_T(l)} \quad (6.2)$$

2817 where  $\rho$  is the pileup energy density, and  $h^\pm, h^0, \gamma, l$ , represent the charged hadron,  
 2818 neutral hadrons, photons, and the lepton, respectively. The radius  $R$  of the cone  
 2819 depends on the  $p_T$  of the lepton according to

$$R = \frac{10 \text{ GeV}}{\min[\max(p_T(l), 50 \text{ GeV}), 200 \text{ GeV}]}, \quad (6.3)$$

2820 The  $p_T$  dependence of the cone size allows for greater signal efficiency. Setting a  
 2821 cut on  $I_{mini}$  below a given threshold ensures that the lepton is locally isolated, even  
 2822 in boosted systems. The effect of pileup is mitigated using the so-called effective area  
 2823 correction  $\mathcal{A}$  listed in Table 6.3.

$ \eta $ range	$\mathcal{A}(e)$ neutral/charged	$\mathcal{A}(\mu)$ neutral/charged
0.0 - 0.8	0.1607 / 0.0188	0.1322 / 0.0191
0.8 - 1.3	0.1579 / 0.0188	0.1137 / 0.0170
1.3 - 2.0	0.1120 / 0.0135	0.0883 / 0.0146
2.0 - 2.2	0.1228 / 0.0135	0.0865 / 0.0111
2.2 - 2.5	0.2156 / 0.0105	0.1214 / 0.0091

**Table 6.3:** Effective areas, for electrons and muons used to mitigate the effect of pileup by using the so-called effective area correction.

2824 A loose cut on  $I_{mini}$  is applied to pre-select the muon and electron candidates;  
 2825 however, the full shape is used in the lepton MVA discriminator when performing the  
 2826 signal lepton selection.

2827 **Jet-related variables**

2828 In order to reject misidentified leptons from  $b$ -jets, mostly coming from  $t\bar{t}$ +jets,  
 2829 Drell-Yan+jets, and W+jets events, the vertexing and isolation described in previous  
 2830 sections are complemented with additional variables related to the closest recon-  
 2831 structed jet to the lepton, i.e., the PF jets reconstructed<sup>3</sup> around the leptons with  
 2832  $\Delta R = \sqrt{(\eta^l - \eta^{jet})^2 + (\phi^l - \phi^{jet})^2} < 0.5$ . The identification variables used in the lep-  
 2833 ton MVA discriminator are the ratio  $p_T^l/p_T^{jet}$ , the CSV b-tagging discriminator value  
 2834 of the jet, the number of charged tracks of the jet, and the relative  $p_T$  given by

$$p_T^{rel} = \frac{(\vec{p}_{jet} - \vec{p}_l) \cdot \vec{p}_l}{\|\vec{p}_{jet} - \vec{p}_l\|}. \quad (6.4)$$

2835 **LeptonMVA discriminator**

2836 Electrons and muons passing the basic selection process described above are referred  
 2837 to as *loose leptons*. Additional discrimination between signal leptons and background  
 2838 leptons is crucial considering that the rate of  $t\bar{t}$  production is much larger than the  
 2839 signal, hence, an overwhelming background from  $t\bar{t}$  production is present. To maxi-  
 2840 mally exploit the available information in each event to that end, the dedicated lepton  
 2841 MVA discriminator, based on a boosted decision tree (BDT) algorithm, has been built  
 2842 so that all the identification variables can be used together.

2843 The lepton MVA discriminator training is performed using simulated signal Loose  
 2844 leptons from the  $t\bar{t}H$  MC sample and non-prompt leptons from the  $t\bar{t}$  +jets MC  
 2845 sample, separately for muons and electrons.  $t\bar{t}$  background contribution gets reduced  
 2846 because it is not possible to have two same-sign prompt leptons in  $t\bar{t}$ , so one of them  
 2847 has to be non-prompt, therefore, it gets suppressed by a leptonMVA cut.

---

<sup>3</sup> Charged hadrons from PU vertices are not removed prior to the jet clustering.

2848       The input variables used include vertexing, isolation and jet-related variables, the  
 2849      $p_T$  and  $\eta$  of the lepton, the electron MVA eID discriminator and the muon segment-  
 2850     compatibility variables. An additional requirement known as the *tight-charge* require-  
 2851     ment is imposed by comparing two independent measurements of the charge, one using  
 2852     the ECAL supercluster position and the other from the tracker as described in Sec-  
 2853     tion 4.5.1; thus, the consistency in the measurements of the electron charge is ensured  
 2854     so that events with a wrong electron charge assignment are rejected; this variable is  
 2855     particularly used in the  $2lss$  channel to suppress opposite-sign events for which the  
 2856     charge of one of the leptons has been mismeasured. The tight-charge requirement for  
 2857     muons is represented by the requirement of a consistently well measured track trans-  
 2858     verse momentum given by  $\Delta p_T/p_T < 0.2$ . Leptons are selected for the final analysis  
 2859     if they pass a given threshold of the BDT output, and are referred to as *tight leptons*  
 2860     in the following.

2861       The validation of the lepton MVA algorithm and the lepton identification variables  
 2862     is performed using data in various control regions; the details about that validation  
 2863     are not discussed here but can be found in Reference [151].

## 2864     **Selection definitions**

2865     Electron and muon object identification is defined in three different sets of selections  
 2866     criteria; the *Loose*, *Fakeable Object*, and *Tight* selection. These three levels of selection  
 2867     are designed to serve for event level vetoes, the fake rate estimation application region  
 2868     (see Section 6.7.2), and the final signal selection, respectively. The  $p_T$  of fakeable  
 2869     objects is defined as  $0.85 \times p_T(\text{jet})$ , where the jet is the one associated to the lepton  
 2870     object. This mitigates the dependence of the fake rate on the momentum of the  
 2871     fakeable object and thereby improves the precision of the method.

2872     Tables 6.4 and 6.5 list the full criteria for the different selections of muons and

2873 electrons.

Cut	Loose	Fakeable object	Tight
$ \eta  < 2.4$	✓	✓	✓
$p_T$	$> 5 \text{ GeV}$	$> 15 \text{ GeV}$	$> 15 \text{ GeV}$
$ d_{xy}  < 0.05 \text{ (cm)}$	✓	✓	✓
$ d_z  < 0.1 \text{ (cm)}$	✓	✓	✓
$\text{SIP}_{3D} < 8$	✓	✓	✓
$I_{\text{mini}} < 0.4$	✓	✓	✓
is Loose Muon	✓	✓	✓
jet CSV	—	$< 0.8484$	$< 0.8484$
is Medium Muon	—	—	✓
tight-charge	—	—	✓
lepMVA $> 0.90$	—	—	✓

**Table 6.4:** Requirements on each of the three muon selections. In the cases where the cut values change between the selections, those values are listed in the table. Otherwise, whether the cut is applied is indicated.

2874 In addition to the previously defined requirements for jets, they are required to  
 2875 be separated from any lepton candidates passing the fakeable object selections by  
 2876  $\Delta R > 0.4$ .

### 2877 6.5.2 Lepton selection efficiency

2878 Efficiencies of reconstructing and selecting loose leptons are measured both for muons  
 2879 and electrons using a tag and probe method on both data and MC, using  $Z \rightarrow \ell^+ \ell^-$   
 2880 [160]. The scale factors are derived from the ratio of efficiencies  $\varepsilon_i(p_T, \eta)$  measured  
 2881 for a given lepton in data/MC, according to

$$\rho(p_T, \eta) = \frac{\varepsilon_{\text{data}}(p_T, \eta)}{\varepsilon_{\text{MC}}(p_T, \eta)}. \quad (6.5)$$

2882 The scale factor for each event is used to correct the weight of the event in the  
 2883 full sample; therefore, the full simulation correction is given by the product of all  
 2884 the individual scale factors. The scale factors used in this thesis are inherited from

Cut	Loose	Fakeable Object	Tight
$ \eta  < 2.5$	✓	✓	✓
$p_T$	$> 7 \text{ GeV}$	$> 15 \text{ GeV}$	$> 15 \text{ GeV}$
$ d_{xy}  < 0.05 \text{ (cm)}$	✓	✓	✓
$ d_z  < 0.1 \text{ (cm)}$	✓	✓	✓
$\text{SIP}_{3D} < 8$	✓	✓	✓
$I_{\text{mini}} < 0.4$	✓	✓	✓
MVA eID $> (0.0, 0.0, 0.7)$	✓	✓	✓
$\sigma_{in\eta} < (0.011, 0.011, 0.030)$	—	✓	✓
$H/E < (0.10, 0.10, 0.07)$	—	✓	✓
$\Delta\eta_{in} < (0.01, 0.01, 0.008)$	—	✓	✓
$\Delta\phi_{in} < (0.04, 0.04, 0.07)$	—	✓	✓
$-0.05 < 1/E - 1/p < (0.010, 0.010, 0.005)$	—	✓	✓
$p_T^{\text{ratio}}$	—	$> 0.5^\dagger / -$	—
jet CSV	—	$< 0.3^\dagger / < 0.8484$	$< 0.8484$
tight-charge	—	—	✓
conversion rejection	—	—	✓
Number of missing hits	$< 2$	$== 0$	$== 0$
lepton MVA $> 0.90$	—	—	✓

**Table 6.5:** Criteria for each of the three electron selections. In cases where the cut values change between selections, those values are listed in the table. Otherwise, whether the cut is applied is indicated. In some cases, the cut values change for different  $\eta$  ranges. These ranges are  $0 < |\eta| < 0.8$ ,  $0.8 < |\eta| < 1.479$ , and  $1.479 < |\eta| < 2.5$  and the respective cut values are given in the form (value<sub>1</sub>, value<sub>2</sub>, value<sub>3</sub>). For the two  $p_T^{\text{ratio}}$  and CSV rows, the cuts marked with a  $\dagger$  are applied to leptons that fail the lepton MVA cut, while the loose cut value is applied to those that pass the lepton MVA cut.

2885 Reference [151] which in turns inherited them from leptonic SUSY analyses using  
 2886 equivalent lepton selections.

2887 The efficiency of applying the tight selection as defined in Tables 6.4 and 6.5 on the  
 2888 loose leptons is determined by using a tag and probe method on a sample of Drell-Yan  
 2889 enriched events. Figures 6.8 and 6.9 show the efficiencies for the  $2lss$  channel and  $3l$   
 2890 channel respectively. Efficiencies in the  $2lss$  channel have been produced including  
 2891 the tight-charge requirement, while for the  $3l$  channel it is not included. The number  
 2892 of passed and failed probes is determined from a fit to the invariant mass of the  
 2893 dilepton system. Simulation is corrected using these scale factors; note that they

2894 depend on  $\eta$  and  $p_T$ .

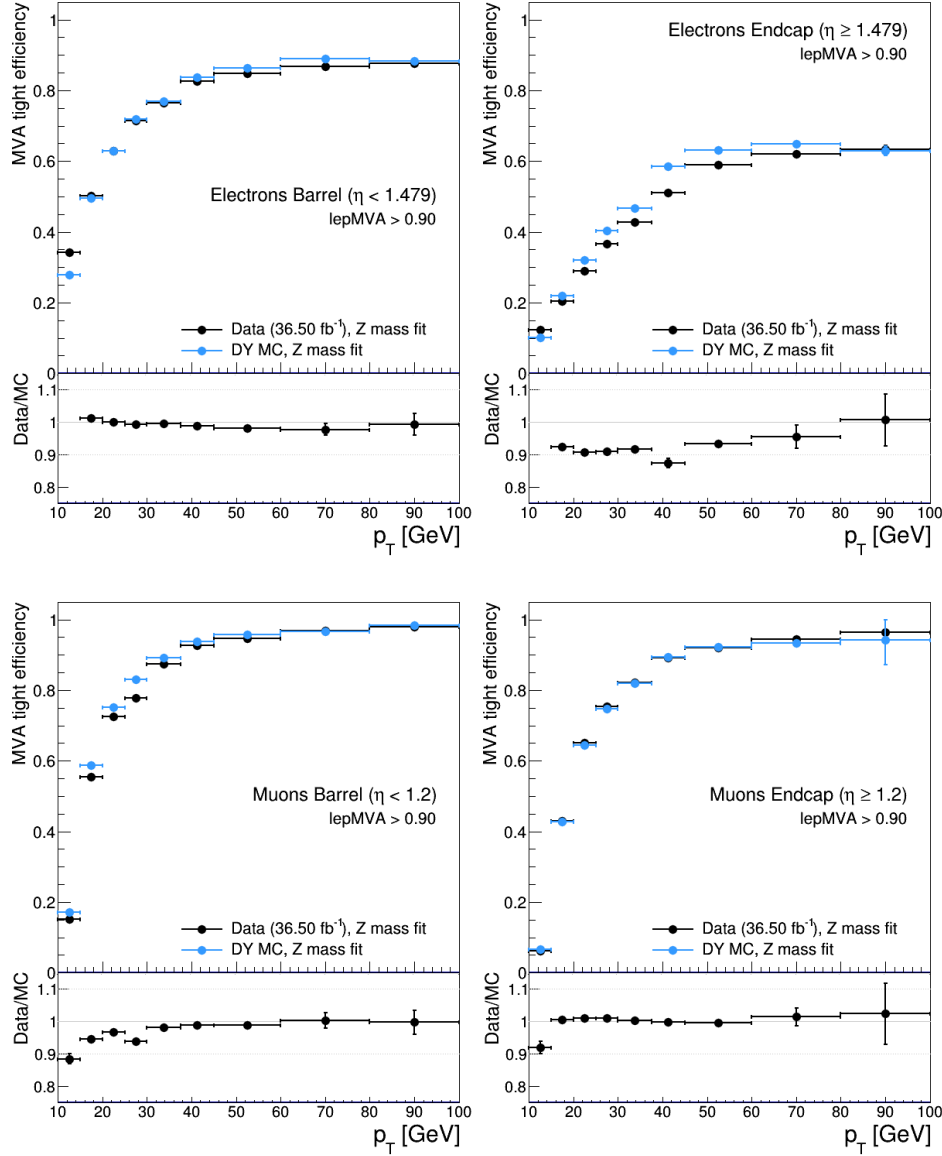


**Figure 6.8:** Tight vs loose selection efficiencies for electrons (top), and muons (bottom), for the 2lss definition, i.e., including the tight-charge requirement. The lower panes show the data/MC ratios.

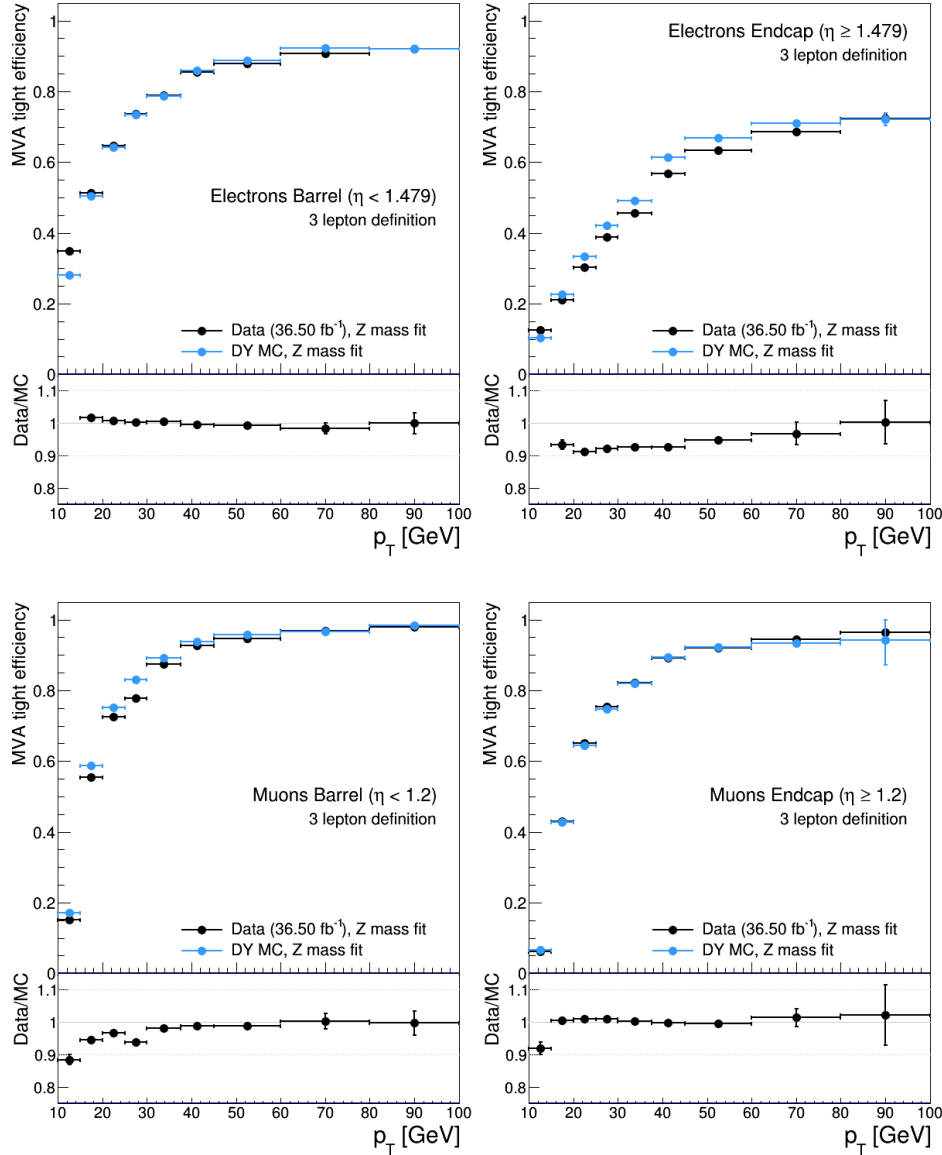


**Figure 6.9:** Tight vs loose selection efficiencies for electrons (top), and muons (bottom), for the  $3l$  channel not including the tight-charge requirement. The lower panes show the data/MC ratios.

### 2895 6.5.3 Jets and $b$ -jet tagging

2896 In this analysis, jets are reconstructed by clustering PF candidates using the anti- $k_t$   
 2897 algorithm with parameter distance  $\Delta R = 0.4$ ; those charged hadrons that are not  
 2898 consistent with the selected primary vertex are discarded from the clustering. The

jet energy is then corrected for the varying response of the detector as a function of transverse momentum  $p_T$  and pseudorapidity  $\eta$ . Jets are selected for use in the analysis only if they have  $p_T > 25$  GeV and are separated from any selected leptons by  $\Delta R > 0.4$ .

Jets coming from the primary vertex and jets coming from pile-up vertices are distinguished using a MVA discriminator based on the differences in the jet shapes, in the relative multiplicity of charged and neutral components, and in the different fraction of transverse momentum which is carried by the most energetic components. Jet tracks are also required to be identified as coming from the primary vertex.

Jets originated from the hadronization of a  $b$  quark are selected using a MVA likelihood discriminant which uses track-based lifetime information and reconstructed secondary vertices (CSV algorithm). Only jets within the CMS tracker acceptance ( $\eta < 2.4$ ) are identified with this tool. Data samples are used to measure the efficiency of the  $b$ -jet tagging and the probability to misidentify jets from light quarks or gluons; in both cases the measurements are parametrized as a function of the jet  $p_T$  and  $\eta$  and latter used to correct differences between the data and MC simulation in the  $b$  tagging performance, by applying per-jet weights to the simulation, dependent on the jet  $p_T$ ,  $\eta$ ,  $b$  tagging discriminator, and flavor (from the MC generation/simulation truth information) [153]. The per-event weight is taken as the product of the per-jet weights, including those of the jets associated to the leptons. The weights are derived from  $t\bar{t}$  and Z+jets events.

Two working points are defined, based on the CSV algorithm output: *loose* working point with a  $b$  signal tagging efficiency of about 83%, and *medium* working point with  $b$ -tagging efficiency of about 69% [154]. Tagging of jets from charm quarks have efficiencies of about 40% and 18% for loose and medium working points respectively, while for jets with only light quarks the efficiencies are 10% and 1.5% respectively.

2925 Separate scale factors are applied to jets originating from bottom/charm quarks and  
 2926 from light quarks in simulated events to match the tagging efficiencies measured in  
 2927 the data.

2928 **6.6 Event selection**

2929 Events are selected considering the features of the signal process and the decay sig-  
 2930 nature as described in Section 6.2. At the trigger level, events are selected to contain  
 2931 either one, two, or three leptons with minimal  $p_T$  thresholds:

- 2932 • single-lepton trigger → 24 GeV for muons and at 27 GeV for electrons
- 2933 • double-lepton triggers → leading and sub-leading leptons: 17 and 8 GeV for  
 2934 muons and 23 and 12 GeV for electrons.
- 2935 • three-lepton triggers → threshold on the third hardest lepton in the event: 5  
 2936 and 9 GeV for muons and electrons, respectively.

2937 The offline event selection level targets the specific topology of the  $tHq$  signal with  
 2938  $H \rightarrow WW$  and  $t \rightarrow Wb \rightarrow l\nu b$ ; therefore, the resulting state is composed of three  
 2939 W bosons, one  $b$  quark, and a light spectator quark at high rapidity. The selection  
 2940 criteria for the two channels exploited in this analysis are summarized in Table 6.6.  
 2941 This selection includes contributions from  $H \rightarrow \tau\tau$  and  $H \rightarrow ZZ$  as well.

2942 In the  $2lss$  channel, events with additional tight leptons are vetoed as well as those  
 2943 for which a loose lepton pair has an invariant mass below 12 GeV. A threshold in  $p_T$  of  
 2944 the leading and sub-leading leptons is also required. Events where the two electrons  
 2945 have invariant mass within 10 GeV of the Z boson mass (*Z-veto*) are discarded in order  
 2946 to reject events from DY+jets production with charge misidentified electrons; charge  
 2947 misidentification can occurs for muons too, but the charge misassignment probability

<b>Same-sign <math>\ell\ell</math> channel <math>e^\pm\mu^\pm, \mu^\pm\mu^\pm</math></b>		<b><math>\ell\ell\ell</math> channel</b>
		Have fired one of the corresponding trigger paths
		No loose leptons with $m_{\ell\ell} < 12\text{GeV}$
		One or more $b$ tagged jets (CSV medium) $ \eta  < 2.4$
		One or more non-tagged jets: central $\rightarrow p_T > 25\text{ GeV},  \eta  < 2.4$ forward $\rightarrow p_T > 40\text{ GeV},  \eta  > 2.4$
Exactly two tight same-sign leptons		Exactly three tight leptons
Lepton $p_T > 25/15\text{GeV}$		Lepton $p_T > 25/15/15\text{GeV}$
Electrons are triple-charge consistent.		No OSSF lepton pair with $ m_{\ell\ell} - m_Z  < 15\text{GeV}$
Muon $p_T$ resolution: $\Delta p_T/p_T < 0.2$ .		
No ee pair with $ m_{ee} - m_Z  < 10\text{GeV}$		

**Table 6.6:** Summary of event pre-selection.

for muons was found to be negligible [145] for this analysis, therefore, the Z-veto is applied only to electrons. In addition, contribution from the associated production of two W bosons of equal charge and two light jets  $W^\pm W^\pm qq$  and from same-sign W boson pairs can also be produced in double parton scattering (DPS) processes, where each of the colliding protons gives two partons, resulting in two hard interactions.

In the  $3l$  lepton channel, leptons are required to have respectively  $p_T > 25\text{ GeV}, > 15\text{ GeV}$ , and  $> 15\text{ GeV}$ . Events with an opposite-sign same-flavor lepton combination (OSSF) with invariant mass within 15 GeV of the Z boson mass are discarded in order to reject events from  $WZ + \text{jets}$  production.

## 6.7 Background modeling and predictions

The dominant background contribution is expected to arise from top quark production processes, either  $t\bar{t}$  pair production or in  $t\bar{t}$  associated production with a W/Z. Processes with production of single top quarks also contribute, mainly in the associated production with a Z boson ( $tZq$ ) or when produced with both a W and a Z boson ( $tZW$ ). Background contamination from diboson processes is strongly suppressed by imposing the Z-veto, vetoing additional leptons and requiring  $b$ -jets in the event.

2964        The selection criteria in Table 6.6 represent a relatively loose selection that allows  
 2965        to maintain a large signal efficiency while suppressing the backgrounds; that selection  
 2966        is called *pre-selection*. The events obtained from the pre-selection are then used to  
 2967        extract the signal contribution in a second analysis step, using BDT discriminators  
 2968        against the main backgrounds of  $t\bar{t}W/t\bar{t}Z$  and non-prompt leptons from  $t\bar{t}$ . The  
 2969        shape of the discriminator variables is then fit to the observed data distribution to  
 2970        estimate the signal and background yields, simultaneously for all channels.

2971        Irreducible backgrounds are reliably estimated from MC simulated events, as will  
 2972        be shown; therefore, in this analysis all backgrounds involving prompt leptons are  
 2973        estimated in this way. Reducible backgrounds, like non-prompt lepton backgrounds,  
 2974        are not well predicted by simulation, hence, they are estimated using data-driven  
 2975        methods.

### 2976        **6.7.1 $t\bar{t}V$ and diboson backgrounds**

2977        Backgrounds from  $t\bar{t}W$  and  $t\bar{t}Z$  processes are estimated using simulated events, cor-  
 2978        rected for data/MC differences and inefficiencies (trigger and lepton selection) in the  
 2979        same way as signal events. Their production cross sections are calculated at NLO of  
 2980        QCD and EWK, considering theoretical uncertainties from unknown higher orders of  
 2981        12% for  $t\bar{t}W$  and 10% for  $t\bar{t}Z$ . Additional uncertainties arise from the knowledge of  
 2982        PDFs and  $\alpha_s$  of about 4% each for  $t\bar{t}W$  and  $t\bar{t}Z$ .

2983        The diboson contribution is also estimated from simulated events; however, the  
 2984        overall normalization of this process is obtained from a dedicated control region.  
 2985        The motivation behind that strategy is that even though the measured inclusive  
 2986        cross section for diboson processes ( $WZ, ZZ$ ) is in good agreement with the NLO  
 2987        calculations [151], that agreement is perturbed when leptonic Z decays and hadronic

2988 jets in the final state are required; those requirements are precisely the ones that  
 2989 make the diboson production a background for the  $tHq$  signal. Thus, by using a  
 2990 dedicated control region dominated by  $WZ$  production<sup>4</sup>, the overall normalization is  
 2991 constrained.

2992 The control region is defined by the presence of at least three leptons, of which  
 2993 one opposite-sign pair must be compatible with a  $Z$  boson decay, i.e., invert the  
 2994  $Z$ -veto which makes the control region orthogonal to signal region; the  $b$ -jet tagging  
 2995 requirements is also inverted with respect to the signal region, i.e., require two not  
 2996  $b$ -jets. A scale factor is extracted from the predicted distribution of  $WZ$  events in the  
 2997 control region, and the observed data, while keeping other processes fixed; this factor  
 2998 is used to scale the diboson prediction in the signal selection region. More details  
 2999 about the procedure used can be found in Reference [151] from where the scale factor  
 3000 is taken.

3001 In order to test the usability of the diboson background scale factor in this analysis,  
 3002 a  $Z$ -enriched control region<sup>5</sup> was defined by inverting the  $Z$ -veto and requiring exactly  
 3003 three tight leptons with  $p_T > 25/15/15$  GeV, one or more jets passing the CSVv2 loose  
 3004 working point and less than four central jets. Figure 6.10 shows the distribution of  
 3005 three variables in the diboson control region; the good agreement between MC and  
 3006 data motivates the adoption of the diboson background scale factor.

3007 Most of the diboson events passing the signal selection contain jets from light  
 3008 quarks and gluons that are incorrectly tagged as  $b$ -jets; it makes the estimate mainly  
 3009 sensitive to the experimental uncertainty in the mis-tag rate rather than the theore-  
 3010 tical uncertainty in the jet flavor composition. The overall uncertainty assigned to  
 3011 the diboson prediction is estimated from the statistical uncertainty due to the limited

---

<sup>4</sup>  $ZZ$  background is strongly reduced by the cut on MET.

<sup>5</sup> This control region is different from the one used to find the scale factor.

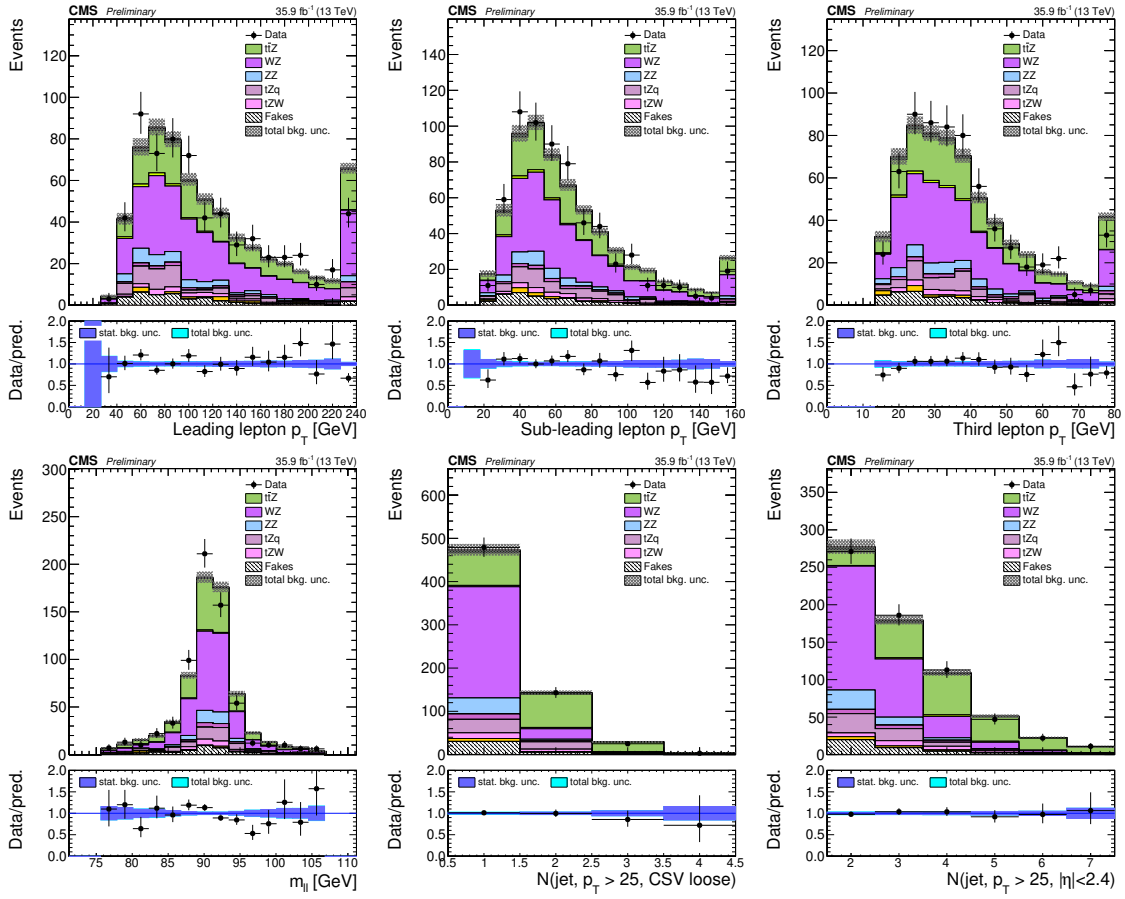


**Figure 6.10:** Kinematic distributions in the diboson control region.

sample size in the control region (30%), the residual background in the control region (20%), the uncertainties on the  $b$ -tagging rate (10-40%), and from the knowledge of PDFs and the theoretical uncertainties of the extrapolation (up to 10%).

### 6.7.2 Non-prompt and charge mis-ID backgrounds

The non-prompt lepton background contribution to the final selection is estimated using the fake factor method. The main idea of the method is to define a control region of events enriched in the background to estimate and determine a factor that relates (extrapolates) these events to those in the signal region. The method is data-driven in the sense that the control sample is selected from data, and the extrapolation

3021 factor is measured from data.

3022 In the signal region of this analysis, non-prompt leptons are predominantly pro-  
 3023 duced in  $t\bar{t}$  events, with a much smaller contribution from Drell-Yan production;  
 3024 therefore, the control region, also known as the *application region*, is defined by modi-  
 3025 fying the event selection criteria in such a way that most of the events after selection  
 3026 are  $t\bar{t}$  events and thus the misidentification rate is increased; hence, in the application  
 3027 regions, the tight definition for electrons and muons are replaced by the the *fakeable*  
 3028 object definitions in Tables 6.4 and 6.5. Since the fakeable definition is a loosened  
 3029 version of the tight definition, in the context of fake rates, the fakeable definition  
 3030 becomes the loose selection.

3031 The ratio between the number of events that pass both the loose and tight selec-  
 3032 tions, and the number of events that pass the loose selection but fail the tight one,  
 3033 corresponds to the *loose-to-tight ratio or fake factor/rate* ( $f$ ). The measurement of  
 3034 the fake factor is made using two background dominated data samples, collected with  
 3035 dedicated triggers, as a function of  $p_T$  and  $|\eta|$  and separately for muons and electrons:

- 3036 • A sample dominated by QCD multijet events, collected using single lepton trig-  
 3037 gers at relatively high  $p_T$  thresholds. It is used to extract ratios for lepton  
 3038 candidates with  $p_T$  above 30 GeV.
- 3039 • A sample dominated by  $Z + \text{jets}$  events, where the two high- $p_T$  leptons resulting  
 3040 from the  $Z$  decay are used to trigger the events without biasing the  $p_T$  spectrum  
 3041 of a third lepton at low transverse momentum. It is used to determine the ratios  
 3042 for low- $p_T$  leptons.

3043 Processes like  $W + \text{jets}$ ,  $Z + \text{jets}$ ,  $WZ$  and  $ZZ$  produce prompt leptons that  
 3044 contaminate the samples; thus, they are suppressed by vetoing additional leptons in

3045 the selection, and the residual contamination is then subtracted using the transverse  
 3046 mass as a discriminating variable.

3047 The extrapolation from the application region to the signal region is performed  
 3048 by weighting the events in the application region using the fake factor according to  
 3049 the following rules:

3050 • events with one lepton failing the tight criteria are weighted with the factor  
 3051  $\frac{f}{(1-f)}$  for the estimate to the signal region.

3052 • events with two leptons (i,j) failing the tight criteria are weighted with the factor  
 3053  $-\frac{f_i f_j}{(1-f_i)(1-f_j)}$  for the estimate to the signal region.

3054 • events with three leptons (i,j,k) failing the tight criteria are weighted with the  
 3055 factor  $\frac{f_i f_j f_k}{(1-f_i)(1-f_j)(1-f_k)}$  for the estimate to the signal region.

3056 Figure 6.11 shows the fake rates for electrons and muons used in this analysis  
 3057 which were taken from the studies in Reference [151].

3058 The resulting prediction of the event yield in the signal selection carries an uncer-  
 3059 tainty of 30-50% which is composed of the statistical uncertainty in the measurement  
 3060 of the fake rates due to prescaling of lepton triggers, the uncertainty in the subtraction  
 3061 of residual prompt leptons from the control region, and from testing the closure of the  
 3062 method in simulated background events; hence, it is one of the dominant limitations  
 3063 on the performance of multilepton analyses in general and this analysis in particular.

3064 Finally, an additional source of background arises in the  $2lss$  channel from events  
 3065 with an originally opposite-sign lepton pair for which the charge of one of the leptons  
 3066 is misidentified (*charge mis-ID*); usually this happens because of the conversion of  
 3067 hard bremsstrahlung photons emitted from the initial lepton, hence, it is more likely  
 3068 to happen for electrons than for muons.

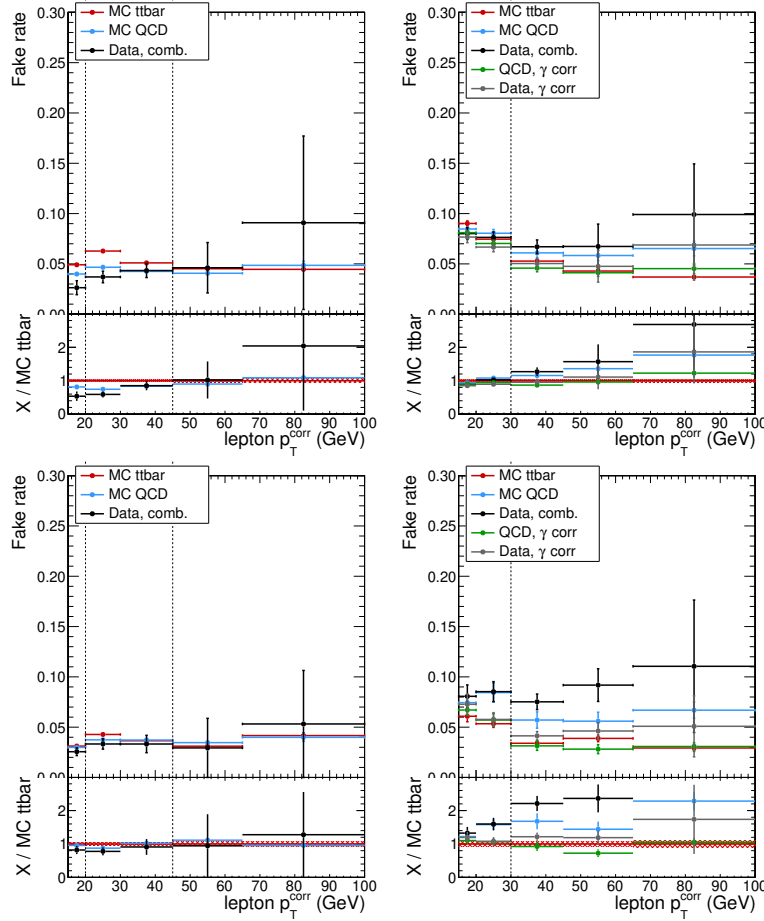


**Figure 6.11:** Fake rate measurement in events in data for muons (left column) and electrons (right column). Predictions from simulated events in the measurement region (blue) and from non-prompt leptons in  $t\bar{t}$  (red) are included for comparison. Top row is for  $|\eta| < 2.5$  and bottom row for  $|\eta| > 2.5$ .

3069        The charge mis-ID background is estimated from the yield of opposite-sign events  
 3070        in the signal region by measuring the charge mis-ID probability in same-sign and  
 3071        opposite-sign events compatible with a Z boson decay, in several bins of  $p_T$  and  $\eta$ ,  
 3072        and weighting events with opposite-sign leptons in the signal selection.

3073        The charge mis-ID probability is found to be negligible for this analysis for muons,  
 3074        whereas for electrons it ranges from about 0.02% in the barrel section ( $|\eta| < 1.48$ )  
 3075        up to about 0.35% in the detector endcaps ( $1.48 < |\eta| < 2.5$ ), as shown in Table 6.7  
 3076        and Figure 6.12.

Data	$10 \leq p_T < 25 \text{ GeV}$	$25 \leq p_T < 50 \text{ GeV}$	$50 \text{ GeV} \leq p_T$
$0 \leq \eta < 1.48$	$0.0442 \pm 0.0011$	$0.0179 \pm 0.0004$	$0.0262 \pm 0.0020$
$1.48 \leq \eta < 2.5$	$0.1329 \pm 0.0066$	$0.1898 \pm 0.0014$	$0.3067 \pm 0.0113$
MC			
$0 \leq \eta < 1.48$	$0.0378 \pm 0.0016$	$0.0222 \pm 0.0003$	$0.0233 \pm 0.0015$
$1.48 \leq \eta < 2.5$	$0.0956 \pm 0.0044$	$0.2108 \pm 0.0027$	$0.3157 \pm 0.0018$

**Table 6.7:** Electron charge mis-ID probabilities (in percent), determined in data (top) and Drell-Yan MC (bottom) [151].

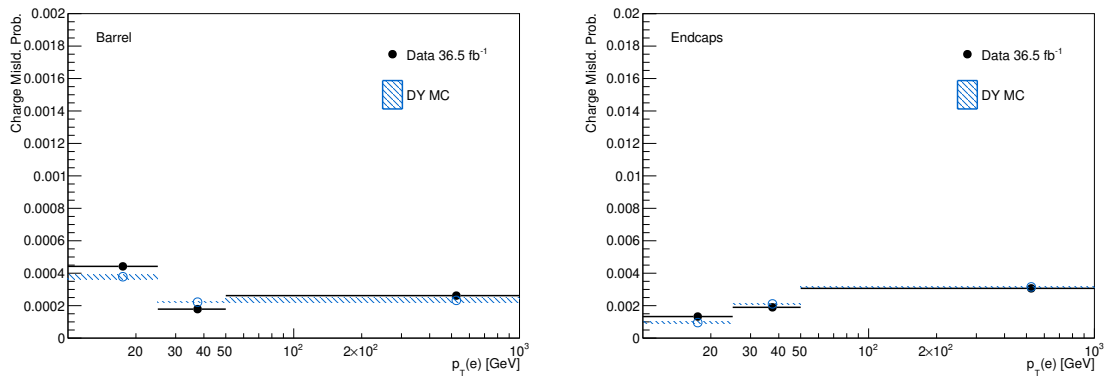


**Figure 6.12:** Electron charge mis-ID probabilities as a function of  $p_T$  for  $|\eta| < 2.5$  (left) and  $|\eta| < 2.5$  (right) [151].

3077     The contribution from charge mis-ID electrons in signal selection of this analysis  
 3078   comes mainly from  $t\bar{t}$  and Drell-Yan events. The systematic uncertainty of the nor-  
 3079   malization of the charge mis-ID estimate is evaluated at about 30%, arising from a  
 3080   slight disagreement of the mis-ID probability between data and simulation. Given  
 3081   that it only affects the  $e\mu$  channel, its impact on the final sensitivity is very limited.

## 3082   **6.8 Pre-selection yields**

3083   The expected and observed event yields of the pre-selection are shown in Table 6.8;  
 3084   Figure 6.13 shows the distributions of some relevant kinematic variables, normalized  
 3085   to the cross section of the respective processes and to the integrated luminosity. The

3086 remaining variable distributions are shown in Appendix B.1.

	$3\ell$	$\mu^\pm \mu^\pm$	$e^\pm \mu^\pm$
$t\bar{t}W$	$22.50 \pm 0.35$	$68.03 \pm 0.61$	$97.00 \pm 0.71$
$t\bar{t}Z/\gamma^*$	$32.80 \pm 1.79$	$25.89 \pm 1.12$	$64.82 \pm 2.42$
$WZ$	$8.22 \pm 0.86$	$15.07 \pm 1.19$	$26.25 \pm 1.57$
$ZZ$	$1.62 \pm 0.33$	$1.16 \pm 0.29$	$2.86 \pm 0.45$
$W^\pm W^\pm qq$	–	$3.96 \pm 0.52$	$6.99 \pm 0.69$
$W^\pm W^\pm(\text{DPS})$	–	$2.48 \pm 0.42$	$4.17 \pm 0.54$
VVV	$0.42 \pm 0.16$	$2.99 \pm 0.34$	$4.85 \pm 0.43$
ttt	$1.84 \pm 0.44$	$2.32 \pm 0.45$	$4.06 \pm 0.57$
tZq	$3.92 \pm 1.48$	$5.77 \pm 2.24$	$10.73 \pm 3.03$
tZW	$1.70 \pm 0.12$	$2.13 \pm 0.13$	$3.91 \pm 0.18$
$\gamma$ conversions	$7.43 \pm 1.94$	–	$23.81 \pm 6.04$
Non-prompt	$25.61 \pm 1.26$	$80.94 \pm 2.02$	$135.34 \pm 2.83$
Charge mis-ID	–	–	$58.50 \pm 0.31$
All backgrounds	$106.05 \pm 3.45$	$210.74 \pm 3.61$	$443.30 \pm 8.01$
$tHq (\kappa_t = -1.0)$	$7.48 \pm 0.14$	$18.48 \pm 0.22$	$27.41 \pm 0.27$
$tHW (\kappa_V = -1.0)$	$7.38 \pm 0.16$	$7.72 \pm 0.17$	$11.23 \pm 0.20$
$t\bar{t}H$	$18.29 \pm 0.41$	$24.18 \pm 0.48$	$35.21 \pm 0.58$
Signal + Backgrounds	$139.20 \pm 3.49$	$261.12 \pm 3.65$	$517.15 \pm 8.03$
Data ( $35.9 \text{ fb}^{-1}$ )	127	280	525

**Table 6.8:** Expected and observed yields for  $35.9 \text{ fb}^{-1}$  after the pre-selection in all final states. Uncertainties are statistical only.

3087 For the  $tH$  and  $t\bar{t}H$  processes, the largest contribution comes from Higgs decays  
 3088 to WW (about 75%), followed by  $\tau\tau$  (about 20%) and ZZ (about 5%). Other Higgs  
 3089 production modes contribute negligible event yields (< 5% of the  $tH + t\bar{t}H$  yield) as  
 3090 shown in Table 6.9. Table 6.10 shows the acceptance×efficiency for the pre-selection  
 3091 criteria in Table 6.6.

3092 A significant fraction of selected data events (about 50% in the dilepton channels,  
 3093 and about 80% in the trilepton channel) also passes the selection used in the dedicated  
 3094 search for  $t\bar{t}H$  in multilepton channels [151]. This is particularly important when  
 3095 considering a possible combination of the measurements from both studies. More  
 3096 details about the overlap between these two analyses are presented in Appendix E.

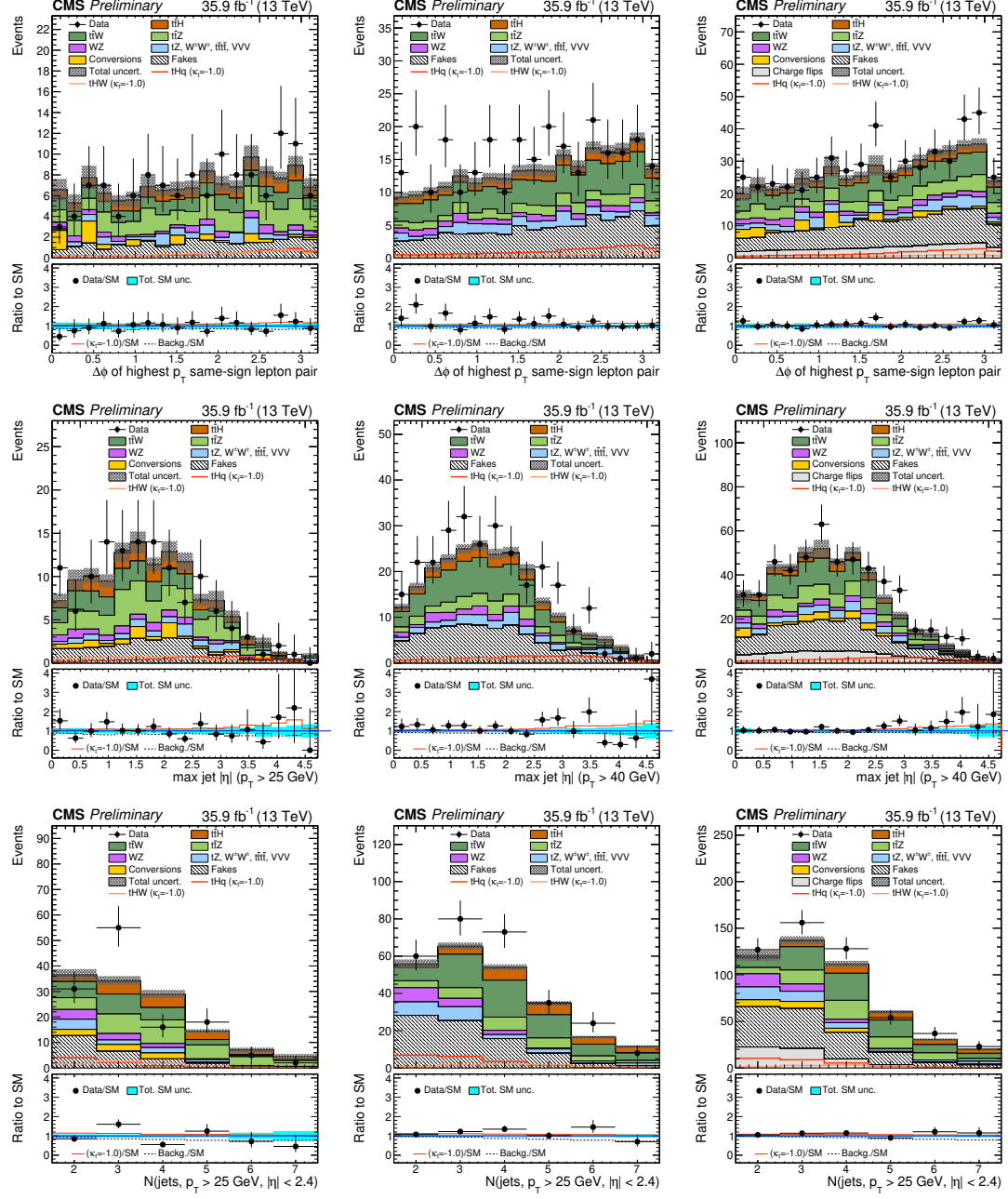


**Figure 6.13:** Distributions of discriminating variables for the event pre-selection for the three lepton channel (left column), same-sign  $\mu^\pm\mu^\pm$  channel (middle column), the same-sign  $e^\pm\mu^\pm$  channel (right column), normalized to  $35.9 \text{ fb}^{-1}$ , before fitting the signal discriminant to the observed data. Uncertainties are statistical and unconstrained (pre-fit) normalization systematics. The shape of the two  $tH$  signals for  $\kappa_t = -1.0$  is shown, normalized to their respective cross sections for  $\kappa_t = -1.0, \kappa_V = 1.0$ .

	$3\ell$	$\mu^\pm\mu^\pm$		
$tHq$ (Inclusive)	<b>6.57</b>	100.0%	<b>17.38</b>	100.0%
$tHq(H \rightarrow WW)$	4.84	73.9%	13.33	76.9%
$tHq(H \rightarrow \tau\tau)$	1.04	15.9%	3.62	20.6%
$tHq(H \rightarrow ZZ)$	0.48	7.2%	0.37	2.2%
$tHq(H \rightarrow \mu\mu)$	0.21	3.0%	0.04	0.2%
$tHq(H \rightarrow \gamma\gamma)$	< 0.01	0.1%	0.02	0.1%
$tHq(H \rightarrow bb)$	< 0.01	< 0.1%	0.01	< 0.1%
$tHW$ (Inclusive)	<b>7.32</b>	100.0%	<b>7.62</b>	100.0%
$tHW(H \rightarrow WW)$	5.50	76.9%	5.60	74.1%
$tHW(H \rightarrow \tau\tau)$	1.40	20.6%	1.81	23.1%
$tHW(H \rightarrow ZZ)$	0.31	2.2%	0.21	2.7%
$tHW(H \rightarrow \mu\mu)$	0.12	0.2%	0.01	0.1%
$tHW(H \rightarrow \gamma\gamma)$	< 0.01	< 0.1%	< 0.01	< 0.1%
$tHW(H \rightarrow bb)$	< 0.01	< 0.1%	< 0.01	< 0.1%

**Table 6.9:** Signal yields split by decay channels of the Higgs boson. Forward jet  $p_T$  cut at 25 GeV.

	$3\ell$	$\mu^\pm\mu^\pm$	$e^\pm\mu^\pm$
$t\bar{t}W$	0.25	0.75	1.07
$t\bar{t}Z/\gamma^*$	0.36	0.29	0.71
$tHq$ ( $\kappa_t = -1.0$ )	0.03	0.06	0.10
$tHW$ ( $\kappa_V = -1.0$ )	0.14	0.15	0.21
$t\bar{t}H$	0.24	0.32	0.46

**Table 6.10:** Acceptance×efficiency (%) for signal and main background events pre-selection.

## 3097 6.9 Signal discrimination

3098 The production cross sections for the signal processes  $tHq$ ,  $tHW$ , and  $t\bar{t}H$  is only  
 3099 about 600 fb (the enhancement provided by inverted couplings,  $\kappa_t = -1$  almost double  
 3100 them), resulting in a small signal to background ratio even for a tight selection. A  
 3101 multivariate method is hence employed to train discriminators to separate  $tH$  signal  
 3102 events from the dominant background events.

3103 **6.9.1 MVA classifiers evaluation**

3104 Several MVA classifier algorithms were evaluated in order to determine the most  
 3105 appropriate method for this analysis<sup>6</sup>. The comparison is based on the performance  
 3106 of the classifiers, encoded in the plot of the background rejection as a function of the  
 3107 signal efficiency (ROC curve). The top row of Figure 6.14 shows the ROC curves for  
 3108 evaluated methods; two separated trainings were performed in the  $3l$  channel: against  
 3109  $t\bar{t}$  (right) and  $t\bar{t}V$  (left) processes.

3110 In both cases, the gradient boosted decision tree *BDTG* (*BDTA\_GRAD* in the  
 3111 plot) classifier offers the best results, followed by the adaptive BDT classifier (*BDTA*);  
 3112 the several Fisher classifiers tested, which differ in their parameters and/or boosting  
 3113 method, offer similar performance among them, while the k-Nearest Neighbour (kNN)  
 3114 classifier performance is below the rest of the classifiers. The corresponding ROC  
 3115 curves and in the  $2lss$  channel for trainings against  $t\bar{t}V$ (left) and  $t\bar{t}$  (right) processes  
 3116 are shown in the bottom row of Figure 6.14; the BDTG performance is similar to  
 3117 that in the  $3l$  channel.

3118 **6.9.2 Discriminating variables**

3119 The classifier chosen to separate the  $tHq$  signal from the main backgrounds is the  
 3120 *BDTG* classifier, trained on simulated signal and background events. The samples  
 3121 used in the training are the  $tHq$  sample in Table 6.2, the samples marked with an \*  
 3122 in Table A.4 and the samples in the third section in Table A.4.

3123 As explained in Section 5.2.1, a set of discriminating variables are given as input to  
 3124 the *BDTG* which combines the individual discrimination power of each input variable

---

<sup>6</sup> The choice of the tested algorithms was based on the recommendations provided by the official TMVA user guide, the experience from previous analyses and considering the expertise of the members of the  $tHq$  and  $t\bar{t}H$  analyses groups. Only the BDT classifier is described in this thesis and a detailed description of all available methods can be found in Reference [127].

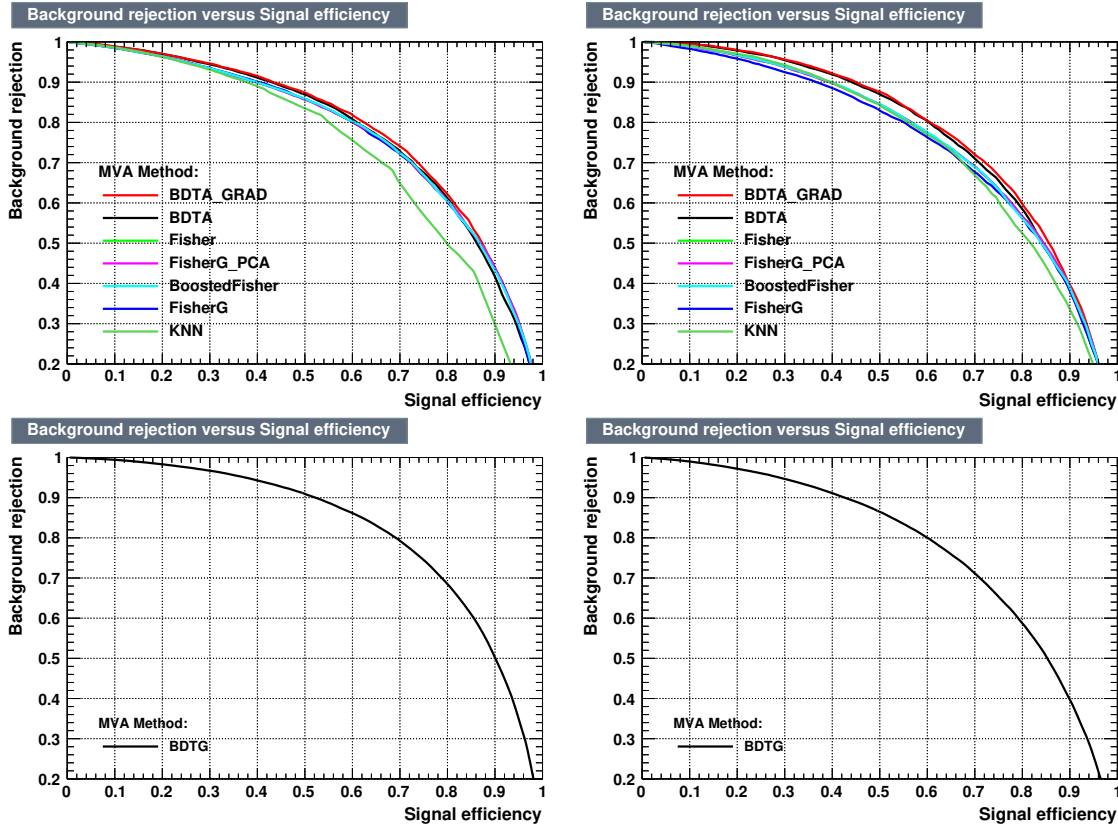


**Figure 6.14:** Top: Background rejection vs signal efficiency (ROC curves) for various MVA classifiers in the  $3l$  channel for training against  $t\bar{t}V$  (left) and  $t\bar{t}$  (right). Bottom: background rejection vs signal efficiency (ROC curve) in the  $2lss$  channel for a single discriminator: BDTG, against  $t\bar{t}V$  (left) and  $t\bar{t}$  (right).

3125 to produce a quantity with the maximum discrimination power. Table 6.11 lists the  
 3126 input variables used in the BDTG trainings for this analysis. The same set of input  
 3127 variables was used to produce the plots for MVA classifiers evaluation.

3128 BDTG input variables reflect those features that differentiate the signal process  
 3129 from the background processes.

3130 The first two input variables in Table 6.11 are related to the jet multiplicity in the  
 3131 events. As shown in the diagrams of the Figure 6.15, signal events are expected to  
 3132 have one forward jet, one  $b$ -jet, and two (zero) light jets in the  $2lss(3l)$  channel. Note  
 3133 that in the  $2lss$  channel light jets originate from a W boson which could be off-shell;

Variable name	Description
nJet25	Number of jets with $p_T > 25$ GeV, $ \eta  < 2.4$
nJetEta1	Number of jets with $ \eta  > 1.0$ , non-CSV-loose
MaxEtaJet25	Max. $ \eta $ of any (non-CSV-loose) jet with $p_T > 25$ GeV
deltaFwdJetClosestLep	$\Delta\eta$ forward light jet and closest lepton
deltaFwdJetBJet	$\Delta\eta$ forward light jet and hardest CSV loose jet
deltaFwdJet2BJet	$\Delta\eta$ forward light jet and second hardest CSV loose jet
Lep3Pt/Lep2Pt	$p_T$ of the 3 <sup>rd</sup> lepton (2 <sup>nd</sup> for 2lss)
totCharge	Sum of lepton charges
minDRll	Min $\Delta R$ any two leptons
dphiHighestPtSSPair	$\Delta\phi$ of highest $p_T$ same-sign lepton pair

**Table 6.11:** BDTG input variables. First section lists variables related to jet multiplicity, second section lists variables related to forward jet activity and variables related to lepton kinematics are listed in third section.

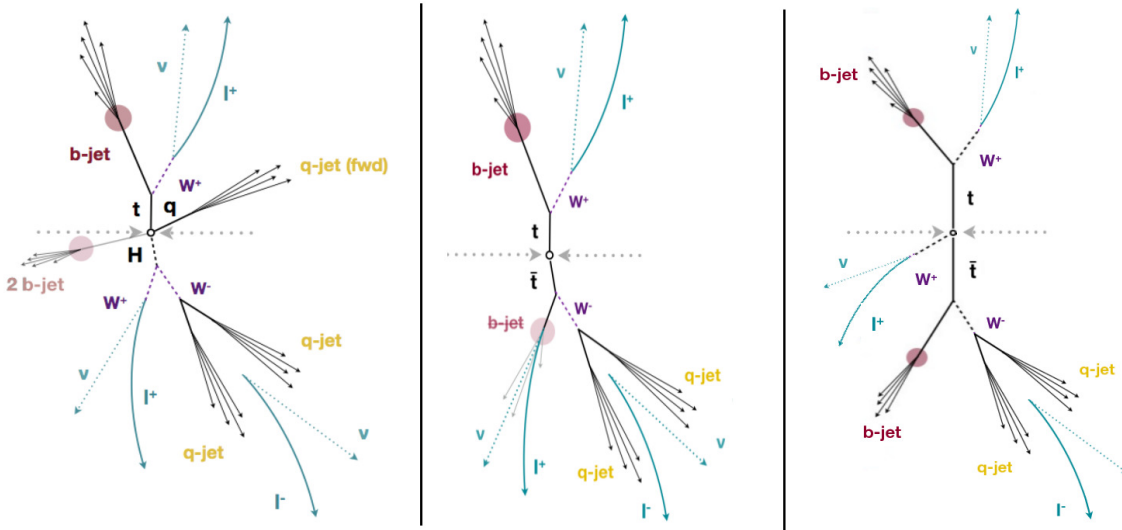


**Figure 6.15:** BDT input variables are defined based on the features of the signal and background processes. Diagrams for signal and the two dominant backgrounds:  $tHq$  (left),  $t\bar{t}$  (middle) and  $t\bar{t}W$  (right) processes. The second  $b$ -jet in  $tHq$  process, indicated in the diagram as an opaque jet, originates from the spectator  $\bar{b}$  quark remaining from the gluon splitting into a  $b\bar{b}$  pair.

3134 if one of these jets is too soft ( $p_T < 25$  GeV) it does not get reconstructed and the  
 3135 event is not identified as a signal event. In the case of  $t\bar{t}$  events, one  $b$ -jet and two  
 3136 light jets (zero for 3l channel) are expected, one fewer than for signal events. For  $t\bar{t}W$   
 3137 events, the number of jets is the same as for signal events but usually there are more

3138 final state radiation jets than in signal. Thus, nJet25 accounts for the number of jets  
 3139 in the event while nJetEta1 accounts for the number of forward jets.

3140 The second section of variables in Table 6.11 is related to the forward jet activity  
 3141 and the location of the leptons and other jets with respect to the forward jet;  
 3142 leptons and  $b$ -jets are expected to be central in both signal and background events.  
 3143 MaxEtaJet25 evaluates how forward are jets in the event.  $\text{detaFwdJetClosestLep}$   
 3144 evaluates how separated in  $\eta$  the forward jet is from the leptons and  $b$ -jets in the  
 3145 event; in background events leptons and jets are central and then closer to each other  
 3146 than in signal events where this separation is large. The same reasoning applies for  
 3147  $\text{detaFwdJetBjet}$ .

3148  $\text{detaFwdJet2Bjet}$  evaluates the separation in  $\eta$  between the light forward jet and  
 3149 the second  $b$ -jet. As described in Chapter 2, in the four flavor scheme,  $b$  quarks are not  
 3150 allowed inside the proton, therefore, the incoming  $b$  quark involved in  $tHq$  process is  
 3151 originated from a gluon splitting into a  $b\bar{b}$  pair, hence, the second  $b$ -jet in  $tHq$  process  
 3152 comes from the remaining  $\bar{b}$  quark acting as a spectator and appearing in the final  
 3153 state as a forward  $b$ -jet. This second  $b$ -jet tends to be very forward and then it is not  
 3154 always reconstructed. For signal events with two forward jets, one forward and the  
 3155 other backward,  $\text{detaFwdJet2Bjet}$  would be larger than for background events with  
 3156 two  $b$ -jets for which  $b$ -jets are central and then less separated from the light forward  
 3157 jet.

3158 The third section of variables in Table 6.11 is related to the lepton kinematics  
 3159 encoding the distinctive behavior of leptons in signal events and background events.  
 3160 In  $tHq$  and  $t\bar{t}$  events, same-sign leptons are back to back; for three lepton events,  
 3161 the two opposite sign leptons are closer together. In  $t\bar{t}W$  events, leptons tends to be  
 3162 distributed throughout the space; thus  $\text{minDRll}$  and  $\text{dphiHighestPtSSPair}$  account  
 3163 for these features.

3164 Lep2Pt and Lep3Pt represent the  $p_T$  of the second and third lepton in  $2lss$  and  
 3165 ( $3l$ ) events respectively. In  $t\bar{t}$  the fake lepton is expected to have lower  $p_T$  than the  
 3166 corresponding lepton in signal events; in  $t\bar{t}W$  events, all leptons are expected to be  
 3167 high  $p_T$  leptons, therefore their correspondent leptons in signal events are expected  
 3168 to have lower  $p_T$ .

3169 Finally, totCharge is the sum of the lepton charges in the final state; for  $tHq$   
 3170 events, it is expected to be asymmetrically distributed with an excess of positive  
 3171 charge because the proton have more  $u$  quarks than  $d$  quarks, therefore, more  $W^+$   
 3172 bosons are expected and then more positive leptons in the final state. The total  
 3173 charge in  $t\bar{t}$  events is expected to be symmetrically distributed since the final state is  
 3174 neutral while for  $tHW$  events the distribution is expected to be asymmetric due to  
 3175 the presence of the  $W$  boson.

3176 Plots in Figure 6.16 shows the BDTG input variables distributions for the signal  
 3177 and background samples in the  $3l$  channels; these plots exhibit the features described  
 3178 above.

3179 All the input variables have some discrimination power, however, that power is  
 3180 bigger for some of them. For instance, the third lepton  $p_T$  plot (top left in Figure 6.16)  
 3181 shows some discrimination power against  $WZ$  and  $VVV$  backgrounds; although this  
 3182 variable discriminates only against these two backgrounds, it is useful for the overall  
 3183 background discrimination.

3184 The same or equivalent input variables are found to perform well for both  $3l$  and  
 3185  $2lss$  channels. Figure B.4 shows the corresponding input variables distribution plots  
 3186 for the  $2lss$  channel.

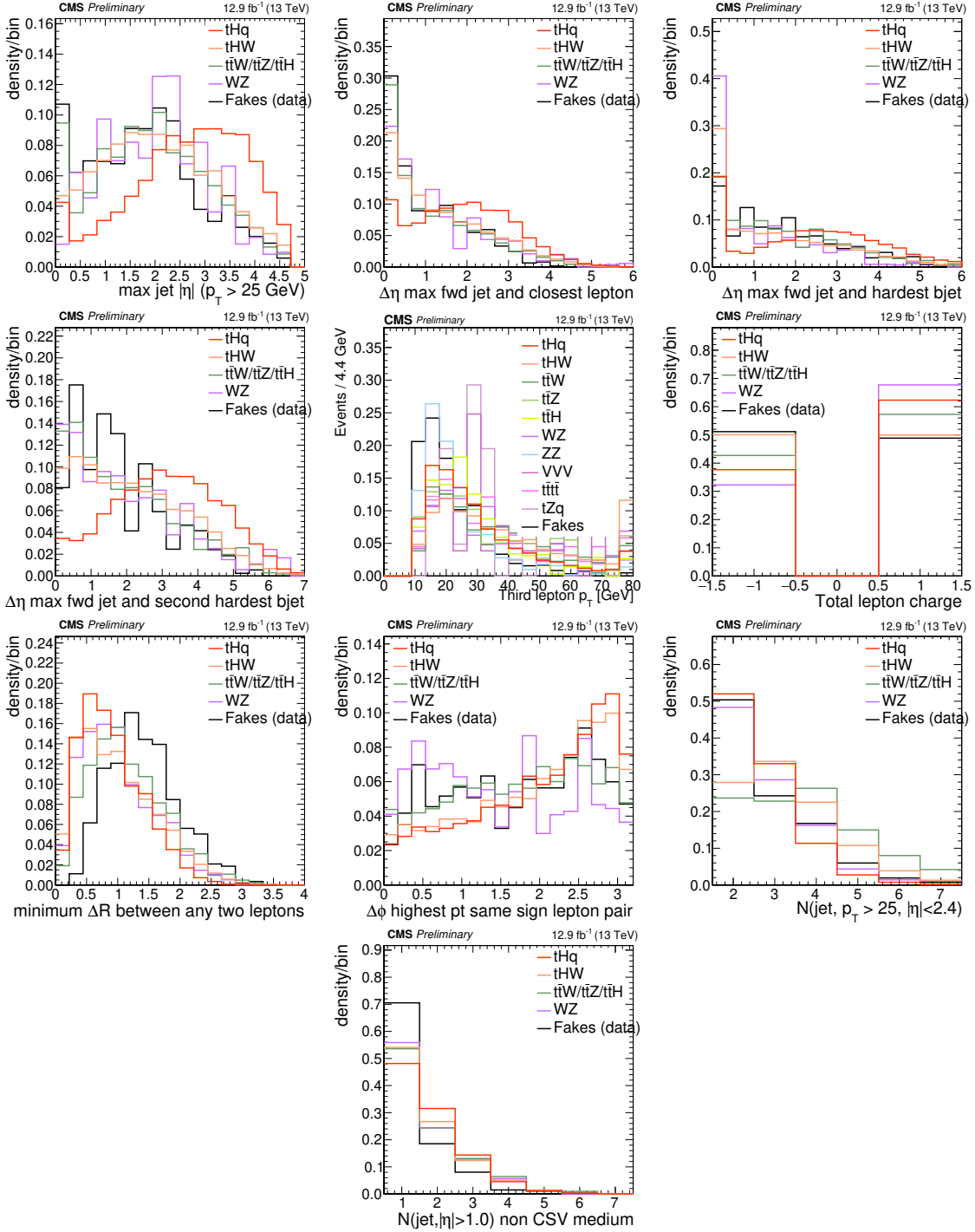


**Figure 6.16:** Distributions of the BDTG classifier input variables for signal discrimination, normalized to equal area, in the  $3l$  channel.

3187 **Discrimination power from BDTG classifier**

3188 The discrimination power of the input variables can also be evaluated from the BDTG  
 3189 training, exclusively for the training samples, i.e., dominant backgrounds ( $t\bar{t}$  and  $t\bar{t}V$ );  
 3190 the training samples are submitted to the selection cuts on Table 6.6.

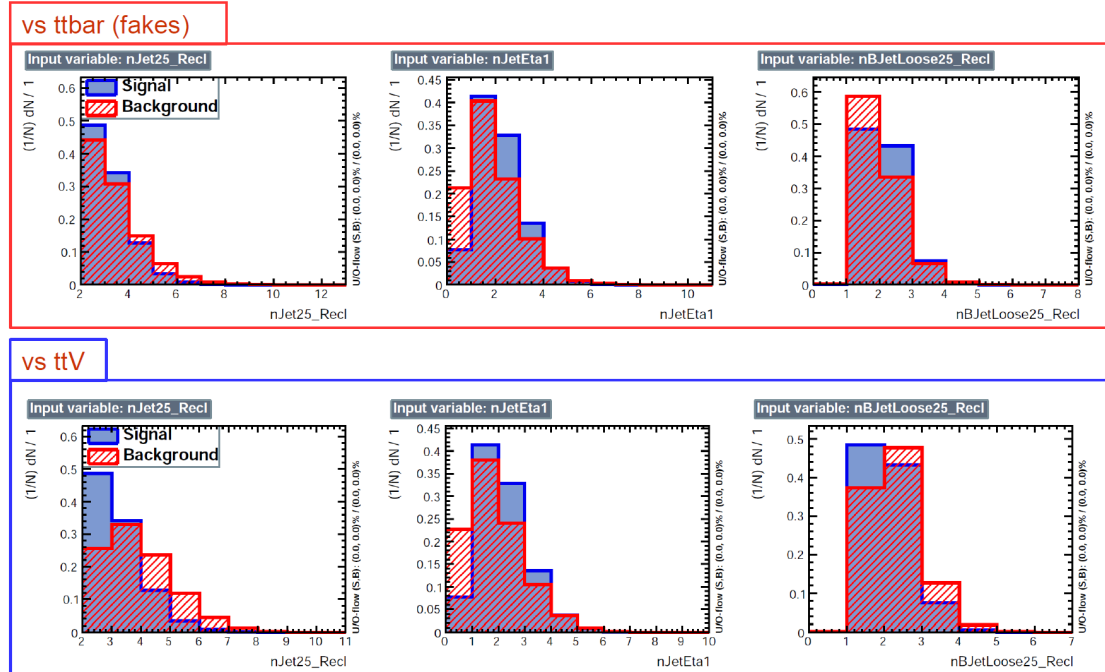


**Figure 6.17:** BDT input variables as seen by BDTG classifier for the  $3l$  channel,  $tHq$  (blue) discriminated against background (red),  $t\bar{t}$  (top) and  $t\bar{t}V$ (bottom).

3191 Figure 6.17 shows the comparison between input variables for the two trainings  
 3192 in the  $3l$  channel; it reveals that some variables show opposite behavior for the two  
 3193 background sources, which results in potentially screening the discrimination power  
 3194 if they were to be used in a single discriminant, i.e., if the training would join  $t\bar{t}$  and  
 3195  $t\bar{t}V$ . For some other variables the distributions are similar in both background cases.  
 3196 In contrast to the distributions in Figure 6.16 only the dominant backgrounds are  
 3197 included; however, the discrimination power agrees among plots.

Figures B.5, B.6, B.7, and B.8 show the input variables distributions for the  $2lss$  and  $3l$  channels as seen by the BDTG classifier.

## Input variables correlations

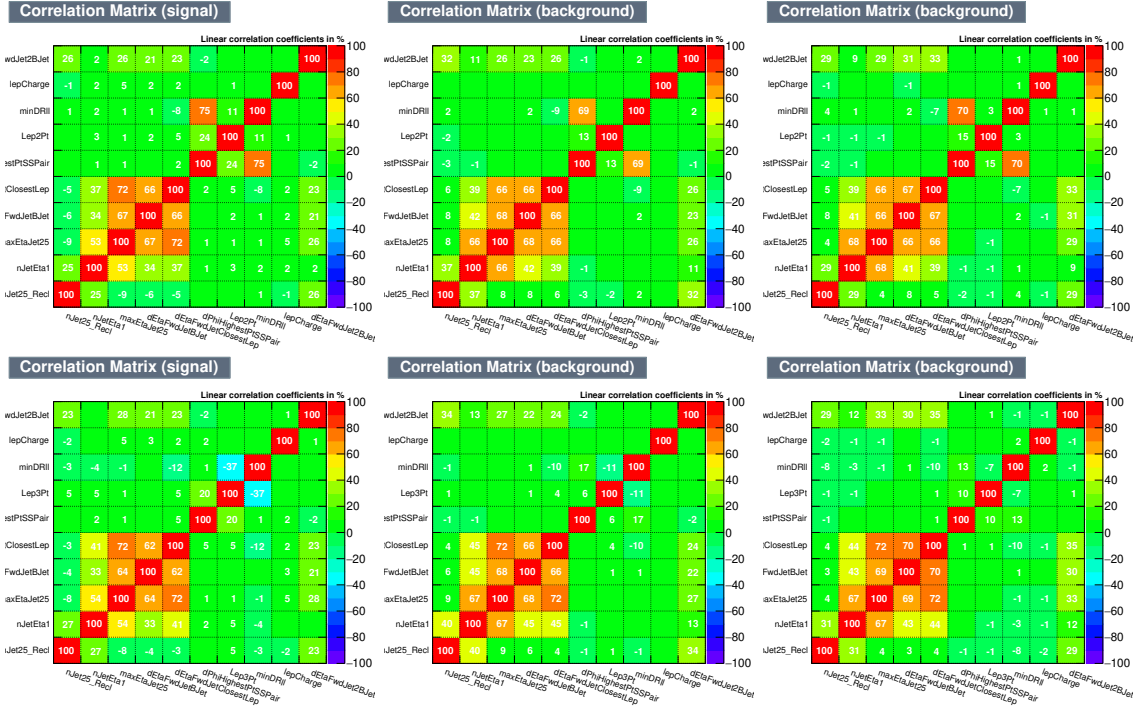


**Figure 6.18:** Signal (left),  $t\bar{t}$  background (middle), and  $t\bar{t}V$  background (right.) correlation matrices for the input variables in the BDTG classifier for the  $2lss$  and  $3l$  channels.

From Table 6.11, it is clear that the input variables are correlated to some extent. These correlations play an important role for some MVA methods like the Fisher discriminant method in which the first step consist of performing a linear transformation to an phase space where the correlations between variables are removed. In the case of BDT, correlations do not affect the performance. Figure 6.18 shows the linear correlation coefficients for signal and background for the two training cases (the signal values are identical by construction). As expected, strong correlations appear for variables related to the forward jet activity.

### 3209 6.9.3 BDTG classifiers response

3210 After the training stage, the BDTG classifier is tested to ensure its ability to discrim-  
 3211 inate between simulated signal and background events. The BDTG classifier output  
 3212 distributions for signal and backgrounds in the  $3l$  channel are shown in Figure 6.19.  
 3213 As expected, a good discrimination power is obtained using default discriminator  
 3214 parameter values; some overtraining, represented in the differences between the test  
 3215 (histogram) and the training (dots), is also visible.

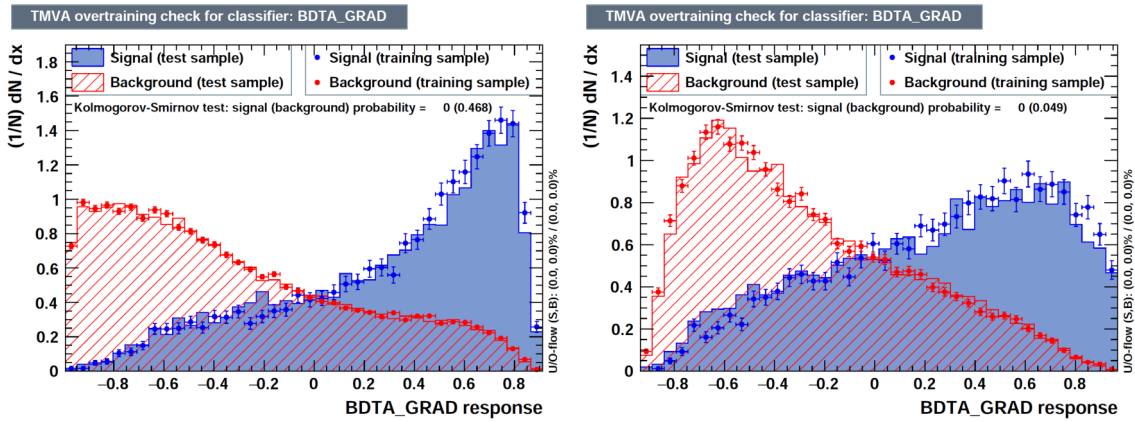


**Figure 6.19:** BDTG classifier output for trainings against  $t\bar{t}V$ (left) and  $t\bar{t}$  (right). Default BDTG parameters have been used.

3216 In order to explore further optimization in the BDTG performance, several changes  
 3217 from the default BDTG parameters were tested; Table 6.12 lists the set of parameters  
 3218 found to be most discriminant with minimal overtraining as shown in Figure 6.20.

TMVA.Types.kBDT		
Option	Default	Used
NTrees	200	800
BoostType	AdaBoost	Grad
Shrinkage	1	0.1
nCuts	20	50
MaxDepth	3	

**Table 6.12:** Configuration used in the final BDTG training. Parameters not listed were not tested.

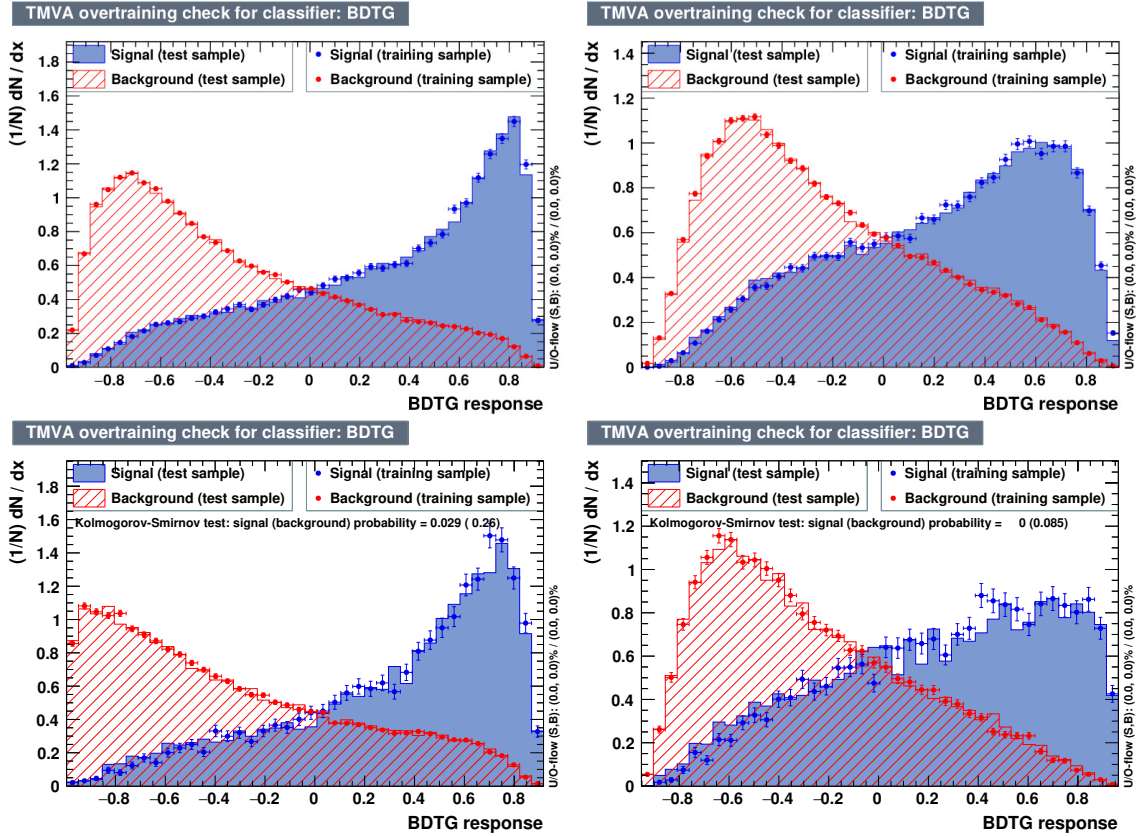


**Figure 6.20:** BDTG classifiers output for training against  $t\bar{t}V$  (left) and  $t\bar{t}$  (right) for  $2lss$  channel (top) and  $3l$  channel (bottom).

3219     The ranking of the input variables by their importance in the classification process  
 3220    is shown in Table 6.13; for both trainings the rankings show almost the same five  
 3221    variables in the first places.

### 3222    **6.9.4 Additional discriminating variables**

3223    Given that the forward jet in background processes could have been originated from  
 3224    pileup, two additional discriminating variables accounting for that were tested. These  
 3225    additional variables describe the forward jet momentum (`fwdJetPt25`) and the forward  
 3226    jet identification (`fwdJetPUID`); their distributions in the  $3l$  channel are shown in  
 3227    Figure 6.21. The forward jet identification distribution shows that for both signal

$t\bar{t}$ training		$t\bar{t}V$ training		
Rank	Variable	Importance	Variable	Importance
1	minDRll	1.329e-01	dEtaFwdJetBJet	1.264e-01
2	dEtaFwdJetClosestLep	1.294e-01	Lep3Pt	1.224e-01
3	dEtaFwdJetBJet	1.209e-01	maxEtaJet25	1.221e-01
4	dPhiHighestPtSSPair	1.192e-01	dEtaFwdJet2BJet	1.204e-01
5	Lep3Pt	1.158e-01	dEtaFwdJetClosestLep	1.177e-01
6	maxEtaJet25	1.121e-01	minDRll	1.143e-01
7	dEtaFwdJet2BJet	9.363e-02	dPhiHighestPtSSPair	9.777e-02
8	nJetEta1	6.730e-02	nJet25_Recl	9.034e-02
9	nJet25_Recl	6.178e-02	nJetEta1	4.749e-02
10	lepCharge	4.701e-02	lepCharge	4.116e-02
1	dEtaFwdJetClosestLep	1.394e-01	maxEtaJet25	1.357e-01
2	minDRll	1.359e-01	dEtaFwdJet2BJet	1.267e-01
3	maxEtaJet25	1.308e-01	dEtaFwdJetBJet	1.200e-01
4	dPhiHighestPtSSPair	1.116e-01	Lep2Pt	1.196e-01
5	Lep2Pt	1.111e-01	dEtaFwdJetClosestLep	1.145e-01
6	dEtaFwdJetBJet	1.067e-01	minDRll	1.077e-01
7	dEtaFwdJet2BJet	8.906e-02	nJet25_Recl	1.020e-01
8	nJetEta1	6.445e-02	dPhiHighestPtSSPair	8.232e-02
9	nJet25	6.254e-02	nJetEta1	5.948e-02
10	lepCharge	4.848e-02	lepCharge	3.198e-02

**Table 6.13:** Input variables ranking for BDTG classifiers for the trainings in the  $2lss$  channel (first section) and  $3l$  channel (second section). For both trainings the rankings show almost the same 5 variables in the first places.

and background, jets are mostly originated from the primary vertex.

The testing was performed by including in the BDTG input one variable at a time, so the discrimination power of each variable can be evaluated individually, and then both simultaneously. fwdJetPUID was ranked the last place in importance (11) in both trainings ( $t\bar{t}V$  and  $t\bar{t}$ ) while fwdJetPt25 was ranked 3 in the  $t\bar{t}V$  training and 7 in the  $t\bar{t}$  training. When training using 12 variables, fwdJetPt25 was ranked 5 and 7 in the  $t\bar{t}V$  and  $t\bar{t}$  trainings respectively, while fwdJetPUID was ranked 12 in both cases.

The improvement in the discrimination performance provided by the additional variables is about 1%, so it was decided not to include them in the procedure. Table 6.14 shows the ROC-integral for all the testing cases performed.

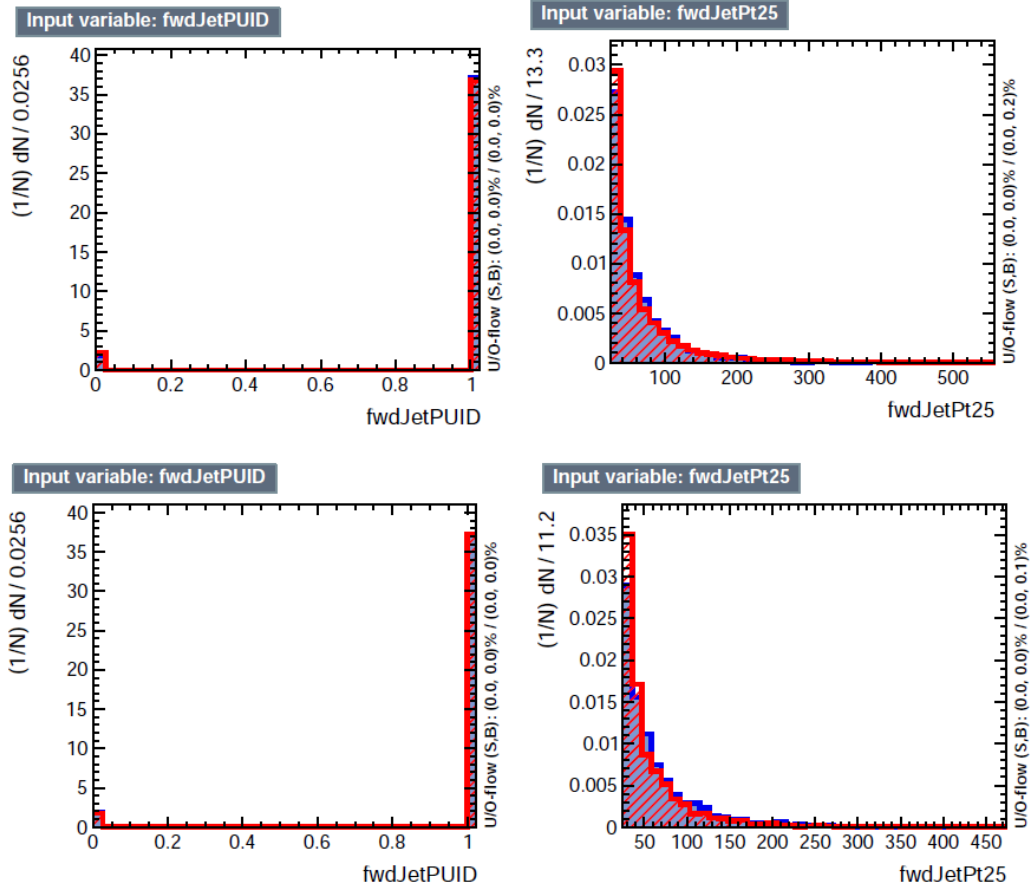


**Figure 6.21:** Additional discriminating variables distributions for  $t\bar{t}V$  training (top row) and  $t\bar{t}$  training (bottom row) in the  $3l$  channel. The origin of the jets in the forward jet identification distribution is tagged as 0 for *pileup jets* while *primary vertex jets* are tagged as 1.

	ROC-integral	
	$t\bar{t}V$	$t\bar{t}$
base 10 var	0.848	0.777
+ <code>fwdJetPUID</code>	0.849	0.777
+ <code>fwdJetPt25</code>	0.856	0.787
12 var	0.856	0.787

**Table 6.14:** ROC-integral for all the testing cases performed in the evaluation of the additional variables discriminating power. The improvement in the discrimination performance provided by the additional variables is about 1% .

3239 **6.9.5 Signal extraction procedure**

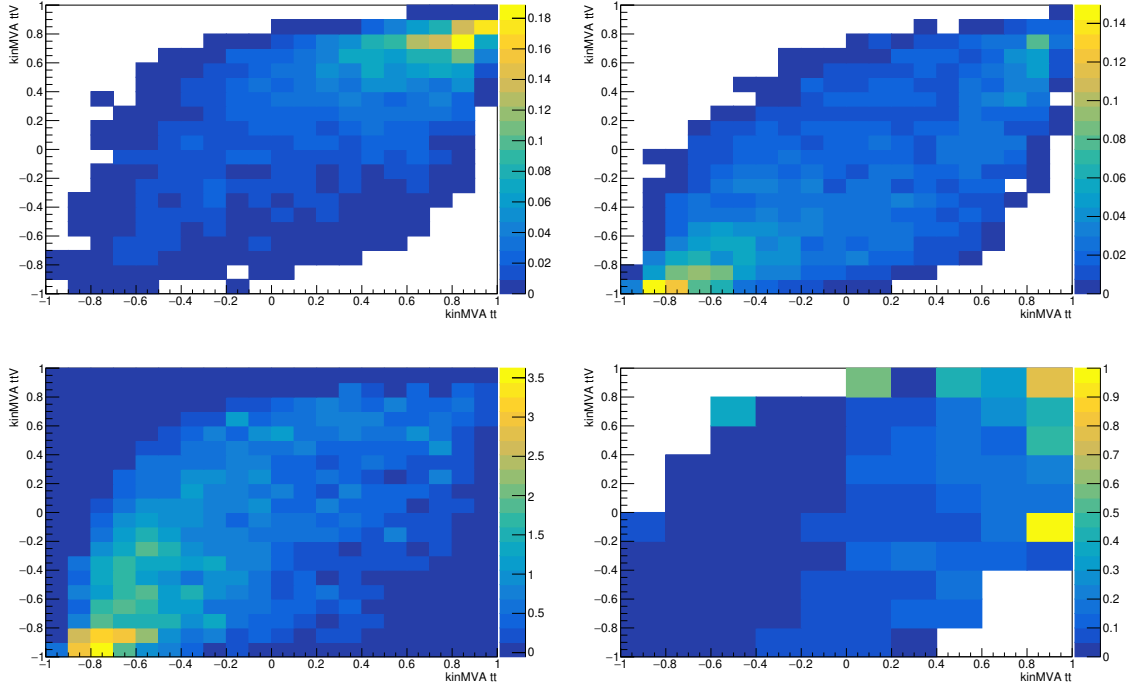


**Figure 6.22:** BDT classifier output planes (training vs.  $t\bar{t}$  on x-axis and vs.  $t\bar{t}V$  on y-axis) for the  $tHq$  and  $tHW$  signals (top row), and for the combined backgrounds (bottom left). Bottom right: S/B ratio (combining  $tHq$  and  $tHW$ ) in the same plane. Plots are for 3l channel.

3240 Once the two BDTG classifiers introduced in the previous section are trained  
 3241 against the dominant backgrounds in each channel, they are used to classify the events  
 3242 in the samples; their outputs are then used to evaluate the signal cross section limits  
 3243 in a fit to the classifier shape. Figure 6.22 shows the expected output distributions in a  
 3244 2D plane of one training vs. the other, i.e.,  $t\bar{t}V$  vs.  $t\bar{t}$ . The top row shows the 2D planes  
 3245 for  $tHq$  and  $tHW$  signals, while the bottom left plot shows the corresponding 2D  
 3246 plane for the combined backgrounds, which are evaluated as in the final background  
 3247 prediction, i.e., these are not the samples used in the BDTG training and this includes  
 3248 data-driven backgrounds. The signal (combining of  $tHq$  and  $tHW$ ) to background

3249 ratio (S/B) is shown in the bottom right plot of Figure 6.22.

3250        Each event is now classified into one of ten 2D-bins according to its position in the  
 3251 plane, as shown in Figure 6.23. The number of bins is chosen such that no bins are  
 3252 entirely empty for any process. The bin boundary positions and number of bins have  
 3253 been studied and optimized with respect to the expected limit on the signal strength  
 3254 (see Appendix C.1).

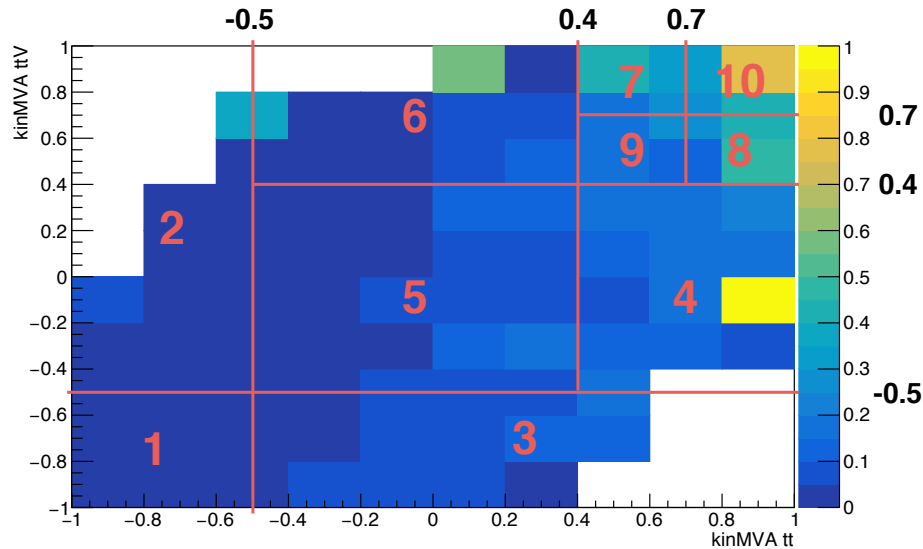


**Figure 6.23:** Binning overlaid on the S/B ratio map on the plane of classifier outputs.

3255        From this event categorization, a 1D histogram of expected distribution is pro-  
 3256 duced for each signal and background process, and fit to the observed data (or the  
 3257 Asimov dataset for expected limits).

## 3258        6.10 Forward jet mismodeling

3259        As said in previous section, among the features of the  $tHq$  signature is the presence  
 3260 of a forward jet that serves as a powerful discriminating variable; unfortunately, its  
 3261  $\eta$  distribution is poorly modeled in simulation as shown in the distributions of some

variables related to the forward jet for MC and data in Figure 6.24. The disagreement of the  $\eta$  distribution of forward jets for a  $p_T$  cut of 25 GeV (row two, columns two and three) is clearly visible, especially at higher values of  $|\eta|$ ; the multiplicity for central jets (row three column three) is also poorly described. The  $t\bar{t}$  background in this analysis is modeled with a data-driven method and these disagreements do not directly affect the  $t\bar{t}$  contribution in the analysis; they do however, reflect the expected agreement in these distributions for the irreducible backgrounds and the signal.

To estimate the effect of a mismodeled forward jet distribution, a reweighting of the events in simulation based on the normalized data/MC ratio in a control region is performed; as a result, an alternative shape of the BDT output distributions that reflects a hypothetical perfect data/MC agreement is derived.

Using a sample of dileptonic  $t\bar{t}$  events, the control region is defined by requiring two opposite-sign tight leptons in the  $e\mu$  channel, with at least two jets and at least one medium CSV tagged jet. (Otherwise the selection is identical to the same-sign  $e^\pm\mu^\pm$  channel selection).

The effect of higher  $p_T$  cuts on the forward jet has been studied for three values: 25, 30 and 40 GeV. In order to take into account the data/MC disagreement in the high  $\eta$  regions, the events are weighted accordingly to the data/MC ratio of the unity normalized control plots shown in Figure 6.25. The data/MC agreement in the forward jet  $\eta$  distribution improves significantly at higher jet  $p_T$ s.

Table 6.15 shows the scale factors obtained for the three  $p_T$  values. The expected limit on cross section in the  $3l$  was used to determine the most appropriate forward jet  $p_T$  cut; higher  $p_T$  cut improves the limit from 1.54 at 25 GeV to 1.51 at 30 GeV and 1.50 at 40 GeV. The impact of the data/MC disagreement for forward jet  $\eta$  is observed to reduce with higher  $p_T$  cuts. Figures F.1, F.2 and F.3 show this reduction

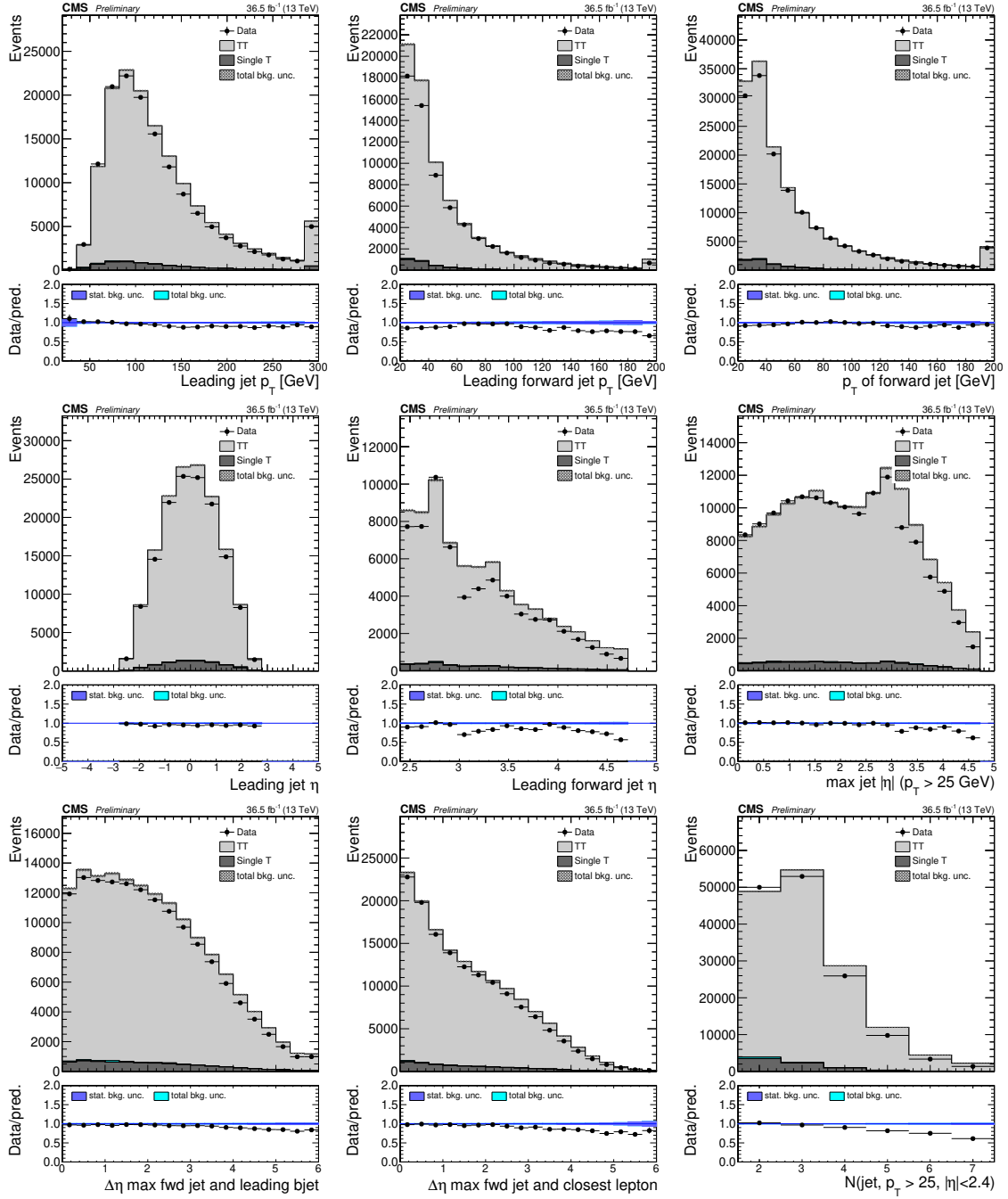


**Figure 6.24:** Kinematic distributions in the  $t\bar{t}$ -enriched opposite-sign  $e\mu$  selection. Top row: leading central ( $\eta < 2.4$ ) jet  $p_T$  (left), leading forward ( $\eta > 2.4$ ) jet  $p_T$  (middle),  $p_T$  of non-CSV-loose jet with highest  $\eta$  (“light forward jet”) (Right). Middle row:  $\eta$  distribution of the jets in the top row. Bottom row:  $\Delta\eta$  between light forward jet and leading CSV-loose tagged jet;  $\Delta\eta$  between light forward jet and closest lepton; number of central jets.

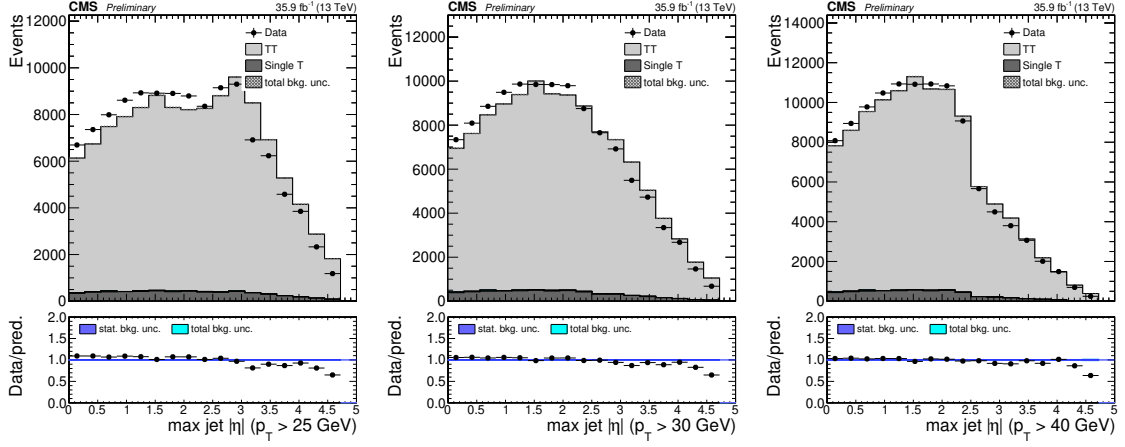


**Figure 6.25:** Pseudorapidity distributions of the most forward, non-CSV-loose tagged jet in the  $t\bar{t}$ -enriched opposite-sign  $e\mu$  selection for the three  $p_T$  cut values studied.

3288 in the impact of the forward jet  $\eta$  nuisance in the fit.

## 3289 6.11 Signal model

3290 It is worth remembering that the main goal of this analysis is to test the compatibility  
 3291 of points in the parameter space of Higgs-to-vector boson and Higgs-to-top quark cou-  
 3292 plings. This is achieved by using simulated  $tHq$ ,  $tHW$ , and  $t\bar{t}H$  signal events which  
 3293 are weighted to reflect the impact of different couplings on kinematic distributions,  
 3294 and together with different predictions of the respective production cross sections and  
 3295 branching ratios, to produce limits on the cross section for different values of  $\kappa_V$  and  
 3296  $\kappa_t$ . See Section 6.4.3 and Table A.3 for the set of  $\kappa_t$  and  $\kappa_V$  values generated. The  
 3297 slight shape dependence of the BDTG classifier outputs as a function of the couplings  
 3298 is shown in Appendix D.

3299 In addition to the  $(\kappa_t, \kappa_V)$  dependence of the  $tHq$  and  $tHW$  production cross  
 3300 sections, due to interference, the cross section of  $t\bar{t}H$  depends quadratically on  $\kappa_t$   
 3301 according to [161]:

$\eta$ range	$p_T > 25$ GeV	$p_T > 30$ GeV	$p_T > 40$ GeV
0 – 0.278	1.0925	1.0566	1.0326
0.278 – 0.556	1.0920	1.0617	1.0407
0.556 – 0.833	1.0675	1.0459	1.0244
0.833 – 1.111	1.0888	1.0593	1.0340
1.111 – 1.389	1.0759	1.0508	1.0322
1.389 – 1.667	1.0109	0.9847	0.9661
1.667 – 1.944	1.0727	1.0448	1.0239
1.944 – 2.222	1.0715	1.0457	1.0169
2.222 – 2.500	1.0112	0.9871	0.9746
2.500 – 2.778	1.0387	0.9942	0.9816
2.778 – 3.056	0.9687	0.9427	0.9200
3.056 – 3.333	0.8137	0.8695	0.9092
3.333 – 3.611	0.9010	0.9387	0.9807
3.611 – 3.889	0.8685	0.8887	0.9213
3.889 – 4.167	0.9277	0.9466	1.0135
4.167 – 4.444	0.8111	0.8278	0.8637
4.444 – 4.722	0.6497	0.6485	0.6367
4.722 – 5.000	1.0000	1.0000	1.0000
Exp. limit ( $\ell\ell\ell$ )	$r < 1.54$	$r < 1.51$	$r < 1.50$

**Table 6.15:** Data/MC scale factors for  $\eta$  distribution of most forward, non-tagged jet with three different  $p_T$  cuts, see Figure 6.25.

$$\sigma(tHq) = (2.633\kappa_t^2 + 3.578\kappa_V^2 - 5.211\kappa_t\kappa_V) * \sigma_{SM}(tHq), \quad (6.6)$$

$$\sigma(tHW) = (2.909\kappa_t^2 + 2.310\kappa_V^2 - 4.220\kappa_t\kappa_V) * \sigma_{SM}(tHW), \quad (6.7)$$

$$\sigma(t\bar{t}H) = \kappa_t^2 * \sigma_{SM}(t\bar{t}H). \quad (6.8)$$

3302      The Higgs branching fractions to vector bosons depend on  $\kappa_V$ , and the overall  
 3303      Higgs decay width depend both on  $\kappa_t$  and  $\kappa_V$  when considering resolved top quark  
 3304      loops in the  $H \rightarrow \gamma\gamma$ ,  $H \rightarrow Z\gamma$ , and  $H \rightarrow gg$  decays. The relative contributions from  
 3305       $H \rightarrow WW$ ,  $H \rightarrow ZZ$ , and  $H \rightarrow \tau\tau$  also change with changing  $\kappa_V$ .  
 3306      If the Higgs-to-tau coupling modifier ( $\kappa_\tau$ ) is assumed to be equal to  $\kappa_t$ , the relative

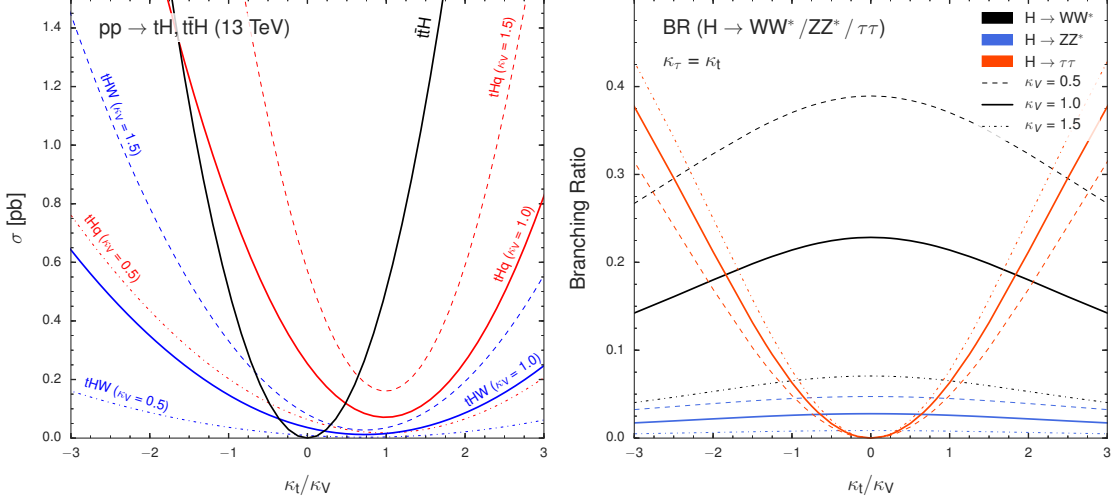


**Figure 6.26:** Scaling of the  $tHq$ ,  $tHW$ , and  $t\bar{t}H$  production cross sections (left) and of the  $H \rightarrow WW^*$ ,  $H \rightarrow \tau\tau$ , and  $H \rightarrow ZZ^*$  branching ratios (right), as a function of  $\kappa_t/\kappa_V$ , for three different values of  $\kappa_V$ .

3307 fractions of  $WW$ ,  $ZZ$ , and  $\tau\tau$  in the event selection will only depend on the ratio of  
 3308  $\kappa_t/\kappa_V$ ; thus, any limit set at any given value of  $\kappa_t/\kappa_V$  is valid for all values of  $\kappa_t$  and  
 3309  $\kappa_V$  with that ratio, and could then be compared with theoretical predictions of cross  
 3310 sections at different values of either modifier. Figure 6.26 shows the  $tHq$ ,  $tHW$  and  
 3311  $t\bar{t}H$  cross sections (left) and the Higgs boson branching ratios  $H \rightarrow WW$ ,  $H \rightarrow ZZ$ ,  
 3312 and  $H \rightarrow \tau\tau$  (right) as a function of the  $\kappa_t/\kappa_V$  ratio.

3313 Thus, this analysis sets an upper limit on the combined cross section times branch-  
 3314 ing ratio of  $tHq$ ,  $tHW$ , and  $t\bar{t}H$  as a function of the ratio  $\kappa_t/\kappa_V$ , under the assumption  
 3315 of  $\kappa_t = \kappa_\tau$ .

3316 A Similar interpretation can be made if instead of reporting the limits as a function  
 3317 of the  $\kappa_t/\kappa_V$  ratio, they are reported as a function of the relative strength of Higgs-top  
 3318 and Higgs-vector-boson couplings, multiplied by the relative sign

$$f_t = \text{sign}\left(\frac{\kappa_t}{\kappa_V}\right) \times \frac{\kappa_t^2}{\kappa_t^2 + \kappa_V^2}. \quad (6.9)$$

3319        This parameter covers the full space between  $-1.0$  and  $1.0$ , with the SM at  $0.5$ .  
 3320        Absolute values of  $1.0$  or  $0.0$  would correspond to purely Higgs-top and purely Higgs-V  
 3321        couplings, respectively.  
 3322        Table 6.16 shows the points in the  $\kappa_t/\kappa_V$  and  $f_t$  parameter space that are mapped  
 3323        by the 51 individual  $\kappa_t$  and  $\kappa_V$  points.

$f_t$	$\kappa_t/\kappa_V$	$\kappa_V = 0.5$	$\kappa_V = 1.0$	$\kappa_V = 1.5$
-0.973	-6.000	-3.00		
-0.941	-4.000	-2.00		
-0.900	-3.000	-1.50	-3.00	
-0.862	-2.500	-1.25		
-0.800	-2.000	-1.00	-2.00	-3.00
-0.692	-1.500	-0.75	-1.50	
-0.640	-1.333			-2.00
-0.610	-1.250		-1.25	
-0.500	-1.000	-0.50	-1.00	-1.50
-0.410	-0.833			-1.25
-0.360	-0.750		-0.75	
-0.308	-0.667			-1.00
-0.200	-0.500	-0.25	-0.50	-0.75
-0.100	-0.333			-0.50
-0.059	-0.250		-0.25	
-0.027	-0.167			-0.25
0.000	0.000	0.00	0.00	0.00
0.027	0.167			0.25
0.059	0.250		0.25	
0.100	0.333			0.50
0.200	0.500	0.25	0.50	0.75
0.308	0.667			1.00
0.360	0.750		0.75	
0.410	0.833			1.25
0.500	1.000	0.50	1.00	1.50
0.610	1.250		1.25	
0.640	1.333			2.00
0.692	1.500	0.75	1.50	
0.800	2.000	1.00	2.00	3.00
0.862	2.500	1.25		
0.900	3.000	1.50	3.00	
0.941	4.000	2.00		
0.973	6.000	3.00		

**Table 6.16:** The 33 distinct values of  $\kappa_t/\kappa_V$  and  $f_t$  as mapped by the 51  $\kappa_t$  and  $\kappa_V$  points.

3324        The overall Higgs decay width (modified by both  $\kappa_t$  and  $\kappa_V$ ) becomes irrelevant  
 3325   if limits are quoted as absolute cross sections rather than multiples of the expected  
 3326   cross section (which depends on it).

3327        The 1D histograms of events as categorized in regions of the 2D BDTG plane are  
 3328   then used in a maximum likelihood fit of signal and background shapes, where the  
 3329    $tHq$ ,  $tHW$ , and  $t\bar{t}H$  signals are floating with a common signal strength modifier  $r$ ,  
 3330   producing a 95% C.L. upper limit the observed cross section of  $tHq + tHW + t\bar{t}H$ .

3331        This procedure is done separately for each point  $(\kappa_t, \kappa_V)$  where the cross sections  
 3332   and branching fractions are scaled accordingly in each point. Limits at fixed values of  
 3333    $\kappa_t/\kappa_V$  are by construction identical. Tables G.1–G.3 and G.4–G.6 in Appendix G show  
 3334   the scalings of cross section times branching fraction, as well as branching fractions  
 3335   alone for each of the Higgs decay modes and each of the signal components.

## 3336        6.12 Systematic uncertainties

3337        The uncertainties present in this analysis can be either of a statistical nature given the  
 3338   size of the samples and the probabilistic nature of the processes, or of a systematic  
 3339   nature. The systematic uncertainties are associated with theoretical uncertainties  
 3340   originating in the limited knowledge of the processes, and also with experimental  
 3341   uncertainties originating for instance from the limited resolution of the detectors. In  
 3342   this section, the contributions to the systematic uncertainties from all the sources in  
 3343   this analysis are considered.

3344        Rate uncertainties associated to the application of scaling factors for the affected  
 3345   processes, and shape uncertainties which affect not only the normalization but also  
 3346   the shape of certain distributions, compose the systematic uncertainties. The latter  
 3347   can affect the analysis during the event selection; therefore, these systematic shape

3348    uncertainties are applied to the simulation samples.

3349    **Experimental uncertainties:**

- 3350    • *Luminosity.* The measurement of the integrated luminosity delivered to the  
3351    CMS Experiment during the 2016 LHC proton-proton run at a center-of-mass  
3352    energy of 13 TeV was performed using the Pixel Cluster Counting method,  
3353    while the absolute luminosity scale calibration was derived from an analysis of  
3354    Van der Meer Scans. The overall uncertainty of the luminosity measurement is  
3355    estimated to be 2.5% [162].
- 3356    • *Lepton efficiencies.* Systematic uncertainties in the signal selection efficiency  
3357    arise from correction factors applied to the simulated events in order to better  
3358    match the measured detector performance, and also from theoretical uncertain-  
3359    ties in the modeling of the signal process. Data/MC differences in the trigger  
3360    efficiency accounted with scale factors applied to correct for them, lepton recon-  
3361    struction and identification performance, and lepton selection efficiency carry a  
3362    combined uncertainty of about 5% per lepton.
- 3363    • *Jet-related uncertainties.* Jet energy corrections affect the uncertainty in the  
3364    signal selection efficiency; they are evaluated by varying the correction factors  
3365    within their uncertainties and propagating the effects to the final results by  
3366    recalculating the kinematic quantities. The effects of the jet energy scale uncer-  
3367    tainties and  $b$ -tagging efficiency are evaluated using dedicated shape templates  
3368    derived from a variation of the jet energy scale within its uncertainty and from  
3369    varying the  $b$ -tagging jet data/MC scale factors within their uncertainty. For  
3370    the forward jet mismodeling an alternative shape of the BDT output distribu-  
3371    tions that reflects a hypothetical perfect data/MC agreement was derived as  
3372    described in section 6.10.

3373       **Theory uncertainties**

3374       The uncertainties from unknown higher orders of  $tHq$  and  $tHW$  production cross  
 3375       sections are estimated from a change in the  $Q^2$  scale of double and half the initial  
 3376       value, evaluated for each point of  $\kappa_t$  and  $\kappa_V$ . The  $t\bar{t}H$  signal component has an  
 3377       uncertainty of about +5.8/-9.2% from  $Q^2$  scale variations and a further 3.6% from  
 3378       the knowledge of PDFs and  $\alpha_s$  [57]. Uncertainties related to the choice of PDF set is  
 3379       estimated to be about 3.7% for  $tHq$  and about 4.0% for  $tHW$ .

3380       The theoretical uncertainties from unknown higher orders for  $t\bar{t}W$  and  $t\bar{t}Z$  are  
 3381       12% and 10% respectively; additional uncertainties from the knowledge of PDFs and  
 3382        $\alpha_s$  of about 4% each for  $t\bar{t}W$  and  $t\bar{t}Z$  are estimated. The uncertainties for the Higgs  
 3383       branching fractions are of order 1-2%.

3384       **Backgrounds**

3385       Besides the theory uncertainties on  $t\bar{t}W$  and  $t\bar{t}Z$ , uncertainties of the smaller irre-  
 3386       ducible backgrounds and the charge mis-identification estimate are covered with flat  
 3387       normalization uncertainties. The  $WZ$  uncertainty due to the scale factor is derived  
 3388       during the background estimation using the control region.

3389       **Fake rate closure uncertainties**

3390       The dominant uncertainty on the background rates is associated with the estimate  
 3391       of the non-prompt lepton contribution using a fake rate method; the main normal-  
 3392       ization uncertainty comes from limited statistics in the data control region, and the  
 3393       subtraction of residual prompt lepton contribution as stated in Section 6.7.2. Shape  
 3394       variations describing data/MC differences and deviations in closure test are evaluated  
 3395       as shape uncertainties.

3396       In order to determine the systematic uncertainties associated with the fake rates,  
 3397       the method is evaluated using MC samples; the fake rate is measured in a QCD MC  
 3398       sample and then compared to the yields from a MC  $t\bar{t}$  sample so that the differences

sets the scale for the uncertainty on the fake rate method. Explicitely, the BDTG classifier output shapes from a pure MC count of fake leptons (in  $t\bar{t}$ ) and from the application of fake-rates as measured in QCD MC, applied in  $t\bar{t}$  MC events, are compared. The difference in the resulting normalization and output shapes, for both trainings vs.  $t\bar{t}$  and vs.  $t\bar{t}V$ , are estimated and propagated to the fit as normalization and shape variations; Figures 6.28 and 6.27 show the results of these closure tests.

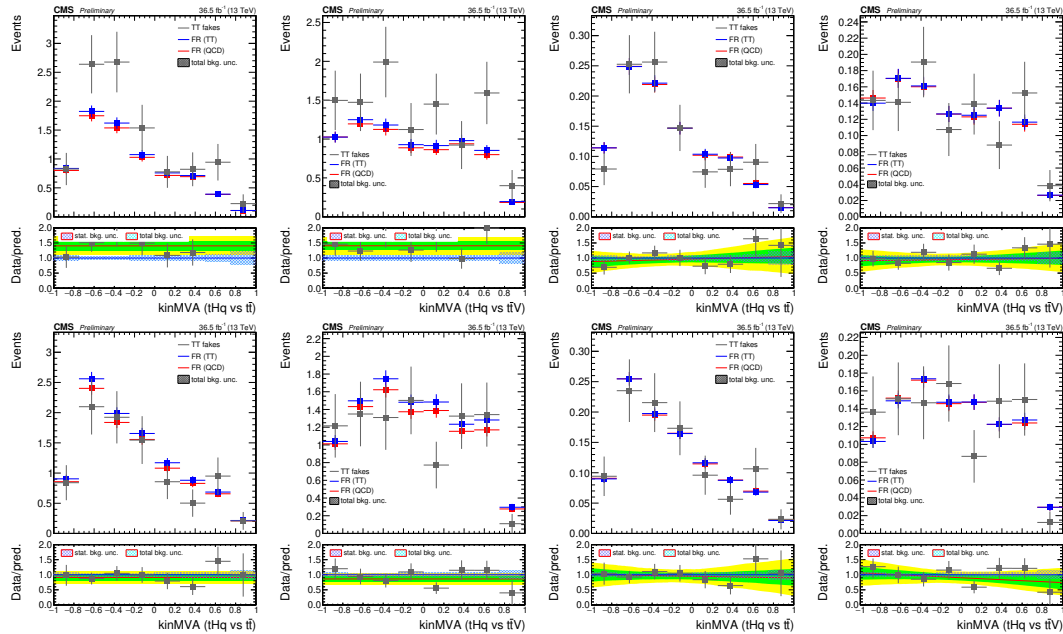


**Figure 6.27:** BDT outputs comparing  $t\bar{t}$  MC to a fake-rate prediction using fake rates measured in QCD MC. Agreement in normalization is estimated from the plots in the two left columns, shape disagreement is estimated from the (normalized) plots in the two right columns. From top to bottom rows: three lepton selection with electron fakes, three lepton selection with muon fakes.

Table 6.17 list all the systematic uncertainties currently considered in the analysis.

## 6.13 Results

As a result of applying the event pre-selection on the dataset, 127 events are observed in the  $3l$  channel, 280 in the  $2lss \mu^\pm \mu^\pm$  channel and 525 in the  $2lss e^\pm \mu^\pm$  channel

Source	Channel	Size
<b>Experimental uncertainties</b>		
Luminosity	all	1.026
Loose lepton efficiency		1.02 per lepton
Tight lepton efficiency		1.03 per lepton
Trigger efficiency	$\mu^\pm\mu^\pm$ $e^\pm\mu^\pm$ $\ell\ell\ell$	1.01 1.01 1.03
Jet energy scale	all	templates
Forward jet modeling	all	templates, see Table 6.15
$b$ -jet tagging efficiency	all	templates
<b>Theory uncertainties</b>		
$Q^2$ scale ( $tHq$ )	all	0.92–1.06 (depending on $\kappa_t$ , $\kappa_V$ )
$Q^2$ scale ( $tHW$ )	all	0.93–1.05 (depending on $\kappa_t$ , $\kappa_V$ )
$Q^2$ scale ( $t\bar{t}H$ )	all	0.915/1.058
$Q^2$ scale ( $t\bar{t}W$ )	all	1.12
$Q^2$ scale ( $t\bar{t}Z$ )	all	1.11
pdf ( $t\bar{t}H$ )	all	1.036
pdf $gg$ ( $t\bar{t}Z$ )	all	0.966
pdf $q\bar{q}$ ( $t\bar{t}W$ )	all	1.04
pdf $qg$ ( $tHq$ )	all	1.037
pdf $qg$ ( $tHW$ )	all	1.040
<b>Higgs branching fractions</b>		
param_alphaS	all	1.012
param_mB	all	0.981
HiggsDecayWidthTHU_hqq	all	0.988
HiggsDecayWidthTHU_hvv	all	1.004
HiggsDecayWidthTHU_hll	all	1.019
<b>Backgrounds</b>		
$WZ$ control region statistics	$\ell\ell\ell$	1.10
$WZ$ control region backgrounds	$\ell\ell\ell$	1.20
$WZ$ modeling	$\ell\ell\ell$	1.07
$WZ + 2$ jet background	$\mu^\pm\mu^\pm, e^\pm\mu^\pm$	1.50
Rare SM processes	all	1.50
Charge flips	$e^\pm\mu^\pm$	1.30
<b>Fake rate estimate</b>		
Electron FR measurement		templates
Muon FR measurement		templates
Electron closure	$e^\pm\mu^\pm$	0.94 norm., (0.98 ( $t\bar{t}$ ))/1.07 ( $t\bar{t}V$ )) shape var.
	$\ell\ell\ell$	1.40 norm., (1.09 ( $t\bar{t}$ ))/1.05 ( $t\bar{t}V$ )) shape var.
Muon closure	$\mu^\pm\mu^\pm$	1.07 norm., (0.97 ( $t\bar{t}$ ))/0.91 ( $t\bar{t}V$ )) shape var.
	$e^\pm\mu^\pm$	1.09 norm., (1.06 ( $t\bar{t}$ ))/1.03 ( $t\bar{t}V$ )) shape var.
	$\ell\ell\ell$	1.09 norm., (0.95 ( $t\bar{t}$ ))/0.83 ( $t\bar{t}V$ )) shape var.

**Table 6.17:** Pre-fit size of systematic uncertainties.

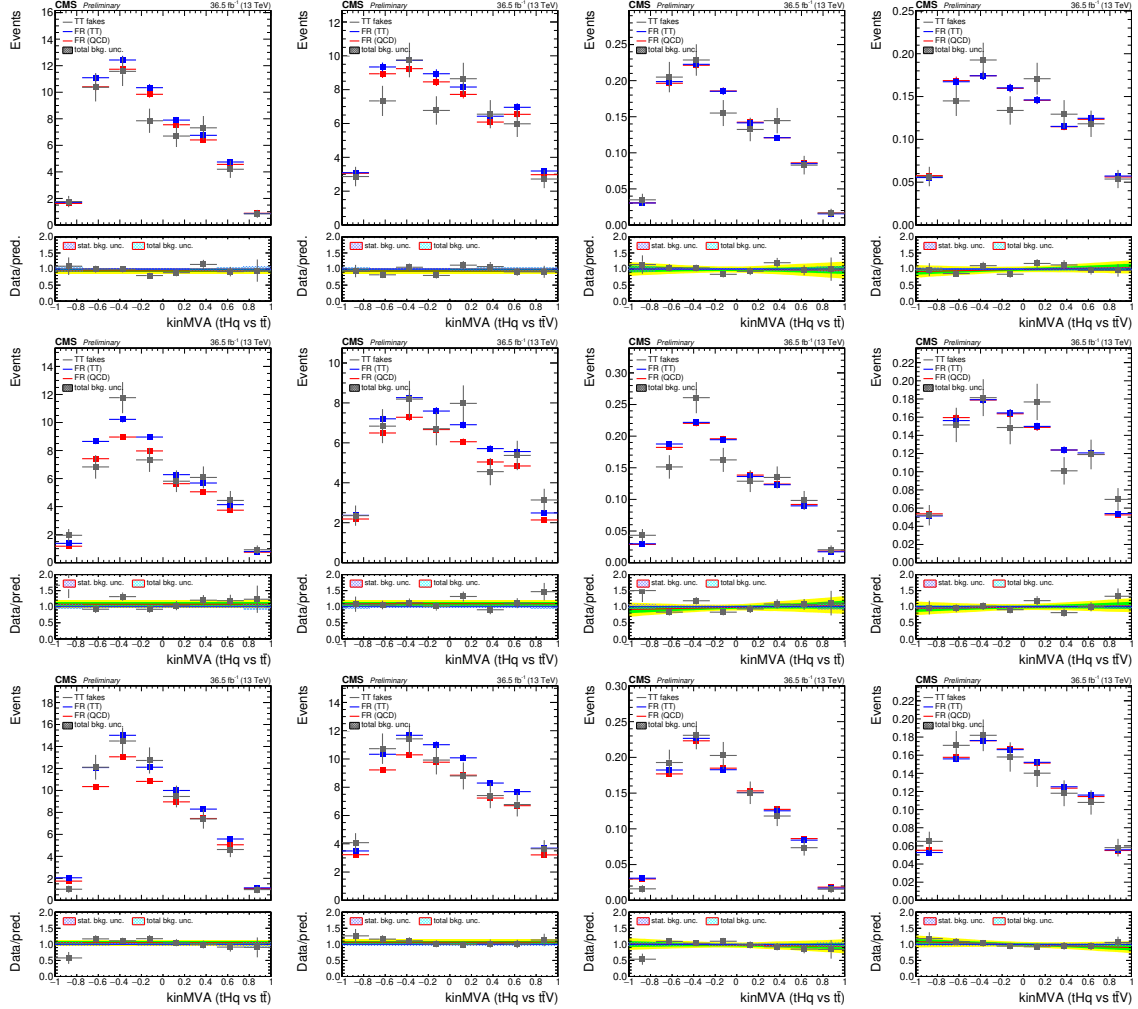


**Figure 6.28:** BDT outputs comparing  $t\bar{t}$  MC to a fake-rate prediction using fake rates measured in QCD MC. Agreement in normalization is estimated from the plots in the two left columns, shape disagreement is estimated from the (normalized) plots in the two right columns. From top to bottom rows: same-sign  $e^\pm \mu^\mp$  selection with electron fakes, same-sign  $e^\pm \mu^\mp$  selection with muon fakes, same-sign  $\mu^\pm \mu^\mp$  selection.

as shown in Table 6.8. These events are then classified into one of ten categories, depending on the output of the two BDTG classifiers and according to the optimized binning strategy.

The pre-fit distributions of BDTG outputs are shown in Figure 6.29, while the pre-fit distributions in the final binning used in the signal extraction are shown in Figure 6.30.

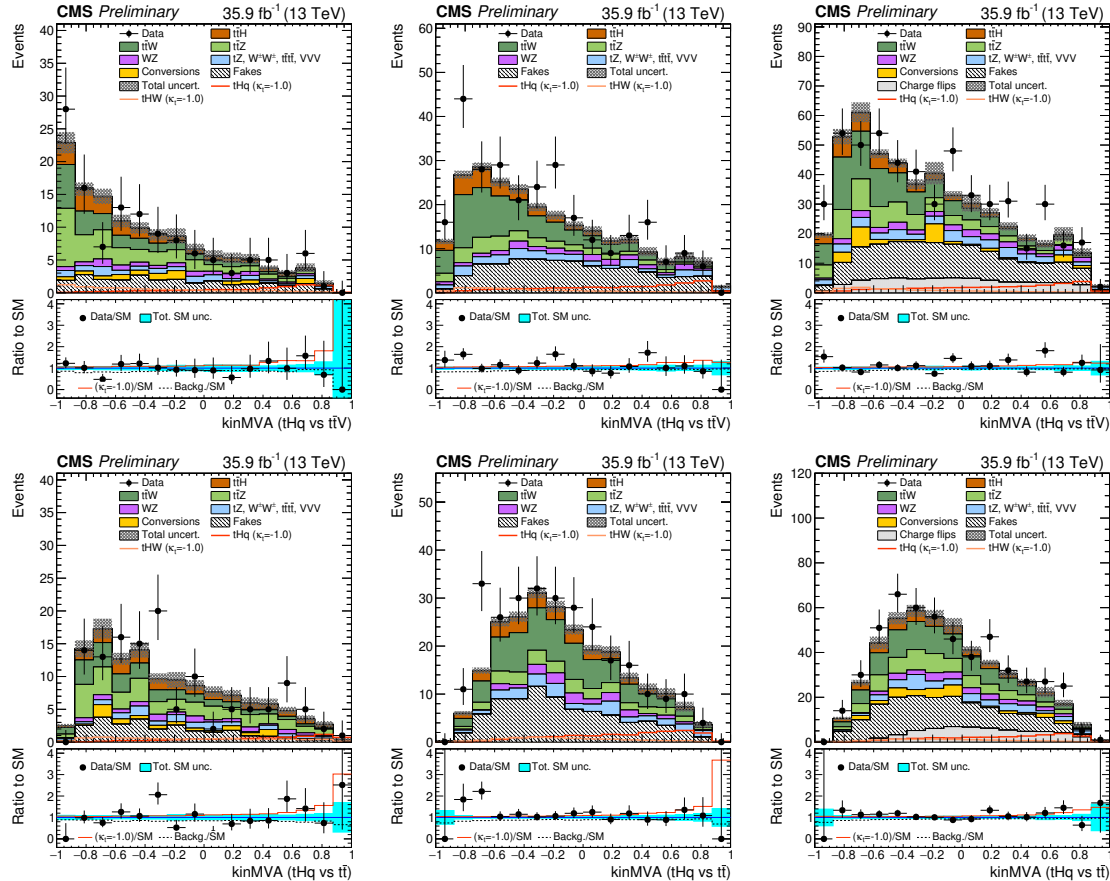


**Figure 6.29:** Pre-fit BDT classifier outputs, for the three-lepton channel (left),  $\mu^{\pm}\mu^{\pm}$  (center), and  $e^{\pm}e^{\pm}$  (right), for  $35.9 \text{ fb}^{-1}$ , for training against  $t\bar{t}V$  (top row) and against  $t\bar{t}$  (bottom row). In the box below each distribution, the ratio of the observed and predicted event yields is shown. The shape of the two  $tH$  signals for  $\kappa_t = -1.0$  is shown, normalized to their respective cross sections for  $\kappa_t = -1.0, \kappa_V = 1.0$ . The grey band represents the unconstrained (pre-fit) statistical and systematical uncertainties

3415     The expected signal and background shapes for the distribution in the 1D his-  
 3416     togram (with ten bins) are fit to the observed data in a maximum likelihood fit, for  
 3417     all three channels simultaneously and separately for the signal shapes for each of the  
 3418     33  $\kappa_t/\kappa_V$  coupling configuration points.

3419     The  $tH$  and  $t\bar{t}H$  production cross sections and the Higgs decay branching ratios are  
 3420     modified in each point with the Higgs-top ( $\kappa_t$ ) and Higgs-vector boson ( $\kappa_V$ ) coupling

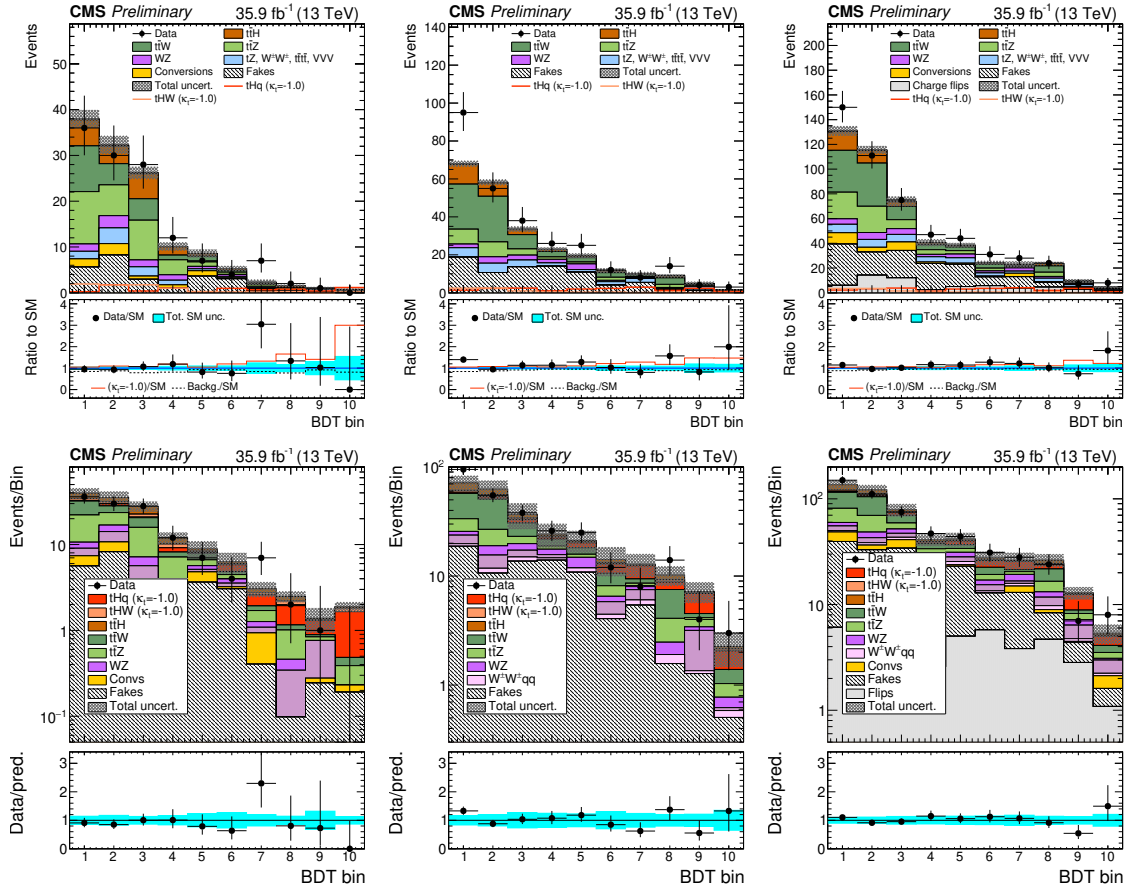


**Figure 6.30:** Expected (pre-fit) distributions in the final binning used for the signal extraction, for (from left to right) the three lepton channel, the  $\mu^+\mu^-$  channel, and the  $e^+\mu^-$  channel. Linear scale (top row), and logarithmic scale (bottom row).

strength and the Higgs-tau coupling strength modifier ( $\kappa_\tau$ ) is assumed to be equal to  $\kappa_t$ ; the rest of the parameters are assumed to be at the SM predicted values. The combined signal shape is then uniquely defined by the ratio of  $\kappa_t/\kappa_V$ . In the fit, the signal components,  $tH$  and  $t\bar{H}$ , are floated with a common signal strength modifier (defined as the ratio to the expected cross section) to produce a 95% C.L. upper limit on the observed  $tH + t\bar{H}$  cross section times the combined branching ratio of  $H \rightarrow WW^* + ZZ^* + \tau\tau$ .

The post-fit categorized BDTG output distributions obtained in the maximum likelihood fit to extract the limits, are shown in Figure 6.31.

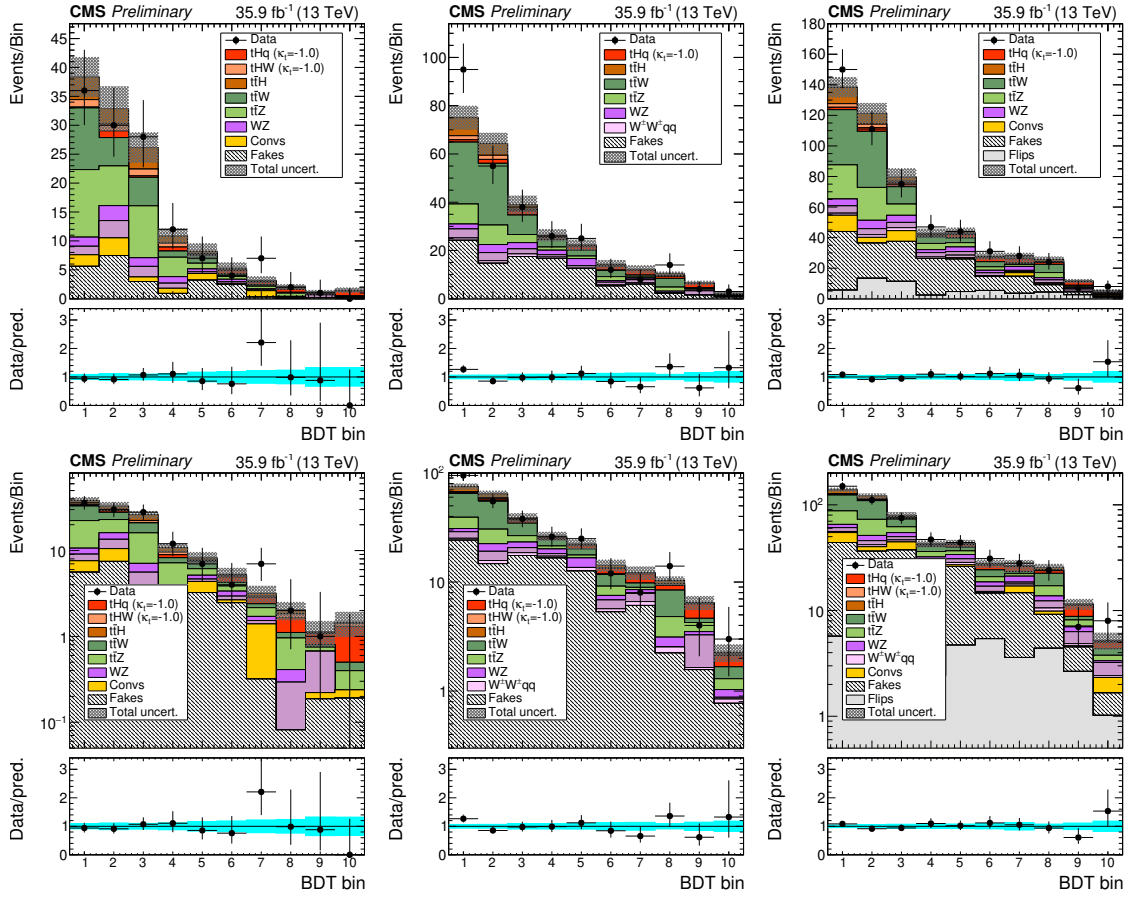


**Figure 6.31:** Post-fit distributions in the final binning used for the signal extraction, for (from left to right) the three lepton channel, the  $\mu^\pm\mu^\pm$  channel, and the  $e^\pm\mu^\pm$  channel. Linear scale (top row), and logarithmic scale (bottom row).

3430 As expected, the signal contribution is very small compared to the background  
 3431 ground contribution; however, it is possible to see the signal contribution by subtracting  
 3432 the background from the overall BDT output distributions as shown in Figure  
 3433 6.32 for the inverted coupling scenario ( $\kappa_V = 1, \kappa_t = -1$ ) and Figure 6.33 for the SM-like  
 3434 scenario ( $\kappa_V = 1, \kappa_t = 1$ ).

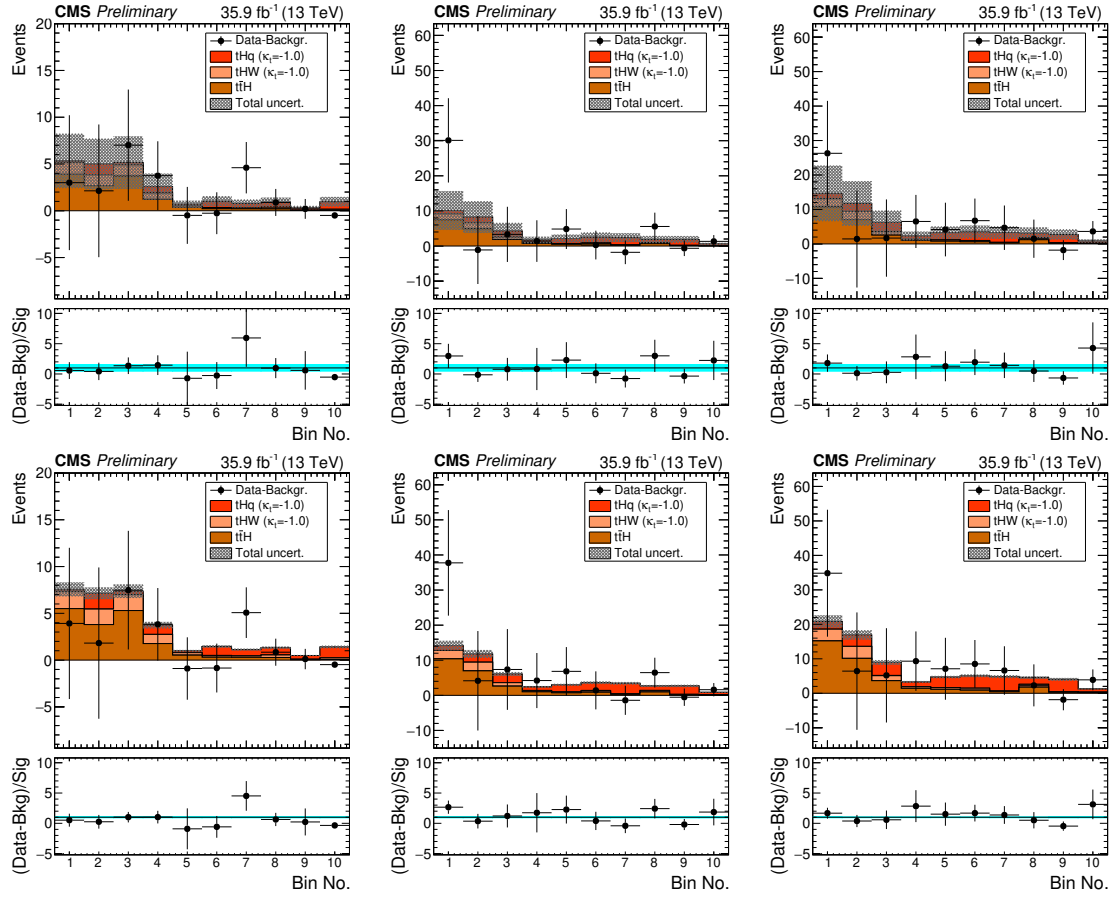


**Figure 6.32:** Background-subtracted pre-fit (top) and post-fit (bottom) distributions in the final binning used for the signal extraction, for three lepton channel (left), the  $\mu^\pm\mu^\pm$  channel (center), and the  $e^\pm\mu^\pm$  channel (right). For a fit in the inverted couplings scenario ( $\kappa_V = 1, \kappa_t = -1$ ).

### 3435 6.13.1 $CL_S$ and cross section limits

3436 Table A.5 lists the expected background only, the expected SM-like Higgs signal, and  
 3437 the observed 95% C.L. upper limits on the  $tH + t\bar{t}H$  production cross section times  
 3438  $H \rightarrow WW^* + ZZ^* + \tau\tau$  branching ratio (in pb); the corresponding plots are shown  
 3439 in Figure 6.34 for  $\kappa_V = 1$ . The expected background-only limit is calculated on an  
 3440 Asimov dataset, while the expected SM-like limit is calculated on an Asimov dataset  
 3441 that includes the SM-like  $tH$  and  $t\bar{t}H$  signals.

3442 An excess of more than  $2\sigma$  is observed for the SM configuration ( $\kappa_t/\kappa_V = 1$ )

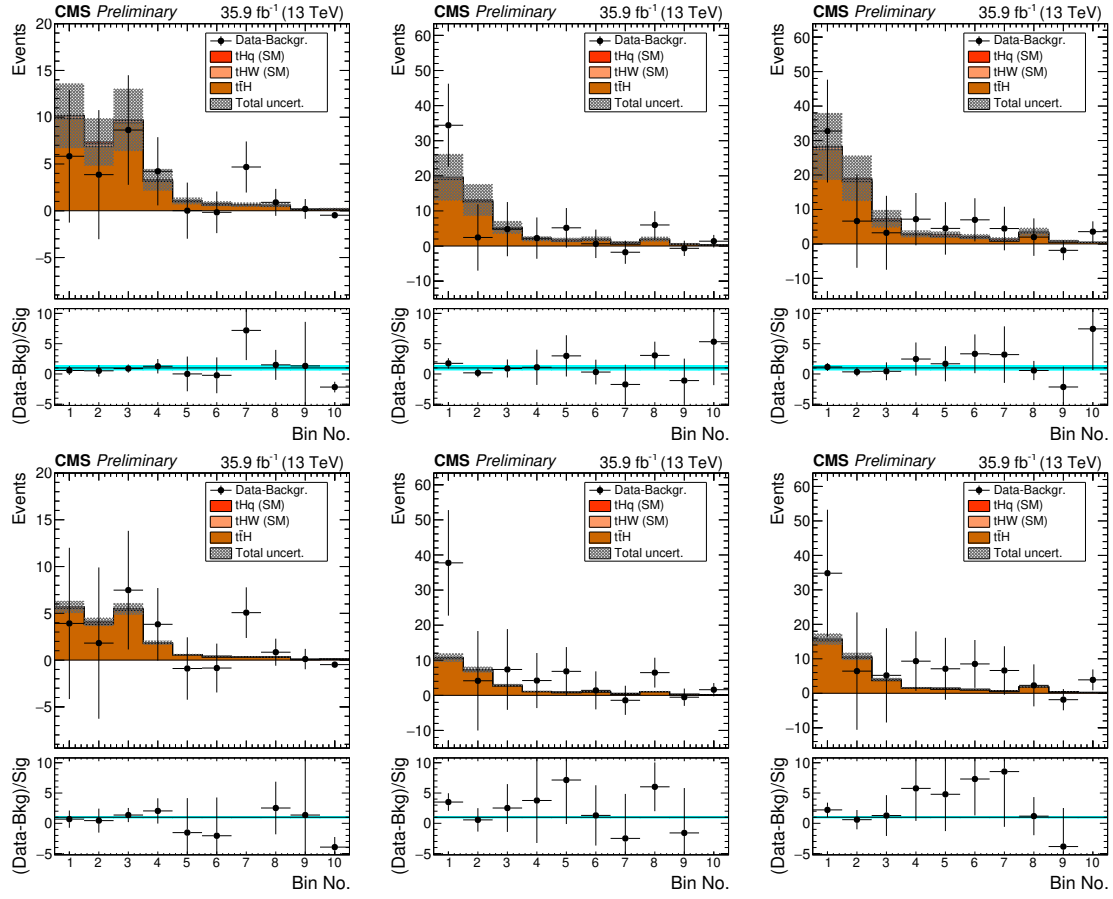


**Figure 6.33:** Background-subtracted pre-fit (top) and post-fit (bottom) distributions in the final binning used for the signal extraction, for the three lepton channel (left), the  $\mu^\pm\mu^\pm$  channel (center), and the  $e^\pm\mu^\pm$  channel (right). For a fit in the SM-like scenario ( $\kappa_t = \kappa_V = 1$ ).

for the background-only expected limit; however, the inclusion of the SM-like  $tH$  and  $t\bar{H}$  signals reveals that the excess is actually about  $1\sigma$ ; furthermore, looking at  $\kappa_t/\kappa_V = 0$ , i.e., the  $t\bar{H}$  component in the signal is zero, it is evident that the origin of the excess is mostly due to the presence of the  $t\bar{H}$  component in the signal, given that the deviation of the observed limit from the expected one is much smaller than  $1\sigma$ ; this is consistent with the results presented in Reference [151]. It is also evident that, given the dependence of the  $t\bar{H}$  cross section on  $\kappa_t^2$  the source of the asymmetry (the peak in the right side) in both background-only and SM-like limits is induced by

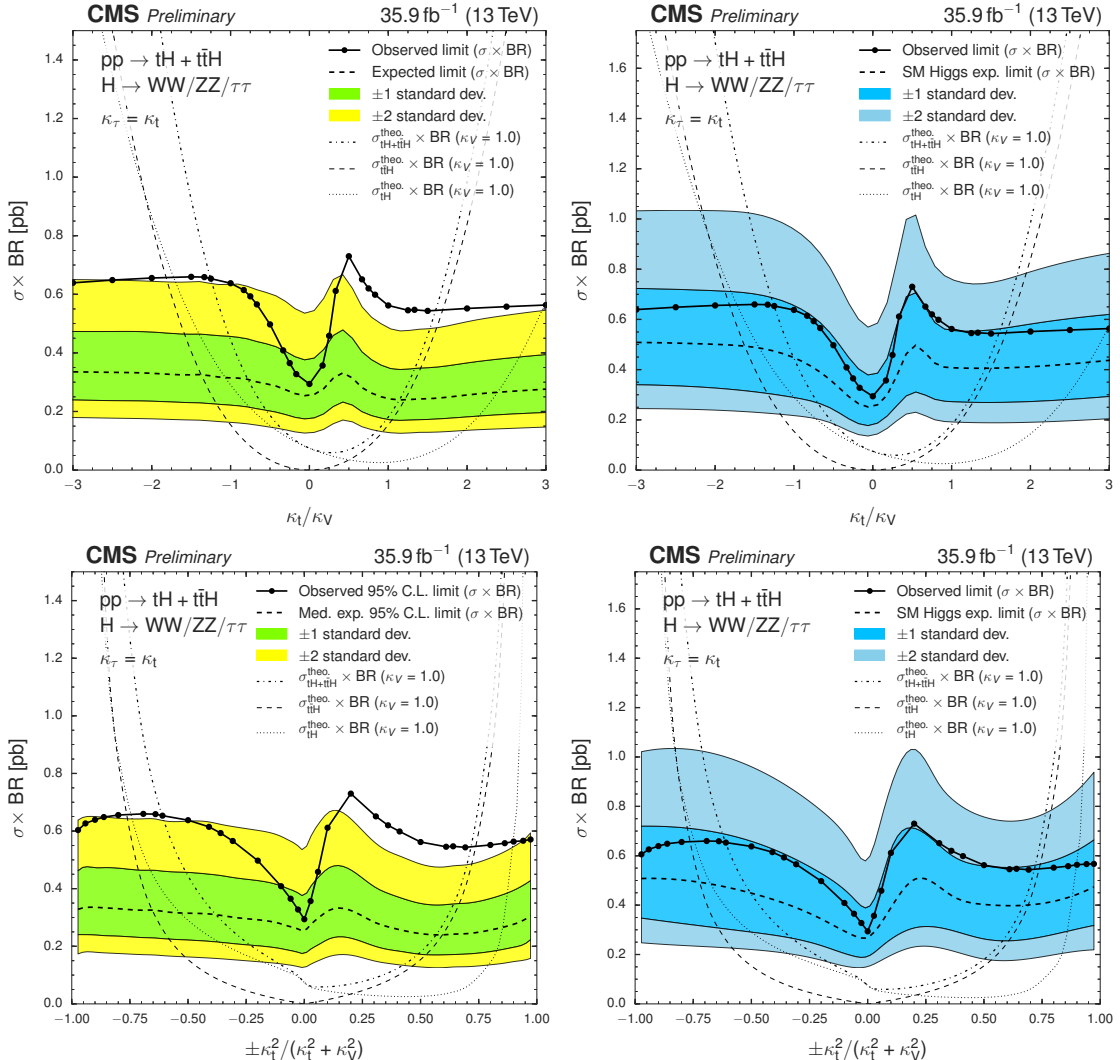


**Figure 6.34:** Left (Right): Expected background-only (SM-like including  $t\bar{t}H$  and  $tH$  signals) and observed asymptotic limits on the combined  $tH + t\bar{t}H$  cross section times modified BR as a function of  $\kappa_t/\kappa_V$  (top) and  $\text{sign}(\kappa_t/\kappa_V) \times \frac{\kappa_t^2}{(\kappa_t^2 + \kappa_V^2)}$  (bottom) for the combination of three lepton channel,  $\mu^\pm\mu^\pm$ , and  $e^\pm\mu^\pm$  channel.

3451 the  $tH$  component of the signal.

3452 Comparing the observed upper limit with the theoretical prediction of the  $tH + t\bar{t}H$   
 3453 cross section times BR for  $\kappa_V = 1.0$  constrains the allowed range of coupling config-  
 3454 urations  $\kappa_t/\kappa_V$  to between about -1.25 and +1.60. as shown in the top right plot in  
 3455 Figure 6.35.

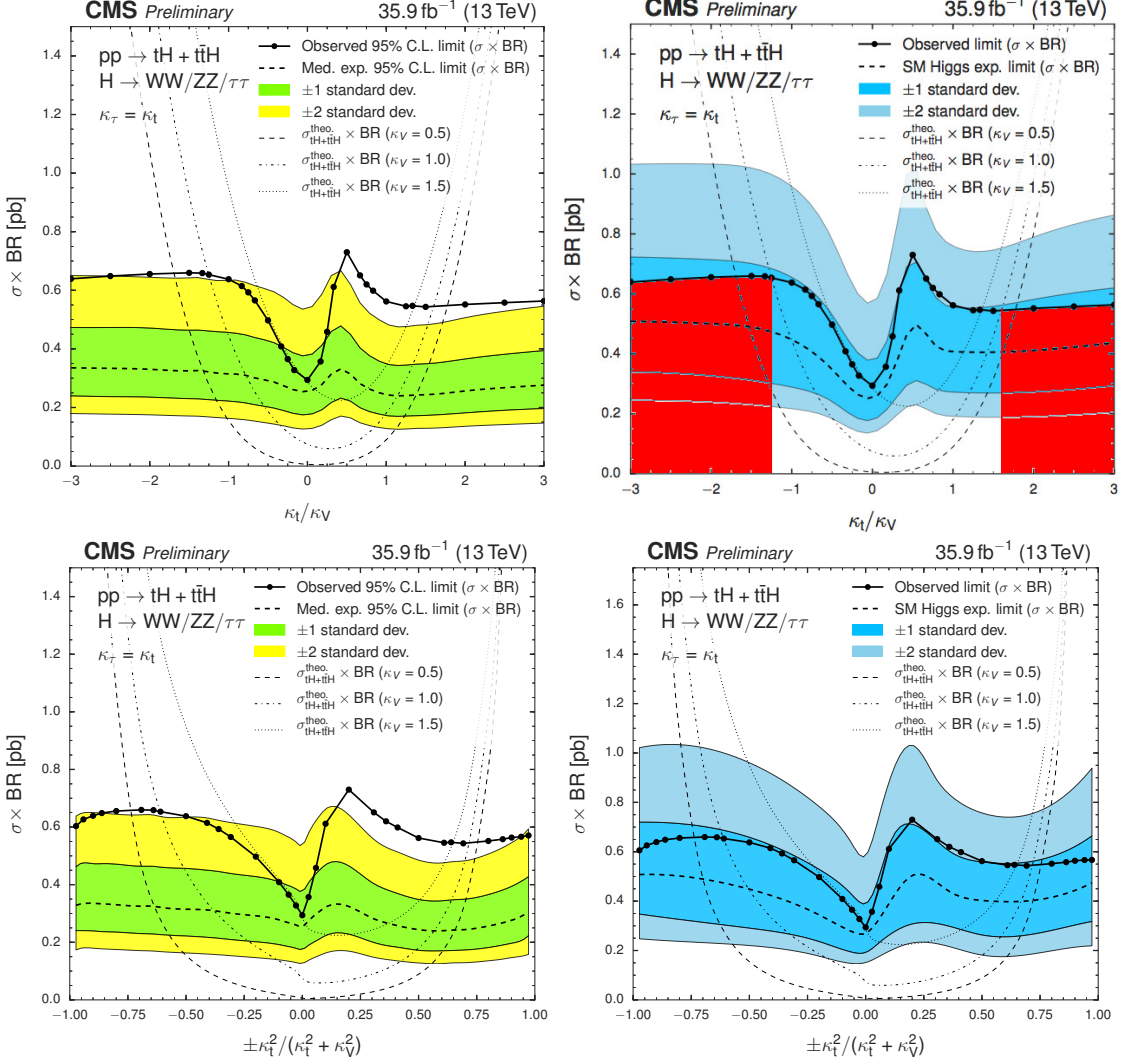


**Figure 6.35:** Left (Right): Expected background-only (SM-like including  $t\bar{t}H$  and  $tH$  signals) and observed asymptotic limits on the combined  $tH + t\bar{t}H$  cross section times modified BR as a function of  $\kappa_t/\kappa_V$  (top) and  $\text{sign}(\kappa_t/\kappa_V) \times \frac{\kappa_t^2}{(\kappa_t^2 + \kappa_V^2)}$  (bottom) for the combination of three lepton channel,  $\mu^\pm \mu^\pm$ , and  $e^\pm \mu^\pm$  channel. Theoretical  $tH + t\bar{t}H$  cross section curves have been included for  $\kappa_V = 0.5, 1.0, 1.5$ . Red areas on the top right plot correspond to the excluded regions.

3456     The scan of  $-2\Delta\log(\mathcal{L})$  shown in Figure 6.36 reveals additional details. In each  
 3457     point, the hypothesis of signal strength equal to one, i.e., where the signal processes  
 3458     are kept fixed at their theoretical expectations, is tested against a fit with floating sig-  
 3459     nal strength. The  $tH$  and  $t\bar{t}H$  components are varied with a common signal strength

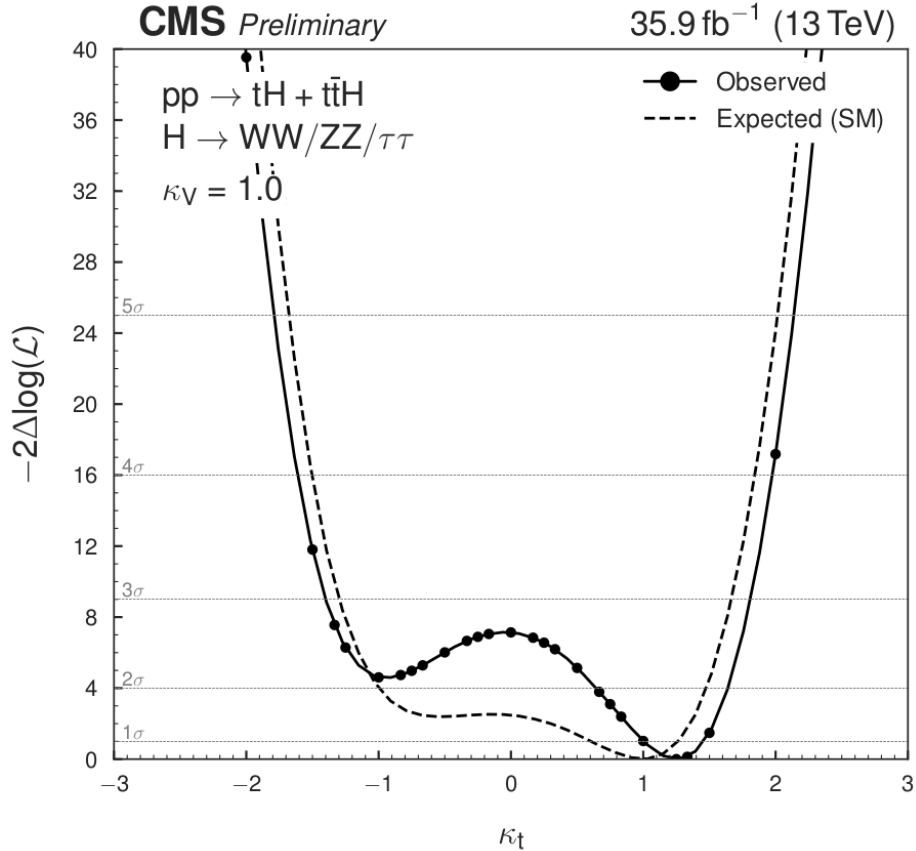


**Figure 6.36:** Scan of  $-2\Delta \log(\mathcal{L})$  for the combined fit of the  $tH + t\bar{t}H$  signal strength on the data (solid line), and on an Asimov dataset corresponding to the SM expectations (dashed line).

3460 and each curve was normalized to have a minimum value of zero.

3461 By looking at the minima of the fits, positive values of  $\kappa_t$  are favored over negative  
 3462 values; in the SM case by about  $1.5\sigma$  and in the data case by more than  $2\sigma$ ; in  
 3463 particular, the fit for the SM expectation favors  $\kappa_t = 1$  over  $\kappa_t = -1$  by  $2\sigma$ . From the  
 3464 fit for data, the most probable value is  $\kappa_t = 1.25^{+0.15}_{-0.25}$ , thus,  $\kappa_t$  is compatible with the  
 3465 SM.

3466 The scan also shows that values outside the range of about [0.65, 1.60] are excluded  
 3467 at 95% C.L. which means that negative values of  $\kappa_t$  are completely excluded at 95%  
 3468 C.L.; although this seems not consistent with the exclusion based on the cross section

limits, is not unexpected because only an upper limit on the cross section was set; thus, by looking at a lower limit on the cross section, it would be possible to exclude the region around  $\kappa_t/\kappa_V = 0$  where the prediction is lower than what is actually observed. The difference of observed and expected fits around  $\kappa_t = 0$  is led by the fact that the predicted  $t\bar{t}H$  cross section vanishes at  $\kappa_t = 0$  while the data shows an excess of  $t\bar{t}H$ -like events.

Scenario	Channel	Obs. Limit (pb)	Exp. Limit (pb)		
			Median	$\pm 1\sigma$	$\pm 2\sigma$
$\kappa_t/\kappa_V = -1$	$\mu^\pm \mu^\pm$	1.00	0.58	[0.42, 0.83]	[0.31, 1.15]
	$e^\pm \mu^\pm$	0.84	0.54	[0.39, 0.76]	[0.29, 1.03]
	$lll$	0.70	0.38	[0.26, 0.56]	[0.19, 0.79]
	Combined	<b>0.64</b>	<b>0.32</b>	[0.22, 0.46]	[0.16, 0.64]
$\kappa_t/\kappa_V = 1$ (SM-like)	$\mu^\pm \mu^\pm$	0.87	0.41	[0.29, 0.58]	[0.22, 0.82]
	$e^\pm \mu^\pm$	0.59	0.37	[0.26, 0.53]	[0.20, 0.73]
	$lll$	0.54	0.31	[0.22, 0.43]	[0.16, 0.62]
	Combined	<b>0.56</b>	<b>0.24</b>	[0.17, 0.35]	[0.13, 0.49]

**Table 6.18:** Expected and observed 95% C.L. upper limits on the  $tH + t\bar{t}H$  production cross section times  $H \rightarrow WW^* + \tau\tau + ZZ^*$  branching ratio for a scenario of inverted couplings ( $\kappa_t/\kappa_V = -1.0$ , top rows) and for a standard-model-like signal ( $\kappa_t/\kappa_V = 1.0$ , bottom rows), in pb. The expected limit is calculated on a background-only Asimov dataset and quoted with  $\pm 1\sigma$  and  $\pm 2\sigma$  probability ranges.

The observed limit of about 0.64 pb on a signal shape expected for  $\kappa_t/\kappa_V = -1.0$  and for the combination of all three channels corresponds to 1.4 times the expected  $tH + t\bar{t}H$  cross section with  $\kappa_t = -1.0$ ,  $\kappa_V = 1.0$ . In the SM scenario ( $\kappa_t/\kappa_V = 1.0$ ), the observed upper limit on the cross section times branching ratio is 0.56 pb, corresponding to 3.1 times the expected SM cross section of  $tH + t\bar{t}H$ . The summary of the results for the ITC and SM-like scenarios split by channel are presented in Table 6.18, whereas the summary of the expected and observed CL<sub>S</sub> limits (at 95%C.L.) on the signal strength of combined  $tH + t\bar{t}H$  production in each channel, and for different combinations thereof, for the ITC and SM-like scenarios are presented in Table 6.23.

Scenario	Channel	Obs. Limit	Exp. Limit				
			$-2\sigma$	$-1\sigma$	Median	$+1\sigma$	$+2\sigma$
$\kappa_V = 1.0$	$\mu^\pm \mu^\pm$	2.3	0.71	0.94	1.32	1.88	2.60
$\kappa_t = -1.0$	$e^\pm \mu^\pm$	1.9	0.65	0.87	1.21	1.71	2.32
	$\ell\ell\ell$	1.6	0.43	0.59	0.86	1.26	1.78
	Combined ( $\mu\mu, 3\ell$ )	<b>1.6</b>	0.40	0.54	<b>0.78</b>	1.12	1.57
	Combined ( $\mu\mu, e\mu, 3\ell$ )	<b>1.4</b>	0.37	0.50	<b>0.71</b>	1.03	1.43
(SM)	$\mu^\pm \mu^\pm$	4.9	1.20	1.61	2.27	3.24	4.54
$\kappa_V = 1.0$	$e^\pm \mu^\pm$	3.3	1.10	1.48	2.07	2.95	4.06
$\kappa_t = 1.0$	$\ell\ell\ell$	3.0	0.91	1.22	1.73	2.49	3.47
	Combined ( $\mu\mu, 3\ell$ )	<b>3.4</b>	0.79	1.07	<b>1.51</b>	2.17	3.01
	Combined ( $\mu\mu, e\mu, 3\ell$ )	<b>3.1</b>	0.71	0.96	<b>1.36</b>	1.94	2.70

**Table 6.19:** Expected and observed CL<sub>S</sub> limits (at 95% C.L.) on the signal strength of combined  $tH + t\bar{t}H$  production in each channel, and for different combinations of them, for a scenario with inverted couplings ( $\kappa_V = 1.0, \kappa_t = -1.0$ , top section), and for the standard model ( $\kappa_V = \kappa_t = 1.0$ , bottom section). Numbers are for  $35.9 \text{ fb}^{-1}$ .

### 3484 6.13.2 Best fit

3485 The best-fit results for the signal strength in all the 33  $\kappa_t/\kappa_V$  configurations are also  
 3486 listed in Table A.5; the inverted top coupling (ITC) and the SM-like scenarios are  
 3487 highlighted there and summarized in Table 6.20. The individual contributions from  
 3488 all the channels to the best-fit signal strength for the SM-like Higgs signal are listed  
 3489 in Table 6.21.

Scenario	Best fit signal strength	Best fit $\sigma \times BR$	Significance Obs.(exp.)
$\kappa_t/\kappa_V = -1.0$	$0.68 \pm 0.40$	$0.30 \pm 0.18 \text{ pb}$	$1.70\sigma(2.51\sigma)$
$\kappa_t/\kappa_V = 1.0$	$1.82^{+0.66}_{-0.67}$	$0.33 \pm 0.12 \text{ pb}$	$2.73\sigma(1.50\sigma)$

**Table 6.20:** Best fit for signal strength  $r$  and corresponding best fit cross section for the combined  $tH + t\bar{t}H$  cross section times modified branching ratio for the combination of all three channels, for the ITC and the SM-like scenarios.

3490 In the SM scenario, a signal strength of 1.82 is obtained which corresponds to a  
 3491 cross section of 0.33 pb. The observed significance of the signal, in a background-  
 3492 only hypothesis, is  $2.7\sigma$ , with an a-priori expected significance of  $1.5\sigma$ . For the  
 3493 ITC scenario, the best fit signal strength is 0.68, corresponding to a significance

$\ell\ell\ell$	$r = 1.44^{+0.91}_{-0.84}$
$e^\pm\mu^\pm$	$r = 1.42^{+1.06}_{-1.03}$
$\mu^\pm\mu^\pm$	$r = 2.75^{+1.22}_{-1.11}$
Combined	$r = 1.82^{+0.76}_{-0.69}$
Expected	$r = 1.00^{+0.70}_{-0.65}$

**Table 6.21:** Best-fit signal strengths for a SM-like Higgs signal for the individual channels.

of  $1.7\sigma$  ( $2.5\sigma$  expected); a scan of the observed and expected significances over the  $\kappa_t/\kappa_V$  configurations is shown in Fig. 6.37. Note that the fit favors a signal strength compatible with zero for a scenario with  $\kappa_t = 0$  (where the  $t\bar{t}H$  component vanishes).

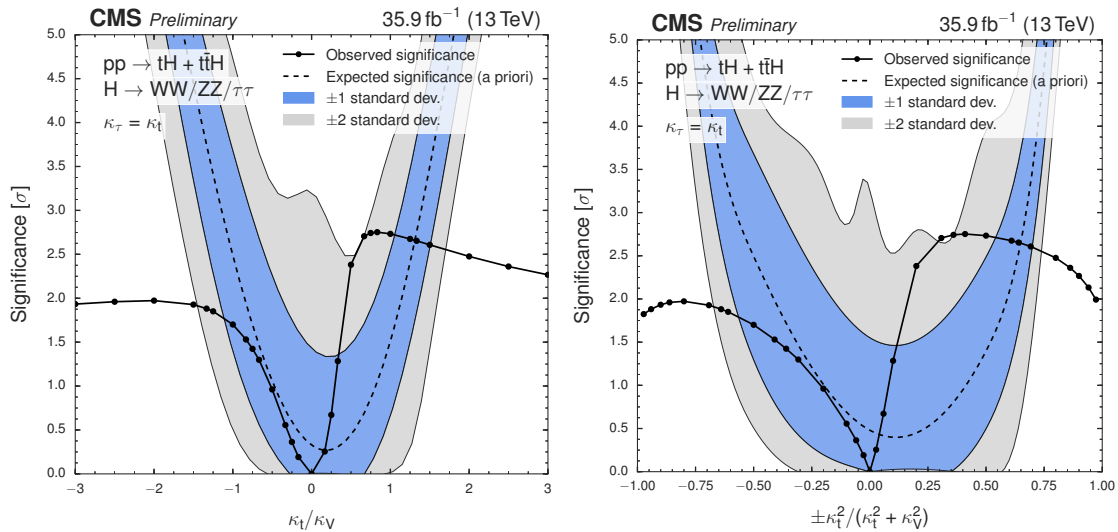


**Figure 6.37:** Observed and a priori expected significance of the fit result (in a background-only hypothesis) as a function of  $\kappa_t/\kappa_V$  (top) and  $f_t$  (bottom) for the combination of three lepton channel,  $\mu^\pm\mu^\pm$ , and  $e^\pm\mu^\pm$  channel.

A scan over the best fit values of the combined cross section times modified BR is shown in Figure 6.38. The fact that the best fit signal strength at  $\kappa_t = 0$ , where the  $t\bar{t}H$  component of the signal is zero, is compatible with zero implies that the best fit for the cross section is also compatible with zero, which again reveals that the excess in the cross section limit with respect to the expectation is not  $tH$ -like but  $t\bar{t}H$ -like.

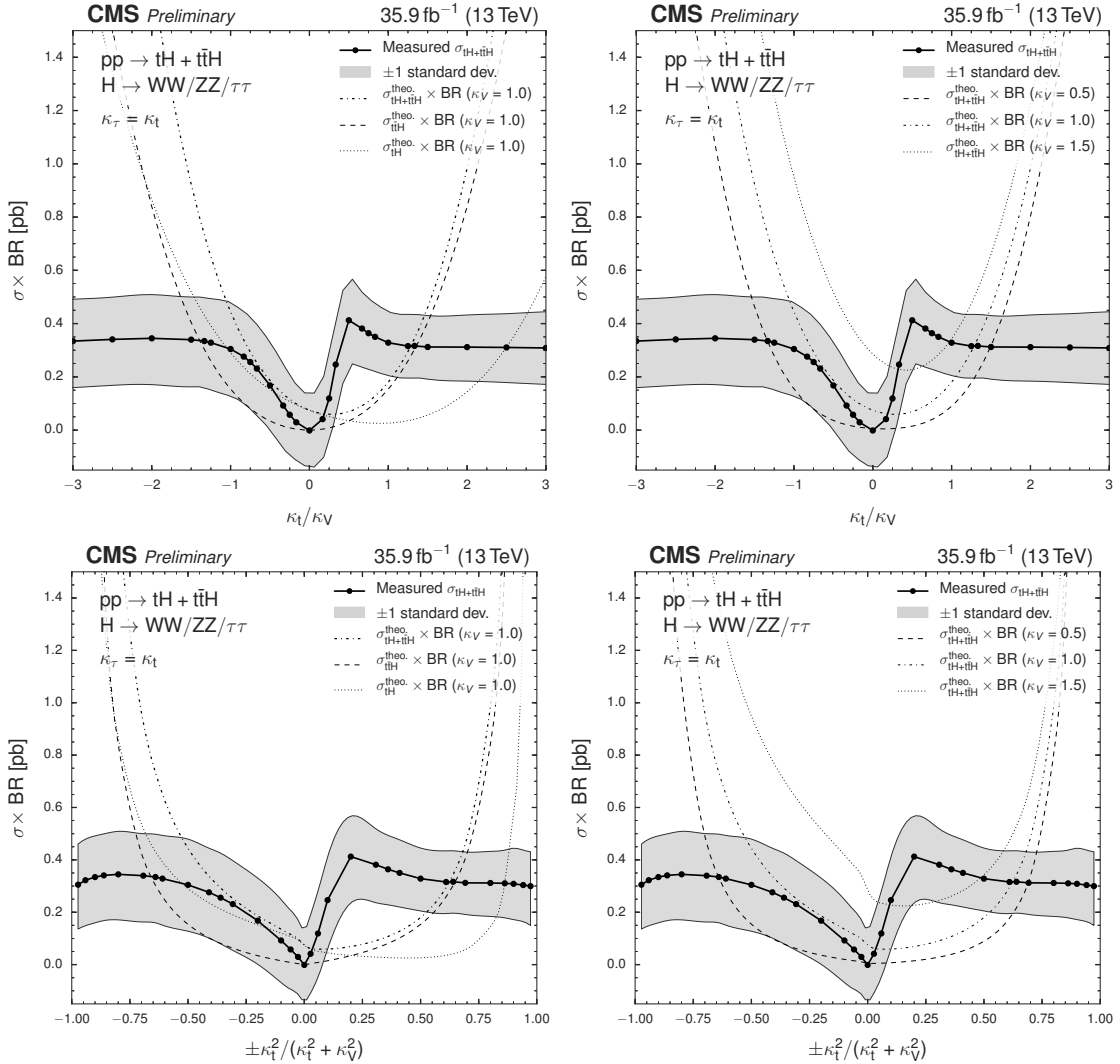


**Figure 6.38:** Best fit values of the combined  $tH + t\bar{t}H$  cross section times modified BR as a function of  $\kappa_t/\kappa_V$  (top) and  $\text{sign}(\kappa_t/\kappa_V) \times \frac{\kappa_t^2}{(\kappa_t^2 + \kappa_V^2)}$  (bottom) for the combination of three lepton channel,  $\mu^\pm\mu^\pm$ , and  $e^\pm\mu^\pm$  channel. In the left column plots, parabolas correspond to the theoretical cross section for  $tH$ ,  $t\bar{t}H$  and  $b+t\bar{t}H$  with  $\kappa_V = 1$ ; in the right column plot the parabolas correspond to  $tH + t\bar{t}H$  for  $\kappa_V = 0.5, 1.0, 1.5$ .

### 3502 6.13.3 Effect of the nuisance parameters

3503 The post-fit behavior of the most important nuisance parameters is presented in the  
 3504 pulls and impacts plots in Figures 6.39 and 6.40; additional pulls and impacts can  
 3505 be found in Appendix B.4

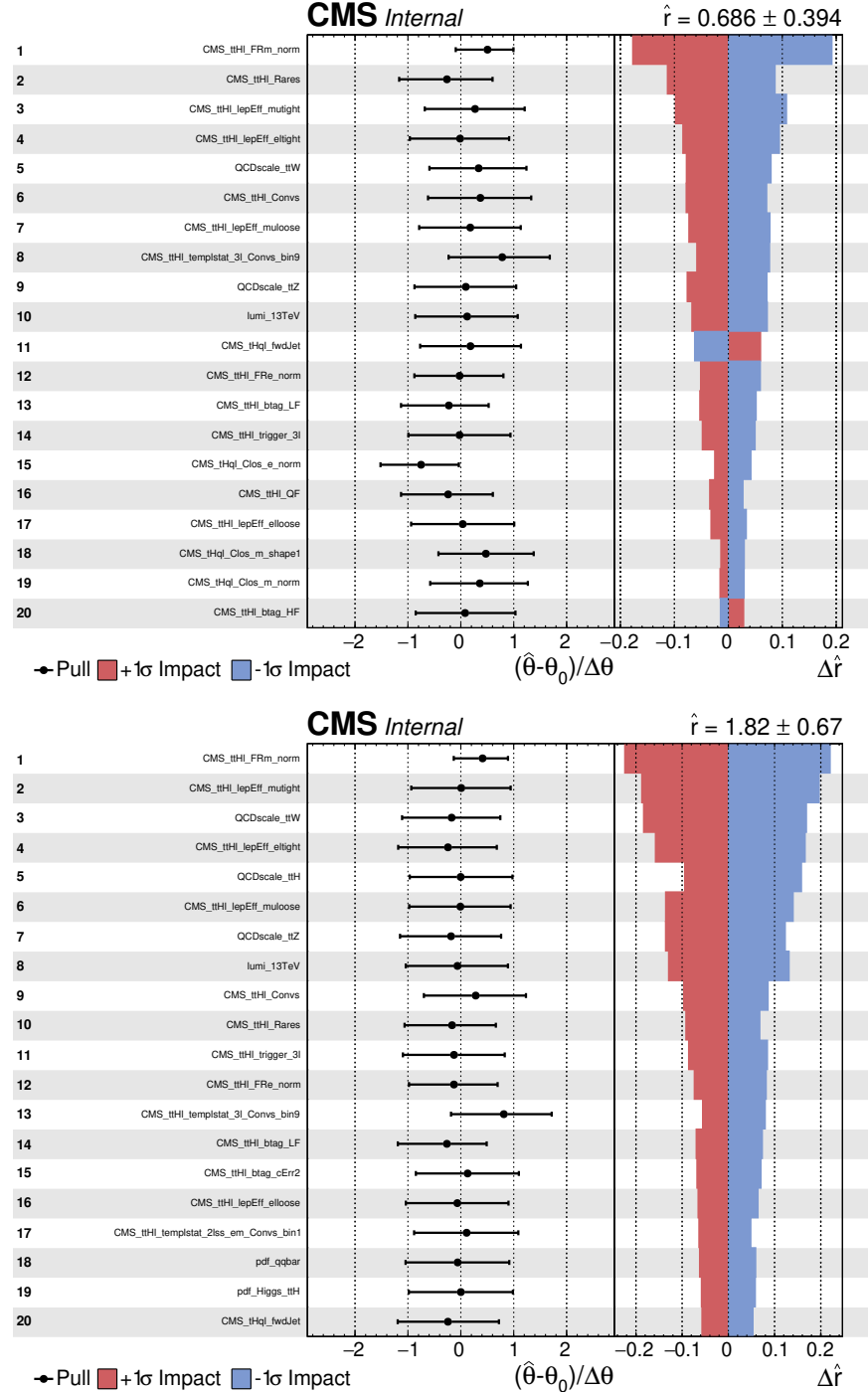


**Figure 6.39:** Post-fit pulls and impacts of the 20 nuisance parameters with largest impacts for the fit on the observed data, for the ITC (top) and SM (bottom) hypotheses.

3506        Most of the nuisance parameters stay close to their initial values, i.e., the esti-  
 3507        mations of all the nuisances are consistent with the observations in this dataset, up  
 3508        to the limited statistical power available. The biggest impact on the signal strength  
 3509        limits is associated with the fake rates for muons, followed by the lepton efficiencies  
 3510        and nuisances associated with the QCD scales. The lower impact in the ITC scenario  
 3511        is associated with the b-tag and  $tHq$  closure normalization and shape nuisances, while  
 3512        in the SM scenario, nuisances associated with the forward jet in  $tHq$  and PDFs have  
 3513        the lower impact in the signal strength limit.

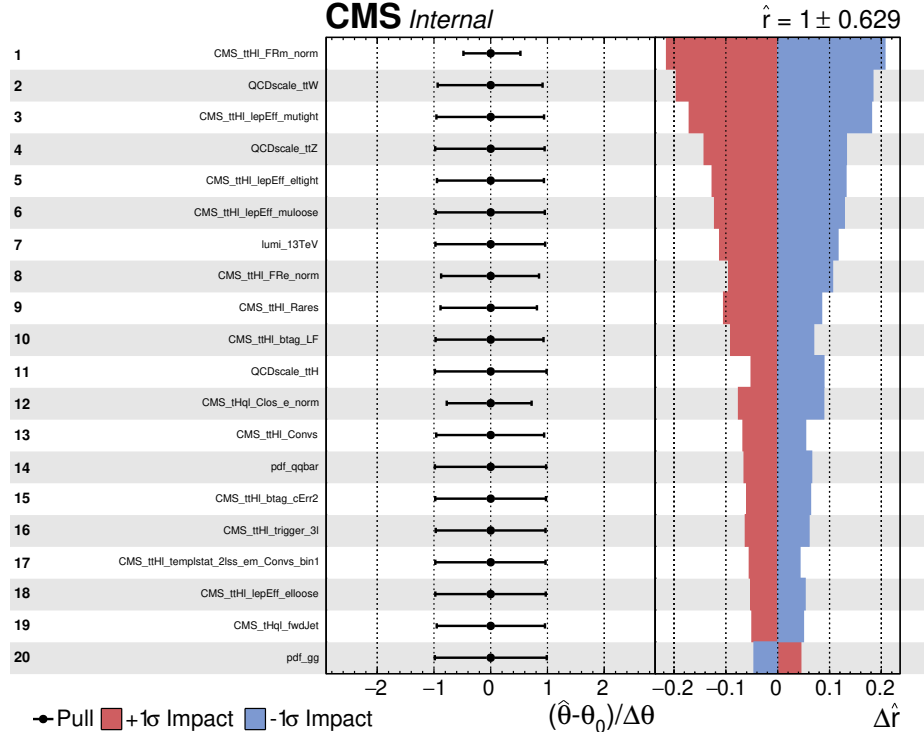


**Figure 6.40:** Post-fit pulls and impacts of the 20 nuisance parameters with largest impacts for a fit to the Asimov dataset with fixed signal strength, for the  $\kappa_t/\kappa_V = -1.0$  hypothesis.

3514        The sensitivity of the analysis is limited by systematic uncertainties, predomi-  
 3515        nantly by those concerning the normalizations of the main background components,  
 3516        i.e., the non-prompt lepton estimation, the scale uncertainties for  $t\bar{t}W$  and  $t\bar{t}Z$ , as

3517 well as by the uncertainties on the measured lepton efficiency.

## 3518 6.14 CP-mixing in $tH$ process

3519 The sensitivity of the  $tH$  production process to CP mixing in the Higgs boson sector  
3520 was explored in Section 2.6; the theoretical model postulates the existence of a generic  
3521 spin-0 particle  $X_0$  with a CP-symmetry violating interaction with the top quark but  
3522 SM-like interaction with the W boson.

$\cos(\alpha_{CP})$	Cross section (pb)		
	$tHq$	$tHW$	$t\bar{t}H$ (Extrap. NLO)
-1.0	$0.794^{+2.8}_{-4.0}$	$0.146^{+0.2}_{-0.2}$	0.503
-0.9	$0.728^{+2.7}_{-4.1}$	$0.135^{+0.2}_{-0.2}$	0.426
-0.8	$0.664^{+2.7}_{-4.2}$	$0.123^{+0.2}_{-0.2}$	0.356
-0.7	$0.601^{+2.8}_{-4.0}$	$0.112^{+0.2}_{-0.2}$	0.296
-0.6	$0.546^{+2.9}_{-4.3}$	$0.102^{+0.2}_{-0.2}$	0.242
-0.5	$0.497^{+3.1}_{-4.2}$	$0.092^{+0.2}_{-0.2}$	0.198
-0.4	$0.446^{+3.1}_{-4.5}$	$0.083^{+0.2}_{-0.2}$	0.160
-0.3	$0.398^{+3.2}_{-4.6}$	$0.074^{+0.2}_{-0.2}$	0.132
-0.2	$0.353^{+3.5}_{-4.8}$	$0.066^{+0.2}_{-0.2}$	0.112
-0.1	$0.314^{+3.7}_{-4.9}$	$0.059^{+0.2}_{-0.2}$	0.100
0.0	$0.275^{+3.6}_{-5.2}$	$0.052^{+0.2}_{-0.2}$	0.095
0.1	$0.242^{+4.0}_{-5.5}$	$0.045^{+0.2}_{-0.2}$	0.100
0.2	$0.211^{+4.1}_{-5.8}$	$0.040^{+0.2}_{-0.2}$	0.112
0.3	$0.182^{+4.1}_{-6.1}$	$0.035^{+0.2}_{-0.2}$	0.132
0.4	$0.156^{+4.4}_{-6.5}$	$0.030^{+0.2}_{-0.2}$	0.160
0.5	$0.134^{+4.5}_{-6.6}$	$0.026^{+0.2}_{-0.2}$	0.198
0.6	$0.116^{+4.7}_{-6.9}$	$0.023^{+0.2}_{-0.2}$	0.242
0.7	$0.100^{+5.0}_{-7.1}$	$0.020^{+0.2}_{-0.2}$	0.296
0.8	$0.087^{+4.8}_{-7.1}$	$0.018^{+0.2}_{-0.2}$	0.357
0.9	$0.077^{+4.7}_{-7.0}$	$0.017^{+0.2}_{-0.2}$	0.426
1.0	$0.071^{+4.2}_{-6.7}$	$0.016^{+0.2}_{-0.2}$	0.503

**Table 6.22:** Production cross sections for  $tHq$ ,  $tHW$  and  $t\bar{t}H$  at  $\sqrt{s} = 13$  TeV, as a function of  $\cos(\alpha_{CP})$ . Uncertainties on the cross section are based on scale variations and given in %. The  $t\bar{t}H$  NLO cross sections are interpolated to the angles for which the LHE weights in the signal MC samples are available [164].

3523 The LHE reweighting procedure used in the couplings analysis is used in this CP  
3524 mixing analysis; thus, a  $tX_0q$  simulation sample was produced, containing 21 event  
3525 weights for different CP-mixing angles ( $\alpha_{CP}$ ) ranging from values of  $\cos(\alpha_{CP}) = 1$

3526 to  $\cos(\alpha_{CP}) = -1$  in steps of 0.1. The extremes of that range correspond to the  
 3527 previously studied points SM ( $\kappa_t = 1$ ) and the ITC ( $\kappa_t = -1$ ). The sample was produced  
 3528 at LO with MadGraph5\_aMCatNLO, requiring the leptonic decay of the top quark.  
 3529 The  $tHq$ ,  $tHW$ , and  $t\bar{t}H$  cross sections are scaled to their NLO predictions and are  
 3530 listed in Table 6.22. The shape variations of the  $t\bar{t}H$  process with  $\cos(\alpha_{CP})$  are  
 3531 expected to be negligible in the range of values studied here where the cross section  
 3532 contribution is dominated by  $tH$  processes; however, the production of a private  $t\bar{t}H$   
 3533 sample including the CP-mixing weights is ongoing so that they can be included in a  
 3534 future refinement of the analysis.

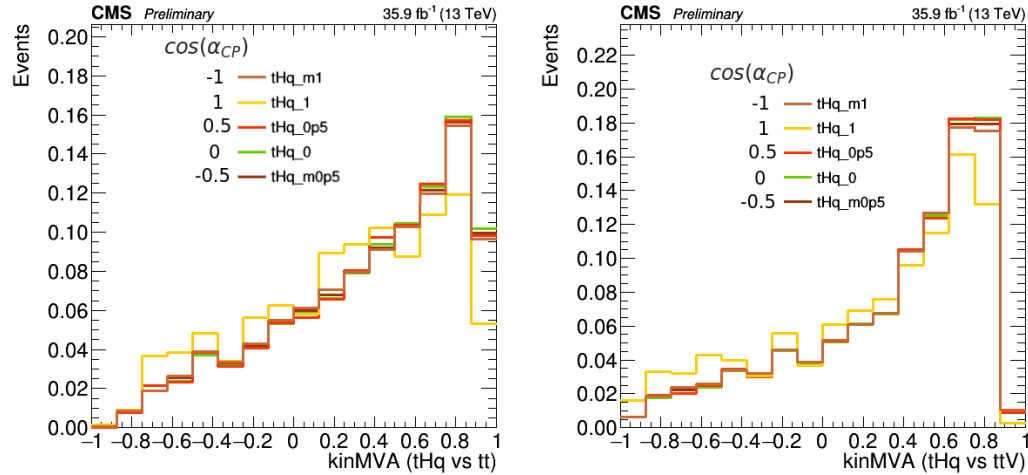


**Figure 6.41:** BDT shape variations for five CP-mixing angles. The trainings use the same set of input variables and samples as for the  $\kappa_t/\kappa_V$  study. Since there are no big variations between BDT output, only one training was performed.

3535 The set of BDTG input variables and training parameters are the same as for the  
 3536  $\kappa_t/\kappa_V$  analysis, as they already were optimized. Figure 6.41 shows that the shape  
 3537 variations for five values of  $\cos(\alpha_{CP})$ ; since there are no significant variations, it is  
 3538 not necessary to perform BDT trainings for each CP-mixing angle.

3539 After performing the simultaneous fit to the observed data for all channels, the  
 3540 asymptotic limits are calculated for each of the CP-mixing angles. Figure 6.42 shows

3541 the expected background-only, SM-like, and observed asymptotic  $CL_s$  limits at 95%  
 3542 C.L. on the combined  $tH + t\bar{H}$  cross section times BR as a function of  $\cos(\alpha_{CP})$   
 3543 for the combination of the  $3l$ ,  $\mu^\pm\mu^\pm$ , and  $e^\pm\mu^\pm$  channels for all studied CP-mixing  
 3544 angles; the corresponding values are listed in Table G.7. The SM-like limits and cross  
 3545 section limits have been calculated on an Asimov dataset that includes SM-like  $tH$   
 3546 and  $t\bar{H}$  signals.

3547 The interpolation between estimated values was made using a cubic spline fit. Ta-  
 3548 ble 6.23 summarizes the upper limits for the ITC ( $\cos(\alpha_{CP}) = -1$ ), SM ( $\cos(\alpha_{CP}) =$   
 3549 1), and fully pseudo-scalar ( $\cos(\alpha_{CP}) = 0$ ) CP-mixing configurations.

Scenario	Obs. Limit	Exp. Limit		
		Median	$\pm 1\sigma$	$\pm 2\sigma$
$\cos(\alpha_{CP}) = -1$	0.594	0.299	[0.210,0.423]	[0.155,0.592]
$\cos(\alpha_{CP}) = 1$	0.555	0.238	[0.170,0.340]	[0.126,0.470]
$\cos(\alpha_{CP}) = 0$	0.469	0.279	[0.195,0.404]	[0.143,0.563]

**Table 6.23:** Expected (for background only) and observed 95% C.L. upper limits (in pb), for the combined  $tH + t\bar{H}$  cross section times branching ratio for the combination of all three channels, for different ITC, SM, and fully pseudo-scalar CP-mixing scenarios.

3550 The CP-mixing limits are consistent with the limits obtained in the  $\kappa_t$ - $\kappa_V$  anal-  
 3551 ysis as expected; however, in the CP-mixing case it is not possible to exclude any  
 3552 region/value in the  $\alpha_{CP}$  phase space. The excess of more than  $2\sigma$  observed in the SM  
 3553 scenario for the background-only expected limit, and that was also observed in the  
 3554  $\kappa_t$ - $\kappa_V$  analysis, is again reduced to about  $1\sigma$  when the SM-like  $tH$  and  $t\bar{H}$  signals are  
 3555 included in the calculation of the expectations; however, as said above, the fact that  
 3556 the  $t\bar{H}$  sample does not include the CP-mixing weights implies that no conclusive  
 3557 statement can be made.

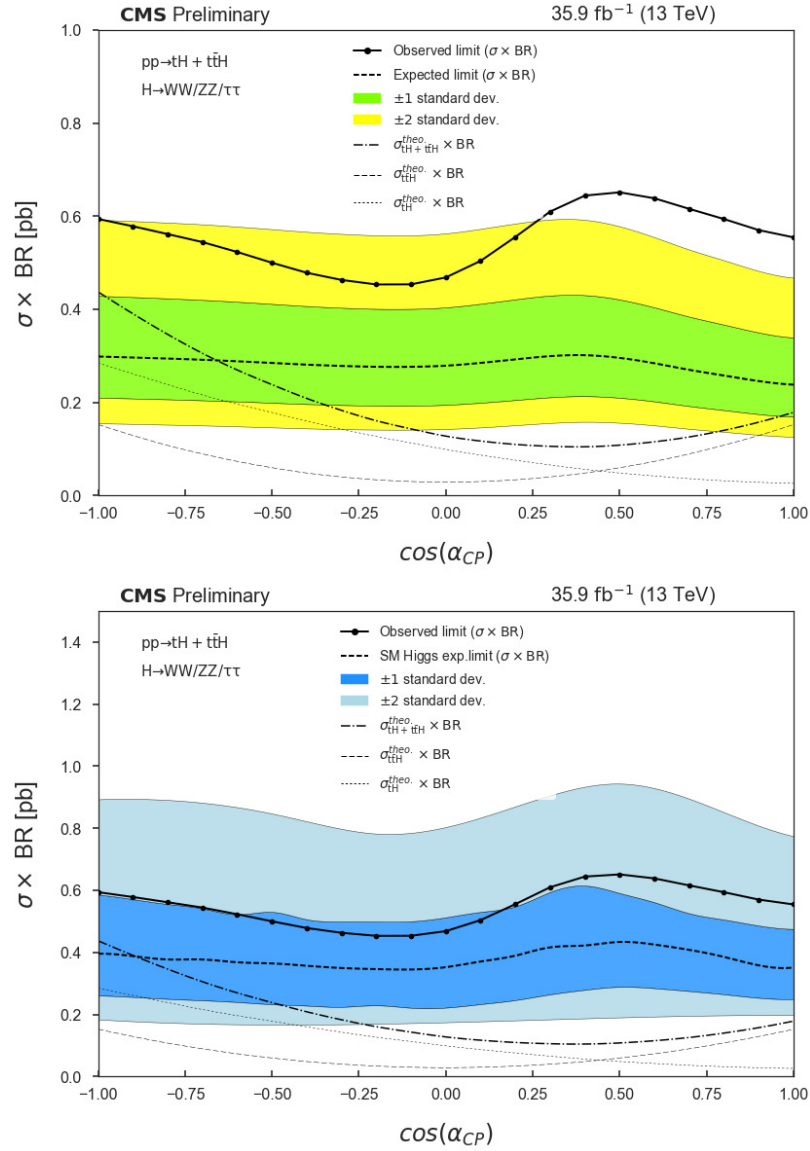


**Figure 6.42:** Top (bottom): Expected background-only (SM-like including  $t\bar{H}$  and  $tH$  signals) and observed asymptotic limits on the combined  $tH + t\bar{H}$  cross section times BR as a function of  $\cos(\alpha_{CP})$  for the combination of three lepton channel,  $\mu^\pm\mu^\pm$ , and  $e^\pm\mu^\pm$  channel. Theoretical  $tH + t\bar{H}$  cross section curves have been included.

3558

## CHAPTER 7

3559

### Phase 1 FPix upgrade module production

#### 3560 7.1 Introduction

3561 In chapter 3, a description of the CMS pixel detector used during the collection of  
3562 the data sets considered in this analysis was presented. During a technical stop in  
3563 2017, the complete CMS pixel detector was replaced in order to support the high  
3564 performance of the CMS experiment under the higher radiation conditions produced  
3565 by the increasing instantaneous luminosity delivered by the LHC accelerator. It also  
3566 was designed to address and mitigate the identified weaknesses in the previous system.

3567 In this chapter, a description of the upgraded detector will be presented. Emphasis  
3568 will be put on the contributions made by the University of Nebraska - Lincoln (UNL)  
3569 HEP group. The contribution consisted of the assembly of about 600 of the modules  
3570 that make up the Phase 1<sup>1</sup> upgraded forward pixel detector (FPix); in particular,  
3571 the gluing and encapsulation stages will be described in detail since they are my  
3572 contributions. A complete description of the upgrade design and plans is presented in  
3573 Reference [79] which is the main source of the information contained in this section  
3574 unless additional references are provided.

<sup>1</sup> During the CMS experiment lifetime, several upgrades will be performed to correct issues and improve performance; the first version of the detector is known as Phase 0, thus, future upgrades are named Phase1 and so on.

## 3575 7.2 CMS pixel detector upgrade

3576 The previous pixel detector was designed to record the first three space-points near  
 3577 the interaction region, in the range of  $|\eta| < 2.5$ , at an instantaneous luminosity of  
 3578  $1 \times 10^{34} \text{ cm}^{-2}\text{s}^{-1}$  and a bunch crossing each 25 ns, efficiently and with high precision.  
 3579 An average pileup of about 25 simultaneous overlapping events is expected under  
 3580 those conditions. An increment in the luminosity would affect the performance of the  
 3581 detector, due to the degradation of the sensors and the readout system resulting from  
 3582 the radiation exposure, reducing track reconstruction efficiency and increasing the  
 3583 data losses; furthermore, if the LHC were to run with 50 ns bunch spacing at twice  
 3584 the luminosity, the data losses would increase almost exponentially to losses of 50%  
 3585 for the innermost layer due to the increasing higher data rates and the limited existing  
 3586 buffer size. An illustration of the foreseen reduced performance in tracking efficiency  
 3587 is shown in Figure 7.1 in the case of simulated  $t\bar{t}$  events at instantaneous luminosity  
 3588 up to  $2 \times 10^{34} \text{ cm}^{-2}\text{s}^{-1}$  with 25 ns and 50 ns bunch spacing. The increasing fake  
 3589 rate is also shown. In conclusion, the previous pixel detector was not able to perform  
 3590 efficiently under the new luminosity, pileup, radiation, and running conditions.

3591 The new system is designed to offer high performance under these new operational  
 3592 conditions; it is composed of low-mass silicon pixel detectors arranged in four-layers  
 3593 and three-disks that provide high performance tracking in the high luminosity envi-  
 3594 ronment.

3595 The upgraded detector is expected to provide higher efficiencies, lower fake rates,  
 3596 and lower dead-time/data-loss, which translate in better muon ID, b tagging, pho-  
 3597 ton/electron ID, and tau reconstruction, at both HLT and offline levels. No details  
 3598 about the performance of the upgraded pixel detector are given here since that mat-  
 3599 ter falls beyond the purpose of this document; however, it is documented in Refer-

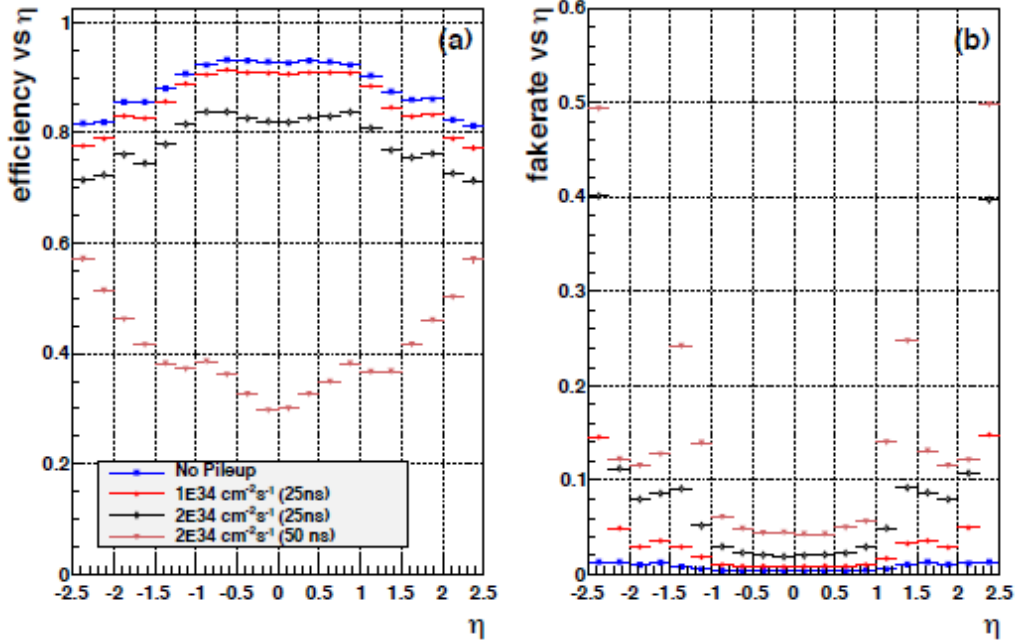


**Figure 7.1:** Expected performance of the previous pixel detector in simulated  $t\bar{t}$  events: a) track-finding efficiency; b) fake rate. Conventions are the same for both plots, considering zero pileup (blue squares), average pileup of 25 (red dots), average pileup of 50 (black diamonds), and average pileup of 100 (magenta triangles).

3600 ence [165].

3601 Figure 7.2 shows the layout of the upgraded pixel detector compared to the old  
 3602 one. The old three-layer barrel (BPix), two-disk endcap (FPix) system is replaced  
 3603 with a four-layer barrel, three-disk endcap system. The additional barrel layer and  
 3604 forward disk provide redundancy for the track pattern recognition and reconstruction.

### 3605 **7.3 Phase 1 FPix upgrade**

3606 The Phase 1 upgraded FPix system is composed of three disks in each endcap, located  
 3607 at each end of the barrel detector, with a radial coverage ranging from 4.5 to 16.1 cm.  
 3608 The first disk is located along the beam line at 29.1 cm from the IP, while the second  
 3609 and third disks are located at 39.6 cm and 51.6 cm from the IP; each disk consists of

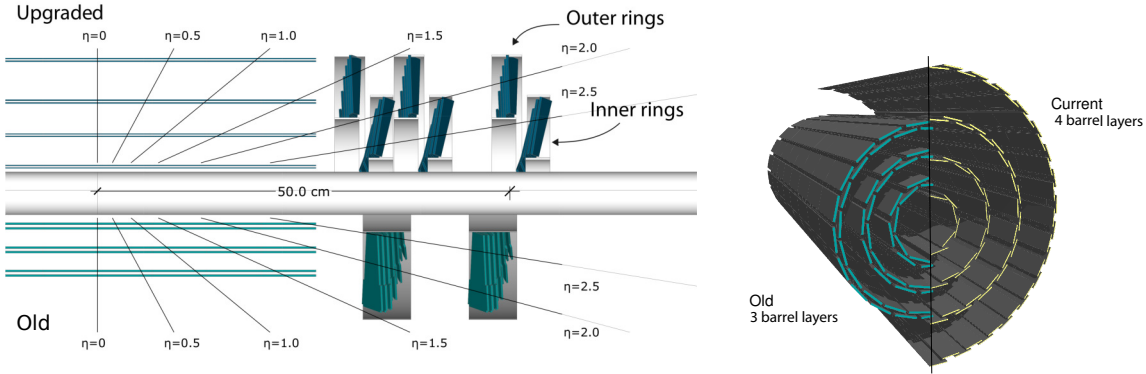


**Figure 7.2:** Layout and comparison of the layers and disks in the upgraded and old pixel detectors.

3610 two half disks. Some of the main features of the upgraded FPix System are:

- 3611     • Pixel size:  $100 \times 150 \mu\text{m}$
- 3612     • Only one type of module: 2x8 ROC modules
- 3613     • Modules oriented radially to improve resolution in  $r - \phi$ .
- 3614     • Minimize the gap in 4-hit coverage between the end of the 4th-barrel layer and
- 3615       the forward-most disk.
- 3616     • All three identical disks on each side of the IP.

3617     Figure 7.3 shows a schematic structure of the FPix half disk; each half disk is  
 3618 composed of two sections, inner and outer, where the pixel modules are assembled.

3619     In total, there are 56 modules (896 ROCs) per half-disk, 34 modules in the outer  
 3620 ring and 22 modules in the inner ring. The pixel modules are attached to the blades  
 3621 by a pair of module holders. Modules are designed to be removable and replace-  
 3622 able without disassembling the half-disks; thus those modules that suffer failure or  
 3623 degradation can be easily replaced during an annual technical stop.

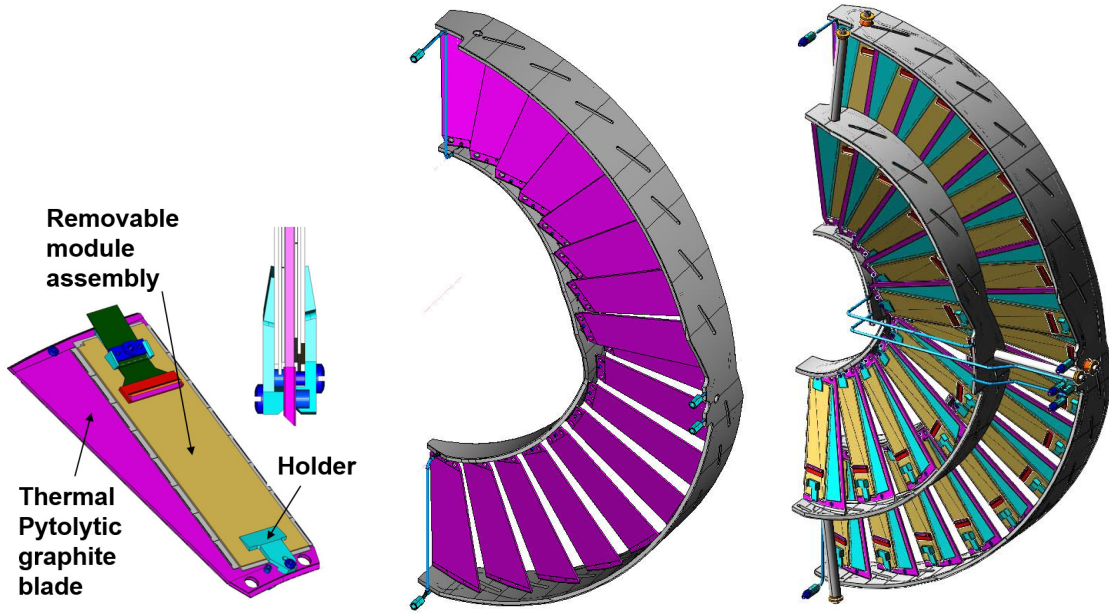


**Figure 7.3:** FPix half disk design; FPix module (left) mounted on a blade, outer half disk (center), assembled half disk (right).

Blades on the outer assembly are rotated by 20° forming a turbine-like geometry; in addition, they are arranged in an inverted cone array with the blades tilted by 12° towards the IP in order to guarantee excellent resolution in both the azimuthal and radial directions throughout the FPix acceptance angle for the inner assembly.

## 7.4 FPix module structure

The upgraded CMS pixel detector is composed of 1184 pixel modules in the BPix sector with a total 79 million of pixels; the FPix sector contains 672 with approximately 45 million pixels. Figure 7.4 shows a schematic view of the FPix module structure. The n<sup>+</sup>-in-n *Silicon sensor* is bump bonded to the 16 ROC to form the detector unit known as *Bump-Bonded Module* (BBM) with 66560 pixels. The *High Density Interconnect* (HDI) is glued on top of the BBM and wirebonded to the ROCs to provide them the required signals and power. The modules are attached to the

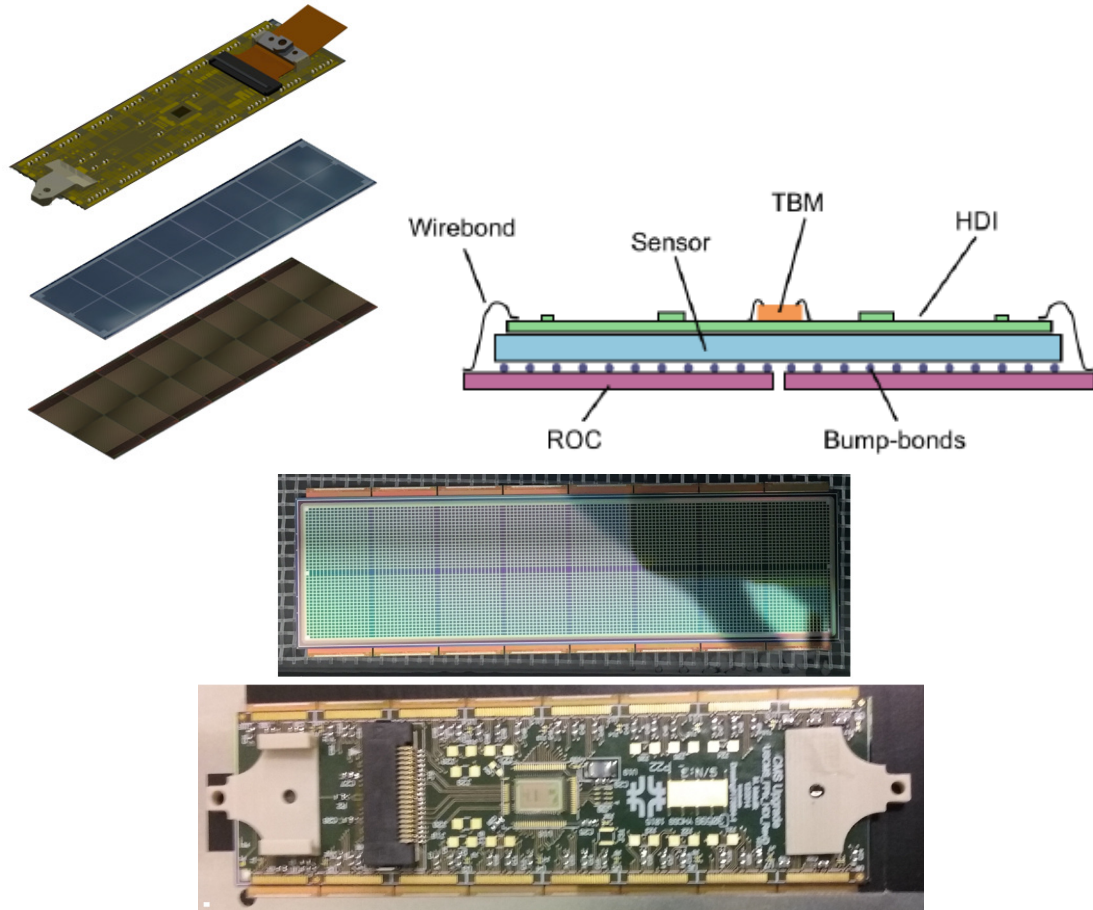


**Figure 7.4:** Top: FPix module structure; The bare silicon sensor is bump-bonded to the ROCs to form the BBM; then the HDI is glued on top of the BBM and wirebonded to the ROCs. Bottom: pictures of actual BBM and HDI.

3636 support structure using the end holders glued to the HDI.

## 3637 **7.5 FPix module assembly**

3638 The construction of the modules for the upgraded FPix system was divided between  
 3639 two sites located at Purdue University and at UNL; testing facilities were located  
 3640 at the University of Kansas and Fermi National Accelerator Laboratory (Fermilab).  
 3641 The integration facility was at Fermilab.

3642 The BBM was prepared by a commercial vendor, while the HDI was populated at

3643 Fermilab, with all the electronic components like resistors, capacitors and the central  
 3644 component known as *Token Bit Manager* (TBM), which is in charge of managing the  
 3645 information coming from the silicon sensors and going to the ROCs. Both BBM and  
 3646 HDI were sent to the assembly sites ready to be glued together.

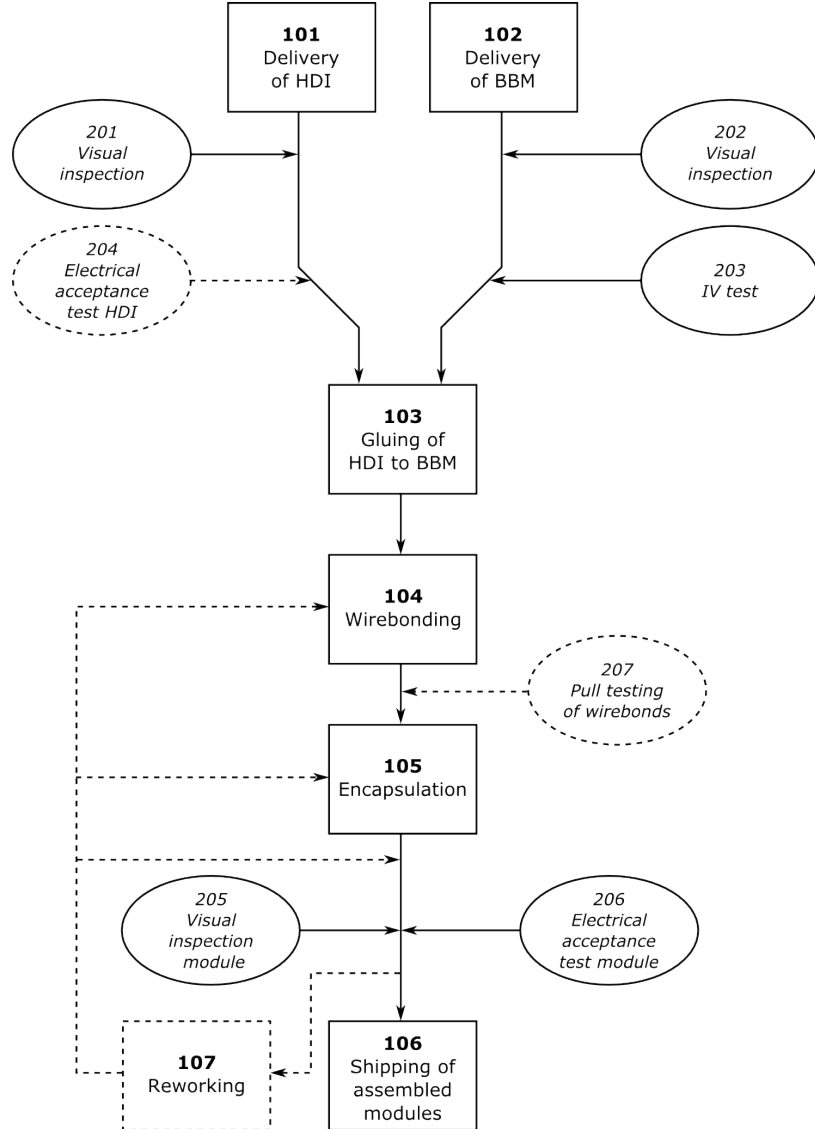


**Figure 7.5:** UNL module assembly work flow. Dashed lines represent occasional quality testing and reworking procedures; 10X numbers represent the stage within the assembly procedure while 20X numbers represent testing stages along the assembly procedure.

3647 The module production procedure was designed according to a production line

3648 structure. Figure 7.5 shows the work flow followed at the UNL assembly site. Once  
3649 the BBM and HDI had arrived, they were submitted to visual inspection looking  
3650 for defects, scratches, dents or short circuits. Modules passing the visual inspection  
3651 were tested for electrical acceptance and performance. BBM and HDI were then  
3652 glued employing robotic a pick-and-place machine that integrates optical tools, pat-  
3653 tern recognition algorithms, and glue dispensing; the semi-automated gluing process  
3654 improves the uniformity of the technique. After ten hours of curing, glued mod-  
3655 ules were moved to the wirebonding station where ROCs and HDI were electrically  
3656 connected employing semi-automated ultrasonic wirebonding machines; occasionally,  
3657 some of the wires were pull tested for quality control. After this step, modules were  
3658 fully functional, hence, a basic functionality test was done on a subset of modules to  
3659 control the manufacturing process.

3660 In the next stage, the wirebonds were encapsulated with an elastomeric com-  
3661 pound (*Sylgard*) in order to protect them against mechanical damage and electrical  
3662 shorts; the encapsulation process was performed employing the robotic pick-and-place  
3663 machine which also integrates the encapsulant dispensing system. Once the encap-  
3664 sulation ends, modules were mounted on module holders and submitted to a heat cycle  
3665 to cure the sylgard.

3666 The module assembly sites were also responsible for the testing and characteriza-  
3667 tion of the assembled pixel modules. That testing included visual inspection, electrical  
3668 acceptance, performance testing under controlled temperature conditions that sim-  
3669 ulate the expected operational conditions; in case of any necessary reworking, the  
3670 modules were returned to the appropriate stage.

3671 In the final stage, the assembled and tested modules were shipped to the University  
3672 of Kansas for further characterization.

3673 Each stage in the assembly procedure is documented in a *Standard Operating Pro-*

3674 *cedure* (SOP) document that describes the procedures to be followed by the operator.

3675 The full set of SOPs can be found in Reference [166].

3676 In the following sections, a detailed description of the gluing and encapsulation  
3677 stages will be presented. The full set of tools was designed by Dr. Frank Meier  
3678 Aeschbacher.

### 3679 **7.5.1 Pick and place machine setup**

3680 Figure 7.6 shows the full setup used to perform the gluing and encapsulation steps.

3681 The gantry used in the setup is a custom made *AGS15000 Series Gantry*, fabricated  
3682 by Aerotech [167], which offers translational motion in 3D ensuring coverage of any  
3683 position in the work field; in addition, rotational motion is provided in the *gantry*  
3684 *head* in the usual x-y plane (gantry table plane).

3685 A set of eight hard-anodized aluminum chucks, composed of a *base chuck* and a  
3686 *plate chuck* each, henceforth chuck and plate respectively, were designed to house the  
3687 parts and tools needed along the gluing process; Figure 7.7 shows the details of a  
3688 chuck.

3689 Each chuck was connected to an independent vacuum line such that the plate was  
3690 held fixed; both pieces are polished to seal the vacuum with no use of O-rings. The  
3691 three screws serve as references for aligning the plates with the chucks. There are  
3692 four types of plates: the HDI/BBM plate, the glue reservoir plate, the stamp plate,  
3693 the weight plate.

#### 3694 **Chucks**

3695 Four chucks were used to accommodate sixteen BBMs (four per plate); the holes in  
3696 the BBM/HDI plate (see Figure 7.8) are intended to hold the BBM/HDI safely fixed

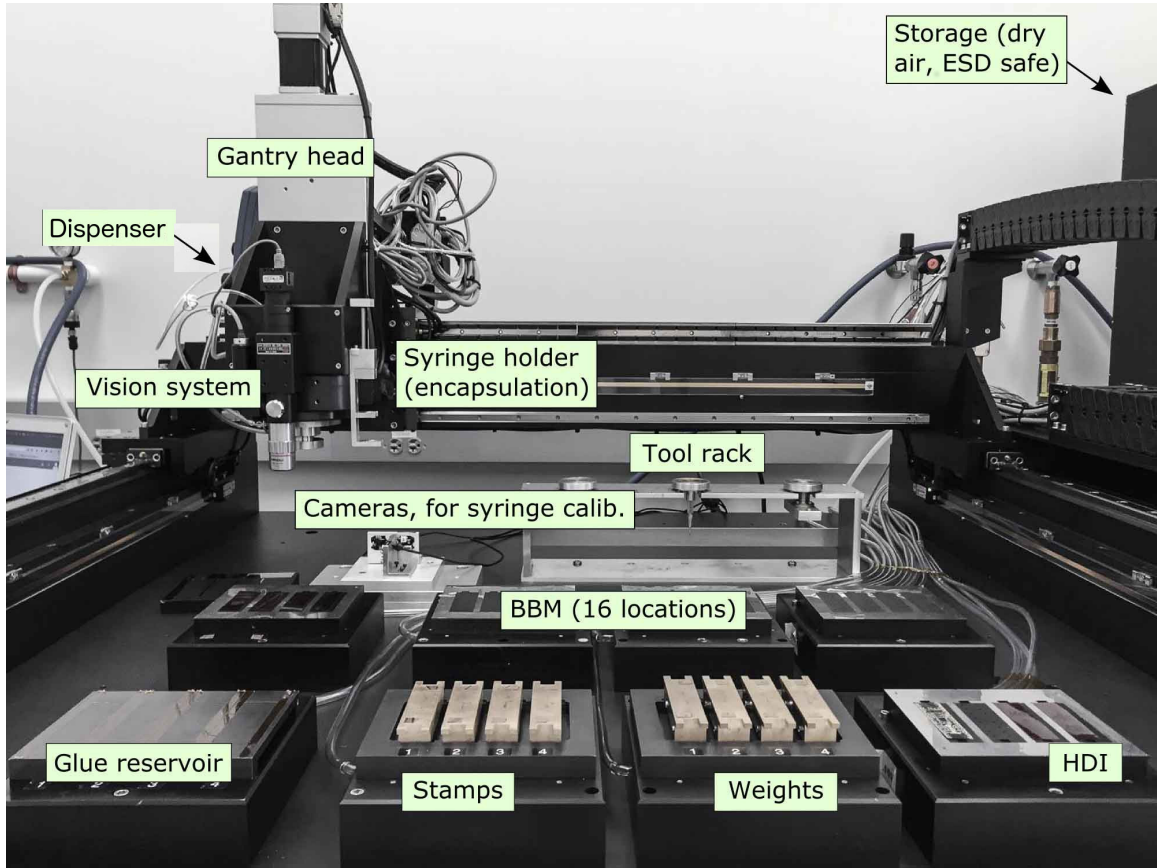


**Figure 7.6:** Full gluing and encapsulation setup.

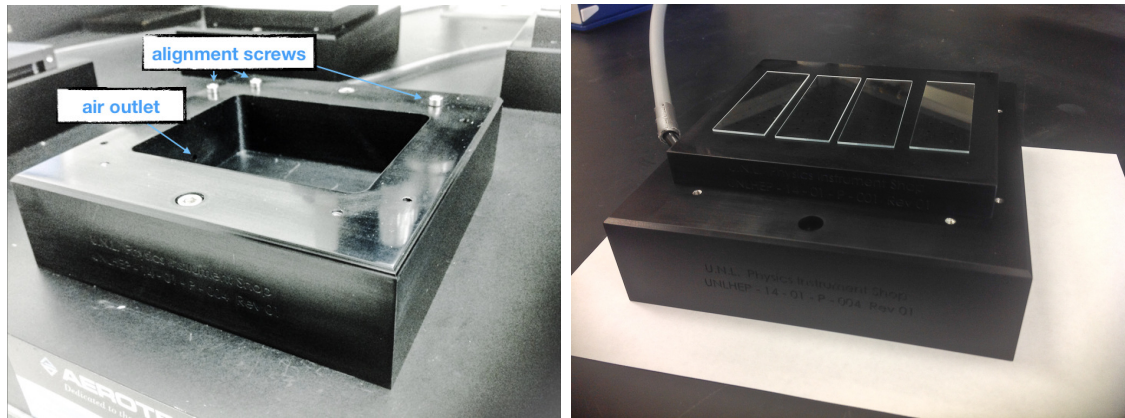


**Figure 7.7:** Left: Chuck detailed internal view. Right: full chuck housing glass slides. The vacuum connection is visible on the left.

3697 to the plate by the action of the vacuum, while the stencil (100  $\mu\text{m}$  in thickness)  
 3698 allows for a very accurate positioning of the BBM/HDI; it is thin enough that the

3699 alignment is controlled by the edges of the ROC and no force is applied to the sensor.



**Figure 7.8:** Left: BBM/HDI plate with a mock module that reproduces the BBM features. Center: the pockets in the top and bottom sides accommodate the module holders. Right: bare HDI and BBM showing the alignment provided by the stencil.

3700 One chuck was dedicated to accommodate four HDIs. Although BBM/HDI plates  
 3701 have the same design, the HDI chuck has four independent pockets instead of only a  
 3702 big one, in order to enable the release of one HDI at a time; hence, it was connected to  
 3703 four vacuum lines. That was not required for the BBMs because they were not moved  
 3704 from their original location. An additional adjustment was made to the HDI plate in  
 3705 response to the HDI back surface which is not totally flat but has irregularities; these  
 3706 irregularities caused vacuum leaks that were addressed by adding a kapton tape layer  
 3707 to the HDI plate, as shown in the picture in the center of Figure 7.8. The carved  
 3708 canals served to improve the vacuum action and sealing.

3709 One chuck held the *glue reservoir* plate, as shown in Figure 7.9. Each of the four  
 3710 reservoirs is a pocket just  $100\ \mu\text{m}$  deep, suitable for retaining sufficient glue to be  
 3711 applied to the BBM.

3712 The remaining two chucks housed the *stamp plate* and the *weight plate* which in  
 3713 turn housed the *stamp* and *weight tools* as shown in Figure 7.10.



**Figure 7.9:** Glue reservoir plate. The four pockets are  $100 \mu\text{m}$  deep.

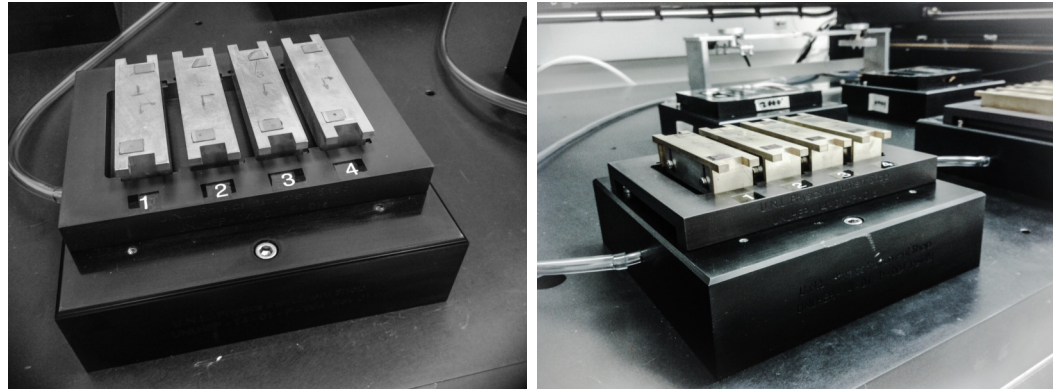


**Figure 7.10:** Chucks housing stamp tools(left) and weight tools(right).

#### 3714 Stamp and weight tools

3715 Stamp and weight tools are a set of custom made tools, all produced by the UNL  
 3716 Physics department machine shop (see Figure 7.11). The very first design of the  
 3717 weight tool included four stainless steel blades and two springs; the blades matched  
 3718 the rows of eight ROC bond pads on the HDI to apply force while curing. The  
 3719 springs apply force to the module end holders on the HDI. The final design of the  
 3720 tool eliminates the issues associated with the alignment of the blades, by integrating  
 3721 them into the design in the form of narrow blade-like brass edges. The weight tools  
 3722 were made with 260 g of brass.

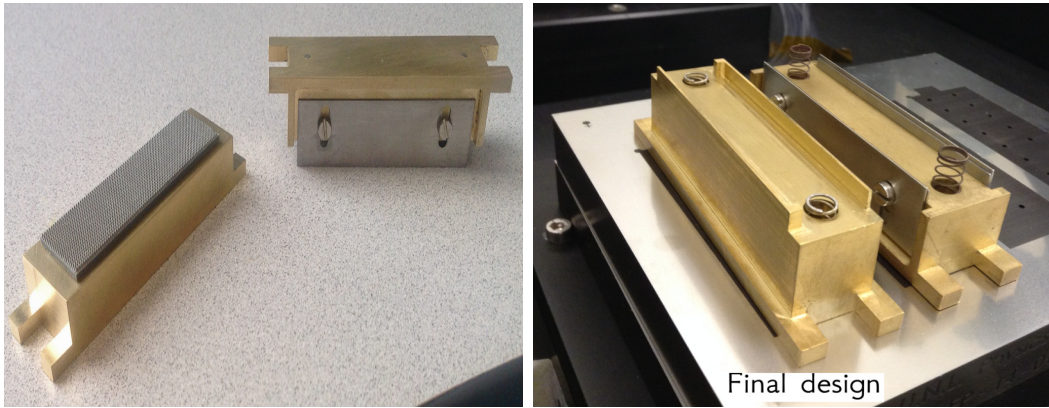


**Figure 7.11:** Stamp and weight tools. Both tools are made of brass; the stamp tool includes a rubber stamp while the weight tool includes four stainless steel blades to apply force while curing. The final weight tool design eliminates the blades (right).

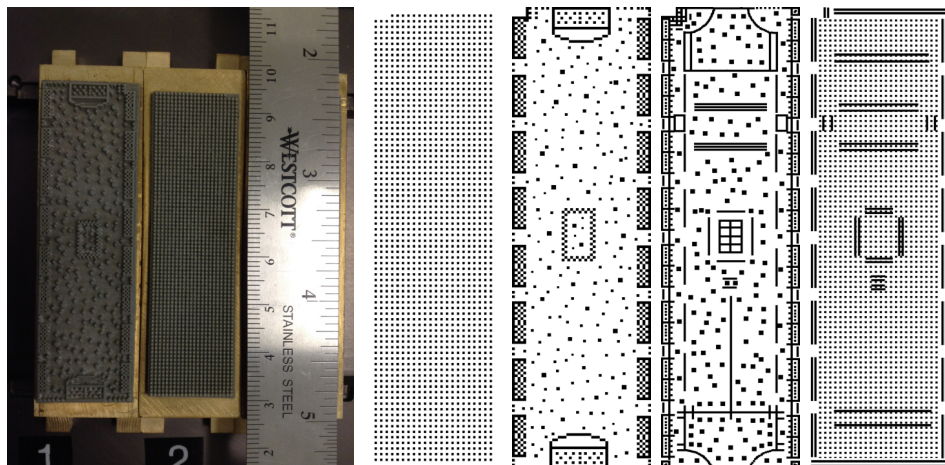


**Figure 7.12:** Stamp patterns evaluated along the glue testing process; the picture on the left shows the first two versions mounted on the stamp tool while the final version is on the right.

3723        The stamp tool is composed of a brass piece of 200 g and a rubber stamp piece  
 3724        attached to the bottom side of the brass piece; it is used to pick the glue from the glue  
 3725        reservoir and then stamp it over the BBM. An extensive testing process was performed  
 3726        in order to determine the most appropriate features of the gluing strategy. Figure 7.12  
 3727        shows the four stamp patterns tested and a picture of the first two attached to the  
 3728        stamp tools; the variations of the stamp pattern design were based on the results of  
 3729        testing for:

3730     • the amount of glue dispensed, and in particular the glue spreading out of the HDI  
 3731 area. An excess of glue, scattered beyond the HDI edge would go between the  
 3732 ROC and the sensor, affecting the functionality of the bump bonds connecting  
 3733 them; in the case of the high voltage (HV) pad, it was observed that the excess  
 3734 of glue covers the pad on the sensor, making impossible to wire it. The amount  
 3735 of glue deposited on top of BBM depends on several variables: the dipping time  
 3736 of the stamp tool in the glue reservoir, the time that the stamp tool is in contact  
 with the BBM, and the depth of the glue reservoir. In the case of the dipping



**Figure 7.13:** Pictures of a test of the amount of glue dispensed as a function of the glue reservoir depth. The glue reservoir depth was varied by adding kapton tape (left), and the test were conducted by gluing plain HDI on top of glass slides (middle and right.)

3738 and stamping times, it was found that there is not a strong dependence and  
 3739 those times were set to 10 seconds; in the case of the glue reservoir depth, the  
 3740 dependence is stronger. Several glue tests where conducted by gluing plain HDIs  
 3741 to glass slides; Figure 7.13 shows pictures from a glue test with three different  
 3742 glue reservoir depths ( $100\ \mu\text{m}$ ,  $255\ \mu\text{m}$  and  $410\ \mu\text{m}$ ). The results show not only  
 3743 that the deeper the glue reservoir, the bigger is the amount of glue deposited,  
 3744 as expected, but also that the spreading out is critical for depths greater than  
 3745  $200\ \mu\text{m}$ . A redesign of the rubber stamp pattern was made in order to reduce  
 3746 the amount of glue deposited in the HDI pads regions; that adjustment led to  
 3747 the final rubber stamp pattern.

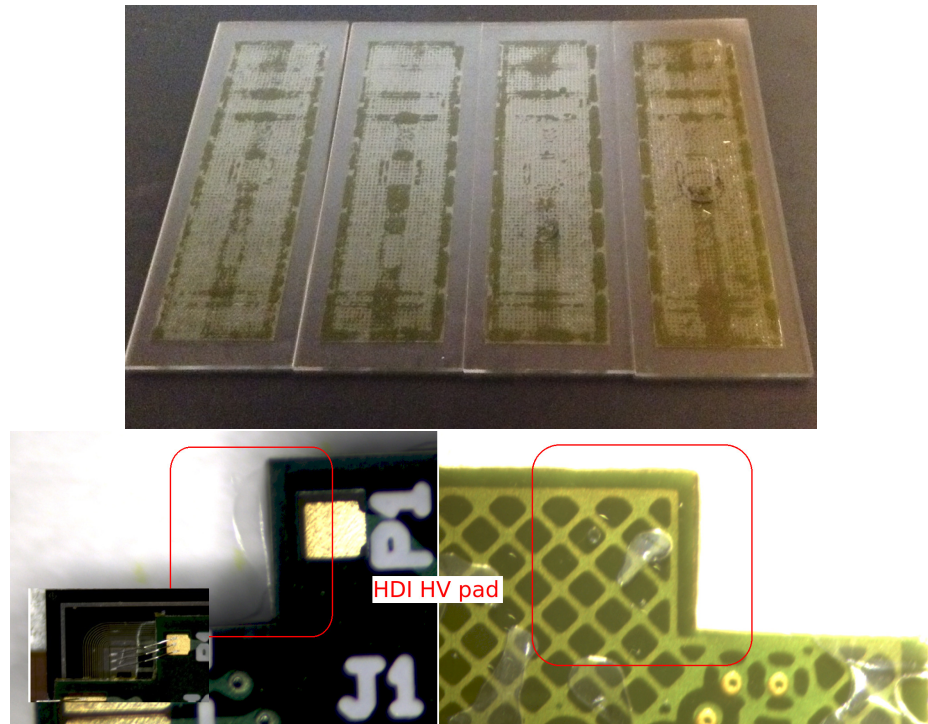


**Figure 7.14:** Results from a glue test using the final stamp pattern, which proves the support provided to the HDI bond pads and the HV pad and the almost null glue spreading out.

3748 • the size of contact area, and in particular the support given to the edges of the

3749 HDI where the bond pads and the HV pad are located. This is a critical aspect,  
 3750 given that the wirebonding relies on the steadiness of the pads to be connected.  
 3751 Figure 7.14 shows the outcomes of a glue test using the final stamp pattern; note  
 3752 the support provided to the HDI bond pads and the HV pad and the almost  
 3753 null glue spreading out; it justifies why this stamp pattern was chosen.

3754 The final tool designs used during the module production are indicated in Figures  
 3755 7.11 and 7.12, while the optimal glue reservoir depth was found to be 100  $\mu\text{m}$ .

3756 **Grabber and picker tools**

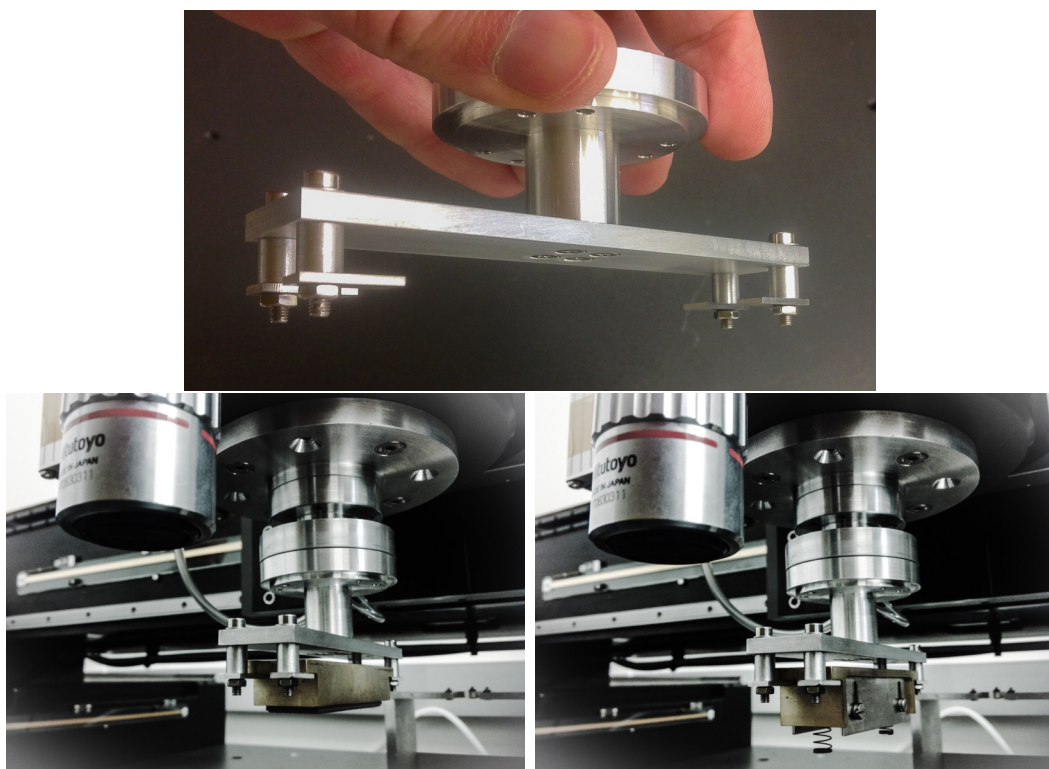


**Figure 7.15:** Top: Grabber tool used to grab the stamp and weight tools from their houses to the BBM location. Bottom: grabber tool holding the stamp (left) and weight (right) tools.

3757 In order to move the stamp and weight tools from their houses to the glue reservoir

3758 and to the BBM location, a *grabber tool* was designed. The grabber tool was held on  
 3759 a tool rack located in the back of the gantry table and it gets attached to the gantry  
 3760 head by using an adapter and the vacuum system as shown in Figure 7.15.

3761 The gantry head adapter is attached to the rotary motor that provides the angular  
 3762 motion, therefore, the grabber tool is able to grab the stamp and weight tools and  
 3763 adjust their alignment in agreement with the BBM orientation. The force with which  
 3764 the glue was applied on the BBM was controlled by the weight of the brass piece;  
 3765 in a similar way, the force applied to the HDI-BBM sandwich was controlled by the  
 3766 weight of the tool and the springs.

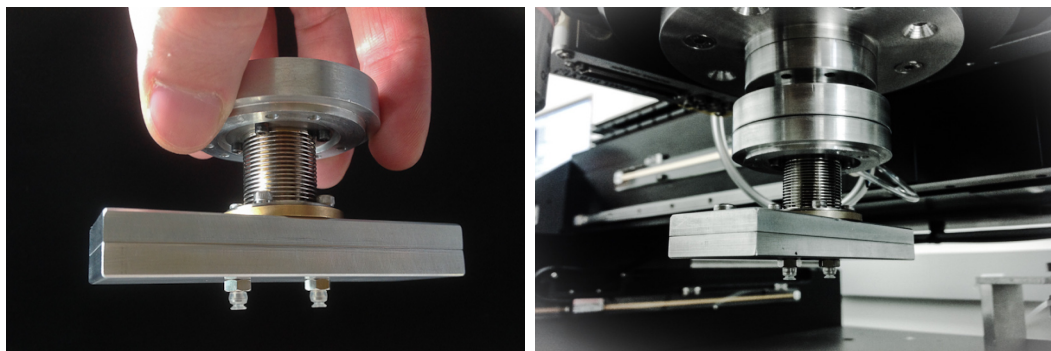


**Figure 7.16:** The pick and place tool picks the HDI from its chuck and place it on top of the BBM.

3767 The pick of the HDI and place on top of the BBM was performed using the *Picker*  
 3768 *tool* shown in Figure 7.16. As with the grabber tool, the picker tool was held at  
 3769 the tool rack until the gantry head went to its location and catches it using vacuum;  
 3770 an independent vacuum line is used to capture the HDI from its chuck slot. The  
 3771 alignment was performed while the HDI was being moved to the BBM location.

### 3772 Vision system

3773 A vision hardware system, attached to the gantry head, was used to locate the module  
 3774 components and tools employed in the assembly process. It is composed of a IDS HD

3775 digital camera and a Mitutoyo wide-field video microscope unit (WIDE VMU) as  
 3776 shown in Figure 7.6. The vision hardware was complemented with auto-focus and  
 3777 pattern recognition algorithms.

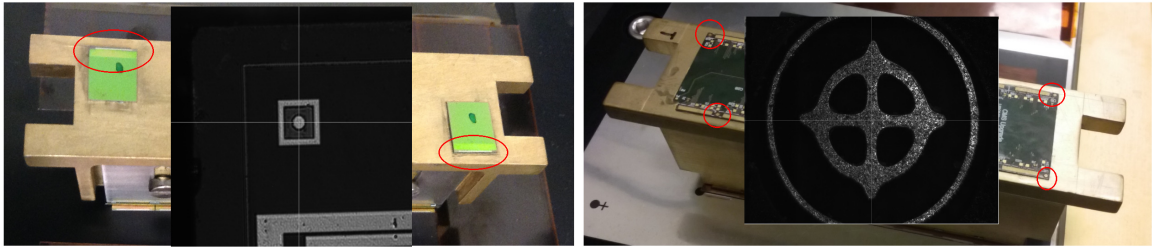


**Figure 7.17:** Fiducial marks attached to the stamp and weight tools. Initially, non-functional ROCs were glued on top of the tools (left) to provide the fiducial marks, which were located in the places indicated by red circles; later they were replaced by plane HDIs (right).

3778 Given that the coarse location of the HDIs, BBMs, stamp and weight tools were  
 3779 well defined by the location of the stencils and plates on the gantry table, the vision  
 3780 system was designed to search for and find fiducial marks present on the materials and  
 3781 tools; these fiducial marks are placed on the HDI and BBM during their fabrication  
 3782 process. In the case of the tools, two methods were used to attach a fiducial mark  
 3783 to them: non-functional ROCs, which have on themselves fiducial marks, were glued  
 3784 on top of the tools as shown in Figure 7.17, however, during the gluing and cleaning  
 3785 processes the fiducial marks were usually covered with glue remainders or broken,  
 3786 making their frequent replacement necessary; the second method consisted of gluing  
 3787 plane HDIs on top of the tools, which not only solved the issues with the destruction  
 3788 of the fiducial marks but also simplified the pattern recognition.

3789 The procedure to find the fiducial marks started by moving the camera to an  
 3790 initial default calibrated position above the element, HDI, BBM or tool, such that  
 3791 the image in the field of view of the camera contains the fiducial mark; then, the auto-  
 3792 focus algorithm found the best focus by measuring the contrast of pictures taken by

3793 the camera at ten different positions in  $z$  direction around a default position where  
 3794 it was assumed the best focus was; these ten contrasts were then fitted to a Gaussian  
 3795 distribution where the maximum of the fitting was assigned to the best focus.

3796 Once the best focus was found, the gantry head moved the camera to that posi-  
 3797 tion, took a new picture and sent it to feed the pattern recognition algorithm which  
 3798 use k-means clustering to separate the foreground from the background; then, the  
 3799 foreground (Fiducial + noise) was dilated to close any small holes in the image and  
 3800 to extract contours from the image.

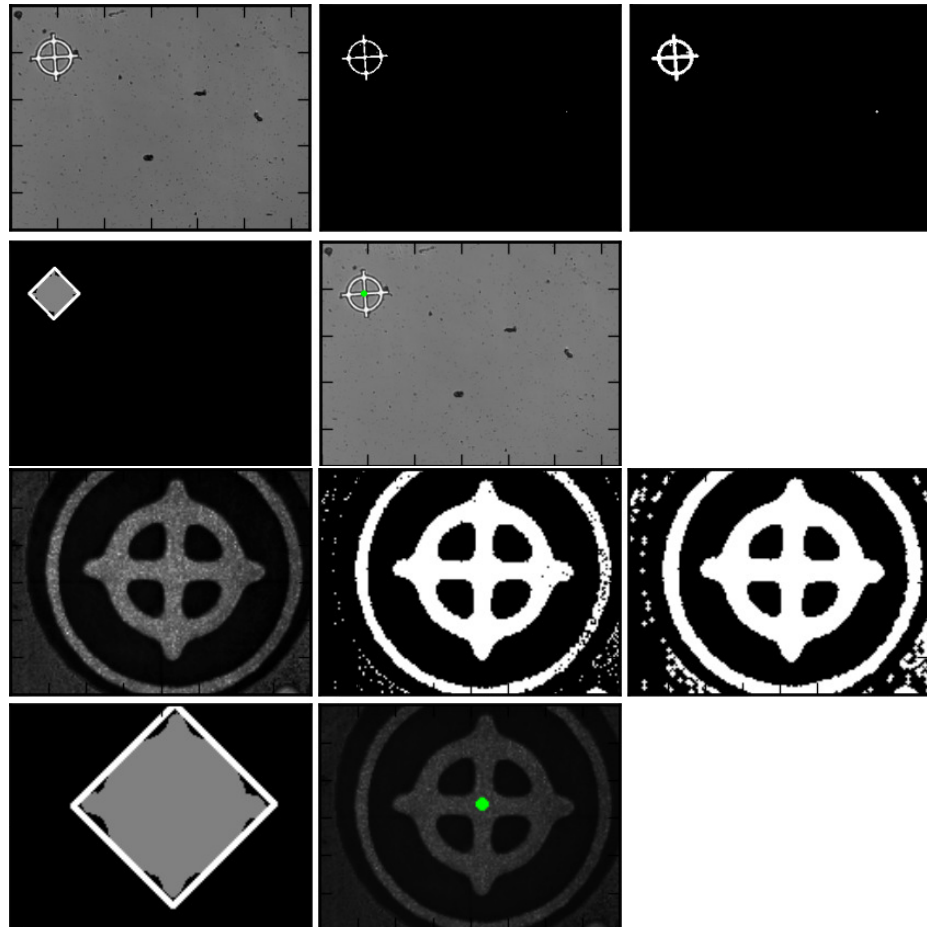


**Figure 7.18:** Fiducial mark recognition: BBM (two top rows) and HDI (two bottom rows). The input image is processed to define contours; after filtering, the centroid of the recognized fiducial mark is returned by the algorithm and indicated in the input image by the green dot.

3801       The fiducial mark features are parametrized in terms of its size and aspect ratio  
 3802      with respect to the field of view of the camera, therefore, by filtering the contours on  
 3803      size and aspect ratio it is assured that one and only one contour passes filters. Later,  
 3804      the algorithm calculates the minimum bounding box and centroid of the fiducial mark  
 3805      to finally return the centroid as fiducial mark center and the distance between centroid  
 3806      and box center as a measure of goodness. In order to reduce the processing time, the  
 3807      input image resolution was reduced by a factor of eight. The algorithm was written  
 3808      by Caleb Fangmeier and is documented in Reference [168] from where Figure 7.18  
 3809      was taken.

3810     **Gantry head center-camera offset (GHCO)**

3811     The *global coordinate system* of the setup is centered in the so-called *home position*  
 3812    located in the back-left side of the gantry table; thus, the origin of the coordinate  
 3813    system is defined by the position of the gantry head center when it is placed at home  
 3814    position. Any distance is then measured by comparing the gantry head center position  
 3815    at a given location and the home position. While the tool adapter is concentric to the  
 3816    gantry head (and then its coordinates are the same as the gantry), the camera has  
 3817    an offset with respect to the origin of the global coordinate system because the vision  
 3818    system is not located at the gantry head center, therefore, any location provided by  
 3819    the vision system has to be corrected by this offset, known as *Gantry head center-*  
 3820   *camera offset (GHCO)*.

3821     To determine the GHCO, a set of 40 marks (scratches) were made on a glass  
 3822    slide using a needle shaped tool with the tip made of carbide (see Figure 7.19);  
 3823    the locations of the scratches were predefined and known as commanded positions.  
 3824    Later, the camera was moved to find the scratches and their locations were tagged  
 3825    as observed positions. In principle, the difference between the commanded and the

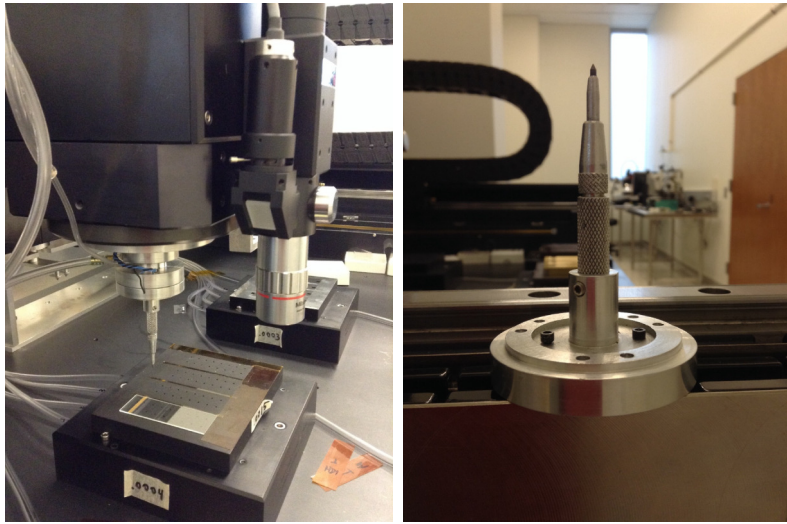


**Figure 7.19:** Setup used to measure the GHCO

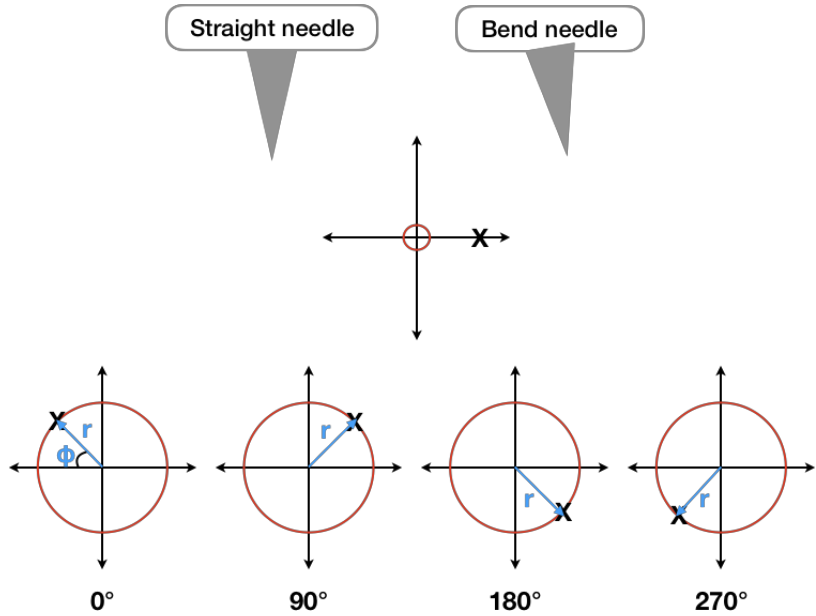


**Figure 7.20:** Scratches scheme if the tool is not straight

3826 observed positions provide a measurement of the GHCO, but it cannot be assumed  
 3827 that the needle tool is straight, i.e., if the tip of the tool coincides with the gantry  
 3828 head center; in order to take into account this fact when calculating the offset, a  
 3829 scratching scheme was designed; it is showed in Figure 7.20. In the ideal case, the

3830 scratch is made right in the commanded position (red circle), but if the needle is not  
3831 straight, the scratch will be shifted (black cross). A rotation of the tool can be used  
3832 to determine how bend is the needle tip.

3833 A precise procedure for measuring the GHCO is performed by a labVIEW program  
3834 (*offset\_fitting.vi*) which implements the following steps

3835 • pick the needle tool from the tool rack,

3836 • move the gantry to the first scratch position (the commanded position),

3837 • make the scratch moving the tool down.

3838 • move the tool back up

3839 • move the gantry to the next scratch commanded position.

3840 • Repeat the process to make nine more scratches.

3841 • Rotate the tool by  $\theta = 90^\circ$  and repeat the process to make ten new scratches.

3842 • Rotate the tool by additional  $90^\circ$  (now the total rotation is  $\theta = 180^\circ$ ) and make  
3843 ten more scratches.

3844 • Rotate the tool by additional  $90^\circ$  (now the total rotation is  $\theta = 270^\circ$ ) and make  
3845 ten more scratches.

3846 • Move the camera to the first scratch position and locate the center of the scratch,  
3847 capture the position.

3848 • Repeat the process to locate the rest of the scratches.

3849 The operator only interacts with the program by capturing the positions. The  
3850 output of the program is a text file that contains all the commanded and observed

3851 positions. The set of measurements are statistically treated, using the linear least  
 3852 squares fitting technique. The model describing the location of the scratches system  
 3853 is parametrized by a linear combination of a set of functions weighted by a set of  
 3854 parameters;

$$y(x) = f(y, \mathbf{a}) = a_1 f_1(x) + a_2 f_2(x) + \dots + a_p f_p(x) \quad (7.1)$$

3855 The residuals, which correspond to the difference between the predicted value  
 3856 from model ( $f(x_i, \mathbf{a})$ ) and the measured value  $y_i$ , are calculated using

$$r_i = y_i - f(x_i \mathbf{a}), \quad (7.2)$$

3857 one wants to minimize these residuals and more specifically their squares ( $S$ ). The fit  
 3858 will provide the values of the parameters  $\mathbf{a}$ , so that the model is totally defined. In  
 3859 matrix form, for a set of measurements  $(x, y)$  :

$$\mathbf{Y} = A\mathbf{a} \quad (7.3)$$

3860

$$S = \mathbf{r}^T \mathbf{r} \quad (7.4)$$

3861 The matrix  $A$  encloses the features of the system/model, the vector  $\mathbf{a}$  encloses the  
 3862 parameters under evaluation and the vector  $\mathbf{Y}$  encloses the taken measurements and  
 3863 the predictions made by the model. After the minimization, the vector of parameters  
 3864 can be written as:

$$\mathbf{a} = (A^T V^{-1} A)^{-1} A^T V^{-1} \mathbf{Y} \quad (7.5)$$

3865 where  $V$  is the covariance matrix; it contains the information about the correlation

3866 among measurements and the uncertainty of the measurements.

$$V = \begin{pmatrix} \sigma_1^2 & \sigma_{12} & \cdots & \sigma_{1n} \\ \sigma_{21} & \sigma_2^2 & \cdots & \sigma_{2n} \\ \vdots & \vdots & \ddots & \vdots \\ \sigma_{n1} & \sigma_{n2} & \cdots & \sigma_n^2 \end{pmatrix} \quad (7.6)$$

3867 The model for one measurement  $(x, y)$ , i.e., only one scratch, can be written as:

$$\begin{pmatrix} x \\ y \end{pmatrix} - \begin{pmatrix} x_g \\ y_g \end{pmatrix} = \begin{pmatrix} \Delta x_{GHCO} \\ \Delta y_{GHCO} \end{pmatrix} + \begin{pmatrix} c & s \\ -s & c \end{pmatrix} \begin{pmatrix} c' & s' \\ -s' & c' \end{pmatrix} \begin{pmatrix} 1 \\ 0 \end{pmatrix} \quad (7.7)$$

3868 where,  $(x_g, y_g)$  are the commanded positions,  $(\Delta x_{GHCO}, \Delta y_{GHCO})$  are the offset com-  
 3869 ponents in  $x, y$  directions respectively,  $c = r \cos \phi$  and  $s = r \sin \phi$  describe the bending  
 3870 of the needle tool in terms of the radius  $r$  of the circle and the angle  $\phi$  (see Figure 7.20);  
 3871  $c' = \cos \theta$  and  $s' = \sin \theta$  describe the rotations of the tool ( $\theta = 0^\circ, 90^\circ, 180^\circ, 270^\circ$ ) with  
 3872 respect to the  $x$  direction.

3873 The matrix A and the vector of parameter **a** can be written as:

$$A = \begin{pmatrix} 1 & 0 & c' & -s' \\ 0 & 1 & -s' & -c' \end{pmatrix}, \quad \mathbf{a} = \begin{pmatrix} \Delta x_{GHCO} \\ \Delta y_{GHCO} \\ c \\ s \end{pmatrix} \quad (7.8)$$

3874 The matrix A, including the full set of forty pairs of measurements  $(x, y)$ , is a  
 3875  $4 \times 80$  matrix where in the first ten rows  $c' = \cos(\theta = 0) = 1, s' = \sin(\theta = 0) = 0$ ,  
 3876 while in the second ten rows  $c' = \cos(\theta = 90) = 0, s' = \sin(\theta = 90) = 1$  and so on.

3877 The offset\_fitting.vi program integrates a Matlab script that solves the matrix  
 3878 equation 7.5, using the commanded and observed positions measured by the vision

3879 system; the uncertainties were assumed to be the same for all measurements and ad-  
 3880 ditionally it was assumed that the measurements are not correlated, so the covariance  
 3881 matrix is the uncertainty ( $\sigma = 0.01\mu\text{m}$ ) times the  $80 \times 80$  identity matrix. The results  
 3882 for the GHCO and the radius are:

$$\begin{aligned}\Delta x_{GHCO} &= 0.482 \pm 0.008\text{mm} \\ \Delta y_{GHCO} &= -102.362 \pm 0.008\text{mm} \\ r &= 0.042 \pm 0.007\text{mm}.\end{aligned}\tag{7.9}$$

3883 **The dispensing system**

3884 The dispensing system components are shown in Figure 7.21. The dispenser and  
 3885 syringe holder were attached to the gantry head as shown in Figure 7.6. The en-  
 3886 capsulant was a mixture of sylgard curing agent and sylgard base elastomer in a  
 3887 proportion 1:10; the volumes were measured using common syringes, and the mixing  
 3888 was performed on a plastic sheet. Several needle tip sizes were tested in order to  
 3889 optimize the amount of sylgard dispensed in agreement with the pressure provided  
 3890 by the dispenser; the needle chosen has an internal diameter of  $150\ \mu\text{m}$ .

3891 The encapsulation process consist of depositing a sylgard trace over the wires  
 3892 connecting the HDI and ths ROC; it is highly dependent not only on the ability to  
 3893 measure the location of the regions to be encapsulated, which is well managed by  
 3894 the vision system, but also on the ability to know with high precision the position of  
 3895 the needle tip, which added to the fact that for each encapsulation session a new set  
 3896 syringe-needle has to be used, demands a robust method to find the needle tip.

3897 The needle tip calibration procedure was implemented using an additional vision

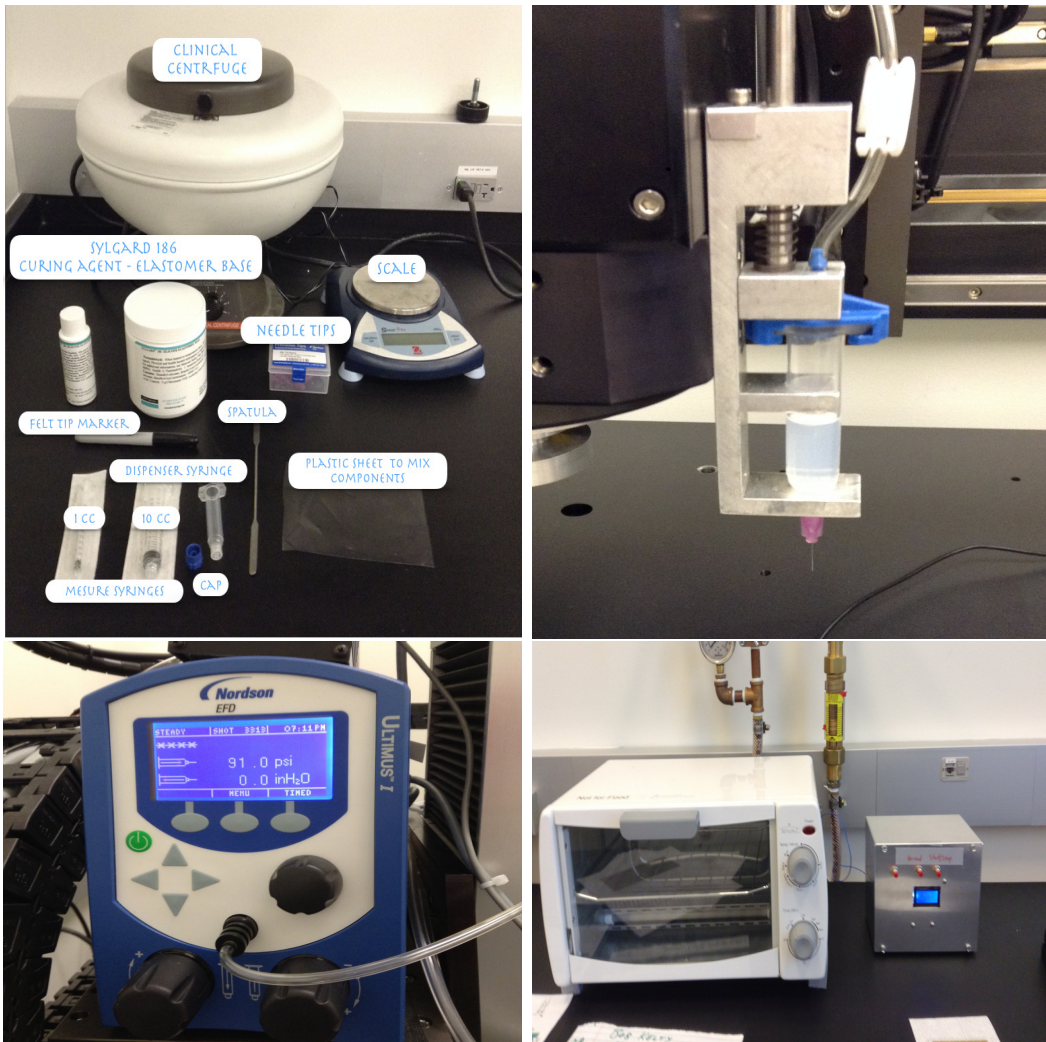


**Figure 7.21:** Dispensing system components.

3898 system composed of two regular web cameras deployed one perpendicular to each  
 3899 other as shown in Figure 7.22, known as *webcam setup*. The reference position acting  
 3900 as the origin of the webcam setup coordinate system (RC) was defined by looking at a  
 3901 ROC placed over a pedestal so that the horizontal plane of the webcams is adjusted;  
 3902 then, using the gantry camera, a fiducial mark on the ROC was located and focused so  
 3903 that the  $z$  coordinate of the fiducial is known ( $RC_z$ ). Later, with a dispenser syringe  
 3904 and a needle tip mounted on the syringe holder, the needle tip was moved to the

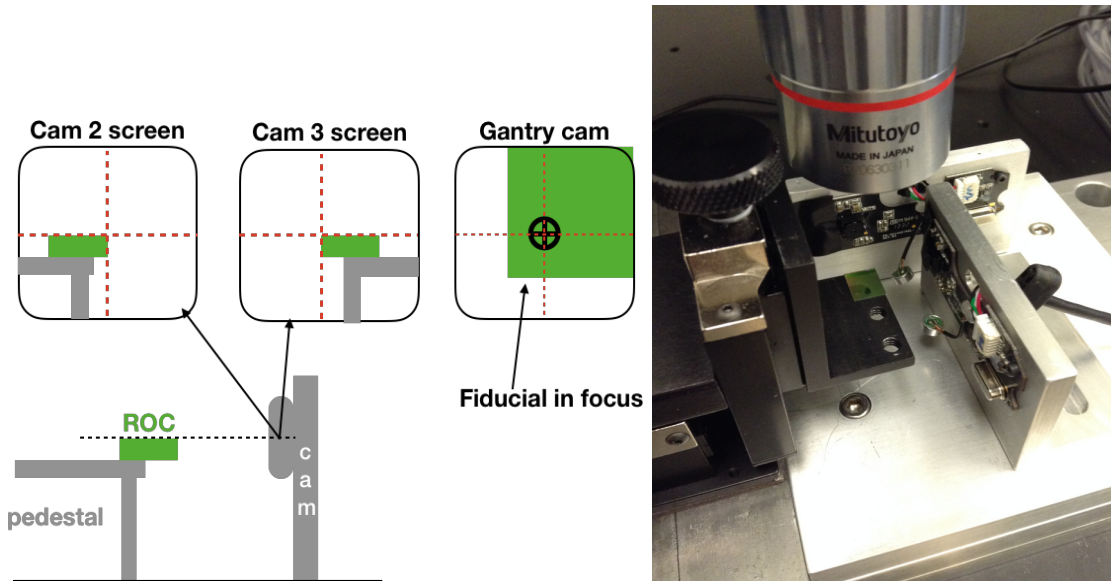


**Figure 7.22:** Webcam setup used to locate the needle tip in 3D.

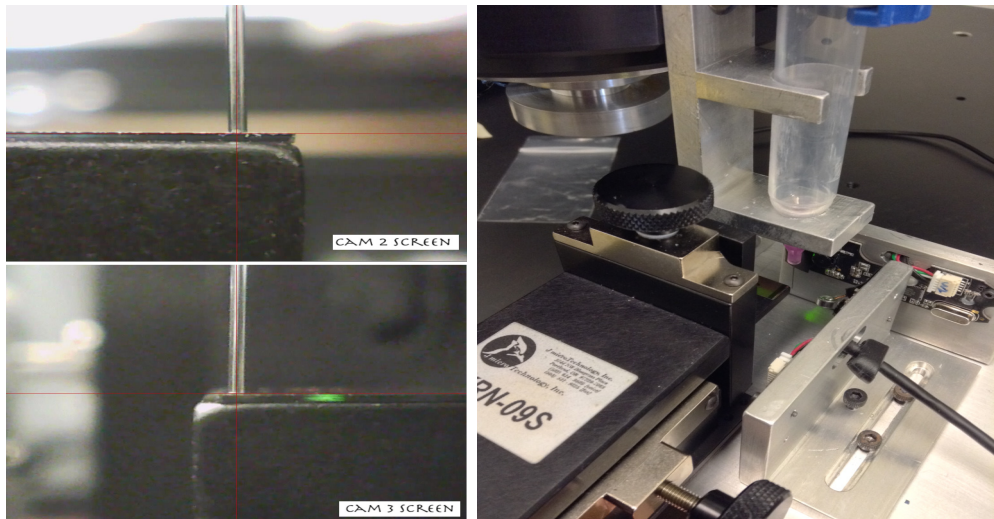


**Figure 7.23:** Webcam setup calibration. The 3D needle tip coordinates define the reference coordinates (origin) of the webcam setup.

3905 position of the fiducial mark on the ROC previously focused; the focuses of webcams  
 3906 were adjusted such that the needle is clearly visible in the screens (see Figure 7.23)  
 3907 and simultaneously in focus for both webcams, while the needle tip is centered in  
 3908 the screen, thus,  $(x, y)$  gantry head coordinates at that position correspond to the

3909  $(RC_x, RC_y)$  coordinates; after the calibration the RC is

$$RC = (17.337, 80.144, 88.486) \text{ mm} \quad (7.10)$$

3910 For any new needle to be used, it is necessary to correct for the needle tip coordi-  
 3911 nates' deviation from the RC; the correction is obtained by moving the new needle tip  
 3912 to the RC position and adjusting the position of the needle tip to get it focused and  
 3913 centered in the webcam setup screens; these modified coordinates (MC) are compared  
 3914 with RC, and the difference is called *Needle Tip Offset* (NTO) (see Figure 7.24); this  
 3915 calibration is connected to the calibration made for the GHCO so that the coordinates  
 3916 provided by the vision system for the regions to be encapsulated are also corrected  
 for the NTO.

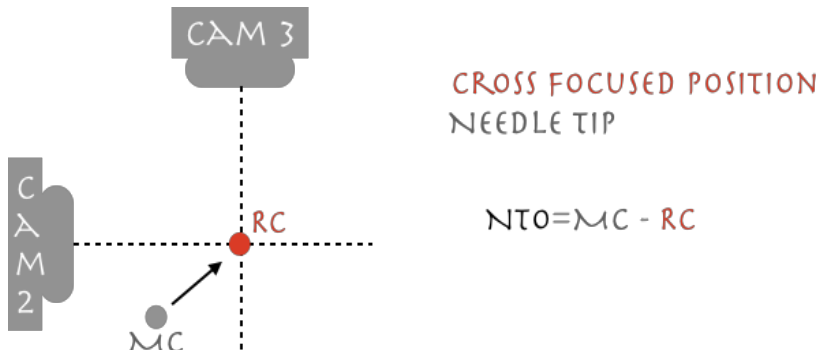


**Figure 7.24:** Needle tip offset measurement.

3917

### 3918 Space-time synchronization of the sylgard deposition

3919 The requirement imposed to the sylgard deposition over the modules, HDI and BBM  
 3920 sides, is to cover all the bond pads including the wire bonds; to do that, several  
 3921 parameters were optimized. First, when the sylgard starts to flow out of the needle,  
 3922 it is necessary that the sylgard drop gets in touch with a surface/object before it gets  
 3923 too heavy to fall down and prevent a continuous flow. Also, it is desired that the

3924 sylgard drop touches the HDI/BBM bondpads/surface first, rather than the wires  
 3925 themselves; in the former case, the sylgard spreads along the surface while in the  
 3926 latter case the sylgard sticks to the wires and it does not spread. Thus, the distance  
 3927 between the needle tip and the surface is a critical factor.

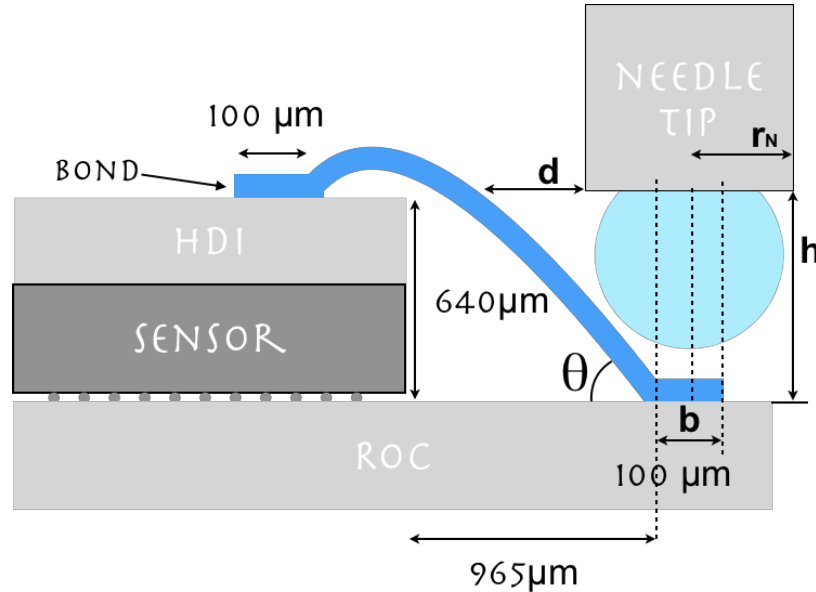


Figure 7.25: Wire bond region.

3928 Figure 7.25 shows a schematic of the wire bond region and some typical dimensions  
 3929 involved. The slope of the wire is about  $34^\circ$  but can vary according to the wirebonding  
 3930 conditions. Going too close to the surface would make the needle tip to touch and  
 3931 break the wires. If the reference to deposit the sylgard is chosen to be the center of  
 3932 the bond, i.e., the center of the needle will be right above the center of the bond, then  
 3933 a simple calculation of the height ( $h$ ) necessary to have the wire at a safe distance  
 3934 from the needle tip is given by

$$h = \left( d + r_N - \frac{b}{2} \right) \tan(\theta) \quad (7.11)$$

3935 where  $d$  is the distance from the needle tip edge to the wire (safe distance),  $r_N$  is the

$\theta(^{\circ})$	d( $\mu\text{m}$ )			
	100	150	200	250
30	207.8	236.7	265.6	294.4
45	360.0	410.0	460.0	510.0
60	623.5	710.1	796.7	883.3

**Table 7.1:** Values of the needle tip height  $h$  ( $\mu\text{m}$ ) for several combinations of parameters  $d$  and  $\theta$ .

3936 external needle radius ( $310\mu\text{m}$ ),  $b$  is the size of the bond ( $100\mu\text{m}$ ) and  $\theta$  describe the  
 3937 slope of the wire. Table 7.1 shows the values of  $h$  for several combinations of  $d$  and  
 3938  $\theta$  ( $r_N$  and  $b$  fixed). Given the typical slope of the wires,  $h = 236.7 \mu\text{m}$  was chosen as  
 3939 the needle tip height.

3940 The next optimization was performed on the parameters defining the sylgard de-  
 3941 position kinematics. The basic sylgard deposition process consists of depositing a syl-  
 3942 gard trace along a path defined by the initial and final positions  $(x_i, y_i, z_i), (x_f, y_f, z_f)$ .  
 3943 To make sure that all the wirebonds are covered, it is necessary to synchronize the  
 3944 dispenser action and the gantry motion. The top side of Figure 7.26 shows an sketch  
 3945 of the gantry speed and dispenser action as a function of the time. When the dis-  
 3946 penser is open the sylgard starts to flow out of the needle, however, the sylgard needs  
 3947 some time to flow out and get touch the surface of the HDI/BBM, thus, there should  
 3948 be a time delay between the dispenser valve opening and the movement of the gantry;  
 3949 it is called  $\Delta t_0$ . Accordingly, after the valve is closed, there is a remaining sylgard  
 3950 flowing, so the valve should be closed before the gantry reaches the end of the way;  
 3951 this time delay is called  $\Delta t_1$ .

3952 To find these time delays, the strategy sketched in the bottom side of Figure 7.26  
 3953 was implemented in a LabVIEW program; it proceeds as follows: with the dispenser  
 3954 needle loaded and mounted on the syringe holder and the needle tip calibrated, a set  
 3955 of sylgard marks are deposited over a glass slide. The first is a control mark at  $x_0$ ,

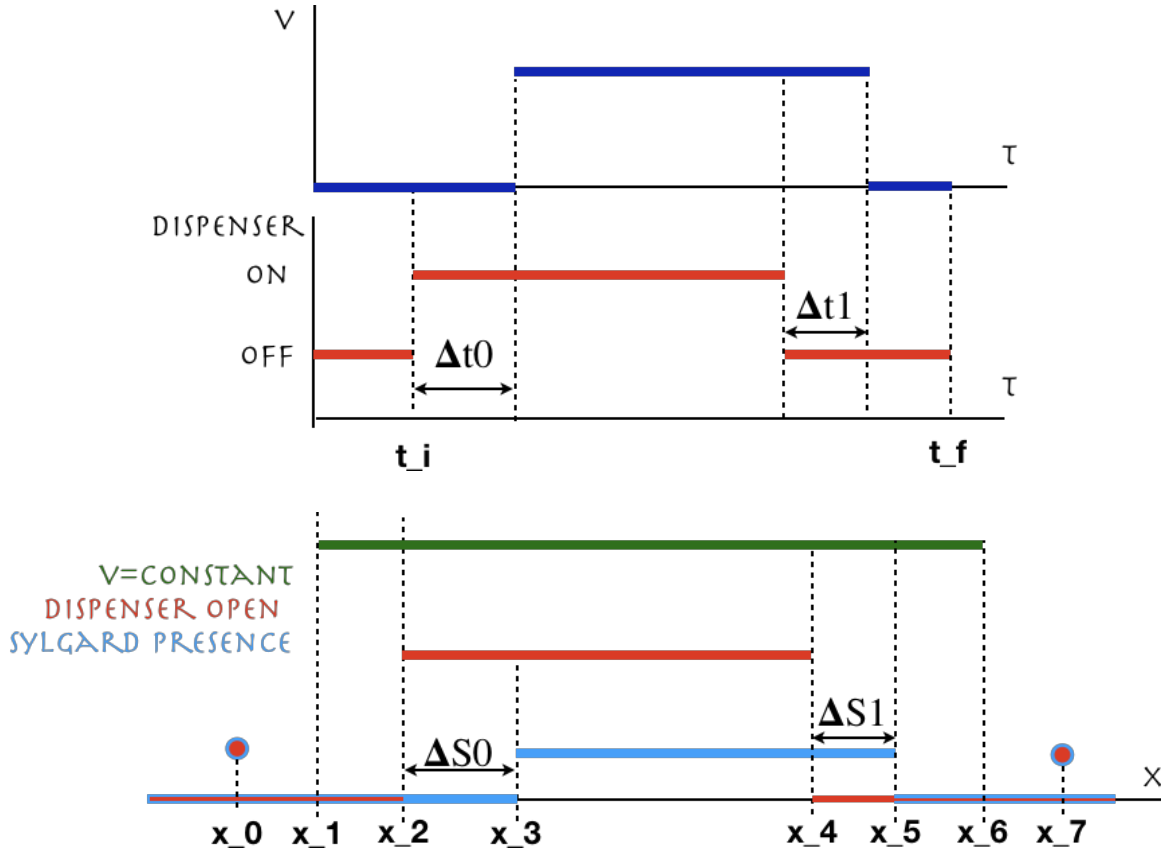


**Figure 7.26:** Sylgard deposition synchronization. Top: sketch of the gantry velocity and dispenser action as a function of the time. Bottom: sketch of the strategy designed to determine the time delays.

3956 then, at  $x_1$  the gantry starts to move at constant speed  $v$ ; at  $x_2$  the dispenser valve is  
 3957 opened; at  $x_3$  the sylgard gets in contact with the glass slide and it starts to spread.  
 3958 At  $x_4$ , the dispenser valve is closed, but some sylgard is still flowing out until  $x_5$ . At  
 3959  $x_6$ , the gantry stops and finally, at  $x_7$  another sylgard control mark is deposited. The  
 3960 time delays are given by

$$\Delta t_0 = \frac{\Delta S_0}{v} = \frac{x_3 - x_2}{v}, \quad (7.12)$$

$$\Delta t_1 = \frac{\Delta S_1}{v} = \frac{x_5 - x_4}{v} \quad (7.13)$$

3961       Figure 7.27 shows the results from two attempts to measure the time delays. In  
 3962       the first attempt, the samples were taken at intervals of five minutes at 1 mm/s; the  
 3963       sylgard traces started to break up after seven samples. The reason of the breaking  
 3964       up is that the sylgard gets thicker with time so that the speed of the gantry needs to  
 3965       be decreased. In the second attempt, the speed was decreased when the breaking up  
 3966       showed up; in total, forty samples spaced by five minutes were taken at six values of  
 3967       the speed (0.6,0.5,0.4,0.3,0.25) mm/s.

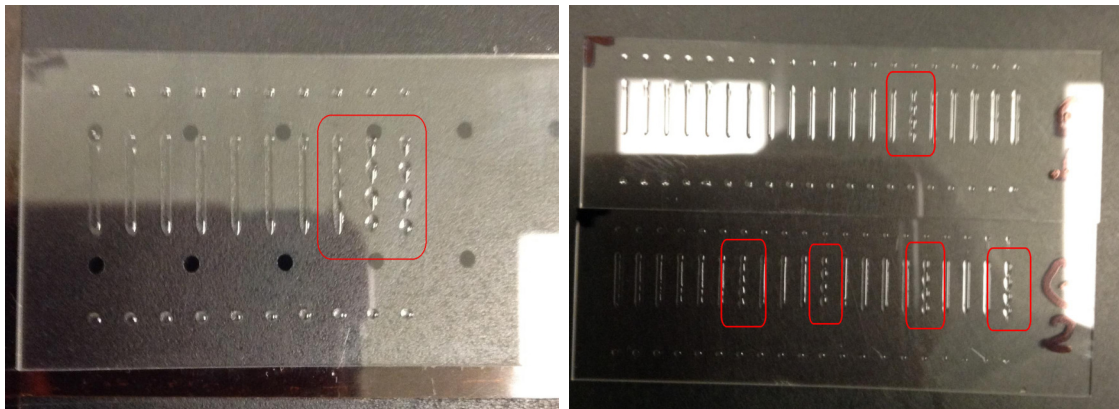


**Figure 7.27:** Time delay measurement. Left: ten samples spaced by 5 minutes at 1mm/s. Right: forty samples spaced by 5 minutes, adjusting the speed to eliminate the breaking up.

3968       Figure 7.28 (top) shows the speed evolution as a function of time for the forty  
 3969       samples; the quadratic fit (modified) corresponds to a function that models a consis-  
 3970       tent reduction of the gantry speed in time such that the breaking up of the sylgard  
 3971       traces is avoided. This fitting function was implemented in the LabVIEW program  
 3972       used to take the samples for the time delay calculation; the results are shown in the  
 3973       bottom side of Figure 7.28 where it is clear that the implementation of the speed  
 3974       function meets the requirements. This speed function is called the *deposition speed*.  
 3975       From this test it is also possible to extract the time delay functions (given that  
 3976       the deposition speed is a function of the time it is expected that the time delays also

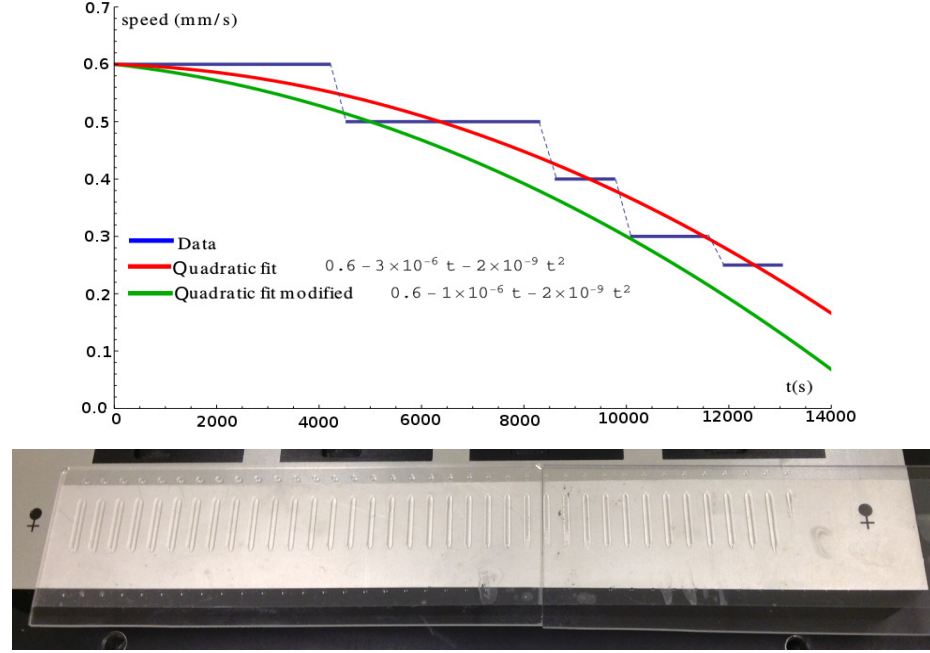


**Figure 7.28:** Top: speed evolution in time for the time delays determination. Bottom: time delays determination experiment after the implementation of the speed function. After 3.5 hours of data taking, there is no sign of sylgard breaking up.

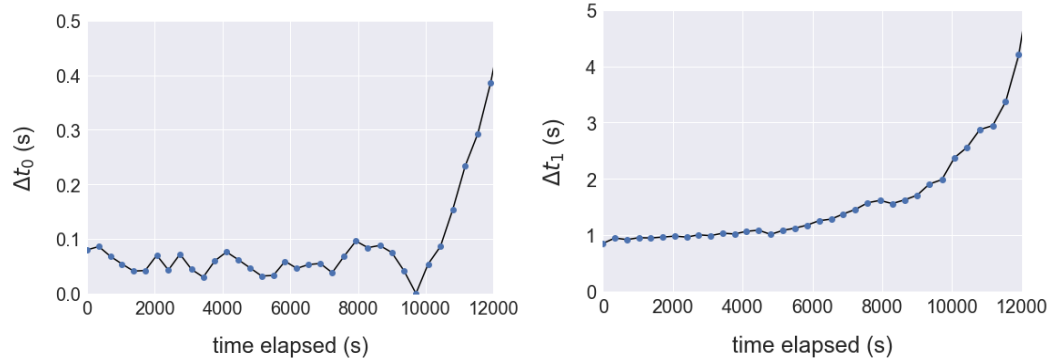


**Figure 7.29:** Time delay functions  $\Delta t_0$  and  $\Delta t_1$ . In the time range of the typical encapsulation process, time delays are approximated by a constant; conservative values were adopted:  $\Delta t_0 = 0.1$  s,  $\Delta t_1 = 1$  s.

3977 depends on time); they are shown in Figure 7.29.

3978 The typical encapsulation time per module is about five minutes, therefore, a full  
 3979 encapsulation session would last about one and a half hours in total, counting the  
 3980 time used to find the fiducial marks on the HDIs/BBMs and the regions where the

3981 sylgard will be deposited. In that time range,  $\Delta t_0$  and  $\Delta t_1$  could be approximated  
 3982 by a constant; a conservative choice was adopted:  $\Delta t_0 = 0.1$  s,  $\Delta t_1 = 1$  s.

3983 **7.5.2 The gluing routine**

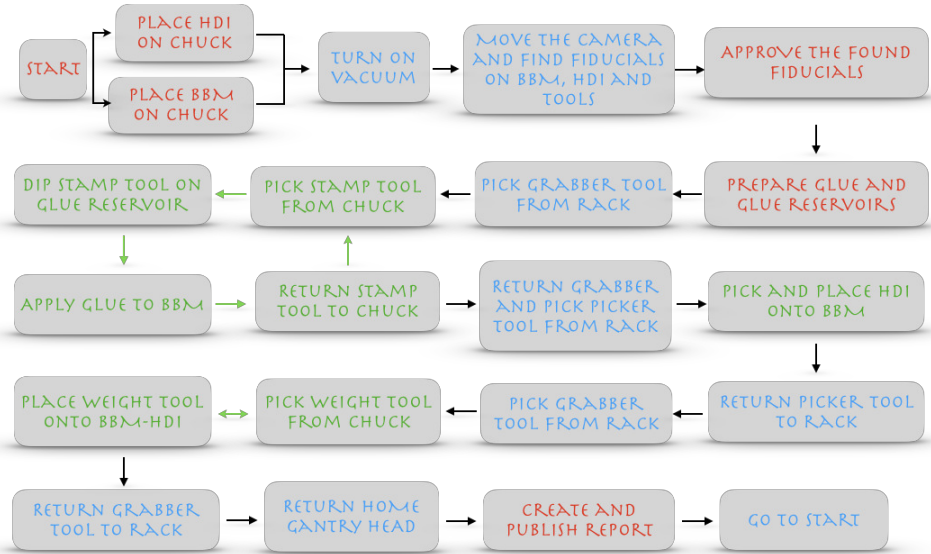


**Figure 7.30:** Gluing routine workflow.

3984 A gluing session was defined as the process where four modules are assembled.  
 3985 The gluing routine workflow is shown in Figure 7.30; steps in blue are those per-  
 3986 formed by the gantry automatically; the green steps represent the steps that are  
 3987 performed repeatedly by the gantry in the same session, and the red steps repre-  
 3988 sent those performed by the operator. The routine was implemented in a LabVIEW  
 3989 program (*Gluing\_main.vi*) that controls the sequence. The *Main front panel* of the  
 3990 gluing routine, shown in Figure 7.31, gathers the most relevant information about  
 3991 the gluing session, while each step in the routine has its dedicated front panel. The  
 3992 module gluing sequence begins by manually placing pre-tested BBMs, HDIs and tools  
 3993 on their chucks.

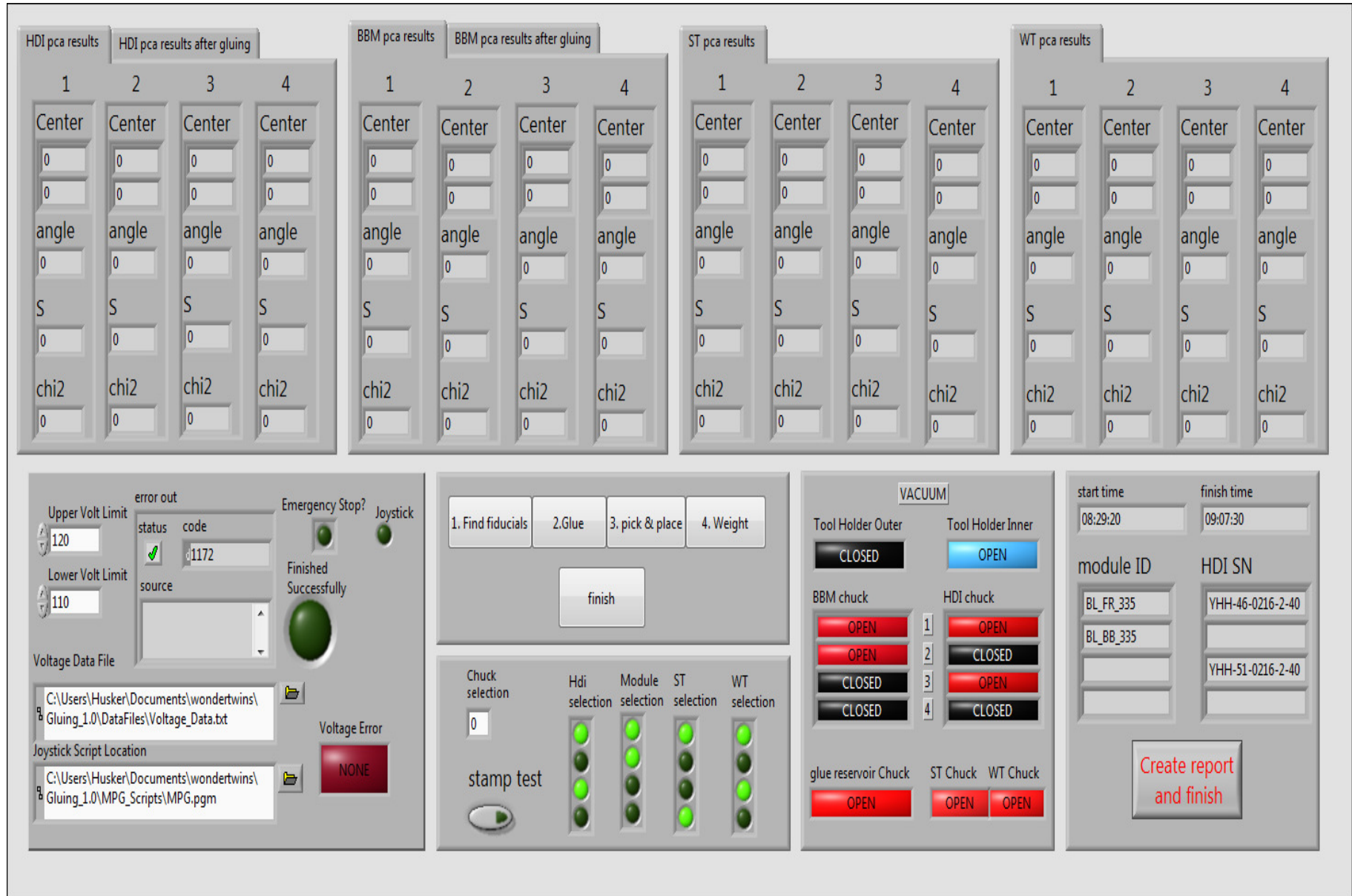
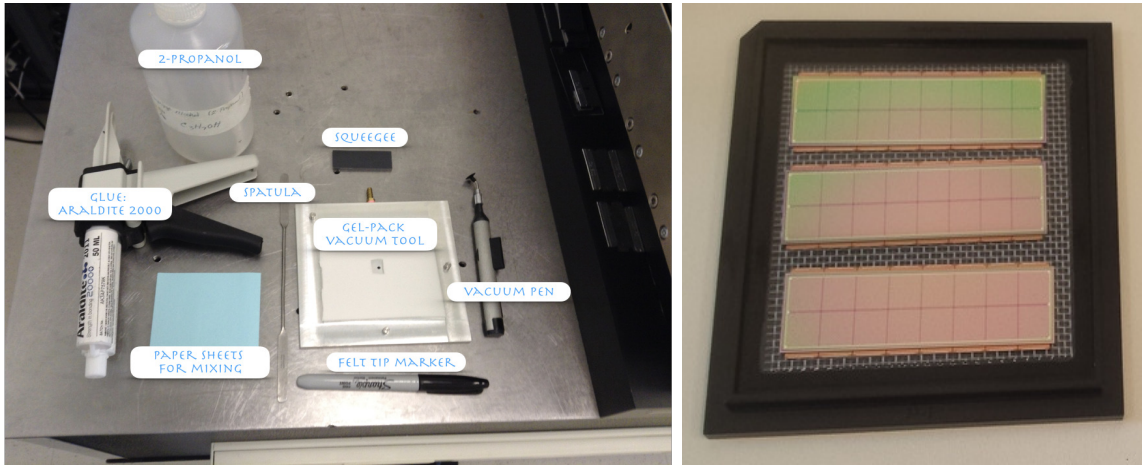


Figure 7.31: Gluing routine LabVIEW front panel.

3994       Figure 7.32 shows the materials used during the gluing session; the square alu-  
 3995 minum tool is used to hold the BBM's container while the vacuum pen is used to  
 3996 manipulate the BBMs.



**Figure 7.32:** Materials used during gluing stage (left). BBMs on container(right).

3997       Once the parts are in place, and the program is run, the BBM and HDI iden-  
 3998 tification information (serial numbers) is collected<sup>2</sup> in the first step as well as the  
 3999 configuration of the gantry table, i.e., the BBM/HDI slots and tools to be used so  
 4000 that the vacuum system is properly activated.

4001       The camera is moved to view, recognize and find the fiducials locations on the  
 4002 BBMs, HDIs and tools. These locations are stored and shown in the Main and *Find*  
 4003 *fiducials* front panels so that the operator can identify abnormal values from extreme  
 4004 misalignment and pattern recognition fails; that usually occurs when the plates are  
 4005 not properly placed on the chucks and/or when the fiducials do not appear in the  
 4006 camera field of view. In those cases, a manual fiducial finding option is available. The  
 4007 find fiducial front pannel is shown in Figure 7.33 and a sample of the found fiducials  
 4008 on a HDI and a BBM is shown in Figure 7.34 indicating the located center of the  
 4009 fiducial with a green dot.

<sup>2</sup> A batch numbering strategy was designed to identify the modules internally at UNL.

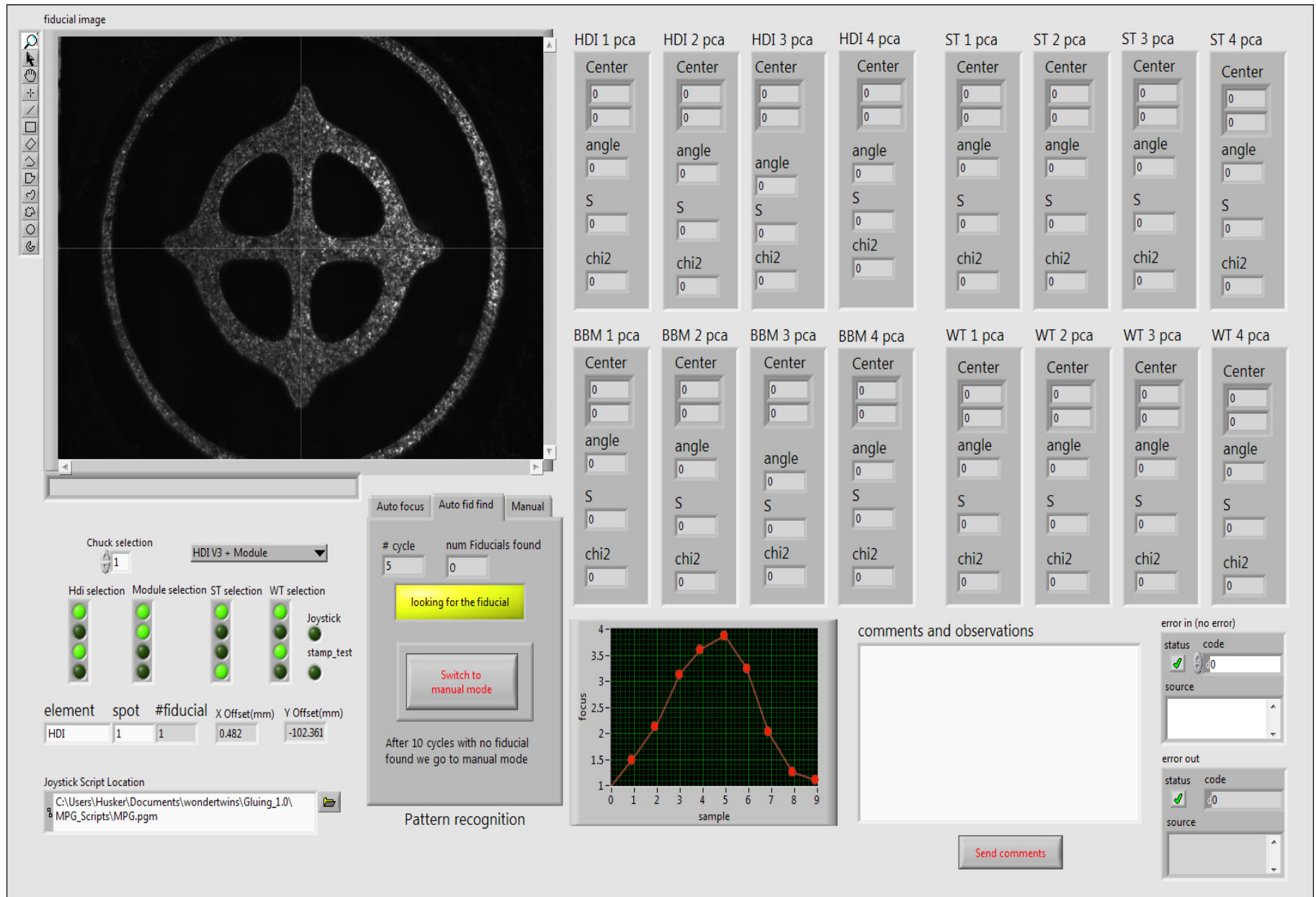
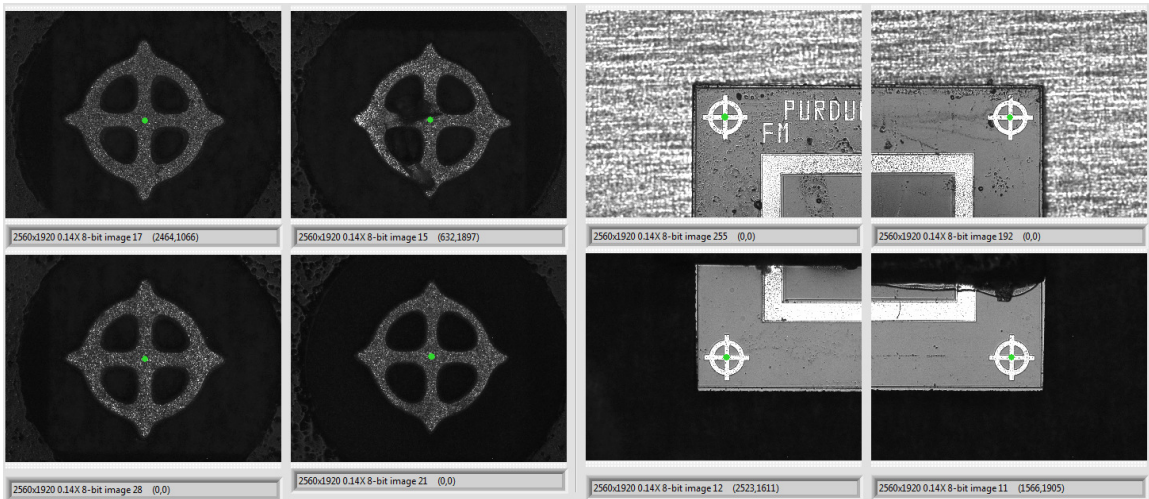


Figure 7.33: Fiducial finder LabVIEW front panel.

4010 After all the fiducials are identified, the operator has to check them and perform  
 4011 the necessary adjustments. Usually, the glue was prepared in parallel to the fiducial  
 4012 identification, reducing the session time.



**Figure 7.34:** Fiducial finder step LabVIEW front panel.

4013 The glue application step starts by picking up the grabber tool from the tool  
 4014 rack, and grabbing the stamp tools from their chuck; after dipping the stamp tool in  
 4015 the glue reservoir, the epoxy is dispensed on the BBMs. The procedure is repeated  
 4016 as many times as the number of modules involved in the session, each time using a  
 4017 different stamp tool and a different glue reservoir slot. The step finishes by returning  
 4018 the grabber tool to the tool rack. The routine provides full freedom to choose any  
 4019 available combination of stamp tool, glue reservoir slot and BBM; this feature is  
 4020 particularly useful for glue testing and commissioning. The grabber tool is then  
 4021 returned to the tool rack and the picker tool is picked, so that the HDIs are picked  
 4022 from their plate slots and placed on top of the BBMs (making the alignment with  
 4023 respect to BBMs); again, the routine allows for different combinations of BBM-HDI.  
 4024 The front panels for both, gluing and pick-and-place steps, are shown in Figure 7.35.  
 4025 Later, the picker tool is returned to the tool rack.

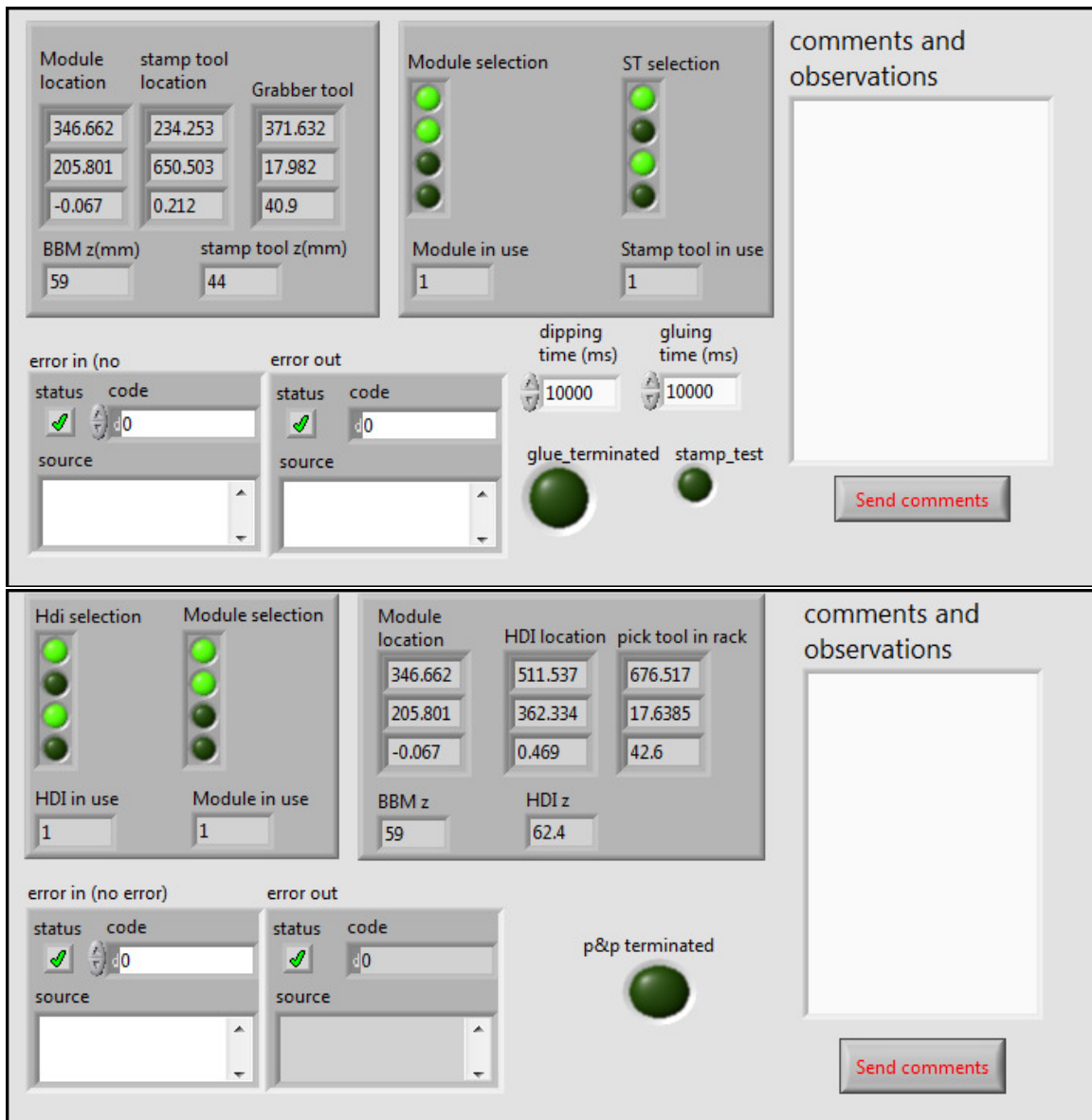


**Figure 7.35:** Gluing (top) and pick-and-place (bottom) LabVIEW front panels.

4026 In the weight step of the routine, the grabber tool is picked again from the tool  
 4027 rack in order to move the weight tools from their plate slots to the BBM locations.  
 4028 The front panel for this step is similar to the gluing front panel. Later, the grabber  
 4029 tool is returned to the tool rack and the gantry head is moved back to the home  
 4030 position. Figure 7.36 shows pictures of the glue reservoir plate loaded with glue,

4031 BBMs after the glue deposition, BBM-HDI after pick-and-place, and weight tools  
 4032 over the assembled modules.

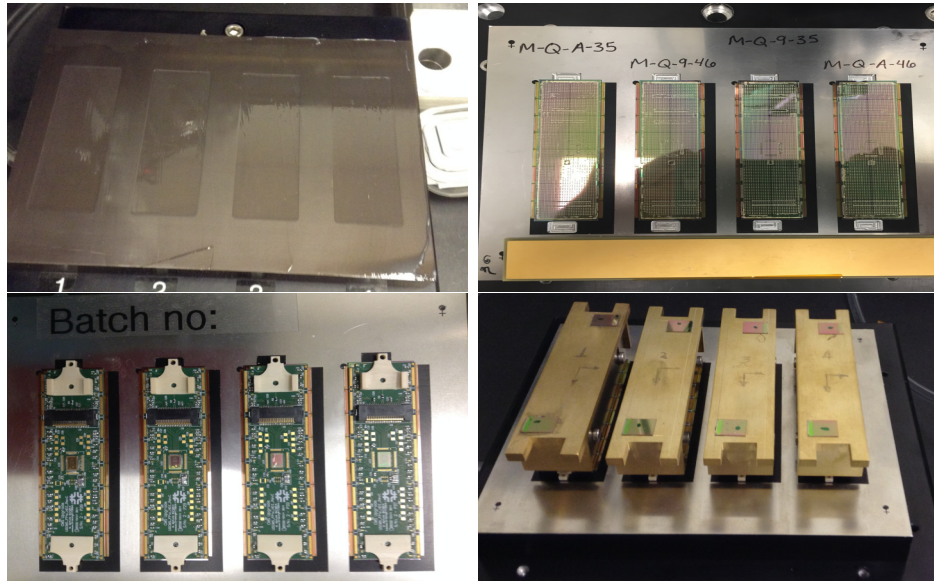


**Figure 7.36:** Gluing steps pictures. Top: glue reservoir loaded (left), glue dispensed on BBMs (right). Bottom: BBM-HDI after pick-and-place(left), weight tools over assembled modules(right).

4033 The last step of the routine consists of creating and publishing the gluing ses-  
 4034 sion report (see Figure 7.37) in the UNL silicon lab electronic logbook (ELOG) and  
 4035 updating the database created to keep track of the assembly progress.

4036 At the end of the full cycle, the stamp plate with stamp tools is moved to be  
 4037 cleaned thoroughly using water and 2-propanol at a sink outside the clean room;  
 4038 They are allowed to dry and then brought back to gantry table. The assembled  
 4039 modules are left to cure eight hours, typically overnight. The fully detailed SOP  
 4040 (SOP-103) for the gluing stage can be found in Reference [169], while several videos  
 4041 showing the gluing routine in action can be found in References [170, 171].

Manufacturing of modules: Glued HDI on BBM

---

Procedure performed according to SOP 103-v0

---

**Date:** 7/3/2016

**Finish time:** 3/7/2016-09:07:30

**Start time:** 3/7/2016-08:29:20

**pressure:** 69

**operator:** Jmonroy

**Araldite batch no. :** ADE0254200

**Software version:** dev

**Object status updated in Purdue database (Justify in comments):** yes

---

List id of parts involved in table below:

**Chuck No. :2**

BBM ID	HDI S/N
BL FR 335	YHH46-0216-2-40
BL BB 335	
	YHH51-0216-2-40

Special observations and comments:

Orientation:

Glueing:

Pick&place:

Weight:

Others:

**Figure 7.37:** Gluing session report.

### 4042 7.5.3 The encapsulation routine

4043 Following the assembly, HDIs were wirebonded to the ROCs using a semi-automated  
 4044 ultrasonic wirebonding machine. Pull tests of wirebonds were performed on a sample  
 4045 of modules for quality control; a picture of one of the sixteen ROCs wirebonded to  
 4046 its HDI counterpart is shown in Figure 7.38. The wirebonds were encapsulated with  
 4047 an elastomeric compound in order to protect them from mechanical damage and to  
 4048 avoid possible shortcut circuits.

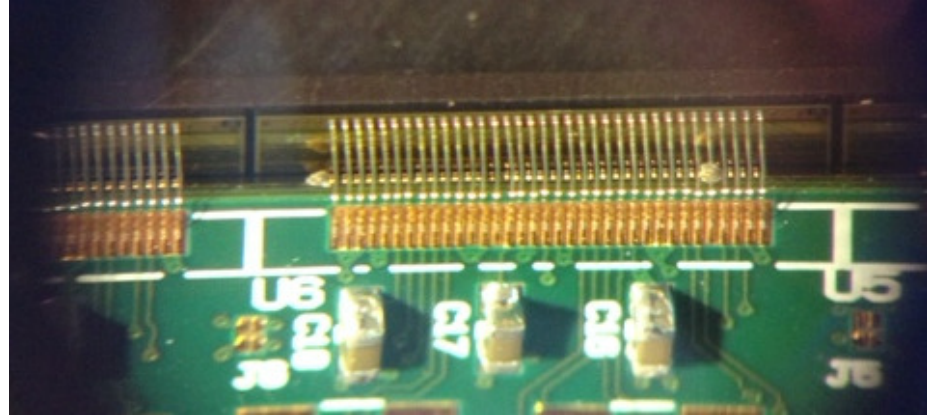


**Figure 7.38:** ROC-HDI wirebonding.

4049        The encapsulation was performed using the robotic gantry and the dispensing  
 4050 system described in Section 7.5.1; the step by step instructions are documented in  
 4051 SOP-105 [172]. After the wirebonding, the plates with the modules were taken back to  
 4052 the gantry table and placed in the BBM chucks. The encapsulation strategy is based  
 4053 on a simple routine: by stating the initial conditions, i.e., the initial ( $R_i$ ) and final  
 4054 ( $R_f$ ) reference positions, the time elapsed after sylgard preparation, time delays, and  
 4055 needle tip location, the gantry head is moved to  $R_i$  and the encapsulant is deposited  
 4056 following the structure sketched in Figure 7.26 (top). The sylgard trace is required  
 4057 to fully cover the HDI/BBM bond pads without spreading out in between the sensor  
 4058 and the ROC.

4059        An encapsulation session was defined as the process where eight modules are en-  
 4060 capsulated following the encapsulation routine workflow shown in Figure 7.39; steps  
 4061 in red correspond to actions performed by the user; steps in blue are those performed  
 4062 by the gantry automatically while the step in green is performed by the gantry re-  
 4063 peatedly during the same encapsulation session. The routine was implemented in a  
 4064 LabVIEW program controlling the sequence, taking advantage of the routines created  
 4065 during the implementation of the gluing stage.

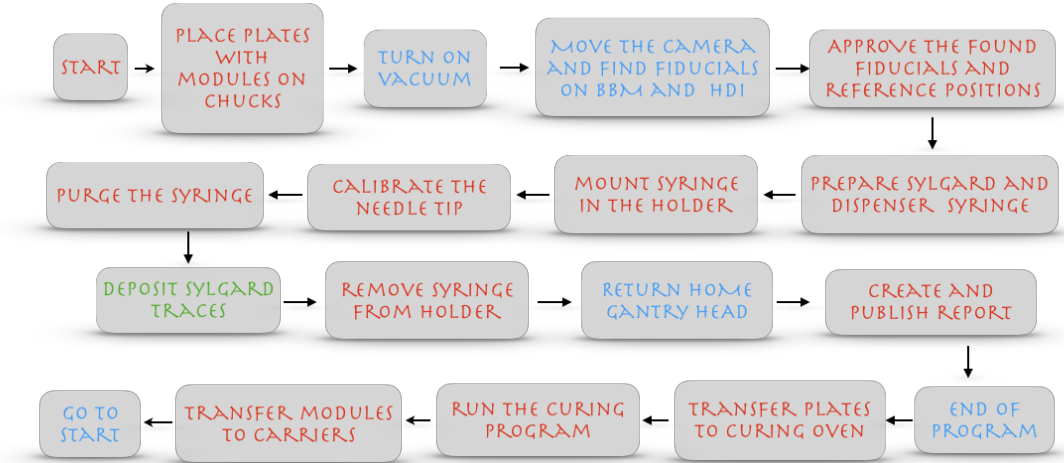


**Figure 7.39:** Encapsulation workflow. Steps in red correspond to interactions with the user; steps in blue are those performed by the gantry automatically while the step in green is performed by the gantry repeatedly during the same encapsulation session.

4066        The main routine is composed of two steps, although each step involves more than  
 4067        one substep. Again, the most important information about the session is gathered  
 4068        in the main front panel as shown in Figure 7.40. The encapsulation routine involves  
 4069        much less vacuum manipulation given that there are no movable elements.

4070        The module encapsulation sequence begins by moving the wirebonded modules  
 4071        from the storage cabinet to the chucks; since the session involves eight modules,  
 4072        only two chucks are made available in the routine. Once the module identification  
 4073        information and gantry table configuration are provided by the operator, the vacuum  
 4074        is activated accordingly.

4075        In the first step, the vision system is used to locate the fiducial marks on the  
 4076        BBMs and HDIs, the same used in the gluing stage, and the reference positions that  
 4077        define the sylgard traces to be deposited.

4078        These reference positions  $R_i$  and  $R_f$  define the length of the sylgard trace as shown  
 4079        in Figure 7.41; they are determined from the bond pad locations which in turn are  
 4080        found using the information from the BBM/HDI design technical specifications,

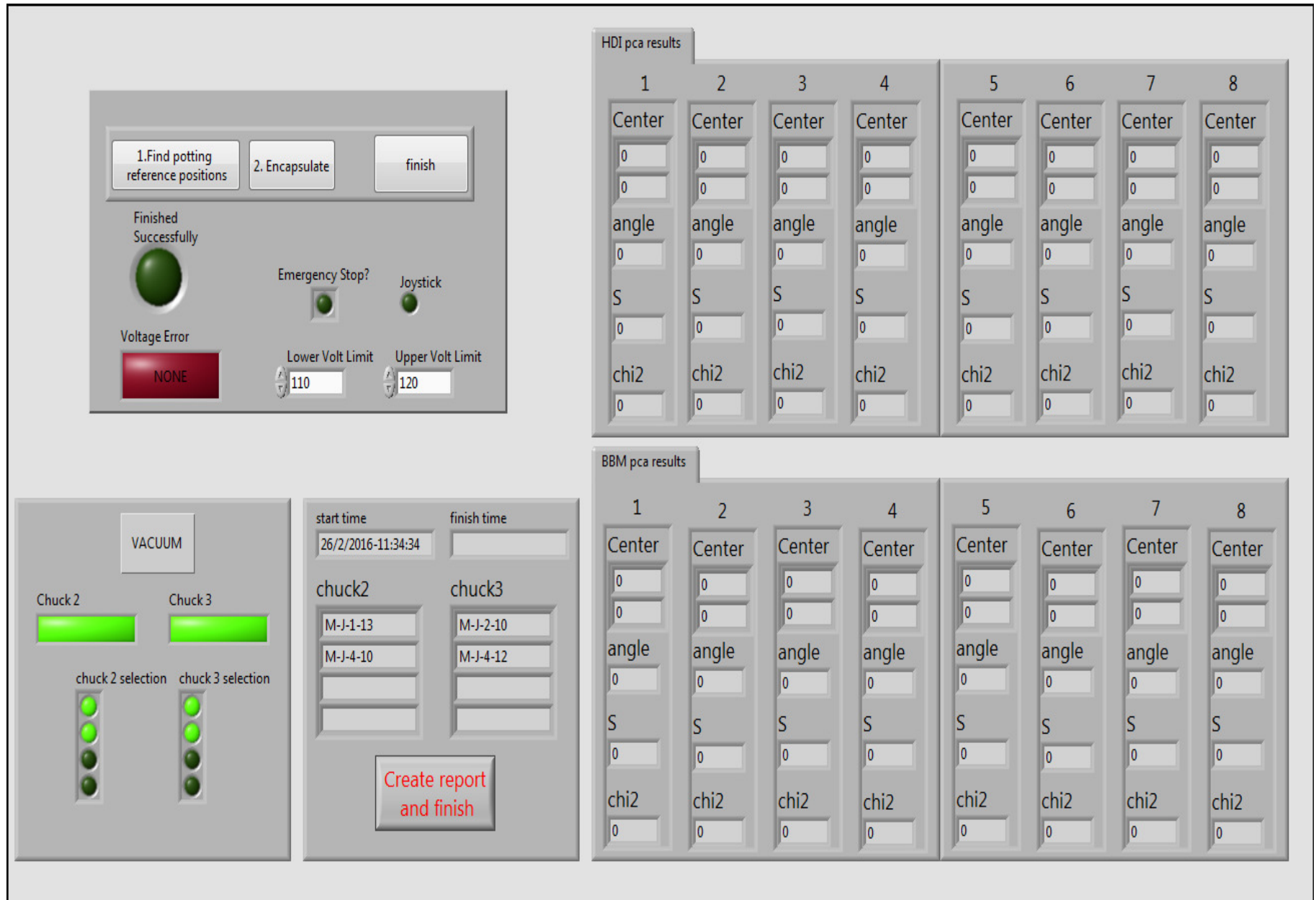
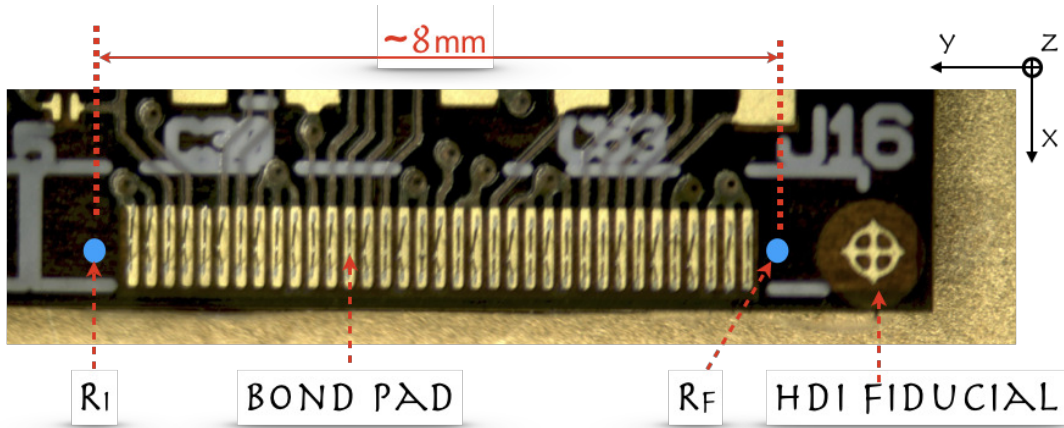


Figure 7.40: Encapsulation LabVIEW main front panel.

i.e., knowing the location of the fiducial marks on the BBM/HDI, it is possible to locate with precision the location of the bond pads. Originally,  $R_i$  was identified with the center of the first bond pad, while  $R_f$  was identified with the center of the last bond pad; however, the initial testing showed that this identification resulted in some of the pads not being fully covered. At first, the proposed solution was to extend  $\Delta t_0$  and eliminate  $\Delta t_i$  which would increase the amount of sylgard in the trace ends, but further testing showed that the additional amount of sylgard, resulting from an extended  $\Delta t_0$ , did not provide a full solution. A simple solution was to move the reference positions a bit away from the bond pad center as showed in Figure 7.41; this adjustment was implemented in the routine.



**Figure 7.41:** Encapsulation region. The sylgard trace, defined by the reference positions  $R_i$  and  $R_f$ , is required spread out to fully cover the bond pads.

In general, the sylgard trace lives in 3D because the module is not perfectly aligned with respect to the gantry coordinate system (and neither is the HDI) and even though the ROCs are flat the HDI could be bent; therefore, the gantry motion during the sylgard deposition is carried out in 3D. The displacements in each direction are determined from the reference positions and the motions are done in the same time interval, thus, the speed for each direction is different; however, the displacement

4097 in  $y$ -direction, i.e., the length of the set of bond pads which is about 8 mm, is much  
4098 larger than the displacement in  $x$  and  $z$  directions, which are expected to be about 10-  
4099 50  $\mu\text{m}$ , so essentially the speed in  $y$ -direction is essentially the same as the deposition  
4100 speed.

4101 The fact that the HDI is not perfectly flat implies that even though the technical  
4102 specifications can provide a very precise estimation of the references in the  $x - y$   
4103 plane and to some extend the information from the fiducials locations can provide a  
4104 measurement of the variation in  $z$ -direction, it is still necessary to set the reference  
4105 positions independently for each sylgard trace in order to foreseen any bump in the  
4106 HDI.

4107 After the reference positions have been determined, they are approved by the  
4108 operator or adjusted according to the parameters described above; in case of failure,  
4109 a manual mode is available. Figure 7.42 shows pictures with the reference positions  
4110 chosen for a module.

4111 The next step is the sylgard preparation; 1 cc of sylgard elastomer are mixed with  
4112 0.1 cc of curing agent over a plastic sheet and then transferred to the dispenser syringe  
4113 using the spatula. Later, the dispenser syringe is placed in a clinical centrifuge in  
4114 order to eliminate the air bubbles; finally the dispenser syringe is installed in the  
4115 syringe holder attached to the gantry head. This process takes about ten minutes  
4116 and is required to be done in the shortest time possible given that sylgard gets thicker  
4117 with time; the mixing time has to be noted and input into the program in order to  
4118 control the deposition speed.

4119 The needle tip is installed once the dispenser syringe is mounted in the holder,  
4120 then, the needle tip calibration is performed using the webcam setup; before to start  
4121 dispensing the sylgard, the syringe is purged to eliminate the air trapped between the  
4122 syringe mouth and the needle tip.

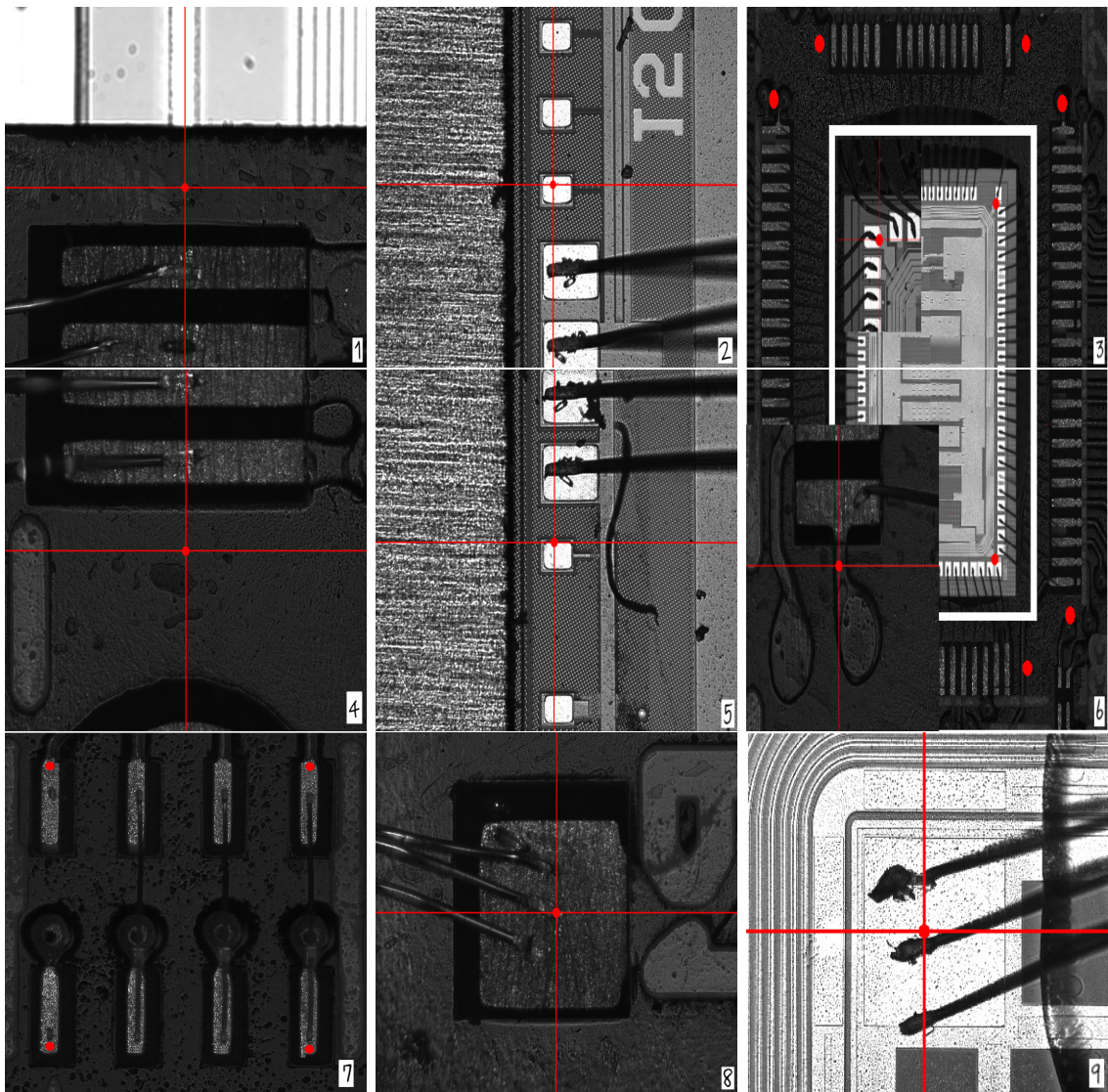


**Figure 7.42:** Encapsulation reference positions for one module. 1 and 4 show the reference positions for one of the HDI bond pads sets, while 2 and 5 show the corresponding reference positions for the bond pads on the BBM side. 3 and 6 show the reference points for the TBM; 7, 8 and 9 show the reference positions for the address pads, the HV pad on HDI and the HV pad on BBM respectively.

4123 In total, the encapsulation of one module is composed by 32 sylgard traces covering  
 4124 the bonds connecting the HDI and each of the 16 ROCs per module, eight sylgard  
 4125 traces covering the bonds connection the TBM and the HDI, two sylgard traces  
 4126 covering the bonds of the address pads, and two sylgard drops covering the HV pads;

4127 each module is encapsulated in about five minutes. Figure 7.43 shows the sylgard  
 4128 deposition front panel.

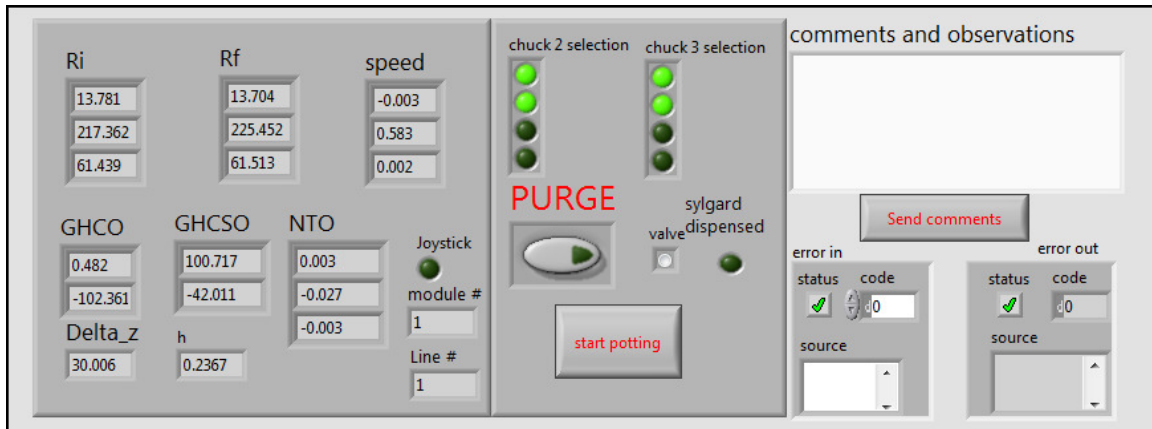


**Figure 7.43:** Sylgard deposition LabVIEW front panel.

Manufacturing of modules: Glued HDI on BBM

---

Procedure performed according to SOP 105-v0

---

Date: 1/29/2016	Finish time: 29/1/2016-17:49:38
Start time: 29/1/2016-16:45:27	pressure: 89.5
operator: Jmonroy	Sylgard batch no. : 8092903
Software version: dev	
<i>Object status updated in Purdue database (Justify in comments): yes</i>	

---

List id of parts involved in table below:

UNL batch(es) No.:na

Chuck2	Chuck 3
M-H-1-29	M-H-1-43
M-G-2-26	M-H-2-26

Special observations and comments:

Orientation:

Encapsulation:

Others:

**Figure 7.44:** Encapsulation session report.

4129 After the sylgard deposition step, the syringe is removed from the holder and the

4130 gantry head goes back to home position. The work at the gantry table ends with the  
 4131 generation and publication of the encapsulation session report (see Figure 7.44).

4132 At the end of the full cycle, a visual inspection of the sylgard traces is performed in  
 4133 order to ensure the quality of the encapsulation; in case of defects, the encapsulation  
 4134 procedure is repeated taking the reference positions in agreement with the regions  
 4135 that are not fully sylgard-covered. Several videos showing the encapsulation routine  
 4136 in action can be found in Reference [171].

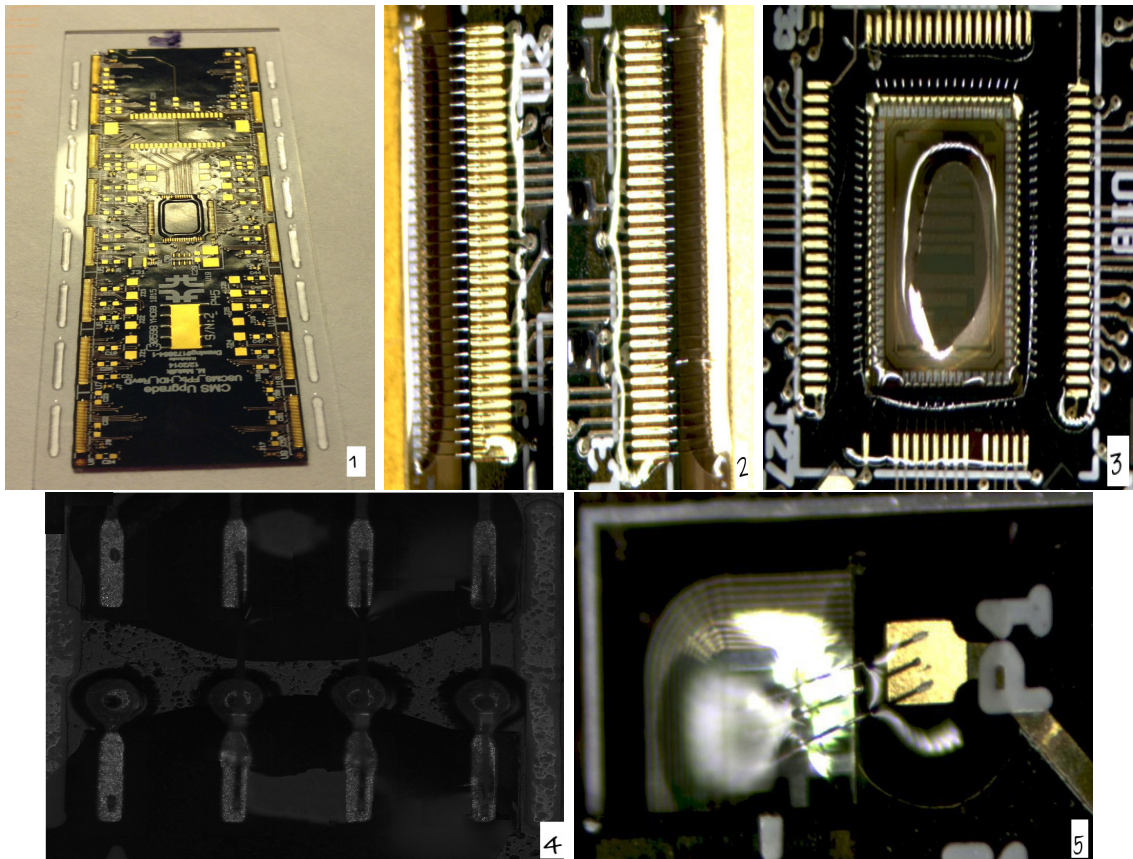


**Figure 7.45:** Encapsulation results. 1 shows an encapsulation test. 2-5 show the results from a module encapsulation for two sets of ROC-HDI traces, TBM, address pads and HV pads respectively.

4137 Later, the plates with the encapsulated modules were transferred into the curing  
 4138 oven where they are submitted to a thermal cycle keeping them at 50 C for one hour.

4139 The curing procedure is not included in the encapsulation routine and no details are  
4140 provided about it in this document. Figure 7.45 shows a picture of an encapsulation  
4141 test using a plain HDI glued on a glass slide; also, pictures of an encapsulated module  
4142 confirming the quality of the encapsulation.

4143 The module assembly sites were also responsible for the testing and characteriza-  
4144 tion of the assembled pixel modules; therefore, modules were tested at room temper-  
4145 ature ( $\sim 17$  C) while monitoring ROC digital and analog currents. The very last step  
4146 in the production line was the shipment to the X-ray characterization site located  
4147 at the University of Kansas. Figure 7.46 shows a module in the carrier ready to be  
4148 shipped; a plastic lid, not shown, was used to fully cover the module.

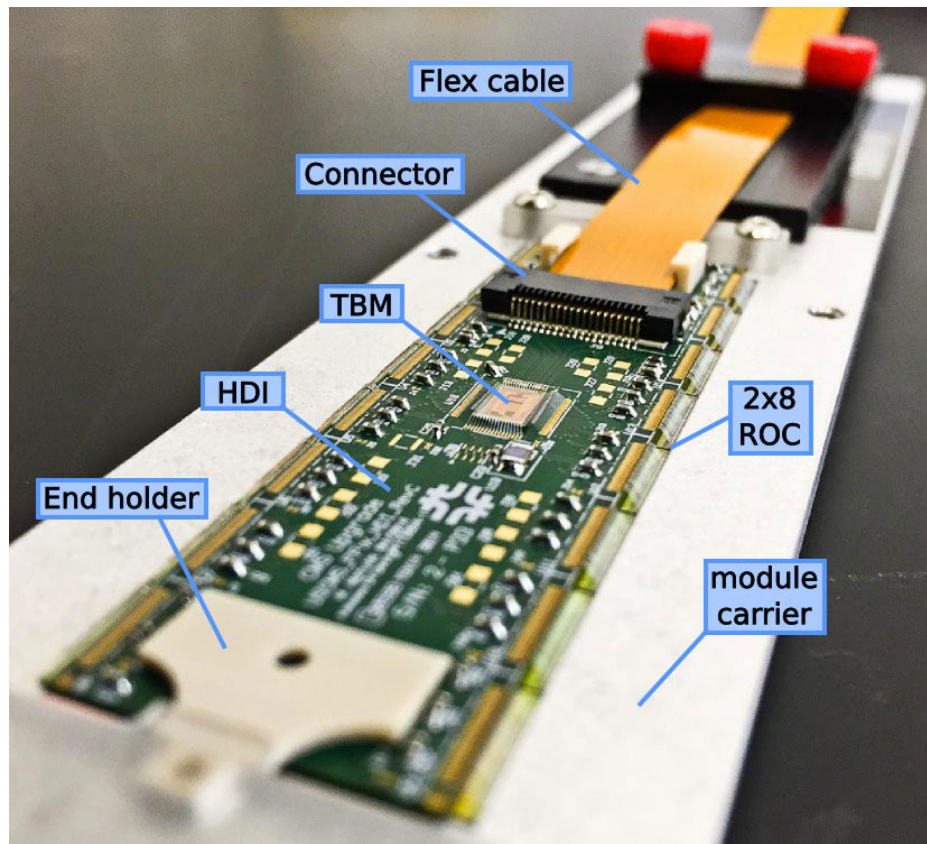


**Figure 7.46:** Module in carrier. A plastic lid was used to fully cover the module.

4149 **7.5.4 FPix module production yields**

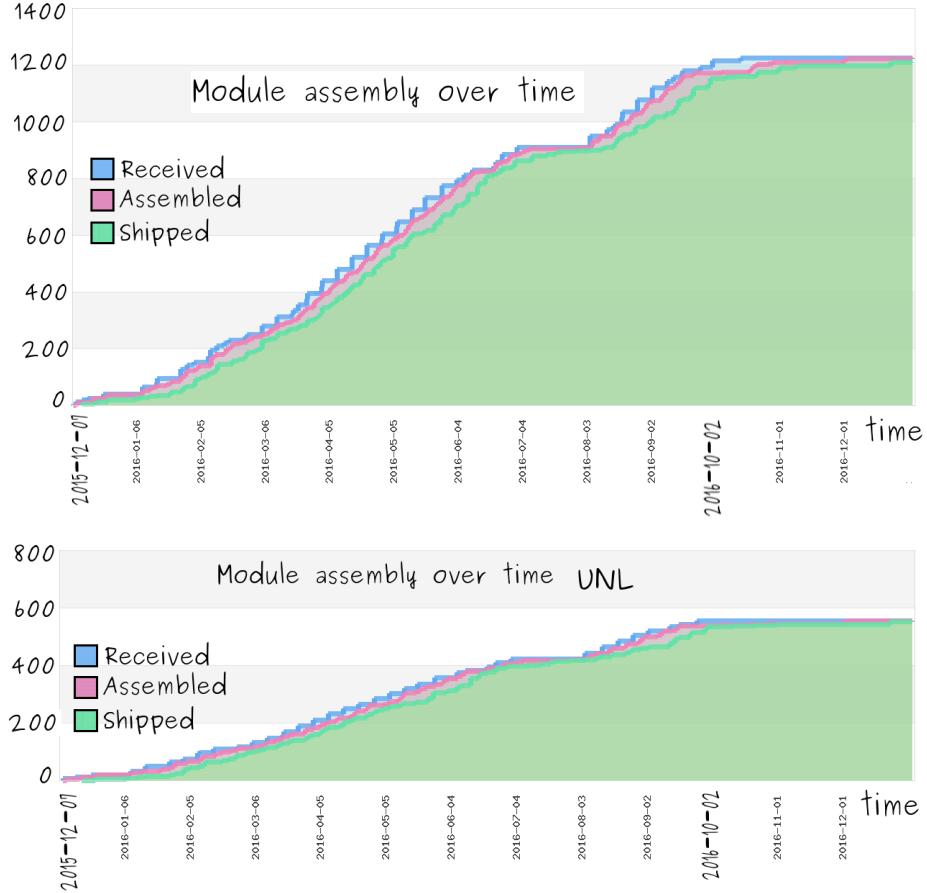


**Figure 7.47:** Module assembly over time for both assembly sites (top) and for UNL (bottom).

4150       Figure 7.47 shows the module assembly over time for both assembly sites, Purdue  
 4151      University and UNL, and for UNL only; in total 1224 were assembled and shipped to  
 4152      the integration site (SiDet-Fermilab), 555 of them at UNL. The module production  
 4153      lasted thirteen months with an interruption at the seventh month due to technical  
 4154      issues faced by the BBM provider. During that time, assembly sites worked in the  
 4155      fixing defective modules and in the assembly of the stocked parts. Although by the  
 4156      sixth month, there were enough modules to build the FPix, not all of them were of  
 4157      optimal quality; the module qualification will be described in the next paragraphs.

		Grade		
	Criteria	A	B	C
IV performance	$I_{-150V}$	$< 2\mu A$	$< 10\mu A$	$> 10\mu A$
	$I_{-150V}/I_{-100V}$	$< 2$	$< 2$	$> 2$
Pixel defects	Sum per ROC	$< 1\%$	$< 4\%$	$> 4\%$

**Table 7.2:** FPix module grading scheme. The overall module grade is assigned as the worse of the IV grade and the pixel defect grade.

4158 Spare modules were assembled after the tenth month of production.

4159 At SiDet, all modules were submitted to extensive testing in order to ensure they  
 4160 were fully functional and fulfill the performance requirements; a detailed description  
 4161 of the complete set of tests is documented in Reference [173].

4162 After testing, each module was given a grade based on its IV performance and its  
 4163 single pixel defects as stated in Table 7.2. The IV performance refers to two aspects;  
 4164 on one side, the amount of leakage current at the expected operating bias voltage  
 4165 ( $I_{-150V}$ ), and on other side, to the breakdown voltage which should be higher than  
 4166 -150 V. If the breakdown voltage is lower than -150 V, the ratio  $I_{-150V}/I_{-100V}$  should  
 4167 be small, otherwise it should be large.

4168 Figure 7.48 shows the module grading yields over time as well as the module grad-  
 4169 ing yields by batch received at the integration site; while in the first weeks of module  
 4170 production the modules were mainly C-graded, due to a combination of failures in  
 4171 the quality of the HDIs and BBM received at the assembly sites and technical issues  
 4172 involving the production line, the quality of the modules was improved and about 620  
 4173 A-graded modules were produced in the whole production time. At the integration  
 4174 time, not enough A-graded modules were available, therefore, B-graded modules were  
 4175 used to complete the 672 modules installed in the FPix detector; B-grade modules  
 4176 were installed in the outermost rings. C-graded modules were not used. Figure 7.49  
 4177 shows the FPix installed in the CMS detector.

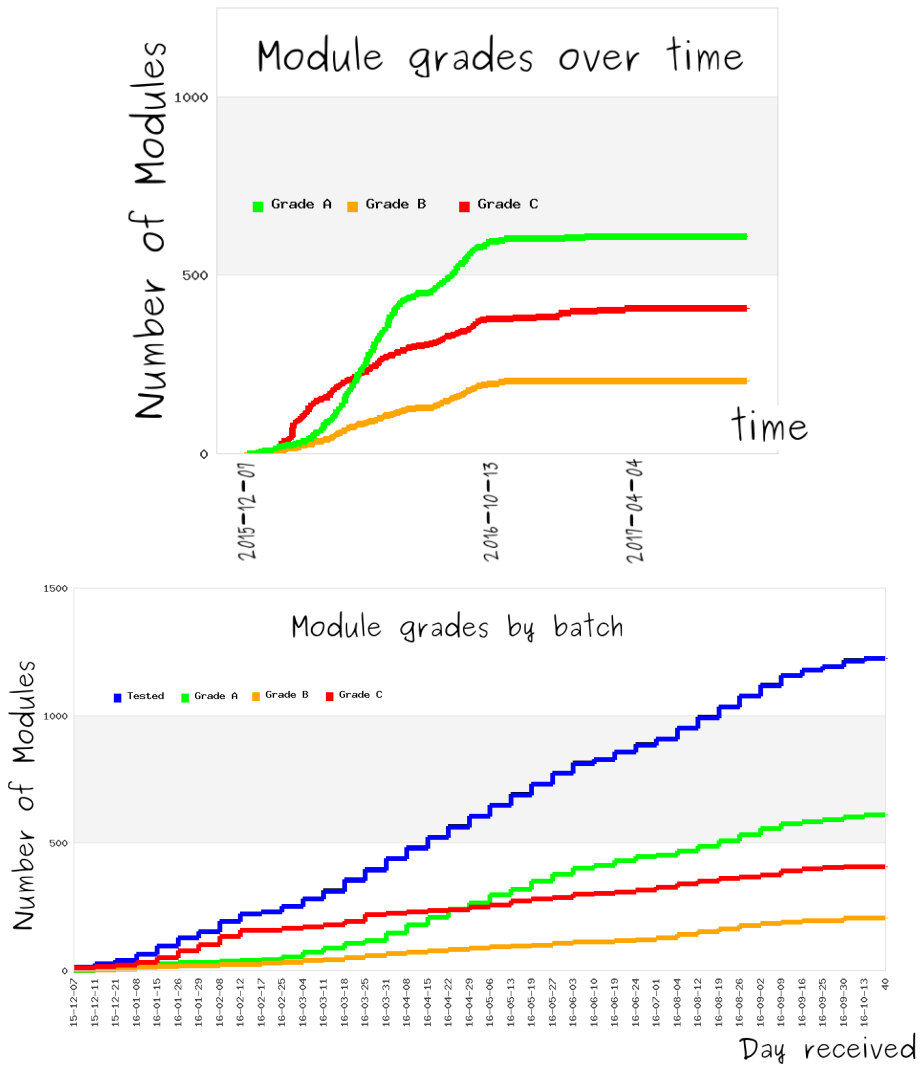


**Figure 7.48:** Module grade over time (top) and per received batch at the integration site (bottom).

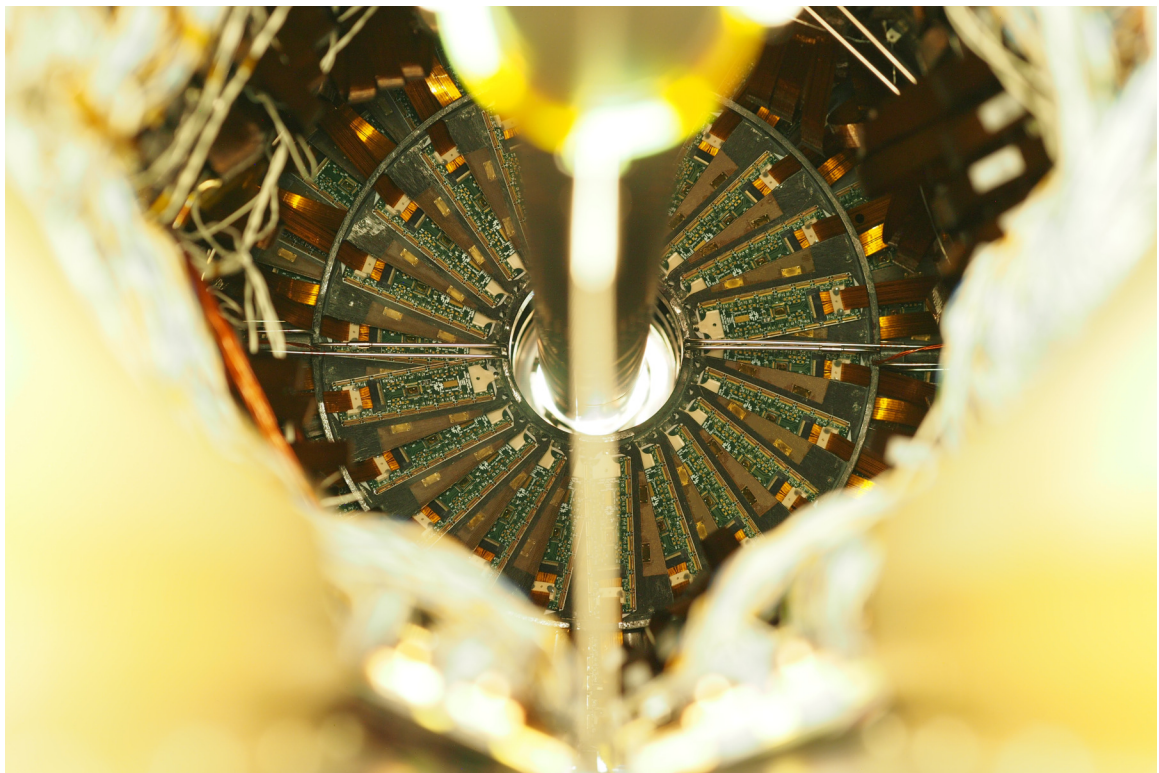


**Figure 7.49:** FPix installed in the CMS detector.

4178

## CHAPTER 8

---

4179

### Conclusions

---

## **8.1 Search for production of a Higgs boson and a single top quark in multilepton final states in pp collisions at $\sqrt{s} = 13$ TeV**

4183 In this thesis, a search for the production of a Higgs boson in association with a single  
 4184 top quark has been presented, using the CMS detector and the full 2016 data sample  
 4185 of  $pp$  collisions at  $\sqrt{s} = 13$  TeV, corresponding to an integrated luminosity of 35.9  
 4186  $\text{fb}^{-1}$ . Three channels have been analyzed, looking at the Higgs boson decaying to a  
 4187 pair of W or Z bosons, or two  $\tau$  leptons and the leptonic decay of the top: two same-  
 4188 sign leptons ( $\mu\mu, e\mu$ ) and three leptons. This process benefits from an enhancement  
 4189 in the production cross section in the case of anomalous top-Higgs couplings and the  
 4190 results are used to constrain these couplings.

4191 The analysis was performed on the basis of the existing analysis *Search for  $t\bar{t}H$  in*  
 4192 *multilepton final states at  $\sqrt{s} = 13$  TeV* [151], to which several elements were added: a  
 4193 dedicated signal discrimination strategy based on multivariate analysis, implemented  
 4194 through the usage of boosted decision trees (BDT) which, after a parameter optimiza-  
 4195 tion process, showed a better performance compared to several other discriminators

4196 like Fisher and K-NN methods. A binned shape fitting on the BDT output was used  
 4197 to extract the signal. The main addition was the interpretation of the results in  
 4198 terms of the ratio of the coupling modifiers ( $\kappa_t, \kappa_V$ ), which differs from previous  $tH$   
 4199 analyses and even from the base  $t\bar{t}H$  analysis; therefore, it was necessary to adapt  
 4200 the systematic uncertainties and background estimations.

4201 Combining the results from all three channels yields a 95% confidence level (C.L.)  
 4202 upper limit on the production cross section times branching ratio of events containing  
 4203 a SM Higgs boson of 0.56 pb; the expected limit is 0.24 pb. In the case of the inverted  
 4204 top-Higgs coupling a combined upper limit on the production cross section times  
 4205 branching ratio of 0.64 pb has been set with an expected limit of 0.32 pb.

4206 Values of the ratio of top-Higgs coupling modifier  $\kappa_t$  and Higgs-vector boson cou-  
 4207 pling modifier  $\kappa_V$  that are outside the range -1.25 to +1.60 are excluded at 95% C.L.  
 4208 for  $\kappa_V = 1.0$ , which is in agreement with the SM predictions. These results of the  
 4209 analysis have been made public by the CMS collaboration in an analysis note [163]  
 4210 and a Physics Analysis Summary [148].

4211 The sensitivity of the  $tH$  process to the CP-mixing phase angle ( $\alpha_{CP}$ ) in the  
 4212 Higgs sector was investigated under the assumption of a generic spin-0 particle  $X_0$   
 4213 with CP-symmetry violating interaction with the top quark but SM-like interaction  
 4214 with the W boson, by using Monte Carlo samples generated for several Higgs bo-  
 4215 son coupling configurations, including the SM scenario ( $\cos(\alpha_{CP})=1$ ) and the ITC  
 4216 scenario ( $\cos(\alpha_{CP})=-1$ ).

4217 Combining the results from all three channels yields a 95% confidence level (C.L.)  
 4218 upper limit on the production cross section times branching ratio of events containing  
 4219 a SM Higgs boson of 0.55 pb has been set, while for the case of the ITC scenario a  
 4220 combined upper limit on the production cross section times branching ratio of 0.60 pb  
 4221 has been set; the expected limits are 0.30 pb and 0.24. These limits are in agreement

4222 with the results from the  $\kappa_t/\kappa_V$  study; however, in the CP-mixing case it is not  
 4223 possible to exclude any region/value in the  $\alpha_{CP}$  phase space.

4224 Currently, a combination with the  $tH$  analysis in the  $H \rightarrow b\bar{b}$  Higgs decay channel  
 4225 and with a reinterpretation of the  $t\bar{t}H$  result in the  $H \rightarrow \gamma\gamma$  decay channel is in  
 4226 preparation for publication.

4227 The sensitivity of the analysis is limited by systematic uncertainties, mainly by  
 4228 those associated to the normalizations of the major background components, i.e., the  
 4229 non-prompt lepton estimation, the scale uncertainties for  $t\bar{t}W$  and  $t\bar{t}Z$ , as well as by  
 4230 the uncertainties on the measured lepton efficiency. In the future refinements of the  
 4231 analysis, the reduction of the systematic uncertainties will be a crucial aspect. In  
 4232 addition, increasing the amount of data analyzed will allow for a better background  
 4233 constraining, by increasing the number of bins in the final S/B ratio map, so that  
 4234 the dominance of backgrounds can be well established by regions and then be better  
 4235 constrained.

## 4236 8.2 Phase 1 FPix upgrade module production

4237 Building a detector involves many challenges, and the HEP group at UNL accepted  
 4238 the leading role of assembling the modules that compose the forward pixel detector of  
 4239 the CMS detector at CERN. The commissioning of the full pixel module production  
 4240 line started from scratch in late 2012 and by 2015 the same yield level as highly  
 4241 experienced groups was reached; this by itself is a big achievement given the leading  
 4242 role assumed by the students involved.

4243 The inclusion of the robotic pick-and-place machine in the assembly provided a  
 4244 shorter production time and uniformity of production assembly technique. In total,  
 4245 45% (555) of the FPix modules were assembled at UNL.

4246        Each stage in the production line went through an optimization process to reduce  
4247    the assembly time while increasing the quality of the produced modules. In particular,  
4248    in the gluing and encapsulation stages everything was optimized to be done with one  
4249    hand, turning out to be more efficient since it involved fewer steps and fewer hands-on  
4250    touches, increasing the yield of the production.

4251

## APPENDIX A

---

4252

### Datasets and triggers

---

Dataset name
/JetHT/Run2016X-23Sep2016-vY/MINIAOD
/HTMHT/Run2016X-23Sep2016-vY/MINIAOD
/MET/Run2016X-23Sep2016-vY/MINIAOD
/SingleElectron/Run2016X-23Sep2016-vY/MINIAOD
/SingleMuon/Run2016X-23Sep2016-vY/MINIAOD
/SinglePhoton/Run2016X-23Sep2016-vY/MINIAOD
/DoubleEG/Run2016X-23Sep2016-vY/MINIAOD
/MuonEG/Run2016X-23Sep2016-vY/MINIAOD
/DoubleMuon/Run2016X-23Sep2016-vY/MINIAOD
/Tau/Run2016B-23Sep2016-v3/MINIAOD
/JetHT/Run2016H-PromptReco-v3/MINIAOD
/HTMHT/Run2016H-PromptReco-v3/MINIAOD
/MET/Run2016H-PromptReco-v3/MINIAOD
/SingleElectron/Run2016H-PromptReco-v3/MINIAOD
/SingleMuon/Run2016H-PromptReco-v3/MINIAOD
/SinglePhoton/Run2016H-PromptReco-v3/MINIAOD
/DoubleEG/Run2016H-PromptReco-v3/MINIAOD
/MuonEG/Run2016H-PromptReco-v3/MINIAOD
/DoubleMuon/Run2016H-PromptReco-v3/MINIAOD

**Table A.1:** Full 2016 dataset used in the analysis. In the first section of the table are listed the 23Sep2016 samples; in the Run2016X-23Sep-vY label, X:B-G tag the run period while Y:1,3 tag the version of the data sample. Second section list the PromptReco version of the dataset.

Same-sign dilepton (==2 muons)
HLT_Mu17_TrkIsoVVL_Mu8_TrkIsoVVL_DZ_v*
HLT_Mu17_TrkIsoVVL_TkMu8_TrkIsoVVL_DZ_v*
HLT_IsoMu22_v*
HLT_IsoTkMu22_v*
HLT_IsoMu22_eta2p1_v*
HLT_IsoTkMu22_eta2p1_v*
HLT_IsoMu24_v*
HLT_IsoTkMu24_v*
Same-sign dilepton (==2 electrons)
HLT_Ele23_Ele12_CaloIdL_TrackIdL_IsoVL_DZ_v*
HLT_Ele27_eta2p1_WP Loose_Gsf_v*
HLT_Ele27_WPTight_Gsf_v*
HLT_Ele25_eta2p1_WPTight_Gsf_v*
Same-sign dilepton (==1 muon, ==1 electron)
HLT_Mu23_TrkIsoVVL_Ele8_CaloIdL_TrackIdL_IsoVL_v*
HLT_Mu8_TrkIsoVVL_Ele23_CaloIdL_TrackIdL_IsoVL_v*
HLT_Mu23_TrkIsoVVL_Ele8_CaloIdL_TrackIdL_IsoVL_DZ_v*
HLT_Mu8_TrkIsoVVL_Ele23_CaloIdL_TrackIdL_IsoVL_DZ_v*
HLT_IsoMu22_v*
HLT_IsoTkMu22_v*
HLT_IsoMu22_eta2p1_v*
HLT_IsoTkMu22_eta2p1_v*
HLT_IsoMu24_v*
HLT_IsoTkMu24_v*
HLT_Ele27_WPTight_Gsf_v*
HLT_Ele25_eta2p1_WPTight_Gsf_v*
HLT_Ele27_eta2p1_WP Loose_Gsf_v*
Three lepton
HLT_DiMu9_Ele9_CaloIdL_TrackIdL_v*
HLT_Mu8_DiEle12_CaloIdL_TrackIdL_v*
HLT_TripleMu_12_10_5_v*
HLT_Ele16_Ele12_Ele8_CaloIdL_TrackIdL_v*
HLT_Mu23_TrkIsoVVL_Ele8_CaloIdL_TrackIdL_IsoVL_v*
HLT_Mu23_TrkIsoVVL_Ele8_CaloIdL_TrackIdL_IsoVL_DZ_v*
HLT_Mu8_TrkIsoVVL_Ele23_CaloIdL_TrackIdL_IsoVL_v*
HLT_Mu8_TrkIsoVVL_Ele23_CaloIdL_TrackIdL_IsoVL_DZ_v*
HLT_Ele23_Ele12_CaloIdL_TrackIdL_IsoVL_DZ_v*
HLT_Mu17_TrkIsoVVL_Mu8_TrkIsoVVL_DZ_v*
HLT_Mu17_TrkIsoVVL_TkMu8_TrkIsoVVL_DZ_v*
HLT_IsoMu22_v*
HLT_IsoTkMu22_v*
HLT_IsoMu22_eta2p1_v*
HLT_IsoTkMu22_eta2p1_v*
HLT_IsoMu24_v*
HLT_IsoTkMu24_v*
HLT_Ele27_WPTight_Gsf_v*
HLT_Ele25_eta2p1_WPTight_Gsf_v*
HLT_Ele27_eta2p1_WP Loose_Gsf_v*

**Table A.2:** Table of high-level triggers considered in the analysis.

		<i>tHq</i>		<i>tHW</i>		
$\kappa_V$	$\kappa_t$	sum of weights	cross section [pb]	sum of weights	cross section [pb]	LHE weights
1.0	-3.0	35.700022	2.991	11.030445	0.6409	LHEweight_wgt[446]
1.0	-2.0	20.124298	1.706	5.967205	0.3458	LHEweight_wgt[447]
1.0	-1.5	14.043198	1.205	4.029093	0.2353	LHEweight_wgt[448]
1.0	-1.25	11.429338	0.9869	3.208415	0.1876	LHEweight_wgt[449]
1.0	-1.0		0.7927		0.1472	
1.0	-0.75	7.054998	0.6212	1.863811	0.1102	LHEweight_wgt[450]
1.0	-0.5	5.294518	0.4723	1.339886	0.07979	LHEweight_wgt[451]
1.0	-0.25	3.818499	0.3505	0.914880	0.05518	LHEweight_wgt[452]
1.0	0.0	2.627360	0.2482	0.588902	0.03881	LHEweight_wgt[453]
1.0	0.25	1.719841	0.1694	0.361621	0.02226	LHEweight_wgt[454]
1.0	0.5	1.097202	0.1133	0.233368	0.01444	LHEweight_wgt[455]
1.0	0.75	0.759024	0.08059	0.204034	0.01222	LHEweight_wgt[456]
1.0	1.0	0.705305	0.07096	0.273617	0.01561	LHEweight_wgt[457]
1.0	1.25	0.936047	0.0839	0.442119	0.02481	LHEweight_wgt[458]
1.0	1.5	1.451249	0.1199	0.709538	0.03935	LHEweight_wgt[459]
1.0	2.0	3.335034	0.2602	1.541132	0.08605	LHEweight_wgt[460]
1.0	3.0	10.516125	0.8210	4.391335	0.2465	LHEweight_wgt[461]
1.5	-3.0	45.281492	3.845	13.426212	0.7825	LHEweight_wgt[462]
1.5	-2.0	27.606715	2.371	7.809713	0.4574	LHEweight_wgt[463]
1.5	-1.5	20.476088	1.784	5.594971	0.3290	LHEweight_wgt[464]
1.5	-1.25	17.337465	1.518	4.635978	0.2749	LHEweight_wgt[465]
1.5	-1.0	14.483302	1.287	3.775902	0.2244	LHEweight_wgt[466]
1.5	-0.75	11.913599	1.067	3.014744	0.1799	LHEweight_wgt[467]
1.5	-0.5	9.628357	0.874	2.352505	0.1410	LHEweight_wgt[468]
1.5	-0.25	7.627574	0.702	1.789184	0.1081	LHEweight_wgt[469]
1.5	0.0	5.911882	0.5577	1.324946	0.08056	LHEweight_wgt[470]
1.5	0.25	4.479390	0.4365	0.959295	0.05893	LHEweight_wgt[471]
1.5	0.5	3.331988	0.3343	0.692727	0.04277	LHEweight_wgt[472]
1.5	0.75	2.469046	0.2558	0.525078	0.03263	LHEweight_wgt[473]
1.5	1.0	1.890565	0.2003	0.456347	0.02768	LHEweight_wgt[474]
1.5	1.25	1.596544	0.1689	0.486534	0.02864	LHEweight_wgt[475]
1.5	1.5	1.586983	0.1594	0.615638	0.03509	LHEweight_wgt[476]
1.5	2.0	2.421241	0.2105	1.170602	0.06515	LHEweight_wgt[477]
1.5	3.0	7.503280	0.5889	3.467546	0.1930	LHEweight_wgt[478]
0.5	-3.0	27.432685	2.260	8.929074	0.5136	LHEweight_wgt[479]
0.5	-2.0	13.956013	1.160	4.419093	0.2547	LHEweight_wgt[480]
0.5	-1.5	8.924438	0.7478	2.757611	0.1591	LHEweight_wgt[481]
0.5	-1.25	6.835341	0.5726	2.075247	0.1204	LHEweight_wgt[482]
0.5	-1.0	5.030704	0.4273	1.491801	0.08696	LHEweight_wgt[483]
0.5	-0.75	3.510528	0.2999	1.007273	0.05885	LHEweight_wgt[484]
0.5	-0.5	2.274811	0.1982	0.621663	0.03658	LHEweight_wgt[485]
0.5	-0.25	1.323555	0.1189	0.334972	0.01996	LHEweight_wgt[486]
0.5	0.0	0.656969	0.06223	0.147253	0.008986	LHEweight_wgt[487]
0.5	0.25	0.274423	0.02830	0.058342	0.003608	LHEweight_wgt[488]
0.5	0.5	0.176548	0.01778	0.068404	0.003902	LHEweight_wgt[489]
0.5	0.75	0.363132	0.03008	0.177385	0.009854	LHEweight_wgt[490]
0.5	1.0	0.834177	0.06550	0.385283	0.02145	LHEweight_wgt[491]
0.5	1.25	1.589682	0.1241	0.692099	0.03848	LHEweight_wgt[492]
0.5	1.5	2.629647	0.2047	1.097834	0.06136	LHEweight_wgt[493]
0.5	2.0	5.562958	0.4358	2.206057	0.1246	LHEweight_wgt[494]
0.5	3.0	14.843102	1.177	5.609519	0.3172	LHEweight_wgt[495]

**Table A.3:**  $\kappa_V$  and  $\kappa_t$  combinations generated for the two signal samples and their NLO cross sections. The *tHq* cross section is multiplied by the branching fraction of the enforced leptonic decay of the top quark (0.324) [152].

Sample	$\sigma$ [pb]
TTWJetsToLNu_TuneCUETP8M1_13TeV-amcatnloFXFX-madspin-pythia8	0.2043
TTZToLLNuNu_M-10_TuneCUETP8M1_13TeV-amcatnlo-pythia8	0.2529
/store/cmst3/group/susy/gpetrucc/13TeV/u/TTLL_m1to10_LO_NoMS_for76X/	0.0283
WGToLNuG_TuneCUETP8M1_13TeV-madgraphMLM-pythia8	585.8
ZGTo2LG_TuneCUETP8M1_13TeV-amcatnloFXFX-pythia8	131.3
TGJets_TuneCUETP8M1_13TeV_amcatnlo_madspin_pythia8	2.967
TGJets_TuneCUETP8M1_13TeV_amcatnlo_madspin_pythia8	2.967
TTGJets_TuneCUETP8M1_13TeV-amcatnloFXFX-madspin-pythia8	3.697
WpWpJJ_EWK-QCD_TuneCUETP8M1_13TeV-madgraph-pythia8	0.03711
ZZZ_TuneCUETP8M1_13TeV-amcatnlo-pythia8	0.01398
WWZ_TuneCUETP8M1_13TeV-amcatnlo-pythia8	0.1651
WZZ_TuneCUETP8M1_13TeV-amcatnlo-pythia8	0.05565
WW_DoubleScattering_13TeV-pythia8	1.64
tZq_ll_4f_13TeV-amcatnlo-pythia8_TuneCUETP8M1	0.0758
ST_tW11_5f_LO_13TeV-MadGraph-pythia8	0.01123
TTTT_TuneCUETP8M1_13TeV-amcatnlo-pythia8	0.009103
WZTo3LNu_TuneCUETP8M1_13TeV-powheg-pythia8	4.4296
ZZTo4L_13TeV_powheg_pythia8	1.256
TTJets_SingleLeptFromTbar_TuneCUETP8M1_13TeV-madgraphMLM-pythia8	182.1754 *
TTJets_SingleLeptFromT_TuneCUETP8M1_13TeV-madgraphMLM-pythia8	182.1754 *
TTJets_DiLept_TuneCUETP8M1_13TeV-madgraphMLM-pythia8	87.3 *
DYJetsToLL_M-10to50_TuneCUETP8M1_13TeV-amcatnloFXFX-pythia8	18610
DYJetsToLL_M-50_TuneCUETP8M1_13TeV-madgraphMLM-pythia8	6024
WJetsToLNu_TuneCUETP8M1_13TeV-amcatnloFXFX-pythia8	61526.7
ST_tW_top_5f_inclusiveDecays_13TeV-powheg-pythia8_TuneCUETP8M1	35.6
ST_tW_antitop_5f_inclusiveDecays_13TeV-powheg-pythia8_TuneCUETP8M1	35.6
ST_t-channel_4f_leptonDecays_13TeV-amcatnlo-pythia8_TuneCUETP8M1	70.3144
ST_t-channel_antitop_4f_leptonDecays_13TeV-powheg-pythia8_TuneCUETP8M1	26.2278
ST_s-channel_4f_leptonDecays_13TeV-amcatnlo-pythia8_TuneCUETP8M1	3.68064
WWTo2L2Nu_13TeV-powheg	10.481
ttWJets_13TeV_madgraphMLM	0.6105
ttZJets_13TeV_madgraphMLM	0.5297/0.692

**Table A.4:** List of background samples used in this analysis (CMSSW 80X). The first section of the table lists the samples used in simulation to extract the final yields and shapes; the second section lists the samples of the processes for which the yields are estimated from data. The MC simulation is used to design the data driven methods and in the derivation of the associated systematic uncertainties. The third section lists the leading order  $t\bar{t}W$  and  $t\bar{t}Z$  samples, which in addition to the ones marked with a \*, where used in the BDT training.

$f_t$	$\kappa_t/\kappa_V$	Bg-only exp.	SM exp.	Obs. lim.	Best fit $r$ [pb]	Best fit $\sigma$
-0.973	-6.000	0.328 $^{+0.136}_{-0.090}$	0.507 $^{+0.206}_{-0.158}$	0.603	0.013 $^{+0.007}_{-0.007}$	0.305 $^{+0.155}_{-0.169}$
-0.941	-4.000	0.335 $^{+0.137}_{-0.098}$	0.509 $^{+0.215}_{-0.166}$	0.627	0.036 $^{+0.018}_{-0.020}$	0.322 $^{+0.157}_{-0.174}$
-0.900	-3.000	0.335 $^{+0.138}_{-0.096}$	0.510 $^{+0.215}_{-0.172}$	0.639	0.075 $^{+0.036}_{-0.039}$	0.334 $^{+0.160}_{-0.173}$
-0.862	-2.500	0.334 $^{+0.139}_{-0.097}$	0.505 $^{+0.217}_{-0.173}$	0.649	0.119 $^{+0.056}_{-0.061}$	0.341 $^{+0.160}_{-0.174}$
-0.800	-2.000	0.330 $^{+0.141}_{-0.095}$	0.500 $^{+0.212}_{-0.176}$	0.656	0.202 $^{+0.097}_{-0.103}$	0.345 $^{+0.165}_{-0.176}$
-0.692	-1.500	0.325 $^{+0.139}_{-0.095}$	0.485 $^{+0.209}_{-0.172}$	0.660	0.369 $^{+0.178}_{-0.191}$	0.340 $^{+0.164}_{-0.176}$
-0.640	-1.333	0.325 $^{+0.139}_{-0.097}$	0.482 $^{+0.210}_{-0.173}$	0.659	0.456 $^{+0.231}_{-0.238}$	0.334 $^{+0.169}_{-0.174}$
-0.610	-1.250	0.321 $^{+0.140}_{-0.095}$	0.474 $^{+0.210}_{-0.169}$	0.653	0.505 $^{+0.252}_{-0.272}$	0.328 $^{+0.164}_{-0.177}$
<b>-0.500</b>	<b>-1.000</b>	<b>0.315 <math>^{+0.142}_{-0.093}</math></b>	<b>0.450 <math>^{+0.213}_{-0.160}</math></b>	<b>0.638</b>	<b>0.685 <math>^{+0.395}_{-0.396}</math></b>	<b>0.304 <math>^{+0.175}_{-0.176}</math></b>
-0.410	-0.833	0.312 $^{+0.138}_{-0.095}$	0.424 $^{+0.210}_{-0.147}$	0.615	0.819 $^{+0.498}_{-0.526}$	0.276 $^{+0.168}_{-0.177}$
-0.360	-0.750	0.307 $^{+0.138}_{-0.093}$	0.409 $^{+0.200}_{-0.136}$	0.593	0.874 $^{+0.581}_{-0.601}$	0.256 $^{+0.170}_{-0.176}$
-0.308	-0.667	0.301 $^{+0.138}_{-0.092}$	0.384 $^{+0.198}_{-0.124}$	0.566	0.915 $^{+0.655}_{-0.689}$	0.231 $^{+0.165}_{-0.174}$
-0.200	-0.500	0.292 $^{+0.136}_{-0.090}$	0.345 $^{+0.181}_{-0.109}$	0.497	0.895 $^{+0.879}_{-0.871}$	0.166 $^{+0.163}_{-0.162}$
-0.100	-0.333	0.278 $^{+0.132}_{-0.086}$	0.303 $^{+0.156}_{-0.092}$	0.409	0.679 $^{+1.159}_{-0.679}$	0.092 $^{+0.157}_{-0.092}$
-0.059	-0.250	0.268 $^{+0.129}_{-0.083}$	0.283 $^{+0.152}_{-0.085}$	0.365	0.515 $^{+1.285}_{-0.515}$	0.059 $^{+0.148}_{-0.059}$
-0.027	-0.167	0.260 $^{+0.125}_{-0.081}$	0.266 $^{+0.135}_{-0.077}$	0.328	0.297 $^{+1.434}_{-0.297}$	0.029 $^{+0.142}_{-0.029}$
0.000	0.000	0.254 $^{+0.123}_{-0.079}$	0.252 $^{+0.123}_{-0.073}$	0.294	0.002 $^{+1.776}_{-0.002}$	0.000 $^{+0.132}_{-0.000}$
0.027	0.167	0.275 $^{+0.132}_{-0.086}$	0.284 $^{+0.148}_{-0.084}$	0.357	0.650 $^{+2.514}_{-0.650}$	0.040 $^{+0.154}_{-0.040}$
0.059	0.250	0.297 $^{+0.141}_{-0.093}$	0.329 $^{+0.171}_{-0.099}$	0.458	2.015 $^{+3.098}_{-2.015}$	0.119 $^{+0.183}_{-0.119}$
0.100	0.333	0.322 $^{+0.148}_{-0.099}$	0.405 $^{+0.220}_{-0.135}$	0.611	4.147 $^{+2.802}_{-3.103}$	0.246 $^{+0.166}_{-0.184}$
0.200	0.500	0.324 $^{+0.141}_{-0.096}$	0.505 $^{+0.212}_{-0.181}$	0.730	5.982 $^{+2.174}_{-2.559}$	0.413 $^{+0.150}_{-0.177}$
0.308	0.667	0.281 $^{+0.122}_{-0.082}$	0.462 $^{+0.172}_{-0.159}$	0.651	4.186 $^{+1.492}_{-1.574}$	0.382 $^{+0.136}_{-0.144}$
0.360	0.750	0.268 $^{+0.116}_{-0.079}$	0.442 $^{+0.160}_{-0.154}$	0.620	3.392 $^{+1.214}_{-1.253}$	0.364 $^{+0.130}_{-0.135}$
0.410	0.833	0.258 $^{+0.112}_{-0.075}$	0.427 $^{+0.162}_{-0.147}$	0.599	2.754 $^{+0.999}_{-1.022}$	0.351 $^{+0.127}_{-0.130}$
<b>0.500</b>	<b>1.000</b>	<b>0.244 <math>^{+0.105}_{-0.072}</math></b>	<b>0.401 <math>^{+0.154}_{-0.137}</math></b>	<b>0.562</b>	<b>1.821 <math>^{+0.657}_{-0.671}</math></b>	<b>0.328 <math>^{+0.118}_{-0.121}</math></b>
0.610	1.250	0.240 $^{+0.104}_{-0.070}$	0.394 $^{+0.154}_{-0.133}$	0.545	1.072 $^{+0.399}_{-0.403}$	0.315 $^{+0.118}_{-0.119}$
0.640	1.333	0.242 $^{+0.105}_{-0.071}$	0.398 $^{+0.156}_{-0.136}$	0.547	0.921 $^{+0.354}_{-0.352}$	0.316 $^{+0.122}_{-0.121}$
0.692	1.500	0.244 $^{+0.106}_{-0.071}$	0.401 $^{+0.159}_{-0.136}$	0.543	0.678 $^{+0.262}_{-0.261}$	0.312 $^{+0.120}_{-0.120}$
0.800	2.000	0.256 $^{+0.109}_{-0.075}$	0.416 $^{+0.169}_{-0.138}$	0.552	0.317 $^{+0.123}_{-0.129}$	0.311 $^{+0.121}_{-0.127}$
0.862	2.500	0.268 $^{+0.114}_{-0.078}$	0.433 $^{+0.169}_{-0.142}$	0.558	0.170 $^{+0.070}_{-0.072}$	0.310 $^{+0.127}_{-0.130}$
0.900	3.000	0.276 $^{+0.118}_{-0.080}$	0.442 $^{+0.177}_{-0.144}$	0.563	0.102 $^{+0.042}_{-0.044}$	0.308 $^{+0.128}_{-0.134}$
0.941	4.000	0.290 $^{+0.122}_{-0.084}$	0.459 $^{+0.184}_{-0.149}$	0.566	0.046 $^{+0.020}_{-0.021}$	0.304 $^{+0.134}_{-0.140}$
0.973	6.000	0.306 $^{+0.122}_{-0.081}$	0.474 $^{+0.192}_{-0.150}$	0.571	0.016 $^{+0.007}_{-0.008}$	0.300 $^{+0.131}_{-0.150}$

**Table A.5:** Expected (for background only, and for a SM-like Higgs signal) and observed 95% C.L. upper limits (in pb), and best fit signal strength  $r$  and corresponding best fit cross section for the combined  $tH + t\bar{t}H$  cross section times modified branching ratio for the combination of all three channels, for different values of  $\kappa_t/\kappa_V$  or the equivalent  $f_t$  numbers.

4253

## APPENDIX *B*

---

4254

### Aditional plots

---

#### 4255 **B.1 Pre-selection kinematic variables**

4256 Figures B.1, B.2 and B.3 show the distributions of some relevant kinematic variables,  
4257 normalized to the cross section of the respective processes and to the integrated  
4258 luminosity.

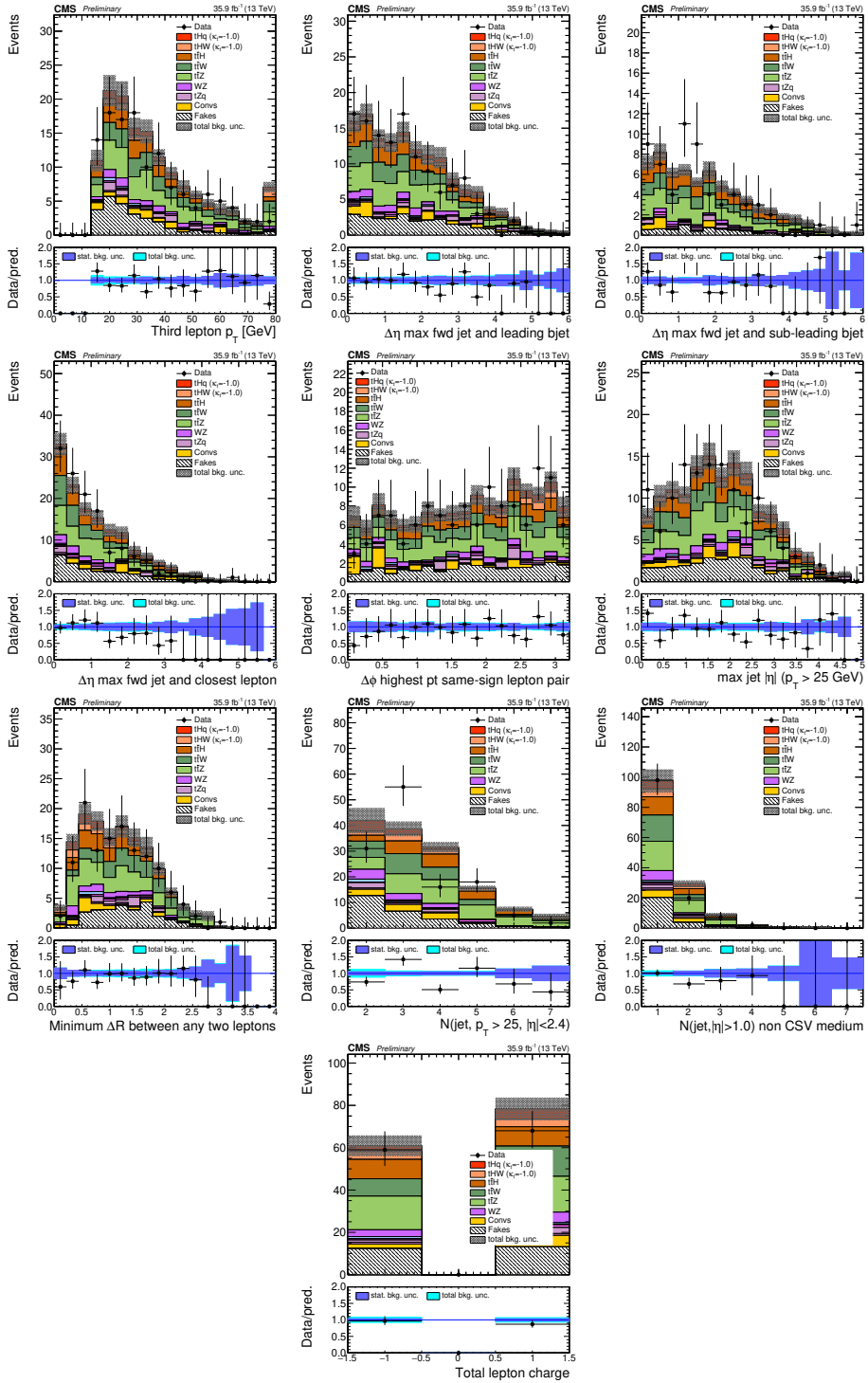


**Figure B.1:** Distributions of input variables to the BDT for signal discrimination, three lepton channel, normalized to their cross section and to  $35.9 \text{ fb}^{-1}$ .

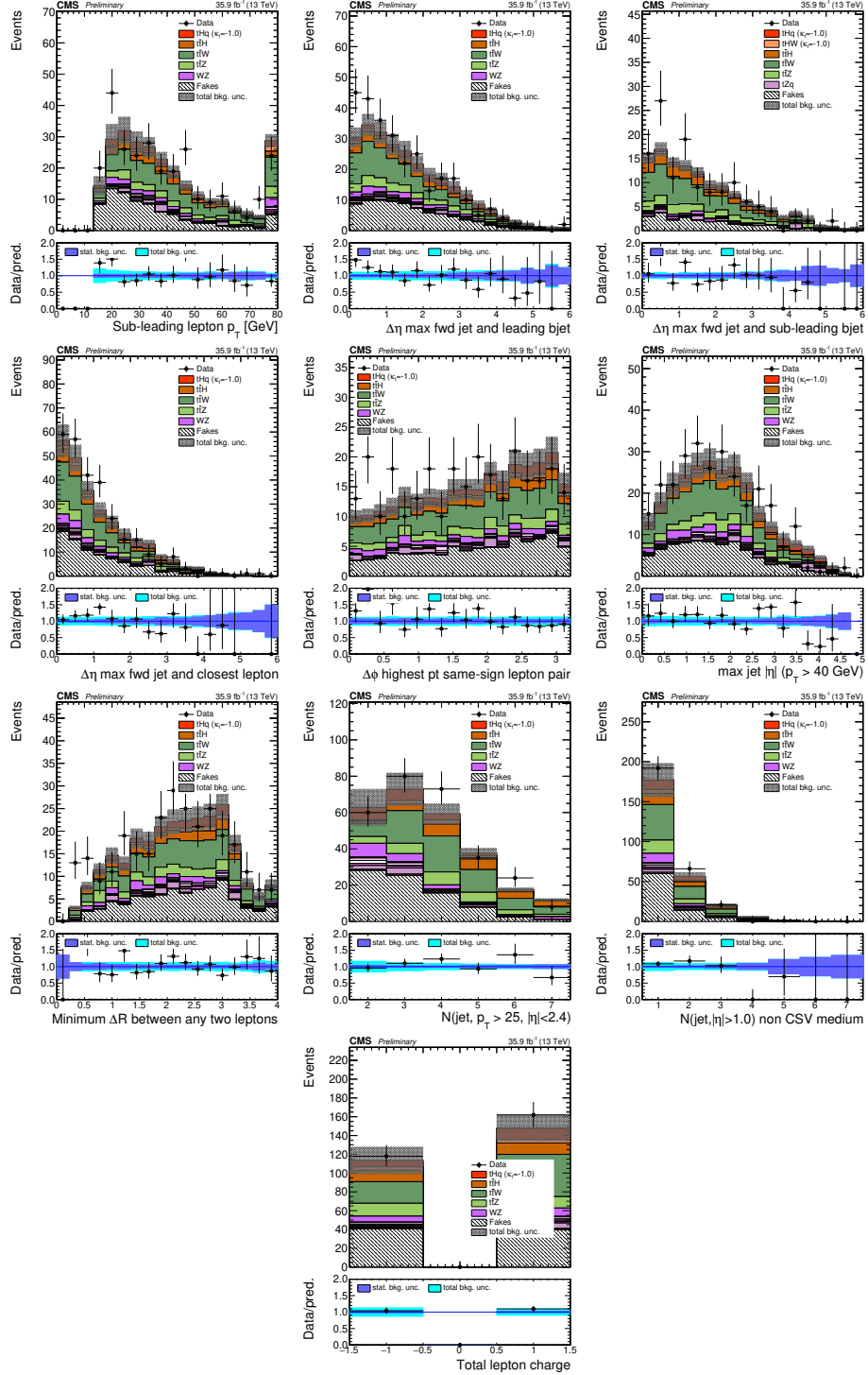


**Figure B.2:** Distributions of input variables to the BDT for signal discrimination, in  $\mu^\pm \mu^\pm$  channel, normalized to their cross section and to  $35.9 \text{ fb}^{-1}$ .

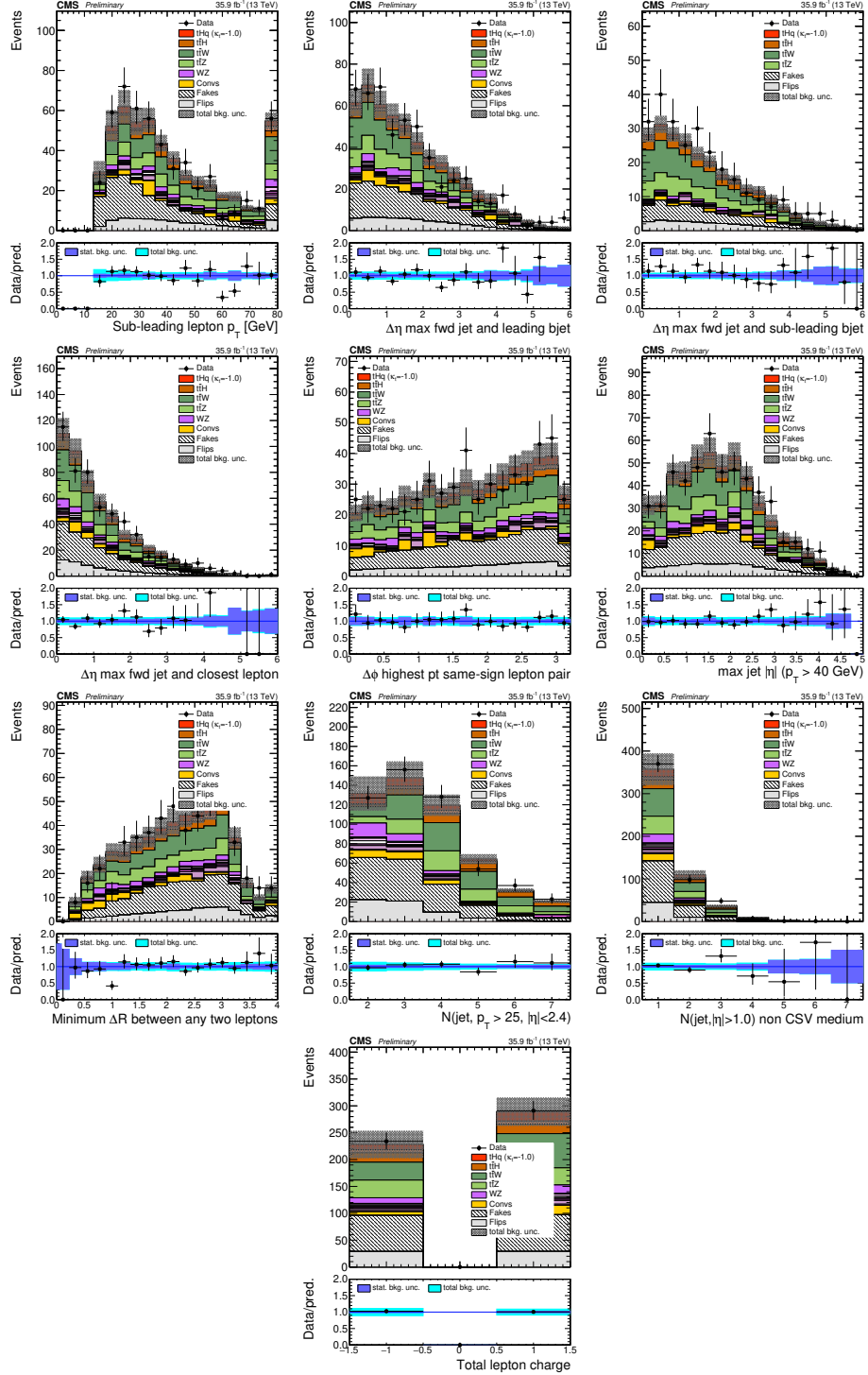


**Figure B.3:** Distributions of input variables to the BDT for signal discrimination, in  $e^\pm\mu^\pm$  channel, normalized to their cross section and to  $35.9 \text{ fb}^{-1}$ .

4259 **B.2 BDTG input variables for  $2lss$  channel**

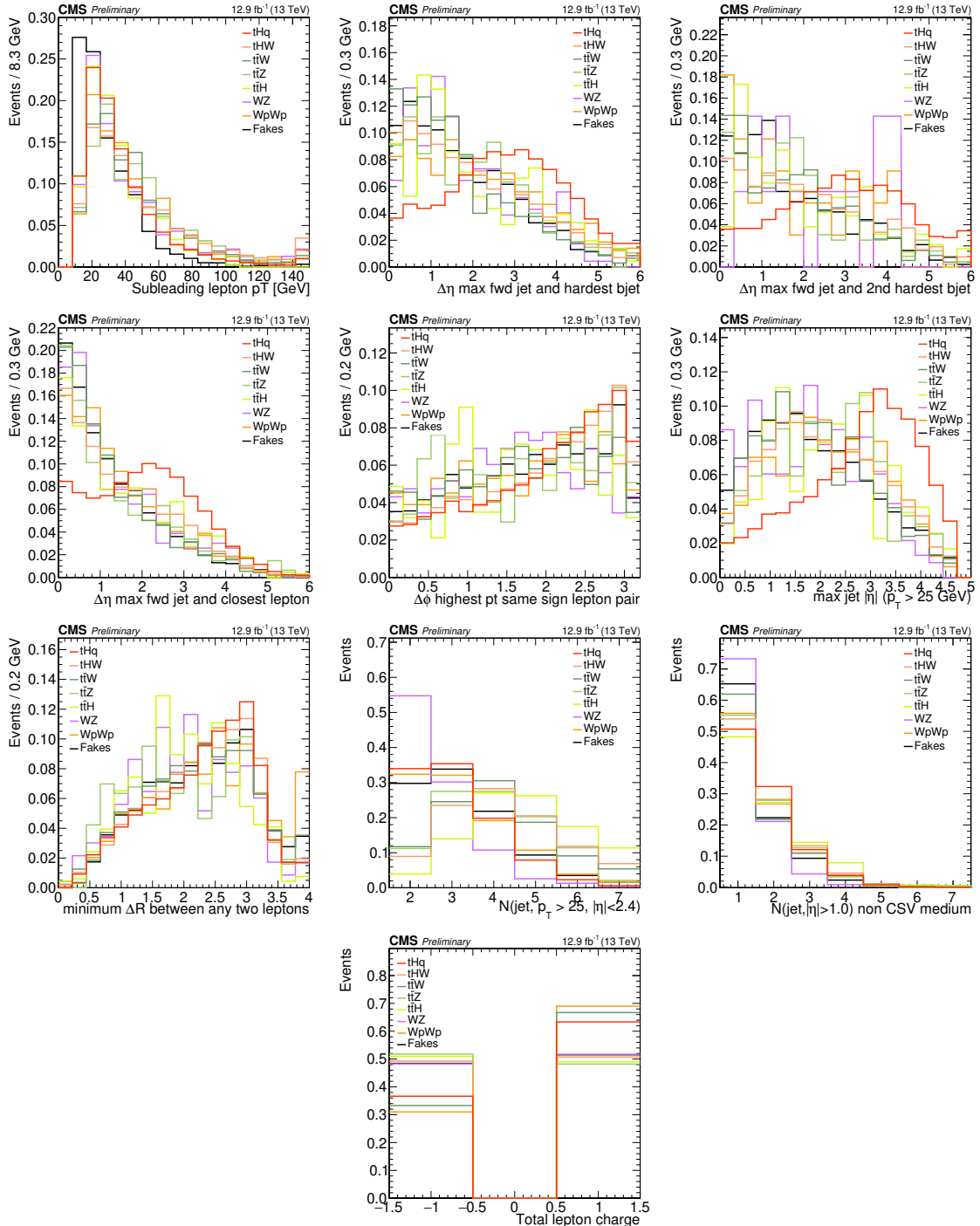


**Figure B.4:** Distributions of input variables to the BDT for signal discrimination, normalized to the equal area, for the  $2lss$  channel.

4260 **B.3 Input variables distributions from BDTG**  
 4261 classifiers

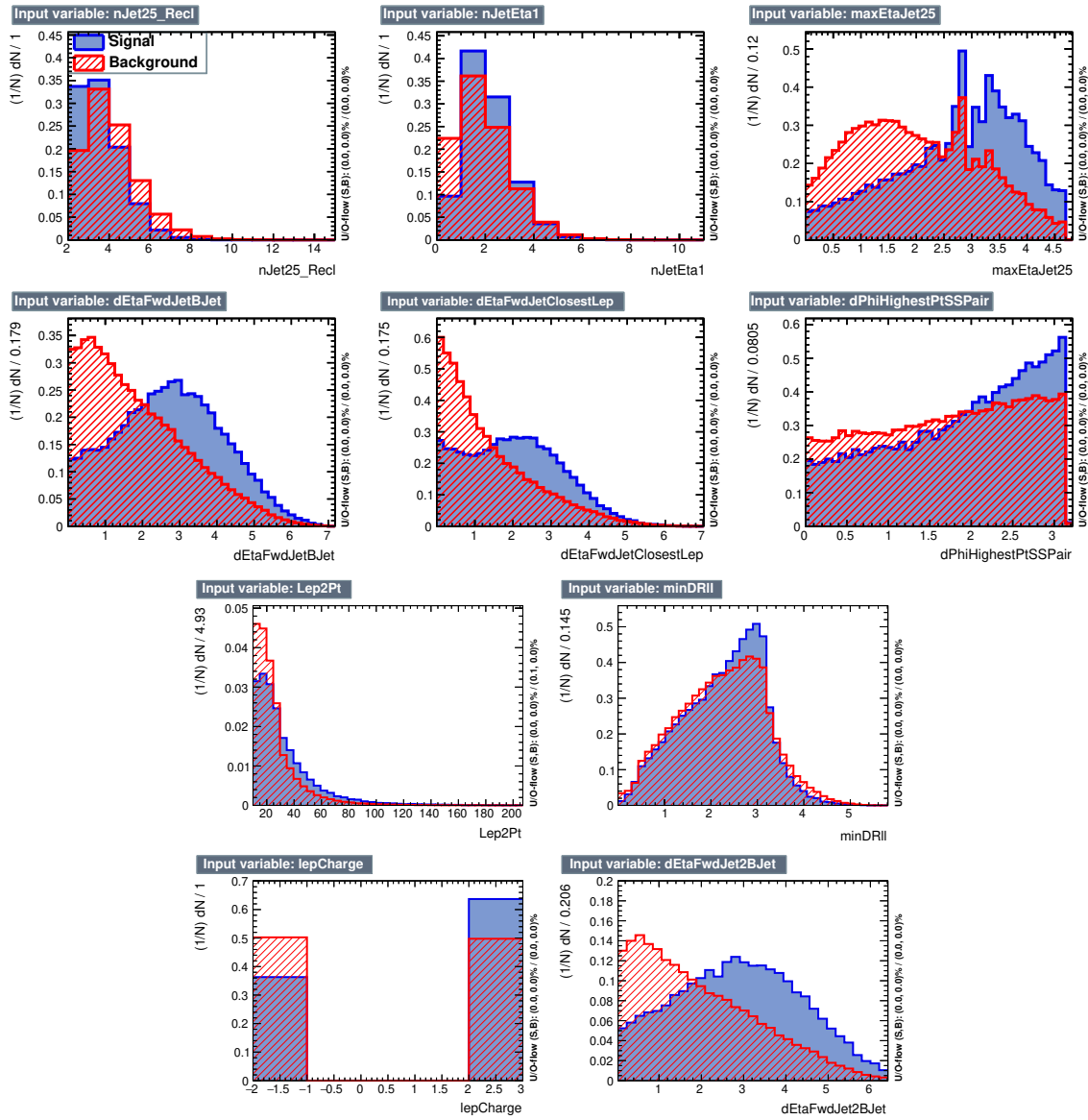


**Figure B.5:** BDT input variables as seen by BDTG classifier for the  $2lss$  channel,  $tHq$  signal (blue) discriminated against  $t\bar{t}$  background (red).

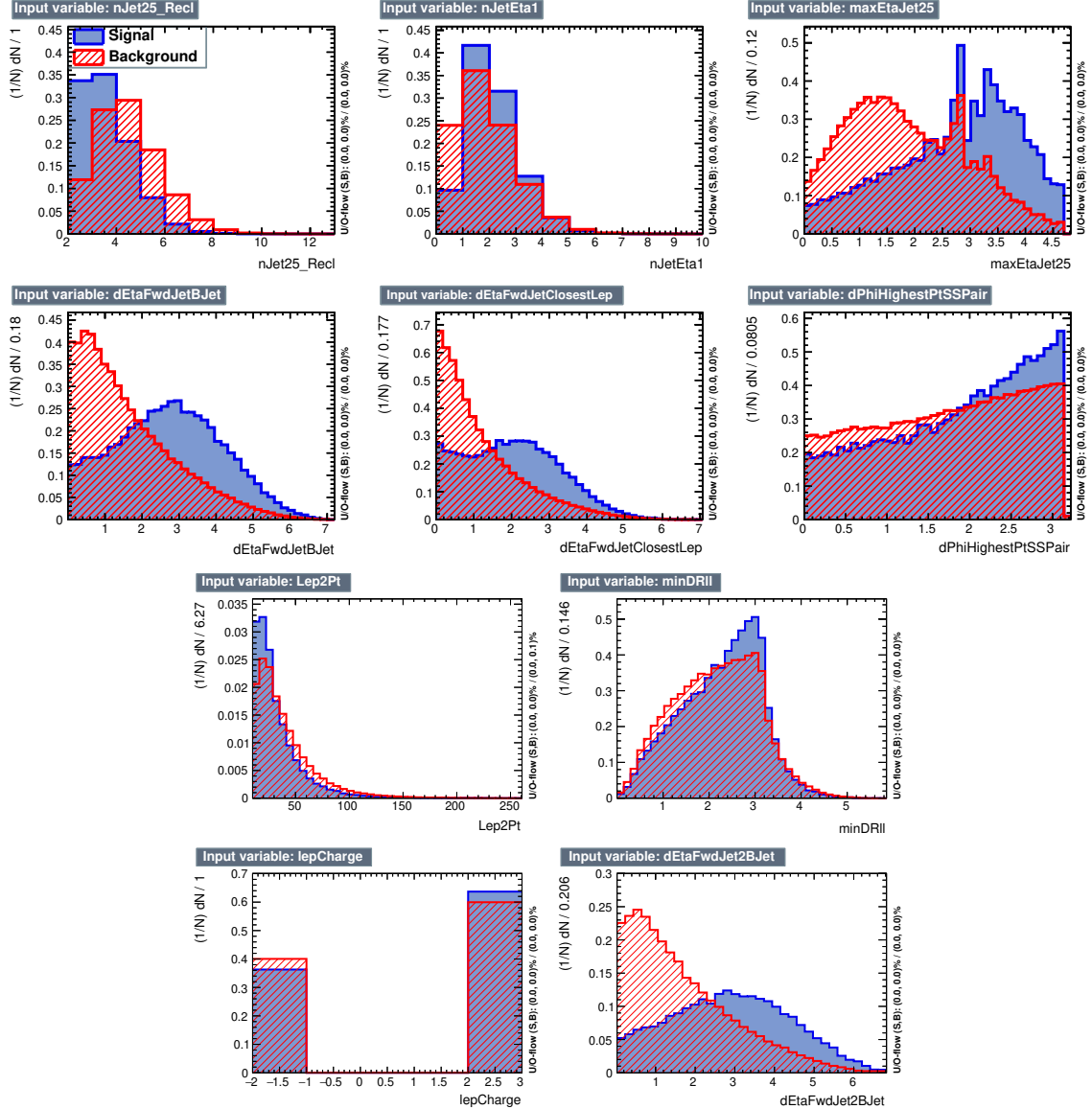


**Figure B.6:** BDT input variables as seen by BDTG classifier for the  $2lss$  channel,  $tHq$  signal(blue) discriminated against  $t\bar{t}V$  background (red).

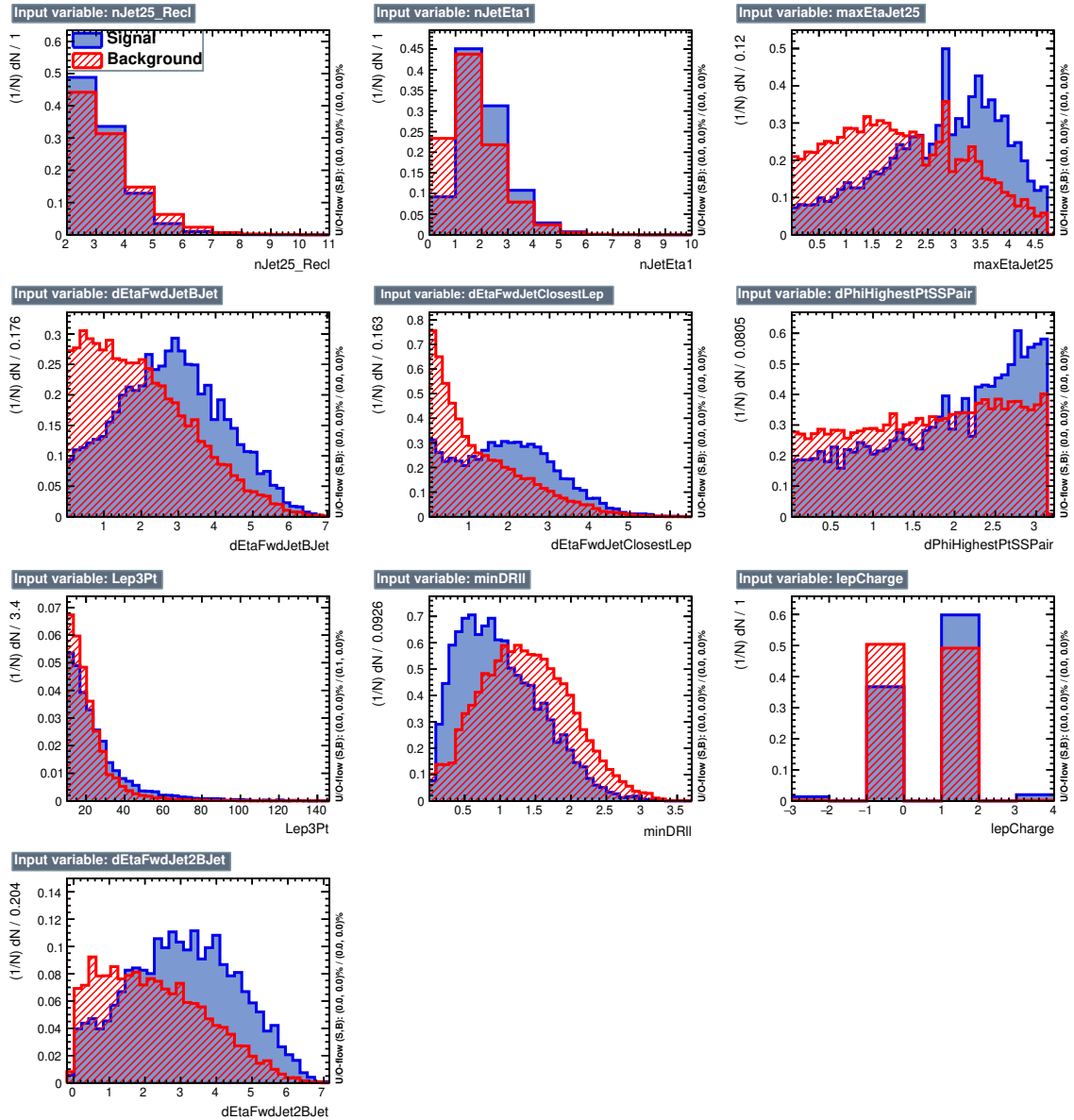


**Figure B.7:** BDT input variables as seen by BDTG classifier for the  $3l$  channel,  $tHq$  signal (blue) discriminated against  $t\bar{t}$  background (red).

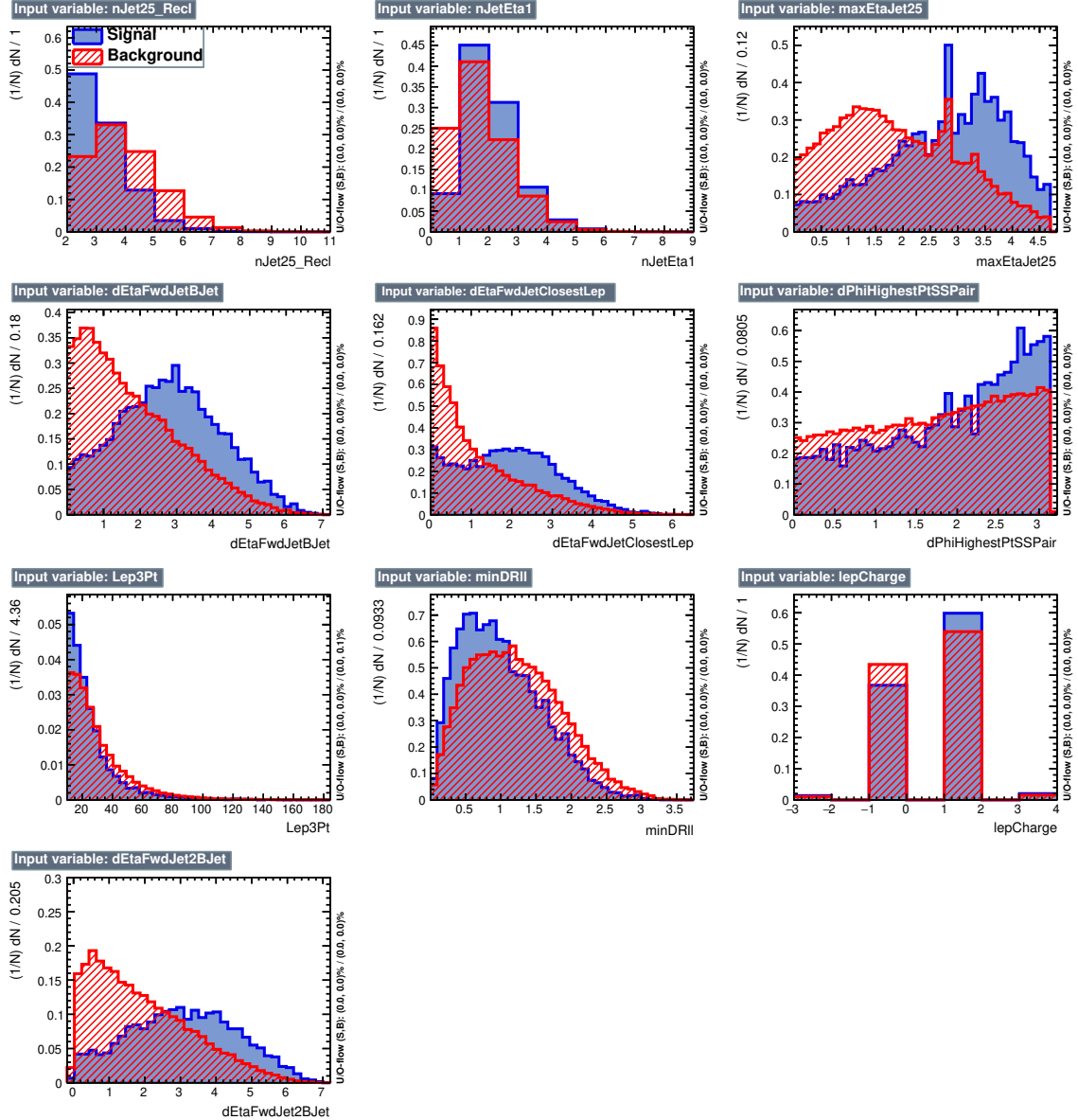


**Figure B.8:** BDT input variables as seen by BDTG classifier for the  $3l$  channel,  $tHq$  signal (blue) discriminated against  $t\bar{t}V$  background (red).

4262 **B.4 Pulls and impacts**

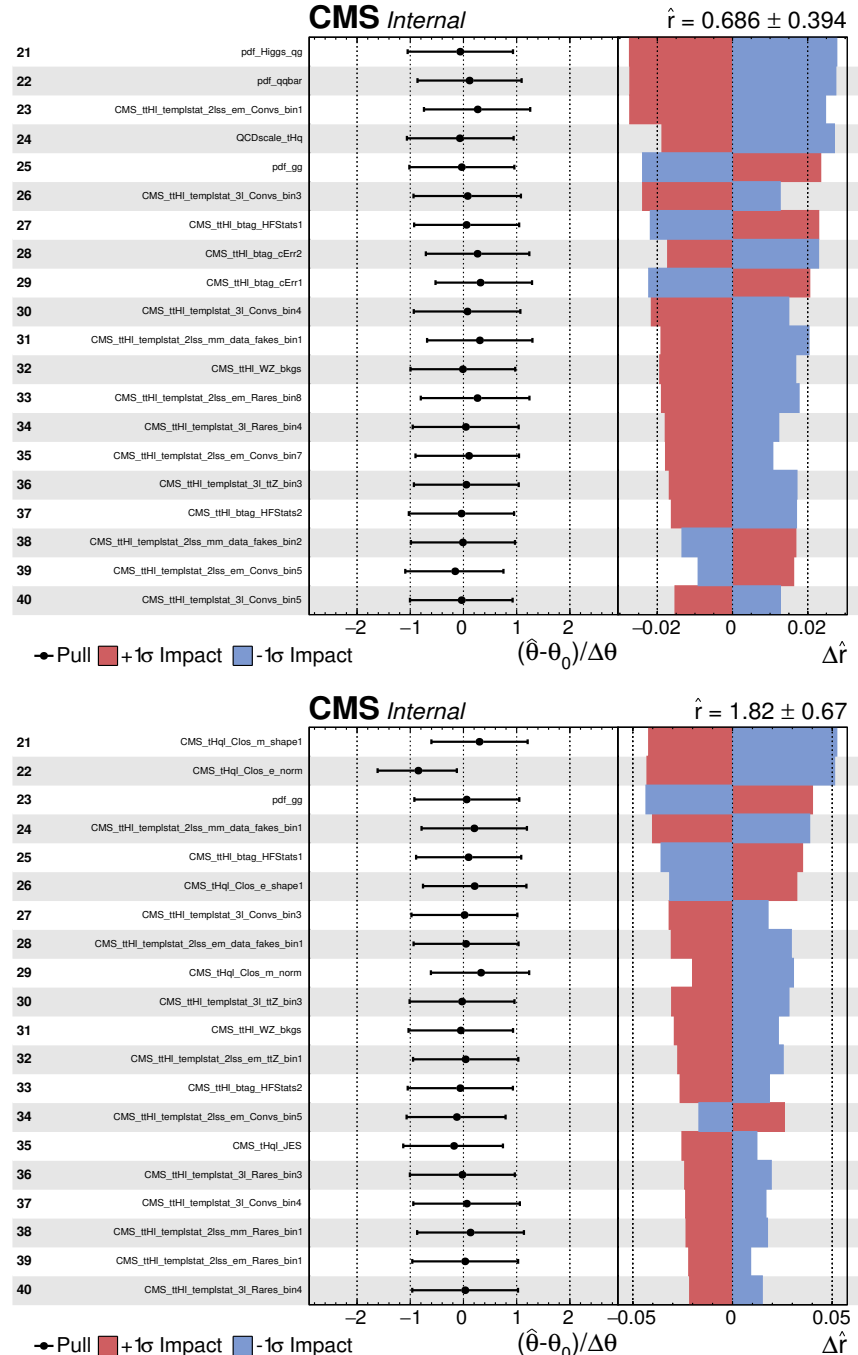


**Figure B.9:** Post-fit pulls and impacts of the next 20 nuisance parameters with largest impacts for the fit on the observed data, for the ITC (top) and SM (bottom) hypotheses. Continuation of pulls and impacts shown in Figure 6.39

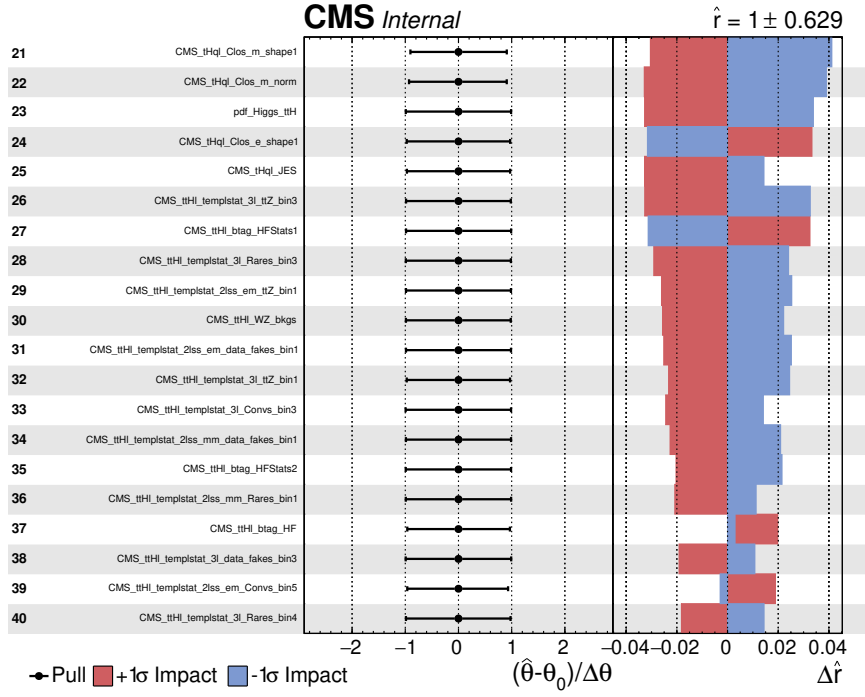


**Figure B.10:** Post-fit pulls and impacts of the next 20 nuisance parameters with largest impacts for a fit to the Asimov dataset with fixed signal strength, for the  $\kappa_t/\kappa_V = -1.0$  hypothesis. Continuation of pulls and impacts shown in Figure B.10

4263

## APPENDIX C

---

4264

### Binning and selection optimization

---

#### 4265 C.1 Binning and selection optimization

4266 The effect of the choice of pre-selection cuts and the number of bins of the 1D his-  
 4267 togram on the cross section limit is evaluated by varying the most important cuts and  
 4268 re-calculating the limit in each case. In this analysis, the optimization was performed  
 4269 in the  $3l$  channel, by evaluating the upper limits on the  $tHq + tHW$  expected signal  
 4270 strength only (without  $t\bar{t}H$  component), always evaluated at  $\kappa_t = -1.0$ ,  $\kappa_V = 1.0$ .

4271 Table C.1 shows several variations explored, compared with a baseline; the baseline  
 4272 is similar to the selection reported in Table 6.6 but only a loose CSV jet and a Z veto  
 4273 of  $\pm 10$  GeV are required.

4274 The optimal limit is found when requiring a slightly tighter selection with respect  
 4275 to the baseline. The optimal selection is reported in Table 6.6.

4276 The signal strength limit also depends on the chosen binning in the 2D plane as  
 4277 the S/B ratio varies across the plane, hence, several sizes and binning combinations  
 4278 were tested in order to improve the limit. Figure C.1 shows some of the binning  
 4279 combinations tested; in the default combination all the bins have the same size, while  
 4280 the best limit was found for a set of 10 bins. The bin borders and the resulting limits  
 4281 are shown in Table C.2.

Selection	Variation	Expected limit
Baseline		< 2.93
Loose CSV tags	$\geq 1 \rightarrow \geq 2$	< 3.81
Medium CSV tags	$\geq 0 \rightarrow \geq 1$	< 2.76
Light forward jet $\eta$	$\geq 0 \rightarrow \geq 1$	< 2.94
Light forward jet $\eta$	$\geq 0 \rightarrow \geq 1.5$	< 3.00
MET > 30 GeV		< 2.91
Z veto ( $ m_{\ell\ell} - m_Z $ )	$> 10\text{GeV} \rightarrow > 15\text{ GeV}$	< 2.79
One medium CSV + 15 GeV Z veto	combined	< 2.62

**Table C.1:** Signal strength limit variation as a function of tighter cuts. The baseline selection corresponds to a looser selection compared to the one reported in Table 6.6 where only a CSV-loose  $b$ -jet is required, and the Z veto is loosened to  $\pm 10$  GeV. The optimal selection determined here corresponds to the baseline plus the two variations in the last row.

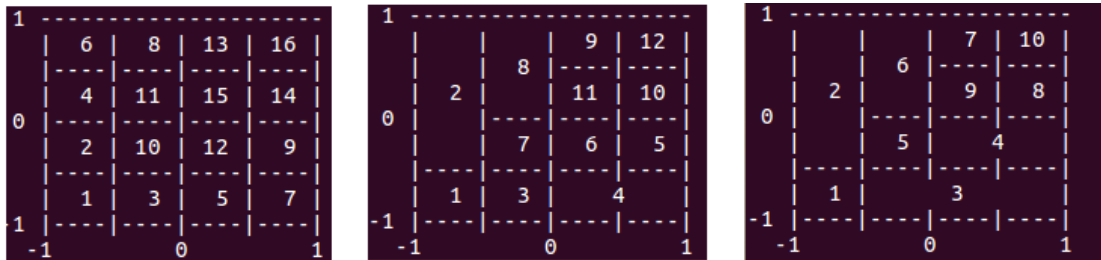


**Figure C.1:** Binning combination scheme.

Number of bins	Bin borders						Expected limit
	$x_1$	$x_2$	$x_3$	$y_1$	$y_2$	$y_3$	
16 (default)	-0.5	0.0	0.5	-0.5	0.0	0.5	< 2.91
16	-0.5	0.3	0.7	-0.5	0.3	0.7	< 2.83
10	-0.5	0.0	0.5	-0.5	0.0	0.5	< 2.93
10	-0.5	0.0	0.7	-0.5	0.0	0.7	< 2.86
10	-0.5	0.0	0.7	-0.5	0.0	0.5	< 2.84
10	-0.5	0.0	0.5	-0.5	0.0	0.7	< 2.87
<b>10</b>	<b>-0.5</b>	<b>0.4</b>	<b>0.7</b>	<b>-0.5</b>	<b>0.4</b>	<b>0.7</b>	<b>&lt; 2.81</b>

**Table C.2:** Limit variation as a function of bin size. The final bin borders used in the  $3l$  channel are indicated in bold.

4282 Combining the optimization of binning and using the tighter pre-selection cuts,  
 4283 the expected limit in the  $3l$  channel alone reaches **r<2.59**.

4284 A similar binning optimization was made for  $2lss$  channel, including other binning  
 4285 combinations. First, the  $3l$  channel binning was used to estimate the expected limit,  
 4286 then, bin borders were varied to obtain the best possible expected limit. The bin  
 4287 borders and the resulting signal strength limits for the same-sign dimuon channel are  
 4288 shown in Table C.3.

Number of bins	Bin borders						Expected limit
	$x_1$	$x_2$	$x_3$	$y_1$	$y_2$	$y_3$	
16	-0.5	0.4	0.7	-0.5	0.4	0.7	< 1.72
12	-0.5	0.4	0.7	-0.5	0.4	0.7	< 1.72
12	-0.3	0.4	0.7	-0.5	0.4	0.7	< 1.71
12	-0.3	0.3	0.7	-0.5	0.4	0.7	< 1.71
12	-0.3	0.3	0.7	-0.4	0.4	0.7	< 1.70
12	-0.3	0.3	0.7	-0.3	0.4	0.7	< 1.70
12	-0.3	0.3	0.7	-0.3	0.2	0.7	< 1.68
12	-0.3	0.3	0.7	-0.3	0.1	0.7	< 1.70
12	-0.3	0.3	0.7	-0.3	0.2	0.6	< 1.70
10	-0.5	0.4	0.7	-0.5	0.4	0.7	< 1.75
<b>10</b>	<b>-0.3</b>	<b>0.3</b>	<b>0.7</b>	<b>-0.3</b>	<b>0.2</b>	<b>0.6</b>	<b>&lt; 1.69</b>

**Table C.3:** Limit variation as a function of bin size in the same-sign dimuon channel. (In bold: the final bin borders used in the  $2lss$  channel.)

4289 The expected limit was found to be **r<1.69** for optimized bin borders in 10 bins  
 4290 and optimized pre-selection cuts.

## 4291 C.2 Other binning strategies

4292 Two additional strategies of clustering regions in the 2D plane of  $BDTG_{tt}$  vs  $BDTG_{t\bar{t}V}$   
 4293 into bins were attempted, following studies done and documented in great detail in  
 4294 Reference [151]. A brief description is provided in the following.

### 4295 Clustering by S/B ratio

4296 In this method, the 2D plane is clustered into a given number of bins corresponding  
 4297 to regions where S/B is within a certain range. The bin borders are determined

such that the number of background events in each bin is approximately equal. The resulting regions for  $2lss$  and  $3l$  events are shown in Figure C.2, while the expected distribution of signal and dominant backgrounds are shown in Figure C.3.

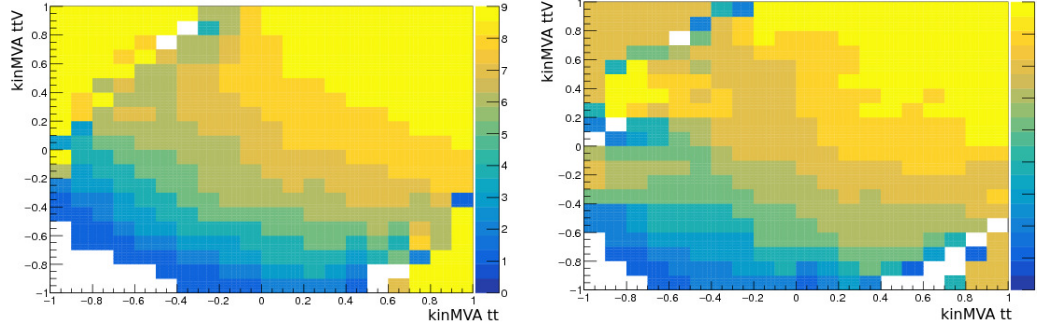


**Figure C.2:** Binning by S/B regions for  $2lss$  (left) and  $3l$  (right).

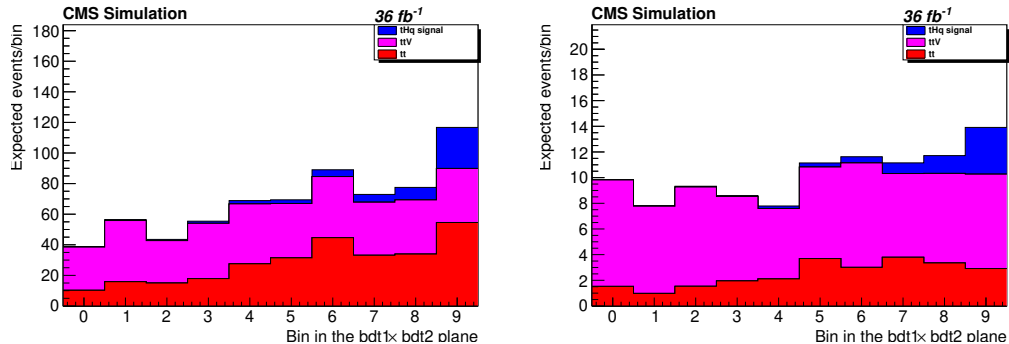


**Figure C.3:** Final bins (corresponding to S/B regions in the 2D plane) for  $2lss$  and  $3l$  (right).

Using this method, the resulting limits (for the  $\kappa_t = -1, \kappa_V = 1$  scenario) are about 20% worse than with the binning in Section ???:  $\mu^\pm\mu^\pm$  changed from 1.82 to 2.15,  $3l$  changed from 1.52 to 1.75.

#### 4304 ***k*-Means geometric clustering**

This method employs a recursive application of the *k*-means algorithm (see Appendix D in Reference [151]) to separate the 2D plane into geometric regions. The resulting clustering (using the  $t\bar{t}H$  multilepton code on  $tHq$  signal and  $t\bar{t}$  and  $t\bar{t}V$  background

4308 events) is shown in Figure C.4. The expected distribution of events for the signal  
 and dominant backgrounds in these bins is shown in Fig. C.5.

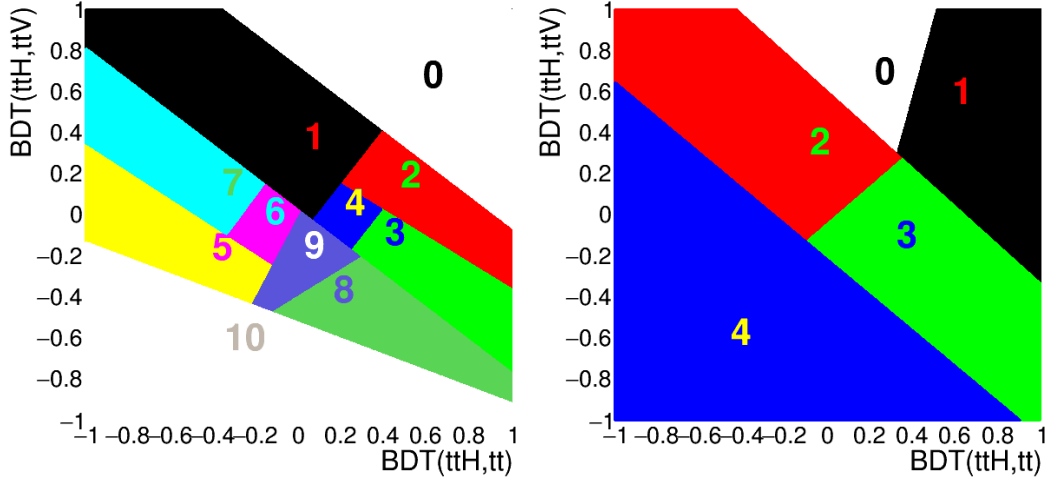


**Figure C.4:** Binning into geometric regions using a  $k$ -means algorithm for  $2lss$  (left) and  $3l$  (right).

4309

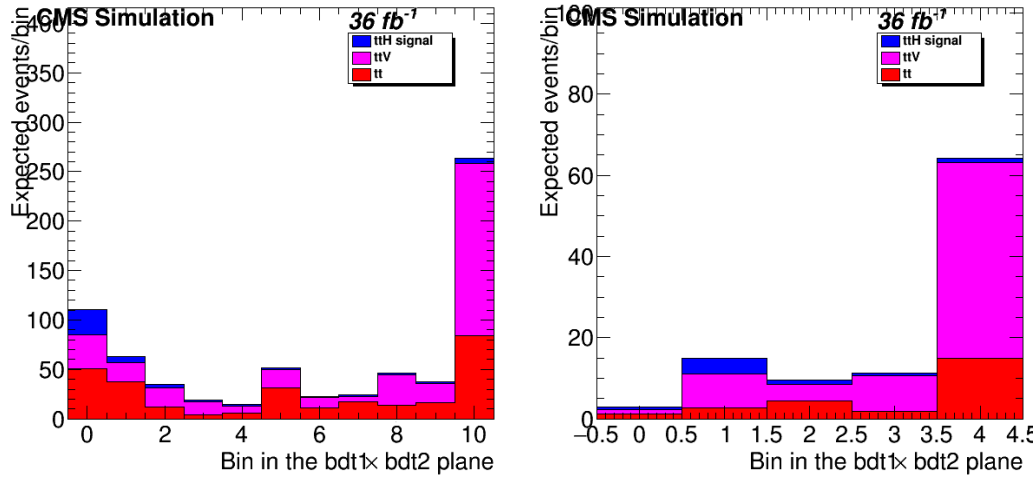


**Figure C.5:** Final bins using a  $k$ -means algorithm for  $2lss$  (left) and  $3l$  (right). Note that the bin numbering here is such that signal-like bins are lower.

4310     Similarly to the S/B ratio binning, the limits using the  $k$ -means clustering are  
 4311 significantly worse than those of the bins described before. In the  $\mu^\pm\mu^\pm$  channel, the  
 4312 limit deteriorates from 1.82 to 2.05, whereas in  $3l$  it changes from 1.58 to 1.78.

4313

## APPENDIX D

4314

### BDTG output variation with $\kappa_V$ and $\kappa_t$

4315 The BDTG classifier output was described in Section in the  $\kappa_t = -1, \kappa_V = 1$  scenario; the  
 4316 change of BDTG classifiers output shape when varying the  $\kappa_V/\kappa_t$  coupling scenario  
 4317 is shown in Figure D.1 in the  $3l$  channel for five different values of  $\kappa_t$ , with  $\kappa_V$  fixed  
 at 1.0.

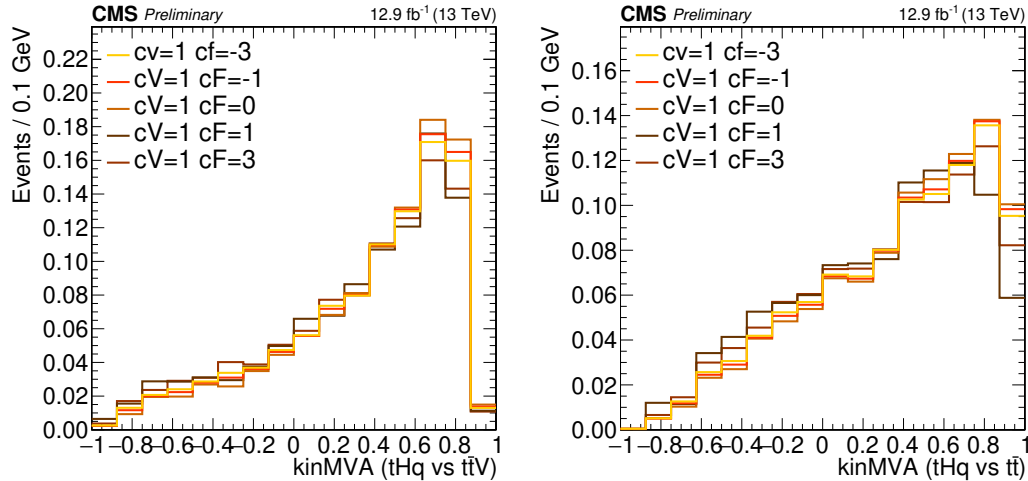


**Figure D.1:** Change of the BDTG classifiers output when varying  $\kappa_t$  coupling ( $\kappa_V$  is fixed at 1.0). Training vs.  $t\bar{t}V$  (right) and vs.  $t\bar{t}$  (left).

4318

4319 Given that the BDT classifier output shape does not change, it is enough to train  
 4320 the BDTG in one of the  $\kappa_t/\kappa_V$  points. It was chosen the SM point.

4321

---

## APPENDIX E

---

4322

### *tHq-tt̄H overlap*

---

4323 This section provides a quick overview of the differences and commonalities in event  
 4324 selections between this analysis and the  $t\bar{t}H$  multilepton search [151]. The object  
 4325 selections of the two analysis are perfectly synchronized due to shared frameworks  
 4326 and samples. The only exception is the usage of forward jets ( $|\eta| > 2.4, p_T > 40$  GeV)  
 4327 in this analysis. Such jets are not considered in the  $t\bar{t}H$  analysis.

4328 Table E.1 gives an overview of the main differences in the event selections. Here,  
 4329  $E_T^{miss}_{LD}$  is defined as  $E_T^{miss} \times 0.00397 + H_T^{miss} \times 0.00265$ . Untagged jets in the  $tHq$   
 4330 analysis are jets that do not pass the CSV loose working point and are either central  
 4331 ( $|\eta| < 2.4, p_T > 25$  GeV) or forward ( $|\eta| < 2.4, p_T > 40$  GeV). All jets in the  $t\bar{t}H$   
 4332 analysis are selected with  $p_T > 25$  GeV. Lepton  $p_T$  cuts and the trigger selections are  
 4333 identical.

Channel	<i>tHq</i>	<i>t̄H</i>
3l	Z veto, 15 GeV $N_{jets}^{b, med.} \geq 1$ $\geq 1$ un-tagged jet	Z veto, 10 GeV $N_{jets}^{b, med.} \geq 1$ OR $N_{jets}^{b, loose} \geq 2$ $E_T^{miss}_{LD} > 0.2$ OR $N_{jets}^{centr.} \geq 4$
2lss	$N_{jets}^{b, med.} \geq 1$ $\geq 1$ un-tagged jet	$N_{jets}^{b, med.} \geq 1$ OR $N_{jets}^{b, loose} \geq 2$ $N_{jets}^{central} \geq 4$

**Table E.1:** Differences in event selection between this analysis and the  $t\bar{t}H$  multilepton analysis.

4334       Table E.2 shows the total event yields in the individual channels, and the yield  
 4335       of shared events between each channel, for the  $tHq$  signal sample, the  $t\bar{t}H$  signal  
 4336       sample, and the data. In the data, for the  $3l$  channel, about 80% of events passing  
 4337       the  $tHq$  selection also pass the  $t\bar{t}H$  selection, constituting about 70% of that channel.  
 4338       In the  $2lss$  channel, about 50% of data events passing the  $tHq$  selection also pass the  
 4339        $t\bar{t}H$  selection, but these events constitute almost 90% of the  $t\bar{t}H$  selection in those  
 4340       channels. Similar overlaps are also seen in the  $tHq$  and  $t\bar{t}H$  signal samples.

4341       There is no migration between different channels and different selections, i.e., no  
 4342       events passing the selection of a given  $tHq$  channel pass the selection of any other  
 4343       channels of  $t\bar{t}H$  and vice versa.

$tHq$ sample	$tHq$	$t\bar{t}H$	Common	(% $tHq$ )	(% $t\bar{t}H$ )
$\mu^\pm\mu^\pm$	7400	2353	2166	29.3	92.1
$e^\pm\mu^\pm$	11158	3600	3321	29.8	92.2
$e^\pm e^\pm$	3550	1106	1025	28.9	92.7
$\ell\ell\ell$	3115	2923	2347	75.3	80.3

$t\bar{t}H$ sample	$tHq$	$t\bar{t}H$	Common	(% $tHq$ )	(% $t\bar{t}H$ )
$\mu^\pm\mu^\pm$	32612	28703	26547	81.4	92.5
$e^\pm\mu^\pm$	48088	42521	39164	81.4	92.1
$e^\pm e^\pm$	15476	12869	11896	76.9	92.4
$\ell\ell\ell$	26627	30598	25288	95.0	82.6

Data	$tHq$	$t\bar{t}H$	Common	(% $tHq$ )	(% $t\bar{t}H$ )
$\mu^\pm\mu^\pm$	280	160	140	50.0	87.5
$e^\pm\mu^\pm$	525	280	242	46.1	86.4
$e^\pm e^\pm$	208	90	79	38.0	87.8
$\ell\ell\ell$	126	154	104	82.5	67.5

**Table E.2:** Individual and shared event yields between this analysis ( $tHq$ ) and  $t\bar{t}H$  multilepton selections.

4344

## APPENDIX *F*

4345

### Forward jet impact plots

4346 The impact of the data/MC disagreement for forward jet  $\eta$  is observed to be reduced  
4347 with higher  $p_T$  cuts. With a cut of 25 GeV in the  $p_T$  of the forward jet, the forward  
4348 jet nuisance have the biggest impact in the fit (it is in the first place in Figure F.1);  
4349 when the  $p_T$  cut is increased to 30 GeV and 40 GeV, there is a reduction in the impact  
4350 of the forward jet  $\eta$  nuisance in the fit as shown in Figures F.2 and F.3.

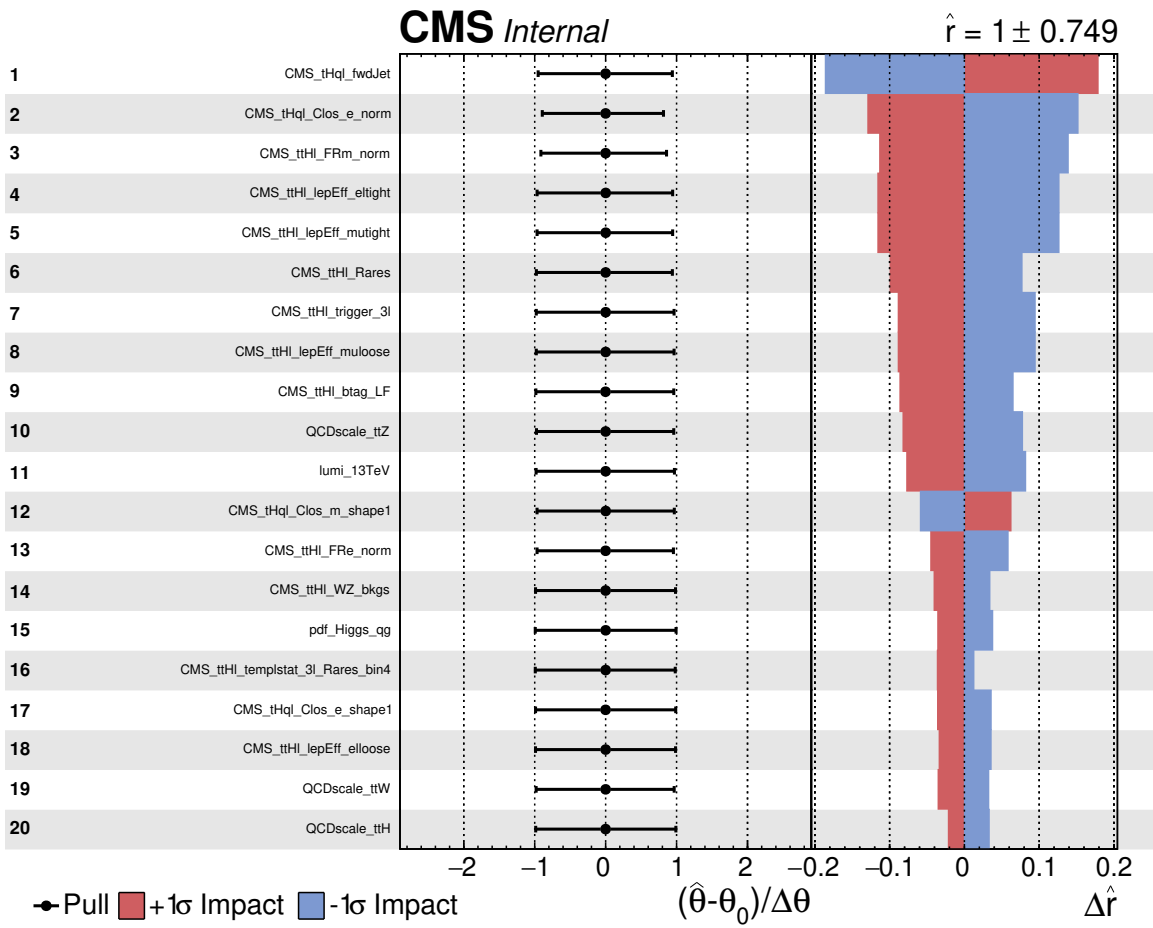


**Figure F.1:** Post-fit pulls and impacts of the 20 nuisance parameters with  $p_T$  cut of 25 GeV for the forward jet.

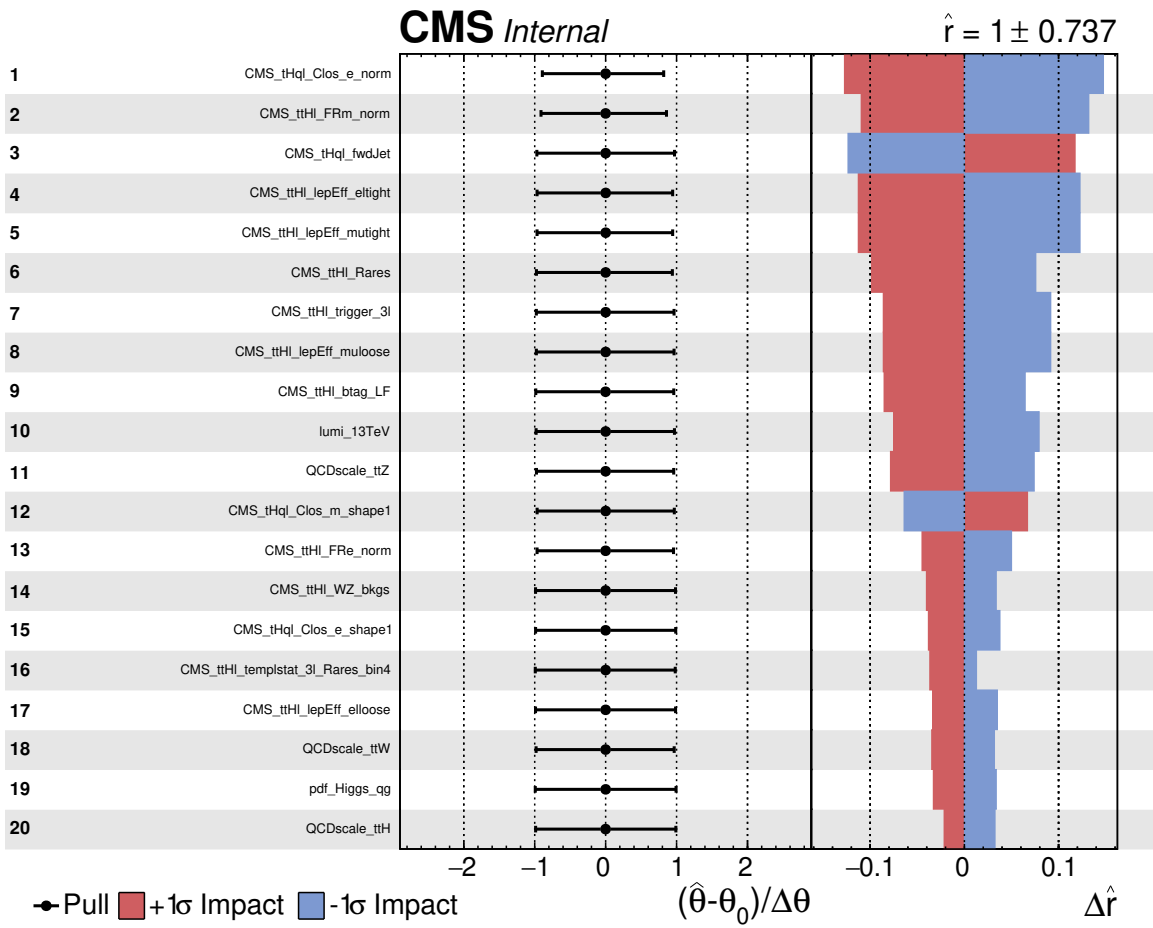


**Figure F.2:** Post-fit pulls and impacts of the 20 nuisance parameters with  $p_T$  cut of 30 GeV for the forward jet.

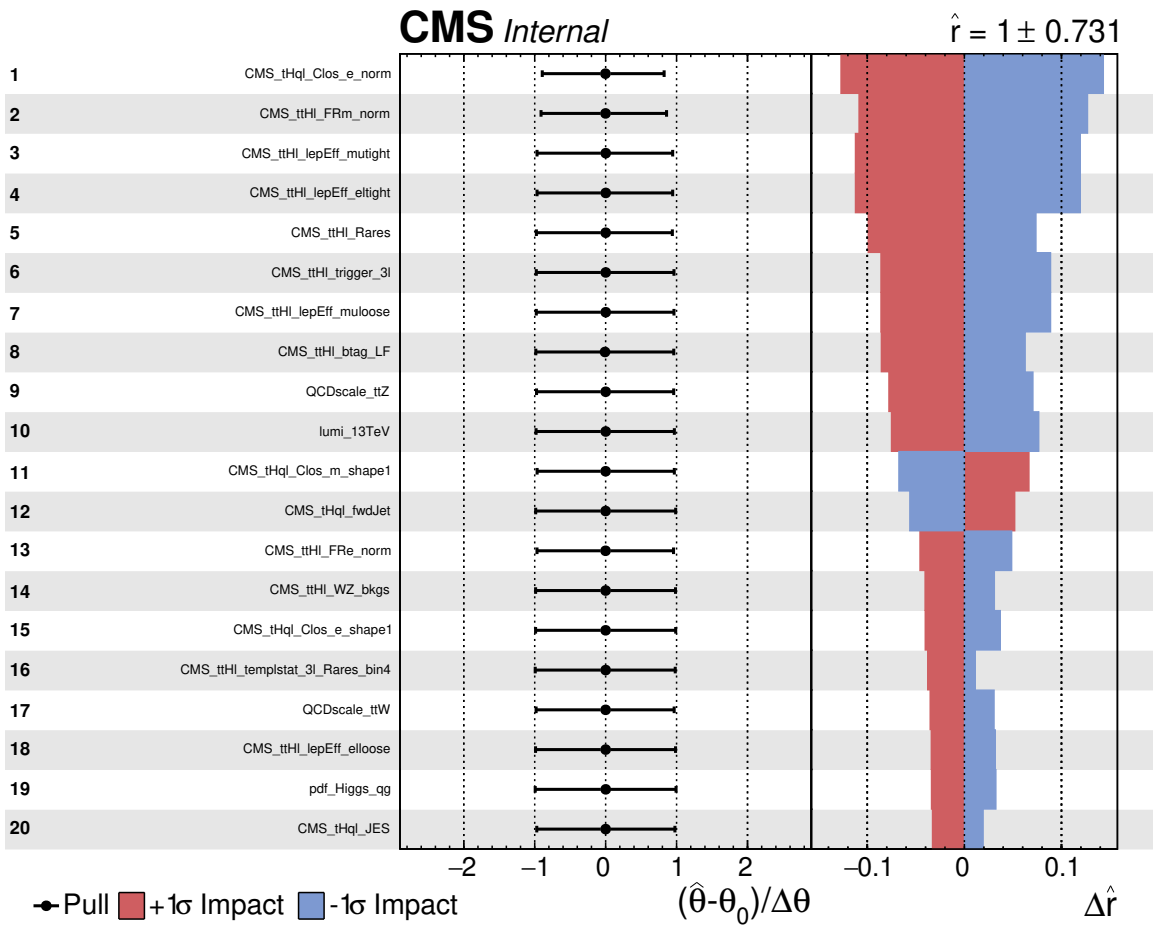


**Figure F.3:** Post-fit pulls and impacts of the 20 nuisance parameters with  $p_T$  cut of 40 GeV for the forward jet.

4351

## APPENDIX *G*

---

4352

### Cross section and branching ratio scalings

---

$\kappa_V$	$\kappa_t$	HWW	HZZ	H $\tau\tau$	H $\mu\mu$	Hbb	Hcc	H $\gamma\gamma$	HZ $\gamma$	Hgg
0.5	-6.0	0.0827	0.0827	11.9098	11.9098	0.3308	0.3308	0.3308	0.3308	0.3308
0.5	-4.0	0.1417	0.1417	9.0699	9.0699	0.5669	0.5669	0.5669	0.5669	0.5669
0.5	-3.0	0.1889	0.1889	6.7999	6.7999	0.7555	0.7555	0.7555	0.7555	0.7555
0.5	-2.5	0.2173	0.2173	5.4325	5.4325	0.8692	0.8692	0.8692	0.8692	0.8692
0.5	-2.0	0.2478	0.2478	3.9647	3.9647	0.9912	0.9912	0.9912	0.9912	0.9912
0.5	-1.5	0.2782	0.2782	2.5034	2.5034	1.1126	1.1126	1.1126	1.1126	1.1126
0.5	-1.333	0.2877	0.2877	2.0448	2.0448	1.1508	1.1508	1.1508	1.1508	1.1508
0.5	-1.25	0.2922	0.2922	1.8264	1.8264	1.1689	1.1689	1.1689	1.1689	1.1689
0.5	-1.0	0.3048	0.3048	1.2194	1.2194	1.2194	1.2194	1.2194	1.2194	1.2194
0.5	-0.833	0.3122	0.3122	0.8665	0.8665	1.2487	1.2487	1.2487	1.2487	1.2487
0.5	-0.75	0.3154	0.3154	0.7097	0.7097	1.2617	1.2617	1.2617	1.2617	1.2617
0.5	-0.667	0.3184	0.3184	0.5666	0.5666	1.2736	1.2736	1.2736	1.2736	1.2736
0.5	-0.5	0.3235	0.3235	0.3235	0.3235	1.2938	1.2938	1.2938	1.2938	1.2938
0.5	-0.333	0.3272	0.3272	0.1451	0.1451	1.3087	1.3087	1.3087	1.3087	1.3087
0.5	-0.25	0.3285	0.3285	0.0821	0.0821	1.3139	1.3139	1.3139	1.3139	1.3139
0.5	-0.167	0.3294	0.3294	0.0367	0.0367	1.3177	1.3177	1.3177	1.3177	1.3177
0.5	0.0	0.3302	0.3302	0.0000	0.0000	1.3207	1.3207	1.3207	1.3207	1.3207
0.5	0.167	0.3294	0.3294	0.0367	0.0367	1.3177	1.3177	1.3177	1.3177	1.3177
0.5	0.25	0.3285	0.3285	0.0821	0.0821	1.3139	1.3139	1.3139	1.3139	1.3139
0.5	0.333	0.3272	0.3272	0.1451	0.1451	1.3087	1.3087	1.3087	1.3087	1.3087
0.5	0.5	0.3235	0.3235	0.3235	0.3235	1.2938	1.2938	1.2938	1.2938	1.2938
0.5	0.667	0.3184	0.3184	0.5666	0.5666	1.2736	1.2736	1.2736	1.2736	1.2736
0.5	0.75	0.3154	0.3154	0.7097	0.7097	1.2617	1.2617	1.2617	1.2617	1.2617
0.5	0.833	0.3122	0.3122	0.8665	0.8665	1.2487	1.2487	1.2487	1.2487	1.2487
0.5	1.0	0.3048	0.3048	1.2194	1.2194	1.2194	1.2194	1.2194	1.2194	1.2194
0.5	1.25	0.2922	0.2922	1.8264	1.8264	1.1689	1.1689	1.1689	1.1689	1.1689
0.5	1.333	0.2877	0.2877	2.0448	2.0448	1.1508	1.1508	1.1508	1.1508	1.1508
0.5	1.5	0.2782	0.2782	2.5034	2.5034	1.1126	1.1126	1.1126	1.1126	1.1126
0.5	2.0	0.2478	0.2478	3.9647	3.9647	0.9912	0.9912	0.9912	0.9912	0.9912
0.5	2.5	0.2173	0.2173	5.4325	5.4325	0.8692	0.8692	0.8692	0.8692	0.8692
0.5	3.0	0.1889	0.1889	6.7999	6.7999	0.7555	0.7555	0.7555	0.7555	0.7555
0.5	4.0	0.1417	0.1417	9.0699	9.0699	0.5669	0.5669	0.5669	0.5669	0.5669
0.5	6.0	0.0827	0.0827	11.9098	11.9098	0.3308	0.3308	0.3308	0.3308	0.3308

**Table G.1:** Scalings of Higgs decay branching ratios vs.  $\kappa_t$  and  $\kappa_V = 0.5$ .

$\kappa_V$	$\kappa_t$	HWW	HZZ	H $\tau\tau$	H $\mu\mu$	Hbb	Hcc	H $\gamma\gamma$	HZ $\gamma$	Hgg
1.0	-6.0	0.3122	0.3122	11.2408	11.2408	0.3122	0.3122	0.3122	0.3122	0.3122
1.0	-4.0	0.5144	0.5144	8.2305	8.2305	0.5144	0.5144	0.5144	0.5144	0.5144
1.0	-3.0	0.6651	0.6651	5.9862	5.9862	0.6651	0.6651	0.6651	0.6651	0.6651
1.0	-2.5	0.7517	0.7517	4.6979	4.6979	0.7517	0.7517	0.7517	0.7517	0.7517
1.0	-2.0	0.8412	0.8412	3.3647	3.3647	0.8412	0.8412	0.8412	0.8412	0.8412
1.0	-1.5	0.9271	0.9271	2.0859	2.0859	0.9271	0.9271	0.9271	0.9271	0.9271
1.0	-1.333	0.9534	0.9534	1.6941	1.6941	0.9534	0.9534	0.9534	0.9534	0.9534
1.0	-1.25	0.9658	0.9658	1.5091	1.5091	0.9658	0.9658	0.9658	0.9658	0.9658
1.0	-1.0	1.0000	1.0000	1.0000	1.0000	1.0000	1.0000	1.0000	1.0000	1.0000
1.0	-0.833	1.0196	1.0196	0.7075	0.7075	1.0196	1.0196	1.0196	1.0196	1.0196
1.0	-0.75	1.0283	1.0283	0.5784	0.5784	1.0283	1.0283	1.0283	1.0283	1.0283
1.0	-0.667	1.0362	1.0362	0.4610	0.4610	1.0362	1.0362	1.0362	1.0362	1.0362
1.0	-0.5	1.0495	1.0495	0.2624	0.2624	1.0495	1.0495	1.0495	1.0495	1.0495
1.0	-0.333	1.0593	1.0593	0.1175	0.1175	1.0593	1.0593	1.0593	1.0593	1.0593
1.0	-0.25	1.0627	1.0627	0.0664	0.0664	1.0627	1.0627	1.0627	1.0627	1.0627
1.0	-0.167	1.0652	1.0652	0.0297	0.0297	1.0652	1.0652	1.0652	1.0652	1.0652
1.0	0.0	1.0672	1.0672	0.0000	0.0000	1.0672	1.0672	1.0672	1.0672	1.0672
1.0	0.167	1.0652	1.0652	0.0297	0.0297	1.0652	1.0652	1.0652	1.0652	1.0652
1.0	0.25	1.0627	1.0627	0.0664	0.0664	1.0627	1.0627	1.0627	1.0627	1.0627
1.0	0.333	1.0593	1.0593	0.1175	0.1175	1.0593	1.0593	1.0593	1.0593	1.0593
1.0	0.5	1.0495	1.0495	0.2624	0.2624	1.0495	1.0495	1.0495	1.0495	1.0495
1.0	0.667	1.0362	1.0362	0.4610	0.4610	1.0362	1.0362	1.0362	1.0362	1.0362
1.0	0.75	1.0283	1.0283	0.5784	0.5784	1.0283	1.0283	1.0283	1.0283	1.0283
1.0	0.833	1.0196	1.0196	0.7075	0.7075	1.0196	1.0196	1.0196	1.0196	1.0196
1.0	1.0	1.0000	1.0000	1.0000	1.0000	1.0000	1.0000	1.0000	1.0000	1.0000
1.0	1.25	0.9658	0.9658	1.5091	1.5091	0.9658	0.9658	0.9658	0.9658	0.9658
1.0	1.333	0.9534	0.9534	1.6941	1.6941	0.9534	0.9534	0.9534	0.9534	0.9534
1.0	1.5	0.9271	0.9271	2.0859	2.0859	0.9271	0.9271	0.9271	0.9271	0.9271
1.0	2.0	0.8412	0.8412	3.3647	3.3647	0.8412	0.8412	0.8412	0.8412	0.8412
1.0	2.5	0.7517	0.7517	4.6979	4.6979	0.7517	0.7517	0.7517	0.7517	0.7517
1.0	3.0	0.6651	0.6651	5.9862	5.9862	0.6651	0.6651	0.6651	0.6651	0.6651
1.0	4.0	0.5144	0.5144	8.2305	8.2305	0.5144	0.5144	0.5144	0.5144	0.5144
1.0	6.0	0.3122	0.3122	11.2408	11.2408	0.3122	0.3122	0.3122	0.3122	0.3122

**Table G.2:** Scalings of Higgs decay branching ratios vs.  $\kappa_t$  and  $\kappa_V = 1.0$ .

$\kappa_V$	$\kappa_t$	HWW	HZZ	H $\tau\tau$	H $\mu\mu$	Hbb	Hcc	H $\gamma\gamma$	HZ $\gamma$	Hgg
1.5	-6.0	0.6424	0.6424	10.2785	10.2785	0.2855	0.2855	0.2855	0.2855	0.2855
1.5	-4.0	1.0028	1.0028	7.1307	7.1307	0.4457	0.4457	0.4457	0.4457	0.4457
1.5	-3.0	1.2477	1.2477	4.9909	4.9909	0.5545	0.5545	0.5545	0.5545	0.5545
1.5	-2.5	1.3802	1.3802	3.8338	3.8338	0.6134	0.6134	0.6134	0.6134	0.6134
1.5	-2.0	1.5115	1.5115	2.6870	2.6870	0.6718	0.6718	0.6718	0.6718	0.6718
1.5	-1.5	1.6322	1.6322	1.6322	1.6322	0.7254	0.7254	0.7254	0.7254	0.7254
1.5	-1.333	1.6682	1.6682	1.3175	1.3175	0.7414	0.7414	0.7414	0.7414	0.7414
1.5	-1.25	1.6851	1.6851	1.1702	1.1702	0.7489	0.7489	0.7489	0.7489	0.7489
1.5	-1.0	1.7310	1.7310	0.7693	0.7693	0.7693	0.7693	0.7693	0.7693	0.7693
1.5	-0.833	1.7570	1.7570	0.5419	0.5419	0.7809	0.7809	0.7809	0.7809	0.7809
1.5	-0.75	1.7684	1.7684	0.4421	0.4421	0.7860	0.7860	0.7860	0.7860	0.7860
1.5	-0.667	1.7788	1.7788	0.3517	0.3517	0.7906	0.7906	0.7906	0.7906	0.7906
1.5	-0.5	1.7962	1.7962	0.1996	0.1996	0.7983	0.7983	0.7983	0.7983	0.7983
1.5	-0.333	1.8089	1.8089	0.0891	0.0891	0.8039	0.8039	0.8039	0.8039	0.8039
1.5	-0.25	1.8133	1.8133	0.0504	0.0504	0.8059	0.8059	0.8059	0.8059	0.8059
1.5	-0.167	1.8165	1.8165	0.0225	0.0225	0.8073	0.8073	0.8073	0.8073	0.8073
1.5	0.0	1.8191	1.8191	0.0000	0.0000	0.8085	0.8085	0.8085	0.8085	0.8085
1.5	0.167	1.8165	1.8165	0.0225	0.0225	0.8073	0.8073	0.8073	0.8073	0.8073
1.5	0.25	1.8133	1.8133	0.0504	0.0504	0.8059	0.8059	0.8059	0.8059	0.8059
1.5	0.333	1.8089	1.8089	0.0891	0.0891	0.8039	0.8039	0.8039	0.8039	0.8039
1.5	0.5	1.7962	1.7962	0.1996	0.1996	0.7983	0.7983	0.7983	0.7983	0.7983
1.5	0.667	1.7788	1.7788	0.3517	0.3517	0.7906	0.7906	0.7906	0.7906	0.7906
1.5	0.75	1.7684	1.7684	0.4421	0.4421	0.7860	0.7860	0.7860	0.7860	0.7860
1.5	0.833	1.7570	1.7570	0.5419	0.5419	0.7809	0.7809	0.7809	0.7809	0.7809
1.5	1.0	1.7310	1.7310	0.7693	0.7693	0.7693	0.7693	0.7693	0.7693	0.7693
1.5	1.25	1.6851	1.6851	1.1702	1.1702	0.7489	0.7489	0.7489	0.7489	0.7489
1.5	1.333	1.6682	1.6682	1.3175	1.3175	0.7414	0.7414	0.7414	0.7414	0.7414
1.5	1.5	1.6322	1.6322	1.6322	1.6322	0.7254	0.7254	0.7254	0.7254	0.7254
1.5	2.0	1.5115	1.5115	2.6870	2.6870	0.6718	0.6718	0.6718	0.6718	0.6718
1.5	2.5	1.3802	1.3802	3.8338	3.8338	0.6134	0.6134	0.6134	0.6134	0.6134
1.5	3.0	1.2477	1.2477	4.9909	4.9909	0.5545	0.5545	0.5545	0.5545	0.5545
1.5	4.0	1.0028	1.0028	7.1307	7.1307	0.4457	0.4457	0.4457	0.4457	0.4457
1.5	6.0	0.6424	0.6424	10.2785	10.2785	0.2855	0.2855	0.2855	0.2855	0.2855

**Table G.3:** Scalings of Higgs decay branching ratios vs.  $\kappa_t$  and  $\kappa_V = 1.5$ .

$\kappa_V$	$\kappa_t$	ttHWW	ttHZZ	ttH $\tau\tau$	tHqWW	tHqZZ	tHq $\tau\tau$	tHWWW	tHWZZ	tHW $\tau\tau$
0.5	-6.0	2.9775	2.9775	428.7530	9.2066	9.2066	1325.7460	9.7660	9.7660	1406.3049
0.5	-4.0	2.2675	2.2675	145.1182	7.5740	7.5740	484.7357	7.8819	7.8819	504.4411
0.5	-3.0	1.7000	1.7000	61.1988	6.1214	6.1214	220.3702	6.2562	6.2562	225.2227
0.5	-2.5	1.3581	1.3581	33.9529	5.1857	5.1857	129.6430	5.2277	5.2277	130.6931
0.5	-2.0	0.9912	0.9912	15.8589	4.1227	4.1227	65.9633	4.0762	4.0762	65.2197
0.5	-1.5	0.6259	0.6259	5.6327	2.9838	2.9838	26.8544	2.8645	2.8645	25.7805
0.5	-1.333	0.5112	0.5112	3.6333	2.6025	2.6025	18.4974	2.4648	2.4648	17.5190
0.5	-1.25	0.4566	0.4566	2.8538	2.4154	2.4154	15.0962	2.2700	2.2700	14.1878
0.5	-1.0	0.3048	0.3048	1.2194	1.8696	1.8696	7.4784	1.7078	1.7078	6.8310
0.5	-0.833	0.2166	0.2166	0.6012	1.5271	1.5271	4.2386	1.3605	1.3605	3.7760
0.5	-0.75	0.1774	0.1774	0.3992	1.3657	1.3657	3.0729	1.1987	1.1987	2.6970
0.5	-0.667	0.1417	0.1417	0.2521	1.2111	1.2111	2.1553	1.0451	1.0451	1.8598
0.5	-0.5	0.0809	0.0809	0.0809	0.9236	0.9236	0.9236	0.7640	0.7640	0.7640
0.5	-0.333	0.0363	0.0363	0.0161	0.6720	0.6720	0.2981	0.5249	0.5249	0.2328
0.5	-0.25	0.0205	0.0205	0.0051	0.5618	0.5618	0.1405	0.4231	0.4231	0.1058
0.5	-0.167	0.0092	0.0092	0.0010	0.4622	0.4622	0.0516	0.3334	0.3334	0.0372
0.5	0.0	0.0000	0.0000	0.0000	0.2953	0.2953	0.0000	0.1909	0.1909	0.0000
0.5	0.167	0.0092	0.0092	0.0010	0.1755	0.1755	0.0196	0.1010	0.1010	0.0113
0.5	0.25	0.0205	0.0205	0.0051	0.1339	0.1339	0.0335	0.0762	0.0762	0.0191
0.5	0.333	0.0363	0.0363	0.0161	0.1043	0.1043	0.0463	0.0647	0.0647	0.0287
0.5	0.5	0.0809	0.0809	0.0809	0.0809	0.0809	0.0809	0.0809	0.0809	0.0809
0.5	0.667	0.1417	0.1417	0.2521	0.1044	0.1044	0.1859	0.1480	0.1480	0.2634
0.5	0.75	0.1774	0.1774	0.3992	0.1329	0.1329	0.2991	0.1993	0.1993	0.4485
0.5	0.833	0.2166	0.2166	0.6012	0.1720	0.1720	0.4775	0.2620	0.2620	0.7272
0.5	1.0	0.3048	0.3048	1.2194	0.2811	0.2811	1.1243	0.4200	0.4200	1.6801
0.5	1.25	0.4566	0.4566	2.8538	0.5119	0.5119	3.1993	0.7270	0.7270	4.5438
0.5	1.333	0.5112	0.5112	3.6333	0.6041	0.6041	4.2939	0.8449	0.8449	6.0051
0.5	1.5	0.6259	0.6259	5.6327	0.8096	0.8096	7.2863	1.1020	1.1020	9.9179
0.5	2.0	0.9912	0.9912	15.8589	1.5402	1.5402	24.6428	1.9827	1.9827	31.7238
0.5	2.5	1.3581	1.3581	33.9529	2.3549	2.3549	58.8716	2.9329	2.9329	73.3233
0.5	3.0	1.7000	1.7000	61.1988	3.1686	3.1686	114.0678	3.8625	3.8625	139.0502
0.5	4.0	2.2675	2.2675	145.1182	4.6200	4.6200	295.6829	5.4873	5.4873	351.1881
0.5	6.0	2.9775	2.9775	428.7530	6.6207	6.6207	953.3740	7.6698	7.6698	1104.4467

**Table G.4:** Scalings of cross section times BR, for the different  $t\bar{t}H$ ,  $tHq$ ,  $tHW$  signal components and  $\kappa_V = 0.5$ .

$\kappa_V$	$\kappa_t$	ttHWW	ttHZZ	ttH $\tau\tau$	tHqWW	tHqZZ	tHq $\tau\tau$	tHWWW	tHWZZ	tHW $\tau\tau$
1.0	-6.0	11.2408	11.2408	404.6686	40.4768	40.4768	1457.1666	41.3681	41.3681	1489.2533
1.0	-4.0	8.2305	8.2305	131.6886	34.2339	34.2339	547.7422	33.8480	33.8480	541.5676
1.0	-3.0	5.9862	5.9862	53.8759	28.5396	28.5396	256.8562	27.3983	27.3983	246.5850
1.0	-2.5	4.6979	4.6979	29.3616	24.8511	24.8511	155.3195	23.3557	23.3557	145.9734
1.0	-2.0	3.3647	3.3647	13.4590	20.6360	20.6360	82.5440	18.8497	18.8497	75.3987
1.0	-1.5	2.0859	2.0859	4.6933	16.0557	16.0557	36.1254	14.0919	14.0919	31.7068
1.0	-1.333	1.6941	1.6941	3.0102	14.4942	14.4942	25.7545	12.5059	12.5059	22.2216
1.0	-1.25	1.5091	1.5091	2.3579	13.7201	13.7201	21.4377	11.7273	11.7273	18.3239
1.0	-1.0	1.0000	1.0000	1.0000	11.4220	11.4220	11.4220	9.4484	9.4484	9.4484
1.0	-0.833	0.7075	0.7075	0.4909	9.9372	9.9372	6.8953	8.0059	8.0059	5.5552
1.0	-0.75	0.5784	0.5784	0.3254	9.2212	9.2212	5.1869	7.3200	7.3200	4.1175
1.0	-0.667	0.4610	0.4610	0.2051	8.5229	8.5229	3.7917	6.6579	6.6579	2.9620
1.0	-0.5	0.2624	0.2624	0.0656	7.1807	7.1807	1.7952	5.4076	5.4076	1.3519
1.0	-0.333	0.1175	0.1175	0.0130	5.9375	5.9375	0.6584	4.2814	4.2814	0.4748
1.0	-0.25	0.0664	0.0664	0.0042	5.3616	5.3616	0.3351	3.7730	3.7730	0.2358
1.0	-0.167	0.0297	0.0297	0.0008	4.8163	4.8163	0.1343	3.3009	3.3009	0.0921
1.0	0.0	0.0000	0.0000	0.0000	3.8183	3.8183	0.0000	2.4676	2.4676	0.0000
1.0	0.167	0.0297	0.0297	0.0008	2.9624	2.9624	0.0826	1.7981	1.7981	0.0501
1.0	0.25	0.0664	0.0664	0.0042	2.5928	2.5928	0.1620	1.5284	1.5284	0.0955
1.0	0.333	0.1175	0.1175	0.0130	2.2612	2.2612	0.2507	1.3014	1.3014	0.1443
1.0	0.5	0.2624	0.2624	0.0656	1.7115	1.7115	0.4279	0.9742	0.9742	0.2435
1.0	0.667	0.4610	0.4610	0.2051	1.3198	1.3198	0.5871	0.8188	0.8188	0.3643
1.0	0.75	0.5784	0.5784	0.3254	1.1834	1.1834	0.6657	0.8042	0.8042	0.4524
1.0	0.833	0.7075	0.7075	0.4909	1.0852	1.0852	0.7530	0.8301	0.8301	0.5760
1.0	1.0	1.0000	1.0000	1.0000	1.0000	1.0000	1.0000	1.0000	1.0000	1.0000
1.0	1.25	1.5091	1.5091	2.3579	1.1380	1.1380	1.7782	1.5278	1.5278	2.3872
1.0	1.333	1.6941	1.6941	3.0102	1.2492	1.2492	2.2197	1.7691	1.7691	3.1434
1.0	1.5	2.0859	2.0859	4.6933	1.5628	1.5628	3.5163	2.3434	2.3434	5.2727
1.0	2.0	3.3647	3.3647	13.4590	3.1023	3.1023	12.4092	4.6362	4.6362	18.5449
1.0	2.5	4.6979	4.6979	29.3616	5.2667	5.2667	32.9167	7.4799	7.4799	46.7493
1.0	3.0	5.9862	5.9862	53.8759	7.7435	7.7435	69.6914	10.5403	10.5403	94.8625
1.0	4.0	8.2305	8.2305	131.6886	12.7892	12.7892	204.6276	16.4642	16.4642	263.4266
1.0	6.0	11.2408	11.2408	404.6686	20.9516	20.9516	754.2573	25.5403	25.5403	919.4497

**Table G.5:** Scalings of cross section times BR, for the different  $t\bar{t}H$ ,  $tHq$ ,  $tHW$  signal components and  $\kappa_V = 1.0$ .

$\kappa_V$	$\kappa_t$	ttHWW	ttHZZ	ttH $\tau\tau$	tHqWW	tHqZZ	tHq $\tau\tau$	tHWWW	tHWZZ	tHW $\tau\tau$
1.5	-6.0	23.1266	23.1266	370.0260	96.1923	96.1923	1539.0768	95.1080	95.1080	1521.7272
1.5	-4.0	16.0441	16.0441	114.0913	81.6690	81.6690	580.7570	77.3512	77.3512	550.0531
1.5	-3.0	11.2295	11.2295	44.9178	68.8703	68.8703	275.4812	62.9086	62.9086	251.6344
1.5	-2.5	8.6261	8.6261	23.9614	60.7939	60.7939	168.8720	54.1622	54.1622	150.4505
1.5	-2.0	6.0458	6.0458	10.7481	51.7152	51.7152	91.9381	44.6227	44.6227	79.3293
1.5	-1.5	3.6725	3.6725	3.6725	41.9469	41.9469	41.9469	34.6991	34.6991	34.6991
1.5	-1.333	2.9643	2.9643	2.3410	38.6171	38.6171	30.4971	31.4016	31.4016	24.7987
1.5	-1.25	2.6330	2.6330	1.8284	36.9629	36.9629	25.6687	29.7807	29.7807	20.6810
1.5	-1.0	1.7310	1.7310	0.7693	32.0233	32.0233	14.2326	25.0144	25.0144	11.1175
1.5	-0.833	1.2192	1.2192	0.3760	28.7953	28.7953	8.8803	21.9653	21.9653	6.7740
1.5	-0.75	0.9948	0.9948	0.2487	27.2234	27.2234	6.8058	20.5014	20.5014	5.1254
1.5	-0.667	0.7914	0.7914	0.1565	25.6778	25.6778	5.0772	19.0767	19.0767	3.7720
1.5	-0.5	0.4491	0.4491	0.0499	22.6628	22.6628	2.5181	16.3435	16.3435	1.8159
1.5	-0.333	0.2006	0.2006	0.0099	19.7986	19.7986	0.9758	13.8117	13.8117	0.6807
1.5	-0.25	0.1133	0.1133	0.0031	18.4397	18.4397	0.5122	12.6364	12.6364	0.3510
1.5	-0.167	0.0507	0.0507	0.0006	17.1281	17.1281	0.2123	11.5203	11.5203	0.1428
1.5	0.0	0.0000	0.0000	0.0000	14.6443	14.6443	0.0000	9.4640	9.4640	0.0000
1.5	0.167	0.0507	0.0507	0.0006	12.3858	12.3858	0.1535	7.6760	7.6760	0.0951
1.5	0.25	0.1133	0.1133	0.0031	11.3529	11.3529	0.3154	6.8916	6.8916	0.1914
1.5	0.333	0.2006	0.2006	0.0099	10.3820	10.3820	0.5117	6.1783	6.1783	0.3045
1.5	0.5	0.4491	0.4491	0.0499	8.6227	8.6227	0.9581	4.9621	4.9621	0.5513
1.5	0.667	0.7914	0.7914	0.1565	7.1299	7.1299	1.4098	4.0411	4.0411	0.7990
1.5	0.75	0.9948	0.9948	0.2487	6.4888	6.4888	1.6222	3.6932	3.6932	0.9233
1.5	0.833	1.2192	1.2192	0.3760	5.9148	5.9148	1.8241	3.4176	3.4176	1.0540
1.5	1.0	1.7310	1.7310	0.7693	4.9627	4.9627	2.2057	3.0782	3.0782	1.3681
1.5	1.25	2.6330	2.6330	1.8284	4.0340	4.0340	2.8014	3.0873	3.0873	2.1440
1.5	1.333	2.9643	2.9643	2.3410	3.8531	3.8531	3.0429	3.2206	3.2206	2.5434
1.5	1.5	3.6725	3.6725	3.6725	3.6725	3.6725	3.6725	3.6725	3.6725	3.6725
1.5	2.0	6.0458	6.0458	10.7481	4.4580	4.4580	7.9254	6.3144	6.3144	11.2255
1.5	2.5	8.6261	8.6261	23.9614	6.8533	6.8533	19.0368	10.4359	10.4359	28.9887
1.5	3.0	11.2295	11.2295	44.9178	10.3536	10.3536	41.4143	15.4728	15.4728	61.8913
1.5	4.0	16.0441	16.0441	114.0913	18.9646	18.9646	134.8595	26.5208	26.5208	188.5926
1.5	6.0	23.1266	23.1266	370.0260	35.9359	35.9359	574.9741	46.2619	46.2619	740.1909

**Table G.6:** Scalings of cross section times BR, for the different  $t\bar{t}H$ ,  $tHq$ ,  $tHW$  signal components and  $\kappa_V = 1.5$ .

$\cos(\alpha_{CP})$	Exp.	SM exp.	Obs.	Best fit $\sigma[pb]$ .	Best fit r
-1.0	0.299 <sup>0.130</sup> <sub>-0.088</sub>	0.396 <sup>0.190</sup> <sub>-0.135</sub>	0.594	0.284 <sup>0.183</sup> <sub>-0.171</sub>	0.650 <sup>0.418</sup> <sub>-0.391</sub>
-0.9	0.297 <sup>0.130</sup> <sub>-0.088</sub>	0.388 <sup>0.184</sup> <sub>-0.132</sub>	0.578	0.268 <sup>0.182</sup> <sub>-0.171</sub>	0.686 <sup>0.466</sup> <sub>-0.438</sub>
-0.8	0.294 <sup>0.129</sup> <sub>-0.088</sub>	0.377 <sup>0.179</sup> <sub>-0.127</sub>	0.562	0.251 <sup>0.181</sup> <sub>-0.171</sub>	0.725 <sup>0.522</sup> <sub>-0.493</sub>
-0.7	0.292 <sup>0.129</sup> <sub>-0.087</sub>	0.377 <sup>0.165</sup> <sub>-0.132</sub>	0.545	0.235 <sup>0.179</sup> <sub>-0.170</sub>	0.768 <sup>0.587</sup> <sub>-0.556</sub>
-0.6	0.288 <sup>0.128</sup> <sub>-0.086</sub>	0.368 <sup>0.155</sup> <sub>-0.128</sub>	0.523	0.215 <sup>0.177</sup> <sub>-0.169</sub>	0.798 <sup>0.658</sup> <sub>-0.627</sub>
-0.5	0.285 <sup>0.127</sup> <sub>-0.086</sub>	0.365 <sup>0.166</sup> <sub>-0.132</sub>	0.500	0.194 <sup>0.176</sup> <sub>-0.167</sub>	0.813 <sup>0.739</sup> <sub>-0.701</sub>
-0.4	0.281 <sup>0.126</sup> <sub>-0.085</sub>	0.357 <sup>0.150</sup> <sub>-0.128</sub>	0.479	0.175 <sup>0.174</sup> <sub>-0.165</sub>	0.840 <sup>0.833</sup> <sub>-0.792</sub>
-0.3	0.279 <sup>0.125</sup> <sub>-0.084</sub>	0.350 <sup>0.150</sup> <sub>-0.125</sub>	0.463	0.162 <sup>0.173</sup> <sub>-0.162</sub>	0.884 <sup>0.943</sup> <sub>-0.884</sub>
-0.2	0.277 <sup>0.124</sup> <sub>-0.084</sub>	0.346 <sup>0.153</sup> <sub>-0.117</sub>	0.453	0.153 <sup>0.172</sup> <sub>-0.153</sub>	0.954 <sup>0.1068</sup> <sub>-0.954</sub>
-0.1	0.277 <sup>0.124</sup> <sub>-0.084</sub>	0.345 <sup>0.155</sup> <sub>-0.123</sub>	0.454	0.154 <sup>0.171</sup> <sub>-0.154</sub>	1.075 <sup>1.197</sup> <sub>-1.075</sub>
0.0	0.279 <sup>0.125</sup> <sub>-0.084</sub>	0.353 <sup>0.161</sup> <sub>-0.130</sub>	0.469	0.167 <sup>0.173</sup> <sub>-0.164</sub>	1.304 <sup>1.356</sup> <sub>-1.282</sub>
0.1	0.285 <sup>0.127</sup> <sub>-0.086</sub>	0.371 <sup>0.160</sup> <sub>-0.137</sub>	0.504	0.197 <sup>0.177</sup> <sub>-0.167</sub>	1.683 <sup>1.508</sup> <sub>-1.427</sub>
0.2	0.293 <sup>0.129</sup> <sub>-0.087</sub>	0.390 <sup>0.159</sup> <sub>-0.143</sub>	0.556	0.246 <sup>0.180</sup> <sub>-0.171</sub>	2.234 <sup>1.639</sup> <sub>-1.552</sub>
0.3	0.300 <sup>0.130</sup> <sub>-0.089</sub>	0.416 <sup>0.178</sup> <sub>-0.152</sub>	0.610	0.303 <sup>0.182</sup> <sub>-0.171</sub>	2.860 <sup>1.723</sup> <sub>-1.612</sub>
0.4	0.302 <sup>0.129</sup> <sub>-0.088</sub>	0.422 <sup>0.193</sup> <sub>-0.143</sub>	0.644	0.349 <sup>0.177</sup> <sub>-0.166</sub>	3.331 <sup>1.693</sup> <sub>-1.587</sub>
0.5	0.296 <sup>0.125</sup> <sub>-0.086</sub>	0.434 <sup>0.157</sup> <sub>-0.145</sub>	0.651	0.374 <sup>0.165</sup> <sub>-0.159</sub>	3.452 <sup>1.527</sup> <sub>-1.467</sub>
0.6	0.284 <sup>0.120</sup> <sub>-0.082</sub>	0.425 <sup>0.136</sup> <sub>-0.141</sub>	0.639	0.377 <sup>0.155</sup> <sub>-0.150</sub>	3.261 <sup>1.339</sup> <sub>-1.298</sub>
0.7	0.270 <sup>0.114</sup> <sub>-0.078</sub>	0.408 <sup>0.118</sup> <sub>-0.133</sub>	0.616	0.366 <sup>0.147</sup> <sub>-0.140</sub>	2.910 <sup>1.167</sup> <sub>-1.111</sub>
0.8	0.258 <sup>0.109</sup> <sub>-0.074</sub>	0.386 <sup>0.120</sup> <sub>-0.120</sub>	0.594	0.354 <sup>0.141</sup> <sub>-0.132</sub>	2.530 <sup>1.006</sup> <sub>-0.945</sub>
0.9	0.246 <sup>0.104</sup> <sub>-0.071</sub>	0.358 <sup>0.128</sup> <sub>-0.105</sub>	0.570	0.341 <sup>0.135</sup> <sub>-0.126</sub>	2.161 <sup>0.857</sup> <sub>-0.798</sub>
1.0	0.238 <sup>0.101</sup> <sub>-0.069</sub>	0.351 <sup>0.125</sup> <sub>-0.101</sub>	0.555	0.331 <sup>0.132</sup> <sub>-0.121</sub>	1.851 <sup>0.736</sup> <sub>-0.679</sub>

**Table G.7:** Expected (for background only, and for a SM-like Higgs signal) and observed 95% C.L. upper limits (in pb), and best fit signal strength  $r$  and corresponding best fit cross section for the combined  $tH + t\bar{H}$  cross section times branching ratio for the combination of all three channels, for different values of  $\cos(\alpha_{CP})$ .

4353

---

## References

---

- 4354 [1] J. Schwinger. "Quantum Electrodynamics. I. A Covariant Formulation". Physical Review. 74 (10): 1439-61, (1948). <https://doi.org/10.1103/PhysRev.74.1439>
- 4355
- 4356
- 4357 [2] R. P. Feynman. "Space-Time Approach to Quantum Electrodynamics". Physical Review. 76 (6): 769-89, (1949). <https://doi.org/10.1103/PhysRev.76.769>
- 4358
- 4359 [3] S. Tomonaga. "On a Relativistically Invariant Formulation of the Quantum Theory of Wave Fields". Progress of Theoretical Physics. 1 (2): 27-42, (1946).
- 4360
- 4361 <https://doi.org/10.1143/PTP.1.27>
- 4362 [4] D.J. Griffiths, "Introduction to electrodynamics". 4th ed. Pearson, (2013).
- 4363 [5] F. Mandl, G. Shaw. "Quantum field theory." Chichester, Wiley (2009).
- 4364 [6] F. Halzen, and A.D. Martin, "Quarks and leptons: An introductory course in modern particle physics". New York: Wiley, (1984) .
- 4365
- 4366 [7] File: Standard\_Model\_of\_Elementary\_Particle\_dark.svg. (2017, June 12) Wikimedia Commons, the free media repository. Retrieved November 27, 2017 from <https://www.collegiate-advanced-electricity.com/single-post/2017/04/10/The-Standard-Model-of-Particle-Physics>.
- 4367
- 4368
- 4369

- 4370 [8] E. Noether, "Invariante Variationsprobleme", Nachrichten von der Gesellschaft  
4371 der Wissenschaften zu Göttingen, mathematisch-physikalische Klasse, vol. 1918,  
4372 pp. 235-257, (1918).
- 4373 [9] C. Patrignani et al. (Particle Data Group), Chin. Phys. C, 40, 100001 (2016)  
4374 and 2017 update.
- 4375 [10] M. Goldhaber, L. Grodzins, A.W. Sunyar "Helicity of Neutrinos", Phys. Rev.  
4376 109, 1015 (1958).
- 4377 [11] Palanque-Delabrouille N et al. "Neutrino masses and cosmology with Lyman-  
4378 alpha forest power spectrum", JCAP 11 011 (2015).
- 4379 [12] M. Gell-Mann. "A Schematic Model of Baryons and Mesons". Physics Letters.  
4380 8 (3): 214-215 (1964).
- 4381 [13] G. Zweig. "An SU(3) Model for Strong Interaction Symmetry and its Breaking"  
4382 (PDF). CERN Report No.8182/TH.401 (1964).
- 4383 [14] G. Zweig. "An SU(3) Model for Strong Interaction Symmetry and its Breaking:  
4384 II" (PDF). CERN Report No.8419/TH.412(1964).
- 4385 [15] M. Gell-Mann. "The Interpretation of the New Particles as Displaced Charged  
4386 Multiplets". Il Nuovo Cimento 4: 848. (1956).
- 4387 [16] T. Nakano, K. Nishijima. "Charge Independence for V-particles". Progress of  
4388 Theoretical Physics 10 (5): 581-582. (1953).
- 4389 [17] N. Cabibbo, "Unitary symmetry and leptonic decays" Physical Review Letters,  
4390 vol. 10, no. 12, p. 531, (1963).

- 4391 [18] M.Kobayashi, T.Maskawa, “CP-violation in the renormalizable theory of weak  
4392 interaction,” Progress of Theoretical Physics, vol. 49, no. 2, pp. 652-657, (1973).
- 4393 [19] File: Weak Decay (flipped).svg. (2017, June 12). Wikimedia Com-  
4394 mons, the free media repository. Retrieved November 27, 2017  
4395 from [https://commons.wikimedia.org/w/index.php?title=File:  
4396 Weak\\_Decay\\_\(flipped\)\.svg&oldid=247498592](https://commons.wikimedia.org/w/index.php?title=File:Weak_Decay_(flipped)\.svg&oldid=247498592).
- 4397 [20] Georgia Tech University. Coupling Constants for the Fundamental Forces(2005).  
4398 Retrieved January 10, 2018, from [http://hyperphysics.phy-astr.gsu.edu/  
4399 hbase/Forces/couple.html#c2](http://hyperphysics.phy-astr.gsu.edu/hbase/Forces/couple.html#c2)
- 4400 [21] M. Strassler. (May 31, 2013).The Strengths of the Known Forces. Retrieved Jan-  
4401 uary 10, 2018, from [https://profmattstrassler.com/articles-and-posts/  
4402 particle-physics-basics/the-known-forces-of-nature/  
4403 the-strength-of-the-known-forces/](https://profmattstrassler.com/articles-and-posts/particle-physics-basics/the-known-forces-of-nature/the-strength-of-the-known-forces/)
- 4404 [22] S.L. Glashow. “Partial symmetries of weak interactions”, Nucl. Phys. 22 579-  
4405 588, (1961).
- 4406 [23] A. Salam, J.C. Ward. “Electromagnetic and weak interactions”, Physics Letters  
4407 13 168-171, (1964).
- 4408 [24] S. Weinberg, “A model of leptons”, Physical Review Letters, vol. 19, no. 21, p.  
4409 1264, (1967).
- 4410 [25] M. Peskin, D. Schroeder, “An introduction to quantum field theory”. Perseus  
4411 Books Publishing L.L.C., (1995).
- 4412 [26] A. Pich. “The Standard Model of Electroweak Interactions” <https://arxiv.org/abs/1201.0537>
- 4413

- 4414 [27] G. Arnison et al. (UA1 Collaboration), Phys. Lett. B 122, 103 (1983).
- 4415 [28] M. Banner et al. (UA2 Collaboration), Phys. Lett. B 122, 476 (1983).
- 4416 [29] G. Arnison et al. (UA1 Collaboration), Phys. Lett. B 126, 398 (1983).
- 4417 [30] P. Bagnaia et al. (UA2 Collaboration), Phys. Lett. B 129, 130 (1983).
- 4418 [31] F.Bellaiche. (2012, 2 September). “What’s this Higgs boson anyway?”. Retrieved  
4419 from: <https://www.quantum-bits.org/?p=233>
- 4420 [32] M. Endres et al. Nature 487, 454-458 (2012) doi:10.1038/nature11255
- 4421 [33] F. Englert, R. Brout. “Broken Symmetry and the Mass of Gauge  
4422 Vector Mesons”. Physical Review Letters. 13 (9): 321-23.(1964)  
4423 doi:10.1103/PhysRevLett.13.321
- 4424 [34] P.Higgs. “Broken Symmetries and the Masses of Gauge Bosons”. Physical Re-  
4425 view Letters. 13 (16): 508-509,(1964). doi:10.1103/PhysRevLett.13.508.
- 4426 [35] G.Guralnik, C.R. Hagen and T.W.B. Kibble. “Global Conservation Laws  
4427 and Massless Particles”. Physical Review Letters. 13 (20): 585-587, (1964).  
4428 doi:10.1103/PhysRevLett.13.585.
- 4429 [36] CMS collaboration. “Observation of a new boson at a mass of 125 GeV with  
4430 the CMS experiment at the LHC”. Physics Letters B. 716 (1): 30-61 (2012).  
4431 arXiv:1207.7235. doi:10.1016/j.physletb.2012.08.021
- 4432 [37] ATLAS collaboration. “Observation of a New Particle in the Search for the Stan-  
4433 dard Model Higgs Boson with the ATLAS Detector at the LHC”. Physics Letters  
4434 B. 716 (1): 1-29 (2012). arXiv:1207.7214. doi:10.1016/j.physletb.2012.08.020.

- 4435 [38] ATLAS collaboration; CMS collaboration (26 March 2015). “Combined Mea-  
 4436 surement of the Higgs Boson Mass in pp Collisions at  $\sqrt{s} = 7$  and 8 TeV with  
 4437 the ATLAS and CMS Experiments”. Physical Review Letters. 114 (19): 191803.  
 4438 arXiv:1503.07589. doi:10.1103/PhysRevLett.114.191803.
- 4439 [39] LHC InternationalMasterclasses“When protons collide”. Retrieved from [http://atlas.physicsmasterclasses.org/en/zpath\\_protoncollisions.htm](http://atlas.physicsmasterclasses.org/en/zpath_protoncollisions.htm)
- 4441 [40] CMS Collaboration, “SM Higgs Branching Ratios and Total Decay Widths (up-  
 4442 date in CERN Report4 2016)”. <https://twiki.cern.ch/twiki/bin/view/LHCPhysics/CERNYellowReportPageBR> , last accessed on 17.12.2017.
- 4444 [41] R.Grant V. “Determination of Higgs branching ratios in  $H \rightarrow W^+W^- \rightarrow l\nu jj$   
 4445 and  $H \rightarrow ZZ \rightarrow l^+l^-jj$  channels”. Physics Department, University of Ten-  
 4446 nessee (Dated: October 31, 2012). Retrieved from <http://aesop.phys.utk.edu/ph611/2012/projects/Riley.pdf>
- 4448 [42] LHC Higgs Cross Section Working Group, Denner, A., Heinemeyer, S. et al.  
 4449 “Standard model Higgs-boson branching ratios with uncertainties”. Eur. Phys.  
 4450 J. C (2011) 71: 1753. <https://doi.org/10.1140/epjc/s10052-011-1753-8>
- 4451 [43] D. de Florian et al., LHC Higgs Cross Section Working Group, CERN-2017-  
 4452 002-M, arXiv:1610.07922[hep-ph] (2016).
- 4453 [44] ATLAS and CMS Collaborations, “Measurements of the Higgs boson produc-  
 4454 tion and decay rates and constraints on its couplings from a combined ATLAS  
 4455 and CMS analysis of the LHC pp collision data at  $\sqrt{s} = 7$  and 8 TeV,” (2016).  
 4456 CERN-EP-2016-100, ATLAS-HIGG-2015-07, CMS-HIG-15-002.

- 4457 [45] J. A. Aguilar-Saavedra, R. Benbrik, S. Heinemeyer, and M. Perez-Victoria,  
 4458 “Handbook of vector-like quarks: Mixing and single production”, Phys. Rev. D  
 4459 88 (2013) 094010, doi:10.1103/PhysRevD.88.094010, arXiv:1306.0572.
- 4460 [46] A. Greljo, J. F. Kamenik, and J. Kopp, “Disentangling flavor vio-  
 4461 lation in the top-Higgs sector at the LHC”, JHEP 07 (2014) 046,  
 4462 doi:10.1007/JHEP07(2014)046, arXiv:1404.1278.
- 4463 [47] F. Demartin, F. Maltoni, K. Mawatari, and M. Zaro, “Higgs production in  
 4464 association with a single top quark at the LHC,” European Physical Journal C,  
 4465 vol. 75, p. 267, (2015). doi:10.1140/epjc/s10052-015-3475-9, arXiv:1504.00611.
- 4466 [48] F. Demartin, B. Maier, F. Maltoni, K. Mawatari, and M. Zaro, “tWH associated  
 4467 production at the LHC”, European Physical Journal C, vol. 77, p. 34, (2017).  
 4468 arXiv:1607.05862
- 4469 [49] F. Maltoni, K. Paul, T. Stelzer, and S. Willenbrock, “Associated production  
 4470 of Higgs and single top at hadron colliders”, Phys.Rev. D64 (2001) 094023,  
 4471 [hep-ph/0106293].
- 4472 [50] S. Biswas, E. Gabrielli, F. Margaroli, and B. Mele, “Direct constraints on the  
 4473 top-Higgs coupling from the 8 TeV LHC data,” Journal of High Energy Physics,  
 4474 vol. 07, p. 073, (2013).
- 4475 [51] M. Farina, C. Grojean, F. Maltoni, E. Salvioni, and A. Thamm, “Lifting de-  
 4476 generacies in Higgs couplings using single top production in association with a  
 4477 Higgs boson,” Journal of High Energy Physics, vol. 05, p. 022, (2013).
- 4478 [52] T.M. Tait and C.-P. Yuan, “Single top quark production as a window to physics  
 4479 beyond the standard model”, Phys. Rev. D 63 (2000) 014018 [hep-ph/0007298].

- 4480 [53] CMS Collaboration, “Modelling of the single top-quark production in associa-  
 4481 tion with the Higgs boson at 13 TeV.” <https://twiki.cern.ch/twiki/bin/viewauth/CMS/SingleTopHiggsGeneration13TeV>, last accessed on 16.01.2018.
- 4483 [54] CMS Collaboration, “SM Higgs production cross sections at  $\sqrt{s} =$   
 4484 13 TeV.” <https://twiki.cern.ch/twiki/bin/view/LHCPhysics/CERNYellowReportPageAt13TeV>, last accessed on 16.01.2018.
- 4486 [55] S. Dawson, The effective W approximation, Nucl. Phys. B 249 (1985) 42.
- 4487 [56] S. Biswas, E. Gabrielli and B. Mele, JHEP 1301 (2013) 088 [arXiv:1211.0499  
 4488 [hep-ph]].
- 4489 [57] LHC Higgs Cross Section Working Group, “Handbook of LHC Higgs Cross  
 4490 Sections: 4.Deciphering the Nature of the Higgs Sector”, arXiv:1610.07922.
- 4491 [58] J. Ellis, D. S. Hwang, K. Sakurai, and M. Takeuchi.“Disentangling Higgs-Top  
 4492 Couplings in Associated Production”, JHEP 1404 (2014) 004, [arXiv:1312.5736].
- 4493 [59] CMS Collaboration, V. Khachatryan et al., “Precise determination of the mass  
 4494 of the Higgs boson and tests of compatibility of its couplings with the standard  
 4495 model predictions using proton collisions at 7 and 8 TeV,” arXiv:1412.8662.
- 4496 [60] ATLAS Collaboration, G. Aad et al., “Updated coupling measurements of the  
 4497 Higgs boson with the ATLAS detector using up to  $25 \text{ fb}^{-1}$  of proton-proton  
 4498 collision data”, ATLAS-CONF-2014-009.
- 4499 [61] File:Cern-accelerator-complex.svg. Wikimedia Commons, the free media repos-  
 4500 itory. Retrieved January, 2018 from <https://commons.wikimedia.org/wiki/File:Cern-accelerator-complex.svg>

- 4502 [62] J.L. Caron , “Layout of the LEP tunnel including future LHC infrastructures.”,  
4503 (Nov, 1993). A C Collection. Legacy of AC. Pictures from 1992 to 2002. Re-  
4504 trieved from <https://cds.cern.ch/record/841542>
- 4505 [63] M. Vretenar, “The radio-frequency quadrupole”. CERN Yellow Report CERN-  
4506 2013-001, pp.207-223 DOI:10.5170/CERN-2013-001.207. arXiv:1303.6762
- 4507 [64] L.Evans. P. Bryant (editors). “LHC Machine”. JINST 3 S08001 (2008).
- 4508 [65] CERN Photographic Service.“Radio-frequency quadrupole, RFQ-1”, March  
4509 1983, CERN-AC-8303511. Retrieved from <https://cds.cern.ch/record/615852>.
- 4511 [66] CERN Photographic Service “Animation of CERN’s accelerator network”, 14  
4512 October 2013. DOI: 10.17181/cds.1610170 Retrieved from <https://videos.cern.ch/record/1610170>
- 4514 [67] C.Sutton. “Particle accelerator”.Encyclopedia Britannica. July 17,  
4515 2013. Retrieved from <https://www.britannica.com/technology/particle-accelerator>.
- 4517 [68] L.Guiraud. “Installation of LHC cavity in vacuum tank.”. July 27 2000. CERN-  
4518 AC-0007016. Retrieved from <https://cds.cern.ch/record/41567>.
- 4519 [69] J.L. Caron, “Magnetic field induced by the LHC dipole’s superconducting coils”.  
4520 March 1998. AC Collection. Legacy of AC. Pictures from 1992 to 2002. LHC-  
4521 PHO-1998-325. Retrieved from <https://cds.cern.ch/record/841511>.
- 4522 [70] AC Team. “Diagram of an LHC dipole magnet”. June 1999. CERN-DI-9906025  
4523 retrieved from <https://cds.cern.ch/record/40524>.

- 4524 [71] CMS Collaboration “Public CMS Luminosity Information”. [https://twiki.cern.ch/twiki/bin/view/CMSPublic/LumiPublicResults#2016\\\_\\\_proton\\_proton\\_13\\_TeV\\_collis](https://twiki.cern.ch/twiki/bin/view/CMSPublic/LumiPublicResults#2016\_\_proton_proton_13_TeV_collis), last accessed 24.01.2018
- 4525
- 4526
- 4527 [72] J.L Caron. “LHC Layout” AC Collection. Legacy of AC. Pictures from 1992  
4528 to 2002. September 1997, LHC-PHO-1997-060. Retrieved from <https://cds.cern.ch/record/841573>.
- 4529
- 4530 [73] J.A. Coarasa. “The CMS Online Cluster:Setup, Operation and Maintenance  
4531 of an Evolving Cluster”. ISGC 2012, 26 February - 2 March 2012, Academia  
4532 Sinica, Taipei, Taiwan.
- 4533 [74] CMS Collaboration. “The CMS experiment at the CERN LHC” JINST 3 S08004  
4534 (2008).
- 4535 [75] CMS Collaboration. “CMS detector drawings 2012” CMS-PHO-GEN-2012-002.  
4536 Retrieved from <http://cds.cern.ch/record/1433717>.
- 4537 [76] Davis, Siona Ruth. “Interactive Slice of the CMS detector”, Aug. 2016,  
4538 CMS-OUTREACH-2016-027, retrieved from <https://cds.cern.ch/record/2205172>
- 4539
- 4540 [77] R. Breedon. “View through the CMS detector during the cooldown of the  
4541 solenoid on February 2006. CMS Collection”, February 2006, CMS-PHO-  
4542 OREACH-2005-004, Retrieved from <https://cds.cern.ch/record/930094>.
- 4543 [78] Halyo, V. and LeGresley, P. and Lujan, P. “Massively Parallel Computing and  
4544 the Search for Jets and Black Holes at the LHC”, Nucl.Instrum.Meth. A744  
4545 (2014) 54-60, DOI: 10.1016/j.nima.2014.01.038”

- 4546 [79] A. Dominguez et. al. “CMS Technical Design Report for the Pixel Detector  
4547 Upgrade”, CERN-LHCC-2012-016. CMS-TDR-11.
- 4548 [80] CMS Collaboration. “Description and performance of track and primary-vertex  
4549 reconstruction with the CMS tracker,” Journal of Instrumentation, vol. 9, no.  
4550 10, p. P10009,(2014).
- 4551 [81] CMS Collaboration and M. Brice. “Images of the CMS Tracker Inner Bar-  
4552 rel”, November 2008, CMS-PHO-TRACKER-2008-002. Retrieved from <https://cds.cern.ch/record/1431467>.
- 4554 [82] M. Weber. “The CMS tracker”. 6th international conference on hyperons, charm  
4555 and beauty hadrons Chicago, June 28-July 3 2004.
- 4556 [83] CMS Collaboration. “Projected Performance of an Upgraded CMS Detector at  
4557 the LHC and HL-LHC: Contribution to the Snowmass Process”. Jul 26, 2013.  
4558 arXiv:1307.7135
- 4559 [84] L. Veillet. “End assembly of HB with EB rails and rotation inside SX ”,Jan-  
4560 uary 2002. CMS-PHO-HCAL-2002-002. Retrieved from <https://cds.cern.ch/record/42594>.
- 4562 [85] J. Puerta-Pelayo.“First DT+RPC chambers installation round in the UX5 cav-  
4563 ern.”. January 2007, CMS-PHO-OREACH-2007-001. Retrieved from <https://cds.cern.ch/record/1019185>
- 4565 [86] X. Cid Vidal and R. Cid Manzano. “CMS Global Muon Trigger” web site:  
4566 Taking a closer look at LHC. Retrieved from [https://www.lhc-closer.es/taking\\_a\\_closer\\_look\\_at\\_lhc/0.lhc\\_trigger](https://www.lhc-closer.es/taking_a_closer_look_at_lhc/0.lhc_trigger)

- 4568 [87] WLCG Project Office, “Documents & Reference - Tiers - Structure,”  
 4569 (2014). <http://wlcg.web.cern.ch/documents-reference> , last accessed on  
 4570 30.01.2018.
- 4571 [88] CMS Collaboration. “CMSSW Application Framework”, <https://twiki.cern.ch/twiki/bin/view/CMSPublic/WorkBookCMSSWFramework>,  
 4572 last accesses 06.02.2018
- 4574 [89] A. Buckleya, J. Butterworthb, S. Giesekec, et. al. “General-purpose event gen-  
 4575 erators for LHC physics”. arXiv:1101.2599v1 [hep-ph] 13 Jan 2011
- 4576 [90] A. Quadt. “Top Quark Physics at Hadron Colliders”. Advances in the Physics  
 4577 of Particles and Nuclei. Springer-Verlag Berlin Heidelberg. DOI: 10.1007/978-  
 4578 3-540-71060-8 (2007)
- 4579 [91] DurhamHep Data Project, “The Durham HepData Project - PDF Plotter.”  
 4580 <http://hepdata.cedar.ac.uk/pdf/pdf3.html> , last accessed on 02.02.2018.
- 4581 [92] G. Altarelli and G. Parisi. “ASYMPTOTIC FREEDOM IN PARTON LAN-  
 4582 GUAGE”, Nucl.Phys. B126:298 (1977).
- 4583 [93] Yu.L. Dokshitzer. Sov.Phys. JETP 46:641 (1977)
- 4584 [94] V.N. Gribov, L.N. Lipatov. “Deep inelastic e p scattering in perturbation the-  
 4585 ory”, Sov.J.Nucl.Phys. 15:438 (1972)
- 4586 [95] F. Maltoni, G. Ridolfi, and M. Ubiali, “b-initiated processes at the LHC: a  
 4587 reappraisal,” Journal of High Energy Physics, vol. 07, p. 022, (2012).
- 4588 [96] B. Andersson, G. Gustafson, G.Ingelman and T. Sjostrand, “Parton fragmen-  
 4589 tation and string dynamics”, Physics Reports, Vol. 97, No. 2-3, pp. 31-145,  
 4590 1983.

- 4591 [97] CMS Collaboration, “Event generator tunes obtained from underlying event  
4592 and multiparton scattering measurements;” European Physical Journal C, vol.  
4593 76, no. 3, p. 155, (2016).
- 4594 [98] J. Alwall et. al., “The automated computation of tree-level and next-to-leading  
4595 order differential cross sections, and their matching to parton shower simula-  
4596 tions,” Journal of High Energy Physics, vol. 07, p. 079, (2014).
- 4597 [99] T. Sjöstrand and P. Z. Skands, “Transverse-momentum-ordered showers and  
4598 interleaved multiple interactions,” European Physical Journal C, vol. 39, pp.  
4599 129–154, (2005).
- 4600 [100] S. Frixione, P. Nason, and C. Oleari, “Matching NLO QCD computations with  
4601 Parton Shower simulations: the POWHEG method,” Journal of High Energy  
4602 Physics, vol. 11, p. 070, (2007).
- 4603 [101] S. Agostinelli et al., “GEANT4: A Simulation toolkit,” Nuclear Instruments  
4604 and Methods in Physics, vol. A506, pp. 250–303, (2003).
- 4605 [102] J.Allison et.al.,“Recent developments in Geant4”, Nuclear Instruments and  
4606 Methods in Physics Research A 835 (2016) 186-225.
- 4607 [103] CMS Collaboration “Full Simulation Offline Guide”, <https://twiki.cern.ch/twiki/bin/view/CMSPublic/SWGuideSimulation>, last accessed 04.02.2018
- 4609 [104] A. Giammanco. “The Fast Simulation of the CMS Experiment” J. Phys.: Conf.  
4610 Ser. 513 022012 (2014)
- 4611 [105] A.M. Sirunyan et. al. “Particle-flow reconstruction and global event description  
4612 with the CMS detector”, JINST 12 P10003 (2017) <https://doi.org/10.1088/1748-0221/12/10/P10003>.

- 4614 [106] The CMS Collaboration. “ Description and performance of track and pri-  
 4615       mary vertex reconstruction with the CMS tracker”. JINST 9 P10009 (2014).  
 4616       doi:10.1088/1748-0221/9/10/P10009
- 4617 [107] J. Incandela. “Status of the CMS SM Higgs Search” July 4, 2012. Pdf slides.  
 4618       Retrieved from [https://indico.cern.ch/event/197461/contributions/1478917/attachments/290954/406673/CMS\\_4July2012\\_Final.pdf](https://indico.cern.ch/event/197461/contributions/1478917/attachments/290954/406673/CMS_4July2012_Final.pdf)
- 4620 [108] P. Billoir and S. Qian, “Simultaneous pattern recognition and track fitting by  
 4621       the Kalman filtering method”, Nucl. Instrum. Meth. A 294 219. (1990).
- 4622 [109] W. Adam, R. Fruhwirth, A. Strandlie and T. Todorov, “Reconstruction of  
 4623       electrons with the Gaussian sum filter in the CMS tracker at LHC”, eConf  
 4624       C 0303241 (2003) TULT009 [physics/0306087].
- 4625 [110] K. Rose, “Deterministic Annealing for Clustering, Compression, Classification,  
 4626       Regression and related Optimisation Problems”, Proc. IEEE 86 (1998) 2210.
- 4627 [111] R. Fruhwirth, W. Waltenberger and P. Vanlaer, “ Adaptive Vertex Fitting”,  
 4628       CMS Note 2007-008 (2007).
- 4629 [112] CMS collaboration, “Performance of CMS muon reconstruction in pp collision  
 4630       events at  $\sqrt{s} = 7 \text{ TeV}$  ”, JINST 7 P10002 2012, [arXiv:1206.4071].
- 4631 [113] Coco, Victor and Delsart, Pierre-Antoine and Rojo-Chacon, Juan and Soyez,  
 4632       Gregory and Sander, Christian, “Jets and jet algorithms”, Proceedings,  
 4633       HERA and the LHC Workshop Series on the implications of HERA for LHC  
 4634       physics: 2006-2008, pag. 182-204. <http://inspirehep.net/record/866539/files/access.pdf>, (2009), doi:10.3204/DESY-PROC-2009-02/54

- 4636 [114] M. Cacciari, G. P. Salam, and G. Soyez, “The anti- $k_t$  jet clustering algorithm,”  
4637 Journal of High Energy Physics, vol. 04, p. 063, (2008).
- 4638 [115] S. Catani, Y. L. Dokshitzer, M. H. Seymour, and B. R. Webber, “Longitudi-  
4639 nally invariant  $K_t$  clustering algorithms for hadron hadron collisions”, Nuclear  
4640 Physics B, vol. 406, pp. 187–224, (1993).
- 4641 [116] Y.L. Dokshitzer, G.D. Leder, S.Moretti, and B.R. Webber, “Better jet clustering  
4642 algorithms,” Journal of High Energy Physics, vol. 08, p. 001, (1997).
- 4643 [117] B. Dorney. “Anatomy of a Jet in CMS”. Quantum Diaries. June  
4644 1st, 2011. Retrieved from [https://www.quantumdiaries.org/2011/06/01/  
4645 anatomy-of-a-jet-in-cms/](https://www.quantumdiaries.org/2011/06/01/anatomy-of-a-jet-in-cms/)
- 4646 [118] The CMS Collaboration.“Event Displays from the high-energy collisions at 7  
4647 TeV”, May 2010, CMS-PHO-EVENTS-2010-007, Retrieved from [https://cds.  
4648 cern.ch/record/1429614](https://cds.cern.ch/record/1429614).
- 4649 [119] The CMS collaboration. “Determination of jet energy calibration and transverse  
4650 momentum resolution in CMS”. JINST 6 P11002 (2011). [http://dx.doi.org/  
4651 10.1088/1748-0221/6/11/P11002](http://dx.doi.org/10.1088/1748-0221/6/11/P11002)
- 4652 [120] The CMS Collaboration, “Introduction to Jet Energy Corrections at  
4653 CMS.”. <https://twiki.cern.ch/twiki/bin/view/CMS/IntroToJEC>, last ac-  
4654 cessed 10.02.2018.
- 4655 [121] CMS Collaboration Collaboration. “Identification of b quark jets at the CMS  
4656 Experiment in the LHC Run 2”. Tech. rep. CMS-PAS-BTV-15-001. Geneva:  
4657 CERN, (2016). <https://cds.cern.ch/record/2138504>.

- 4658 [122] CMS Collaboration Collaboration. “Performance of missing energy reconstruction  
4659 in 13 TeV pp collision data using the CMS detector”. Tech. rep. CMS-PAS-  
4660 JME16-004. Geneva: CERN, 2016. <https://cds.cern.ch/record/2205284>.
- 4661 [123] CMS Collaboration, “New CMS results at Moriond (Electroweak) 2013”,  
4662 Retrieved from [http://cms.web.cern.ch/sites/cms.web.cern.ch/files/styles/large/public/field/image/HIG13004\\_Event01\\_0.png?itok=LAWZzPHR](http://cms.web.cern.ch/sites/cms.web.cern.ch/files/styles/large/public/field/image/HIG13004_Event01_0.png?itok=LAWZzPHR)
- 4665 [124] CMS Collaboration, “New CMS results at Moriond (Electroweak) 2013”,  
4666 Retrieved from [http://cms.web.cern.ch/sites/cms.web.cern.ch/files/styles/large/public/field/image/TOP12035\\_Event01.png?itok=uMdnSqzC](http://cms.web.cern.ch/sites/cms.web.cern.ch/files/styles/large/public/field/image/TOP12035_Event01.png?itok=uMdnSqzC)
- 4669 [125] K. Skovpen. “Event displays highlighting the main properties of heavy flavour  
4670 jets in the CMS Experiment”, Aug 2017, CMS-PHO-EVENTS-2017-006. Re-  
4671 trieval from <https://cds.cern.ch/record/2280025>.
- 4672 [126] G. Cowan. “Topics in statistical data analysis for high-energy physics”.  
4673 arXiv:1012.3589v1
- 4674 [127] A. Hoecker et al., “TMVA-Toolkit for multivariate data analysis”  
4675 arXiv:physics/0703039v5 (2009)
- 4676 [128] L. Lista. “Statistical Methods for Data Analysis in Particle Physics”, 2nd  
4677 ed. Springer International Publishing. (2017) <https://dx.doi.org/10.1007/978-3-319-62840-0>

- 4679 [129] I. Antcheva et al., “ROOT-A C++ framework for petabyte data storage, sta-  
 4680       tistical analysis and visualization ,” Computer Physics Communications, vol.  
 4681       182, no. 6, pp. 1384â€¢1385, (2011).
- 4682 [130] Y. Coadou. “Boosted decision trees”, ESIPAP, Archamps, 9 Febru-  
 4683       ary 2016. Lecture. Retrieved from [https://indico.cern.ch/event/472305/contributions/1982360/attachments/1224979/1792797/ESIPAP\\_MVA160208-BDT.pdf](https://indico.cern.ch/event/472305/contributions/1982360/attachments/1224979/1792797/ESIPAP_MVA160208-BDT.pdf)
- 4686 [131] J.H. Friedman. “Greedy function approximation: A gradient boosting ma-  
 4687       chine”. Ann. Statist. Volume 29, Number 5 (2001), 1189-1232. [https://projecteuclid.org/download/pdf\\_1/euclid-aos/1013203451](https://projecteuclid.org/download/pdf_1/euclid-aos/1013203451).
- 4689 [132] W. Verkerke and D. Kirkby, “The RooFit toolkit for data modeling,” arXiv  
 4690       preprint physics, (2003).
- 4691 [133] CMS Collaboration, “Documentation of the RooStats-based statistics  
 4692       tools for Higgs PAG”. <https://twiki.cern.ch/twiki/bin/view/CMS/SWGuideHiggsAnalysisCombinedLimit>, last accessed on 08.04.2018.
- 4694 [134] F. James, M. Roos, “MINUIT: Function minimization and error analysis”. Cern  
 4695       Computer Centre Program Library, Geneve Long Write-up No. D506, 1989
- 4696 [135] J. Neyman and E. S. Pearson, “On the problem of the most efficient tests of  
 4697       statistical hypotheses”. Springer-Verlag, (1992).
- 4698 [136] A.L. Read. “Modified frequentist analysis of search results (the  $CL_s$  method),”  
 4699       (2000). CERN-OPEN-2000-205.
- 4700 [137] C. Palmer. “Searches for a Light Higgs with CMS”, CMS-CR-2012-215. <https://cds.cern.ch/record/1560435>.

- 4702 [138] A. Wald, “Tests of statistical hypotheses concerning several parameters when  
 4703 the number of observations is large”, Transactions of the American Mathematical  
 4704 society, vol. 54, no. 3, pp. 426–482, (1943).
- 4705 [139] G. Cowan, K. Cranmer, E. Gross, and O. Vitells, “Asymptotic formulae for  
 4706 likelihood-based tests of new physics”, European Physical Journal C, vol. 71,  
 4707 p. 1554, (2011).
- 4708 [140] S. S. Wilks, “The Large-Sample Distribution of the Likelihood Ratio for Testing  
 4709 Composite Hypotheses”, Annals of Mathematical Statistics, vol. 9, pp. 60–62,  
 4710 (03, 1938).
- 4711 [141] G. Aad et al. (ATLAS Collaboration, CMS Collaboration). “Combined Mea-  
 4712 surement of the Higgs Boson Mass in pp Collisions at  $\sqrt{s} = 7$  and 8 TeV  
 4713 with the ATLAS and CMS Experiments”. Phys. Rev. Lett. 114, 191803.  
 4714 <https://arxiv.org/pdf/1503.07589.pdf>.
- 4715 [142] B. Hespel, F. Maltoni, and E. Vryonidou, “Higgs and Z boson associated pro-  
 4716 duction via gluon fusion in the SM and the 2HDM”, JHEP 06 (2015) 065,  
 4717 [https://dx.doi.org/10.1007/JHEP06\(2015\)065](https://dx.doi.org/10.1007/JHEP06(2015)065), arXiv:1503.01656.
- 4718 [143] ATLAS Collaboration, “Measurements of Higgs boson pro-  
 4719 duction and couplings in diboson final states with the AT-  
 4720 LAS detector at the LHC”, Phys. Lett. B726 (2013) 88–119,  
 4721 doi:10.1016/j.physletb.2014.05.011, 10.1016/j.physletb.2013.08.010,  
 4722 arXiv:1307.1427. [Erratum: Phys. Lett.B734,406(2014)].
- 4723 [144] CMS Collaboration, “Search for the associated production of a Higgs boson  
 4724 with a single top quark in proton-proton collisions at  $\sqrt{s} = 8$  TeV”, JHEP 06  
 4725 (2016) 177, doi:10.1007/JHEP06(2016)177, arXiv:1509.08159.

- 4726 [145] B. Stieger, C. Jorda Lope et al., “Search for Associated Production of a Single  
 4727 Top Quark and a Higgs Boson in Leptonic Channels”, CMS Analysis Note CMS  
 4728 AN-14-140, 2014.
- 4729 [146] M. Peruzzi, C. Mueller, B. Stieger et al., “Search for ttH in multilepton final  
 4730 states at  $\sqrt{s} = 13$  TeV”, CMS Analysis Note CMS AN-16-211, 2016.
- 4731 [147] CMS Collaboration, “Search for H to bbar in association with a single top quark  
 4732 as a test of Higgs boson couplings at  $\sqrt{s} = 13$  TeV”, CMS Physics Analysis  
 4733 Summary CMS-PAS-HIG-16-019, 2016.
- 4734 [148] CMS Collaboration, “Search for production of a Higgs boson and a single top  
 4735 quark in multilepton final states in proton collisions at  $\sqrt{s} = 13$  TeV”, CMS  
 4736 Physics Analysis Summary CMS-PAS-HIG-17-005, 2016.
- 4737 [149] CMS Collaboration. “The CMS data quality monitoring software: experience  
 4738 and future prospects”, J. Phys.: Conf. Ser. 513 (2014) 032024
- 4739 [150] CMS Collaboration, “PdmV2016Analysis,” (2016). <https://twiki.cern.ch/twiki/bin/viewauth/CMS/PdmV2016Analysis#DATA>, last accessed 11.04.2016.
- 4741 [151] M. Peruzzi, F. Romeo, B. Stieger et al., “Search for ttH in multilepton final  
 4742 states at  $\sqrt{s} = 13$  TeV”, CMS Analysis Note CMS AN-17-029, 2017.
- 4743 [152] B. Maier, “SingleTopHiggProduction13TeV”, February, 2016. <https://twiki.cern.ch/twiki/bin/viewauth/CMS/SingleTopHiggsGeneration13TeV>.
- 4745 [153] B. WG, “BtagRecommendation80XReReco”, February, 2017. <https://twiki.cern.ch/twiki/bin/view/CMS/BtagRecommendation80XReReco>.

- 4747 [154] CMS Collaboration, “Identification of b quark jets at the CMS Experiment  
 4748 in the LHC Run 2”, CMS Physics Analysis Summary CMS-PAS-BTV-15-001,  
 4749 2016.
- 4750 [155] CMS Collaboration, “Baseline muon selections for Run-II.” <https://twiki.cern.ch/twiki/bin/viewauth/CMS/SWGuideMuonIdRun2>, last accessed on  
 4751 24.02.2018.
- 4753 [156] G. Petrucciani and C. Botta, “Two step prompt muon identification”, January,  
 4754 2015. <https://indico.cern.ch/event/368007/contribution/2/material/slides/0.pdf>.
- 4756 [157] CMS Collaboration, “Performance of electron reconstruction and selection with  
 4757 the CMS detector in proton-proton collisions at  $\sqrt{s} = 8$  TeV”. JINST 10 P06005,  
 4758 2015. <https://doi.org/10.1088/1748-0221/10/06/P06005>
- 4759 [158] H. Brun and C. Ochando, “Updated Results on MVA eID with 13 TeV samples”,  
 4760 October, 2014. <https://indico.cern.ch/event/298249/contribution/3/material/slides/0.pdf>.
- 4762 [159] K. Rehermann and B. Tweedie, “Efficient Identification of Boosted Semileptonic  
 4763 Top Quarks at the LHC”, JHEP 03 (2011) 059, [https://dx.doi.org/10.1007/JHEP03\(2011\)059](https://dx.doi.org/10.1007/JHEP03(2011)059), arXiv:1007.2221.
- 4765 [160] CMS Collaboration. “Tag and Probe”, <https://twiki.cern.ch/twiki/bin/view/CMSPublic/TagAndProbe>, last accessed on 02.03.2018.
- 4767 [161] CMS Collaboration. “ $\kappa$  coupling modifiers”, [https://twiki.cern.ch/twiki/bin/view/LHCPhysics/LHCHXSWG2KAPPA#t\\_ch\\_qbtHq](https://twiki.cern.ch/twiki/bin/view/LHCPhysics/LHCHXSWG2KAPPA#t_ch_qbtHq), last accessed on  
 4768 27.04.2018.

- 4770 [162] CMS Collaboration, “CMS Luminosity Measurement for the 2016 Data Taking  
4771 Period,” (2017). CMS-PAS-LUM-17-001.
- 4772 [163] J. Monroy, P.Das, B. Stieger et al., “Search for tHq in multilepton final states  
4773 at  $\sqrt{s} = 13$  TeV”, CMS Analysis Note CMS AN-16-378, 2016.
- 4774 [164] T. Chwalek 1 , N. Faltermann 1 , S. Fink 1 , et. al., “Investigating the top-  
4775 Yukawa coupling with the production of a Higgs boson in association with a  
4776 single top quark in the  $H \rightarrow b\bar{b}$  decay channel. CMS Analysis Note CMS AN-  
4777 16-065, Version 4, 2017.
- 4778 [165] CMS Tracker Group. “The Performance plots for Phase 1 Pixel De-  
4779 tector 2017” [https://twiki.cern.ch/twiki/bin/view/CMSPublic/  
4780 PixelOfflinePlotsAugust2017#Alignment\\_of\\_the\\_forward\\_pixels](https://twiki.cern.ch/twiki/bin/view/CMSPublic/PixelOfflinePlotsAugust2017#Alignment_of_the_forward_pixels), last  
4781 accessed on 01.05.2018
- 4782 [166] UNL Silicon pixel group “Pixel Phase-I activities at University of  
4783 Nebraska-Lincoln (UNL)”[https://twiki.cern.ch/twiki/bin/view/CMS/  
4784 UNLPixelPhaseI](https://twiki.cern.ch/twiki/bin/view/CMS/UNLPixelPhaseI), last accessed on 01.05.2018.
- 4785 [167] Aerotech (n.d.). “AGS15000 Series”, retrieved from [https://www.  
4786 aerotech.com/product-catalog/gantry-system/ags15000.aspx?p=%2fproduct-catalog%2fgantry-system.aspx%3f](https://www.aerotech.com/product-catalog/gantry-system/ags15000.aspx?p=%2fproduct-catalog%2fgantry-system.aspx%3f)
- 4788 [168] C. Fangmeier. “Fiducial recognition”, 2016. Github repository,[https://github.com/cfangmeier/Small/blob/master/JupyterNotebooks/  
4789 Fiducial\\_Recognition.ipynb](https://github.com/cfangmeier/Small/blob/master/JupyterNotebooks/Fiducial_Recognition.ipynb)  
4790

- 4791 [169] F. Meier and J. Monroy “ SOP 103 - Module assembly: Gluing of  
4792 HDI to BBM”, retrieved from <https://twiki.cern.ch/twiki/pub/CMS/>  
4793 UNLPixelPhaseI/UNL-PxPhI-SOP-103-v0.pdf, last accessed on 05.30.2018.
- 4794 [170] F. Meier “ Forward Pixel Module Glueing at UNL” YouTube, Sep. 15, 2014,  
4795 retrieved from <https://www.youtube.com/watch?v=ofdntTIwKY4>.
- 4796 [171] J. Monroy (n.d). Home [YouTube Channel]. Retrieved from <https://www.youtube.com/channel/UCi7S7vhYpieL0y2KJ0SS0eg>.
- 4798 [172] F. Meier and J. Monroy “ SOP 105 - Module assembly: Encapsula-  
4799 tion of wirebonds”, retrieved from <https://twiki.cern.ch/twiki/pub/CMS/>  
4800 UNLPixelPhaseI/UNL-PxPhI-SOP-103-v0.pdf, last accessed on 05.30.2018.
- 4801 [173] J. Antonelli. “FPix Module Testing Reference Guide”, Sep. 2015, retrieved  
4802 from <https://cms-docdb.cern.ch/cgi-bin/DocDB/RetrieveFile?docid=12690&filename=fpix-module-testing-reference-guide.pdf&version=5>